Journal of Experimental and Theoretical Physics, Vol. 90, No. 2, 2000, pp. 227–239.
Translated from Zhurnal Éksperimental'noĭ i Teoreticheskoĭ Fiziki, Vol. 117, No. 2, 2000, pp. 261–274.

GRAVITATION, ASTROPHYSICS

Characteristic Features of Microlensing by Noncompact Objects of Dark Matter

V. A. Sirota*

Lebedev Institute of Physics, Russian Academy of Sciences, Leninskiĭ pr. 53, Moscow, 117924 Russia
**e-mail: singlim@td.lpi.ru*

Received September 10, 1999

Abstract—A theory of microlensing by nonbaryonic bodies is developed. The characteristic features of lensing by noncompact transparent objects with a singular density distribution are investigated. The conditions under which additional peaks appear in the brilliance curve and the characteristics of these peaks are determined. The effect of a compact baryonic nucleus on the brilliance curve is studied. © *2000 MAIK "Nauka/Interperiodica".*

1. INTRODUCTION

Gravitational lensing, i.e., the deflection of light rays by a massive body, was first observed during a solar eclipse in 1919 when the sun occulted the stars. Gravitational lensing was subsequently observed during observations of quasars. In this case the lensing objects were galaxies. For microlensing, i.e., when the gravitational lens is an object with stellar mass, individual images cannot be resolved. However, the focusing action of the lens appreciably and even substantially increases the point brilliance of the light source. If the relative velocities of the lensing object and the source are sufficiently high, for example, if they are located in the halo of our galaxy, then the temporal variation of point brilliance can be seen in the observations.

Observations of gravitational microlensing of stars in the Large and Small Magellanic Clouds by objects located in the galactic halo were proposed by Paczynski in 1986 [1]. Such observations have been conducted since 1993 [2–6]. They have become a new step in the study of dark matter. These observations revealed in the halo of our galaxy the existence of a substantial number of invisible objects with masses $(0.05–1)M_\odot$. According to the observational statistics, they comprise a substantial fraction (possibly greater than 50%) of the total mass of the halo.

Since the probability of lensing of a given star at a given moment in time is very small ($\sim 10^{-7}$), a large number of stars must be followed simultaneously for a long time in order to perform observations. The candidates in a microlensing event are extracted from the data by a variety of criteria, including achromaticity and absence of recurrence.

Aside from observations of the Magellanic Clouds, observations of microlensing in the direction of the galactic center are also being conducted [7–9]. The probability of microlensing is an order of magnitude higher in this region, and more than 300 events have already been discovered. Aside from investigations of the galactic center, this direction is used to test new technology and methods, including for studying "exotic" cases of microlensing in which the observed brilliance curve is strongly different from the "standard" curve corresponding to a point lens and source. Such deviations arise (see the detailed description in [10, 11]), for example, for a binary lens [12, 13], a binary source, or a source whose angular size is comparable to the characteristic microlensing parameter [14].

Initially it was assumed [1, 4] that objects which are seen during observations of microlensing in the halo are brown, red, and white dwarfs, neutron stars, or Jupiter-type planets, consisting of ordinary baryonic matter. However, a large number of observed objects could lead in this case to a contradiction with the hypothesis of the nonbaryonic nature of dark matter, which, in turn, raises substantial difficulties from the standpoint of cosmological theories. It is unclear how to explain the origin of these stars or planets on the basis of the theory of evolution of galaxies. The theory of nucleosynthesis must explain a very high initial fraction of metal nuclei. In addition, these observations [15, 16] attest that the masses of most lensing objects are quite large $(0.5–1)M_\odot$, and the hypotheses of "Jupiters" and brown dwarfs become unsatisfactory. In this case, microlenses must be dim stars, and such an interpretation makes it difficult to match the microlensing data with the direct optical observations using the Hubble telescope [17].

In this connection, it has been hypothesized [18] that for microlensing in the halo it is not Jupiter-type and cold stars that are observed, but rather objects of a small-scale hierarchical structure of dark matter which consist of nonbaryonic matter. The question of the masses, sizes, structure, and lifetimes of such objects and their distribution in the galactic halo is examined in detail in [19]. It is shown that under certain conditions on the spectrum of the initial fluctuations their masses lie in the range

$$M_x \sim (0.01–1)M_\odot \quad (1)$$

1063-7761/00/9002-0227$20.00

corresponding to the objects observed in microlensing. However, the sizes of these objects with the masses (1) are found to be of the order of

$$R_x \sim (10^{13}–10^{15})\ \text{cm}. \quad (2)$$

This is several orders of magnitude larger than the sizes of baryonic bodies of the same mass (though, on the other hand, it is much smaller than the sizes of cold gas clouds). For this reason, such nonbaryonic objects are also said to be noncompact [19, 20].

This fact is important, specifically, because the quantity (2) is of the same order of magnitude as the Einstein radius, which is a characteristic parameter of microlensing. For this reason, noncompact objects cannot be treated as point microlenses. The finiteness of their size and density distribution must be taken into account. The metric of a gravitational lens is, in this case, different from the Schwarzschild metric. A theory of gravitational microlensing by noncompact objects has been constructed in [19, 20]. Comparing this theory with the observational results [19, 21, 22] shows that noncompact objects which are candidates for microlenses are, at least in some lenses, preferable to compact objects. However, it is impossible to draw an unequivocal conclusion on the basis of the observational data discussed. Thus, the question of the baryonic or nonbaryonic nature of the objects observed during microlensing is closely related with the question of whether microlenses are compact or noncompact objects and requires further investigation. It is also of great interest to develop a theory for determining new possibilities for manifestations of noncompact objects.

Specifically, in [23] it is indicated that so-called three-ray microlensing is possible when the lensing object is transparent. The caustic surfaces arising in this case lead to the appearance of additional peaks in the brilliance curve. This raises the following questions: Can these data be used to reveal noncompact objects? Can the presence or absence of peaks be interpreted as indicating a nonbaryonic nature of a lensing body? To answer these questions it is necessary to analyze the conditions under which additional peaks appear, and in so doing the properties of nonbaryonic objects must be taken into account realistically. Such an analysis is the subject of the present paper.

The form of the brilliance curve, like the position of the caustic surfaces, depends on the mass distribution in the gravitational lens. In [23], an object with constant density is studied. This is impossible for a body of nonbaryonic dark matter bound by gravitational forces. Indeed, as shown in [19, 24, 25], the density distribution possesses a singularity at the center and follows the scaling law

$$\rho(r) \propto r^{-\alpha}, \quad \alpha \approx 1.8. \quad (3)$$

The presence of a small fraction of baryonic matter in a nonbaryonic object can also play an important role. This matter emits energy and gradually settles at the center as the object is formed, thereby forming a compact baryonic nucleus [19].

In the present paper the conditions for the appearance and form of additional peaks on the brilliance curve in the case of a noncompact transparent lensing object with the singular density distribution (3) are studied. The influence of the compact nucleus on the lensing curve is analyzed.

The general principles of gravitational lensing are presented in Section 2. A point lens is studied in detail in Section 3. A theory of microlensing for an extended (noncompact) spherically symmetric gravitational lens with a prescribed density distribution is constructed in Section 4. In Section 5, the brilliance curves produced by point and noncompact lenses are compared, a method for making such a comparison is developed, and the regions where the differences between the brilliance curves are greatest are determined. The effect of a compact baryonic nucleus on the lensing curve of a noncompact object is investigated in Section 6.

2. TRAJECTORY OF A LIGHT RAY IN A SPHERICALLY SYMMETRIC GRAVITATIONAL FIELD

The metric in a spherically symmetric gravitational field can be written as

$$ds^2 = e^{\nu(t,r)}c^2dt^2 - e^{\lambda(t,r)}dr^2 - r^2(d\theta^2 + \sin^2\theta d\phi^2), \quad (4)$$

where $\nu(t, r)$ and $\lambda(t, r)$ are arbitrary functions [26, 27]. The energy–momentum tensor for "dust-like" matter with zero pressure has the form

$$T^{\mu\nu} = \rho(x)u^\mu u^\nu,$$

where u^μ is the 4-velocity and $\rho(x)$ is the density. We shall assume the gravitational field to be weak, so that $4\pi G\rho = \Delta\Phi$, where $\Phi(r)$ is the gravitational potential, and we shall neglect the motion of the matter, $u^\mu = (1, \mathbf{0})$. Then, from the condition that the tensor $T^{\mu\nu}$ (and hence the Einstein tensor) is diagonal follows $\dot\lambda \equiv 0$. The condition $\dot\nu \equiv 0$, i.e., a stationary metric, can be attained by a change of the variable t. The remaining components of Einstein's equations give three equations for the functions ν and λ:

$$\frac{1}{r^2} - e^{-\lambda}\left(\frac{1}{r^2} - \frac{\lambda'}{r}\right) = \frac{8\pi G}{c^2}T_0^0 = e^\nu\frac{2}{c^2}\Delta\Phi,$$

$$\frac{1}{r^2} - e^{-\lambda}\left(\frac{1}{r^2} + \frac{\nu'}{r}\right) = \frac{8\pi G}{c^2}T_1^1 = 0,$$

$$-\frac{1}{2}e^{-\lambda}\left(\nu'' + \frac{\nu'^2}{2} + \frac{\nu' - \lambda'}{r} - \frac{\nu'\lambda'}{2}\right)$$

$$= \frac{8\pi G}{c^2}T_2^2 = \frac{8\pi G}{c^2}T_3^3 = 0.$$

Solving these equations to first order in ν and λ, and taking account of the fact that

$$\Delta\Phi = \Phi'' + \frac{2}{r}\Phi',$$

we obtain

$$\nu = \frac{2}{c^2}\Phi(r), \quad \lambda = \frac{2}{c^2}r\Phi'(r). \tag{5}$$

We note that the metric can be put into an isotropic form by a change of the variable r,

$$ds^2 = e^{\nu}c^2dt^2 - e^{\tilde{\lambda}}(d\tilde{r}^2 + \tilde{r}^2d\theta^2 + \tilde{r}^2\sin^2\theta d\phi^2),$$

where

$$\nu = -\tilde{\lambda} = \frac{2}{c^2}\Phi(r)$$

follows from equation (5) to first order in ν and $\tilde{\lambda}$.

The equation for the trajectory of a light ray in a space with the metric (4) has the form [28, 27]

$$\left(\frac{du}{d\phi}\right)^2 + u^2e^{-\lambda} - \frac{1}{R^2}e^{-\nu-\lambda} = 0, \quad u = r^{-1}. \tag{6}$$

Here, R is the impact parameter of the ray, and the angle ϕ is measured in the plane of the ray.[1]

The solution of the of equation (6) to zero order in ν and λ is the straight line

$$u^{(0)} = \frac{1}{R}\cos(\phi - \phi_0). \tag{7}$$

The first correction gives

$$u^{(1)} = \frac{1}{2R} \times \left\{\int^{\phi}\left(\frac{\nu+\lambda}{\sin^2(\phi'-\phi_0)} - \frac{\lambda\cos^2(\phi'-\phi_0)}{\sin^2(\phi'-\phi_0)}\right)d\phi' + C_1\right\} \times \sin(\phi-\phi_0), \tag{8}$$

where the integral is calculated along the straight line (7).

Calculation of the angle between the asymptotes (u =0) gives the total deflection of the ray:[2]

$$\Theta(R) = \int_0^{\pi/2}(\lambda(r) + r\nu'(r))d\phi', \quad r(\phi') = R/\cos\phi'. \tag{9}$$

[1] Strictly speaking, the parameter R in equation (6) differs from the distance of closest approach R_0 by an amount of the order of ν: $R_0 = Re^{\nu(R_0)/2}$.

[2] We note that the deflection of the ray can also be calculated directly from equation (6), integrating the equation and taking the first approximation in Φ. In so doing, indicating the limits of integration, the Footnote 1 must be taken into account.

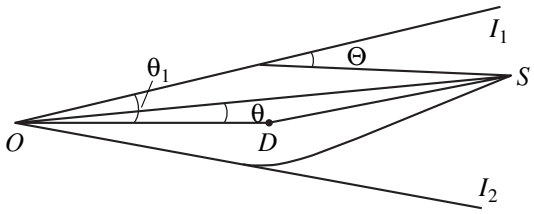

Fig. 1. Geometry of a gravitational lens: the relative arrangement of the observer O, lens D, and source S.

Using equation (5), this expression can be written in terms of the potential Φ as

$$\Theta(R) = \frac{4}{c^2}\int_0^{\pi/2} r\Phi'(r)d\phi', \quad r(\phi') = R/\cos\phi'. \tag{10}$$

Thus, we have found the angle of deflection $\Theta(R)$ of a ray as a function of the impact parameter in a prescribed potential.

We shall now consider the relative arrangement of the observer, lens, and light source (Fig. 1).

Let θ be the angle between the directions from the observer O to the lens D and the light source (star) S, and L_D and L_S the distances to the lens and to the star, respectively, where $L_{SD} = L_S - L_D$. On account of the curving of the light rays, the observer will see in the ODS plane two images I_1 and I_2 instead of a point star. We denote by θ_1 the angle between the directions to the lens D and the image. Then, from geometric considerations (see Fig. 1 and, for example, [10]), taking account of the smallness of the angles θ, θ_1, and Θ, we obtain the formula

$$\theta_1 \pm \theta = \frac{L_{SD}}{L_S}\Theta(R), \quad R = \theta_1 L_D, \tag{11}$$

which relates the angles θ and θ_1. The symbol $\pm$ is used so that all angles would be positive.

3. MICROLENSING BY COMPACT BODIES

Let us consider gravitational lensing when the lensing object is compact, i.e., when the size of the object is negligibly small. The potential produced by an object of mass M in this case can be written in the form

$$\Phi_s(r) = -\frac{GM}{r}. \tag{12}$$

Substituting into equation (10) the potential (12) and integrating, we arrive at the Schwarzschild value $\Theta = \Theta_s(R)$:

$$\Theta_s(R) = \frac{4GM}{c^2R}. \tag{13}$$

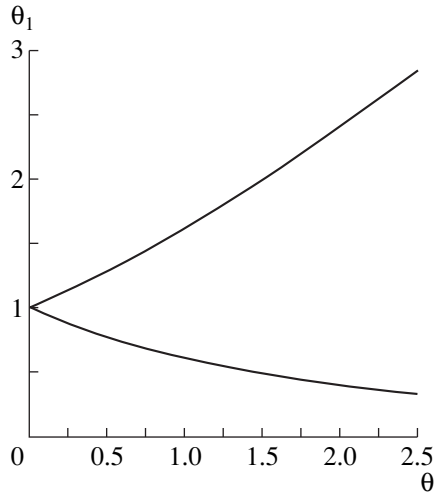

Fig. 2. Position of the images $\theta_1(\theta)$ for a point lens. The angles were normalized to the Einstein angle θ_0 (14).

Substituting the Schwarzschild function (13) into equation (11) gives a dimensionless quantity, the angle θ_0,

$$\theta_0^2 = \frac{4GM}{c^2}\frac{L_{SD}}{L_S L_D}, \tag{14}$$

or the Einstein radius

$$R_E^2 = (L_D\theta_0)^2 = \frac{4GM}{c^2}\frac{L_{SD}L_D}{L_S}. \tag{15}$$

The relation (11) itself becomes in this case a quadratic equation

$$\theta_1(\theta_1 \pm \theta) = \theta_0^2, \tag{16}$$

which always possesses two solutions $\theta_1(\theta)$.

The Einstein radius gives the characteristic size of the lens. The lensing object is compact, if its size r_b is much less than R_E. This condition always holds well for planets or stars in the galactic halo.

The dependence of $\theta_1^{\pm}$ on the angle θ is displayed in Fig. 2. It reflects the change in the angular position $\theta_1^{\pm}$ of the images as a function of the angle θ between the directions from the observer to the lens and to the source. As $\theta \longrightarrow 0$, the images merge. As $\theta \longrightarrow \infty$, one image approaches the star and the other approaches the lens. (As will be seen below, the point brilliance of the second image in this case approaches zero.)

Under the real conditions of microlensing experiments the characteristic distance to a lensing object in the galactic halo is $L_D \sim 10$ kpc. For an object of mass $M \sim 1M_\odot$, the angle between the images is $\theta_1 \sim 0.001''$. Such small angles make it impossible to resolve images using currently available means. However, the existence of gravitational focusing can be established according to the change in the point brilliance of the star being lensed.

The coefficient of increase in the point brilliance Ω is equal to the ratio of the total angular area of the images to the area of the source. It can be expressed in terms of the position of the source and the images as follows:

$$\Omega = \sum \frac{\theta_1}{\theta}\left|\left(\frac{d\theta_1}{d\theta}\right)_\theta\right|. \tag{17}$$

Here, the sum extends over both branches of $\theta_1(\theta)$.

Hence we obtain, substituting the expression (16),

$$\Omega_s = \frac{\theta^2 + 2\theta_0^2}{\theta\sqrt{\theta^2 + 4\theta_0^2}}. \tag{18}$$

We now take account of the fact that the picture of the increase in the point brilliance of a star is not stationary: the observer, the lens *D*, and the star *S* possess certain virial velocities. As a result, the angle θ changes with time. Since only the relative velocity is relevant, it can be assumed that the observer and star are at rest and the lensing object moves with velocity $v_\perp$ in a plane perpendicular to the line of sight. Then, the angle θ between the directions to the source *S* and the lens *D* is

$$\theta = \sqrt{\theta_{\min}^2 + \left(\frac{v_\perp(t - t_{\min})}{L_D}\right)^2},$$

where $t_{\min}$ is the moment of closest approach and $\theta_{\min}$ is the angular distance attained at this moment between *D* and *S* (the impact parameter).

Finally, using the expression (18), we obtain the time dependence of the coefficient of increase in the point brilliance of the star [4]:

$$A_s(t) = A_s[u(t)] = \frac{u^2 + 2}{u\sqrt{u^2 + 4}},$$
$$u(t) = \left[u_{\min}^2 + \left(\frac{2(t - t_{\min})}{\hat{t}}\right)^2\right]^{1/2}. \tag{19}$$

Here, $u(t) = \theta(t)/\theta_0$, $u_{\min} = \theta_{\min}/\theta_0$, and $\hat{t}$ is the characteristic lensing time, which is related with $v_\perp$ as

$$\hat{t} = 2R_E/v_\perp = 2L_D\theta_0/v_\perp. \tag{20}$$

The relative motion of the lens and source corresponds to the motion of a point in the plot of $\Omega_s(x)$ from $x \longrightarrow +\infty$ to $x_{\min}$ and back. Therefore, $A_s(t)$ is a symmetric "bell-shaped" function with a maximum value

$$A_{s\max} = \Omega_s(\theta_{\min}),$$

independent of the light frequency. It is the function $A(t)$ that is measured in observations.

Thus, for a compact lens the form of the curve $A(t)$ is determined completely by two parameters: the

impact parameter $u_{\min}$ (or the value of A at the maximum) and the duration $\hat{t}$ of the event.

4. MICROLENSING BY NONCOMPACT OBJECTS

The theory expounded above concerns compact bodies whose size r_b is much smaller than the Einstein radius:

$$r_b \ll R_E.$$

For noncompact objects of dark matter the reverse condition usually holds:

$$R_x \geq R_E. \tag{21}$$

Indeed, according to equation (2) the size R_x of an object with mass $M \sim (0.1\text{–}1)M_\odot$ is of the order of 10^{14}–10^{15} cm. This is 3–10 times greater than the Einstein radius for bodies of the same mass located at a distance $L_D \sim 10$ kpc characteristic for lensing in the halo. Thus, the microlensing theory needs to be extended to the case of noncompact objects with characteristic sizes (21). We underscore that such an extension of the microlensing theory is of interest only for nonbaryonic objects: baryonic objects of such size and mass cannot exist in the galaxy. We also note that a feature of nonbaryonic objects that is important for microlensing is their optical transparency: a light ray is not absorbed, even if it passes very close to the center of the lens. This property, incidentally, does not hold for objects with a baryonic nucleus. Such objects will be considered in Section 6.

Thus, we shall study gravitational lensing for the case where the lens size R_x cannot be neglected. We shall use the density distribution (3) for $r \leq R_x$. The density distribution

$$\rho = \begin{cases} \dfrac{(3-\alpha)M_x}{4\pi R_x^2}\left(\dfrac{r}{R_x}\right)^{-\alpha}, & \alpha = 1.8, \quad r < R_x \\ 0, & r > R_x \end{cases} \tag{22}$$

corresponds to the potential

$$\Phi(r) = \begin{cases} -\dfrac{GM_x}{R_x}\left[\dfrac{3-\alpha}{2-\alpha} - \dfrac{1}{2-\alpha}\left(\dfrac{r}{R_x}\right)^{2-\alpha}\right], & r \leq R_x \\ -\dfrac{GM_x}{r}, & r > R_x. \end{cases} \tag{23}$$

Once again, the curvature of the trajectory of a light ray for a spherically symmetric potential $\Phi(r)$ can be described by equations (6)–(10). Now, instead of equation (13) we obtain for the total deflection of the ray between the asymptotes

$$\Theta(R) = \frac{4GM_x}{c^2 R_x} f(R/R_x), \tag{24}$$

$$f(\xi) = \begin{cases} \dfrac{1-\sqrt{1-\xi^2}}{\xi} - \dfrac{\xi\sqrt{1-\xi^2}}{\alpha-1} \\ \quad + \dfrac{\alpha}{\alpha-1}\xi^{2-\alpha}\displaystyle\int_\xi^1 \frac{x^\alpha dx}{\sqrt{1-x^2}}, \quad \xi \leq 1 \\ 1/\xi, \quad \xi > 1. \end{cases} \tag{25}$$

For $R > R_x$ the expression for Θ is identical to the Schwarzschild expression. We note that the integral in equation (25) can be expressed in terms of a hypergeometric function:

$$\int_\xi^1 \frac{x^\alpha dx}{\sqrt{1-x^2}} = \sqrt{1-\xi^2}\,F\left(-\frac{(\alpha-1)}{2}, \frac{1}{2}, \frac{3}{2}, 1-\xi^2\right).$$

The angle θ_1 between the direction to the lens D and the direction to the image is once again related with the position θ of the source S relative to the lens by equation (11):

$$\theta_1 \pm \theta = \frac{L_{SD}}{L_S}\Theta(R_1), \quad R_1 = \theta_1 L_D.$$

However, the quantity $\Theta(R)$ is now determined by the expression (24) instead of (13). Since the function $\Theta(R)$ is complicated, it is more convenient to switch from the variables θ and θ_1 to the variables $x = \theta L_D/R_x$ and $x_1 = \theta_1 L_D/R_x$ and to introduce, instead of the Einstein angle θ_0, the constant

$$Q = \frac{4GM_x}{c^2}\frac{1}{R_x^2}\frac{L_{SD}L_D}{L_S} = \left(\frac{R_E}{R_x}\right)^2. \tag{26}$$

Then, equation (11) assumes the form

$$x_1 \pm x = Qf(x_1), \tag{27}$$

where the function $f(x_1)$ is given by equation (25).

We shall now estimate Q. If the lensed star S is located in the Large Magellanic Cloud (LMC) ($L_S = 5$ kpc) and the lens parameters correspond to the average values $M_x = 0.5M_\odot$ and $R_x = 4 \times 10^{14}$ cm indicated in the Introduction, then the largest possible value of Q (for $L_D = L_S/2$) is $Q \approx 0.08$, i.e., $R_x/R_E \simeq 3.5$.

An example of the function $x_1(x)$ for various values of Q is presented in Fig. 3a.

It is evident that, in contrast to the case of a point lens, the plot possesses three branches, i.e., for impact parameter $x < x_c(Q)$ there are three and not two images. The quantities $x_1^{(1),(2)}(0)$ are the ordinates of the "first" and "second" branches at $x = 0$, corresponding to the Einstein angle in the case of a point lens, and it increases monotonically with Q. For $Q \geq 1$ we have $x_1(0) = R_E/R_x$.

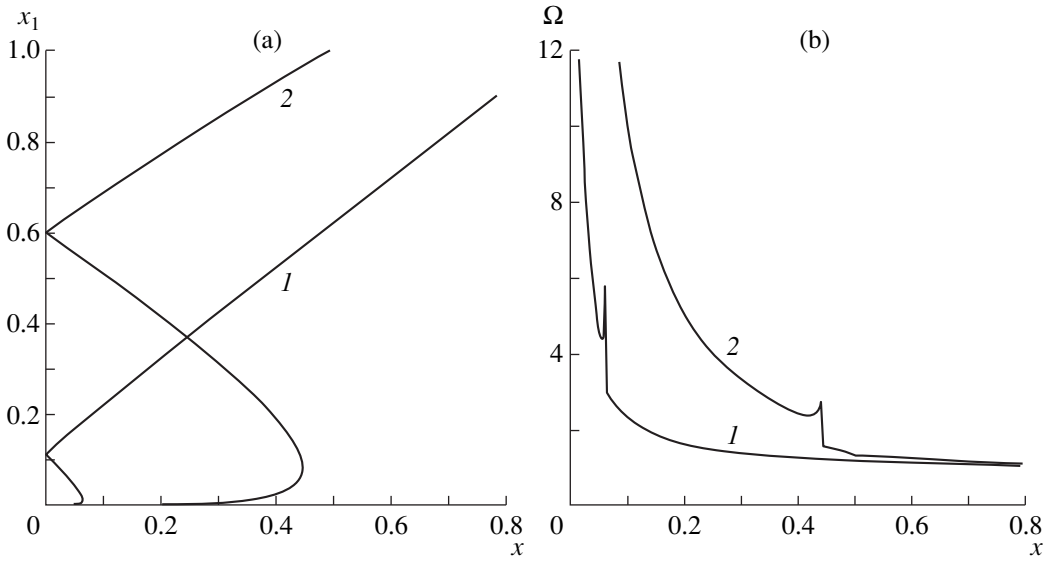

Fig. 3. (a) Positions of images $x_1(x)$ and (b) coefficient of increase $\Omega(x)$ for a noncompact lens for various values of the parameter $Q = 0.1$ (*1*) and 0.5 (*2*).

The quantity $y_c = x_1^{(2),(3)}(x_c)$, which gives the value of x_1 for which the second and third images merge, is determined by the equation

$$(dx/dx_1)\big|_{y_c} = 0,$$

whence follows

$$1 - Qf'(y_c) = 0.$$

For large Q it is limited by the value $\hat{y}$: $f'\hat{y} = 0$ and $\hat{y} \approx 0.39$. The value of $x_c = Qf(y_c) - y_c$, however, grows without bound as Q increases. Thus, as Q increases, the third branch of the plot "hugs" the x axis.

The increase in the point brilliance Ω of a star, as determined by the expression (17), also depends now on the parameter Q. Using equation (27), we obtain for our case

$$\Omega_Q = \sum \frac{x_1}{x} \frac{1}{|1 - Qf'(x_1)|}. \qquad (28)$$

Just as in the case of a point lens, $\Omega_Q \longrightarrow \infty$ as $x \longrightarrow 0$. However, there arises another point where the coefficient of increase becomes infinite,[3] specifically, the point x_c of the caustic. Thus, a narrow "one-sided" peak appears in the plot of $\Omega_Q(x)$ (Fig. 3b) at the point $x = x_c$.

The existence of a third ray and the appearance of a caustic in the case of a transparent noncompact lens were first indicated in [23].[4] We note, however, that the singular density distribution (22) gives a much narrower peak than the smooth distribution. The peak itself corresponds to a much larger impact parameter x_c, and the quantity y_c is less than for a smooth distribution. (In [23] the density is assumed to be constant inside the lensing object.) Conversely, increasing the exponent in equation (22) to $\alpha = 2$, corresponding to a logarithmic potential at the center $\Phi \propto \ln r$, changes $f(\xi)$ in equation (25) to

$$\tilde{f}(\xi) = \begin{cases} \arccos\xi + (1 - \sqrt{1-\xi^2})/\xi, & \xi \le 1 \\ 1/\xi, & \xi > 1. \end{cases}$$

Neither a caustic nor a third image arises for such a distribution, and the second image vanishes for $x = (\pi/2)Q$.

It is easy to estimate the width of the peak. Let the total point brilliance of the second and third branches be Ω_0 at the boundary of the peak (the impact parameter is $x_c - \delta x$). Of course, for $x > x_c$ the total point brilliance is zero. Then, using the definition of y_c we obtain from equations (17) and (28) near x_c

$$\Omega_0 = \sum_{(2),(3)} \frac{x_1}{x}\left|\frac{dx_1}{dx}\right| \simeq 2\frac{y_c}{x_c}\frac{1}{-Qf''(y_c)|\delta x_1|}.$$

Since $\delta x = (1/2)(d^2x/dx_1^2)\big|_{y_c}(\delta x_1)^2$, we obtain

$$\delta x = 2\left(\frac{y_c}{x_c}\right)^2 \frac{1}{-Qf''(y_c)}\frac{1}{\Omega_0^2}. \qquad (29)$$

The estimate (29) shows that the width of the peak for fixed Ω_0 is maximum for $Q \sim 0.6$ (the value of δx is then of the order of $5 \times 10^{-3}\Omega_0^{-2}$) and vanishes when $Q \longrightarrow 0$ and $Q \longrightarrow \infty$. We denote by $\overline{\delta x}$ the width of the peak,

[3] In reality, the height of the peak is bounded because of the finite angular size of the light source. In addition, the presence of a nontransparent baryonic body at the center of the lensing object plays an important role (see Section 6).

[4] I thank G.V. Chibisov for a detailed discussion of the questions concerning microlensing and for pointing out the possibility of three-ray microlensing.

Parameters of $\Omega_Q(x)$ for various values of Q

Q	1	0.8	0.5	0.1	0.05	0.01
x_c	0.997	0.776	0.445	0.064	0.027	0.0037
$\overline{\delta x}$	7×10^{-2}	5.5×10^{-2}	2.5×10^{-2}	3.5×10^{-3}	1.5×10^{-3}	2.5×10^{-4}
$\overline{\delta x}/\sqrt{Q}$	7×10^{-2}	6.2×10^{-2}	3.5×10^{-2}	1.1×10^{-2}	7×10^{-3}	2.5×10^{-3}
$\overline{\delta x}/x_{1.34}$	0.07	0.07	0.05	0.01	0.008	0.007
$x_c/\sqrt{Q}$	1.00	0.87	0.63	0.20	0.12	0.04
$A(x_c-\overline{\delta x})$	1.63	1.78	2.39	4.36	4.68	4.97
$A(x_c+0)$	1.17	1.23	1.58	3.05	3.28	3.47

measured from the local minimum of the function $\Omega_Q(x)$ up to the caustic point. In order for the estimate (29) to be close to $\overline{\delta x}$, the quantity Ω_0 must be chosen as ~0.5. This correspondence, however, break down for large values $Q \geq 1$, where the minimum becomes increasingly less pronounced and corresponds to an increasingly smaller difference of the point brilliance Ω_0.

The quantities characterizing the curve $\Omega_Q(x)$ for various values of Q are presented in the table. The value $\overline{\delta x}/\sqrt{Q} = \overline{\delta x}/(R_E/R_x)$ characterizes the ratio of the width of the peak $\overline{\delta x}$ and the width of the "main" maximum. Indeed, if the characteristic lensing time is $\hat{t} = 2R_E/v_\perp$ (see equation (20)), and δt is the characteristic passage time of the "secondary" peak, then $\overline{\delta x}/\sqrt{Q} = 2\delta t/\hat{t}$. It is evident that this quantity is small (4–5% for $Q \sim 0.5$–0.8) and decreases with Q.

Since for a noncompact lens the value $x = \sqrt{Q} = R_E/R_x$ corresponds to different coefficients of increase with different values of Q, a row giving the values of $\overline{\delta x}/x_{1.34}$, where $x_{1.34}$ is the value of the parameter x for which the increase is 1.34, which in the compact-lens model corresponds to the Einstein radius, is included in the table for comparison. For $Q \sim 1$, we have $x_{1.34} \sim x_c$.

The quantity $x_c/\sqrt{Q}$ characterizes the position of the "additional" peak on the lensing curve with respect to the point R_E/R_x. It is evident that for $Q \leq 1$ the caustic point lies inside R_E, and it approaches the center as Q decreases, so that for small Q the "additional" peak merges with the "main" peak. For $Q > 1$ the caustic lies outside R_E/R_x on the wings of the curve, and it recedes as Q increases.

The values of $A(x_c + 0)$ and $A(x_c - \overline{\delta x})$ show the difference of the coefficient of increase of Ω_Q on different sides of the peak. As one can see from Fig. 3b, the sharp change in point brilliance beyond the caustic is an important feature of the brilliance curve. Since the absolute magnitude of the differential increases as Q decreases, it can be observed in observations of events with $Q < 1$ even if the narrow peak itself remained undetected.

We underscore that for $Q > 1$ the third image and caustic do not vanish even though the lensing object is smaller than the Einstein radius. However, for large Q the caustic point $x_c = Qf(y_c) - y_c \approx Qf(\hat{y}) \longrightarrow \infty$, and the quantity $x_c/\sqrt{Q}$ also increases. The quantity $\overline{\delta x}$ (as is evident from the table) increases. However, this happens because the curve becomes "flatter" near a local minimum. However, if the width of the peak (29), calculated according to a fixed difference of the intensity Ω_0, is considered, then

$$\delta x \approx \frac{2}{\Omega_0^2}\left(\frac{\hat{y}}{Qf(\hat{y})}\right)^2\left(-\frac{1}{Qf''(\hat{y})}\right) \sim Q^{-3}$$

decreases rapidly as Q increases. The absolute values of the point brilliance on different sides of the peak also decrease, and the position and point brilliance of the first image as a function of x approach the "Schwarzschild" values corresponding to a point lens. For this reason, for large Q the difference between noncompact and compact lenses becomes increasingly less noticeable.

The temporal variation of the parameter x due to the relative motion of the lensing object is described by the formula

$$x = \sqrt{x_{\min}^2 + \left(\frac{v_\perp t}{R_x}\right)^2},$$

where $x_{\min} = \theta_{\min}L_D/R_x$ and $\theta_{\min}$ is, once again, the impact parameter. As the lens moves, the point brilliance of the star varies

$$A(t) = \Omega_Q(x(t)).$$

Examples of plots of $A(t)$ (only for $t > 0$) are displayed in Fig. 4 for various values of the constant Q. The time scale corresponds to $\tau = R_x/v_\perp$. For $v_\perp = 200$ km/s and $R_x = 4\times10^{14}$ cm, we have $\tau = 2\times10^7$ s. For comparison, plots of $A(t)$ are presented for a point

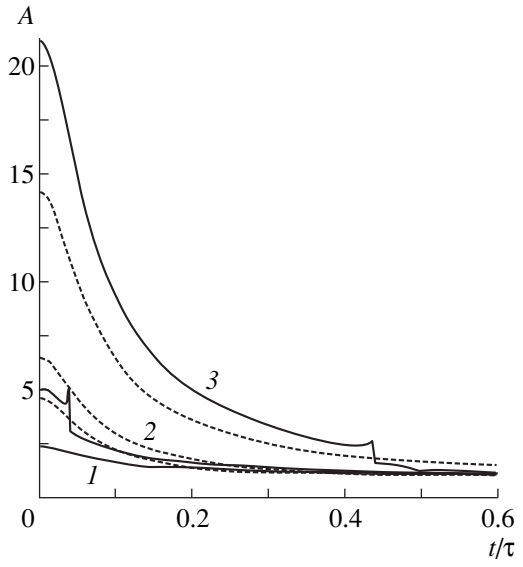

Fig. 4. Brilliance curve $A(t)$ for various values of $Q = 0.05$ (*1*), 0.1 (*2*), and 0.5 (*3*) (dashed lines for point lens). Time in units of $\tau = R_x/v_\perp$, $x_{\min} = 0.05$.

lens with the same values of the lens mass M, distance L_D to the lens, and impact angles $\theta_{\min}$. It is important that for a noncompact body the form of the brilliance curve is determined not by two but rather by three parameters. These parameters can be the point brilliance $A_{\max}$ at the maximum, the duration of lensing $\hat{t} = 2R_E/v_\perp$, and $Q = (R_E/R_x)^2$.

The "secondary" maximum in the dependence $\Omega_Q(x)$ appears on the lensing curve in the form of two additional symmetrically arranged one-sided peaks. As Q decreases, the width $\overline{\delta x}$ of the range of parameters corresponding to the "additional" intensity peak decreases (in the units R_x and $R_E - \overline{\delta x}/\sqrt{Q}$). This circumstance can make it more difficult to see additional peaks in the observations. Thus, for $R_x = 4 \times 10^{14}$ cm, $v_\perp = 200$ km/s, and $Q = 0.08$, we have $\overline{\delta x} \sim 3 \times 10^{-3}$, and the time interval in which the point brilliance will increase rapidly is $\delta t \simeq R_x \overline{\delta x}/v_\perp \simeq 17$ h. If the observations of each star are performed once per day (as done at the MACHO experiment), this increase can become unnoticeable or it could be perceived as a random excursion. At the same time, as noted above, a sharp "stepped" jump in point brilliance beyond the caustic could be seen in the observations.

On the other hand, for small Q the peaks occur for large amplitudes and can strongly distort the "main" maximum of the brilliance curve. If $x_{\min}$ is somewhat smaller than x_c, the width of the additional peaks can increase substantially, and they can become even wider than the central peak of finite height. However, if $x_{\min}$ lies in the region of growth of the curve $\Omega_Q(x)$, $x_c - \overline{\delta x} < x_{\min} < x_c$, the central maximum vanishes completely. Thus, quite exotic lensing curves are possible for certain values of the parameters. However, in contrast to binary lens or binary light sources [10], the lensing curves produced by a centrally symmetric noncompact lens are always symmetric.

We also note that for small amplitudes $A_{\max}$, when the impact parameter $x_{\min} > x_c$, no additional peaks occur in the lensing curve, and the curve is bell-shaped, just as in the case of a point lens.

5. COMPARISON OF THE BRILLIANCE CURVES PRODUCED BY NONCOMPACT AND COMPACT LENSES

The exact form of the brilliance curve of a compact object is determined by the following parameters: the mass M_x of the lensing body, the distance L_D to the body, the relative velocity $v_\perp$, the impact parameter $\theta_{\min}$, and the distance L_S to the lensed star. For a noncompact object there is an additional parameter, the size R_x of the body. The brilliance curves corresponding to compact and noncompact lenses with the same values of the parameters M_x, L_D, $v_\perp$, $\theta_{\min}$, and L_S are presented in Fig. 4.

The difficulty of a real problem is that we do not know these parameters. The theoretical brilliance curve is adjusted so as to obtain the best agreement between theory and observations. Therefore, to determine whether or not a lensing object is compact or noncompact we must compare the lensing curves which are closest to one another and not curves which correspond to the same values of the parameters. We shall now determine how the difference between these curves can be characterized.

The problem is formulated as follows. A brilliance curve $A_c(t)$ of a compact body with a prescribed amplitude A_0 and characteristic duration $\hat{t}_c$ is given. The brilliance curve for a noncompact lens is characterized by three parameters: the amplitude A_{n0}, the duration $\hat{t}_n$, and the size R_x/R_E of the lensing body (or the parameter Q (26)).

The problem is to find the amplitude A_{n0} and with width $\hat{t}_n$ for which the difference between the compact $A_c(t)$ and noncompact $A_{nc}(t)$ brilliance curves is a minimum for fixed value of the ratio R_x/R_E. For this, we construct the functional

$$J = \int (A_{nc}(t) - A_c(t))^2 \frac{dt}{\hat{t}_c}. \qquad (30)$$

This is a dimensionless quantity, which can characterize the difference between the noncompact and compact brilliance curves. Now, varying the amplitude A_{n0} and the characteristic time $\hat{t}_n$ of a noncompact brilliance curve arbitrarily, we find a minimum of J for

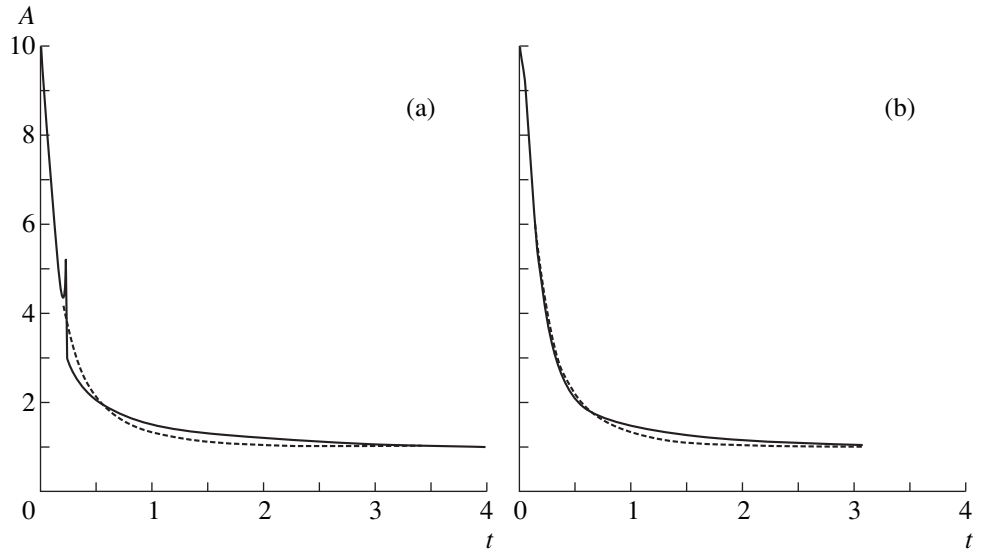

Fig. 5. (a) Examples of "noncompact" curves closest to a given "compact" curve (dashed line): noncompact lens with no nucleus ($J = 0.11$); (b) noncompact lens with a baryonic nucleus, $\lambda = 0.01$ ($J = 0.05$). $Q = 0.1$, amplitude of a "compact" curve $A_{c0} = 10$, time is normalized to $\hat{t}_c$.

fixed A_c and Q. This minimum then describes the difference between the closest brilliance curves for noncompact and compact lenses.

An example of the corresponding closest brilliance curve with $Q = 0.1$ is displayed in Fig. 5a. The integral J for $0.01 \le Q \le 1$ varies from 0.02 to 0.4; it increases with the amplitude $A_{\max}$ and increases as Q decreases for $Q \le 0.1$. As one can see from Fig. 5a, the largest discrepancy between the curves is produced by the "additional" peaks and the sharp drop following these peaks in the curve corresponding to a noncompact object. In addition, a substantial difference is observed on the wings of the brilliance curves in the region $|t - t_{\min}| > \hat{t}_c$, and for small Q the curve corresponding to a noncompact lens passes above the compact curve. To understand the reason for this we shall examine the asymptotic behavior of the brilliance curves in this region. The condition $|t - t_{\min}| \gg \hat{t}_c$ is equivalent to $u(t) = \theta(t)/\theta_0 \gg 1$ or $R \gg R_E$. Then, for a point (compact) lens we obtain from equation (19)

$$A_c(t) - 1 \simeq \frac{2}{u^4}, \quad u(t) = \frac{R}{R_E} \simeq \frac{|t - t_{\min}|}{\hat{t}_c/2}, \qquad R \gg R_E. \tag{31}$$

For a noncompact lens, a region of intermediate asymptotic behavior appears on the wings of the brilliance curve:

$$R_E < R \ll R_x. \tag{32}$$

The brilliance curve in this region can be calculated assuming

$$x = \frac{R}{R_x} \ll 1, \quad Q = \left(\frac{R_E}{R_x}\right)^2 \ll 1. \tag{33}$$

Since the function $f(\xi)$ is bounded, we find from equation (27) the position of the image as

$$x_1^+ = x + Qf(x) + O(Q^2),$$

which is the only image in the range under study (since, according to the table, for $Q < 1$ we have $x/x_c > x/\sqrt{Q} = R/R_E > 1$).

We obtain from equation (28), taking account the asymptotic behavior of the function $f(\xi)$ in the limit $\xi \longrightarrow 0$,

$$A_{nc}(t) - 1 \simeq \frac{3-\alpha}{\alpha-1}\alpha C\frac{Q}{x^{\alpha-1}} + \frac{3-\alpha}{\alpha-1}Q + O(Qx^2) \sim \frac{Q^{(3-\alpha)/2}}{u^{\alpha-1}}, \quad C = F\left(-\frac{\alpha-1}{2}, \frac{1}{2}, \frac{3}{2}, 1\right) \simeq 0.8. \tag{34}$$

Thus, for a noncompact lens, in the "transitional" region (32) we have instead of the behavior $A \propto u^{-4}$ the behavior $A \propto u^{1-\alpha}$. This difference produces substantially more slowly decaying wings of the brilliance curve, which are seen in Fig. 5.

In what follows, however, the relation between the brilliance curves for the cases of compact and noncompact lenses changes. For $R > R_x$ and $Q < 1$, for a noncompact lens, as is evident from equations (25) and (27), one image coincides with the image from a point lens and the second image is absent. As follows from

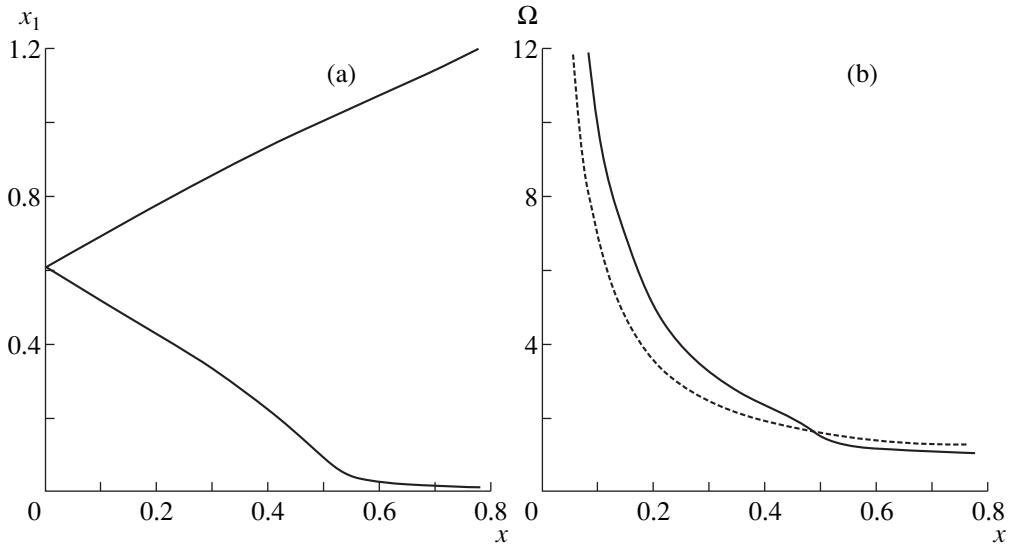

Fig. 6. Curves of (a) the position of the images $x_1(x)$ and (b) coefficient of increase $\Omega(x)$ for a noncompact lens with a baryonic nucleus of mass $M_b > \lambda_c(Q)M_x$; $Q = 0.5$, $\lambda = 0.01$. Dashed line displays coefficient of increase for a point lens with the same parameters.

equation (28), the difference of the coefficient of increase from unity here is half that obtained for a compact lens:

$$A_{nc}(t) - 1 \simeq \frac{4Q^2}{x^4} = \frac{1}{u^4}, \quad u(t) = \frac{R}{R_E} \gg 1, \qquad x = \frac{R}{R_x} > 1. \tag{35}$$

Therefore, as $t \longrightarrow \infty$ the brilliance curve corresponding to a noncompact lens passes below the compact curve.

As the parameter Q increases, the region of intermediate asymptotic behavior (32) and (33) becomes narrower, and for $Q > 1/2$ the brilliance curve behind the caustic immediately enters the region where the position and point brilliance of the image are described by the formulas for a point lens, i.e., in the region of the "far" asymptotic behavior (35).

6. EFFECT OF A BARYONIC NUCLEUS ON THE LENSING CURVE OF A NONCOMPACT OBJECT

In the preceding discussion we studied the simplest model of a density distribution of a noncompact object characterized by a single parameter—the radius R_x of the body. However, a substantial amount of baryonic matter could be trapped in a nonbaryonic object during the period when the object is formed. This matter can then emit energy and settle to the center, forming a baryonic nucleus. The fraction of baryonic matter with respect to the total mass of a noncompact object should be, on the average, of the order of the fraction of baryonic matter in the universe, i.e., ~5%. The existence of such a baryonic nucleus could have a substantial effect on microlensing.

Let us consider a gravitational lens with the density distribution of nonbaryonic matter (22) and a baryonic nucleus of mass $M_b = \lambda M_x$ at the center. We shall assume the baryonic nucleus to be point-like (the justification for this approximation is discussed below). The potentials produced by the baryonic and nonbaryonic components add together, and instead of equation (25) we have

$$f_\lambda(\xi) = f(\xi) + \lambda/\xi. \tag{36}$$

As $\xi \longrightarrow 0$, the function f_λ, in contrast to f, grows without bound. For this reason, the second image, just as in the case of a point-like ("Schwarzschild") lens, is always present, i.e., equation (11) has for any x at least two solutions. However, depending on the ratio of the parameters Q and λ, two variants of a plot of $x_1(x)$ are possible (and, correspondingly, $\Omega(x)$). For nuclear mass greater than the critical value $\lambda_c(Q)M_x$, neither a third image nor a caustic arises (see Fig. 6), and the plot is qualitatively the same as in the case of a point lens (Fig. 2). However, if $\lambda < \lambda_c(Q)$, then there exist two caustics at the points x_{c1} and x_{c2}, between which there are four images (see Fig. 7). As $\lambda \longrightarrow 0$, one caustic point x_{c1} approaches x_c, and the other approaches zero. As λ increases, both caustics move away from the center and merge at $\lambda = \lambda_c(Q)$.

The first variant (no caustic) occurs if the function $x(x_1)$, given by equation (27) together with (36), does not have an extremum:

$$\forall x_1: \quad f'(x_1) - \lambda/x_1^2 < 1/Q. \tag{37}$$

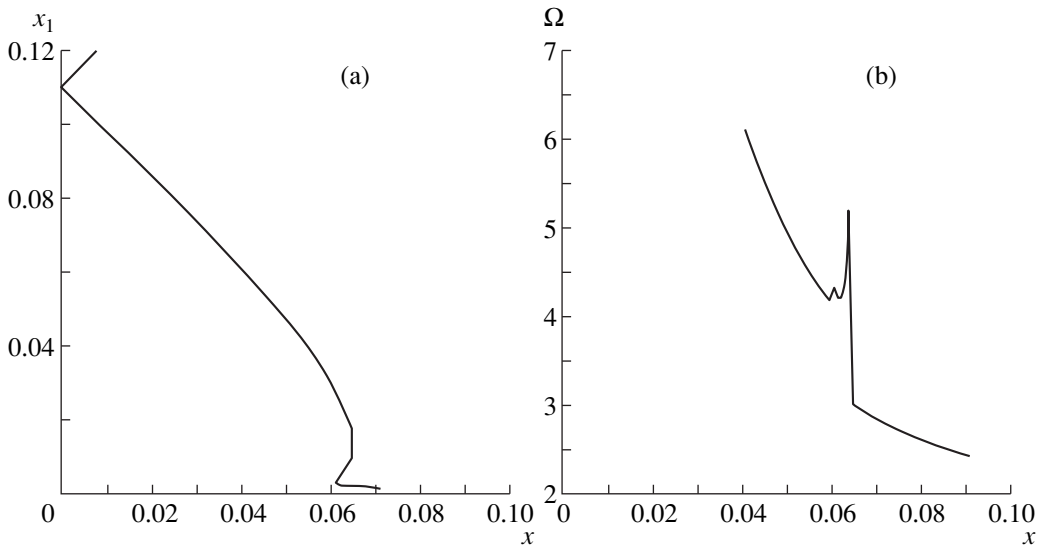

Fig. 7. Same as in Fig. 6 but for a baryonic nucleus of mass $M_b < \lambda_c(Q)M_x$; $Q = 0.1$, $\lambda = 2 \times 10^{-4}$.

Thus, the critical value λ_c is determined by the expression

$$\lambda_c(Q) = \max_{x_1}(x_1^2 f'(x_1) - x_1^2/Q).$$

The point at which a maximum is realized gives the value x_1 at the caustic point. The function $\lambda_c(Q)$ increases with Q from zero to a finite value

$$\lambda_0 = \lambda_c(\infty) = \max_{x_1}(x_1^2 f'(x_1)) \approx 0.023.$$

For $Q \leq 1$ it is described very well by an approximate expression which is obtained by expanding $f(\xi)$ in a series in powers of ξ:

$$\xi^2 f'(\xi) - \frac{\xi^2}{Q} = \frac{\alpha(2-\alpha)}{\alpha-1}C\xi^{3-\alpha} - \left(\frac{3-\alpha}{2(\alpha-1)} + \frac{1}{Q}\right)\xi^2 + O(\xi^4).$$

Here, $C = F(-(\alpha-1)/2, 1/2, 3/2, 1) \simeq 0.8$ cm (see equation (34)). The maximum is reached at the point

$$\xi \simeq \left[\alpha(2-\alpha)C\Big/\left(\frac{2(\alpha-1)}{Q(3-\alpha)} + 1\right)\right]^{\frac{1}{\alpha-1}}.$$

Hence, we obtain for the critical value λ_c

$$\lambda_c(Q) \simeq \frac{1}{2}(\alpha(2-\alpha)C)^{\frac{2}{\alpha-1}}\left(1 + \frac{2(\alpha-1)}{(3-\alpha)Q}\right)^{-\frac{3-\alpha}{\alpha-1}}.$$

It is evident that the critical fraction of baryonic mass is very small. For $Q = 1$, we have $\lambda_c(1) \simeq 6.6 \times 10^{-3}$, and for $Q = 0.01$ we have $\lambda_c(0.01) \simeq 1.5 \times 10^{-5}$. Thus, more than two images can occur only if the amount of baryonic matter is very small, and caustics do not arise for the average fraction of baryonic mass $\lambda \sim 5\%$.

For $\lambda < \lambda_c(q)$, as shown in Fig. 7, the coefficient of increase of $\Omega(x)$ becomes infinite on each caustic. However, the second ("inner") peak is very narrow (in Fig. 7, because of computational inaccuracy near the caustic, the peak is shown to be wider than it actually is). The width of this "inner" peak δx_{c2} can be estimated by taking account of the fact that λ and the value $x_1(x_{c2}) = y_{c2}$ at the point of the caustic x_{c2} is much less than unity. It follows from the vanishing of the derivative dx/dx_1 that at the point of the caustic we have

$$\lambda = y_{c2}^2 f'(y_{c2}) - \frac{1}{Q}y_{c2}^2.$$

Retaining only terms which are of first order in y_{c2} and taking account of equations (27) and (29), we obtain

$$\lambda \sim y_{c2}^{3-\alpha}, \quad x_{c2} \sim y_{c2}^{2-\alpha},$$

$$\delta x_{c2} \sim \frac{(y_{c2}/x_{c2})^2}{-f''(y_{c2})} \sim y_{c2}^{2(\alpha-1)+\alpha} \sim \lambda^{\frac{3\alpha-2}{3-\alpha}} \sim \lambda^3.$$

Apparently, it would be extremely difficult to observe such a narrow peak. For this reason, the observed brilliance curve for such small values of λ would appear to be virtually the same as in the absence of a point nucleus.

Conversely, for $\lambda > \lambda_c$ a nucleus even for comparatively small mass can substantially change the brilliance curve, "smoothing" the maximum in it. The brilliance curve becomes more like the "Schwarzschild" curve. Figure 5b shows the brilliance curve produced by a lens with $Q = 0.1$ and $\lambda = 0.01$, which is closest to a given brilliance curve corresponding to the point lens. Comparing with Fig. 5a shows that the additional peak

vanishes, and the behavior of the curve in the wings remains the same.

Opaqueness of the nucleus. Thus, we have determined the effect of the presence of a point baryonic nucleus on lensing. The cutoff of the power-law density distribution can also have an effect, but it is easy to show that it does not change qualitatively either the position or the number of images or the form of the coefficient of increase in point brilliance.

On the other hand, a baryonic body is opaque, and light rays passing closer than the radius R_b to the center of the lens are absorbed. Thus, the position of the images, which is shown in Figs. 3a, 6a, and 7a, becomes distorted: all points lying below $x_1 = R_b/R_x$ vanish. Correspondingly, the coefficient of increase in point brilliance should also change. However, assuming a baryonic nucleus mass $M_b \sim 0.05M_x$, the density in the nucleus $\rho \sim 1$ g/cm^3, for $M_x = 0.5M_\odot$ we obtain $R_b \sim 3.5 \times 10^{10}$ cm (which is approximately five times greater than the radius of Jupiter), and for $R_x = 4 \times 10^{14}$ cm ($Q \simeq 1$) we have $R_b/R_x \sim 10^{-4}$. It is evident from Figs. 3a and 6a that this value is very small compared with the characteristic values of x_1, and the image corresponding to the bottom branch of the graph vanishes in the cases where this contribution to the total point brilliance is essentially zero. For this reason, the absorption caused by the baryonic nucleus can be neglected. However, the effect of its potential is much larger.

7. CONCLUSIONS

The question of whether or not the invisible objects observed during microlensing in the galactic halo are compact is of fundamental importance for determining the nature of these objects and of the dark matter as a whole. From this standpoint it is important to develop the aspects of microlensing theory that could provide criteria and methods for answering this question experimentally.

As shown above, the main differences between the brilliance curves produced by noncompact lenses from the curves produced by compact (point) lenses lie in the possibility of the appearance of additional maxima in the brilliance curve and in the behavior of the curve in the wings.

The additional "one-sided" peaks arranged symmetrically relative to the central maximum are quite narrow (with widths up to several hours), which could make them difficult to observe. At the same time the point brilliance difference on different sides of the peak increases as the width of the peak decreases, and it can be observed even if the narrow peak itself became unobservable.

We note that secondary maxima can also arise in microlensing by baryonic objects. This happens when a binary lens or a binary star as the light source. However, the brilliance curve is then, generally speaking, asymmetric. The question of why additional peaks appear can be solved in each specific case by analyzing the shape and position of the peaks.

In the presence of a compact baryonic nucleus of mass equal to several percent of the total mass of the object, the additional maxima vanish and the point brilliance differences become strongly smoothed. The brilliance curve, just as in the case of a point lens, is "bell-shaped." The largest differences from a curve corresponding to a compact lens should be expected in this case on the wings of the brilliance curve.

Analysis of the observations of one of the microlensing events [29] gives for a point lens a value of the parameter normalized to the number of degrees of freedom $\chi^2 = 1.75$; the assumption that the object is noncompact and has no baryonic nucleus gives an optimal normalized value $\chi^2 = 1.77$ for $Q = 3.6 \pm 0.1$, which signifies a somewhat worse agreement of this hypothesis with observations. However, for a noncompact body with a point nucleus (relative mass $M_b/M_x = 5\%$) the minimum normalized value of χ^2 is obtained for $Q = 0.235 \pm 0.001$ and is $\chi^2 = 1.71$. Thus, the model of a noncompact lens with a nucleus is in this case somewhat preferable to the point-lens model.

The mass of a lensing object in all three models is $M_x \simeq 0.02M_\odot$ (with the distance to the object 10 kpc and velocity 200 km/s). The Einstein radius is $R_E = 3 \times 10^{13}$ cm in the first two models and 2.7×10^{13} cm in the last model. The size of the nonbaryonic object is $R_x = 1.6 \times 10^{13}$ cm in the model without a nucleus ($Q = 3.6$) and $R_x = 5.7 \times 10^{13}$ cm in a model with a baryonic nucleus ($Q = 0.235$). These quantities all agree with theoretical estimates (1) and (2).

In summary, the question of whether or not the objects of dark matter which are observed during microlensing are compact is closely related with the question of their nature and requires further investigation. First it is necessary to obtain more complete and accurate observational data.

ACKNOWLEDGMENT

I thank A.V. Gurevich, K.P. Zybin, and G.V. Chibisov for valuable discussions.

REFERENCES

1. B. Paczyn´ski, Astrophys. J. **304**, 1 (1986).
2. C. Alcock, C. W. Akerlof, R. A. Allsman, *et al.*, Nature **365**, 621 (1993).
3. E. Aubourg, P. Bareyre, S. Brehin, *et al.*, Nature **365**, 623 (1993).
4. C. Alcock, R. A. Allsman, T. S. Axelrod, *et al.*, Phys. Rev. Lett. **74**, 2867 (1995).
5. C. Alcock, R. A. Allsman, D. Alves, *et al.*, Astrophys. J. **486**, 697 (1997).
6. T. Vandehei, K. Griest, C. Alcock, *et al.*, in *Abstract of the American Astronomy Society Meeting, 1998*, Vol. 192, Pap. No. 07.03.

7. C. Alcock, R. A. Allsman, D. Alves, *et al.*, Astrophys. J. **479**, 119 (1997).
8. F. Derue, C. Afonso, C. Alard, *et al.*, submitted to Astron. Astrophys. (1999); astro-ph/9903209.
9. A. Udalski, M. Szymanski, K. Z. Stanek, *et al.*, Acta Astron. **44**, 165 (1994).
10. A. F. Zakharov and M. V. Sazhin, Usp. Fiz. Nauk **168**, 1041 (1998).
11. A. F. Zakharov, *Gravitational Lenses and Microlenses* (Yanus, Moscow, 1997).
12. C. Alcock, R. A. Allsman, D. Alves, *et al.*, Astrophys. J. **518**, 44 (1999).
13. A. Udalski, M. Szymanski, S. Mao, *et al.*, Astrophys. J. Lett. **436**, L103 (1994).
14. C. Alcock, W. H. Allen, R. A. Allsman, *et al.*, Astrophys. J. **491**, 436 (1997).
15. W. Sutherland, C. Alcock, R. A. Allsman, *et al.*, in *Proceedings of the 1st International Workshop on the Identification of Dark Matter, Sheffield, UK*, Ed. by N. Spooner (World Sci., Singapore, 1996), p. 200; astro-ph/9611059.
16. C. Alcock, R. A. Allsman, D. Alves, *et al.*, Astrophys. J. Lett. **499**, L9 (1998).
17. C. Flynn, A. Gould, and J. Bahcall, Astrophys. J. Lett. **466**, L55 (1996).
18. A. V. Gurevich and K. P. Zybin, Phys. Lett. A **208**, 276 (1995).
19. A. V. Gurevich, K. P. Zybin, and V. A. Sirota, Usp. Fiz. Nauk **167**, 913 (1997).
20. A. V. Gurevich, K. P. Zybin, and V. A. Sirota, Phys. Lett. A **214**, 232 (1996).
21. A. V. Gurevich, K. P. Zybin, and V. A. Sirota, in *Proceedings of the 2nd Sakharov Conference on Physics, Moscow, 1996* (World Sci., Singapore, 1997), p. 127.
22. M. V. Sazhin, A. G. Yagola, and A. V. Yakubov, Phys. Lett. A **219**, 199 (1996).
23. D. L. Ossipov and V. E. Kuryan, Phys. Lett. A **223**, 157 (1996).
24. A. V. Gurevich and K. P. Zybin, Zh. Éksp. Teor. Fiz. **94** (1), 3 (1988) [Sov. Phys. JETP **67**, 1 (1988)].
25. A. V. Gurevich and K. P. Zybin, Usp. Fiz. Nauk **165**, 723 (1995) [Phys. Usp. **38**, 687 (1995)].
26. L. D. Landau and E. M. Lifshitz, *The Classical Theory of Fields* (Nauka, Moscow, 1988; Pergamon, Oxford, 1975, 4th ed.).
27. A. L. Zel'manov and V. G. Agakov, *Elements of the General Theory of Relativity* (Nauka, Moscow, 1989).
28. S. Weinberg, *Gravitation and Cosmology: Principles and Applications of the General Theory of Relativity* (Wiley, New York, 1972; Mir, Moscow, 1975).
29. D. Bennett, C. Alcock, R. Cook, *et al*., in *Abstract of the American Astronomy Society Meeting, 1995*, Vol. 187, Pap. No. 47.07.

Translation was provided by AIP

Journal of Experimental and Theoretical Physics, Vol. 90, No. 2, 2000, pp. 240–249.
Translated from Zhurnal Éksperimental'noĭ i Teoreticheskoĭ Fiziki, Vol. 117, No. 2, 2000, pp. 275–285.

ATOMS, SPECTRA, RADIATION

Description of Diffraction and Focusing of Ultrashort Pulses on the Basis of a Nonstationary Kirchhoff–Sommerfeld Method

E. M. Mikhaĭlov and P. A. Golovinskiĭ*

Voronezh State Architecture and Civil Engineering Academy, Voronezh, 394006 Russia
**e-mail: golovinsk@phys.vgasa.voronezh.su*

Received April 12, 1999

Abstract—The scalar problem of the propagation of a plane-wave pulse behind a diaphragm is solved. The calculation is performed on the basis of the nonstationary Kirchhoff–Sommerfeld integral and decomposition of the pulse in terms of wavelets. Two types of diaphragms, circular and square, are studied. The propagation of a pulse under focusing conditions is calculated. The Green's function of the diffraction problem for a circular opening with and without aberration-free focusing is constructed. *© 2000 MAIK "Nauka/Interperiodica".*

1. INTRODUCTION

More and more new experimental results are now being obtained in laser physics using pulses which are focused in space and compressed in time. This field is now an independent direction in the optics of femtosecond laser pulses [1]. The experimental observation of focusing of short laser pulses and nonlinear Thompson scattering [2, 3] as well as the generation of hard X-rays by focusing pulsed radiation on a metallic target [4] are very impressive. Various theoretical models, used to described pulses [5–7], as well as new proposed experiments on the interaction of pulses with electrons [8–11] are based on a description of laser radiation in the form of Gaussian beams [12, 13]. Estimates show that the series of laser types is approaching, with respect to their parameters, the physical limit in terms of energy extracted in one pulse. The natural reserve for further increasing the peak intensity of laser pulses lies in not only spatial focusing but also in maximum temporal compression of the pulses. A scheme has already been realized for one of the most promising titanium-sapphire lasers where the pulse duration is decreased to 5 fsec [14]. The pulse length becomes comparable to the wavelength, and the theory of quasistationary Gaussian wave beams [12, 13] is no longer applicable. The new experimental possibilities make it necessary to develop an adequate theory of diffraction and focusing of ultrashort pulses. A step in this direction has been made in [15] for the problem of the diffraction by an opening in an infinite flat screen on the basis of the nonstationary Kirchhoff–Sommerfeld diffraction approximation. In [15] it is shown that the theory of diffraction of monochromatic fields can be effectively extended to the strongly nonstationary case and the diffraction of a half-period of an electromagnetic pulse is studied.

At the same time these questions have attracted specialists on the pulse generation and propagation in the radio and microwave ranges. In [16] the author arrived, simultaneously with and independently of [15], at a nonstationary formulation of the Kirchhoff method and used this formulation to calculate the diffraction of a square pulse with infinite duration by a circular diaphragm. This formulation of the problem could be of interest in acoustics and other applications where linear diffraction of ultrashort pulses occurs under weak dispersion conditions. We note that while making definite progress in the correct formulation of the problem, the works [15, 16] do not completely resolve the problem of diffraction and focusing of ultrashort pulses. Thus, in [15] the question of constructing unified methods for calculating the diffraction of ultrashort pulses of arbitrary shape remains open. The solution contained in [16] for a step pulse makes it possible in principle to elaborate the theory further for pulses of arbitrary shape on the basis of the Duhamel integral, but this extension is not made. For the problem of focusing of ultrashort pulses, it is touched upon only in passing in [15], and the problem is not posed at all in [16]. The present paper is devoted to the development of a systematic approach to the construction of a theory of diffraction and focusing of ultrashort pulses on the basis of the application of wavelets and the construction of the nonstationary Green's functions as the response to a delta-function pulse. The scalar approximation is used in this paper.

The classical stationary Kirchhoff method for solving diffraction problems consists of using an integral theorem according to which the value of a function ψ, which is a solution of the scalar Helmholtz equation, at an arbitrary point $M(x, y, z)$ inside a closed volume is expressed in terms of the value of the function ψ and its first derivative on the surface bounding this volume [17]. The Kirchhoff method is an adequate mathematical expression of the Huygens–Fresnel principle, according to which the disturbance at a point in space M is a result of the interference of waves emitted by

secondary sources. These sources lie on a surface located between the point M and the real source of the waves. A nonstationary expression relating the value of the field ψ on the boundary and inside a closed region of space, can also be obtained [18]. If there are no field sources inside the volume, Kirchhoff's theorem holds:

$$\psi = \int_{-\infty}^{\tau} dt' \int_{S(V)} \psi \nabla G(\mathbf{R}, t-t') - G(\mathbf{R}, t-t') \nabla \psi d\mathbf{S} = \frac{1}{4\pi} \int_{S(V)} \left(\frac{1}{R} \nabla - \frac{1}{cR} \nabla R \frac{\partial}{\partial t} - \nabla \frac{1}{R} \right) \psi \Big|_{t' = t - R/c} d\mathbf{S}, \quad (1)$$

where

$$\mathbf{R} = \mathbf{r} - \mathbf{r}',$$

and

$$G(\mathbf{R}, t-t') = \begin{cases} 0, & t < t' \\ -\dfrac{c}{4\pi} \dfrac{\delta(R - c(t-t'))}{R}, & t > t' \end{cases}$$

is the Green's function of the nonstationary scalar wave equation, which describes the propagation of a wave from a point with radius vector $\mathbf{r}'$ at time t' to a point with radius vector $\mathbf{r}$ at time t.

We shall use this formula to determine the field of a wave transmitted through a screen with an opening. The value of the field at the point of interest is determined only by the values of the field and its derivative on the first surface of the shadow side of the screen and the opening. The approximate Kirchhoff boundary conditions correspond to the following assumptions: ψ and $\nabla\psi$ vanish everywhere except at the openings; in the openings the values of ψ and $\nabla\psi$ are the same as in the absence of a screen. For quasistationary fields these approximations are, as a rule, quite accurate.

Sommerfeld's method [18] for choosing the Green's function eliminates the need to give simultaneously the boundary conditions for the field and its derivative along the normal when studying diffraction by a screen. The corresponding nonstationary Green's functions

$$G_{\mp} = -\frac{c}{4\pi} \frac{\delta(|\mathbf{r} - \mathbf{r}'| - c|t-t'|)}{|\mathbf{r} - \mathbf{r}'|} \mp \frac{c}{4\pi} \frac{\delta(|\mathbf{r} - \mathbf{r}_1'| - c(t-t'))}{|\mathbf{r} - \mathbf{r}_1'|},$$

where $\mathbf{r} = (x, y, z)$ are the coordinates of the observation point, $\mathbf{r}' = (\xi, \eta, -\zeta)$ are the coordinates of the field source, and $\mathbf{r}_1' = (\xi, \eta, \zeta)$ are the coordinates of the image field source symmetric to the real source about the surface of a flat screen.

We shall employ the substitution of G_+ in the Kirchhoff integral (1). This procedure is more convenient in nonstationary calculations. The result is

$$G_+ = 0,$$

$$\nabla G_+ = -2 \frac{c}{4\pi} \frac{\partial}{\partial \zeta} \frac{\delta(R - c(t-t'))}{R}, \quad (2)$$

$$\psi = \int_{-\infty}^{\tau} dt' \int_{S(V)} \psi \nabla G_+ d\mathbf{S} = \frac{1}{2\pi} \frac{\partial}{\partial z} \int_S \frac{\psi(\xi, \eta, \zeta, t')}{R} \Big|_{\zeta = 0,\, t' = t - R/c} dS, \quad (3)$$

where the fact that $\partial/\partial\zeta = -\partial/\partial z$ has been taken into account.

If ψ on the right-hand side of equation (3) is replaced by the unperturbed value of the field, then we obtain a method for calculating nonstationary diffraction problems on the basis of the nonstationary Kirchhoff–Sommerfeld integral.

2. TRANSMISSION OF A PULSE THROUGH A SQUARE OPENING

We shall now consider the transmission of an electromagnetic plane-wave pulse through a square opening. We shall consider a wavelet as the profile of a plane wave [19, 20].

The wavelets consist of a complete orthonormal set of functions that is different from the Fourier set. This set makes it possible to represent a function as a series expansion with respect to such a set. The entire z axis can be covered using appropriate transformations of a localized function which rapidly approaches zero. Obvious operations are translation along the axis and scaling of the argument in order to reproduce the scale of the nonuniformities.

If scaling in powers of two is used for definiteness, then the generated set of functions is $\psi(2^j z - k)$, where j and k are integers

A basic wavelet from which the entire set of wavelet functions is obtained by translations and dilatations is taken as the basis. We introduce the scalar product

$$\langle p, q \rangle = \int_{-\infty}^{\infty} p(z) q^*(z) dz$$

and the norm $\|p\| = \langle p, p \rangle^{1/2}$. If the generating function ψ is normalized, then the normalized wavelets of the family $\{\psi_{jk}\}$ have the form

$$\psi_{jk}(z) = 2^{j/2} \psi(2^j z - k).$$

The family $\{\psi_{jk}\}$ forms an orthonormalized basis, so that

$$\langle \psi_{jk}, \psi_{lm} \rangle = \delta_{jl} \delta_{km},$$

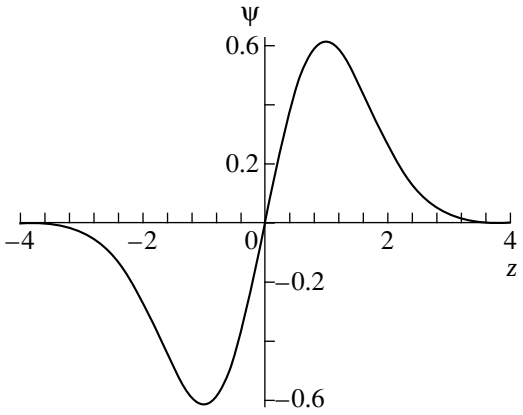

Fig. 1. Shape of the basic wavelet with $a = 1$ and $b = 0$.

and each function $f \in L^2(R)$ can be represented as a uniformly converging series

$$f(z) = \sum_{j,k=-\infty}^{\infty} c_{jk}\psi_{jk}(z).$$

For example, a function of the form [19]

$$\psi_m(z) = (-1)^m \partial_z^m \exp(-z^2/2) \tag{4}$$

with fixed m can be taken as the basic wavelet. We shall take the basic wavelet (4) with $m = 1$ (Fig. 1), i.e.,

$$\psi_1(z) = \frac{z-b}{a}\exp\left(-\frac{(z-b)^2}{2a^2}\right).$$

This wavelet resembles a characteristic ultrashort pulse. Let such an initial pulse distribution along the z axis be given. Then, it corresponds to a plane wave propagating along this axis

$$\Psi(\mathbf{r}, t) = \psi_1(z-ct) = \frac{(z-ct-b)}{a} \times \exp\left(-\frac{(z-ct-b)^2}{2a^2}\right). \tag{5}$$

A pulse of arbitrary shape can be expanded in terms of wavelets, the diffraction of each of which is described by equation (3) with the unperturbed field substituted on the right-hand side. Since the problem is linear, the result of diffraction will be a superposition of the corresponding solutions for individual wavelets with the weights of the initial expansion.

Let us substitute the basic wavelet into the nonstationary Kirchhoff–Sommerfeld integral. Then

$$\psi(\mathbf{r}, t) = \frac{1}{2\pi}\frac{\partial}{\partial z}\int_{S(V)} \frac{\Psi(\xi, \eta, 0, t-R/c)}{R}dS = \frac{1}{2\pi}\frac{\partial}{\partial z}\int_{S(V)} \frac{\Psi(R-ct)}{R}dS, \tag{6}$$

where the variables ξ, η, 0 are the coordinates of points in the diaphragm plane, over which the integration extends, $dS = d\xi d\eta$. Using equation (5) we obtain

$$\psi(\mathbf{r}, t) = \frac{1}{2\pi a} \times \frac{\partial}{\partial z}\int_{S(V)} \frac{(R-\tau)\exp(-(R-\tau)^2/2a^2)}{R}dS, \tag{7}$$

where $\tau = ct + b$.

To calculate the integral we shall differentiate the integral with respect to a parameter and represent the formula (7) in the form

$$\psi(\mathbf{r}, r) = \frac{a}{2\pi}\frac{\partial}{\partial z}\frac{\partial}{\partial \tau}\int_{S(V)} \frac{\exp(-(R-\tau)^2/2a^2)}{R}dS. \tag{8}$$

Let the distance from the point under study to the diaphragm be much greater than the dimensions of the diaphragm and let $R \approx r = \sqrt{x^2 + y^2 + z^2}$.

We now represent the vector $\mathbf{R}$ as a difference of vectors $\mathbf{R} = \mathbf{r} - \rho\mathbf{e}$, where $\mathbf{r} = (x, y, z)$ is the radius vector drawn from the center of the diaphragm to the point of observation of the field and $\mathbf{e}$ is a unit vector in the polar direction to the running integration point. Then

$$R = \sqrt{r^2 + \rho^2 - 2\rho\mathbf{e}\cdot\mathbf{r}} \approx r + \frac{\rho^2 - 2\rho(\mathbf{e}\cdot\mathbf{r})}{2r},$$
$$(R-\tau)^2 = \Delta^2 + \Delta\frac{\rho^2 - 2r\rho\cos\theta}{r} + \frac{(\rho^2 - \rho r\cos\theta)^2}{4r^2}, \tag{9}$$

where $\Delta = r - \tau$ and $\rho = \sqrt{\xi^2 + \eta^2}$. The event $\Delta = 0$ means that the central part of a wave pulse from the point (0, 0, 0) on the diaphragm surface has arrived at the point of observation (x, y, z). In the expression (9), θ is the angle between the vectors $\mathbf{r}$ and $\mathbf{e}$. The last term complicates the calculation of the integral (8). In general it cannot be neglected, since it is not small. For this reason, to perform calculations in all space the integral must be calculated numerically. Analytical results can be obtained near the axis. This is often of greatest interest. In this region the parameter $\rho/r \ll 1$. In this approximation we have

$$(R-\tau)^2 = \left[\Delta^2 + \frac{\Delta}{r}(\rho^2 - 2(x\xi + y\eta)) + \frac{(\rho^2 - 2(x\xi + y\eta))^2}{4r^2}\right],$$

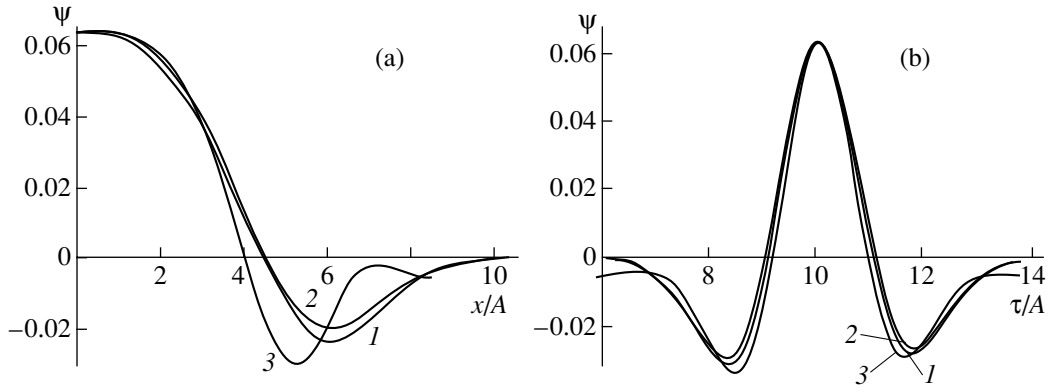

Fig. 2. The field Ψ at the point (0, 0, 10*A*) in the cross-section (a) as a function of the distance *x*/*A* and (b) as a function of the time parameter τ/*A*: *1*—the result of an approximate calculation using equation (14), *2*—the result of a direct numerical integration; and *3*—the result of the calculation by the method of quasistationary Gaussian beams [1].

and the integral in equation (8) can be rewritten as

$$\int \frac{\exp(-(R-\tau)^2/2a^2)}{R} dS = \frac{\exp(-\Delta^2/2a^2)}{r} \times \int \exp\left(-\frac{\Delta}{2a^2 r}\{\rho^2 - 2(x\xi + y\eta)\}\right) d\xi d\eta. \quad (10)$$

When integrating over a square aperture of size $2A \times 2A$ the auxiliary integral factorizes:

$$\int_{-A}^{A}\int_{-A}^{A} \exp[-\alpha(\xi^2 + \eta^2 - 2(x\xi + y\eta))] d\xi d\eta = \int_{-A}^{A} \exp(-\alpha(\xi^2 - 2x\xi)) d\xi \times \int_{-A}^{A} \exp(-\alpha(\eta^2 - 2y\eta)) d\eta = I(x)I(y). \quad (11)$$

The integrals containing the parameters x and y separated. They are identical and can be calculated separately:

$$I(x) = \int_{-A}^{A} \exp(-\alpha(\xi^2 - 2x\xi)) d\xi = \frac{\sqrt{\pi} e^{\alpha x^2}}{2\sqrt{\alpha}} \times [\mathrm{erf}(\sqrt{\alpha}(A - x)) - \mathrm{erf}(-\sqrt{\alpha}(A + x))], \quad (12)$$

where the error function is [21]

$$\mathrm{erf}(x) = \frac{2}{\sqrt{\pi}} \int_0^x \exp(-t^2) dt.$$

Then

$$\int_{-A}^{A} d\xi \int_{-A}^{A} d\eta \frac{\exp(-(R-\tau)^2/2a^2)}{R} = \frac{\exp(-\Delta^2/2a^2)}{r} I(x)I(y),$$

where $I(x)$ is determined by equation (12), and $\alpha = \Delta/2a^2 r$. Therefore the scalar potential is

$$\psi(\mathbf{r}, t) = \frac{a}{2\pi} \frac{\partial}{\partial z} \frac{1}{r} \frac{\partial}{\partial \tau} \exp\left(-\frac{\Delta^2}{2a^2}\right) I(x)I(y). \quad (13)$$

Since the entire dependence of $I(x)$ and $I(y)$ on z and τ is contained in the parameter α, the derivatives of the integral I can be represented in the form

$$\frac{\partial}{\partial z} I(x) = \frac{\partial I(x)}{\partial \alpha} \frac{\partial \alpha}{\partial z} = I'_\alpha(x) \frac{\partial \alpha}{\partial z}.$$

After calculating the derivatives, we obtain

$$\psi(\mathbf{r}, t) = \frac{a}{2\pi} \exp\left(-\frac{\Delta^2}{2a^2}\right) \left[\left(\frac{z}{a^2 r^2} - \frac{\Delta}{a^2 r^2} - \frac{z\Delta^2}{a^4 r^2}\right) \times I(x)I(y) + \left(\frac{1}{2a^2 r^3} + \frac{\Delta z}{2a^4 r^3} - \frac{\Delta \tau z}{2a^4 \tau^4} + \frac{z}{2a^2 r^4}\right) \times (I'_\alpha(x)I(y) + I'_\alpha(x)I(x)) + \frac{\tau z}{a^4 r^5} \times (I''_{\alpha\alpha}(x)I(y) + 2I'_\alpha(x)I'_\alpha(y) + I(x)I''_{\alpha\alpha}(y))\right]. \quad (14)$$

Figures 2a and 2b display the results of the calculations of the diffraction for a square diaphragm with side A at the point (0, 0, 10*A*). The radiation pulse had the form of a wavelet (5) with the parameters $a = A$ and $b = 0$. A comparison shows that the numerical integration using the formula (8) agrees well with calculations

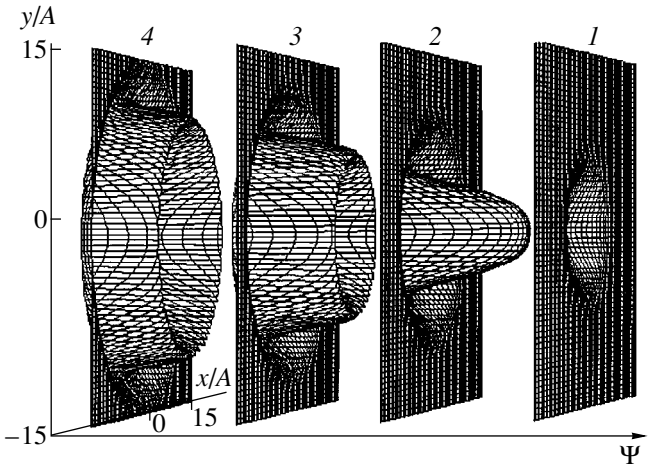

Fig. 3. Transverse distribution of the field $\Psi(x, y)$ of a diffracted pulse in the plane $z = 10A$ at different moments in time $\tau/A = 8$ (*1*), 10 (*2*), 12 (*3*), 14 (*4*).

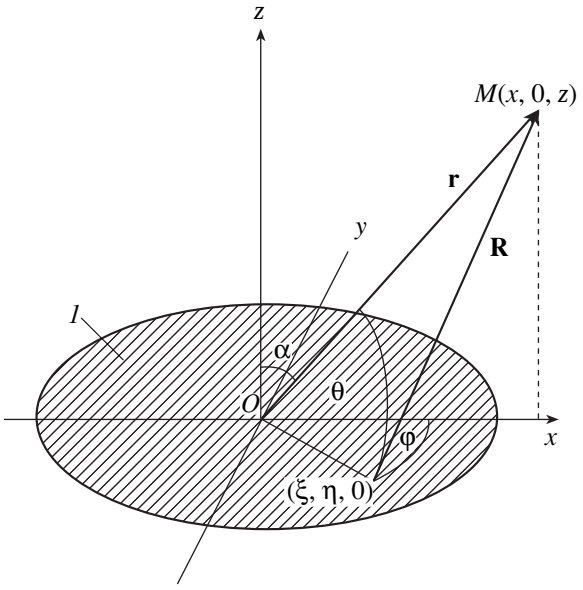

Fig. 4. System of coordinates for calculating the Kirchhoff integral in the case of a circular diaphragm (*1*): $M(x, 0, z)$ point of observation of the field, α—angle between the vector **r** and the *z* axis, φ—polar angle of the vector $(\xi, \eta, 0)$ in the plane of the diaphragm, θ—angle between the vectors **r** and ρ**e**.

using the approximate formula (14). The discrepancy between the numerical and analytic calculations does not exceed 3%. It is interesting to note that the form of the pulse found by direct numerical integration is more asymmetric relative to the center of the pulse, in contrast to the form calculating using the approximate formula. A calculation by the method of quasistationary Gaussian beams was performed for the time $t = 0$, since this method assumes simultaneous modulation of the entire pulse along the *z* axis. A comparison shows that the method of quasistationary Gaussian beams reproduces satisfactorily the longitudinal structure of the pulse after the diaphragm but agrees poorly with the more accurate calculations for the transverse distribution of the field. This is because the phase relations between the plane-wave components of the pulse are not adequately taken into account in the method of quasistationary Gaussian beams.

Figure 3 displays the transverse distribution of the field of a wave in the $z = 10A$ plane at different moments in time. It is evident that before the maximum value of the scalar potential of the wave there is a region with the opposite value of the potential, which does not occur in the initial pulse (5). In time, the maxima of the field shift away from the *z* axis and decrease in amplitude.

3. TRANSMISSION OF A PULSE THROUGH A CIRCULAR OPENING

We shall now consider the transmission of an electromagnetic plane wave through a circular opening. Once again we take a wavelet as the profile of the plane wave.

We shall calculate the integral in equation (8) in cylindrical coordinates. We choose a coordinate system in which the polar axis is oriented along the *z* axis. We place the **r** vector in the *xz* plane, as shown in Fig. 4. Assuming the function $1/R$ to be slowly varying, we remove $1/r$ from the integrand and write

$$\psi(\mathbf{r}, t) = \frac{a}{2\pi}\frac{\partial}{\partial z}\frac{\partial}{\partial \tau}\frac{I}{r}, \tag{15}$$

where

$$I = \int_0^{2\pi} d\varphi \int_0^A \exp\left(-\frac{(R-\tau)^2}{2a^2}\right)\rho\, d\rho, \tag{16}$$

φ is the polar angle, and *A* is the radius of the opening. Let the point of interest lie at a distance from the diaphragm that is large compared with the dimensions of the diaphragm, $r \gg A$. Then

$$R = \sqrt{r^2 + \rho^2 - 2\rho\cos\theta} \approx r + \frac{\rho^2 + 2\rho\cos\theta}{2r},$$

$$R - \tau \approx \Delta + \frac{\rho^2 - 2\rho\cos\theta}{2r}.$$

On the basis of Fig. 4 we obtain

$$\tan\theta = \cos\varphi\tan\alpha,$$

where α is the angle between the *z* axis and the vector **r**. Hence

$$\cos\theta = \frac{\cot\theta}{\sqrt{1-\cot^2\theta}} = \frac{\cos\varphi\tan\alpha}{\sqrt{1+\cos^2\varphi\tan^2\alpha}}. \tag{17}$$

We introduce the parameter $\beta = \tan\alpha = \sqrt{x^2 + y^2}/z$. It follows from equation (17) that, up to the second

order in β,

$$\cos\theta = \frac{\beta\cos\varphi}{\sqrt{1+\beta^2\cos^2\varphi}} \approx \beta\cos\varphi. \qquad (18)$$

Using the symmetry of the problem and the approximations made above, we can obtain an analytic answer on the radiation axis. In this case, integrating in the plane of the diaphragm, $\cos\theta$ is always zero. For this reason, the integral over φ is 2π and we have instead of equation (16)

$$I = 2\pi\int_0^A \exp\left(-\frac{1}{2a^2}\left(\Delta+\frac{\rho^2}{2r}\right)\right)\rho d\rho$$
$$= 2\pi\left[ar\sqrt{\frac{\pi}{2}}\left\{\mathrm{erf}\left(\frac{\sqrt{2}(A^2+2\Delta r)}{4ar}\right)-\mathrm{erf}\left(\frac{\Delta}{a\sqrt{2}}\right)\right\}\right]. \qquad (19)$$

Substituting the expression obtained into equation (15) for ψ, we obtain

$$\psi(\mathbf{r},t) = -\frac{\Delta z}{ar}\exp\left(-\frac{\delta^2}{2a^2}\right)+\frac{z}{2ar^2}$$
$$\times\left[(A^2+2\Delta r)\left(1+\frac{\Delta}{r}\right)-\frac{1}{2r^2}(A^2+2\Delta r)^2\right] \qquad (20)$$
$$\times\exp\left(\frac{A^2+2\Delta\rho}{8a^2r^2}\right).$$

We now consider the field in the region near the axis. For this, we expand the integrand in equation (16) in powers of $\cos\theta$:

$$\exp\left(-\frac{(R-\tau)^2}{2a^2}\right) = \exp\left(-\frac{(\Delta+\rho^2/2r)^2}{2a^2}\right)$$
$$+\frac{\rho}{a^2}\left(\Delta+\frac{\rho^2}{2r}\right)\exp\left(-\frac{(\Delta+\rho^2/2r)^2}{2a^2}\right)\cos\theta+\ldots. \qquad (21)$$

We now take account of the fact that $\cos\theta$ in our approximation is determined by equation (18) and that

$$\int_0^{2\pi}\cos\varphi d\varphi = 0.$$

Up to second order in the parameter β, the integrand in the expression of equation (16) is determined by the first term in equation (21). Therefore, in the region near the axis, to second order in the parameter β, the scalar potential ψ is once again determined by the formula (20).

Figure 5 shows the temporal form of the diffracted pulse on the radiation axis as a function of the characteristic length a/A of the initial pulse. It is evident that for a sufficiently short pulse, for $a < A^2/2z$, the result has the form of two wavelets separated in time by $\Delta t = A^2/2zc$. This agrees with the results of [15] for the diffraction of a half-wave pulse.

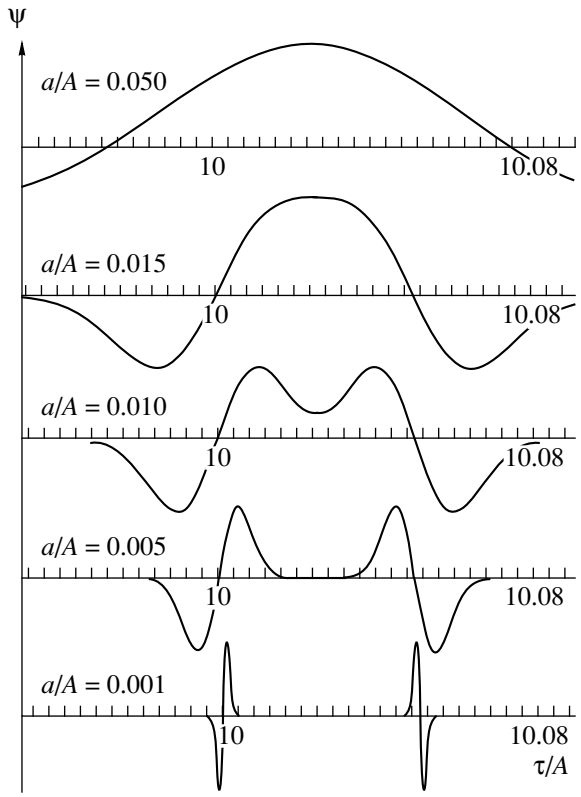

Fig. 5. Behavior of the diffracted pulse Ψ as a function of time τ/A for various values of the ratio of the pulse length a to the radius A of the aperture of the diaphragm.

4. ABERRATION-FREE FOCUSING OF A PULSE

The nonstationary Kirchhoff–Sommerfeld method also makes it possible to study focusing of a pulse. To describe the diffraction of a plane wave on the basis of equation (8), we used the fact that the value of the incident wave is constant on the aperture of the diaphragm. The corresponding flat surface is described by the equation $\zeta = 0$. The action of the focusing apparatus, lying in the diaphragm plane, reduces to distortion of the flat wavefront and transformation of the wavefront into a spherical front. Depending on the convexity of the spherical front, the transmitted wave will be focused or defocused. The equation of a sphere centered at the focal point of the optical system with radius vector $\mathbf{F}$ is $\tilde{r}_\pm = |\mathbf{r}-\mathbf{F}| = \sqrt{(z\pm F)^2+x^2+y^2}$. Here, the minus sign corresponds to focusing and the plus sign corresponds to defocusing. Introducing the equation of a sphere, instead of the equation of a plane, and making the

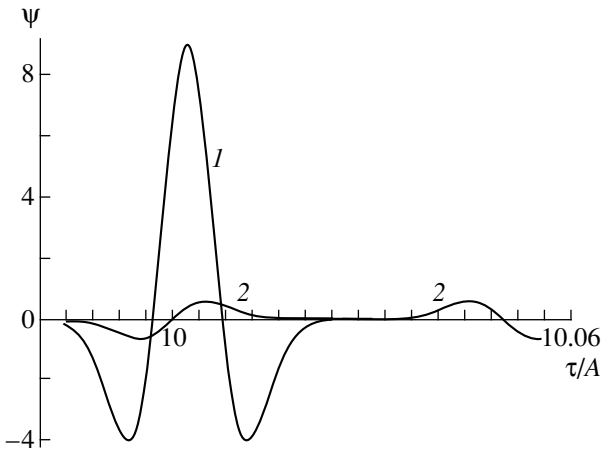

Fig. 6. Comparison of the time dependence of the field Ψ of focused (*1*) and unfocused (*2*) pulses near the focal point.

substitution $z - ct \longrightarrow \tilde{r}_\pm \pm ct - F$ in the phase of the diffracting wave in equation (6), we obtain

$$\psi = \frac{1}{2\pi}\frac{\partial}{\partial z}\int \frac{\Psi(\tilde{r}_\pm \pm ct' - F)}{R}\bigg|_{\zeta = 0,\, t' = t - R/c} dS. \qquad (22)$$

Let the focal length be $F \gg A$, where A are the characteristic dimensions of the diaphragm. Then the distance from the focal point (imaginary focus) to a point in the diaphragm plane can be approximately described as

$$\tilde{r}_\pm = \sqrt{F^2 + \xi^2 + \eta^2} \approx F + \frac{\xi^2 + \eta^2}{2F} = F + \frac{\rho^2}{2F},$$

and equation (22) can be rewritten in the form

$$\psi = \frac{1}{2\pi}\frac{\partial}{\partial z}\int_S \frac{\Psi(\rho^2/2F \pm (ct - R))}{R} dS. \qquad (23)$$

In the limit $F \longrightarrow \infty$, the expression (23) becomes the formula (6) for a plane wave.

Let us now consider the diffraction of a wavelet (5) by a circular opening in the presence of focusing (defocusing). The auxiliary integral (16) now assumes the form

$$I_f = \int_0^{2\pi} d\varphi \int_0^A \exp\left(-\left(R - \tau \pm \frac{\rho^2}{2F}\right)^2 / 2a^2\right)\rho\, d\rho. \qquad (24)$$

In the near-axis approximation, just as in the case without focusing, we have

$$R - \tau \pm \frac{\rho^2}{2F} \approx \Delta + \frac{\gamma\rho^2 - 2\rho\cos\theta}{2r},$$

where $\gamma = 1 \pm r/F$ is the focusing parameter. Once again, we expand the integrand in equation (24) in a series in the small parameter $\cos\theta$:

$$\exp\left(-\frac{(R - \tau \pm \rho^2/2F)^2}{2a^2}\right) = \exp\left(-\frac{(\gamma\Delta + \gamma\rho^2/2r)^2}{2a^2}\right)$$
$$+ \frac{\rho}{a^2}(\Delta + \gamma\rho^2/2r)\exp\left(-\frac{(\Delta + \gamma\rho^2/2r)^2}{2a^2}\right)\cos\theta + \ldots. \qquad (25)$$

Similarly to the planar case, the integral of the second term in equation (25) vanishes. As a result,

$$I_f = 2\pi$$
$$\times\left[\frac{ar}{\gamma}\sqrt{\frac{\pi}{2}}\left\{\mathrm{erf}\left(\frac{\sqrt{2}(\gamma A^2 + 2\Delta r)}{4ar}\right) - \mathrm{erf}\left(\frac{\Delta}{a\sqrt{2}}\right)\right\}\right]. \qquad (26)$$

Performing the differentiation we obtain the answer

$$\psi(\mathbf{r}, t) = -\frac{az}{\gamma r}\left(\frac{1}{\gamma F} - \frac{\Delta}{a^2}\right)\exp\left(-\frac{\delta^2}{2a^2}\right)$$
$$+ \frac{az}{\gamma r}\left[\frac{(\gamma A^2 + 2\Delta r)}{4a^2 r}\left(2 + \frac{2\Delta}{r} - \frac{A^2}{rF}\right)\right. \qquad (27)$$
$$\left. - \frac{1}{4a^2 r^3}(\gamma A^2 + 2\Delta r)^2 - \frac{1}{\gamma F}\right]\exp\left(\frac{(\gamma A^2 + 2\Delta r)}{8a^2 r^2}\right).$$

The expression obtained describes the focusing of a pulse for a negative sign of F and defocusing for a positive sign. Figure 6 displays the results of the calculation of the time dependence of the focused and unfocused pulse near the focal point. It is evident that the unfocused pulse has separated into two wavelets, while the focused pulse consists of a single pulse. The focusing apparatus gives, in accordance with Fermat's principle, the same optical path difference for different rays arising at the focal point. For this reason, the temporal form of the pulse is not distorted. Away from the focal point such compensation is lost and the form of the pulse becomes distorted, just as in the case without focusing.

5. GREEN'S FUNCTION FOR THE PROBLEM OF NONSTATIONARY DIFFRACTION OF A PLANE WAVE

A convenient and universal method for solving linear problems in which it is necessary to find the response of a system to an arbitrary disturbance is to construct the response to a δ-function pulse, i.e., the Green's function $g(\mathbf{r}, t)$.

We shall now consider the transmission of a δ-function pulse through a circular opening. Substituting a

δ-function pulse into the nonstationary Kirchhoff–Sommerfeld integral (6), we obtain

$$g(\mathbf{r}, t) = \frac{1}{2\pi}\frac{\partial}{\partial z}\int\limits_S \frac{\delta(R-\tau)}{R}dS. \qquad (28)$$

We now choose a new coordinate system K' whose origin coincides with the projection of the point (x, y, z) on the diaphragm plane. The $O'z'$ axis is parallel to the Oz axis and the $O'x'$ axis passes through the center of the diaphragm, as shown in Fig. 7. In this coordinate system $z = z'$, $y = y'$, and $R = \sqrt{\rho'^2 + z^2}$ is the distance from the point near the diaphragm to the point under study, and $\rho' = \sqrt{x'^2 + y'^2}$,

$$dR = \frac{2\rho' d\rho'}{R}. \qquad (29)$$

Switching in the integral appearing in equation (28) to integration in polar coordinates ρ' and φ' and using equation (29) we obtain

$$g(\mathbf{r}, t) = \frac{1}{4\pi}\frac{\partial}{\partial z}\int\int \delta(R-\tau)d\varphi dR = \frac{1}{4\pi}\frac{\partial}{\partial z}\phi. \qquad (30)$$

Here, ϕ is the angle which rests on the arc cut by the diaphragm from a circle centered at the origin of the coordinate system K'. This arc consists of the geometric locus of the points located at a distance $\tau = ct$ to which the light propagated from the points in the opening of the diaphragm in the time t from the point of observation of the field (x, y, z). The expression (30) must be interpreted in the sense that

$$\begin{cases} R = \tau \\ \phi = \phi(\tau). \end{cases} \qquad (31)$$

We shall now find an analytical expression for the quantity ϕ. It is evident from Fig. 7 that the $O'x'$ axis is the symmetry axis. For this reason

$$\cos\frac{\phi}{2} = \frac{x'}{\sqrt{x'^2 + y'^2}}.$$

The system of equations for determining the coordinates of the intersection of two circles, one of which is centered at the origin of the coordinate system K' and has radius $\sqrt{x'^2 + y'^2}$ while the other is centered at the origin of the coordinate system K and has radius A, is

$$\begin{cases} x'^2 + y'^2 = \tau^2 - z^2 \\ \left(x' - \sqrt{x^2 + y^2}\right)^2 + y'^2 = A^2. \end{cases}$$

Expanding the brackets and subtracting the first equation from the second equation, we obtain

$$\tau^2 - z^2 - 2x'\sqrt{x^2 + y^2} + x^2 + y^2 = A^2,$$

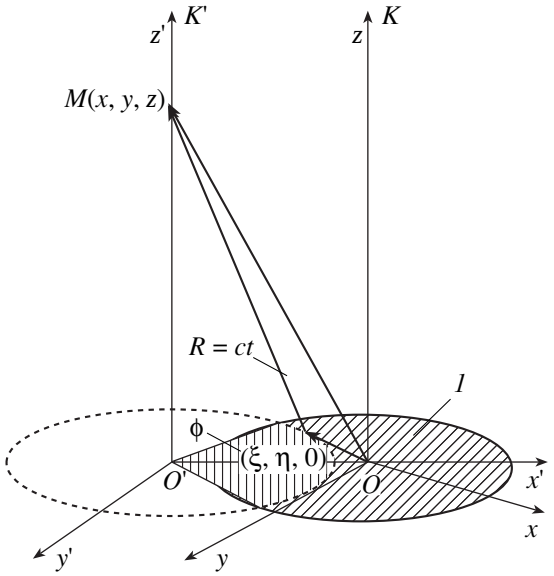

Fig. 7. Coordinate systems K and K' of the Green's function g in the problem of the transmission of a pulse through a circular diaphragm: $M(x, y, z)$—point of observation of the field, *1*—aperture of the diaphragm, ϕ—angle of observation of the arc of a circle from the center O' of the coordinate system K'.

whence

$$x' = \frac{1}{2}\left(\frac{\tau^2 - z^2 + x^2 + y^2 - A^2}{\sqrt{x^2 + y^2}}\right),$$
$$y' = \pm\sqrt{\tau^2 - z^2 - x'^2}. \qquad (32)$$

The condition for the existence of a solution is that the radicand in the equation for y' is positive. Physically, this means that a solution exists if light from the diaphragm has arrived, otherwise $\phi = 0$. Thus,

$$\phi = \begin{cases} 0, & x'^2 < \tau^2 - z^2 \\ 2\arccos\dfrac{x'}{\sqrt{x'^2 + y'^2}}, & x'^2 > \tau^2 - z^2. \end{cases} \qquad (33)$$

If the observation point lies on the axis of the diaphragm, then at any moment in time, when there is enough time for the light to arrive from the diaphragm, the angle ϕ is always 2π, i.e.,

$$\phi = \begin{cases} 0, & \tau^2 - z^2 < 0 \\ 2\pi, & x'^2 > \tau^2 - z^2 \\ 0, & x'^2 < \tau^2 - z^2. \end{cases} \qquad (34)$$

To obtain an expression for the Green's function the formula (34) must be differentiated with respect to z. We shall take account of the fact that the derivative of a unit jump is a δ-function. Then the scalar potential of the field on the radiation axis acquires the character of

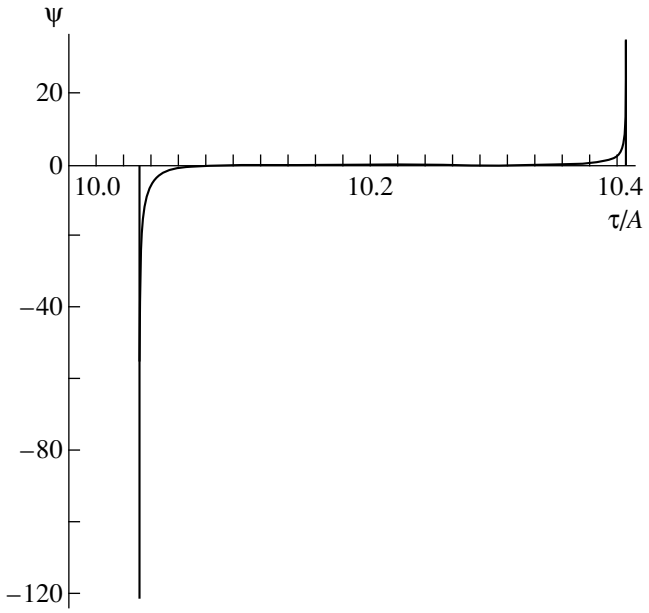

Fig. 8. Spatial distribution of the Green's function along the x axis in the problem of the passage of a plane wave through a diaphragm at the time $\tau/A = 10.5$ and $z/A = 10$.

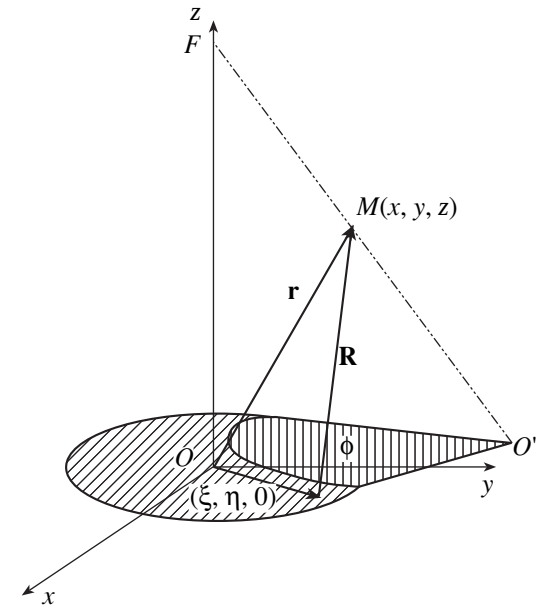

Fig. 9. Coordinate system for calculating the Green's function g_f in the problem of focusing of a pulse: $M(x, y, z)$—point of observation of the field, ϕ—angle of observation of the arc of a circle from the point $O'(xF/(F-r), yF/(F-r), 0)$, F—coordinate of the focus.

two δ-function pulses which are separated in time by $\Delta t = (\sqrt{z^2 + A^2} - z)/c$ and have opposite signs, as shown in Fig. 8. A similar situation is noted in [15], where diffraction of a half-wave pulse of finite width by a circular diaphragm is studied. In [15] it is shown that the energy density of the transmitted wave in the region $\Delta t > \tau_0$ (τ_0 is the duration of the incident pulse) is doubled. The form of the scalar potential changes as the observation point moves in a plane perpendicular to the propagation axis of the wave. The front delta-shaped pulse is broadened, and this broadening becomes maximum for points lying above the boundary of the diaphragm. The second pulse does not undergo strong changes.

We shall now construct the Green's function g_f in the problem of focusing of a pulse, for which once again we use the initial δ-function pulse and the minus sign in equation (22), corresponding to focusing. To calculate the corresponding integral it is necessary to determine the conditions under which the argument of the delta function vanishes. We switch from integration over the surface to integration over the volume. Then

$$g_f(\mathbf{r}, t) = \frac{1}{2\pi}\frac{\partial}{\partial z}\int_V \frac{\delta(r - R + ct - F)\delta(\zeta)}{R} d\xi d\eta d\zeta. \quad (35)$$

The two δ-functions give in space a curve in the form

$$\begin{cases} R - r + \tau - F = 0 \\ \zeta = 0, \end{cases} \quad (36)$$

where R is the distance from a point in the diaphragm to the point of observation, and r is the distance from the focus to a point on the diaphragm. The first equation in equation (36) gives a hyperboloid of revolution with foci at the observation point and at the focal point of the optical system. The second equation gives the plane of the diaphragm. The system of equations (36) describes the line of intersection of a hyperboloid of revolution and a plane, i.e., an ellipse.

Let us now consider the long focal-length approximation, where the diaphragm is small compared with the focal distance and the distance to the observation point, i.e., $A \ll F$ and $A \ll r$. Then the argument of the δ-function can be expanded in the small parameter $\sqrt{\xi^2 + \eta^2}/r$:

$$r - R + \tau - F \approx -\Delta - \left(\frac{r - R}{2rR}\right)(\xi^2 + \eta^2) + \frac{1}{r}(x\xi + \eta y),$$

where $\Delta = r - \tau$. Using the properties of the delta function

$$\delta(-x) = \delta(x), \quad \delta(ax) = \frac{1}{|a|}\delta(x),$$

we obtain

$$\delta\left(-\Delta - \frac{r - F}{2rF}(\xi^2 + \eta^2) + \frac{1}{r}(x\xi + y\eta)\right)$$

$$= \frac{2rF}{r - F}\delta\left(\xi^2 + \eta^2 - \frac{2F}{r - F}(x\xi + y\eta) + \frac{2rF\Delta}{r - F}\right)$$

$$= \frac{2rF}{r-F}\delta\left(\left(\xi - \frac{Fx}{r-F}\right)^2 + \left(\eta - \frac{Fy}{r-F}\right)\right.$$

$$\left. + \frac{2rF\Delta}{r-F} - \frac{F^2}{(r-F)^2}(x^2+y^2)\right).$$

Setting the argument of the δ-function equal to zero gives the equation of a line on which the integrand will be different from zero. Under the assumptions made this is an equation of a circle that is centered at the point O' and has the coordinates $(2xF/(r-F), 2yF/(r-F))$. If the origin of the coordinate system is transferred to the center and the coordinates are transformed to polar coordinates, then the Green's function can be written in the form

$$g_f(\mathbf{r}, t) = \frac{F}{2\pi}\frac{\partial}{\partial z}\frac{\phi}{r-F}, \qquad (37)$$

where ϕ is the angle cut by a circle of radius ρ' (Fig. 9) from the diaphragm.

CONCLUSIONS

The analysis of the diffraction of extremely short pulses on the basis of the nonstationary Kirchhoff–Sommerfeld integral demonstrates that the Huygens–Fresnel principle needs to be modified. We shall formulate it in the nonstationary form as follows: The field produced as a result of diffraction can be found by summing the contributions from regions of the wavefront that are located at a fixed distance, corresponding to the propagation time of the pulse, from the observation point. The contribution of equidistant regions of the front is taken with the same sign for a positive time derivative of the amplitude and with opposite sign for a negative derivative. In application to stationary problems this condition means a phase shift of the interfering waves by $\pi/2$. This eliminates the well-known phase inaccuracy of the stationary formulation [22]. For transmission of short pulses through a narrow diaphragm, the number of oscillations in a pulse increases by one.

Wavelets are a suitable complete basis for describing ultrashort pulses. We found the solution for the diffraction of a wavelet by square and circular openings. For the diffraction of a pulse by a narrow opening, a pulse undergoes conical spreading as it propagates after the diaphragm. Focusing partially compensates this phenomena within the focal distance.

The Green's function for the propagation of a plane wave initially in the form of a Dirac delta function was constructed to describe the propagation of a pulse of arbitrary form through an opening. This function is equal to the derivative of the angular size of an arc, cut by the radius of propagation from the diaphragm, with respect to the direction of propagation. The Green's function for diffraction and focusing provide an alternative to wavelets for calculating pulse propagation. The results obtained can be transferred to a complete vector description of electromagnetic fields on the basis of the Hertz vectors.

ACKNOWLEDGMENTS

We thank I.Ya. Novikov for an introduction to the theory of wavelets, A.V. Berdyshev for assisting in the formulation of the problem, and A.L. Gutman for helpful references.

REFERENCES

1. S. A. Akhmanov, V. A. Vysloukh, and A. S. Chirkin, *The Optics of Femtosecond Pulses* (Nauka, Moscow, 1988).
2. A. B. Borisov, A. V. Borovksiy, V. V. Korobkin, *et al.*, Phys. Rev. Lett. **68**, 2309 (1992).
3. C. Bula, K. T. McDonald, E. J. Prebys, *et al.*, Phys. Rev. Lett. **76**, 3116 (1996).
4. J. D. Kmetec, C. L. Gordon III, J. J. Macklin, *et al.*, Phys. Rev. Lett. **68**, 1527 (1992).
5. A. B. Borisov, A. V. Borovksiy, V. V. Korobkin, *et al.*, Phys. Rev. Lett. **65**, 1753 (1990).
6. H. S. Brandi, C. Manus, G. Mainfray, *et al.*, Laser Phys. **3**, 405 (1993).
7. K. Krushelnick, A. Ting, C. I. Moore, *et al.*, Phys. Rev. Lett. **78**, 4047 (1997).
8. N. B. Narozhnyi and M. S. Fofanov, Zh. Éksp. Teor. Fiz. **110**, 26 (1996) [JETP **83**, 14 (1996)].
9. L. C. Stainhauer and W. D. Kimura, J. Appl. Phys. **72**, 3237 (1992).
10. N. B. Baranova and B. Ya. Zel'dovich, Zh. Éksp. Teor. Fiz. **105**, 469 (1994) [JETP **78**, 249 (1994)].
11. Yu. N. Eremenko and L. S. Mkhitar'yan, Zh. Éksp. Teor. Fiz. **111**, 1554 (1997) [JETP **84**, 851 (1997)].
12. M. B. Vinogradova, O. V. Rudenko, and A. P. Sukhorukov, *The Theory of Waves* (Nauka, Moscow, 1979).
13. A. N. Oraevskiĭ, Zh. Éksp. Teor. Fiz. **111**, 3 (1997) [JETP **84**, 1 (1997)].
14. A. Baltuska, Z. Wei, M. S. Pshenichnikov, and D. A. Wiersma, Opt. Lett. **22**, 102 (1997).
15. V. A. Aleshkevich and V. K. Peterson, Pis'ma Zh. Éksp. Teor. Fiz. **66**, 232 (1997) [JETP Lett. **66**, 344 (1997)].
16. A. L. Gutman, Radiotekh. Élektron. (Moscow) **42**, 271 (1997).
17. A. Sommerfeld, *Optics* (Academic, New York, 1954; Inostrannaya Literatura, Moscow, 1973).
18. M. M. Bredov, V. V. Rumyantsev, and I. N. Toptygin, *Classical Electrodynamics* (Nauka, Moscow, 1953).
19. N. M. Astaf'ev, Usp. Fiz. Nauk **166**, 1145 (1996) [Phys. Usp. **39**, 1085 (1996)].
20. I. Ya. Novikov and S. V. Stechkin, FPM **3**, 1 (1997).
21. M. Abramowitz and I. A. Stegun, *Handbook of Mathematical Functions* (National Bureau of Standards, 1964).
22. G. S. Landsberg, *Optics* (Nauka, Moscow, 1976).

Translation was provided by AIP

Journal of Experimental and Theoretical Physics, Vol. 90, No. 2, 2000, pp. 250–257.
Translated from Zhurnal Éksperimental'noĭ i Teoreticheskoĭ Fiziki, Vol. 117, No. 2, 2000, pp. 286–293.

ATOMS, SPECTRA, RADIATION

Elastic Scattering of Metastable He($2^{1,3}S$) Atoms by Na(3^2S) Atoms at 68 meV

E. Yu. Remeta, V. I. Kelemen, A. N. Zavilopulo, and A. V. Snegurskiĭ*
Institute of Electron Physics, National Academy of Sciences of Ukraine, 8800 Uzhgorod, Ukraine
**e-mail: sneg@iep.uzhgorod.ua*
Received June 14, 1999

Abstract—The spectroscopy of metastable states is used to make the first experimental measurement of the total differential elastic-scattering cross sections of metastable helium atoms in 2^3S and 2^1S states by sodium atoms in the ground state at interaction energy 68 meV in the center-of-mass system. To analyze the experimental data, the partial scattering phases are calculated using the method of phase functions in the optical potential approximation. The analysis makes it possible to give a more detailed interpretation of the structure of the differential cross section. The computed integral cross sections, specifically, Penning ionization, diffusion, viscosity, and spin exchange are discussed. © *2000 MAIK "Nauka/Interperiodica".*

1. INTRODUCTION

The problem of determining the complex interaction potential in a system consisting of an excited atom and an atom in the ground state and the characteristics of the accompanying processes has by now been adequately solved for the interaction of two inert gas atoms. For an interatomic interaction in which one partner is a metal atom, this problem has not been adequately studied. At the same time, data of this kind are very important for analyzing the processes occurring in the active media of metal-vapor lasers, specifically, ion lasers, in different types of plasma, the chemistry of gases, liquids, solids, and so on [1].

The study of elastic collisions of atomic particles is a part of the general investigation of the properties of interatomic interactions and the characteristics of scattering processes. Precise experimental measurements of the differential scattering cross sections and their energy dependences, together with theoretical calculations, can be of help in solving the important problem of determining the optical potential (see, for example, [2]). For this reason, our objective in the present work was to determine the differential elastic scattering cross section (DSC) and to describe theoretically its features and the collisional characteristics for the system of strongly interacting particles He($2^{1,3}S$) + Na(3^2S).

2. THEORETICAL COMPUTATIONAL SCHEME

It is well known that the relative motion of atoms is described in the Born–Oppenheimer adiabatic approximation by the Schrödinger equation (the center-of-mass system and atomic units are used)

$$\left[-\frac{1}{2\mu}\nabla_R^2 + V_{\text{opt}}(\mathbf{R}) - E\right]\Psi(\mathbf{R}) = 0, \qquad (1)$$

where $V_{\text{opt}} = V_R(\mathbf{R}) + iV_I(\mathbf{R})$ is the optical potential for the interaction of the atoms, E is the kinetic energy of the collision, μ is the reduced mass of the atoms, and $\mathbf{R}$ is the distance between the nuclei.

Theoretical methods are now available for obtaining *ab initio* the optical potential describing the interatomic interaction in a system consisting of an excited metastable inert-gas atom (Rg*) and a metal atom (M) [3–6]. In these methods this system is treated as a collisional autoionization complex Rg*M. The optical potentials obtained, which are characterized by very large depths (several hundred meV) of the potential well, can be used for obtaining a detailed description of elastic scattering in the system Rg* + M. In [2] the optical potential for He(2^1S) + Na(3^2S) scattering was determined by a χ^2 fit of the differential scattering cross sections calculated in the semiclassical approximation to the experimentally measured cross sections at collision energies 52, 92, 132, 188, and 207 meV in the range of laboratory scattering angles $\theta_L = 5°–105°$. In [3] the optical potentials for the processes He(2^1S), He(2^3S) + Na(3^2S) were obtained by an *ab initio* calculation in terms of the electron resonance energy and the autoionization width and were used to calculate the DSC in the semiclassical approximation and to determine the Penning ionization cross section in a quite wide energy range: 10–1000 meV. In [4] *ab initio* optical potentials of the systems He(2^3S) + H, Li, Na, and He(2^1S) + Na, which are used for experimental and theoretical analysis of the characteristics of the electron spectra of the Penning ionization process, were obtained from the same assumptions. A similar method was used in [5] for He($2^{1,3}S$) + Mg, Ca, Sr, Ba systems. The values obtained for the potential well of the real part of the optical potential of the systems Rg*M (Rg = He, Ne, Ar, Kr, Xe, M = Li, Na, K, Rb, Cs, Mg, Ca, Sr, Ba, Yb, Hg) on the basis of

the high-resolution electron spectra in Penning ionization are generalized in [6]. In our work [7], the optical potential from [2] was used for quantum-mechanical calculation of the DSC and other characteristics of scattering of He(2^1S) by Na(3^2S) at 68 meV. The DSC obtained in this manner was used for the interpretation of the measured total cross section of He($2^{1,3}S$) + Na(3^2S) processes. In [8, 9] a theoretical phase analysis of these processes at 52, 80, and 92 meV was performed on the basis of the optical potential from [2]. In [10] the optical potential for scattering of He(2^3S) by Na(3^2S) was used for a semiclassical calculation of the Penning ionization cross section and the exchange cross section for scattering of triplet helium in a wide energy range.

Let us consider in greater detail the basic features of the collision of a metastable helium atom with alkali-metal atoms. The interaction in the systems He($2^{1,3}S$) + Na(3^2S) (μ = 6214 a.u.) is characterized by two values of the total spin of the quasimolecular terms. A helium atom in the singlet state is scattered on a single doublet quasimolecular term $^2\Sigma^+$, while for the triplet state the interaction occurs on two terms—the doublet $^2\Sigma^+$ (statistical weight 2/6) and the quartet $^4\Sigma^+$ (statistical weight 4/6). We note that the interaction on the doublet terms is characterized by a complex optical potential, while the interaction on the quartet term is characterized by a real potential. For calculations on the doublet terms we employed the computed potentials from [3], and for the quartet term we used the potential obtained in [10]. The real part of the optical potential in [3] was obtained in the approximation of interacting configurations for NaHe* molecules using a fit to the correct asymptotic dependence—the van-der-Waals potential. The imaginary parts of these optical potentials (autoionization widths) were obtained using the method of Stieltjes moments with a discrete representation of the continuum of the system e^- + $NaHe^+$ in (L^2). The quartet potential $^4\Sigma^+$ was determined on the basis of the rule of averages using the potentials of the systems He(2^3S)–He(2^3S) and Na(3^2S)–Na(3^2S) (see [10]).

The real part of the doublet optical potentials in [3] is characterized by the following parameters for the helium 2^1S (2^3S) state: strong repulsion at distances $R \le 0.2a_0$; zero value at $R_0 \simeq 5.75a_0$ ($4.45a_0$); minimum value V_{Rm} = 300 meV at $R_m = 7.35a_0$ (V_{Rm} = 740 meV, $R_m = 5.85a_0$); and, asymptotic behavior $\propto -C_6/R^6$, C_6 = 3660 a.u. (2220 a.u.), which "starts" approximately at $R_a = 8.22a_0$ ($6.27a_0$). The imaginary part of the optical potentials in [3] are characterized by almost exponential behavior for $R \ge 5a_0$ with a deviation from this behavior in the region $R < 5a_0$. At $6a_0$ the imaginary part decreases for the state 2^1S more rapidly than for 2^3S [3] (for example, for $R = 11a_0$ the triplet part is five times greater than the singlet part). In [10] the quartet potential has the form of a van-der-Waals potential with a positive correction: $-C_6/R^6 + AR^B\exp(-CR)$, C_6 = 1970 a.u. (compare with C_6 = 2220 a.u. for 2^3S [3]), A = 0.0205 a.u., B = 4.81, and $C = 1.206a_0^{-1}$.

The smallness of the collision energy compared with the depth of the potential well requires, in our opinion, that the theoretical method be mainly quantum-mechanical, while ordinarily various modifications of the semiclassical approximation are used. For this reason, we used the method of phase functions [11, 12] with a complex optical potential to perform the theoretical calculation of the scattering phases.

The system of equations for the complex phase function $\delta_l(E, R) = \varepsilon_l(E, R) + i\bar{\eta}_l(E, R)$ can be obtained from equation (1) and has the form

$$\begin{aligned}\frac{d\varepsilon_l}{dR} &= -\frac{1}{4k\eta_l}\{V_R[(1+\eta_l)^2(j_l\cos\varepsilon_l - n_l\sin\varepsilon_l)^2 \\ &- (1-\eta_l)^2(j_l\sin\varepsilon_l + n_l\cos\varepsilon_l)^2] + 2V_I(1-\eta_l^2) \\ &\times (j_l\cos\varepsilon_l - n_l\sin\varepsilon_l)(j_l\sin\varepsilon_l + n_l\cos\varepsilon_l)\}, \\ \frac{d\eta_l}{dR} &= \frac{1}{2k}\{V_I[(1+\eta_l)^2(j_l\cos\varepsilon_l - n_l\sin\varepsilon_l)^2 \\ &- (1-\eta_l)^2(j_l\sin\varepsilon_l + n_l\cos\varepsilon_l)^2] - 2V_R(1-\eta_l^2) \\ &\times (j_l\cos\varepsilon_l - n_l\sin\varepsilon_l)(j_l\sin\varepsilon_l + n_l\cos\varepsilon_l)\}\end{aligned} \quad (2)$$

with the initial conditions

$$\varepsilon_l(E, 0) = 0, \quad \eta_l(E, 0) = 1, \quad (3)$$

where $\eta_l(E, R) = \exp[-2\bar{\eta}_l(E, R)]$, $k^2 = 2\mu E$, and $j_l \equiv j_l(kR)$ and $n_l \equiv n_l(kR)$ are Riccati–Bessel functions. The real $\varepsilon_l(E)$ and imaginary $\bar{\eta}_l(E)$ parts of the partial scattering phase $\delta_l(E)$ are obtained from the corresponding phase functions:

$$\varepsilon_l = \lim\varepsilon_l(E, R), \quad \bar{\eta}_l(E) = -\frac{1}{2}\ln\lim\eta_l(E, R) \quad (4)$$

in the limit $R \longrightarrow \infty$.

It is very difficult to integrate the system (2) numerically, where the integration must start at a finite distance $r > 0$, because of the strong repulsive interaction at short distances and the singular behavior of $n_l(kR)$ for $l > 0$. In [11], the solution of this problem is examined for three types of behavior of the interaction potential $V(R)$ in the limit $R \longrightarrow 0$: nonsingular (or weakly singular), $R^2V(R) \longrightarrow 0$; strongly singular, $R^2V(R) \longrightarrow \infty$; and, intermediate between these two behaviors, $R^2V(R)$ = const. The interaction potential in our prob-

lem is of the first type. For this reason, the initial expression for $\delta_l(E, r)$ will be

$$\varepsilon_l(E, r) \approx -\frac{1}{k}\int_0^r dR\, j_l^2(kR) V_R(R), \qquad \eta_l(E, r) \approx 1. \tag{5}$$

Here, we use the fact that for sufficiently small r only the first term remains in the equation for $\varepsilon_l(E, R)$, in which the second and third terms can be neglected after squaring. Neglecting these terms means that for small l (in our case ≤30) and using an expansion for $j_l(kR)$

$$|\varepsilon_l(E, r)| \ll \frac{(kr)^{2l+1}}{(2l+1)!!(2l-1)!!}, \tag{6}$$

and then for $r \longrightarrow 0$

$$\varepsilon_l(E, r) \approx -\frac{k^{2l+1}}{[(2l+1)!!]^2}\int_0^r dR V_R(R) R^{2l+2}. \tag{7}$$

We note that in [7] analytic expressions were obtained for $\varepsilon_l(E, r)$ and $\eta_l(E, r)$ at small distances ($kr \leq 0.05$), using the optical potential from [2]. The real part of this potential has the form of a modified double Morse potential without the correct van-der-Waals asymptotic behavior. The imaginary part has a simple exponential dependence: $V_I(R) = 40\exp(-1.85R)$ (in a.u.). The expressions obtained in [7] show that the desired parts of the phase function $\delta_l(E, r)$ depend strongly on the orbital angular momentum l, the wave number k, and the parameters of the given optical potential.

We integrated the system of equations (2) with the initial conditions (3) numerically using a fourth-order "prediction–correction" method with automatic monitoring of the magnitude of the step. Here Adams–Bashforth prediction with Adams–Moulton correction and the modification in [13] were used. Using these methods, the partial phases were calculated with accuracy 10^{-4} rad.

The phases for scattering on the doublet terms for orbital angular momenta $l \geq 150$, starting with which the real part of the phases ε_l is less than 0.08 rad and the imaginary part $\bar{\eta}_l$ is essentially zero ($<10^{-16}$ rad), were calculated in the semiclassical approximation. For the quartet term, the phases were calculated only in the semiclassical approximation. For the collision energy 68 meV, which we used, the phases were calculated up to $l_{\max} = 660$ (for two $^2\Sigma^+$ terms) and up to $l_{\max} = 300$ (for one $^4\Sigma^+$ term). It should be noted that the values of the phases in solving equations (2)–(4), starting with $l \geq 145$, approached the semiclassical value and for $\varepsilon_l < 0.09$ rad follow the dependence $\propto l^{-5}$ [14] due to scattering by the van-der-Waals potential. The finite number of partial waves taken into account was dictated by the magnitude of the phases $\varepsilon_l \leq 10^{-4}$ rad. Summarizing everything we have said above about the computational algorithm and the use of the semiclassical approximation, we can state that we definitely obtained three significant figures in the differential and integral cross sections.

We neglected transitions between the terms $^2\Sigma^+$ and $^4\Sigma^+$ (for He(2^3S) + Na(3^2S) scattering) due to the spin–orbit interaction. The phases for each term were calculated independently. This approximation is satisfactory because the interaction between the atoms in the quasimolecule corresponds to a Σ term, where the spin–orbit interaction in the first approximation (with respect to the projection of the total spin) is zero and is very small in the second and first approximations in the spin–spin interaction [15]. Thus, our computational procedure contains both quantum and semiclassical descriptions.

The partial scattering phases $\delta_l(E)$ found were used to find the differential elastic scattering cross sections $d\sigma_{el}/d\Omega_c$ [14, 15]:

$$\frac{d\sigma_{el}(E, \theta_c)}{d\Omega_c} = \frac{g}{4k^2}\left|\sum_l (2l+1)(S_l - 1)P_l(\cos\theta_c)\right|^2, \qquad S_l = \exp[2i\delta_l(E)], \tag{8}$$

where the statistical weights are $g = 1$ for He(2^1S), $g = 1/3$ for He(2^3S) for the doublet terms and $g = 2/3$ for the quartet term.

The dependence (on l) of the real parts of the partial phases for ^1S (^3S) scattering on the $^2\Sigma^+$ terms has a maximum at $l = 37$ (28). This means that scattering is characterized by a glory at small angles.

The differential elastic-scattering cross section of the singlet and triplet metastable states of the helium atoms scattered by a sodium atom at 68 meV, which we calculated in the center-of-mass system in the entire range of angles, are presented in Fig. 1, and the computed cross sections in the laboratory system, taking account of the experimental range of scattering angles, are presented in Fig. 2. As expected, the angular dependence of the cross sections possesses a strong interference structure. Comparing the doublet DSC for He(2^1S) and He(2^3S) (Fig. 1, curves *1*, *2*) shows that they possess low-frequency structure (which is more pronounced for the singlet state) and high-frequency structure. The quartet DSC (curve *3*) possesses only a high-frequency structure (we recall that the quartet scattering phases were calculated semiclassically). The quartet DSC in the range of angles (~0.5°–150°) is somewhat greater than the doublet cross section for the triplet state (compare curves *3* and *2*) and is comparable to the DSC for the singlet state (curve *1*). For this reason, the total DSC over both terms for the triplet state (curve *4*) possesses primarily the features of the quartet DSC, except for the range of angles θ_c = 150°–180°.

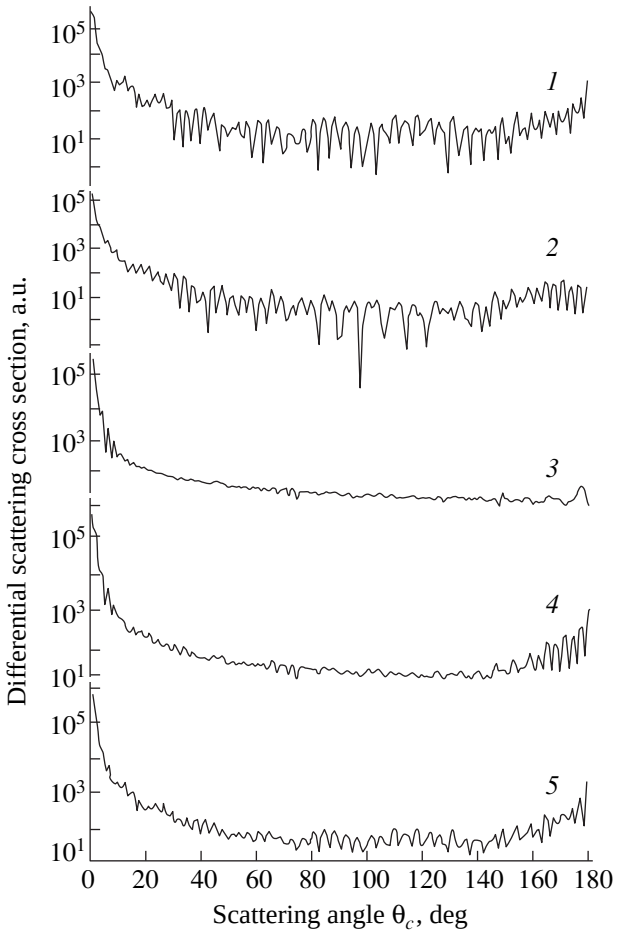

Fig. 1. Computed differential elastic scattering cross sections for metastable He($2^{1,3}S$) atoms scattered by Na(3^2S) atoms, in the center-of-mass system for energy E = 68 meV: *1*—singlet 2^1S state, doublet term; *2*—triplet 2^3S state, doublet term; *3*—triplet 2^3S state, quartet term; *4*—triplet 2^3S state, total over both terms; and *5*—sum over two states.

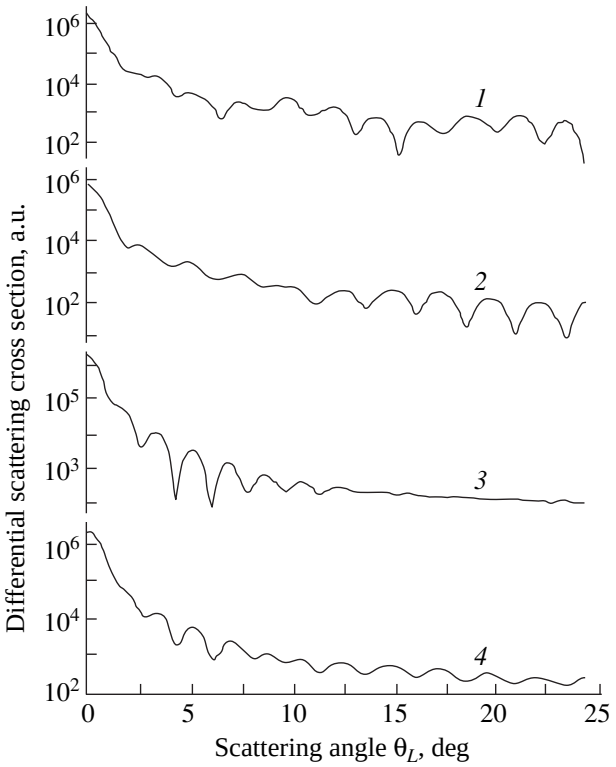

Fig. 2. Same as in Fig 1 but in the laboratory system without summation over the two states of helium.

Thus, it is evident that the theoretical differential elastic-scattering cross sections for individual terms (curves *1*, *2*, *3*) and the total cross sections (curves *4* and *5*) presented in Fig. 1 are characterized by a complicated angular dependence. We also note that the scattering cross section for the singlet and triplet states of helium for the doublet terms (curves *1*, *2*) possess features in common as well as distinguishing features. Specifically, the absolute value of the triplet DSC (curve *2*) is somewhat smaller than the singlet cross section (curve *1*), and their angular dependences in the ranges 5°–40° and 110°–180° are substantially different.

3. EXPERIMENT

The experiment was performed using the overlapping-beams technique and the spectroscopy of metastable states [16]. The beam of metastable atoms was produced using an ultrasonic nozzle-type source with longitudinal electron excitation, and the beam of sodium atoms was formed by a slit-type effusion source. A channel electronic multiplier, making it possible to measure the DSC in a range of scattering angles θ_L = 0.5°–20.5° with angular resolution $\Delta\theta_L$ = 0.5°, served as a detector of the scattered metastable atoms. The scanning step of the DSC curve was 0.5°. As a result of the specific nature of the experiment, selection of metastable atoms with respect to individual states was not performed, so that the measured DSC is a sum for both metastable states (singlet and triplet). The DSC curve obtained (see Fig. 3) is the result of repeated many times scanning of the range of scattering angles, and the relative statistical spread at each point of the experimental curve did not exceed 5%. The "nonideality" of the experimental instrumental function made it necessary to perform additional averaging of the computed DSC taking account of the real parameters of the experiment ($\Delta\theta_L \geq$ 0.5°, $\Delta V_{\mathrm{He}} = \pm 545$ m/sec, $\Delta V_{\mathrm{Na}} = \pm 140$ m/sec). In addition, we note that the uncertainty of the scattering angle (on the average ≈5% for the entire range of angles), the uncertainty of the particle velocity (≈10%), and the uncertainty in detection of the useful signal (≈5%) contribute to the measurement error in the experimental curves. Thus, the total error of the relative measurements taking account of averaging of the experimental curves should not exceed 25%. The confidence interval, determined taking account of what we have said above,

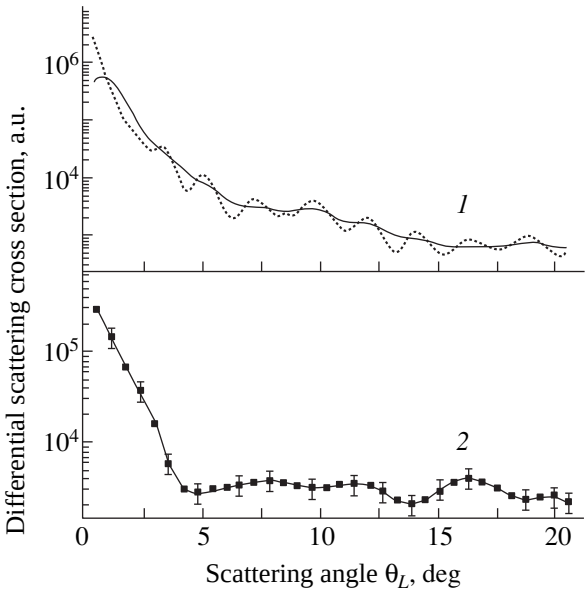

Fig. 3. Differential elastic scattering cross section for metastable He($2^{1,3}S$) atoms scattered by Na(3^2S) atoms in the laboratory system at E = 68 meV (sum over two states): *1*—calculation (a_0^2/sr) without averaging (dotted curve) and with averaging over 1.5° (solid line) and *2*—experimental cross section (arb. units).

is indicated in Fig. 3 and, as we shall see, does not exceed the amplitude of the irregularities of the cross section.

The experimental DSC curve presented in Fig. 3 drops sharply at small scattering angles, which is followed by low-frequency (3°–5°) irregularities of the cross sections on the flat section. To explain this behavior of the total differential cross section we used the theoretical scheme proposed above to calculate the DSC in the laboratory system.

4. DISCUSSION

The total computed DSCs in the laboratory system are presented in Fig. 3 (curve *1*) in comparison with experiment (curve *2*). It is evident that the behavior of the experimental DSCs on the whole agrees with the behavior of the theoretical cross section: a diffraction maximum ($\theta_L < 5°$), followed by interference behavior, which is manifested in the theoretical curves in the form of high-frequency ($\theta_L < 1°$) and low-frequency ($\theta_L \approx 3°$–$5°$) structures. As one can see in Fig. 3, our averaging over the instrumental function smooth the high-frequency structure. The low-frequency structure of the total DSC is determined primarily by the structure of the scattering of 2^1S helium atoms (see also Fig. 2). The structure of the DSC is due to the interference of the scattering waves corresponding to the three branches of the impact parameter as functions of the scattering angles [17]. These three branches of the impact parameter correspond to the three parts of the optical potentials which were used: attraction at the periphery (van-der-Waals potential), central attraction (potential well), and central repulsion at short distances. The kink in the DSC at 5° is probably due to the behavior of these parts of the optical potentials, which influence the formation of the partial phases. Moreover, because of the large depth V_{Rm} of the well in the optical potential and the low collision energy E, the ratio E/V_{Rm} (equal to 0.23 and 0.1 for ^1S and ^3S states) is very small, which makes it possible to assume that the behavior of the DSC for both helium states reflects orbiting phenomenon (periodic oscillations of the nonaveraged DSCs with a step of about 2° in Fig. 3). For orbital angular momenta from l = 37 to l = 76, the partial phase shifts regularly take values which are approximately multiples of π. The experimental minimum at $\theta_L \approx 14°$ and the theoretical minimum at $\theta_L \approx 15°$ could be due to orbiting phenomena for the $^2\Sigma^+$ term, more for scattering of the 2^1S state of helium and less for the 2^3S state.

In [7] we calculated the DSC, using the optical potential from [2], for He(2^1S) scattering. The real part of this potential decreases slowly by a factor of two in the range $R = 0.1$–$0.5a_0$, while the real part of the optical potential in [3] decreases by a factor of approximately 33 in the same range. The imaginary part of the optical potential in [2] is much greater than the imaginary part of the optical potential from [3]: by more than a factor of 10^4 for $R = 0.1a_0$ and a factor of ten for $R = 6a_0$. At large distances, however, it rapidly drops below the imaginary part of the potential from [3], for example, for $R = 15a_0$ by a factor of 1500. In this case, $R_0 = 5.53a_0$, $R_m = 6.3a_0$, and V_{Rm} = 300 meV (compare with the corresponding parameters, presented above, for the optical potential in [3]). The DSC calculated in [7] in the laboratory system did not have low-frequency structure and it was characterized by monotonic behavior, while qualitative agreement with the results of our experiment was observed only on the section up to ≈5°. This behavior agrees with the result of [3], where the DSC for He(2^1S) and E = 52 meV shows smooth behavior for the optical potential from [2] and a kink at 5° for the potential from [3]. Moreover, the DSCs calculated in [7] assuming $V_I(R) = 0$ for angles from 30° to 120° lie above the DSCs obtained for $V_I(R) \neq 0$, which agrees with the behavior of the DSC, described in [1], for He(2^1S) + Ar scattering. Therefore it can be concluded that on the whole the optical potentials from [3] correctly reflect the nature of the interatomic interaction of the system of particles under study.

The scattering phases which we calculated made it possible to give a more complete description of scattering and to obtain ultimately the following integral-type cross sections: diffusion, σ_D; viscosity, σ_η; elastic scat-

Integral-type cross sections for the scattering processes He($2^{1,3}S$) + Na(3^2S) at 68 meV (in units of a_0^2)

Cross section	He(2^1S) + Na(3^2S), doublet	He(2^3S) + Na(3^2S)			Total
		doublet	quartet	subtotal	
σ_{el}	2070	605	1550	2155	4225
σ_i	115	58.0	–	58.0	173
σ	2185	663	1550	2213	4398
σ_D	424	143	132	275	699
σ_η	335	65.9	243	309	644

tering, σ_{el}; absorption (Penning ionization), σ_i; and total, σ [14, 15]:

$$\sigma_D(E) = 2\pi\int d\theta_c \sin\theta_c(1-\cos\theta_c)\frac{d\sigma_{el}}{d\theta_c},$$

$$\sigma_\eta(R) = 2\pi\int d\theta_c \sin^3\theta_c\frac{d\sigma_{el}}{d\theta_c},$$

$$\sigma_{el}(E) = \sum_l \sigma_l(E), \quad \sigma_l(E) = \frac{\pi}{k^2}(2l+1)|S_l-1|^2, \tag{9}$$

$$\sigma_i(E) = \frac{g\pi}{k^2}\sum_l (2l+1)(1-|S_l|^2),$$

$$\sigma(E) = \frac{2\pi}{k^2}\sum_l (2l+1)(1-\mathrm{Re}S_l) = \sigma_{el}(E)+\sigma_i(E)$$

(see table). The contribution of the cross sections for the quartet term $^4\Sigma^+$ for the process He(2^3S) + Na(3^2S) is very large compared with the contribution of the cross sections corresponding to the $^2\Sigma^+$ term: it is comparable to the latter for σ_D, is 3.5 times greater than it for σ_η, and is 2.5 and 2.3 times greater for σ_{el} and σ. In [7], we noted that the inelastic processes have a large effect on the diffusion cross section calculated with the optical potential from [2] for He(2^1S) + Na(3^2S) scattering, which decreases approximately by a factor of two.

The theoretical values of the Penning ionization cross sections σ_i obtained from the computed curve in [3] for 68 meV are approximately $257a_0^2$ and $114a_0^2$ for He(2^1S) and He(2^3S), respectively (compare with our values of σ_i from the table).

The curve of the dependence $\sigma_i(E)$ calculated in [2] using the optical potential obtained in the same work for He(2^1S) scattering lies systematically above the corresponding curve obtained in [3]. The ionization cross section which we calculated with the optical potential from [2] $\sigma_i = 247a_0^2$ is less than that obtained in the same work $\sigma_i = 332a_0^2$ (see [7]). We note here that in [3] (and, apparently, in [2]) the scattering phases were calculated on the basis of only the semiclassical approximation. The experimental value of the cross section σ_i for 50 meV is $214a_0^2$ (±100%) [18]. Thus, the cross section $\sigma_i(E)$ calculated in [7] falls between the values presented in [2] and [18], and our value (68 meV) is substantially less than the theoretical value in [3].

A similar picture is also observed for the ionization cross section for He(2^3S) scattering. There are two experimental values: $\sigma_i \simeq 114a_0^2$ (+5%, –10%) for about 40 meV [19] and $\sigma_i \simeq 86a_0^2$ (±100%) for 50 meV [18]. The computed data in [3] lie above these values, and our computed value (for 68 meV) is much less than the value of σ_i in [3]. We note that the value obtained for σ_i for 68 meV in the semiclassical approximation in [10] is about $122a_0^2$ (taking account of the statistical weight 1/3), which is much greater than (by a factor of two) the values which we obtained and is somewhat greater than σ_i in [3]. We note that the real part of the optical potential in [10] is the "12–6" Lennard-Jones potential with $R_0 = 5.35a_0$, $R_m = 6.0a_0$, and $V_{Rm} = 735$ meV, and the imaginary part has the form $V_I(R) = 0.6\exp(-R)$ [a.u.]. Comparing this potential with the analogous potentials in [3] shows that they coincide near the minimum of the potential and in the asymptotic range, but the potential in [10] has stronger repulsion for $R < R_0$. In [10], the imaginary part of the potential is 50 times greater than the imaginary part of the potential from [3] at short distances and approximately 1.2 times greater at $R = 15a_0$.

The ratio of the ionization cross sections in the processes He(2^1S), He(2^3S) + Na which is determined both experimentally and theoretically, is discussed in [4]. It is asserted that it depends weakly on the collision energy. For 70 meV, according to the experimental data in [4], this ratio is 2.8 (±30%), while according to the experimental data in [20] the ratio is 3.1 (±30%). It follows from the experiment in [18] that for 50 meV

the ratio is 2.5. The theoretical values of this ratio are systematically less than three, which corresponds to the ratio of the statistical weights of the spin-allowed collisions for these processes. Thus, the ratio obtained according to our computed values of the ionization cross sections (see table) is 2.0. The value of the same ratio according to the results of [3] is 2.2 for 50 meV and 2.3 for 68 meV. In [4] the value 2.18 is obtained using the optical potential from [3], while the value is 2.15 with the real part of the optical potential obtained in [4] *ab initio* and the imaginary part from [3]. As one can see, our values agree well with all of these data.

A spin-exchange process, which is possible for scattering of He(2^3S) by Na(3^2S), is indicated in [10]. The amplitude of such a process is $f(m_1, m_2; m_1', m_2'; E, \theta_c) = (2^{1/2}/3)[f_q(E, \theta_c) - f_d(E, \theta_c)]$, where m_1, m_2; m_1', m_2' are the projections of the spins of the Na and He atoms before and after a collision, respectively ($m_1 + m_2 = m_1' + m_2'$), and f_q and f_d are the scattering amplitudes for the quartet (partial phase $\eta_{lq}(E)$) and doublet (partial phase $\delta_{ld}(E) = \varepsilon_{ld}(E) + i\bar{\eta}_{ld}(E)$) terms. The corresponding total spin-exchange cross section has the form

$$\sigma^{tr}(E) = \frac{2\pi}{k^2}\sum_{l=0}^{\infty}(2l+1) \times \{1 + \eta_{ld}^2(E) - 2\eta_{ld}(E)\cos(2[\varepsilon_{ld}(E) - \varepsilon_{lq}(E)])\}, \quad (10)$$

where $\eta_{ld}(E)$ is related with the imaginary part of the phase $\bar{\eta}_{ld}(E)$. Our computed value of the cross section is $\sigma^{tr}(68\ \mu\text{eV}) = 300a_0^2$. The main part of the cross section ($298a_0^2$) was obtained for waves with l ranging from 0 to 149, where ε_{ld} and η_{ld} were found from the quantum-mechanical calculation using the optical potential from [3]. As we have noted above, the phase ε_{lq} was calculated in the semiclassical approximation with the potential from [10]. According to the data from this work, the cross section $\sigma^{tr}(68\ \text{meV})$ was $200a_0^2$. As indicated above, the Penning ionization cross section for He(2^3S) in [10] is greater than our value. This attests to small values of η_{ld} (the partial ionization cross section is proportional to $1 - \eta_{ld}^2$). A consequence of this (see (10)) is that the exchange cross section in [10] is small. Thus, the spin-exchange cross section is very sensitive to the imaginary part of the partial waves and hence to the imaginary part of the optical potential employed.

5. CONCLUSIONS

The experimental and theoretical investigations of the elastic scattering of He($2^{1,3}S$) atoms by Na(3^2S) atoms at 68 meV performed in this work made it possible to interpret for the first time the structure observed in the DSCs at small scattering angles. Thus, we found that the low-frequency structure of the angular dependence of the differential cross sections is due to the interference of the amplitudes from different parts of the interaction potential together with the phenomenon of orbiting. This structure is determined primarily by the characteristic features of scattering of metastable helium atoms in the singlet state.

The quantum-mechanical and semiclassical representations, which we employed for the calculations, for a system of strongly interacting atomic particles Rg*M in the approximation of an optical potential, to find which this system is treated as an autoionization complex, correctly describe the characteristics of elastic scattering at this energy.

The Penning ionization cross sections which we calculated with such optical potentials are in good quantitative agreement with the existing experimental data.

The total spin-exchange cross section for scattering of metastable helium atoms in the triplet state is very sensitive to the magnitude of the imaginary part of the optical potential, and the quantum-mechanical description in this case is decisive.

ACKNOWLEDGMENTS

We thank O.B. Shpenik and I.I. Fabrikant for valuable discussions of the results obtained in this work, J.S. Cohen for providing the data on the optical potential, and H. Hotop, O.I. Zatsarinnom, and I.O. Tsapfel for encouragement and assistance in performing the work.

REFERENCES

1. V. B. Leonas, *Intermolecular Interactions and Collisions of Atoms and Molecules* (VINITI, Moscow, 1980).
2. H. Haberland and W. Weber, J. Phys. B **13**, 4147 (1980).
3. J. S. Cohen, R. L. Martin, and N. F. Lane, Phys. Rev. A **31**, 152 (1985).
4. A. Merz, M. W. Muller, M.-W. Ruf, *et al.*, Chem. Phys. **145**, 219 (1990).
5. M.-W. Ruf, A. J. Yencha, H. Hotop, *et al.*, Z. Phys. D **37**, 219 (1996).
6. H. Hotop, T. E. Roth, M.-W. Ruf, *et al.*, Theor. Chem. Acc. (1998).
7. E. Yu. Remeta, V. I. Kelemen, A. N. Zavilopulo, *et al.*, Ukr. Fiz. Zh. **44**, 1077 (1999).
8. E. Yu. Remeta, V. I. Kelemen, A. V. Snegursky, *et al.*, in *Proceedings of the 19th International Symposium on Physics of Ionised Gases, Zlatibor, Yugoslavia, 1998*, p. 155.
9. E. Yu. Remeta and V. I. Kelemen, in *Proceedings of the 6th EPS Conference on Atomic and Molecular Physics, ECAMP, Siena, Italy, 1998*, p. 4.23.
10. V. A. Kartoshkin, Opt. Spektrosk. **85**, 196 (1998) [Opt. Spectrosc. **85**, 177 (1998)].

11. V. V. Babikov, *The Method of Phase Functions in Quantum Mechanics* (Nauka, Moscow, 1988).
12. F. Calogero, *Variable Phase Approach to Potential Scattering* (Academic, New York, 1967; Mir, Moscow, 1972).
13. G. A. Korn and T. M. Korn, *Mathematical Handbook for Scientists and Engineers* (McGraw-Hill, New York, 1961; Nauka, Moscow, 1978).
14. N. Mott and H. Massey, *The Theory of Atomic Collisions* (Clarendon, Oxford, 1965, 3rd ed.; Mir, Moscow, 1969).
15. L. D. Landau and E. M. Lifshitz, *Quantum Mechanics: The Non-Relativistic Theory* (Nauka, Moscow, 1989; Pergamon, Oxford, 1977, 3rd ed.).
16. A. V. Snegurskiĭ, A. I. Zhukov, and A. N. Zavilopulo, Ukr. Fiz. Zh. **39**, 300 (1994).
17. E. E. Nikitin and S. Ya. Umanskiĭ, *Nonadiabatic Transitions in Slow Atomic Collisions* (Atomizdat, Moscow, 1979).
18. H. Hotor and A. Niehaus, Z. Phys. **238**, 452 (1970).
19. C. E. Johnson, C. A. Tipton, and M. G. Robinson, J. Phys. B **11**, 97 (1978).
20. M.-W. Ruf, A. J. Yencha, and H. Hotor, Z. Phys. D **5**, 9 (1987).

Translation was provided by AIP

Journal of Experimental and Theoretical Physics, Vol. 90, No. 2, 2000, pp. 258–275.
Translated from Zhurnal Éksperimental'noĭ i Teoreticheskoĭ Fiziki, Vol. 117, No. 2, 2000, pp. 294–312.

ATOMS, SPECTRA, RADIATION

Investigation of Amplified Spontaneous X-ray Laser Radiation Using the Equation for the Transverse Correlation Function of the Field

F. A. Starikov*

Russian Federal Nuclear Center 3/4 All-Russia Scientific-Research Institute of Experimental Physics, Sarov, Nizhegorod oblast, 607190 Russia

**e-mail: starikov@otd13.vniief.ru*

Received June 22, 1999

Abstract—A physical model, based on the solution of the quasi-optics equation for the transverse correlation function (TCF) of the field amplitude, is developed for investigating the brightness, angular divergence, and spatial coherence of the amplified spontaneous emission in a laboratory X-ray laser. The model takes account of the spontaneous source of radiation, diffraction, regular refraction, regular amplification taking account of saturation, nonresonance absorption, scattering by small-scale fluctuations of the electron density and the gain, and scattering by random hose-like deviations of the extended plasma medium of the X-ray laser. It is established that the TCF method makes it possible to obtain the final result much more quickly than the basic Monte Carlo method for the parabolic equation for the field amplitude. As a result of the statistical linearization of the equation for the transverse correlation function in the presence of gain saturation, this method overestimates the absolute values of the average intensity of the amplified spontaneous radiation, but the maximum overestimation does not exceed 10%. It is found that fluctuations of the optical parameters of the medium of the X-ray laser degrade the quality of the amplified spontaneous radiation beam, and they are the analog of the nonresonance absorption from the standpoint of the effect on the brightness of the laser and therefore decrease the observed gain. For the characteristic conditions of an X-ray laser with a quasistationary generation scheme, the contribution of small-scale gain fluctuations and random hose-like deviations of the plasma filament of the laser to the scattering of the amplified spontaneous radiation is much smaller than the contribution of small-scale density fluctuations. Calculations of the amplified spontaneous radiation in an X-ray laser, which is produced by unilateral irradiation of a curved target and possesses an asymmetric plasma electron density profile in the gain zone, are performed. It is shown that in the gain saturation regime the coherence length and the coherent power of the amplified spontaneous radiation can be substantially increased, realizing in the gain zone a convex electron density profile instead of a typical concave profile. It is found that this improvement of the coherence occurs only under conditions such that the characteristic depth of the small-scale density fluctuations does not exceed several percent of the typical regular values of the density in the gain zone. © *2000 MAIK "Nauka/Interperiodica".*

1. INTRODUCTION

One of the most important problems of laser physics is to decrease the wavelength of the laser radiation and to develop a laser in the far-UV and soft X-ray ranges $\lambda = 0.2$–100 nm. An X-ray laser will make possible substantial progress in many areas of science, technology, and medicine [1]. One of the most striking examples of this potential application is time- and space-resolved holography of live cells.

The working medium of an X-ray laser is a plasma, which is ordinarily obtained by focusing the radiation from an optical laser into a line on a solid target or in a capillary electric discharge. In the plasma column formed, the X-ray laser radiation develops in a regime of amplified spontaneous radiation. The most promising schemes are those with laser transitions in Ne- or Ni-like ions. Powerful lasers with nanosecond pulses and an energy of hundreds of Joules were first used for pumping [2]. This makes it possible to obtain quasistationary generation. However, there are only a few powerful laser setups in the world, and experiments are quite expensive to perform using them. For this reason, an interesting result was the development of a table-top X-ray laser operating on a capillary discharge, where quasistationary generation of far-UV radiation was obtained without using laser pumping [3]. In addition, lasing was subsequently obtained by irradiating the target with an optical laser with picosecond [4] and femtosecond [5] pulses with ~10–1000 mJ per pulse. The nonstationary transitional amplification regime makes it possible to obtain a gain of tens and hundreds of inverse centimeters. The result of all this is that the X-ray laser is gradually becoming a compact device, accessible to a large number of laboratories as an object of and tool for research [6, 7].

From the mid-1980s to the present lasing has been obtained on more than 100 lines in the range of wavelengths λ with the lower limit lying inside the "water window" (2.33–4.36) nm, which is convenient for holo-

graphic measurements in biology. The brightness and monochromaticity of X-ray lasers are now much higher than those of alternative X-ray sources, which has made it possible to begin the use of X-ray lasers in plasma diagnostics [6, 7]. However, many applications of the X-ray laser cannot be implemented, including holographic applications, because at present the spatial coherence and divergence of X-ray laser radiation is low and much higher than the diffraction limit. Obtaining from an X-ray laser a beam of radiation with angular divergence of the order of the diffraction divergence and a high degree of spatial coherence is at present one of the key problems in this complicated and multilevel problem [8].

The poor quality of an X-ray laser beam is due to at least three factors. In the first place, the spontaneous radiation that must be amplified has a wide divergence. Even if the gain zone is optically uniform, to obtain a single-mode regime with a gain zone of transverse size a the length of the X-ray laser must be $z \sim a^2/\lambda$. For $a \sim 100$ μm and $\lambda = 0.2$–100 nm, z is tens of centimeters and meters. Since for a promising picosecond pumping regime the characteristic length of an X-ray laser is less than 1 cm, it is obvious that the amplified spontaneous radiation is multimode. This problem could be solved by using a master oscillator for such radiation and an amplifier separated from one another by at some distance. But, in the second place, the plasma active medium of an X-ray laser is characterized by large-scale transverse nonuniformity, since during generation the plasma is in a state of expansion. The refraction of the amplified spontaneous radiation causes the radiation to leave the gain zone, which additionally degrades the angular, the energy, and, as a rule, the coherence properties of the radiation. In the third place, one reason for the low quality of the amplified spontaneous radiation beam could be the presence of small-scale random optical irregularities in the X-ray laser. For a laser plasma, they are related with the nonuniformity of the target and its surface, the nonuniformity of irradiation of the target, the filamentation of the pump beam in the plasma, induced scattering of the pump, turbulence, and so on.

It should be noted that work to improve the quality of the amplified spontaneous radiation beam has been conducted in parallel with the search for new active media for an X-ray laser and attempts to decrease the wavelength. The methods for improving the quality of the amplified spontaneous radiation beam in an X-ray laser are described in the review [8]. Striking progress has been achieved by using a preliminary pump pulse [9] and by curving the target [10]. This make it possible to decrease the divergence and increase substantially (by an order of magnitude) the brightness of the X-ray laser operating on transitions in Ne- and Ni-like ions [11]. Nonetheless, the divergence and spatial coherence of amplified spontaneous radiation are far from ideal.

Computational-theoretical investigations play a large role in solving the problem of the quality of an X-ray laser beam. The dynamics of the amplified spontaneous radiation is an integral part of the theoretical description of an X-ray laser, together with the hydrodynamic plasma in the kinetics of the level populations of ions. One method for describing the dynamics of amplified spontaneous radiation is the conventional geometric optics method, which has been used in the approximation of a regularly-nonuniform active media of an X-ray laser (see, for example, [12–16]). However, for characteristic sizes of optical irregularities ~1–10 μm, diffraction can play an appreciable role. Wave effects must also be taken into account when the transverse coherence length of the amplified spontaneous radiation becomes comparable to the beam width. In addition, it is difficult to investigate coherence, which is a purely wave property of amplified spontaneous radiation, by the methods of geometric optics.

Wave effects can be taken into account on the basis of the method of the parabolic equation for the complex amplitude of the radiation field. This method has been used to calculate the amplified spontaneous radiation in a requlary-nonuniform active medium of an X-ray laser (see, for example, [17–23]). The parabolic equation was either simplified using a mode expansion for special profiles of the optical parameters [20–23] or it was solved numerically for arbitrary distributions of the optical parameters [17–19]. But, for a random source of radiation the parabolic equation method requires multiple calculations of the equation (statistical tests) and averaging of the results over an ensemble. This approach requires long computer calculations. The parabolic equation method becomes especially complicated when additional random parameters of the medium are included in the analysis. Switching from a parabolic equation to an equation for the transverse correlation function (TCF) for the amplitude of the field has made it possible to circumvent the problem of averaging over an ensemble of realizations [24–26]. When the transverse coherence length is much less than the beam width, the TCF method makes it possible to obtain a numerical result much more quickly than the parabolic equation method. The TCF method has been used to investigate the formation of amplified spontaneous radiation in an X-ray laser in regularly nonuniform [27–30] and randomly nonuniform [31–34] media with an arbitrary distribution of the optical parameters. In a simplified approach with special profiles of the optical parameters, the TCF method has also been used to investigate the amplified spontaneous radiation in a randomly nonuniform medium of an X-ray laser [35, 36].

The present paper is devoted to three aspects associated with the TCF method and its application for calculation of the dynamics of amplified spontaneous radiation. First, the TCF method with gain saturation is improved. The two-level medium approximation is used to take account of gain saturation in calculations of the amplified spontaneous radiation with the aid of the parabolic equation [17–19]. The equation for the TCF was obtained from the parabolic equation in [24–26] taking account of gain saturation in an approximate form, using statistical linearization of the nonlinear terms of the equation

which take account of the amplification. The result is that the parameters of the amplified spontaneous radiation that are obtained from the equation for the TCF are somewhat different from the average parameters found by the Monte Carlo method for the initial parabolic equation [37, 38]. In the present paper a correction is introduced to the statistical linearization of the equation for the TCF. The improvement of the TCF method permits obtaining data closer to the average-statistical data.

Second, the TCF method is used to study the effect of random irregularities of the parameters of the medium of various types of X-ray lasers on the amplification of the spontaneous radiation. The ordinary fluctuations of the permittivity and gain, analogous to turbulent fluctuations in the atmosphere, as well as hose-like fluctuations (chaotic transverse displacements) of the plasma filament of the X-ray laser are taken into account at the same time [39]. The results of calculations of amplified spontaneous radiation in a three-dimensional randomly inhomogeneous medium are presented. These are the first results published in the literature on X-ray lasers. The effect of gain fluctuations, which are observed in an X-ray laser based on Ne-like yttrium, on the amplified spontaneous radiation is estimated.

Finally, a method for improving the coherent properties of the amplified spontaneous radiation beam in an X-ray laser whose active medium is produced by irradiating a thick target with laser radiation and is characterized by an asymmetric density profile of the expanding plasma in the gain zone is examined. One reason for the remaining low degree of coherence when using a preliminary pump pulse and curving the target is residual refraction, which for the typical concave transverse density profile is of a focusing character. As shown in [30], a convex instead of a concave transverse density profile would substantially improve the coherence of the amplified spontaneous radiation with a curved target because of the residual defocusing effect. In [30] the case of linear gain was examined, whereas in the present paper the behavior of amplified spontaneous radiation with gain saturation, which is achieved in experiments, is investigated. The degree of the possible negative influence of permittivity fluctuations on the improvement of the coherence is determined.

2. THE PARABOLIC EQUATION METHOD

The dynamics of amplified spontaneous radiation in the plasma of an X-ray laser in the quasistationary case is described by a parabolic equation for the slowly varying complex amplitude E of the radiation field [8]:

$$\left[\frac{\partial}{\partial z} + \frac{i}{2k}\frac{\partial}{\partial \mathbf{r}^2} + \frac{ik}{2}[\varepsilon(\mathbf{r}, z) - 1] + \frac{\kappa(\mathbf{r}, z)}{2} - \frac{\alpha(\mathbf{r}, z)/2}{1 + J(\mathbf{r}, z)/J_{sat}}\right]E(\mathbf{r}, z) = S(\mathbf{r}, z), \quad (1)$$

where $\mathbf{r} = \mathbf{i}x + \mathbf{i}y$ is the transverse radius vector, z is the longitudinal coordinate, k is the wave number, κ is the nonresonant absorption coefficient, α is the weak-signal gain, $J = |E|^2$ is the radiation flux density, and J_{sat} is the saturation flux density. The equation (1) describes amplified spontaneous radiation propagating in one direction along the z axis. This corresponds to the "traveling wave" pumping regime of the active medium. The quantity ε in equation (1) is the plasma permittivity determined by the contribution of free electrons [40]:

$$\varepsilon = \eta^2 = 1 - N_e/N_c, \quad (2)$$

where N_e is the free-electron density and N_c is the critical density. For soft X-ray and far-UV ranges ($\lambda = 0.2$–100 nm) $N_c \gg N_e$ in the plasma of an X-ray laser [1], i.e., $\varepsilon \approx 1$.

The source S on the right-hand side of equation (1) is delta-correlated:

$$\langle S(\mathbf{r}_1, z_1)S^*(\mathbf{r}_2, z_2)\rangle = \lambda^2 Q(\mathbf{r}_1)\delta^{(2)}(\mathbf{r}_1 - \mathbf{r}_2)\delta(z_1 - z_2),$$

where Q is the average specific power of the spontaneous noise, measured in W/cm^3 sr. In equation (1) the influence of saturation on the source power is neglected, but it is obvious that in the saturation regime the intensity of the amplified spontaneous radiation is quite high and the role of the source becomes negligible.

It is impossible to solve equation (1) in a general form analytically. Expanding the field amplitude E in terms of transverse modes makes it possible to simplify the initial problem for linear gain ($J \ll J_{sat}$) and for certain model profiles α and ε, where the transverse modes are determined analytically [20–23]. The mode approach is not realized for the saturation regime. The direct numerical solution of equation (1) is of greater practical utility. The transverse grid step is $\Delta x \sim \lambda/\theta_s$, where θ_s is the divergence angle of the radiation from the noise source. As a result of the large divergence of the noise and the smallness of λ, the number of grid points is usually large, and the integration step along z, $\Delta z \sim k(\Delta x)^2$, is small. For this reason, present-day computers make it possible to study only the case of a planar medium (with one transverse coordinate) [18, 38]. In addition, a single solution of the parabolic equation with a random source gives the result of a single statistical test (a realization of a random process). To obtain the average characteristics, the solutions obtained for the parabolic equation must be averaged over an ensemble of realizations [38] or over time [18, 19], and this requires long computer calculations. It is worth noting that the difficulties increase when the randomness of the parameters of the medium is taken into account.

In the numerical calculations below, the finite-difference algorithm described in [41] is used to solve the parabolic equation (1) numerically. The accuracy of the algorithm is much higher than that of spectral methods [18, 19]. The amplitude error of the harmonic solution of the homogeneous equation is zero, and the phase error

is substantially reduced ($\sim(\Delta x)^6$). Splitting according to physical processes is used to take into account the nonuniform terms in the equation.

3. THE METHOD OF THE EQUATION FOR THE TRANSVERSE CORRELATION FUNCTION

3.1. The Equation for the Transverse Correlation Function

To avoid the problem of averaging over an ensemble of realizations, an equation for the second moment of the field amplitude can be obtained from the stochastic equation (1) 3/4 the transverse correlation function $B = \langle E(\mathbf{r}_1, z)E^*(\mathbf{r}_2, z)\rangle$, where the brackets denote statistical averaging.

In performing the averaging we take account of the fact that two types of random optical irregularities are present in the plasma. The first type corresponds to ordinary permittivity and gain fluctuations, which are characterized by a definite spatial spectrum, dispersion, and correlation lengths, i.e., according to the method used for the description, they are similar to, for example, fluctuations of a turbulent atmosphere [42]. These fluctuations can arise as a consequence of various plasma instabilities of the X-ray laser (see [8]). The fluctuations of the second type are due to chaotic deviations of the plasma filament as a whole from a rectilinear form. They can be called axial fluctuations (the term hose-like fluctuations is used in the English-language literature [39]. Hose-like fluctuations could be due to the nonuniformity of the irradiation of the target by radiation from the optical laser. We shall simulate the hose-like fluctuations by a chaotic displacement of the regular gain and refractive index profiles. For this reason, we represent ε and α in the form

$$\begin{aligned}\varepsilon(\mathbf{r}, z) &= \bar{\varepsilon}(\mathbf{r} + \tilde{\mathbf{r}}, z) + \tilde{\varepsilon}(\mathbf{r}, z)\\ &\approx \bar{\varepsilon}(\mathbf{r}, z) + \tilde{\mathbf{r}}(z)\nabla_\perp\bar{\varepsilon}(\mathbf{r}, z) + \tilde{\varepsilon}(\mathbf{r}, z),\\ \alpha(\mathbf{r}, z) &= \bar{\alpha}(\mathbf{r} + \tilde{\mathbf{r}}, z) + \tilde{\alpha}(\mathbf{r}, z)\\ &\approx \bar{\alpha}(\mathbf{r}, z) + \tilde{\mathbf{r}}(z)\nabla_\perp\bar{\alpha}(\mathbf{r}, z) + \tilde{\alpha}(\mathbf{r}, z),\end{aligned}$$

where $\bar{\varepsilon}$ and $\bar{\alpha}$ are the regular components, $\tilde{\varepsilon}$ and $\tilde{\alpha}$ are the fluctuation components, $\tilde{\mathbf{r}}$ is the random transverse displacement of the regular profiles $\bar{\varepsilon}$ and $\bar{\alpha}$, and $\nabla_\perp$ is the transverse gradient. The fluctuations $\tilde{\varepsilon}$, $\tilde{\alpha}$, and $\tilde{\mathbf{r}}$ are statistically independent and possess zero means. We neglect the fluctuations of κ, since $\kappa \ll \alpha$. The general prescription for obtaining the equation for the TCF in a randomly inhomogeneous medium in the Markov approximation can be found, for example, in [42]. In [24, 25] it is extended to the case of an active medium with refraction.

However, the derivation from equation (1) of the equation for the TCF presents a difficulty because of the existence of the flux density $J(\mathbf{r}, z)$ in the denominator of the nonlinear term (1), responsible for amplification with saturation. This problem can be solved by using the method of statistical linearization [43], which reduces to replacing certain fluctuating quantities in the stochastic equation by averages. In the present case, it will consist of replacing $J(\mathbf{r}, z)$ by $\beta B(\mathbf{r}, 0; z)$, where $B(\mathbf{r}, 0; z)$ is the average radiation flux density in the TCF method and β is a parameter that depends on the ratio $B(\mathbf{r}, 0; z)/J_{sat}$, i.e., on the local degree of saturation.

Finally, the equation for the TCF becomes

$$\begin{aligned}&\left[\frac{\partial}{\partial z} + \frac{i}{k}\frac{\partial^2}{\partial\mathbf{r}\partial\mathbf{r}'} + \frac{ik}{2}[\bar{\varepsilon}(\mathbf{r}_1; z) - \bar{\varepsilon}(\mathbf{r}_2; z)]\right.\\ &+ \frac{\kappa(\mathbf{r}_1; z) + \kappa(\mathbf{r}_2; z)}{2} + \frac{\pi k^2}{4}H(\mathbf{r}, \mathbf{r}'; z)\\ &- \frac{\bar{\alpha}(\mathbf{r}_1; z)/2}{1 + \beta B(\mathbf{r}_1, 0; z)/J_{sat}(\mathbf{r}_1; z)}\\ &\left.- \frac{\bar{\alpha}(\mathbf{r}_2; z)/2}{1 + \beta B(\mathbf{r}_2, 0; z)/J_{sat}(\mathbf{r}_2; z)}\right]B(\mathbf{r}, \mathbf{r}'; z)\\ &= \lambda^2 Q(\mathbf{r}; z)\delta(\mathbf{r}'),\end{aligned} \tag{3}$$

where $\mathbf{r} = (\mathbf{r}_1 + \mathbf{r}_2)/2$ and $\mathbf{r}' = \mathbf{r}_1 - \mathbf{r}_2$. Scattering by the fluctuations of the parameters of the medium is determined by the function $H(\mathbf{r}, \mathbf{r}'; z) = H_\varepsilon + H_\alpha + H_h$, where

$$H_\varepsilon(\mathbf{r}, \mathbf{r}'; z) = \frac{A_\varepsilon(\mathbf{r}_1, 0; z) + A_\varepsilon(\mathbf{r}_2, 0; z) - 2A_\varepsilon(\mathbf{r}, \mathbf{r}'; z)}{2\pi}, \tag{4}$$

$$H_\alpha(\mathbf{r}, \mathbf{r}'; z) = -\frac{A_\alpha(\mathbf{r}_1, 0; z) + A_\alpha(\mathbf{r}_2, 0; z) + 2A_\alpha(\mathbf{r}, \mathbf{r}'; z)}{2\pi k^2[1 + \beta B(\mathbf{r}, 0; z)/J_{sat}]^2}, \tag{5}$$

$$H_h(\mathbf{r}, \mathbf{r}'; z) = \frac{A_h(z)}{2\pi}\left[\mathbf{r}'\nabla_\perp^2\bar{\varepsilon}(\mathbf{r}, z) + \frac{2i}{k}\frac{\nabla_\perp\bar{\alpha}(\mathbf{r}, z)}{[1 + \beta B(\mathbf{r}, 0; z)]}\right]^2 \tag{6}$$

are responsible for, respectively, the influence of $\tilde{\varepsilon}$, $\tilde{\alpha}$, and $\tilde{\mathbf{r}}$. For Gaussian correlations of the quasi-uniform fluctuations of $\tilde{\varepsilon}$, $\tilde{\alpha}$, and $\tilde{\mathbf{r}}$ we have

$$\begin{aligned}A_\varepsilon(\mathbf{r}, \mathbf{r}'; z) &= (2\pi)^{1/2}\sigma_\varepsilon^2(\mathbf{r}, z)l_{\varepsilon\|}(\mathbf{r}, z)\\ &\times \exp[-r'^2/2l_{\varepsilon\perp}^2(\mathbf{r}, z)],\end{aligned} \tag{7}$$

$$\begin{aligned}A_\alpha(\mathbf{r}, \mathbf{r}'; z) &= (2\pi)^{1/2}\sigma_\alpha^2(\mathbf{r}, z)l_{\alpha\|}(\mathbf{r}, z)\\ &\times \exp[-r'^2/2l_{\alpha\perp}^2(\mathbf{r}, z)],\end{aligned} \tag{8}$$

$$A_h(z) = (2\pi)^{1/2}L_\perp^2(z)L_\|(z), \tag{9}$$

where σ_ε^2 and σ_α^2 are the variances of $\tilde{\varepsilon}$ and $\tilde{\alpha}$; $l_{\varepsilon\perp}$ and $l_{\varepsilon\|}$ are the transverse and longitudinal correlation lengths of $\tilde{\varepsilon}$; $l_{\alpha\perp}$ and $l_{\alpha\|}$ are the transverse and longitudinal correlation lengths of $\tilde{\alpha}$; and, $L_\perp^2$ and $L_\|$ are, respectively, the dispersion and the longitudinal correlation length of $\tilde{\mathbf{r}}$. The relations (4)–(6) hold when the average flux density of the amplified spontaneous radiation changes little over a distance of the order of the transverse correlation length of the parameters of the medium and the transverse coherence length of the medium.

The general criteria for applicability of the Markov approximation [42] are usually satisfied in the case of an X-ray laser [25]. The restriction on the propagation path length, which occurs in an infinite randomly inhomogeneous medium [42], is absent in the case of a transversely bounded plasma filament of an X-ray laser [33].

3.2. Determination of the Parameter β

In the presence of gain saturation, the parameter β should be such that the parameters of the amplified spontaneous radiation, which are determined from equation (3) for the TCF, would be as close as possible to the truly average quantities. The truly average quantities are found by solving numerically the parabolic equation (1), which is the initial equation for the equation for the TCF. The equation (1) must be solved repeatedly by the Monte Carlo method, averaging the required results over an ensemble of noise realizations.

In previous TCF investigations of the dynamics of the amplified spontaneous radiation it was assumed that $\beta = 1$ in the saturation regime [24–33]. The error in determining the average energy characteristics of the amplified spontaneous radiation which is associated with the statistical linearization of the equation for the TCF with fixed β has been discussed in [37, 38] in the absence of fluctuations of the parameters of the medium. It was shown that $\beta = 1$ makes it possible to describe best the case of deep saturation. In the present paper we introduce a correction into equation (3), using a more complicated dependence of β on $B(\mathbf{r}, 0; z)/J_{sat}$, in order to make the results of integrating the equation as close as possible to the true averages.

Let us consider the dynamics of the amplified spontaneous radiation, neglecting diffraction, refraction, nonresonant losses, and fluctuations of the optical parameters. Such an approximate approach makes it possible to determine analytically the statistical characteristics of the radiation and to perform statistical linearization of the equation for the TCF more accurately. For convenience in performing the analysis, the spontaneous noise in the volume of the medium can be neglected ($S = 0$), replacing this noise by a source in the section $z = 0$. This is justified for sufficiently large gain, when

$$\exp G \gg 1,$$

where

$$G = \int_0^z \alpha(z)dz,$$

which is required for gain saturation. Then, equations (1) and (3) assume the forms, respectively,

$$\frac{\partial J(z)}{\partial z} - \frac{\bar{\alpha}J(z)}{1 + J(z)/J_{sat}} = 0, \quad J(0) = J_s = |E_s|^2, \quad (10)$$

$$\frac{\partial B(z)}{\partial z} - \frac{\bar{\alpha}B(z)}{1 + \beta B/J_{sat}} = 0, \quad B(0) = \langle J_s \rangle, \quad (11)$$

where E_s and J_s are the field amplitude and the flux density of the radiation from the source. The dependence of β on $\langle J \rangle$ is determined from the condition $B = \langle J \rangle$. Then, we obtain from equation (10) with equation (11)

$$\beta = \langle j/(1 + j) \rangle^{-1} - \langle j \rangle^{-1}, \quad (12)$$

where $j = J/J_{sat}$. From equation (12) we can estimate the range of variation of β. We shall assume that the independent components of E_s are distributed according to a Gaussian law with zero mean. When the influence of saturation is weak, $\langle j \rangle \ll 1$, the statistics of the field amplitude remains Gaussian. Then, expanding the right-hand side of equation (12) in a power series in the small parameter $\langle j \rangle$, it follows that $\beta \approx 2$. In the other extreme case, where saturation is deep, i.e., $\langle j \rangle \gg 1$, it is evident from equation (12) that β approaches 1.

The solution of equation (10) can be written in the implicit form

$$\ln(j/j_s) + j - j_s = G, \quad (13)$$

where $j_s = J_s/J_{sat}$. Amplification lengths for which $J \gg J_s$ are interesting, and since $j_s \ll 1$, the term j_s on the left-hand side of equation (3) can be neglected, i.e., $j_s = j\exp(j - G)$. Since E_s is a Gaussian quantity, j_s has an exponential distribution law

$$w(j_s) = \exp[-j_s/\langle j_s \rangle]/\langle j_s \rangle.$$

Using this fact, we obtain the probability distribution function for j:

$$w(j) = \frac{1 + j}{j_0}\exp\left\{-\frac{j}{j_0}\exp[j - j_{\max}] + j - j_{\max}\right\}, \quad (14)$$

where $j_0 = j_{\max} + 1/(1 + j_{\max})$, and $j_{\max}$ corresponds to the maximum of $w(j)$ and satisfies the equation

$$\langle j_s \rangle = j_0 \exp(j_{\max} - G).$$

The quantity j_{max} can also be negative, formally, $j_{max} > -1$, but $w(j)$ is meaningful only for $j > 0$. For fixed j_{max}, we have, using equation (14),

$$\langle j\rangle = \int_0^\infty \exp\left\{-\frac{j}{j_0}\exp[j - j_{max}]\right\} dj,$$

$$\left\langle \frac{j}{1+j}\right\rangle = \int_0^\infty \exp\left\{-\frac{j}{j_0}\exp[j - j_{max}]\right\}\frac{dj}{(1+j)^2}.$$

After the integrals have been calculated numerically, the function $\beta(\langle j\rangle)$ can be determined from equation (12). The result is shown in Fig. 1. The quantity β, as assumed above, varies from 2 in the absence of saturation down to 1 with deep saturation. The transitional region corresponds to the range $10^{-2} \le \langle j\rangle \le 10$. The analytic function

$$\beta(\xi) = 1 + 0.286\exp(-0.7281\xi) + 0.242\exp(-15.86\xi) + 0.471\exp(-3.13\xi), \quad (15)$$

which is used below to solve equation (3) numerically for the TCF with $\xi = B(\mathbf{r}, 0; z)/J_{sat}$, fits the numerical data in Fig. 1 well. The principles of the numerical method for integrating the equation for the TCF are presented in [24]. In a subsequent work [44] the method is improved and the phase error of the numerical solution is substantially decreased.

4. COMPARISON OF THE TCF METHOD WITH THE PARABOLIC EQUATION METHOD

As a check, equation (10) was integrated numerically with α = const by the Monte Carlo method with 10^4 numerical realizations. The values of $\langle j\rangle$ averaged over an ensemble were compared with $b = B/J_{sat}$ obtained by a single numerical solution of equation (11) with $\beta = 1$ (i.e., without correcting the TCF equation) and $\beta(b)$ determined in equation (15) (with a correction). Figure 2 shows plots of the relative difference of b from $\langle j\rangle$ as a function of $\langle j\rangle$ for different values of $\langle j_s\rangle$. For $\langle j_s\rangle = 10^{-3} \ll 1$, the maximum difference of b from $\langle j\rangle$ is about 20% without correction [37], and with a correction it is essentially zero. As the noise level increases with $\langle j_s\rangle = 10^{-1}$ and 1, when equation (14) holds increasingly more approximately, the introduction of the correction (15) does not eliminate the error, but it does make it possible to decrease the error to $\le$5%. The introduction of a correction does not change the result only for a high noise level $\langle j_s\rangle = 10$, but in this case the error is small.

In comparing the results of the TCF and Monte Carlo methods, the effect of fluctuations of the phase of the source radiation in the transverse section of the medium, which are due to the wide angular divergence of the spontaneous radiation, was neglected. The simplified approach does not answer the question of the accuracy of equation (3) in determining the angular distribution of the brightness of the amplified spontaneous radiation. The brightness of the radiation emitted at an angle $\theta = k_\perp/k$ with respect to the optic axis is one of the most important experimentally measured parameters. In the TCF method and in the parabolic equation method the brightness is determined as

$$q_B(\theta, z) = \lambda^{-2}\iint B(\mathbf{r}, \mathbf{r}'; z)\exp(i\mathbf{k}_\perp\mathbf{r}')d\mathbf{r}d\mathbf{r}',$$

$$\langle q(\theta, z)\rangle = \lambda^{-2}\left\langle \left|\int E(\mathbf{r}, z)\exp(i\mathbf{k}_\perp\mathbf{r}')d\mathbf{r}\right|^2\right\rangle.$$

In what follows we shall compare the average brightness of the amplified spontaneous radiation obtained by solving equations (1) and (3) numerically, retaining the transverse differential operators.

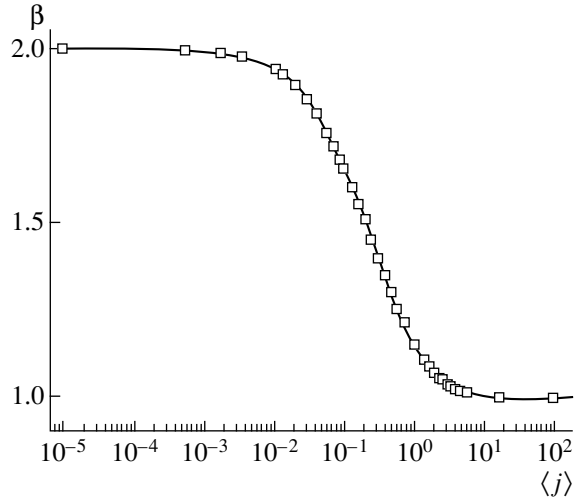

Fig. 1. Numerical dependence of β on $\langle j\rangle$ (squares) and an analytic fit (solid curve).

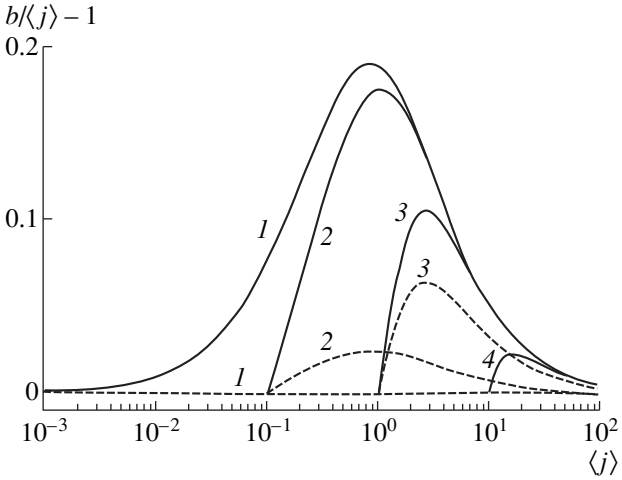

Fig. 2. Plot of $b/\langle j\rangle - 1$ versus $\langle j\rangle$ without correction (solid curves) and with correction (dashed curves) by statistical linearization with $\langle j_s\rangle = 10^{-3}$.

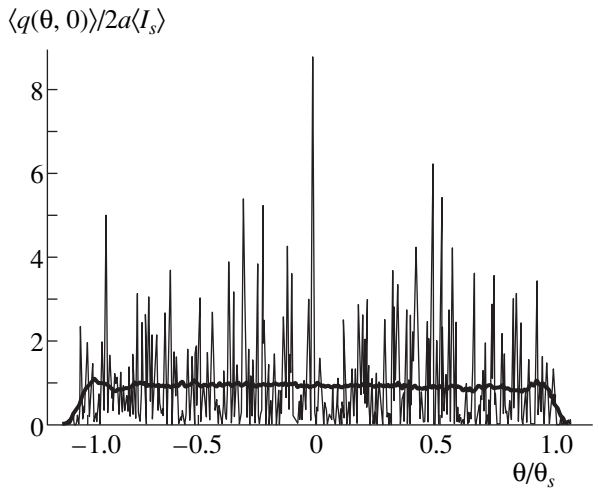

Fig. 3. Average angular brightness distribution of the source radiation with $N_r = 1$ (fine curve) and 900 (heavy curve).

The active medium is assumed to be planar with only the transverse coordinate x. It is difficult to perform three-dimensional calculations of the amplified spontaneous radiation by the parabolic equation method because of the limited present-day computational possibilities [18, 38]. The parameters of the medium and the value $\lambda \approx 21$ nm are characteristic for an X-ray laser operating on $3p$–$3s$ transitions in Ne-like ions with a nuclear charge of about 30 [1]. The half-width of the active medium is $a = 150$ μm, and the length of the laser is $z = 5$ cm. Therefore the geometric divergence angle is $\theta_g = 2a/z = 6$ mrad. Inside the gain zone of the medium (for $|x| \le a$) the gain is uniform and is equal to $\bar{\alpha} = 4$ cm^{-1}. The symmetric defocusing profile $\bar{\varepsilon}$ has the form

$$\bar{\varepsilon} = 1 - \Delta\varepsilon + x^2/z_r,$$

where $z_r = a/(\Delta\varepsilon)^{1/2}$ is the refraction length. This profile has been widely used in the numerical simulation of the dynamics of the radiation in the active medium of an x-ray laser produced by irradiating a thin exploding foil [13, 14, 21–26]. Outside the active medium (for $|x_{1,2}| \ge a$) we set $\alpha = 0$ and $\varepsilon = 1$. We neglect the nonresonant losses and the fluctuations of the optical parameters.

4.1. Simulation of a Random Realization of the Radiation Field

Under the conditions of strong gain, we shall replace the delta-correlated radiation source distributed in the volume of the medium by a source in the plane $z = 0$. In the numerical calculations we consider a partially coherent radiation source with a bounded angular spectrum of half-width θ_s. We write the boundary condition for equation (3) as

$$B(x, x'; 0) = \langle E(x_1, 0)E^*(x_1, 0)\rangle = \begin{cases} \langle I_s\rangle 2\theta_s \mathrm{sinc}(kx'\theta_s), & |x_{1,2}| \le a, \\ 0, & |x_{1,2}| > a. \end{cases} \quad (16)$$

The angular distribution of the average brightness of the source with the TCF (16) has the form

$$q_s(\theta) \simeq \begin{cases} \langle I_s\rangle 2a, & |\theta| \le \theta_s, \\ 0, & |\theta| > \theta_s. \end{cases} \quad (17)$$

For an appropriate choice of θ_s, such a source accurately simulates a delta-correlated source [24]. In the calculations it was assumed that $\theta_s = 10$ mrad, and increasing this quantity had no effect on the final result.

The boundary condition for equation (1) $E(x, 0) = E_s(x)$ in each realization is random. We represent $E_s(x)$ in the form

$$E_s(x) = \varphi_r(x) + i\varphi_i(x),$$

where φ_r and φ_i are real statistically independent functions. We write each function φ_r and φ_i on a grid as a linear combination of random numbers ψ_m:

$$\varphi(x_n) = \sum_{m=-\infty}^{m=\infty} C_m \psi_{m+n}, \quad (18)$$

where $\langle \psi_m \psi_n\rangle = \delta_{mn}$, $C_m = [2I_s\Delta x/\lambda]^{1/2}\theta_s \mathrm{sinc}(km\Delta x\theta_s)$ (see [45]), and Δx is the step in the grid along x with the condition $\Delta x \le \pi/k\theta_s$. It should also be noted that in equation (18) a finite number of terms can be summed, since C_m decreases as the index increases. The summation is of a moving character in space, which saves computer time [45].

The results of the numerical simulation of the radiation source are shown in Fig. 3. The angular distributions of the source brightness, which are averaged over an ensemble with $N_r = 1$ and 900 terms, are given. We note that one realization of the Monte Carlo method gives a good representation only of the width of the region of localization of the average angular spectra $\langle q_s\rangle$ of the radiation source. The brightness fluctuations are deep because of the Gaussian statistics; modulation from 0 up to values 6 to 8 times greater than the average occur. The angular radiation spectrum of the source closely approaches the distribution (17) only for a quite large number of realizations $N_r = 900$.

4.2. Computational Results for the Amplified Spontaneous Radiation

The results obtained by both methods can differ not only because of the approximate nature of the TCF equation but also because of possible numerical errors in each method. For this reason, such a comparison must first be made for linear amplification ($J_{sat} = \infty$), when the results should agree in the ideal situation.

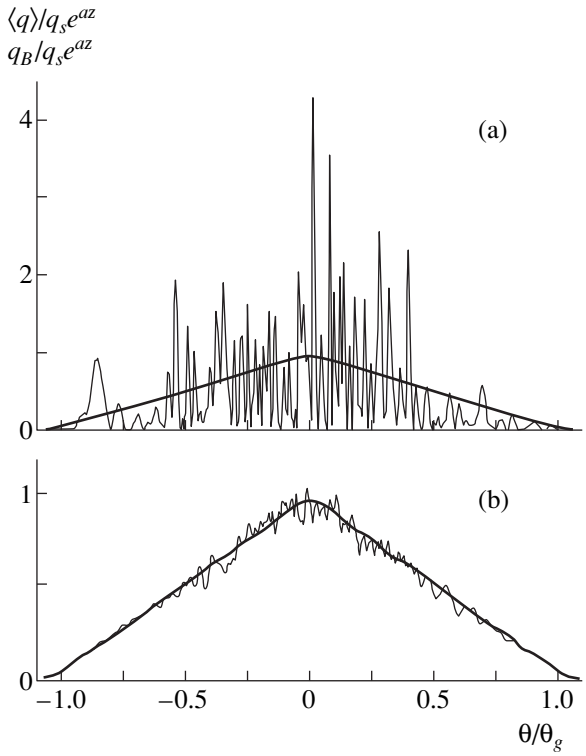

Fig. 4. Plots of the brightness of the amplified spontaneous radiation $\langle q(\theta)\rangle$ (fine curve) and $q_B(\theta)$ (heavy curve) with linear amplification with no refraction for N_r = (a) 1 and (b) 300.

Figure 4 shows the angular distributions of the brightness of the amplified spontaneous radiation for linear amplification and in the absence of refraction for N_r = 1 and 300. The divergence of the radiation is of a geometric character [24]. Once again, a single realization of the Monte Carlo method gives a distorted representation of the profile of the average brightness of the amplified spontaneous radiation. The fluctuations of the brightness remain deep because the Gaussian statistics remains in force. Increasing N_r results in smoothing of the profile $\langle q\rangle$. For N_r = 300 the Monte Carlo method gives a distribution $\langle q\rangle$ which weakly fluctuates around the profile q_B obtained by the TCF method. The results obtained show that the numerical errors are negligible in both methods.

Calculations with gain saturation in the absence of refraction ($\Delta\varepsilon = 0$) were performed for I_s = 1 arb. units and $J_{sat} = 7.5 \times 10^5$ arb. units. For these parameters the average flux density of the amplified spontaneous radiation at the exit of the X-ray laser is close to J_{sat}. Thus, the approximate character of equation (3) should be more strongly manifested here. Figure 5 shows the angular distributions of the brightness of the amplified spontaneous radiation which were obtained by the TCF method and by the Monte Carlo method with the parabolic equation for N_r = 1, 10, and 300. The character of the divergence remains geometric, just as with linear amplification (Fig. 4). Radiation exiting through the end face of the X-ray laser plays the main role. The

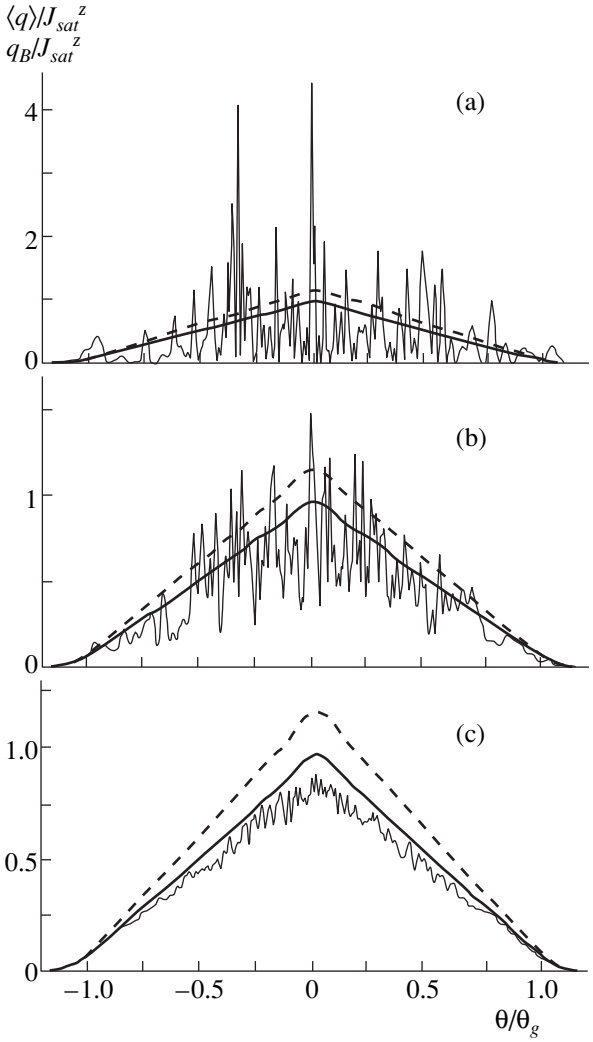

Fig. 5. Plots of the brightness of the amplified spontaneous radiation $\langle q(\theta)\rangle$ (fine curve) and $q_B(\theta)$ with no correction β = 1 (dashed curve) and with correction (heavy curve) by statistical linearization of the equation for the transverse correlation function with gain saturation and with no refraction for N_r = (a) 1, (b) 10, and (c) 300.

deep modulation of the angular spectrum of the amplified spontaneous radiation which occurs for linear amplification remains in a single Monte Carlo realization. The period of the modulation of the brightness at the periphery of the beam is greater than near the axis, i.e., according to [29] the coherence at the periphery of the beam is higher than at the center. It follows from Fig. 5 that the TCF method does not distort the form of the profile of the angular distribution of the average brightness of the radiation. But the fluctuations of the phase of the field increase the error in determining the absolute values of the average brightness by the TCF equation method, without correction, up to ~30%. It is evident from Fig. 5 that correcting the TCF equation makes it possible to decrease the difference between $\langle q\rangle$ and q_B from 30% to ~10%. The impossibility of obtaining complete agreement between the distributions $\langle q\rangle$

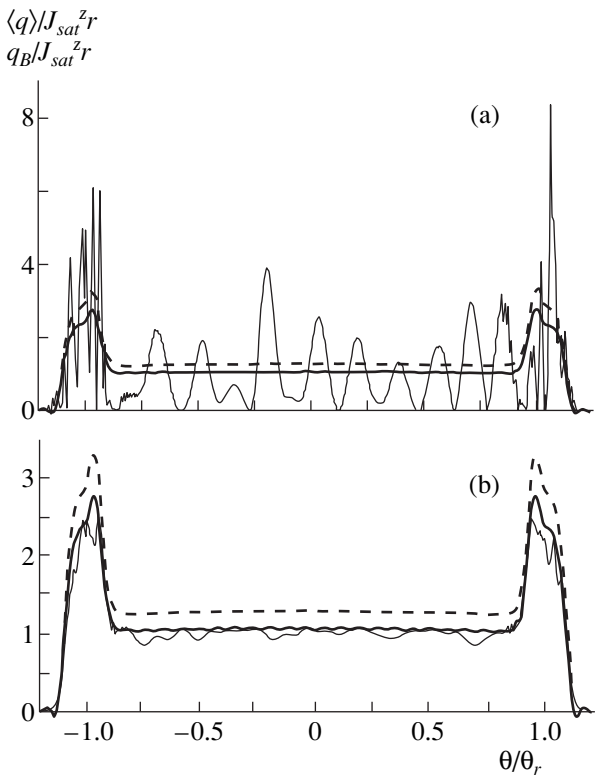

Fig. 6. Plots of the brightness of the amplified spontaneous radiation $\langle q(\theta)\rangle$ (fine curve) and $q_B(\theta)$ without correction (dashed line) and with correction (heavy line) by statistical linearization of the equation for the transverse correlation function with gain saturation and with refraction for $N_r = 1$ (a) and 300 (b).

and q_B using the correction (15) is explained by the approximate nature of the distribution function (14).

The results of similar calculations by the TCF method and the Monte Carlo method with $N_r = 1$ and 300 in the presence of refraction with $\Delta\varepsilon = 10^{-4}$ are displayed in Fig. 6. Here refraction plays a substantial role, since $z_r = 1.5$ cm is much smaller than the length of the X-ray laser. The divergence is of a typical refraction character [26, 28]. In the presence of gain saturation, the spontaneous radiation exiting through the lateral surface of the gain zone forms off-axis peaks at $\theta \approx \pm\theta_r$ in the angular brightness distribution, where $\theta_r = \Delta\varepsilon^{1/2} = 10$ mrad is the refraction angle. However, at locations where the average brightness reaches its maximum value, the spatial coherence of the amplified spontaneous radiation is relatively low. The degree of coherence is higher in the region of the beam near the axis, where the amplified spontaneous radiation which has exited through the end face of the active medium dominates [29]. In one Monte Carlo realization the degree of modulation of the angular spectrum of the amplified spontaneous radiation is high, and the spectrum is smoothed as the number of realizations increases. It is evident that for $\beta = 1$, i.e., without correction of equation (3), the TCF method overestimates the absolute values of $\langle q\rangle$ by ~20–30%. At the same time, the TCF method does not distort the profile $\langle q\rangle$. When the correcting function (15) is used, the difference between $\langle q\rangle$ and q_B decreases substantially.

Thus, correcting a statistical realization makes it possible to increase substantially the accuracy of the TCF equation. As the degree of saturation decreases and increases, the error in determining $\langle q\rangle$ by the TCF method will decrease even more.

We note that in the absence of refraction, the calculation by the TCF method requires ten times less time than a single realization of the parabolic equation, and in the presence of refraction these times are comparable. This is especially remarkable: after all, the equation for the TCF is three-dimensional in the planar-medium approximation, while the parabolic equation is two-dimensional. The point is that in the parabolic equation method the transverse grid step is $\Delta x \sim \lambda/\theta_s$, and for the TCF method $\Delta x' \sim \lambda/\theta_s$, $\Delta x \sim h$, where h is the characteristic transverse nonuniformity of the average flux density, which is of the order of a and much greater than $\Delta x'$. For this reason, in the first place, the step along z in the parabolic equation method $\Delta z \sim k(\Delta x)^2$ [41] is much less than the step in the TCF method $\Delta z \sim k\Delta x\Delta x'$ [24, 52]. In the second place, because of the low degree of coherence of the amplified spontaneous radiation the size of the grid region along x' in the TCF method is much less than $2a$, and the number of grid points in the transverse section is smaller than in the parabolic equation method. In the third place, as noted above, the TCF method does not require averaging over an ensemble. To obtain reliable results by the parabolic equation method, as one can see from Figs. 5 and 6, it is necessary to average over tens and hundreds of realizations. For this reason, the time to obtain a finite average result by the TCF method is less than by the parabolic equation method by a factor of $\sim 10^2$–10^3 in the absence of refraction and by a factor of 10^1–10^2 in the presence of refraction. Hence it follows that the TCF method is much more effective than the parabolic equation method for this class of problems. Characteristically, the literature contains no calculations of the amplified spontaneous radiation in an X-ray laser by the parabolic equation method for a real three-dimensional medium, since such calculations require an unrealistic number of grid points [18], while for the TCF method such calculations have been performed for a regularly nonuniform [24] and randomly-nonuniform media (see below). It is also important to note that when random parameters of the medium are additionally included in the analysis, the TCF method becomes relatively even more effective.

5. ANALYSIS OF THE EFFECT OF FLUCTUATIONS OF THE PARAMETERS OF A MEDIUM ON THE AMPLIFIED SPONTANEOUS RADIATION

We shall assume below that at distances of the order of the correlation lengths the quantities σ_ε and σ_α vary little in the transverse plane. For a qualitative analysis

of the role of the fluctuations $\tilde{\mathbf{r}}$, we shall assume, as done in [39], that the $\bar{\varepsilon}$ and $\bar{\alpha}$ profiles can be represented in the same quadratic form:

$$\bar{\varepsilon} = 1 - \Delta\varepsilon + x^2/z_r, \quad \bar{\alpha} = \alpha_0[1 - \mathbf{r}^2/a^2].$$

Then, using equations (7)–(9), we obtain from equations (4)–(6)

$$H_\varepsilon(\mathbf{r}, \mathbf{r}'; z) = \sqrt{\frac{2}{\pi}}\sigma_\varepsilon^2 l_{\varepsilon\parallel}\left[1 - \exp\left(-\frac{r'^2}{2l_{\varepsilon\perp}^2}\right)\right], \quad (19)$$

$$H_\alpha(\mathbf{r}, \mathbf{r}'; z) = -\sqrt{\frac{2}{\pi}}\frac{\sigma_\alpha^2 l_{\alpha\parallel}[1 + \exp(-r'^2/2l_{\alpha\perp}^2)]}{k^2[1 + \beta B(\mathbf{r}, 0; z)/J_{sat}]^2}, \quad (20)$$

$$H_h(\mathbf{r}, \mathbf{r}'; z) = \frac{4L_\parallel L_\perp^2}{\sqrt{2\pi}z_r^2} \times\left(\mathbf{r}' - i\frac{2\alpha_0}{k\Delta\varepsilon}\mathbf{r}\frac{1}{[1 + \beta B(\mathbf{r}, 0; z)/J_{sat}]}\right)^2. \quad (21)$$

It follows from equation (3) that the terms (21) are proportional to $\mathbf{r}'^2$, $\mathbf{r}^2$, and $i\mathbf{r}\mathbf{r}'$. They lead, respectively, to narrowing of the TCF with respect to $\mathbf{r}'$, broadening with respect to $\mathbf{r}$, and phase modulation of the TCF. Thus, the term with $\mathbf{r}'^2$ leads to scattering of the amplified spontaneous radiation, similar to scattering by fluctuations $\tilde{\varepsilon}$ and $\tilde{\alpha}$. The term with $\mathbf{r}^2$ leads to broadening of the beam as a result of the effective broadening of the regular gain profile. The term with $i\mathbf{r}\mathbf{r}'$ leads to additional regular refraction of the amplified spontaneous radiation.

We shall rewrite equation (3), using equations (19)–(21) and neglecting the nonresonant absorption and gain saturation:

$$\left[\frac{\partial}{\partial z} + \frac{i}{k}\frac{\partial^2}{\partial\mathbf{r}\partial\mathbf{r}'} - \alpha_0 + \frac{ik}{z_r^2}\left(1 - \sqrt{8\pi}\frac{L_\parallel L_\perp^2\alpha_0}{a^2}\right)\right.$$
$$\times\left(\mathbf{r}\mathbf{r}' - i\frac{\alpha_0}{k\Delta\varepsilon}\mathbf{r}^2\right) + \left(\frac{3(ka)^2}{2z_h^3} + \frac{\alpha_0}{4a^2}\right)\mathbf{r}'^2$$
$$+ 3\frac{(kal_{\varepsilon\perp})^2}{z_\varepsilon^2}\left\{1 - \exp\left(-\frac{\mathbf{r}'^2}{2l_{\varepsilon\perp}^2}\right)\right\} - 3\frac{(kal_{\alpha\perp})^2}{z_\alpha^3}$$
$$\left.\times\left\{1 + \exp\left(-\frac{\mathbf{r}'^2}{2l_{\alpha\perp}^2}\right)\right\}\right]B(\mathbf{r}, \mathbf{r}'; z) = \lambda^2 Q(\mathbf{r}, z)\delta(\mathbf{r}'), \quad (22)$$

where

$$z_\varepsilon = [6(2/\pi)^{1/2}(al_{\varepsilon\perp})^2/\sigma_\varepsilon^2 l_{\varepsilon\parallel}]^{1/3},$$

$$z_\alpha = [6(2/\pi)^{1/2}(kal_{\alpha\perp})^2/\sigma_\alpha^2 l_{\alpha\parallel}]^{1/3},$$

$$z_h = [6(2/\pi)^{1/2}(az_r^2)^2/(4L_\parallel L_\perp^2)]^{1/3}$$

is the characteristic scattering length of the amplified spontaneous radiation scattered by the fluctuations $\tilde{\varepsilon}$, $\tilde{\alpha}$, and $\tilde{\mathbf{r}}$, respectively.

The scattering of the amplified spontaneous radiation by the fluctuations $\tilde{\varepsilon}$ in the transversely-bounded medium of an X-ray laser differs substantially from scattering in an infinite medium such as a turbulent atmosphere. It has been studied quite well using the TCF method for a planar medium [31–34]. We present below the computational results obtained for equation (3) for a three-dimensional medium with an axisymmetric distribution of its average parameters. We note that when this situation is simulated by the parabolic equation method, the axial-symmetry approximation cannot be used, because there is no axial symmetry in each realization.

Figure 7 shows the curves of the axial brightness $q(0, z) \equiv q_0(z)$, normalized to the brightness q_s (17) of a spontaneous source, with uniform linear amplification in an axisymmetric medium for $\lambda = 21$ nm, $\Delta\varepsilon = 0$, $\bar{\alpha} = 4$ cm^{-1}, $a = 50$ μm, $l_{\varepsilon\perp} = l_{\varepsilon\parallel} = l_\varepsilon = 1$ μm, and different values of σ_ε. Outside the active medium $\alpha = 0$ and $\varepsilon = 1$. As one can see from Fig. 7, in the absence of fluctuations $\tilde{\varepsilon}$ the on-axis brightness increases exponentially with increasing length of the X-ray laser, i.e., $q_0(z) = q_s\exp(\alpha z)$. It is well known that obtaining such a dependence in an experiment serves as the main proof for the presence of lasing [1]. However, in many experimental situations the gain determined according to the dependence of the brightness of an X-ray laser on the

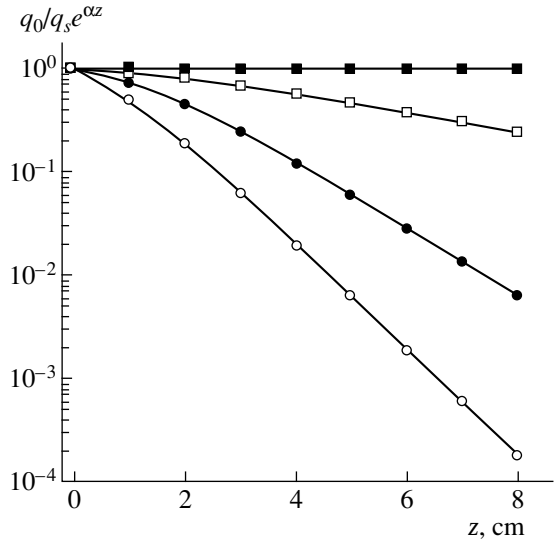

Fig. 7. Plots of the on-axis brightness of the amplified spontaneous radiation $q_0(z)$ in the three-dimensional case for a = 50 μm, $\alpha = 4$ cm^{-1}, $\Delta\varepsilon = 0$, $l_{\varepsilon\perp} = l_{\varepsilon\parallel} = 1$ μm, and $\sigma_\varepsilon = 0$ (■), 2×10^{-5} (□), 4×10^{-5} (●), 6×10^{-5} (○).

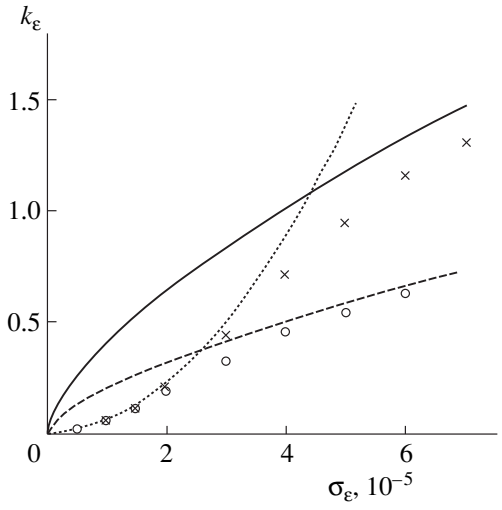

Fig. 8. Numerical dependences of κ_e in the two-dimensional (○) and three-dimensional (×) cases and analytical dependences $3d^2/z_\varepsilon$ (dotted line), $1/z_\varepsilon$ (dashed curve), and $2/z_\varepsilon$ (solid curve) on σ_ε.

length of the laser is much less than the value obtained from kinetic calculations. It is evident from Fig. 7 that in the presence of $\tilde{\varepsilon}$ the curves on a logarithmic scale with $z \geq z_{cs}$ are close to straight lines, i.e.,

$$q_0(z) \propto \exp(\alpha z - \kappa_\varepsilon z).$$

Thus, the scattering of amplified spontaneous radiation by the fluctuations $\tilde{\varepsilon}$ and its "expulsion" through the side surface of an X-ray laser is similar to linear absorption of the amplified spontaneous radiation with a intensity coefficient κ_ε. Therefore the presence of $\tilde{\varepsilon}$ decreases the observed gain and can be one of the reasons for the discrepancy between its experimental value and the value determined in calculations of the population kinetics.

Plots of the quantity $\kappa_\varepsilon(\sigma_\varepsilon)$ determined from the slope of the linear section of the curves $q_0(z)$ are shown in Fig. 8 for two-dimensional planar and three-dimensional axisymmetric media. The character of the function $\kappa_\varepsilon(\sigma)$ is determined by the parameter $d \equiv kal_{\varepsilon\perp}/z_\varepsilon$. For weak fluctuations $\tilde{\varepsilon}$, where $d^3 \ll 1$, we obtain $\kappa_\varepsilon \approx 3d^2/z_\varepsilon \sim \sigma_\varepsilon^2$ [34], and κ_ε is independent of $l_{\varepsilon\perp}$, a, and the geometry of the medium. For strong fluctuations $\tilde{\varepsilon}$, when $d^3 \geq 1$, we have $\kappa_\varepsilon \approx 1/z_\varepsilon$ for a planar medium, i.e., $\kappa_\varepsilon \propto \sigma_\varepsilon^{2/3}$. For a three-dimensional axisymmetric medium $\kappa_\varepsilon \approx 2/z_\varepsilon$, i.e., the losses become twice as great. The effect of $\tilde{\varepsilon}$ on the amplified spontaneous radiation is appreciable for comparatively small values of $\sigma_\varepsilon \geq 10^{-5}$, where $\sigma_\varepsilon \ll \Delta\varepsilon$ and the nonuniformity of the electron density of the plasma is several percent of the maximum regular value in the gain zone.

As one can see from equation (22), the character of the effect of the fluctuations $\tilde{\alpha}$ on the amplified spontaneous radiation is similar to the effect of $\tilde{\varepsilon}$. Instead of $l_{\varepsilon\parallel}$, $l_{\varepsilon\perp}$, σ_ε, and z_ε we must use in the formulas $l_{\alpha\parallel}$, $l_{\alpha\perp}$, σ_α/k, and z_α, respectively. In addition to scattering, the fluctuations $\tilde{\alpha}$ lead to an additional regular amplification against the background $\bar{\alpha}$, since $H_\alpha \neq 0$ at $\mathbf{r}' = 0$. The correction for $\bar{\alpha}$ is $(\pi/2)^{1/2}\sigma_\alpha^2 l_{\alpha\parallel}$. For the same scale and depth of the fluctuations $\tilde{\varepsilon}$ and $\tilde{\alpha}$, the effect of $\tilde{\alpha}$ on the amplified spontaneous radiation is weaker, since they do not directly influence the phase of the radiation. Even if we set $\sigma_\alpha \sim \alpha_0$, for $\lambda \sim 20$ nm, we have $\sigma_\alpha/k \sim 10^{-6}$. This level of fluctuations does not lead to an appreciable influence on the radiation.

In the experiments of [46], intended to measure the quasistationary gain in an X-ray laser on the transition $3p$–$3s$ in Ne-like yttrium ($\lambda = 15.5$ nm), the amplification of the input radiation in a 2-mm long laser was studied, so that the influence of refraction was ruled out. An X-ray laser plasma was obtained by unilateral irradiation of a flat target without a preliminary pulse. The measured average gain was 10–15 cm^{-1}. A small-scale structure was found in the distribution of the time-integrated intensity of the amplified radiation with transverse spot size ~10 μm. Evidently, it is related with the presence of the fluctuations $\tilde{\alpha}$, whose parameters are difficult to measure directly. On the basis of the spot size, $l_{\alpha\perp} \sim 10$ μm. It is quite difficult to draw an unequivocal conclusion about $l_{\alpha\parallel}$. It can only be stated that $l_{\alpha\parallel}$ is appreciably greater than $l_{\alpha\perp}$ and is comparable to the length of the amplifier (2 mm), since substantial amplification, leading to a spotty intensity distribution, should build up in a distance $l_{\alpha\parallel}$. In the two-dimensional calculations below, we take $l_{\alpha\parallel} = 2$ mm, in order to estimate the maximum possible effect. The average profile $\bar{\alpha}(x)$ taken in the calculations is shown in Fig. 9. If we take $\sigma_\alpha = 0.5\bar{\alpha}(x)$, then the characteristic maximum value of α reaches ~15 cm^{-1}. This value and the profile $\bar{\alpha}(x)$ agree with the results obtained in the calculations performed in [47] using the XRASER program. The average electron density profile $\overline{N_e}$ used, which is shown in Fig. 9, is close to the distribution obtained in [47] using the LASNEX computer code. We recall that the relation between $\overline{N_e}$ and $\bar{\varepsilon}$ can be found from equation (2).

Figure 10 showed the brightness distribution q of the amplified spontaneous radiation and the transverse coherence length L_c in the far zone with a three-dimensional spontaneous source, $z = 2.5$ cm, and different values of σ_α. The transverse coherence length L_c near the point x is determined according to the drop of the modulus of the coherence coefficient

$$\mu(x, x'; z) = B(x, x'; z)/[J(x_1; z)J(x_2; z)]^{1/2}$$

along x' to the value $\mu = 0.88$. The coherence length in Fig. 10 is presented in units of $\lambda Z/4R$, where Z is the distance from the X-ray laser to the far-zone plane, R = 200 μm. In the absence of $\tilde{\alpha}$ (for $\sigma_\alpha = 0$) the intensity distribution of the amplified spontaneous radiation is shifted in angle as a result of regular diffraction. In the presence of fluctuations $\sigma_\alpha(x) = 0.5\bar{\alpha}(x)$ with a nonuniform profile $\tilde{\alpha}$, the divergence and coherence of the amplified spontaneous radiation improve somewhat. However, analysis shows that this is a consequence not of the scattering of radiation by $\tilde{\alpha}$, but rather a nonuniform correction to the regular amplification. The regular gain profile is peaked and acquires the form

$$\bar{\alpha}[1 + (\pi/32)^{1/2}\bar{\alpha}l_{\alpha\|}].$$

The narrowing of the zone of maximum regular amplification results in a small improvement of the beam quality. The contribution of $\tilde{\alpha}$ to the average additional gain is appreciable, and its contribution to scattering is not. To check this, calculations were performed for a stronger but uniform field of fluctuations with $\sigma_\alpha = 0.5\bar{\alpha}_{\max} = 5$ cm^{-1}, so that the correction to the regular profile $\bar{\alpha}$ is also uniform and does not change shape. This calculation gave a result that is identical, as one can see from Fig. 10, to the case of no fluctuations $\tilde{\alpha}$. It is worth noting that for pico- and femtosecond pumping regimes, when the average gain is an order of magnitude greater than that in the quasistationary regime, the consequences of fluctuations with $\sigma_\alpha \sim \bar{\alpha}$ will be more serious for the amplified spontaneous radiation.

As far as the effect of hose-like fluctuations $\tilde{\mathbf{r}}$ on the amplified spontaneous radiation is concerned, for a small gain on length $L_\|$ and weak deflections $L_\perp \ll a$ we have in equation (22)

$$(8\pi)^{1/2}L_\|\alpha_0(L_\perp/a)^2 \ll 1.$$

For example, for the conditions considered in [39] with a = 100 μm, $L_\perp$ = 1 μm, $L_\|$ = 10 μm, and $\alpha_0 = 4$ cm^{-1}, we have 2×10^{-6}. For this reason, the relative contribution of the fluctuations $\tilde{\mathbf{r}}$ to the regular refraction and broadening of the beam is negligible. It is evident from equation (22) that the contribution of fluctuations $\tilde{\mathbf{r}}$ to scattering of the amplified spontaneous radiation is of a similar form as the contribution of the relatively large-scale fluctuations $\tilde{\varepsilon}$ and $\tilde{\alpha}$, where the exponential functions in equation (22) can be expanded in a series. The quantities $l_{\varepsilon\|}$, $l_{\varepsilon\perp}$, σ_ε, and z_ε in the case of fluctuations $\tilde{\varepsilon}$ are similar to, respectively, $L_\|$, $L_\perp$, $\sigma_h = 2(L_\perp/z_r)^2$, and z_h in the case of the fluctuations $\tilde{\mathbf{r}}$. For $L_\perp$ = 1 μm, $L_\|$ = 10 μm, and $\Delta\varepsilon \sim 10^{-4}$ we obtain $\sigma_h \sim 10^{-8}$, which is a very small quantity, and $z_h \sim 2.3$ m, which is much greater than the length of the X-ray laser. For this reason, the hose-like fluctuations $\tilde{\mathbf{r}}$ have no effect on the amplified spontaneous radiation for the X-ray laser parameters considered, but they could have a destructive effect when the input coherent radiation is amplified, as was demonstrated in [39].

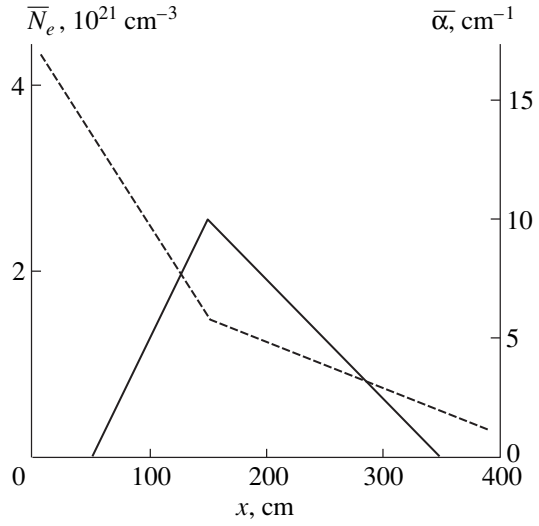

Fig. 9. Regular electron density profiles $\overline{N_e}$ (dashed curve) and gain $\bar{\alpha}$ (solid curve) in an x-ray laser operating on Ne-like yttrium.

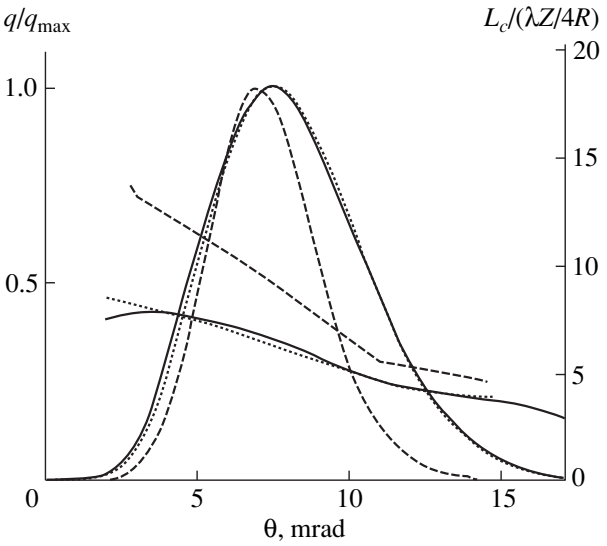

Fig. 10. Brightness distribution of the amplified spontaneous radiation q (bell-shaped curves) and coherence length L_c (inclined curves) in the far zone with $l_{\alpha\perp}$ = 10 μm, $l_{\alpha\|}$ = 0.2 cm, and $\sigma_\alpha = 0$ (solid curves), $\sigma_\alpha = 0.5\bar{\alpha}(x)$ (dashed curves), and $\sigma_\alpha = 0.5\bar{\alpha}_{\max}$ (dotted curves).

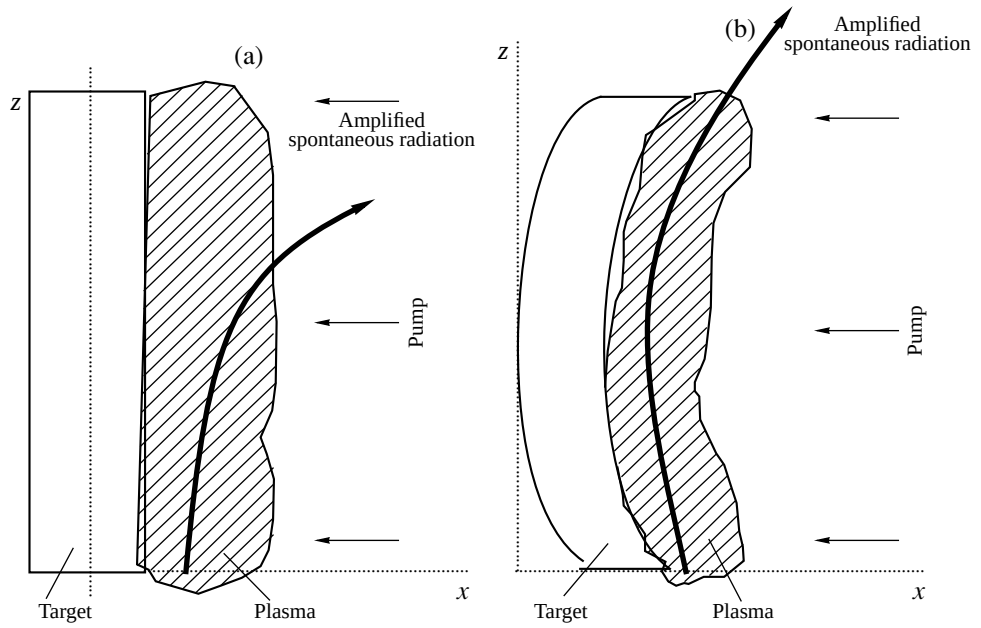

Fig. 11. Diagram of an x-ray laser with (a) a flat and (b) curved target.

6. IMPROVEMENT OF THE SPATIAL COHERENCE OF AN X-RAY LASER

The expanding plasma column of the active medium of a laboratory X-ray laser, produced by unilateral focusing of the radiation from an optical laser into a line on a thick solid target, is characterized by a sharp nonuniformity and asymmetry of the regular transverse profile of the electron density. The gain zone lies in the region where the electron density gradient in the plasma is quite large (Fig. 9). Refraction displaces the amplified spontaneous radiation beam out of the gain zone in the direction away from the target (see Fig. 11a) and causes angular displacement of the beam as a whole in the far zone; this is demonstrated in Fig. 10.

For an X-ray laser operating on Ne-like ions with small nuclear charges of the order of 20-25, the refraction losses are so large that lasing disappears. Irradiation of the target with pump radiation containing a prepulse or several pulses is widely used to decrease refraction [9]. The role of the prepulse is to produce a preliminary plasma, which has enough time to expand, cool down, and acquire a low density gradient before the arrival of the main pulse. The use of a preliminary pump pulse made it possible to detect the laser lines which had not been previously observed because of refraction losses.

But the use of a prepulse does not eliminate but only decreases the refraction by the density. Additional improvement of beam quality is achieved with partial compensation of the refraction distortions using a target curved with a constant radius of curvature in a longitudinal direction [10]. When the target is curved, the propagating radiation is deflected because of refraction, but the plasma medium is also displaced in the direction of defocusing. For this reason the beam passes through the plasma without leaving the gain zone (Fig. 11b). This approach, combined with the preliminary pump pulse, was first implemented in [11]. Since refraction compensation occurs in only one direction x, the two-dimensional case is studied in the calculations.

In the calculations the radiation wavelength is taken to be $\lambda = 21.2$ nm, which is characteristic for a $3p$–$3s$ transition in Ne-like zinc. In the presence of pumping with a preliminary pulse, the expanding plasma is characterized by a regular concave exponential electron density profile:

$$\overline{N_e}(x) = \overline{N_e}^{conc}(x) = N_{e0}\exp(-x/d), \qquad (23)$$

where $N_{e0} = 5.6 \times 10^{20}$ cm^{-3} and $d = 70$ μm. The distribution can be approximated by a model quadratic function

$$\bar{\alpha}(x) = \alpha_0[1 - (x - x_0)^2/a^2], \qquad (24)$$

where $a = 50$ μm, $x_0 = 100$ μm, $\alpha_0 = 4$ cm^{-1}, and $\alpha = 0$ for $|x - x_0| > a$. The $\overline{N_e}^{conc}$ and $\bar{\alpha}$ profiles are shown in Fig. 12. The source intensity is proportional to $\bar{\alpha}$. In the case of a curved target (Fig. 11b) we assume that the regular plasma parameters are determined by the functions (23) and (24), but they depend on $x + Cz^2/2$, where C is the curvature of the target ($Cz \ll 1$).

The basic laws of the dynamics of the power and beam quality of the amplified spontaneous radiation in an X-ray laser with linear amplification were obtained in [30] for flat and curved targets. The experimental facts [48] that the coherence length L_c is on the whole

very small and, moreover, in the presence of strong refraction it is much shorter at the center than at the periphery of the beam (see curves *1* in Fig. 13) were confirmed for a flat target. Choosing the optimal target curvature

$$C_{opt} = \nabla \overline{N}_e(x_0)/2N_c,$$

where $\nabla \overline{N}_e(x_0)$ is the density gradient at the point of maximum amplification, substantially increases the power and brightness of the amplified spontaneous radiation, appreciably increases L_c in the far zone, and gives a more uniform distribution of L_c in the transverse section of the radiation beam (see curves *2* in Fig. 13). However, analysis shows that the coherence length L_c is even less than would be the case for a flat target in the absence of refraction. The reason is that the compensation of refraction as a result of target curvature is incomplete. The residual refraction is a consequence of the nonuniformity of $\nabla \overline{N}_e$ in the gain zone, and for a concave density profile (23) it is of a focusing character. It has been shown in [30] that L_c can be substantially increased, if curving the target gives a residual defocusing effect. This requires a convex density profile in the gain zone.

A convex profile $\overline{N}_e = \overline{N}_e^{conv}(x)$ is shown in Fig. 12. Near the point of maximum gain $x = x_0$ it is described by the function

$$\overline{N}_e(x) = \overline{N}_e^{conv}(x) = \overline{N}_e^{conc}(x_0) + \nabla \overline{N}_e^{conc}(x_0)(x - x_0) - \nabla^2 \overline{N}_e^{conc}(x_0)(x - x_0)^2/2, \quad (25)$$

where the derivatives of the function $\overline{N}_e^{conc}$ (23) are taken at the point $x = x_0$. The relation (25) is different from the series expansion of the function $\overline{N}_e^{conc}(x)$ near the point $x = x_0$ by the sign in front of the last term with the second derivative. Thus, $\overline{N}_e^{conc}(x)$ and $\overline{N}_e^{conv}(x)$ have the same curvature at the center of the gain zone but opposite signs. The value of C_{opt} is the same for both density profiles.

The curves *3* in Fig. 13 correspond to the computational results obtained with $C = C_{opt}$ and a convex profile $\overline{N}_e = \overline{N}_e^{conv}(x)$. The distribution of L_c across the beam is obtained to be uniform, and L_c additionally increases by approximately a factor of 6 compared with the case $\overline{N}_e = \overline{N}_e^{conc}(x)$. This is achieved at the cost of a decrease in the power density by a factor ≈6 and the maximum brightness q_m by a factor of ≈12 as a result of doubling of the divergence. For this reason, the coherent power P_c, which is an important characteristic of the amplified spontaneous radiation and influences the possibility of holographic applications of the X-ray laser, decreases by a factor ≈2. We define P_c for a planar medium as $P_c = q_m L_c$. Therefore, for linear amplification the proposed method for improving the coherence concerns only the coherence length and is not justified energetically from the standpoint of either the brightness or the coherent power.

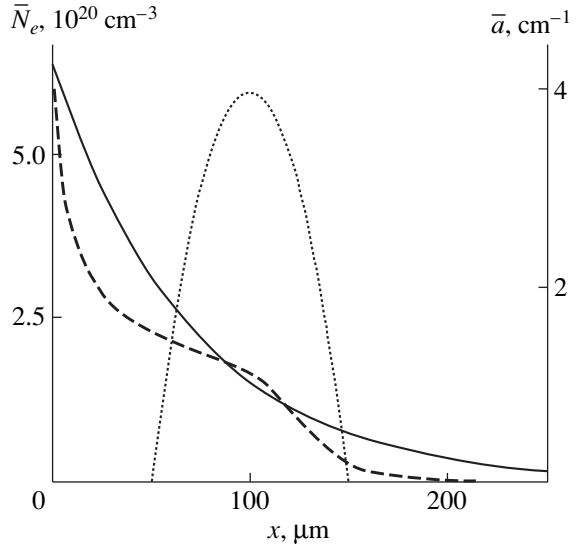

Fig. 12. Regular profiles of the parameters of the active medium of an x-ray laser: exponential concave (solid curve) and convex (dashed curve) electron density profiles and gain profile (dotted curve).

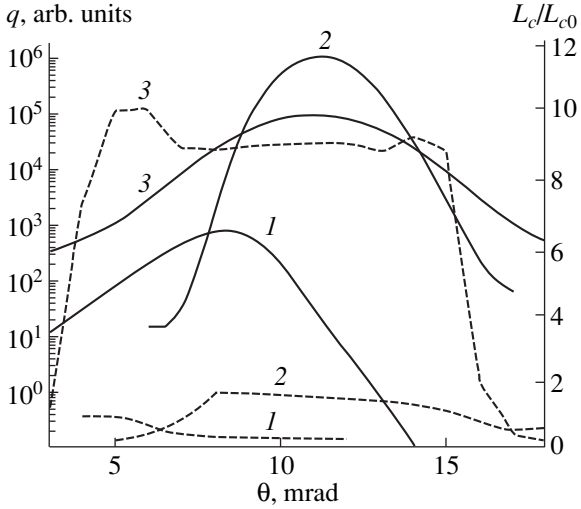

Fig. 13. Brightness distribution of the amplified spontaneous radiation q (solid curves) and coherence length L_c (dashed curves) in the far zone for $z = 5$ cm in the absence of gain saturation for $\overline{N}_e = \overline{N}_e^{conv}$ with $C = 0$ (*1*), $C = C_{opt}$ (*2*), $\overline{N}_e = \overline{N}_e^{conc}$ and in the case $C = C_{opt}$ (*3*) with $\alpha_{c0} = \lambda z/4a$.

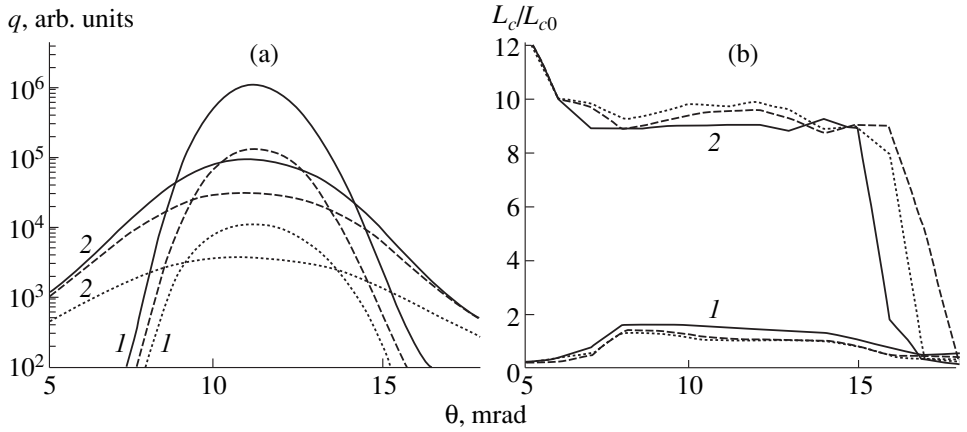

Fig. 14. Distributions of (a) brightness of amplified spontaneous radiation q and (b) coherence length L_c in the far zone with $\overline{N_e} = \overline{N_e}^{conv}$ (*1*) and $\overline{N_e} = \overline{N_e}^{conc}$ (*2*) for $J_{sat}/J_0 = \infty$ (solid curves), 5×10^4 (dashed curves), and 2×10^3 (dotted curves).

However, a positive consequence of curving the target is the possibility of attaining gain saturation, as demonstrated in the experiments of [6, 7]. Figure 14 shows the computational results for the angular distribution of the brightness and the coherence length of amplified spontaneous radiation in the far zone, which were obtained for $\overline{N_e}^{conc}$ and $\overline{N_e}^{conv}$ and various saturation levels, i.e., by varying J_{sat}. The saturation flux density J_{sat} in Fig. 14 is normalized to the value $J_0 = 100 j_s \theta_s/\alpha_0$, i.e., a 100-fold noise radiation flux density. For $J_{sat} = 10^7 J_0$ there is no saturation; for $J_{sat} = 10^6 J_0$ saturation starts to have a weak effect; and, for $J_{sat} = 10^4 J_0$ the flux density of the amplified spontaneous radiation is of the order of J_{sat} at the exit of the X-ray laser.

It is evident from Fig. 14a that gain saturation substantially retards the growth of the brightness of the X-ray laser. Obviously, the higher the brightness achieved in the absence of saturation, the greater the decrease in brightness in the presence of saturation. For this reason, on switching from the profile $\overline{N_e}^{conc}$ to the profile $\overline{N_e}^{conv}$, in the presence of gain saturation the brightness of the amplified spontaneous radiation decreases not by a factor ≈ 12, as happened with linear amplification, but only by a factor ≈ 3. The divergence of the amplified spontaneous radiation increases with the degree of saturation, and on switching from $\overline{N_e}^{conc}$ to $\overline{N_e}^{conv}$ it increases by a factor of 2. The effect of gain saturation on L_c is much smaller, and for $\overline{N_e}^{conc}$ the coherence length decreases somewhat with increasing saturation, while for $\overline{N_e}^{conv}$ it increases somewhat (Fig. 14b). For this reason, on switching from $\overline{N_e}^{conc}$ to $\overline{N_e}^{conv}$ the quantity L_c increases with gain saturation not by a factor ≈ 6, as in the linear amplification, but rather by a factor of ≈ 9. Ultimately, for linear amplification the coherent power with $\overline{N_e}^{conv}$ was two times lower than the level obtained with $\overline{N_e}^{conc}$, but in the presence of gain saturation it was three times higher. Therefore gain saturation makes the proposed method of improving coherence energetically more justified. The drawback is that the divergence increases and the absolute values of the brightness of the amplified spontaneous radiation decrease, but the latter is not as great a problem for holographic applications of X-rays as is the coherence. A graphic argument in support of the proposed method for improving the coherence is that in the presence of gain saturation, for $\overline{N_e}^{conc}$ and $\overline{N_e}^{conv}$, the width of the beam of amplified spontaneous radiation is 30–40 and 6–7 times greater, respectively, than L_c. From the practical standpoint, in the first the radiation is incoherent, and in the second case there is partial coherence.

The improvement of coherence obtained on switching to a convex density profile can be suppressed as a result of scattering by fluctuations of the optical parameters of the medium. Calculations of the amplified spontaneous radiation in the presence of fluctuations $\tilde{\varepsilon}$ with $l_{\varepsilon\perp} = l_{\varepsilon\parallel} = 1$ μm and $\sigma_\varepsilon = 10^{-5}$ and 2×10^{-5} showed that the effect of scattering by $\tilde{\varepsilon}$ on the brightness and divergence of the radiation is negligible for concave as well as convex density profiles. For $\overline{N_e}^{conc}$, the influence of $\tilde{\varepsilon}$ on the coherence length L_c is small, while for $\overline{N_e}^{conv}$ the coherence length decreases substantially as σ_ε increases. A similar "hidden" effect of the fluctuations $\tilde{\varepsilon}$ on the amplified spontaneous radiation has been observed in calculations with a symmetric defocusing density profile [33]. In consequence, the effectiveness

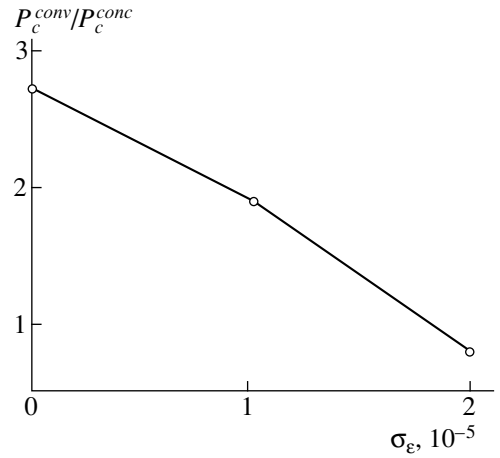

Fig. 15. Ratio of the coherent powers in the far zone with $\overline{N_e} = \overline{N_e}^{conc}$ and $\overline{N_e} = \overline{N_e}^{conv}$ as a function of σ_ε for $J_{sat} = 10^4 J_0$.

of switching from a concave to a convex density profile decreases. For $\sigma_\varepsilon = 10^{-5}$ the coherent power increases on switching from $\overline{N_e}^{conc}$ to $\overline{N_e}^{conv}$ not by a factor of 3 by rather by a factor of 2 (see Fig. 15). This value of σ_ε corresponds to the standard deviation of the electron density 2.5×10^{19} cm^{-3} and is relatively small against the background of the regular values of the density in the gain zone in Fig. 12. For $\sigma_\varepsilon = 2 \times 10^{-5}$ the increase in coherent power is replaced by a drop.

7. CONCLUSIONS

A physical model of the dynamics of amplified spontaneous radiation in an X-ray laser was developed on the basis of a numerical solution of the quasi-optics equation for the transverse correlation function of the complex amplitude of the field in two- and three-dimensional axisymmetric media. The model includes a spontaneous radiation source, diffraction, regular refraction, regular amplification taking account of saturation, nonresonant absorption, scattering by ordinary permittivity and gain fluctuations, and scattering by random hose-like deflections of the extended plasma medium of the X-ray laser. In the derivation of the equation for the TCF, statistical linearization of the nonlinear terms of the equation that are responsible for gain with saturation was performed. It reduces to introducing into these terms of the equation a universal function that depends on the local degree of saturation.

The dynamics of the amplified spontaneous radiation in an X-ray laser with regular refraction was investigated numerically in the approximation of a two-dimensional medium using the TCF method and the Monte Carlo method for the parabolic equation for the amplitude of the field. The parabolic equation method is basic for the TCF method and is accurate when the number of statistical tests is large. The TCF method does not require averaging over an ensemble, but in the presence of saturating gain it is approximate because statistical linearization of the nonlinear terms is used to derive the TCF equation. It was found that the TCF method makes it possible to obtain the final result one to three orders of magnitude more quickly than the parabolic equation method. The statistical linearization of the equation for the TCF does not distort the profile of the average angular distribution of the intensity of the amplified spontaneous radiation, but it somewhat overestimates the absolute values of the intensity. The maxima overestimation, equal to ~10%, is observed when the average radiation intensity is close to the saturation value.

Computational results were presented for the amplified spontaneous radiation computed by the TCF method in a three-dimensional randomly-inhomogeneous axisymmetric medium of an X-ray laser. It was found that the ordinary permittivity fluctuations are the analog of nonresonance absorption from the standpoint of the effect on the brightness of an X-ray laser and therefore decrease the observed gain. The loss factor due to scattering by strong fluctuations in a three-dimensional medium is two times greater than value determined in the planar-medium approximation. The effect of gain fluctuations on the formation of the amplified spontaneous radiation in a laboratory X-ray laser, operating on Ne-like yttrium and obtained by irradiating a thick target with an optical laser, was investigated. It was found that the contribution of fluctuations to the average additional gain is appreciable, and the scattering of the amplified spontaneous radiation by them has essentially no effect. It was shown that hose-like fluctuations of the plasma filament of an X-ray laser result in additional regular amplification and refraction as well as scattering of the amplified spontaneous radiation. However, for characteristic plasma parameters of an X-ray laser with a quasistationary lasing scheme, the influence of hose-like fluctuations on the amplified spontaneous radiation is unnoticeable compared with ordinary fluctuations with the same spatial scale.

A computational-theoretical investigation of the amplified spontaneous radiation in an X-ray laser, which was obtained by irradiating a thick target and contains an asymmetric concave electron density profile in the gain zone, was performed by solving the equation for the TCF. For a flat target the transverse coherence length of the amplified spontaneous radiation is small and its distribution is nonuniform in the transverse section of the radiation beam in the far zone. Curving the target with a constant optimal curvature for partial compensation of refraction appreciably increases the coherence length and gives a uniform distribution of the coherence length in the transverse section of the beam, but from the practical standpoint the amplified spontaneous radiation remains incoherent. For a curved target the coherence

can be additionally increased substantially and the coherence length can be made to approach the width of the amplified spontaneous radiation beam as a result of residual defocusing, realizing a convex electron density profile in the gain zone. It was shown that in the gain saturation regime the degree to which the coherence length increases on switching from a concave to a convex density profile is higher than the degree to which the brightness decreases and the divergence increases. Thus, an increase in the coherence length is accompanied by an increase in the coherent power of the amplified spontaneous radiation; this is important for potential holographic applications of X-ray lasers in biology. It was found that the improvement of the coherence on switching from a concave to a convex density profile may not occur in the presence of appreciable small-scale fluctuations of the plasma density.

ACKNOWLEDGMENTS

I am grateful to B.A. Voinov, V.A. Volkov, P.D. Gasparyan, V.M. Gerasimov, V.A. Eroshenko, G.G. Kochemasov, V.K. Ladagin, A.N. Starostin, and V.D. Urlin for collaboration and helpful discussions of the problems touched upon in this paper and to G.A. Kirillov for encouragement and interest in this work.

REFERENCES

1. R. C. Elton, *X-ray Lasers* (Academic Press, Boston, 1990).
2. D. L. Matthews, P. L. Hagelstein, M. D. Rosen, *et al.*, Phys. Rev. Lett. **54**, 110 (1985).
3. J. J. Rocca, V. N. Shlyaptsev, F. G. Tomasel, *et al.*, Phys. Rev. Lett. **73**, 2192 (1994).
4. P. V. Nickles, M. Shnurer, M. Kalachnikov, *et al.*, Proc. SPIE **2520**, 373 (1995).
5. B. Lemoff, G. J. Yin, G. L. Gordon III, *et al.*, Phys. Rev. Lett. **74**, 1574 (1995).
6. *Proceedings of the IOP Conference on X-ray Lasers 1996*, Ed. by S. Svanberg and C.-G. Wahlström (IOP Publishing, Bristol, 1996), No. 151.
7. *Proceedings of the IOP Conference on X-ray Lasers 1998*, Ed. by Y. Kato, H. Takuma, and H. Daido (IOP Publishing, Bristol, 1999), No. 159.
8. P. D. Gasparyan, F. A. Starikov, and A. N. Starostin, Usp. Fiz. Nauk **168**, 843 (1998) [Phys. Usp. **41**, 461 (1998)].
9. J. Nilsen, B. J. MacGowan, L. B. Da Silva, and J. C. Moreno, Phys. Rev. A **48**, 4682 (1993).
10. J. G. Lunney, Appl. Phys. Lett. **48**, 891 (1986).
11. R. Kodama, D. Neely, Y. Kato, *et al.*, Phys. Rev. Lett. **73**, 3215 (1994).
12. A. G. Zhidkov, A. O. Terskikh, and S. I. Yakovlenko, Kratk. Soobshch. Fiz., No. 9, 27 (1988).
13. R. A. London, Phys. Fluids **31**, 184 (1988).
14. B. Boswell, D. Shvarts, T. Boehly, and B. Yaakobi, Phys. Fluids B **2**, 436 (1990).
15. V. B. Kryuchenkov, A. V. Lukin, P. V. Petrov, and Yu. I. Chernukhin, Kvantovaya Élektron. (Moscow) **17**, 189 (1990).
16. Yu. V. Mokhov, Vopr. At. Nauki Tekh., Ser. Teor. Prikl. Fiz. , No. 1, 29 (1991).
17. A. V. Borovskiĭ, A. L. Galkin, and V. V. Korobkin, Kvantovaya Élektron. (Moscow) **15**, 1457 (1988).
18. M. D. Feit and J. A. Fleck, Jr., J. Opt. Soc. Am. B **7**, 2048 (1990).
19. M. D. Feit and J. A. Fleck, Jr., Opt. Lett. **16**, 76 (1991).
20. G. Hazak and A. Bar-Shalom, Phys. Rev. A **40**, 7055 (1989).
21. R. A. London, M. Strauss, and M. D. Rosen, Phys. Rev. Lett. **65**, 563 (1990).
22. P. Amendt, R. A. London, and M. Strauss, Phys. Rev. A **44**, 7478 (1991).
23. P. Amendt, R. A. London, and M. Strauss, Phys. Rev. A **47**, 4348 (1993).
24. F. A. Starikov, Vopr. At. Nauki Tekh., Ser. Teor. Prikl. Fiz., No. 4, 14 (1989); No. 2, 33 (1990).
25. F. A. Starikov and V. D. Urlin, Kvantovaya Élektron. (Moscow) **18**, 436 (1991).
26. F. A. Starikov, Kvantovaya Élektron. (Moscow) **19**, 527 (1992).
27. V. A. Volkov, V. K. Ladagin, F. A. Starikov, and V. D. Urlin, Kvantovaya Élektron. (Moscow) **18**, 1329 (1991).
28. V. K. Ladagin, F. A. Starikov, and V. D. Urlin, Kvantovaya Éelektron. (Moscow) **20**, 471 (1993).
29. F. A. Starikov, Kvantovaya Élektron. (Moscow) **21**, 343 (1994).
30. F. A. Starikov, Kvantovaya Élektron. (Moscow) **24**, 691 (1997).
31. F. A. Starikov, Kvantovaya Élektron. (Moscow) **20**, 477 (1993).
32. F. A. Starikov, in *Proceedings of the 2nd International Conference on the Physics of Nuclear-Excited Plasma and the Problem of Nuclear-Pumped Lasers, Arzamas-16, 1995*, Vol. 2, p. 260.
33. F. A. Starikov, Kvantovaya Élektron. (Moscow) **23**, 205 (1996).
34. F. A. Starikov, in *Proceedings of the IOP Conference on X-ray Lasers 1996*, Ed. by S. Svanberg and C.-G. Wahlström (IOP Publishing, Bristol, 1996), No. 151, p. 315.
35. V. V. Kolosov, Opt. Atmos. Okeana **8**, 1825 (1995).
36. V. V. Kolosov, R. P. Ratowsky, A. A. Zemlyanov, and R. A. London, Proc. SPIE **2859**, 269 (1996).
37. F. A. Starikov, Vopr. At. Nauki Tekh., Ser. Teor. Prikl. Fiz., No. 3, 20 (1990).
38. V. K. Ladagin, F. A. Starikov, and V. A. Volkov, in *Proceedings of the IOP Conference on X-ray Lasers 1996*, Ed. by S. Svanberg and C.-G. Wahlström (IOP Publishing, Bristol, 1996), No. 151, p. 336.

39. P. Amendt, M. Strauss, and R. A. London, Phys. Rev. A **53**, R23 (1996).

40. L. D. Landau and E. M. Lifshitz, *Electrodynamics of Continuous Media* (Pergamon Press, Oxford, 1960, 1st ed.; Nauka, Moscow, 1981).

41. V. K. Ladagin, Vopr. At. Nauki Tekh, Ser. Metodika Prog. Chisl. Reshen. Zadach Mat. Fiz., No. 1, 19 (1985).

42. S. M. Rytov, Yu. A. Kravtsov, and V. I. Tatarskiĭ, *Introduction to Statistical Radio Physics* (Nauka, Moscow, 1978), Part 2.

43. S. A. Akhmanov, Yu. E. D'yakov, and A. S. Chirkin, *Introduction to Statistical Radio Physics and Optics* (Nauka, Moscow, 1981).

44. V. K. Ladagin and F. A. Starikov, Mat. Model. **10**, 114 (1998).

45. V. P. Kandidov and V. I. Ledenev, Vestn. Mosk. Univ., Ser. 3: Fiz., Astron, **23**, 3 (1982).

46. A. S. Wan, C. A. Back, T. W. Barbee, Jr., *et al.*, in *Proceedings of the IOP Conference on X-ray Lasers 1996*, Ed. by S. Svanberg and C.-G. Wahlström (IOP Publishing, Bristol, 1996), No. 151, p. 504.

47. R. P. Ratowsky *et al.*, Lawrence Livermore Lab. Rep. UCRL-LR **4** (105821-94-2), 63 (1994).

48. F. Albert, B. Rus, Ph. Zeitoun, *et al.*, in *Proceedings of the IOP Conference on X-ray Lasers 1996*, Ed. by S. Svanberg and C.-G. Wahlström (IOP Publishing, Bristol, 1996), No. 151, p. 427.

Translation was provided by AIP

Journal of Experimental and Theoretical Physics, Vol. 90, No. 2, 2000, pp. 276–280.
Translated from Zhurnal Éksperimental'noĭ i Teoreticheskoĭ Fiziki, Vol. 117, No. 2, 2000, pp. 313–318.

ATOMS, SPECTRA, RADIATION

Sums of Products of Coulomb Wave Function over Degenerate States

M. I. Chibisov[1, *], A. M. Ermolaev[2], M. Sherkani[3], and F. Bruiar[4]

[1]*Russian Research Centre Kurchatov Institute, Moscow, 123182 Russia*
[2]*Physique Théorique, Faculté des Sciences CP 227, Université Libre de Bruxelles, B-1050 Bruxelles, Belgium*
[3]*UFR Physique Corpusculaire, FST Fes-Saiss, Morocco*
[4]*Départment de Physique, Unité Fyam, Bâtiment Marc de Hemptinne, B-1348, Louvain-la-Neuve, Belgium*
**e-mail: chib@qq.nfi.kiae.su*

Received August 19, 1999

Abstract—The sums of products of Coulomb wave function over degenerate states are expressed in terms of quadratic forms that depend on the wave function of only one state with zero orbital angular momentum $l = m = 0$. These sums are encountered in many fields in the physics of atoms and molecules, for example, in investigations of the perturbation of degenerate atomic energy levels of a small potential well, a delta-function potential. The sums were found in an investigation of the limit of the Coulomb Green's function $G(\mathbf{r}, \mathbf{r}', E)$, where the energy parameter E approaches an atomic energy level: $E \longrightarrow E_n$, $E_n = -Z^2/2n^2$. The Green's function found by L. Hostler and R. Pratt in 1963 was used. The result obtained is a consequence of the degeneracy of the Coulomb energy levels, which in turn is due to the four-dimensional symmetry of the Coulomb problem.

1. In the problem of the energy levels of a system consisting of negative and positive ions $A^- + B^+$ it is necessary to calculate the sums [1–4]

$$Q_n^{(0)}(R) \equiv \sum_{l,m} \psi^*_{nlm}(\mathbf{R})\psi_{nlm}(\mathbf{R}), \tag{1}$$

$$Q_n^{(1)}(R) \equiv \sum_{l,m} \psi^*_{nlm}(\mathbf{R})\frac{d\psi_{nlm}(\mathbf{R})}{dR} \tag{2}$$

of the Coulomb wave function ψ_{nlm} and their derivatives $d\psi_{nlm}/dR$ over states belonging to the same value of the principal quantum number n (R is the distance from the Coulomb center). The energy levels of the hydrogen atom and hydrogen-like ions H, He^+, Li^{++}, … are degenerate with respect to the angular momentum quantum numbers l and m, so that the summation in equations (1) and (2) extends over bound states with the same energy. The sums (1) and (2) are fundamental, since they belong to the simplest quantum objects.

2. In [1–4] the energy levels of the system $A^- + B^+$ were investigated in the approximation of a delta-function potential, in which these levels are determined by the Coulomb Green's function $G(\mathbf{r}, \mathbf{R}, E)$. An exact expression for this function has been found by Hostler and Pratt [5, 6]:

$$G(\mathbf{r}, \mathbf{r}', E) = \frac{\Gamma(1 - Zn_-)}{2\pi|\mathbf{r} - \mathbf{r}'|}\left(\frac{\partial}{\partial(x/n_-)} - \frac{\partial}{\partial(y/n_-)}\right)$$
$$\times W_{Zn_-,1/2}\left(\frac{x}{n_-}\right)M_{Zn_-,1/2}\left(\frac{y}{n_-}\right), \tag{3}$$
$$x = r + r' + |\mathbf{r} - \mathbf{r}'|, \quad y = r + r' - |\mathbf{r} - \mathbf{r}'|,$$
$$n_- = (-2E)^{-1/2};$$

where M and W are the Whittaker functions, which are solutions of the equation [7]

$$W''_{Zn_-,1/2}(\tau) + \left(-\frac{1}{4} + \frac{Zn_-}{\tau}\right)W_{Zn_-,1/2}(\tau) = 0, \tag{3a}$$

and an identical equation for the function M. The function W is regular at infinity, $\tau \longrightarrow \infty$, and the function M is regular at the origin, $\tau = 0$. The expansion of the Green's function in terms of the eigenfunctions ψ_{nlm} has the form [8]

$$G(\mathbf{r}, \mathbf{r}', E) = \sum_{nlm} \frac{\psi^*_{nlm}(\mathbf{r})\psi_{nlm}(\mathbf{r}')}{E - E_n}, \tag{4}$$

where the summation symbol represents a summation over discrete states with negative energies and integration over the states of the continuum.

The sums (1) and (2) can be calculated in a general form for an arbitrary value of n, by analyzing the expression (3) for the Green's function in the limit $E \longrightarrow E_n$. The Whittaker function M is a linear combination of $W_{nZ,1/2}(\tau)$ and $W_{-nZ,1/2}(-\tau)$ Whittaker functions [7]:

$$\Gamma(1 - Zn_-)M_{Zn_-,1/2}(\tau) = (-1)^{1+Zn_-}$$
$$\times \frac{\Gamma(1 - Zn_-)}{\Gamma(1 + Zn_-)}W_{Zn_-,1/2}(\tau) + (-1)^{Zn_-}W_{-Zn_-,1/2}(-\tau). \tag{5}$$

The function $W_{-Zn_-}(-\tau)$ increases exponentially as $\tau \longrightarrow \infty$. If the energy E is close to an eigenvalue $E_n = -Z^2/2n^2$, then the index of the functions W is close to an integer $Zn_- = n$. In this limit, the first term in equation (5) predominates, and the leading term in the expansion (4) is the resonant term, proportional to $(E - E_n)^{-1}$. Then the Green's function is close to the following expression:

$$G(\mathbf{r}, \mathbf{R}, E \longrightarrow E_n) \simeq \frac{\sum_{l,m} \psi^*_{nlm}(\mathbf{r})\psi_{nlm}(\mathbf{R})}{E - E_n}$$

$$= \frac{1}{(E - E_n)} \frac{Z^2}{\pi n^3 n!(n-1)!} \frac{1}{(x-y)} \left(\frac{n\partial}{\partial(Zy)} - \frac{n\partial}{\partial(Zx)} \right) \times W_{n,1/2}\left(\frac{Zx}{n}\right) W_{n,1/2}\left(\frac{Zy}{n}\right), \quad (6)$$

where an expansion of the resonant gamma function in the limit under study was used:

$$\Gamma(1 - Zn_-) = \frac{\tau}{\Gamma(Zn_-)\sin(\pi Zn_-)}\bigg|_{Zn_- \to n} \longrightarrow \frac{(-1)^n Z^2}{n^3 \Gamma(n)} \frac{1}{E - E_n}.$$

From equation (6) we obtain

$$\sum_{l,m} \psi^*_{nlm}(\mathbf{r})\psi_{nlm}(\mathbf{R}) = \frac{Z^2}{\pi n^3 n!(n-1)!} \frac{1}{(x-y)} \times \left(\frac{n\partial}{\partial(Zy)} - \frac{n\partial}{\partial(Zx)} \right) W_{n,1/2}\left(\frac{Zx}{n}\right) W_{n,1/2}\left(\frac{Zy}{n}\right). \quad (7)$$

The limit of the Green's function (3) as $E \longrightarrow E_n$ was used in [9–11] to calculate the Born amplitudes of the transitions between highly excited states of atoms in collisions with electrons. On summing and averaging over degenerate states these amplitudes depend integrally on the sums (7). In [12] V.A. Fok examined sums similar to the sums (1) and (7), but for wave function in the momentum representation.

The Whittaker function $W_{n,1/2}$ with an integral value of the first index n can be expressed in terms of the normalized Coulomb function ψ_{n00} with zero angular momentum quantum numbers $l = m = 0$. The Coulomb functions of hydrogen-like ions are [13]

$$\psi_{nlm}(\mathbf{r}) = f_{nl}(r) Y_{lm}(\theta, \varphi),$$

$$\phi_{nl}(r) = \text{const} \cdot r f_{nl}(r),$$

$$f_{nl}(r) = \frac{2Z^{3/2}}{n^2(2l+1)!} \sqrt{\frac{(n+l)!}{(n-l-1)!}} \left(\frac{2Zr}{n}\right)^l \times \exp\left(\frac{-Zr}{n}\right) F\left(-n + l + 1;\, 2l + 2;\, \frac{2Zr}{n}\right), \quad (8)$$

$$\phi''_{nl}(r) + 2\left(E_n + \frac{Z}{r} - \frac{l(l+1)}{2r^2}\right)\phi_{nl}(r) = 0, \qquad E_n = -\frac{Z^2}{2n^2}. \quad (9)$$

Switching to the variable τ, the equation (9) for $l = 0$ becomes

$$\phi''_{n0}(\tau) + \left(-\frac{1}{4} + \frac{n}{\tau}\right)\phi_{n0}(\tau) = 0, \quad \tau = \frac{2Zr}{n}, \quad (10)$$

which is identical to the equation (3a) for the function $W_{n,1/2}$. Comparing the asymptotic expressions of the functions W and ϕ_{n0} in the limit $r \longrightarrow \infty$, we obtain the relation

$$W_{n,1/2}(\tau) = (-1)^{n+1} n! \sqrt{\frac{4\pi n}{Z}} \phi_{n0}(\tau), \quad (11)$$

where the function ϕ_{n0} is normalized on a three-dimensional volume (the division of the corresponding radial function by $\sqrt{4\pi}$), and its variable r is replaced by τ.

Substituting the expression (11) into equation (7) we obtain

$$\hat{Q}^{(0)}_n(\mathbf{r}, \mathbf{R}) \equiv \sum_{l,m} \psi_{nlm}(\mathbf{r})\psi^*_{nlm}(\mathbf{R}) = \frac{4Z^2}{n^2} \frac{\phi'_{n0}(\tau_y)\phi_{n0}(\tau_x) - \phi_{n0}(\tau_y)\phi'_{n0}(\tau_x)}{\tau_x - \tau_y}, \quad (12)$$

$$\tau_x = \frac{z}{n}[r + R + |\mathbf{r} - \mathbf{R}|], \qquad \tau_y = \frac{z}{n}[r + R - |\mathbf{r} - \mathbf{R}|].$$

The expression (12) has a more general form than the sums (1) and (2): $\hat{Q}^{(0)}_n(\mathbf{r}, \mathbf{R})$ depends on two vectors, $\mathbf{r}$ and $\mathbf{R}$, and the sums (1) and (2) can be expressed in terms of the particular value of $\hat{Q}^{(0)}_n$ at $\mathbf{r} = \mathbf{R}$ (see below).

Differentiating the expression (12) with respect to the absolute value of R and using equation (10) for the second derivative ϕ''_{n0}, we obtain the more general expression for the second sum

$$\hat{Q}^{(1)}_n(\mathbf{r}, \mathbf{R}) \equiv \sum_{l,m} \psi_{nlm}(\mathbf{r}) \frac{d\psi_{nlm}(\mathbf{R})}{dR} = -\frac{2Z(R - r\cos\alpha)}{n|\mathbf{r} - \mathbf{R}|^3}(\phi'_{n0}(\tau_y)\phi_{n0}(\tau_x) - \phi_{n0}(\tau_y)\phi'_{n0}(\tau_x)) + \frac{4Z^2(R - r\cos\alpha)}{n^2|\mathbf{r} - \mathbf{R}|^2}\left[\phi'_{n0}(\tau_x)\phi'_{n0}(\tau_y)\right. \quad (13)$$

$$+\left(-\frac{1}{4}+\frac{n^2(R-r)}{2ZR(R-r\cos\alpha)}\right)\phi_{n0}(\tau_x)\phi_{n0}(\tau_y)\Bigg],$$

where α is the angle between the vectors **r** and **R**.

In the model with a delta-function potential [4] the sum $\hat{Q}_n^{(0)}(\mathbf{r},\mathbf{R})$, determined by the formula (12), is proportional to the $E \longrightarrow E_n$ limit of the wave function of the system $A^- + B^+$ for the case where the angular momentum of the electron of the isolated ion A^- is zero, $L = 0$. The sum $\hat{Q}_n^{(1)}(\mathbf{r},\mathbf{R})$, determined by the formula (13), is proportional to a similar limit for the case $L = 1$.

To calculate the sum (1), we shall investigate the limit of equation (12) as $\mathbf{r} \longrightarrow \mathbf{R}$. In this limit $y \longrightarrow x$, $\tau_y \longrightarrow \tau_x$, and the numerator in equation (12) approaches zero. The first term in the Taylor series expansion of the numerator in equation (12) is

$$\phi'_{n0}(\tau_y)\phi_{n0}(\tau_x)-\phi_{n0}(\tau_y)\phi'_{n0}(\tau_x)\simeq(\tau_x-\tau_y)$$
$$\times\left[\left(\frac{d\phi_{n0}}{d\tau_x}\right)^2+\left(-\frac{1}{4}+\frac{n}{\tau_x}\right)\phi_{n0}^2(\tau_x)\right]+\ldots.$$

Substituting this expansion into equation (12), we obtain the first sum (1):

$$Q_n^{(0)}(R)\equiv\sum_{l,m}|\psi_{nlm}(\mathbf{R})|^2$$
$$=\left(\frac{d\phi_{n0}(R)}{dR}\right)^2+2\left(E_n+\frac{Z}{R}\right)\phi_{n0}^2(R). \tag{14}$$

We can see that the sum of the squared moduli of the wave function for states with fixed energy and fixed principal quantum number n is, according to equation (14), a quadratic form of a function of only one state (the function $\phi_{n0}(R)$) with zero orbital angular momentum $l = 0$ and the same value of n. The existence of the relation (14) is due to the degeneracy of the Coulomb energy levels: for values of the angular momentum quantum numbers $l \le n-1$ and $-l \le m \le l$ these energies depend only on n and they do not depend on l and m. In the presence of degeneracy, the Green's function at each pole, i.e., in the limit $E \longrightarrow E_n$, is determined by a sum of the products of the wave function of degenerate states; see the spectral expansion (4). In the absence of degeneracy the function $G(\mathbf{r},\mathbf{r}',E)$ depends at the pole on the wave function of only one state.

Using the theorem for the addition of spherical harmonics $Y_{lm}(\theta,\varphi)$ [13, 14], which makes it possible to sum over the magnetic quantum number m, we can transform the double sums (12) and (1), (2) into single sums:

$$\hat{Q}_n^{(0)}(\mathbf{r},\mathbf{R})\equiv\sum_{l,m}\psi_{nlm}(\mathbf{r})\psi^*_{nlm}(\mathbf{R})$$
$$=\frac{1}{4\pi}\sum_l(2l+1)P_l(\cos\alpha)f_{nl}(r)f_{nl}(R), \tag{15}$$

$$Q_n^{(0)}(R)=\frac{1}{4\pi}\sum_l(2l+1)|f_{nl}(R)|^2,$$

$$Q_n^{(1)}(R)=\frac{1}{2}\frac{dQ_n^{(0)}(R)}{dR}=\frac{1}{4\pi}\sum_l(2l+1)f_{nl}(R)\frac{df_{nl}}{dR}. \tag{16}$$

In the limit $\mathbf{r} \longrightarrow \mathbf{R}$ the angle $\alpha = 0$, $\cos\alpha = 1$ and $P_l(1) = 1$, so that the sums (15), (16) and (1), (2) do not depend on the spherical angles of the vector **R**. However, a concrete expression for the right-hand side of equation (14) cannot be obtained from these general formulas: a further summation over l in equations (15) and (16) cannot be performed in a general form. This summation can be done only by using the expression (3), found by Hostler and Pratt [5, 6] by solving exactly the differential equation for the Coulomb Green's function. The specific form of the right-hand side of equation (14) is apparently determined only by the specific nature of the Coulomb field.

3. In the one-dimensional case for a system with a real Hamiltonian it is possible to write down on the basis of the Schrödinger wave equation a linear second-order integrodifferential equation for the squared modulus of the wave function of this system. Multiplying equation (9) by ϕ'_{nl} and integrating once we obtain

$$(\phi'_{nl}(r))^2+2(E_n-U_l(r))\phi_{nl}^2(r)$$
$$=2\int_r^\infty\phi_{nl}^2(r')\frac{dU_l(r')}{dr'}dr', \tag{17}$$

and multiplying equation (9) by ϕ_{nl} and using (17) we obtain an equation for the probability density

$$\rho''_{nl}(r)+8(E_n-U_l(r))\rho_{nl}(r)$$
$$=4\int_r^\infty\rho_{nl}(r')\frac{dU_l(r')}{dr'}dr', \tag{18}$$

$$\rho_{nl}(r)\equiv|\phi_{nl}(r)|^2;\quad U_l(r)\equiv-\frac{Z}{r}+\frac{l(l+1)}{2r^2}.$$

We recall that the radial functions of the bound states ($E < 0$) are real. The following boundary condition was used to derive these equations: $\phi_{nl}(r)$ approaches zero exponentially in the limit $r \longrightarrow \infty$. The equality (17) and equation (18) were used in [15] to investigate the potential on the surface of a metal. Differentiating equation (18) with respect to r, we obtain the equation discussed by Solov'ev [16]:

$$\rho'''+8(E-U)\rho'-4\rho U'=0.$$

Substituting for $l = 0$ the equality (17) into equation (14), we transform the first sum into

$$Q_n^{(0)}(R) \equiv \sum_{l,m} |\psi_{nlm}(\mathbf{R})|^2 = 2\int_R^\infty \phi_{n0}^2(r)\frac{dU_0(r)}{dr}dr. \quad (19)$$

It is easy to see that the integral in equations (17) and (19) is the force (in dimensionless atomic units employed in the present paper) exerted by the nucleus on a portion of the electron charge density located in the range r, ∞. The first sum, $\hat{Q}_n^{(0)}$, is proportional to twice the value of this force.

Using $dU_0/dr = Z/r^2$, equation (19) can be written in the form

$$Q_n^{(0)}(R) \equiv \sum_{l,m} |\psi_{nlm}(\mathbf{R})|^2 = 2Z\int_R^\infty \psi_{n0}^2(r)dr. \quad (19a)$$

Since the right-hand sides of the relation (17) and equation (18) differ only by a numerical factor, the sum (1) can also be written in the form

$$Q_n^{(0)}(R) \equiv \sum_{l,m} |\psi_{nlm}(\mathbf{R})|^2 = \frac{1}{2}\rho''_{n0}(R) + 4(E_n - U_0(R))\rho_{n0}(R). \quad (19b)$$

It is interesting to note that in the semiclassical approximation for the function ϕ_{n0} the right-hand side in equation (14) vanishes. Indeed, in the semiclassical approximation we have

$$\phi_{n0}(R) = \exp(S(R)), \quad (20)$$

$$\exp S((S')^2 + p^2(R)) = 0 \longrightarrow (S')^2 + p^2(R) = 0; \quad p(R) = \sqrt{2(E_n - U(R))}. \quad (21)$$

Substituting equations (20) and (21) into the right-hand side of equation (14), we obtain

$$Q_n^{sc}(R) \simeq \exp(2S)((S')^2 + p^2(R)) = 0. \quad (22)$$

4. The second sum (2) is obtained by differentiating equation (14) with respect to the absolute value of the vector **R** or (which is more difficult) studying the expression (13) in the limit $\mathbf{r} \longrightarrow \mathbf{R}$:

$$Q_n^{(1)}(R) = \frac{1}{2}\frac{dQ_n^{(0)}(R)}{dR} = \sum_{lm}\psi_{nlm}^*(\mathbf{R})\frac{d\psi_{nlm}(\mathbf{R})}{dR} = -Z\psi_{n00}^2(R) = -\frac{Z}{R^2}\phi_{n0}^2(R). \quad (23)$$

This relation can also by easily obtained by differentiating equation (19a).

Figures 1 and 2 display the sums (1) and (2) calculated as functions of the distance R from the nucleus for the hydrogen atom ($Z = 1$): for the excited states $n = 4$, 5, 6, 7, and 8 in the case $Q_n^{(0)}(R)$ (Fig. 1) and $n = 4$ and 8 in the case $Q_n^{(1)}(R)$ (Fig. 2). Both sums were calculated by direct summation over l of equations (15) and (16) and using the equations (14), (19) and (19a), (19b) which we obtained for $Q_n^{(0)}(R)$ and using the formula (23) for $Q_n^{(1)}(R)$. For each sum and fixed value of n, the computational results obtained using all formulas fell on the same curve, i.e., the results obtained by all computational methods were identical. It is evident from Figs. 1 and 2 that the sum $Q_n^{(0)}(R)$ has no zeros for finite values of R. In the limit $R \longrightarrow \infty$, this sum decreases to zero in steps at the center of which the derivative of this sum is zero. In accordance with equation (23) the derivative of the function $Q_n^{(0)}(R)$ is proportional to the square of the function $\psi_{n00}(R)$, which has $n - 1$ zeros.

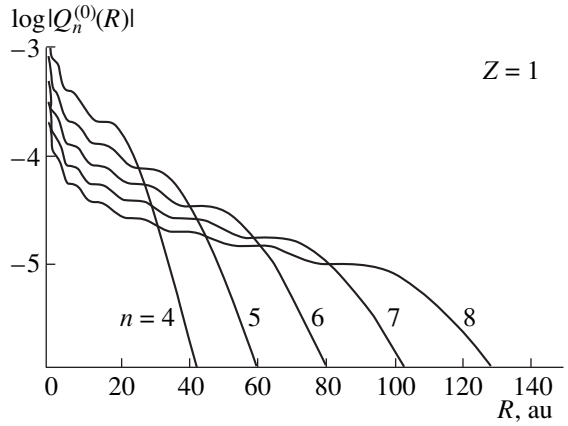

Fig. 1. Sum (1) for the hydrogen atom ($Z = 1$) as a function of the distance R from the nucleus for five values of the principal quantum number $n = 4$–8.

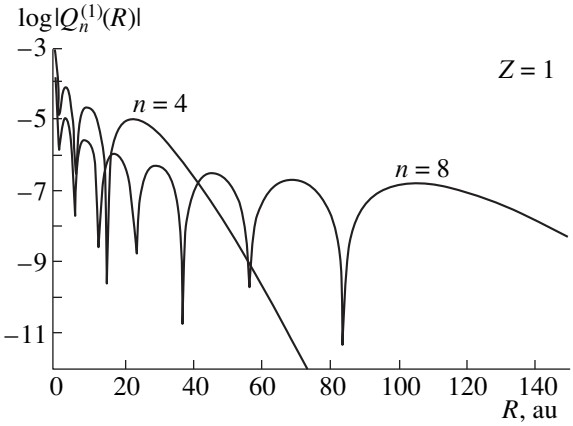

Fig. 2. Sum (*2*) for the hydrogen atom ($Z = 1$) as a function of the distance R from the nucleus for the principal quantum numbers $n = 4$ and 8.

The existence of the relations (14) and (23) is due to the degeneracy of the Coulomb energy levels, which is a consequence of the four-dimensional symmetry of the problem of a hydrogen atom and hydrogen-like ions. In [12] V.A. Fok investigated the Schrödinger equation for the hydrogen atom in the momentum representation and he found that the group of transformations admitted by these equations is identical to the four-dimensional rotation group. The sum of products of wave function in the momentum representation, similar to the sum (1) in the coordinate representation, was also studied in [12]. In [12] an analytical expression depending on the four-dimensional momenta was found for this sum. The question of the relation between the sums in the momentum and coordinate representations is quite complicated and requires an additional investigation.

Works devoted to the properties of the Coulomb Green's function and the four-dimensional symmetry of the hydrogen atom are discussed in the recently published reviews [17, 18]. Our expressions for the sums (1) and (2) can be added to the list of properties of hydrogen-like ions discussed in these reviews.

ACKNOWLEDGMENT

This work was supported by the Russian Foundation for Fundamental Research (project no. 96-15-96815) as part of the program for the support of leading scientific schools.

REFERENCES

1. I. V. Komarov, P. A. Pogorelyĭ, and A. S. Tibilov, Opt. Spektrosk. **27**, 198 (1969).
2. L. P. Presnyakov, Phys. Rev. A **2**, 1720 (1970).
3. T. M. Kereselidze and M. I. Chibisov, Zh. Éksp. Teor. Fiz. **68**, 12 (1975) [Sov. Phys. JETP **41**, 6 (1975)].
4. Yu. N. Demkov and V. N. Ostrovskiĭ, *Zero-Range Potentials and Their Applications in Atomic Physics* (Lenin. Gos. Univ., Leningrad, 1975; Plenum Press, New York, 1988), Ch. 7.4.
5. L. Hostler and R. H. Pratt, Phys. Rev. Lett. **10**, 469 (1963).
6. L. Hostler, J. Math. Phys. **5**, 591 (1964).
7. S. Gradshteĭn and I. M. Ryzhik, *Tables of Integrals, Sums, Series, and Products* (Fizmatgiz, Moscow, 1962).
8. A. I. Baz', Ya. B. Zel'dovich, and A. M. Perelomov, *Scattering, Reactions, and Decays in Nonrelativistic Quantum Mechanics* (Nauka, Moscow, 1971).
9. I. L. Beĭgman, A. M. Urnov, and V. P. Shevel'ko, Zh. Éksp. Teor. Fiz. **58**, 1825 (1970) [Sov. Phys. JETP **31**, 978 (1970)].
10. I. L. Beĭgman and A. M. Urnov, J. Quant. Spectrosc. Radiat. Transf. **14**, 1009 (1974).
11. L. A. Vaĭnshteĭn, I. I. Sobel'man, and E. A. Yukov, *The Excitation of Atoms and Broadening of Spectral Lines* (Nauka, Moscow, 1979).
12. V. A. Fok, Izv. Akad. Nauk SSSR, Otd. Mat. Estestv. Nauk, No. 2, 169 (1935); V. A. Fock, Z. Phys. **98**, 145 (1935).
13. L. D. Landau and E. M. Lifshitz, *Quantum Mechanics: The Non-relativistic Theory* (Nauka, Moscow, 1974; Pergamon Press, Oxford, 1977).
14. A. S. Davydov, *Quantum Mechanics* (Nauka, Moscow, 1973).
15. M. I. Chibisov, Preprint No. IAÉ-4983/7 (Institute of Atomic Energy, Moscow, 1989).
16. E. A. Solov'ev, Pis'ma Zh. Éksp. Teor. Fiz. **39**, 84 (1984) [JETP Lett. **39**, 100 (1984)].
17. A. Maquet, V. Veniard, and T. A. Marian, J. Phys. B: At. Mol. Opt. Phys. **31**, 3743 (1998).
18. N. L. Manakov, V. D. Ovsiannikov, and L. P. Rapoport, Phys. Rep. **141**, 319 (1986).

Translation was provided by AIP

Journal of Experimental and Theoretical Physics, Vol. 90, No. 2, 2000, pp. 281–286.
Translated from Zhurnal Éksperimental'noĭ i Teoreticheskoĭ Fiziki, Vol. 117, No. 2, 2000, pp. 319–325.

ATOMS, SPECTRA, RADIATION

Resonance Compton Scattering in an External Magnetic Field

P. I. Fomin[1, *] and R. I. Kholodov[2]

[1]*Bogolyubov Institute of Theoretical Physics, National Academy of Science of Ukraine, Kiev, 252028 Ukraine*
[2]*Institute of Applied Physics, National Academy of Science of Ukraine, Sumy, 244030 Ukraine*
**e-mail: pfomin@bitp.kiev.ua*

Received September 1, 1999

Abstract—The scattering of a photon by an electron in an external magnetic field under resonant conditions, when the photon energy is close to the splittings between the Landau levels, is investigated. Formulas are obtained for the cross section of the process taking account of the polarization of the electron. For external fields $\sim 10^{12}$ G the resonant Compton cross section is several orders of magnitude greater than the Thompson cross section, and the width of the resonance is tens of electron volts. *© 2000 MAIK "Nauka/Interperiodica".*

1. INTRODUCTION

There is an extensive literature on quantum electrodynamic processes with photons, electrons, and positrons in an external magnetic field, but this subject continues to remain topical on the experimental and theoretical levels. First-order processes in a magnetic field (magnetobremsstrahlung, electron-positron pair production by a photon, and others) have been investigated in detail in the last ten years (see, for example, [1–5]). Less attention has been devoted to the Compton scattering of a photon by an electron [6, 7], since in the general case the probability of such a process is relatively low because it contains an additional power of the fine structure constant.

We wish to show here that in Compton scattering in a magnetic field a resonant increase of the probability is possible when the energy of the incident particles is close to a Landau level of the intermediate particle, which makes such processes physically interesting and observable in practice if the magnetic fields are sufficiently strong. Fields of this magnitude occur, for example, in strongly magnetized neutron stars.

We also note that a similar resonant increase of the cross section can also occur for pair production by equivalent photons [8] in a collision of two fast nuclei with large Z (heavy ions), and the strong magnetic field produced by the nuclei in the region between them at the moment of closest approach can play the role of an external magnetic field. In this region the Coulomb fields of the nuclei mutually compensate one another, and the magnetic fields add. Such a process could be relevant for observable anomalies in the yield of resonant pairs in heavy-ion collisions [9, 10].

In contrast to [7], in the present paper a general relativistic analysis of the process, where the relativistic wavefunction and the Green's function of the electron are used, is made.

In Section 2, using the Green's function of an electron in a magnetic field, an expression for the Coulomb scattering amplitude is obtained in a form convenient for investigating resonance effects. In Section 3 the conditions for the appearance of resonances are analyzed. The general formulas simplify in the approximation where the frequencies of the initial and final photons are low compared with $mc^2/\hbar$. In Section 4 the widths of the resonances are calculated. In the last section the cross section for the resonance Compton effect is calculated for various polarizations of the final electron.

2. AMPLITUDE OF THE PROCESS

The scattering of a photon by an electron in a magnetic field is described by the following Feynman diagrams shown in the figure. The wavy lines in the figure correspond to photons with 4-momenta $\mathbf{k} = (\omega, k)$ and $\mathbf{k}' = (\omega', k')$ that do not interact with the external field. The external solid lines correspond to exact solutions of the Dirac equation for an electron in a uniform magnetic field with the 4-momenta $\mathbf{p} = (\varepsilon_l, 0, p_y, p_z)$ and $\mathbf{p}' = (\varepsilon_l', 0, p_y', p_z')$ (with zero component along the x axis), and the intermediate solid lines denote an electron Green's function in a uniform external magnetic field.

It is convenient to take the wavefunction Ψ of an electron in a uniform constant external magnetic field in the form [11]

$$\Psi(x) = \frac{\exp(-i\mathbf{p}\cdot\mathbf{r})}{\sqrt{S}}\Psi(\zeta), \tag{1}$$

$$\Psi(\zeta) = A_l[i\sqrt{2leH}U_l(\zeta) + (m + \mu\tilde{m})U_{l-1}(\zeta)\gamma_1]u_l,$$

1063-7761/00/9002-0281$20.00 © 2000 MAIK "Nauka/Interperiodica"

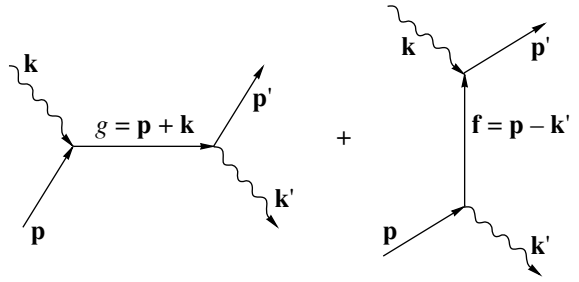

Feynman diagrams of the process where a photon is scattered by an electron in a magnetic field.

where $r = (t, 0, y, z)$, $\mathbf{p} \cdot \mathbf{r} = \varepsilon_l t - p_y y - p_z z$, ε_l is the energy of an electron in the given magnetic field, S is the normalization area in the (yz) plane, $\zeta = \sqrt{eH}\,(x + p_y/eH)$, $U_l(\zeta)$ is a Hermite function of order l, μ is the polarization of an electron which assumes the values +1 and –1, γ_1 is a Dirac matrix in the standard representation, $\tilde{m}^2 = m^2 + 2leH$, the bispinor u_l has the form

$$u_l = \begin{pmatrix} 0 \\ \mu\tilde{m} - \varepsilon_l \\ 0 \\ p_z \end{pmatrix}, \tag{2}$$

A_l is a normalization factor

$$A_l = \begin{cases} \sqrt{\dfrac{\sqrt{eH}(\varepsilon_l + \mu\tilde{m})}{p_z^2 2\tilde{m} 2\varepsilon_l(\tilde{m} + \mu m)}}, & l > 0, \\ \dfrac{1}{\sqrt{\sqrt{eH} 2\varepsilon_0(\varepsilon_0 + m)}}, & l = 0, \quad \mu = -1. \end{cases} \tag{3}$$

The constant magnetic field H is directed along the z axis. The wavefunction (1) corresponds to a gauge of the external field in which the 4-vector potential is defined as

$$A_0 = A_x = A_z = 0, \quad A_y = Hx. \tag{4}$$

The energy spectrum ε_l is

$$\varepsilon_l = \sqrt{m^2 + p_z^2 + 2leH} = \sqrt{\tilde{m}^2 + p_z^2}. \tag{5}$$

The wavefunction (1) is an eigenfunction for operators of the generalized momentum P and the operator corresponding to the polarization of the electron R:

$$P_{ik}\Psi_k^+ = \gamma_{ik}^\mu (p_\mu - eA_\mu)\Psi_k^+ = m\Psi_i^+, \tag{6}$$

$$R_{ik}\Psi_k^+ = \mu\Psi_i^+. \tag{7}$$

We write out the explicit form of these operators:

$$P = \gamma\tilde{\mathbf{p}} + i\sqrt{eH}\gamma_1\partial/\partial\zeta - \sqrt{eH}\gamma_2\zeta, \tag{8}$$

$$R = PF_{\mu\nu}\sigma^{\mu\nu} + F_{\mu\nu}\sigma^{\mu\nu}P = \gamma_5\gamma^\mu S_\mu, \tag{9}$$

where

$$\tilde{\mathbf{p}} = (\varepsilon_l, 0, 0, p_z), \quad F_{\mu\nu} = \partial_\mu A_\nu - \partial_\nu A_\mu,$$
$$\sigma^{\mu\nu} = (\gamma^\mu\gamma^\nu - \gamma^\nu\gamma^\mu)/2, \quad S_\mu = (-p_z, 0, 0, -\varepsilon_l)/\tilde{m}.$$

It should be noted that the expression for the generalized operator (8) contains only one differentiation operator with respect to the variable x ($\zeta = \zeta(x)$). The operators $\hat{p}_0$, $\hat{p}_y$, and $\hat{p}_z$ are replaced by the eigenvalues ε_l, p_y, and p_z, since the dependence of the wavefunction (1) on the variables t, y, z has the form of a plane wave.

For the causal Green's function of the operator (8) we employ the expression

$$G_H(\mathbf{x}_1, \mathbf{x}_2) = \frac{-1}{(2\pi)^3} \times \int d^3\mathbf{g} \exp(-i\mathbf{g} \cdot (\mathbf{r}_1 - \mathbf{r}_2)) G_H(\mathbf{g};\, \rho_1, \rho_2), \tag{10}$$

$$G_H(\mathbf{g};\, \rho_1, \rho_2) = \sqrt{eH} \sum_{n=0}^{\infty} \frac{1}{g_0^2 - \varepsilon_n^2 - i \cdot 0} \times [U_n(\rho_1)U_n(\rho_2)(\gamma\tilde{\mathbf{g}} + m)\alpha + (1 - \delta_{0n})U_{n-1}(\rho_1) \times U_{n-1}(\rho_2)(\gamma\tilde{\mathbf{g}} + m)\beta + (1 - \delta_{0n})i\sqrt{2neH} \times (U_{n-1}(\rho_1)U_n(\rho_2)\gamma_1\alpha - U_n(\rho_1)U_{n-1}(\rho_2)\alpha\gamma_1)],$$

where $d^3\mathbf{g} = dg_0 dg_y dg_z$, $\gamma\tilde{\mathbf{g}} = \gamma_0 g_0 - \gamma_3 g_z$, and $\rho_{1,2} = \sqrt{eH}\,(x_{1,2} + g_y/eH)$ for the first diagram. In the second diagram $\mathbf{g} \longrightarrow \mathbf{f}$, so that $\rho_{1,2} \longrightarrow \eta_{1,2} = \sqrt{eH}\,(x_{1,2} + f_y/eH)$. The matrices α and β have the form

$$\alpha = (1 + i\gamma_2\gamma_1)/2 \quad \beta = (1 - i\gamma_2\gamma_1)/2. \tag{11}$$

We shall construct the amplitude of the process on the basis of the diagrams presented in the figure. Substituting into it the expressions (1) and (10) and using as the quantum photon fields $A(x_{1,2})$ the well-known expressions for the fields of noninteracting photons, we obtain

$$S_{if} = ie^2 \int \mathbf{dx_1 dx_2} \bar{\Psi}(\mathbf{x}_1)[A(\mathbf{x_1})G_H(\mathbf{x_1}, \mathbf{x_2})A'(\mathbf{x_2}) + A'(\mathbf{x_1})G_H G_H(\mathbf{x_1}, \mathbf{x_2})A(\mathbf{x_2})\Psi(\mathbf{x_2}), \tag{12}$$

where $\bar{\Psi}(\mathbf{x_1})$ is the Dirac conjugate of the expression (1), where $\zeta \longrightarrow \xi = \sqrt{eH}\,(x + p_y'/eH)$. Integrating over $dt_{1,2}$, $dy_{1,2}$, $dz_{1,2}$, $d^3\mathbf{g}$, and $d^3\mathbf{f}$ yields

$$S_{if} = \frac{-ie^2(2\pi)^4 e_\mu e_\nu'^*}{VS\sqrt{\omega\omega'}} \delta^3(\mathbf{p} + \mathbf{k} - \mathbf{p}' - \mathbf{k}') \times \int dx_1 dx_2 \bar{\Psi}(\xi_1) Q^{\mu\nu} \Psi(\zeta_2), \tag{13}$$

$$Q^{\mu\nu} = \exp(ik_x x_2 - ik'_x x_1)\gamma^\nu G_H(g; \rho_1, \rho_2)\gamma^\mu$$

$$+ \exp(ik_x x_1 - ik'_x x_2)\gamma^\mu G_H(f; \eta_1, \eta_2)\gamma^\nu,$$

where e_μ and e'_ν are the polarization vectors of the initial and final photons and V is the volume under study. The delta-function corresponds to the conservation laws for the energy and the projections of the momentum on the axes y and z. The following constraints are imposed on the 4-momenta of the intermediate particles (with the exception of their x components):

$$\mathbf{g} = \mathbf{p} + \mathbf{k} = \mathbf{p}' + \mathbf{k}', \quad (14)$$

$$\mathbf{f} = \mathbf{p}' - \mathrm{k} = \mathbf{p} - \mathbf{k}'. \quad (15)$$

3. CONDITIONS FOR RESONANCE SCATTERING

From the conservation laws (14) it is not difficult to obtain, taking account of the dispersion laws for the initial and final particles

$$\omega^2 = \vec{k}^2, \quad \omega'^2 = \vec{k}'^2, \quad \varepsilon_l = \sqrt{\tilde{m}^2 + p_z^2}, \quad (16)$$

$$\varepsilon_{l'} = \sqrt{\tilde{m}'^2 + p_z'^2},$$

where

$$\tilde{m} = \sqrt{m^2 + 2leH}, \quad \tilde{m}' = \sqrt{m'^2 + 2l'eH},$$

the frequency of the final photon expressed in terms of the Landau level numbers l and l', the frequency of the initial photon, and the direction of the incident and emitted photons:

$$\omega' = \frac{1}{1-u}[\varepsilon_l + \omega(1 - vu) - ((\varepsilon_l + \omega(1 - vu))^2 - (\omega^2 + 2\varepsilon_l\omega + 2(l - l')hm^2)(1 - u^2))^{1/2}], \quad (17)$$

where $v = \cos\theta$ and $u = \cos\theta'$ are the cosines of the angles between the direction along the magnetic field and the directions of motion of the initial and final photons, respectively, and $h = H/H_0$ ($H_0 = m^2/e \sim 4.4 \times 10^{13}$ G). For simplicity, the z component of the momentum of the initial electron is assumed to be zero, $p_z = 0$.

For fields that are weak compared with H_0, small values of the Landau level numbers l and l', and low frequencies,

$$(l + l')h \ll 1 \quad \text{and} \quad \omega \ll m, \quad (18)$$

the expression (17) simplifies

$$\omega' = \omega + (l - l')hm. \quad (19)$$

The conditions for a resonance process require that the poles of the Green's function (10) vanish. In the expression for the Green's function (10) only one term remains in the sum. This corresponds to the fact that the intermediate electron is in a definite Landau level. For the first diagram in the figure the resonance condition has the form

$$g_0^2 - \varepsilon_{n1}^2 = g_0^2 - (m^2 + 2n_1hm^2 + g_z^2) = 0. \quad (20)$$

The condition (20) imposes a restriction on the frequency of the initial photon, and taking account of equation (14) we obtain

$$\omega = (\sqrt{\varepsilon_l^2 - 2(n_1 - l)hm^2(1 - v^2)} - \varepsilon_l)/(1 - v^2). \quad (21)$$

In the approximation (18)

$$\omega = (n_1 - l)hm, \text{ and } \omega' = (n_1 - l')hm. \quad (22)$$

The meaning of the expression (22) is obvious: The energy of the initial photon is equal to the splitting between the levels of the intermediate and initial electrons, and the energy of the final photon is equal to the splitting between the levels of the intermediate and final electrons. In this approximation the resonance values of ω and ω' do not depend on the angles of incidence and emission of the photons.

It is evident from equation (22) that ω' is proportional to ω, and the coefficient of proportionality is $(n_1 - l')/(n_1 - l) > 1$, if the Landau level number l of the initial electron is greater than the Landau level number of the final electron l', and $\omega' < \omega$ in the opposite case, where $l' < l$. Thus, for $l = 1$, $n_1 = 2$, and $l' = 0$, doubling of the photon frequency will be observed as a result of the resonance scattering of a photon by an electron. The case $l' = l$ corresponds to elastic scattering.

The resonance condition also occurs for the second diagram in the figure:

$$f_0^2 - \varepsilon_{n2}^2 = f_0^2 - (m^2 + 2n_2hm^2 + f_z^2) = 0. \quad (23)$$

It can be realized in two different cases:

$$\varepsilon_{n2} = \begin{cases} \varepsilon - \omega = \omega' - \varepsilon', \ \varepsilon > \omega \text{ and } \omega' > \varepsilon', \\ \omega - \varepsilon = \varepsilon' - \omega' \ \varepsilon < \omega \text{ and } \omega' < \varepsilon'. \end{cases} \quad (24)$$

The first equality in equation (24) corresponds to a process where the initial electron, emitting the final photon, passes into the intermediate electron, which, absorbing the initial photon, passes into the final electron. In this case the condition (24) imposes the following restriction on the frequency of the final photon:

$$\omega' = (\varepsilon_l - \sqrt{\varepsilon_l^2 - 2(l - n_2)hm^2(1 - u^2)})/(1 - u^2), \quad (25)$$

and in the expression (18)

$$\omega' = (l - n_2)hm, \text{ and } \omega = (l' - n_2)hm. \quad (26)$$

It should be noted that in the case at hand, at resonance, the two conditions for the approximation (18) are identical for the first and second diagrams.

The second equality in equation (24) corresponds to the possibility of resonance Compton scattering via e^-e^+-pair production by the initial photon followed by annihilation of the intermediate positron with the initial electron. In this case, however, in the approximation (18) the cross section is exponentially small because of the factor $\exp(-\omega^2/2hm^2)$, where $\omega^2 \geq 4m^2$. In the preceding cases this factor was of the order of 1.

4. RESONANCE WIDTHS

In what follows, for simplicity, we shall consider processes where the initial electron is in the ground state ($l = 0$). In this case, as one can see from Eq. (25), the resonance in the second diagram does not occur (with the exception of the process where a photon is scattered by an electron via the creation and annihilation of an e^-e^+-pair).

The width of a resonance is determined by the probability of decay of the intermediate state, in this case the probability of emission of a photon with frequency ω' by an intermediate electron with 4-momentum $\mathbf{g} = (\varepsilon_n, 0, g_y, g_z)$, satisfying the condition (14). This is the wellknown process of magnetobremsstrahlung of an electron. However, the expression for the probability must be doubled, since in our case the initial particle is an electron in an intermediate state (see figure), in which summation is performed over the polarization, in contrast to a real electron for which averaging is performed in the initial states. For the differential probability of photon emission per unit time at an angle θ' with respect to the direction of the magnetic field accompanying a transition from the level n to the level l' we have

$$\frac{dW_{nl'}}{du}[-m^2J^2(l', n) + (\tilde{\mathbf{g}}\cdot\tilde{\mathbf{p}}' - m^2) \times (J^2(l', n-1) + J^2(l'-1, n)) - 4m^2h\sqrt{l'n} \times J(l'-1, n-1)J(l', n) - m^2J^2(l'-1, n-1)]\frac{\alpha\omega'}{g_0(g_0-\omega')}, \quad (27)$$

where $\alpha = e^2/\hbar c$, $\tilde{\mathbf{g}}\cdot\tilde{\mathbf{p}}' = g_0\varepsilon_{l'} - g_z p_z'$, and $J(-l', n)$ is a special function of the form

$$J(l', n) = e^{-\eta'/2}\eta^{(n-l')/2} \times \sqrt{\frac{n!}{l'!}}\frac{1}{(n-l')!}F(-l', n-l'+1, \eta'), \quad (28)$$

$F(-l', n-l'+1, \eta)$ is the confluent hypergeometric function, and $\eta' = \omega'^2(1-u^2)/2hm^2$. For a small parameter $\eta' \ll 1$, which for small Landau level numbers is equivalent to the condition (18), the expression (27) can be put into the form

$$\frac{dW_{nl'}}{du} = \alpha mAh^{n-l'+1}(1+u^2)(1-u^2)^{n-l'-1}, \quad (29)$$

where A is a numerical factor

$$A = \frac{(n^2-l'^2)(n-1)!(n-l')^{2n-2l'}}{2^{n-l'}l'!(n-l')!^2}.$$

Integrating over u we obtain the total probability of the process:

$$W_{nl'} = \alpha mh^{n-l'+1} \times \frac{2(n-1)!(n-l')^{2n-2l'}(n+l')(n-l'+1)}{l'!(n-l')!(2n-2l'+1)!!}. \quad (30)$$

According to what we have said above, the width Γ is equal to the sum of the probabilities (30) over l' from 0 to $n-1$. But, in the approximation (18) the term with $l' = n-1$ will be dominant, i.e.,

$$\Gamma = W_{n\,n-1} = \frac{4}{3}(2n-1)\alpha mh^2. \quad (31)$$

The expression for $2/\Gamma$ with $n = 1$ is identical to the emission time of an electron in a magnetic field [12]. For magnetic fields $H \sim 0.1H_0$ the width is $\Gamma \sim 50$ eV.

The width at the pole of the Green's function (10) is introduced in the standard manner by adding to the energy ε_n of the intermediate particle a negative imaginary correction

$$\varepsilon_n \longrightarrow \varepsilon_n - i\Gamma/2. \quad (32)$$

5. CROSS SECTION FOR THE RESONANCE COMPTON EFFECT

The differential probability of the process is determined as the product of the squared modulus of the amplitude (13) by the number dN of final states, which is

$$dN = \frac{SVd^2\mathbf{p}'d^3\mathbf{k}'}{(2\pi)^5}. \quad (33)$$

Averaging over the polarizations of the initial photon, summing over the polarizations of the final photon, and integrating over dp_z' and dp_y', the differential probability can be put into the form

$$dW_{0nl'} = \frac{e^4\delta(m+w-\varepsilon'-w')}{\omega_1\omega_2}\frac{Td^3k'}{V} \times \int dx_1dx_1'dx_2dx_2'\mathrm{Sp}\left\{\rho(\xi_1, \xi_1')Q^{\mu\nu}\rho(\zeta_2, \zeta_2')Q_{\mu\nu}'^{+}\right\}, \quad (34)$$

where $Q^{\mu\nu}$ is only the first term in equation (13), $Q_{\mu\nu}'$ depends on the primed coordinates $x_{1,2}'$, and $\rho(\zeta_2, \zeta_2')$ and $\rho(\xi_1', \xi_1)$ are the polarization density matrices

of the initial and final electrons, which are defined as

$$\rho(\zeta_2, \zeta_2') = \Psi(\zeta_2)\bar{\Psi}(\zeta_2'),$$
$$\rho(\xi_1', \xi_1) = \Psi(\xi_1')\bar{\Psi}(\xi_1). \quad (35)$$

Substituting the expressions (1), (10), and (35) into the expression for the differential probability (34), dividing the latter by the flux density $j = c/V$ of the initial photons and by the time T, and integrating over $d\omega'$ gives a general expression for the differential cross section of the process of interest. The explicit form of this expression is given in the Appendix. The expression depends on the product of two special functions (28) $J_1(l', n)$ and $J_2(0, n)$, the first one depending on the parameter $\eta' = \omega'^2(1 - u^2)/2hm^2$ and the second on the parameter $\eta = \omega^2(1 - v^2)/2hm^2$. In the approximation of small parameters $\eta \sim \eta' \ll 1$, the differential cross section for the Compton effect near resonance with the final electron polarized in a direction opposite to the field ($\mu' = -1$) can be put into the form

$$\frac{d\bar{\sigma}_{0nl'}}{du} = \pi r_0^2 B^- m^2 h^{2n-l'} \times \frac{(1+v^2)(1-v^2)^{n-1}(1+u^2)(1-u^2)^{n-l'-1}}{(\omega-\omega_r)^2 + \Gamma^2/4}, \quad (36)$$

where once again $v = \cos\theta$, $u = \cos\theta'$, $h = eH/m^2$, r_0 is the classical radius of the electron, ω_r is the frequency of the initial photon at resonance (22), and B^- is the following numerical factor

$$B^- = \frac{n^{2n-1}(n-l')^{2n-2l'+1}}{2^{2n-l'}l'!(n-l')!^2}. \quad (37)$$

It is worth noting that the dependence (36) of the differential cross section on the cosine u of the angle of the final photon is identical to the dependence of the differential probability of magnetobremsstrahlung on u. This shows that at resonance the process where a photon is scattered by an electron in a magnetic field divides into two independent processes: absorption of the photon by the electron and magnetobremsstrahlung.

Integrating the expression (36) over u, taking account of Eq. (31), we obtain the total cross section for the Compton effect at resonance

$$\bar{\sigma}_{0nl'} = 9\pi r_0^2 \times \frac{(n-l')^{2n-2l'}n^{2n-1}(n-l'+1)(1+v^2)(1-v^2)^{n-1}}{\alpha^2 h^{4+l'-2n}2^{n+1}(2n-1)^2 l'!(n-l')!(2n-2l'+1)!!}. \quad (38)$$

For $n = 1$, $l' = 0$ after integrating over v, the cross section becomes

$$\bar{\sigma}_{010} = \frac{3}{2}\pi r_0^2\left(\frac{1}{\alpha h}\right)^2 = \sigma_T\frac{3}{4}\left(\frac{m^2c^4}{e^3H}\right)^2, \quad (39)$$

where $\sigma_T = 8\pi r_0^2/3$ is the Thompson cross section. In this case $\omega = \omega'$ and $\varepsilon = \varepsilon'$, which corresponds to elastic scattering. We note that the expression (39) can be written in the form $\bar{\sigma}_{010} = 2\pi\lambda\!\!\!^{-2}$, where $\lambda\!\!\!^-$ is the wavelength of the initial photon. As the magnetic field decreases, $\lambda\!\!\!^-$ increases, which corresponds to an increase in the cross section. But the width of the resonance decreases. For magnetic fields $H \sim 0.1H_0$ the resonance cross section for Compton scattering is six orders of magnitude greater than the Thompson cross section.

Similarly to equation (36), we can obtain an expression for the differential cross section for Compton scattering with the final electron polarized in the direction of the field ($\mu' = +1$):

$$\frac{d\sigma^+_{0nl'}}{du} = \pi r_0^2 B^+ m^2 h^{2n-l'+1} \times \frac{(1+v^2)(1-v^2)^{n-1}(1+u^2)(1-u^2)^{n-l'-1}}{(\omega-\omega_r)^2 + \Gamma^2/4}, \quad (40)$$

where

$$B^+ = \frac{n^{2n-1}(n-l')^{2n-2l'+1}}{2^{2n-l'+1}(l'-1)!(n-l')!^2}. \quad (41)$$

To compare the cross sections (40) and (36) we divide one by the other:

$$\frac{d\sigma^+_{0nl'}/du}{d\bar{\sigma}_{0nl'}/du} = \frac{l'h}{2}. \quad (42)$$

Since the ratio (42) does not depend on the variable u, it will also hold for the total cross sections

$$\sigma^+_{0nl'} = l'h\bar{\sigma}_{0nl'}/2. \quad (43)$$

Finally, we note that since for an electron in the ground state ($l = 0$, $\mu = -1$) the cross section (38) (scattering without reorientation of the electron spin) is $2H_0/l'H \gg 1$ times greater than the cross section (43) (scattering with reorientation of the electron spin), the expression (38) actually also describes resonance cross section of the Compton effect summed over the polarizations of the final electron. In addition, we underscore that the expressions (36)–(40) were obtained in a coordinate system where the initial electron does not have a momentum component in the direction of the magnetic field: $p_z = 0$.

ACKNOWLEDGMENT

We thank S.P. Roshchupkin for helpful discussions.

APPENDIX

An expression for the differential cross section for resonance Compton scattering is presented below for arbitrary polarization μ' of the final electron with no restrictions imposed by the conditions (19). This expression could be helpful for analyzing situations in supercritical fields ($H > H_0$) or with ultrarelativistic particles:

$$\frac{d\sigma_{0nl'}}{du} = \frac{\pi r_0^2 \omega' \sum_{i=1}^{9} A_i}{4\omega\tilde{m}'\varepsilon_n^2(m + \omega(1 - vu) - \omega'(1 - u^2))((g_0 - \varepsilon_n)^2 + \Gamma^2/4)},$$

where

$$A_1 = -J_1^2(l', n)J_2^2(0, n)\frac{2l'hm^2\mu'\tilde{m}'(\tilde{g}^2 + m^2)}{\tilde{m}' + \mu'm + \Delta'},$$

$$A_2 = (J_1^2(l', n)J_2^2(0, n-1) + J_1^2(l', n-1)J_2^2(0, n)) \times \frac{4l'nh^2m^4\mu'\tilde{m}'}{\tilde{m}' + \mu'm + \Delta'},$$

$$A_3 = J_1^2(l'-1, n)J_2^2(0, n)\lambda_{l'}(\tilde{m}' + \mu'm) \times (\mu'\tilde{m}'(\tilde{g}^2 + m^2) - 2mp'\tilde{g}),$$

$$A_4 = J_1^2(l'-1, n)J_2^2(0, n-1)2n\lambda_{l'}hm^2 \times (\tilde{m}' + \mu'm)(\varepsilon' - \mu'\tilde{m}'),$$

$$A_5 = J_1^2(l', n-1)J_2^2(0, n-1)\frac{2l'hm^2}{\tilde{m}' + \mu'm + \Delta'}[2wp'\tilde{g} - \tilde{g}^2(\varepsilon' + \mu'\tilde{m}') + 2mg_0\mu'\tilde{m}' + m^2\varepsilon' - m^2\mu'\tilde{m}'],$$

$$A_6 = -J_1^2(l'-1, n-1)J_2^2(0, n)2n\lambda_{l'}hm^2(\tilde{m}' + \mu'm)\mu'\tilde{m}',$$

$$A_7 = J_1^2(l'-1, n-1)J_2^2(0, n-1) \times \lambda_{l'}(\tilde{m}' + \mu'm)\mu'\tilde{m}'\omega^2(1 - v^2),$$

$$A_8 = J_1(l', n)J_1(l'-1, n-1)J_2^2(0, n)2\sqrt{l'n}\lambda_{l'}hm^3\tilde{m}',$$

$$A_9 = -J_1(l', n)J_1(l'-1, n-1)J_2^2(0, n-1) \times 2\sqrt{l'n}\lambda_{l'}hm^2\tilde{m}'\omega,$$

$$\lambda_{l'} = 1 - \delta_{0l'}, \quad \Delta' = l'hm\delta_{0l'}.$$

REFERENCES

1. A. A. Sokolov and I. M. Ternov, *Radiation from Relativistic Electrons* (Nauka, Moscow, 1983; AIP, New York, 1986).
2. N. P. Klepikov, Zh. Éksp. Teor. Fiz. **26**, 19 (1954).
3. I. M. Ternov, V. G. Bagrov, and R. A. Rzaev, Zh. Éksp. Teor. Fiz. **67**, 453 (1974) [Sov. Phys. JETP **40**, 225 (1975)].
4. V. N. Baier, V. M. Katkov, and V. M. Strakhovenko, Zh. Éksp. Teor. Fiz. **67**, 453 (1974) [Sov. Phys. JETP **40**, 225 (1975)].
5. A. I. Nikishov, Trudy FIAN **111**, 152 (1979).
6. V. Ch. Zhukovskiĭ and I. Kherman, Yad. Fiz. **14**, 150 (1971) [Sov. J. Nucl. Phys. **14**, 851 (1972)].
7. R. W. Bussard, S. B. Alexander, and P. Meszaros, Phys. Rev. D **34**, 440 (1986).
8. P. I. Fomin and R. I. Kholodov, Dokl. Akad. Nauk Ukrainy **12**, 91 (1998).
9. J. Koenig, E. Berdermann, F. Bosch, *et al.*, Z. Phys. A **346**, 153 (1993).
10. R. Bär, A. Balanda, J. Baumann, *et al.*, Nucl. Phys. A **583**, 237 (1995).
11. A. I. Akhiezer and V. B. Berestetskiĭ, *Quantum Electrodynamics*, 3rd ed. (Nauka, Moscow, 1969; Wiley, New York, 1965).
12. V. G. Bagrov, D. M. Gutman, V. N. Rodionov, *et al.*, Zh. Éksp. Teor. Fiz. **71**, 433 (1976) [Sov. Phys. JETP **44**, 228 (1976)].

Translation was provided by AIP

Journal of Experimental and Theoretical Physics, Vol. 90, No. 2, 2000, pp. 287–289.
From Zhurnal Éksperimental'noĭ i Teoreticheskoĭ Fiziki, Vol. 117, No. 2, 2000, pp. 326–328.

PLASMA, GASES

Scaling Law for the Fluid-Solid Phase Transition in Yukawa Systems (Dusty Plasmas)[1]

O. S. Vaulina* and S. A. Khrapak

High Energy Density Research Center, Russian Academy of Sciences, Moscow, 127412 Russia
**e-mail: ipdustpl@redline.ru*

Received June 9, 1999

Abstract—Yukawa systems serve as models for plasmas and colloidal suspensions of charged particles. The state of these systems is determined by two dimensionless parameters: $k = a/\lambda_D$, which is the ratio of the mean interparticle distance to the Debye length λ_D, and $\Gamma = Z_d^2 e^2/aT_d$, which is the ratio of the Coulomb potential energy to the particle temperature T_d (Z_d is the charge of each particle). We propose an empirical scaling law for the critical coupling parameter Γ_c needed for crystallization in Yukawa systems. The dependence of Γ_c on k is in good agreement with recent molecular dynamics simulations. *© 2000 MAIK "Nauka/Interperiodica".*

Systems of small solid particles (dust particles) immersed in plasmas have recently attracted much attention. They arise in a wide variety of plasma environments ranging from the interstellar medium to laboratory plasma devices. A dust particle in a plasma usually acquires an electric charge and interacts with other particles. The interaction potential between macroscopic dust particles depends on their own physical parameters and those of the ambient plasma. The question of the correct potential of interaction between dust particles is not purely fundamental and still remains open. Such effects as the plasma flow anisotropies, dipole effects, and long-range attractive interactions due to shadow effects may play a role when considering different plasma conditions. In order to understand the behavior of dusty plasmas in complicated situations, however, the results for simple and basic cases are indispensable. As one of those cases, an isotropic screened Coulomb potential (or a Yukawa-type potential) is frequently assumed:

$$\phi(r) = \frac{Z_d^2 e^2}{r}\exp\left(-\frac{r}{\lambda_D}\right), \qquad (1)$$

where Z_d is the particle change and λ_D is the screening length. For an isotopic and homogeneous plasma,

$$\lambda_D^{-2} = \lambda_{De}^{-2} + \lambda_{Di}^{-2} \approx \lambda_{Di}^{-2}$$

(if as usual $T_e \gg T_i$), where

$$\lambda_{De(i)} = \sqrt{\frac{T_{e(i)}}{4\pi e^2 n_{e(i)}}}$$

is the electron (ion) Debye length.

[1] This article was submitted by the authors in English.

It was suggested by Ikezi [1] that, when the interparticle potential energy exceeds the kinetic energy, particles in a plasma can form crystalline structures. Laboratory experiments under various plasma conditions have recently demonstrated this possibility [2–8]. Such crystal structures have been also observed in colloidal suspensions of charged particles, where the interaction potential (1) can be also adopted.

The conditions of such crystallization in a system of particles interacting via a screened Coulomb potential are under investigation. For example, molecular dynamics simulations were recently used to study phase diagrams of the Yukawa systems [9–12]. Although some of the assumptions in the simulations (interaction potential, cubic simulation box with periodic boundary conditions) may be not completely suited to some experiments on Coulomb crystallization in dusty plasmas, the results were obtained. In these simulations the state of a system is determined by only two dimensionless parameters,

$$k = a/\lambda_D \quad \text{and} \quad \Gamma = Z_d^2 e^2/aT_d, \qquad (2)$$

which enter into the equations of motion. Here $a = n_a^{-1/3}$ is the mean interparticle distance and n_d is the particle number density. The coupling parameter Γ is roughly the ratio of the unscreened Coulomb potential energy to the kinetic energy per particle (T_d being the particle temperature). Some studies [10, 12] have used normalization that differs slightly from (2). Specifically the Wigner–Seitz radius $\rho = (3/4\pi n_d)^{1/3}$ was used as the length unit instead of a. Note that k and Γ will then be $k' = k(4\pi/3)^{-1/3}$ and $\Gamma' = \Gamma(4\pi/3)^{1/3} \approx 1.612\Gamma$.

In the limit $k \longrightarrow 0$, the Yukawa potential devolves into the long-range Coulomb potential describing the one-component plasma (OCP) system. In this limit,

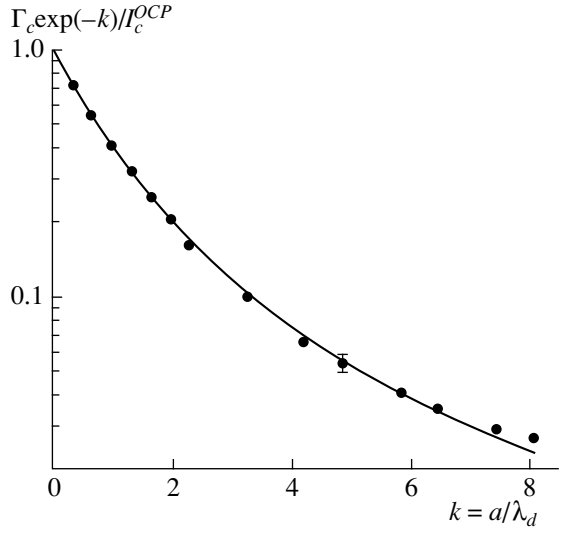

Filled circles are the values of $\Gamma_c \exp(-k)/\Gamma_c^{OCP}$ for various values of k, calculated from the solid-fluid phase transition data of Hamagushi *et al.* [12]. The error bar at $k = 4.84$ ($k' = 3.0$) represents the simulation uncertainties. The solid curve is the function $(1 + k + k^2/2)^{-1}$.

only one parameter Γ describes the fluid-solid phase transition. It is well known [13, 14] that for the OCP system, Γ must exceed the critical value $\Gamma_c \approx 106$ ($\Gamma_c' \approx 170$) to from a Coulomb lattice. For a system with a Yukawa interaction potential, the transition between fluid and solid phases takes place at some critical value Γ_c that depends on the screening parameter k. By analogy with the OCP system, it was first proposed to introduce a coupling parameter that takes screening into account [1],

$$\Gamma_s = \frac{Z_d^2 e^2}{aT_d} \exp(-a/\lambda_D) \equiv \Gamma \exp(-k), \qquad (3)$$

and use the condition $\Gamma_s > 106$ to describe Coulomb solidification, so that $\Gamma_c \approx 106 \exp k$. However, recent numerical simulations show that Γ_c is a more complicated function of k [12].

We have constructed a function $\Gamma_c = \Gamma_c(k)$ that fits the fluid-solid phase transition data of Hamaguchi, Farouki, and Dubin [12] well over a wide range of k (in [12], three different polynomial fits (equations (17)–(19)) were used to fit data over different ranges of k). We assume that the critical value of the coupling parameter depends on k as

$$\Gamma_c = \Gamma_c^{OCP}(1 + k + k^2/2)^{-1} \exp k, \qquad (4)$$

where $\Gamma_c^{OCP} \approx 106.6$ as found in [12].

In table, the values of Γ_c found via numerical simulation [12] and normalized by the right-hand side of equation (4) for various values of k are summarized. It can be seen that for $k \le 1.61$ ($k' \le 1$), the deviation between simulations and equation (4) is less than 1%. This range of k is very often applied to dust crystals in laboratory experiments. For all values of k except the last point $k = 8.06$, equation (4) fit simulation results to within 10%.

In figure, the values of $\Gamma_c \exp(-k)/\Gamma_c^{OCP}$ calculated from the solid-fluid phase transition data of [12] are plotted versus k. In addition, the function $(1 + k + k^2/2)^{-1}$ is plotted. The error bar at $k = 4.84$ ($k' = 3.0$) represents the simulation uncertainties estimated in [12]. It seems that for all values of k (except $k = 8.06$). Equation (4) holds to within the simulations errors. Figure also shows that Γ_s introduced by

k	$\frac{\Gamma_c}{\Gamma_c^{OCP}} \exp(-k)(1 + k + k^2/2)$
0	1.00
0.32	1.01
0.65	1.01
0.97	1.01
1.29	1.00
1.61	0.99
1.93	0.98
2.26	0.95
3.22	0.96
4.19	0.93
4.84	0.96
5.80	0.99
6.45	1.00
7.42	1.08
8.06	1.15

Equation (3) is not an appropriate measure to describe the fluid-solid phase transition.

The form of the melting curve (4) can be obtained using a very simple approach. We consider a one-dimensional lattice of dust particles interacting via a screened Coulomb potential. Moreover, we assume that it is sufficient to include only interactions between nearest neighbor particles. Then the characteristic oscillation frequency of a given particle about its equilibrium position with all other particles held fixed is [15]

$$\omega_0^2 = \frac{4Z_d^2 e^2}{m_d a^3}\left(1 + k + \frac{k^2}{2}\right)\exp(-k),$$

where m_d is the dust particle mass. The mean squared displacement of particles around their equilibrium positions is $\langle \delta u^2 \rangle \sim T_d/m_d\omega_0^2$. According to Lindenmann's rule for the melting transition $\langle \delta u^2 \rangle / a^2 = \text{const}$, we have

$$\frac{Z_d^2 e^2}{aT_d}\left(1 + k + \frac{k^2}{2}\right)\exp(-k) = \text{const} \qquad (5)$$

at the melting curve. Extrapolating (5) to the limit $k \longrightarrow 0$ we finally arrive at (4).

Surely this crude model cannot serve as a physical basis for (4). It considers a one-dimensional lattice (although simulations were performed in 3*D*) and includes only interactions with nearest neighbors (this assumption is valid only when $k \gg 1$). At the present time, (4) must therefore be considered as an empirical relation.

To conclude, we propose a scaling law for the critical coupling parameter Γ_c needed for crystallization in Yukawa systems. The dependence of Γ_c on k is determined by (4). This dependence is consistent with the recent fluid-solid phase transition simulation data obtained by Hamaguchi *et al.* [12] to within the simulation errors over a wide range of *k*. The empirical condition for crystallization,

$$\frac{Z_d^2 e^2}{aT_d}\left(1 + k + \frac{k^2}{2}\right)\exp(-k) \geq 106,$$

can be very useful in a variety of experimental contexts ranging from dusty plasmas to colloidal suspensions.

ACKNOWLEDGMENT

This work was supported by the Russian Foundation for Basic Research, projects nos. 98-02-16825 and 97-02-17565.

REFERENCES

1. H. Ikezi, Phys. Fluids **29**, 1764 (1986).
2. J. H. Chu and Lin I, Phys. Rev. Lett. **72**, 4009 (1994).
3. H. Thomas, G. E. Morfill, V. Demmel, *et al.*, Phys. Rev. Lett. **73**, 652 (1994).
4. A. Melzer, T. Trottenberg, and A. Piel, Phys. Lett. A **191**, 301 (1994).
5. Y. Hayashi and K. Tachibana, Jpn. J. Appl. Phys. **33**, L804 (1994).
6. A. Barkan and R. L. Merlino, Phys. Plasmas **2**, 3261 (1995).
7. V. Fortov, A. Nefedov, O. Petrov, A. Samarian, and A. Chernyshev, Phys. Rev. E **54**, R2236 (1996).
8. V. Fortov, A. Nefedov, V. Torchinsky, V. Molotkov, *et al.*, Phys. Lett. A **229**, 31 (1997).
9. M. Robbins, K. Kremer, and G. Grest, J. Chem. Phys. **88**, 3286 (1988).
10. R. T. Farouki and S. Hamaguchi, Appl. Phys. Lett. **61**, 2973 (1992).
11. M. Stevens and M. Robbins, J. Chem. Phys. **98**, 2319 (1993).
12. S. Hamaguchi, R. T. Farouki, and D. H. E. Dubin, Phys. Rev. E **56**, 4671 (1997).
13. N. Slattery, G. D. Doolen, and H. E. DeWitt, Phys. Rev. A **21**, 2087 (1980).
14. S. Ichimaru, Rev. Mod. Phys. **54**, 1017 (1982).
15. F. Melandso, Phys. Plasmas **3**, 3890 (1996).

Journal of Experimental and Theoretical Physics, Vol. 90, No. 2, 2000, pp. 290–300.
Translated from Zhurnal Éksperimental'noĭ i Teoreticheskoĭ Fiziki, Vol. 117, No. 2, 2000, pp. 329–341.

SOLIDS
Structure

Mössbauer Optics of Synchrotron Radiation at an Isotopic Boundary

V. A. Belaykov[1, *] and S. V. Semenov[2]

[1]*Landau Institute of Theoretical Physics, Russian Academy of Sciences, Chernogolovka, Moscow oblast, 142432 Russia*
**e-mail: bel@landau.ac.ru*

[2]*Russian Research Centre Kurchatov Institute, Moscow, 123182 Russia*

Received April 1, 1999

Abstract—The inelastic coherent Mössbauer scattering (ICMS) of synchrotron radiation at an isotopic boundary—a flat interface between two regions of matter which have different concentrations of the Mössbauer isotope—is investigated theoretically. Attention is focused primarily on the ICMS component for which the absorption of a synchrotron radiation photon by a nucleus occurs with recoil, i.e., with the creation or annihilation of lattice phonons, and the subsequent process of reemission of a photon by the Mössbauer nucleus occurs without recoil, as a result of which radiation is pumped from the wide synchrotron radiation line into the narrow Mössbauer line. Formulas similar to the Fresnel formulas, well known in optics, for the transmission and reflection of light at a dielectric boundary are obtained for ICMS at an isotopic boundary. Specifically, it is shown that the angle of reflection for ICMS at an isotopic boundary is different from the angle of mirror reflection of a synchrotron radiation beam, and the direction of the ICMS transmitted through the isotopic boundary depends on the deviation of its frequency from the exact value of the Mössbauer resonance frequency and in general is different from the direction of propagation of the synchrotron radiation beam. The suppression of ICMS at grazing angles of incidence of the synchrotron radiation beam is analyzed. A similar problem is solved for a plate-shaped sample containing a Mössbauer isotope. It is shown that the specific nature of the ICMS at an isotopic boundary could be helpful in the problem of Mössbauer filtering of synchrotron radiation. © *2000 MAIK "Nauka/Interperiodica".*

1. INTRODUCTION

Recent progress in Mössbauer spectroscopy using synchrotron radiation in the investigation of the phonon spectra of condensed media [1–3] (see also the recent review publications [4, 5]) make detailed investigations of the Mössbauer optics of synchrotron radiation topical. Inelastic coherent Mössbauer scattering (ICMS) of synchrotron radiation, specifically, forward scattering, studied theoretically in [6], is of special interest. In [6] it was shown that ICMS is of special interest for Mössbauer optics of synchrotron radiation. At the first stage of this process, resonance nuclear absorption of a synchrotron radiation photon, the absorption process is accompanied by the emission or absorption of a lattice phonon, while the second stage of scattering, the reemission of a photon, occurs without recoil, i.e., without phonon absorption or emission. This channel of ICMS results in pumping of radiation out of the wide synchrotron radiation line into a narrow Mössbauer radiation line. It is of interest to study the optics of ICMS by an isotopic boundary—a flat interface between regions with different concentrations of the Mössbauer isotope—in connection with, specifically, the problem of Mössbauer filtering of synchrotron radiation.

The isotopic boundary separating the regions of matter with no Mössbauer isotope and the same substance with 100% content of the Mössbauer isotope or with a quite high degree of enrichment of the material with a Mössbauer isotope is a convenient object for investigating Mössbauer scattering of synchrotron radiation. The point is that for radiation which has not undergone a resonance interaction with Mössbauer nuclei this boundary is simply not manifested in optical properties, since the optical characteristics of matter determined by the interaction of the radiation with electrons are identical on both sides of an isotopic boundary. An isotopic boundary separates spatial regions of matter with different optical characteristics only for a narrow spectral band of the synchrotron radiation near the frequency of the Mössbauer transition, where the resonance interaction of radiation with the Mössbauer nuclei is strong. All optical phenomena well known in optics for a dielectric boundary appear in this spectral range: reflection, refraction of radiation at the boundary, and, specifically, total internal (or external) reflection (TIR). For ICMS, as will be shown below, these phenomena all exhibit qualitative characteristic features as compared with the optics of elastic scattering of synchrotron radiation. For this reason, the optics of an isotopic boundary is of interest for experiments studying the interaction of synchrotron radiation with Mössbauer nuclei [7], specifically, experiments on Mössbauer filtering of synchrotron radiation, since the

1063-7761/00/9002-0290$20.00

background due to the interaction of the synchrotron radiation with the electrons in the matter can be eliminated. Indeed, reflection of synchrotron radiation in the spectral ranges for which nuclear resonance scattering of synchrotron radiation is not observed simply does not occur at an isotopic boundary, and for this reason the nonresonance background is completely suppressed in the scattering.

The present paper is devoted to a systematic analysis of the optical characteristics of ICMS at an isotopic boundary (including in the region of TIR) and by a plane-parallel layer of matter enriched with the Mössbauer isotope and submerged in the same material without the Mössbauer isotope. In this paper elastic Mössbauer scattering is completely omitted, since this question has already been exhaustively studied and the corresponding results can be found in a number of monographs (see, for example, [7–9]). Attention is focused on the ICMS component corresponding to resonance nuclear scattering of synchrotron radiation photons, where the creation or annihilation of lattice phonons occurs at the stage of absorption of the primary photon, while the stage of reemission of a photon by the nucleus occurs without the participation of phonons, i.e., without recoil, and therefore the energy of the scattered photon corresponds exactly to the energy of the Mössbauer transition. Formulas similar to the Fresnel formulas, well known in optics, are obtained, and the corresponding formulas are also presented for ICMS in a plate-shaped sample. ICMS at a boundary with a vacuum as well as for a plate-shaped sample in a vacuum is described by the formulas obtained after a simple limit is taken in them. The possibility of experimental observation of the effects in ICMS optics and the advantages of using ICMS at an isotopic boundary for Mössbauer filtering of synchrotron radiation are discussed.

2. BASIC EQUATIONS

Let us consider the ICMS process for a synchrotron radiation pulse propagating in a sample containing nuclei of a Mössbauer isotope, i.e., nuclear resonance scattering processes accompanied by the creation or annihilation of lattice phonons. The generation of ICMS is described by the inhomogeneous Maxwell's equation [6, 10]

$$-\mathrm{rot}\,\mathrm{rot}\,\mathbf{E}_1 = \frac{1}{c^2}(\varepsilon_0+\varepsilon_1)\frac{\partial^2\mathbf{E}_1}{\partial t^2} + \chi^N\mathbf{E}_0(\omega_s, z)\delta(z-v_g t), \quad (1)$$

where ε_0 is the permittivity in the absence of a nuclear interaction, ε_1 is the correction to the permittivity resulting from the nuclear interaction, χ^N is the analog of the nonlinear susceptibility well-known from nonlinear optics [7, 10], ω_s is the frequency of the synchrotron radiation, v_g is the group velocity of the synchrotron radiation pulse, z is the coordinate in the direction of propagation of the pulse, and the electromagnetic field in the sample is represented as a sum of two components: $\mathbf{E} = \mathbf{E}_0 + \mathbf{E}_1$, where $\mathbf{E}_0$ is the unperturbed field of the synchrotron radiation and $\mathbf{E}_1$ is the perturbation due to the interaction of the radiation with Mössbauer nuclei. In what follows, to solve equation (1) we shall first assume that only absorption of the primary photon of synchrotron radiation occurs with recoil, and the reemission of the secondary photons by the nuclei occurs without recoil. Under these assumptions, ε_1 corresponds to elastic resonance scattering of photons. Therefore [7, 10]

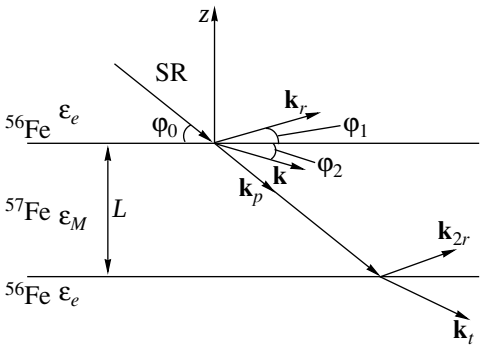

Fig. 1. Illustration for the geometry of ICMS at an isotopic boundary and a layer of matter (SR is synchrotron radiation beam).

$$\varepsilon_0+\varepsilon_1 = \varepsilon_M = \varepsilon_0 + \frac{f^2\Gamma_i N_0}{E_s - E_R + i\Gamma/2}, \quad (2)$$

where f^2 is the Lamb–Mössbauer factor, Γ_i and Γ are the radiation and total widths of the Mössbauer level, the factor N_0 depends on the characteristics of the crystal and the nuclear transition, $E_s = \hbar\omega_s$, and E_R is the resonance energy.

To describe ICMS by an isotopic boundary or a plate bounded by two isotopic boundaries, the solutions of equation (1) must satisfy the boundary conditions at the isotopic boundary or at two boundaries in the case of a plate (Fig. 1). Assuming for simplicity that the density of the Mössbauer isotope is zero outside the plate, we shall seek the solution for the ICMS field in the form

$$\begin{gathered}\mathbf{E}_r\exp(i\mathbf{k}_r\mathbf{r}) \text{ for } z>0 \text{ and } \varepsilon_1 = 0,\\ \mathbf{E}_t\exp(i\mathbf{k}_t\mathbf{r}) \text{ for } z<-L \text{ and } \varepsilon_1 = 0,\\ \mathbf{E}_p\exp(i\mathbf{k}_p\mathbf{r}) + \mathbf{E}_f\exp(i\mathbf{k}\mathbf{r}) + \mathbf{E}_{2r}\exp(i\mathbf{k}_{2r}\mathbf{r})\\ \text{for } 0>z>-L \text{ and } \varepsilon_1\neq 0,\end{gathered} \quad (3)$$

where $\mathbf{k}_r$ and $\mathbf{k}_t$ are the wave vectors of the ICMS photons reflected from and transmitted through the plate, $\mathbf{k}$ and $\mathbf{k}_{2r}$ are the wave vectors of the transmitted beam in the plate and the beam reflected from the second isoto-

pic boundary, $\mathbf{k}_p$ is the wave vector in the particular solution of equation (1), and $\mathbf{E}_r$, $\mathbf{E}_t$, $\mathbf{E}_f$, $\mathbf{E}_{2r}$, $\mathbf{E}_p$, are the amplitudes of the corresponding plane waves.

To refine the wave vectors appearing in the relation (3), it is necessary to satisfy the boundary conditions for the tangential components of the wave vectors. To find the amplitudes introduced above in the relations (3), it is necessary to satisfy the boundary conditions for the tangential components of the electric and magnetic fields. The moduli of the wave vectors are determined by the frequency of the ICMS photons and the permittivities of the plate and the external medium [6, 7]:

$$k_r = k_t = \frac{\omega}{c}\sqrt{\varepsilon_e}, \quad k = k_{2r} = \frac{\omega}{c}\sqrt{\varepsilon_M}, \qquad k_p = \frac{\omega}{c}\frac{1}{\sqrt{\varepsilon_M}}, \tag{4}$$

where ε_M and ε_e are the permittivities on the side of the isotopic boundary containing the Mössbauer isotope (see equation (2)) and on the side of the boundary that does not contain the Mössbauer isotope.

3. BOUNDARY CONDITIONS

As a result of the boundary conditions for the wave vectors, the tangential components of all wave vectors are identical and can be expressed in terms of the angle of incidence of the synchrotron radiation beam as $k_p\cos\varphi_0$ (see Fig. 1).

The boundary conditions for the electric and magnetic fields for waves polarized linearly in a direction orthogonal to the scattering plane lead to the following system of equations for the amplitudes of the waves:

$$\begin{aligned}
&\mathbf{E}_p + \mathbf{E}_f + \mathbf{E}_{2r} = \mathbf{E}_r.\\
&\mathbf{k}_{pz}\mathbf{E}_p + k_z\mathbf{E}_f + \mathbf{k}_{2rz}\mathbf{E}_{2r} = \mathbf{k}_{rz}\mathbf{E}_r,\\
&\mathbf{E}_p\exp(ik_{pz}L) + \mathbf{E}_f\exp(ik_zL)\\
&+ \mathbf{E}_{2r}\exp(ik_{2rz}L) = \mathbf{E}_t\exp(ik_{tz}L).\\
&\mathbf{k}_{pz}\mathbf{E}_p\exp(ik_{pz}L) + \mathbf{k}_z\mathbf{E}_f\exp(ik_zL)\\
&+ \mathbf{k}_{2rz}\mathbf{E}_{2r}\exp(ik_{2rz}L) = \mathbf{k}_{tz}\mathbf{E}_t\exp(ik_{tz}L),
\end{aligned} \tag{5}$$

where the index z marks the wave vector components normal to the isotopic boundary. The system (5) describes the optics of an isotopic boundary and a plate, i.e., a plane-parallel layer containing nuclei of the Mössbauer isotope.

4. ISOTOPIC BOUNDARY

To describe ICMS at an isotopic boundary it is sufficient to use the first pair of equations in the system (5), setting the amplitude $\mathbf{E}_{2r}$ equal to zero. From the boundary conditions for the wave vectors follows an expression for the "reflection" angle for ICMS:

$$\frac{\cos\varphi_0}{\cos\varphi_1} = -\varepsilon_e. \tag{6}$$

Since the difference between the angles of incidence and reflection is small, we can write $\varphi_1 = \varphi_0 + \Delta\varphi_1$ and obtain for $\Delta\varphi_1$

$$\Delta\varphi_1 = -\frac{1-\varepsilon_e}{\varepsilon_e}\cot\varphi_0. \tag{7}$$

Since $\varepsilon_e < 1$, the correction $\Delta\varphi_1$ is negative, i.e., the reflected ICMS ray hugs the isotopic boundary, and $\Delta\varphi_1$ is essentially independent of the ICMS frequency.

The same boundary conditions for the wave vectors give for the angle of refraction φ_2

$$\frac{\cos\varphi_2}{\cos\varphi_0} = \frac{1}{\sqrt{\varepsilon_e\varepsilon_M}}. \tag{8}$$

Setting $\varphi_2 = \varphi_0 + \Delta\varphi_2$, we obtain

$$\Delta\varphi_2 = \left(1 - \frac{1}{\sqrt{\varepsilon_e\varepsilon_M}}\right)\cot\varphi_0. \tag{9}$$

In contrast to the angle of reflection, the correction to the angle of refraction and its sign depend on the ICMS frequency and its difference from the exact value of the Mössbauer resonance frequency, since ε_M depends on the frequency and near the resonance frequency it can be greater or less than 1. For the frequency satisfying the phase matching conditions [6], i.e.,

$$k = k_p. \tag{10}$$

we have $\varphi_2 = \varphi_0$, i.e., the "refracted" ICMS beam propagates strictly in the direction of the primary synchrotron radiation beam.

Just as for X-rays at a vacuum-crystal boundary, for ICMS a "characteristic feature of reflection" appears at an isotopic boundary in the TIR region. However, the manifestation of this feature is completely different from the total internal reflection of X-rays (below). The TIR condition for ICMS is $k_{pt} \geq k$, where k_{pt} is the tangential component of the vector $\mathbf{k}_p$. Hence follows an expression for the critical angle ($\varphi_0 = \varphi_c$) or TIR in transmission

$$\cos\varphi_c = \sqrt{\varepsilon_e\varepsilon_M}. \tag{11}$$

It is evident from equation (11) that because of the frequency dependence of ε_M, the condition for TIR in transmission holds for all ICMS frequencies above the resonant Mössbauer frequency, i.e., for them $\varphi_c > 0$, and the condition may not hold in a frequency range immediately below the resonance frequency, i.e., for the corresponding frequencies $\varphi_c = 0$. In any case, the

critical angle is very small, since from equation (11) follows the expression

$$\varphi_c - \sqrt{2(1-\sqrt{\varepsilon_e\varepsilon_M})}. \tag{12}$$

The ICMS frequencies for which total internal reflection is absent for transmission are determined by the inequality

$$\varepsilon_e\varepsilon_M \geq 1. \tag{13}$$

We note that, strictly speaking, the relations (8), (9), and (11)–(13) contain not ε_M but rather $\mathrm{Re}\varepsilon_M$.

Figure 2 displays the computed spectral dependence of the critical angle φ_c for refraction. The parameters used in the calculations here and below approximately correspond to the case where synchrotron radiation at the isotopic boundary interacts with an iron sample strongly enriched with ^{57}Fe and are presented in Section 9. The figure shows that for ICMS frequency below the resonance value there exists a range of frequencies where the critical angle for transmission is zero, and directly above the resonance frequency there exists approximately the same frequency range where the critical angle for transmission is appreciably greater than the critical angle for reflection. The difference of the corresponding angles reaches of the order of 3 mrad, i.e., it can be easily observed experimentally.

Figure 3 displays the computed spectral dependence of the refraction angle $\Delta\varphi_2$ for ICMS at an isotopic boundary for several grazing angles of synchrotron radiation.

From the first pair of equations of the system (5) we have for the amplitudes E_f and E_r at the isotopic boundary

$$\begin{aligned} E_f &= -E_p\left[\sqrt{1-\left(\frac{\cos\varphi_0}{\varepsilon_e}\right)^2}+\frac{\sin\varphi_0}{\varepsilon_e}\right] \\ &\times\left[\sqrt{1-\left(\frac{\cos\varphi_0}{\varepsilon_e}\right)^2}+\sqrt{\frac{\varepsilon_M}{\varepsilon_e}-\left(\frac{\cos\varphi_0}{\varepsilon_e}\right)^2}\right]^{-1}, \\ E_r &= E_p\left[\sqrt{\frac{\varepsilon_M}{\varepsilon_e}-\left(\frac{\cos\varphi_0}{\varepsilon_e}\right)^2}-\frac{\sin\varphi_0}{\varepsilon_e}\right] \\ &\times\left[\sqrt{1-\left(\frac{\cos\varphi_0}{\varepsilon_e}\right)^2}+\sqrt{\frac{\varepsilon_M}{\varepsilon_e}-\left(\frac{\cos\varphi_0}{\varepsilon_e}\right)^2}\right]^{-1}. \end{aligned} \tag{14}$$

The expressions (14), together with the expression for E_p [6],

$$E_p = \chi^N E_0\left(\frac{\omega}{c}\right)^2\left[k_p^2-(\varepsilon_0+\varepsilon_1)\left(\frac{\omega}{c}\right)^2\right]^{-1}, \tag{15}$$

determine the amplitudes of the ICMS waves reflected from and transmitted through the isotopic boundary.

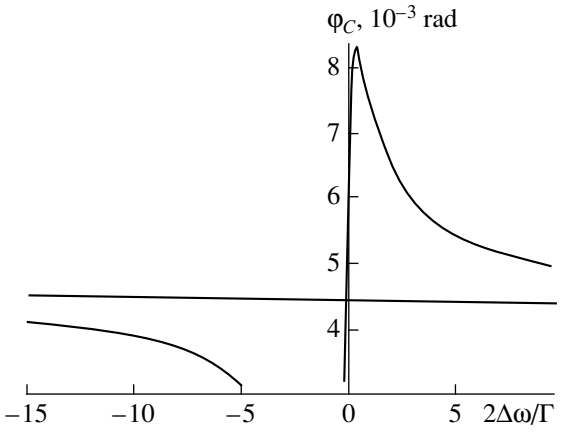

Fig. 2. Computed spectral dependences of the critical angle φ_c for transmission in the case of an isotopic boundary. The horizontal line gives the critical value of the angle φ_s for reflection.

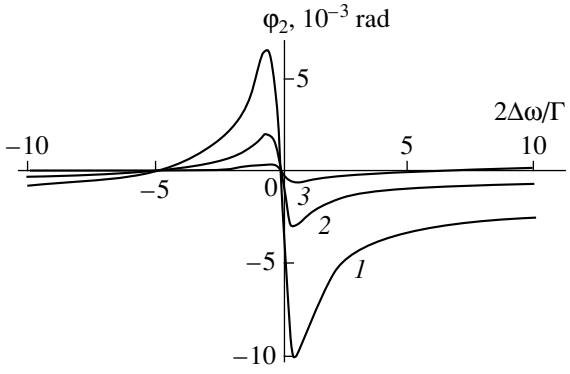

Fig. 3. Computed spectral dependences of the refraction angle $\Delta\varphi_2$ for ICMS at an isotopic boundary for several grazing angles of the synchrotron radiation beam: φ_0 = 0.003 (*1*); 0.01 (*2*); and 0.05 (*3*).

For normal incidence of a synchrotron radiation beam the expressions (14) assume the form

$$\begin{aligned} E_f &= -E_p\frac{1+1/\varepsilon_e}{1+\sqrt{\varepsilon_M/\varepsilon_e}}, \\ E_r &= E_p\frac{\sqrt{\varepsilon_M/\varepsilon_e}-1/\varepsilon_e}{1+\sqrt{\varepsilon_M/\varepsilon_e}}. \end{aligned} \tag{16}$$

Figure 4 shows the spectral dependence of the amplitude of the ICMS wave reflected from the isotopic boundary with normal incidence of the synchrotron radiation beam.

For a fixed frequency of the synchrotron radiation photons, the expressions (14) and (16) give a very low intensity of the reflected ICMS within the energy width of the Mössbauer line. For the ICMS intensity inte-

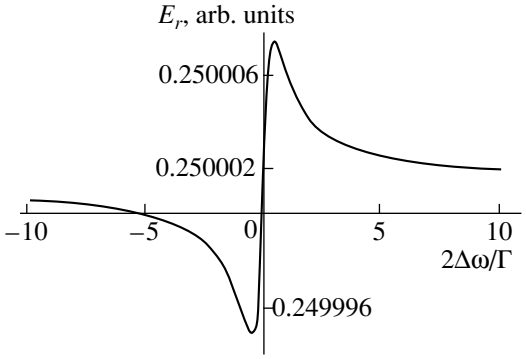

Fig. 4. Computed frequency dependence of the ICMS amplitude for reflection at an isotopic boundary with normal incidence of the beam.

grated over the frequency of the primary synchrotron radiation beam, we obtain from equation (16) the estimate

$$|E_r|^2 \approx \frac{(1-f^2)f^2}{\alpha+1}\frac{|E_0|^2}{16}, \tag{17}$$

where α is the coefficient of internal conversion and $|E_0|^2$ is the spectral density of radiation in the synchrotron radiation beam. This expression shows that the fraction of the resonance component of ICMS reflected at the isotopic boundary is comparable to the intensity of resonance elastic Mössbauer reflection of synchrotron radiation photons [7–9], within the width of the Mössbauer line in the region of the resonance frequency under TIR conditions, i.e., for grazing angles of incidence of the beam. The estimate (17) refers to large angles of incidence (formally for normal incidence of synchrotron radiation on the isotopic boundary), for which the resonance Mössbauer reflection coefficient is very small ($\sim|1-\varepsilon_M|$). For this reason, for large angles of incidence most of the reflected resonance photons are associated with ICMS.

5. INELASTIC COHERENT MÖSSBAUER SCATTERING BY A PLATE

We shall now solve the system (5) for a plate bounded by two isotopic boundaries. For an arbitrary angle of incidence of a synchrotron radiation beam on a plate we obtain

$$\begin{aligned}
E_r &= -E_p\Bigg[\left(\frac{k_{pz}}{k_{tz}}-1\right)(k_{2rz}-k_z)\exp(ik_{pz}L)\\
&\quad+\left(\frac{k_z}{k_{tz}}-1\right)(k_{pz}-k_{2rz})\exp(ik_zL)\\
&\quad+\left(\frac{k_{2rz}}{k_{tz}}-1\right)(k_z-k_{pz})\exp(ik_{2rz}L)\Bigg]\\
&\quad\times\Bigg[(k_{2rz}-k_{rz})\left(\frac{k_z}{k_{tz}}-1\right)\exp(ik_zL)\\
&\quad+(k_{rz}-k_z)\left(\frac{k_{2rz}}{k_{tz}}-1\right)\exp(ik_{2rz}L)\Bigg]^{-1},\\
E_t\exp(ik_{tz}L) &= E_p\Bigg\{\Bigg[\frac{k_z-k_{pz}}{k_{tz}}\exp(ik_zL)\\
&\quad+\frac{(k_{rz}-k_z)(k_{2rz}-k_{pz})}{k_{tz}(k_{2rz}-k_{rz})}\exp(ik_{2rz}L)\Bigg]\\
&\quad\times\exp(ik_{pz}L)-\frac{(k_{rz}-k_z)(k_{2rz}-k_{pz})}{k_{tz}(k_{2rz}-k_{rz})}-\frac{k_z-k_{pz}}{k_{tz}}\Bigg\}\\
&\quad\times\Bigg[\left(\frac{k_z}{k_{tz}}-1\right)\exp(ik_zL)\\
&\quad+\frac{(k_{2rz}-k_{tz})(k_{rz}-k_z)}{k_{tz}(k_{2rz}-k_{rz})}\exp(ik_{2rz}L)\Bigg]^{-1},
\end{aligned} \tag{18}$$

where

$$k_{pz} = \frac{\omega}{c}\frac{\sin\varphi_0}{\sqrt{\varepsilon_e}},\quad k_z = -k_{2rz} = \frac{\omega}{c}\sqrt{\varepsilon_M-\frac{\cos^2\varphi_0}{\varepsilon_e}},$$

$$k_{tz} = -k_{rz} = \frac{\omega}{c}\sqrt{\varepsilon_e-\frac{\cos^2\varphi_0}{\varepsilon_e}}.$$

The equations (18) together with the expression (15) for E_p make it possible to calculate the absolute ICMS intensities for beams reflected and emanating from a plate.

The expressions (18) simplify for normal incidence of synchrotron radiation on a plate:

$$\begin{aligned}
E_r &= E_p\Bigg[\frac{2\sqrt{\varepsilon_M/\varepsilon_e}(1-\varepsilon_e)}{\varepsilon_e(1-\sqrt{\varepsilon_M/\varepsilon_e})}\exp(ik_pL)\\
&\quad+\left(\frac{1}{\varepsilon_e}+\sqrt{\frac{\varepsilon_M}{\varepsilon_e}}\right)\exp(ikL)-\left(\frac{1}{\varepsilon_e}-\sqrt{\frac{\varepsilon_M}{\varepsilon_e}}\right)\\
&\quad\times\frac{1+\sqrt{\varepsilon_M/\varepsilon_e}}{1-\sqrt{\varepsilon_M/\varepsilon_e}}\exp(-ikL)\Bigg]\\
&\quad\times\Bigg[\left(\sqrt{\frac{\varepsilon_M}{\varepsilon_e}}-1\right)\exp(ikL)\\
&\quad-\frac{(1+\sqrt{\varepsilon_M/\varepsilon_e})^2}{\sqrt{\varepsilon_M/\varepsilon_e}-1}\exp(-ikL)\Bigg]^{-1},\\
E_t\exp(ik_tL) &= E_p\Bigg\{\Bigg[\left(\sqrt{\frac{\varepsilon_M}{\varepsilon_e}}-\frac{1}{\varepsilon_e}\right)\exp(ikL)
\end{aligned} \tag{19}$$

$$+\left(\frac{1}{\varepsilon_e}+\sqrt{\frac{\varepsilon_M}{\varepsilon_e}}\right)\frac{1+\sqrt{\varepsilon_M/\varepsilon_e}}{\sqrt{\varepsilon_M/\varepsilon_e}}\exp(-ikL)\Bigg]$$

$$\times\exp(ik_pL)+\left(\frac{1}{\varepsilon_e}+\sqrt{\frac{\varepsilon_M}{\varepsilon_e}}\right)\frac{1+\sqrt{\varepsilon_M/\varepsilon_e}}{\sqrt{\varepsilon_M/\varepsilon_e}-1}$$

$$+\left(\frac{1}{\varepsilon_e}-\sqrt{\frac{\varepsilon_M}{\varepsilon_e}}\right)\Bigg\}\Bigg[\left(\sqrt{\frac{\varepsilon_M}{\varepsilon_e}}-1\right)\exp(ikL)$$

$$-\frac{(1+\sqrt{\varepsilon_M/\varepsilon_e})^2}{\sqrt{\varepsilon_M/\varepsilon_e}-1}\exp(-ikL)\Bigg]^{-1}.$$

It is easy to obtain from the expressions (18) and (19) expressions for ICMS in a plate placed in a vacuum. In this case, however, the synchrotron radiation photons that do not participate in Mössbauer resonance scattering and that produce a nonresonance background, which is not described by equations (18) and (19), also undergo reflection at the boundary of the plate. To suppress this background, time-delayed photon detection is ordinarily used in experiments [4, 5].

As an example, we shall present expressions for the amplitudes of ICMS generated by synchrotron radiation in a plate placed in a vacuum for normal incidence of the beam:

$$E_r = E_p \times\frac{2i(\varepsilon_M-1)\sin kL}{(1-\sqrt{\varepsilon_M})^2\exp(ikL)-(1+\sqrt{\varepsilon_M})^2\exp(-ikL)},$$

$$E_t\exp(ik_tL) = E_p\{4\sqrt{\varepsilon_M}+[(1-\sqrt{\varepsilon_M})^2\exp(ikL) - (1+\sqrt{\varepsilon_M})^2\exp(-ikL)]\exp(ik_pL)\} \times[(1-\sqrt{\varepsilon_M})^2\exp(ikL) - (1+\sqrt{\varepsilon_M})^2\exp(-ikL)]^{-1}. \quad (20)$$

For an arbitrary angle of incidence the expression (18) gives a result for a plate in vacuum if we set $\varepsilon_e \equiv 1$.

The formulas presented above assume that the angle of incidence of the synchrotron radiation beam lies outside the TIR range. ICMS in the TIR range merits a special analysis.

6. INELASTIC COHERENT MÖSSBAUER SCATTERING IN THE RANGE OF TOTAL INTERNAL REFLECTION

We shall now examine the generation of ICMS at an isotopic boundary for extremely small grazing angles of a synchrotron radiation beam, i.e., in the region which for optics ordinarily corresponds to TIR. However, as will be shown below, for ICMS at an isotopic boundary the situation is radically different in this range of angles: ICMS reflection is completely suppressed, so that the corresponding range of angles for ICMS corresponds not to TIR but rather to the complete suppression of reflection.

The condition that the tangential components of the wave vectors match at the isotopic boundary requires

$$k_{pt} = k_p\cos\varphi_0 = k_{rt}, \quad (21)$$

which, because $k_p > k_r$ for small angles φ_0 less than a certain critical angle φ_s, immediately leads to an imaginary value for the normal component of the wave vector $\mathbf{k}_r$, since the normal components of this vector is determined by the expression $\sqrt{k_r^2-k_{pt}^2}$. In turn, this means that the ICMS wave reflected from the isotopic boundary decays for $\varphi_0 < \varphi_s$, i.e., its reflection is absent. Using the expressions for the moduli of these wave vectors, we obtain for the critical angle φ_s for reflection (see Fig. 1)

$$\varphi_s = \sqrt{2(1-\varepsilon_e)} = \sqrt{2}\frac{\omega_p}{\omega}, \quad (22)$$

where ω_p is the plasma frequency.

The characteristic features of an ICMS beam transmitted through an isotopic boundary also appear in the range of complete suppression of reflection.

We call attention to the fact that the critical angle φ_s given by the relation (22) determines the range where there is no ICMS beam reflected from the isotopic boundary and is frequency-independent. The critical angle φ_c for transmission, which is given by the relation (12), determines the angular range where there is not ICMS beam crossing the isotopic boundary, and it is frequency-dependent.

The character of the propagation of an ICMS beam crossing the boundary depends on the offset of its frequency from the exact Mössbauer resonance. For ICMS frequencies above exact resonance, it follows from the condition for the tangential components of the wave vectors that the normal component of the wave vector $\mathbf{k}$ of the ICMS beam crossing the boundary is imaginary for grazing angles φ_0 of the synchrotron radiation beam less than the critical angle φ_s for reflection, i.e., in this range of angles there is no ICMS beam propagating beyond the isotopic boundary. For frequencies below the resonance frequency, in this range of angles of incidence there is a range of frequencies where an ICMS beam propagating beyond the isotopic boundary exists. The lower frequency limit of this range is determined by the condition $k > k_{pt} = k_p\cos\varphi_0$, whence follows the relation

$$\varphi_0^2 > 2(1-\varepsilon_M\varepsilon_e). \quad (23)$$

In the range of grazing angles φ_0 greater than the critical angle φ_s for reflection, where the reflected ICMS

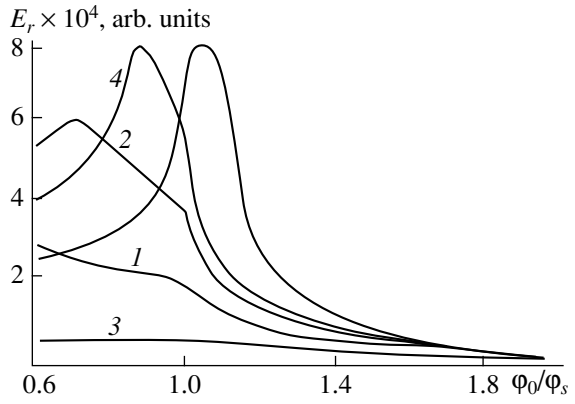

Fig. 5. Computed angular dependences of the amplitude of ICMS reflected from an isotopic boundary for ICSM frequencies $\Delta\omega/\Gamma = -2$ (*1*), -5 (*2*), 0 (*3*), and -10 (*4*).

beam always exists, there may not be an ICMS beam propagating beyond the isotopic boundary in a certain frequency range because of the above-mentioned conditions for the tangential components of the wave vectors for frequency above the resonance value. The upper frequency limit of this range is determined by the relation

$$\varepsilon_M < \frac{1-\varphi_0^2}{\varepsilon_e}. \tag{24}$$

Thus, very unusual characteristics of transmission and reflection of ICMS beams are realized in the range of complete suppression of reflection at the isotopic boundary. Thus, there exist angular ranges of incidence of a synchrotron radiation beam and frequency ranges of ICMS for which there are no ICMS waves propagating on both sides of the isotopic boundary, and there also exist ranges where there is only one propagating ICMS wave—either transmitted or reflected. These properties have a direct bearing on experiments on Mössbauer filtering of synchrotron radiation. However, it should be noted that the suppression of reflection and transmission of ICMS beams through an isotopic boundary, discussed above, can be interpreted in an absolute sense of these concepts only for real permittivities ε_M and ε_e. Since in reality these quantities are complex, the boundaries of the regions where the phenomena discussed appear are "smeared" as a function of the values of the parameters (angles, ICMS frequencies) on which they depend. Figure 5 gives an idea of the behavior of the amplitude of the reflected ICMS wave near the critical angle φ_s for reflection.

7. THICK PLATE

The limiting case of a thick plate enriched with a Mössbauer isotope is of practical interest. Here the term thick is understood to be a sample thickness for which the characteristic Mössbauer solutions are damped in the samples because of strong resonance nuclear absorption, but because electronic absorption is much weaker the intensity of the synchrotron radiation beam does not yet decrease strongly. In this case ICMS beams at the entrance surface of the plate are described by the formulas presented above for an isotopic boundary.

For the exit surface of a plate the ICMS beams are likewise described by simplified formulas. Thus, from the system (5) and equation (18) we have for the amplitude of the ICMS beam transmitted and reflected at the exit surface

$$\begin{aligned} E_t \exp(ik_{tz}L) &= E_p(L)\frac{k_{2rz}-k_{pz}}{k_{2rz}-k_{tz}} \\ &= E_p(L)\left(\sqrt{\varepsilon_M - \frac{\cos^2\varphi_0}{\varepsilon_e}} + \frac{\sin\varphi_0}{\sqrt{\varepsilon_e}}\right) \\ &\times \left(\sqrt{\varepsilon_M - \frac{\cos^2\varphi_0}{\varepsilon_e}} + \sqrt{\varepsilon_e - \frac{\cos^2\varphi_0}{\varepsilon_e}}\right)^{-1}, \\ E_{2r} &= E_p(L)\frac{k_{tz}-k_{pz}}{k_{2rz}-k_{tz}} \\ &= E_p(L)\left(\sqrt{\varepsilon_M - \frac{\cos^2\varphi_0}{\varepsilon_e}} - \frac{\sin\varphi_0}{\sqrt{\varepsilon_e}}\right) \\ &\times \left(\sqrt{\varepsilon_M - \frac{\cos^2\varphi_0}{\varepsilon_e}} + \sqrt{\varepsilon_e - \frac{\cos^2\varphi_0}{\varepsilon_e}}\right)^{-1}. \end{aligned} \tag{25}$$

In the normal-incidence limit these formulas become

$$\begin{aligned} E_t \exp(ik_t L) &= E_p(L)\frac{\sqrt{\varepsilon_M}+1/\sqrt{\varepsilon_e}}{\sqrt{\varepsilon_M}+\sqrt{\varepsilon_e}}, \\ E_{2r} &= E_p(L)\frac{\sqrt{\varepsilon_M}-1/\sqrt{\varepsilon_e}}{\sqrt{\varepsilon_M}+\sqrt{\varepsilon_e}}, \end{aligned} \tag{26}$$

where $E_p(L) = E_p \exp(ik_{pz}L)$ is the amplitude E_p at the exit surface, taking account of the propagation (including damping) of the synchrotron radiation beam in the layer. Figure 6 presented below illustrates the angular dependence of the ICMS amplitude in the transmitted beam in the range of grazing angles of incidence of the synchrotron radiation beam.

8. ABSOLUTE INTENSITY OF ICMS BEAMS

In all formulas presented above the ICMS amplitudes were expressed in terms of the amplitude E_p of the solution of the inhomogeneous Maxwell's equation (1). The absolute value of the intensity of the beams is important in experiments. For this reason, we present below the formulas using the relation (15) between the amplitude E_p and the amplitude of the field E_0 in the

synchrotron radiation beam [6] and thereby relating the intensity of ICMS beams with the spectral density of the beam intensity.

We present first the corresponding expressions for the simplest cases, specifically, for reflection from a thick plate and for transmission of ICMS through a thick plate under normal incidence of a synchrotron radiation beam on it. For a thick plate the expressions (19) simplify:

$$E_r = -E_0\chi^N[(1+\sqrt{\varepsilon_M/\varepsilon_e})(1+\sqrt{\varepsilon_M\varepsilon_e})]^{-1},$$
$$E_t\exp[i(k_t-k_p)L] \qquad (27)$$
$$= E_0\chi^N[(1-\sqrt{\varepsilon_M\varepsilon_e})(1+\sqrt{\varepsilon_M/\varepsilon_e})]^{-1}.$$

It is evident from the expressions (27) that the spectral distribution of the reflected ICMS does not have the character of resonant gamma radiation with parameters close to the spectral distribution of the Mössbauer line, but rather it is strongly broadened compared with Γ (for a thick sample). The spectral range of the reflected ICMS beam is determined by the extinction length l_e due to the electronic absorption mechanism and can be estimated from the relation $kl_e\mathrm{Im}[\varepsilon_M(\Delta\omega)] = 1$. The spectral distribution in the ICMS beam transmitted through the plate has a maximum at the phase matching frequency [6] (the denominator of the expression for E_t contains a factor whose modulus is minimum at the phase-matching frequency). The estimate (17) presented above for the integral intensity of the reflected ICMS beam follows from the expression (27).

Another interesting limiting case, as already mentioned above, is the range of small grazing angles, next to large critical angles φ_s for reflection, where the intensities of the reflected and transmitted ICMS beams reach a maximum [11] (see Figs. 5 and 6). Thus, in this range the amplitude of the ICMS wave transmitted through and reflected from a thick plate is given by the expressions

$$E_t = E_0(L)$$
$$\times\frac{\chi^N\varepsilon_e(\sqrt{\varepsilon_M\varepsilon_e-1+\varphi_0^2/2}+\varphi_0)}{(\sqrt{\varepsilon_M\varepsilon_e-1+\varphi_0^2/2}+\sqrt{\varepsilon_e^2-1+\varphi_0^2/2})(1-\varepsilon_M\varepsilon_e)},$$
$$E_r = E_0(L) \qquad (28)$$
$$\times\frac{\chi^N\varepsilon_e(\sqrt{\varepsilon_M\varepsilon_e-1+\varphi_0^2/2}-\varphi_0)}{(\sqrt{\varepsilon_M\varepsilon_e-1+\varphi_0^2/2}+\sqrt{\varepsilon_e^2-1+\varphi_0^2/2})(1-\varepsilon_M\varepsilon_e)},$$

where the meaning of $E_0(L)$ is the same as in equations (25) and (26).

9. COMPUTATIONAL RESULTS

We shall illustrate the qualitative analysis of the phenomena of the optics of ICMS by an isotopic boundary, performed above, with the results of numerical calculations (Figs. 2–9). As already mentioned above, the parameters used in the calculations approximately correspond to the case of the interaction of synchrotron radiation on an isotopic boundary with an iron sample highly enriched with ^{57}Fe. The corresponding energy of the Mössbauer transition is 14.4 keV. The following values for the parameters were used in the calculations:

$$\mathrm{Re}(1-\varepsilon_e) = 10^{-5}, \quad \mathrm{Im}(1-\varepsilon_e) = 2\times10^{-7},$$
$$\max\mathrm{Re}(\varepsilon_M-1) = 10\mathrm{Re}(1-\varepsilon_e).$$

The values of $\Delta\omega/\Gamma$, where $\Delta\omega$ is the offset of the frequency from the resonance value, Γ is the width of the Mössbauer level, and $t = L(\omega/c)\mathrm{Re}(\Delta\varepsilon_{el})$, where $\Delta\varepsilon_{el}$ is the difference of the permittivity for synchrotron radiation from 1, were taken in the figures as the dimensionless frequency and thickness.

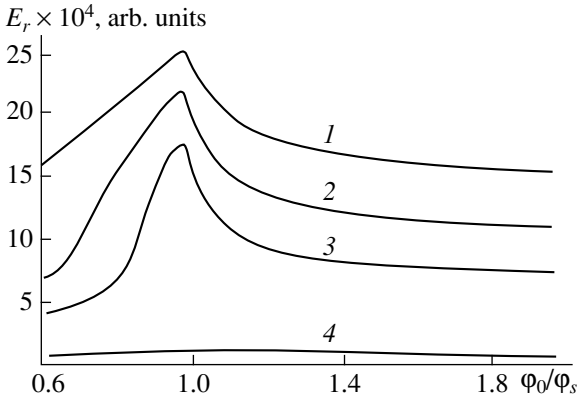

Fig. 6. Computed angular dependences of the amplitude of an ICMS transmitted through a thick plate enriched with a Mössbauer isotope for ICMS frequencies $\Delta\omega/\Gamma = -2$ (*1*), -5 (*2*), -10 (*3*), and 0 (*4*).

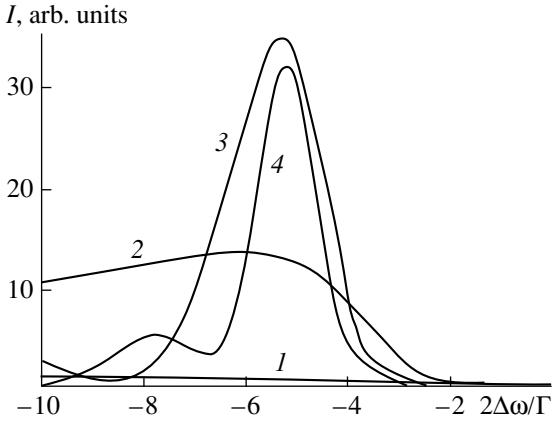

Fig. 7. Spectral distributions of the intensity of the resonant component of ICMS transmitted through a sample as a function of the dimensionless thickness of the layer $t = L(\omega/c)\mathrm{Re}(\Delta\varepsilon_{el})$: $t = 1$ (*1*); 5 (*2*), 15 (*3*), 25 (*4*), for normal incidence of the synchrotron radiation beam.

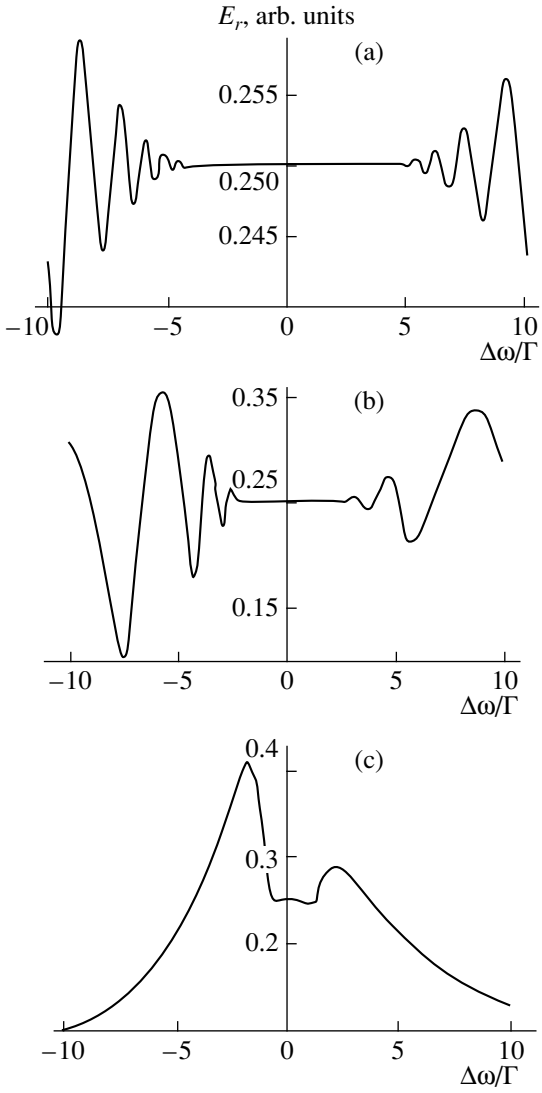

Fig. 8. Computed frequency dependences of the ICMS amplitude for reflection from a plate with finite thickness, enriched with a Mössbauer isotope, for several values of the dimensionless thickness of the plate $t = L(\omega/c)\mathrm{Re}(\Delta\varepsilon_{el})$: t = (a) 100; (b) 25; (c) 1.

The calculations showed that the ICMS line is frequency-broaden compared with Γ and that for a thick sample resonance effects are manifested only as a weak modulation of reflection near the resonance Mössbauer frequency (see Fig. 4).

Figures 5 and 6 show the computed angular dependences of the amplitudes of the transmitted and reflected ICMS waves (for a thick sample) for several values of the ICMS frequency. The curves presented demonstrate that the intensity maxima in the transmitted and reflected ICMS beams are reached for angles of incidence of the synchrotron radiation beam near the critical angle φ_s for reflection (compare with the measurements in [12, 13], which give a sharp scattering maximum for a grazing angle different from zero). The value of the maximum itself depends strongly on the frequency, and the spectral density of the ICMS intensity in the direct beam is higher than in the reflected beam only near the phase-matching frequency (see [11] also).

Figures 7 and 8 display, respectively, the computed frequency dependences of the intensity of the transmitted and the amplitude of the reflected ICMS waves for several values of the thickness. The curves presented demonstrate broadening of the frequency range of the scattered radiation and the concentration of the spectral density of the intensity of the transmitted beam near the phase-matching frequency with an increase in the thickness of the layer.

Figure 9 shows the thickness dependences of the ICMS amplitude for reflection from a plate of finite thickness for several values of the ICMS frequency and normal incidence of the synchrotron radiation beam. These dependences are characterized by very shallow beats (with period λ/2, see Fig. 9a), which are averaged in real experiments, and smooth amplitude variations which decay with thickness.

10. INELASTIC-INELASTIC AND ELASTIC-INELASTIC ICMS COMPONENTS

We shall now briefly discuss the optics of an isotopic boundary for other ICMS components, specifically, the inelastic-inelastic scattering (i.e., with recoil at both stages of scattering) and elastic-inelastic scattering (i.e., with recoil at the photon reemission stage). Although the frequency-integrated ICMS intensity for these components can be comparable to the intensity of the ICMS component examined above, their spectral intensity is much lower than in the initial synchrotron radiation beam. For this reason, their observation, especially in the first beam, is a more difficult problem than for the inelastic-elastic ICMS component already examined.

For the inelastic-inelastic ICMS component, the critical grazing angles for reflection and transmission are the same, they do not depend on the frequency, and they are determined by the relation (22). The synchronization condition (10) [6], which can be presented as $k_p = k$, assumes the form $\varepsilon_e = 1$. Since in reality $\varepsilon_e < 1$, the synchronization condition for this ICMS component cannot be satisfied, and its intensity in the transmitted beam undergoes beats as a function of the sample thickness and does not exceed the value corresponding to a sample thickness equal to the coherence length. This means that this ICMS component is more pronounced in the reflected beam, for which the synchronization condition is not as critical.

In the elastic-inelastic ICMS channel, the group velocity v_g of the synchrotron radiation beam near the Mössbauer resonance frequency is strongly frequency-

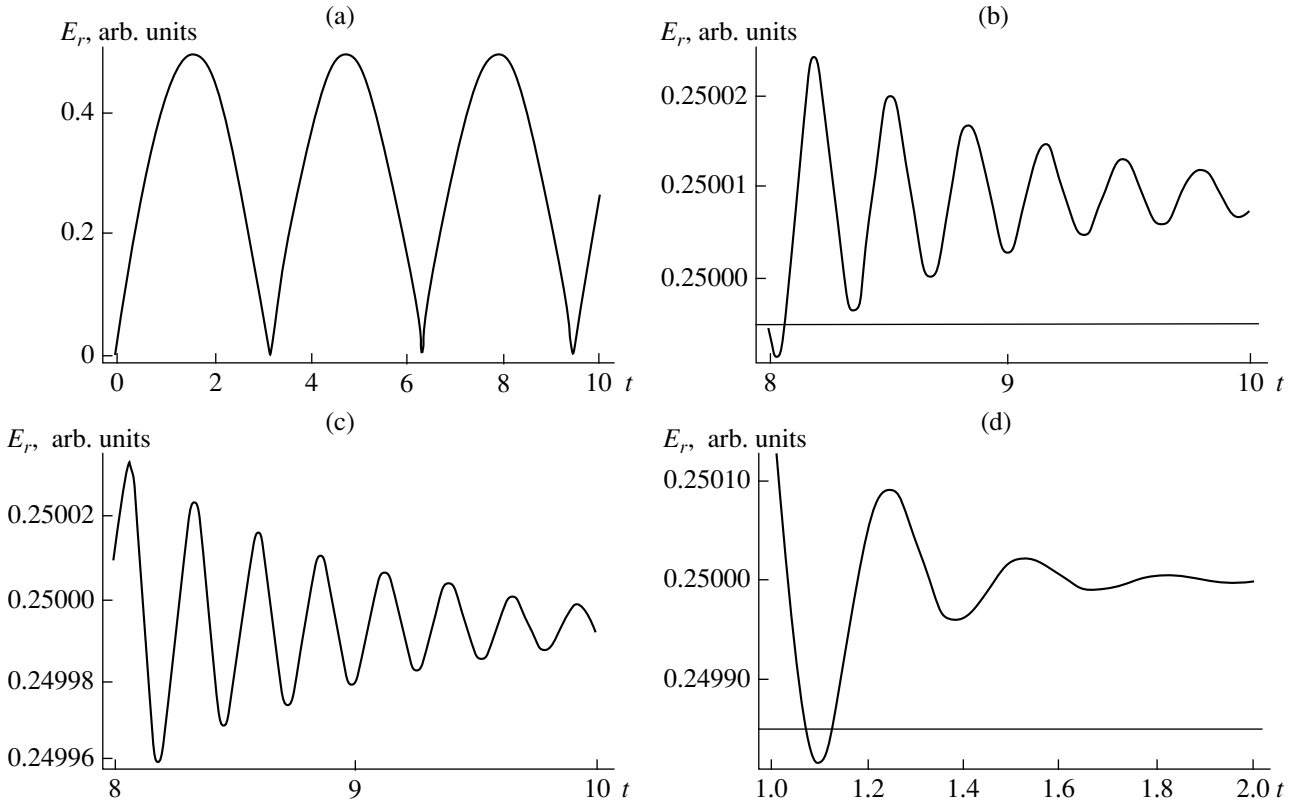

Fig. 9. Computed thickness dependences of the ICMS amplitude for reflection from a plate of finite thickness, enriched with a Mössbauer isotope, for several values of the ICMS frequency: (a) beats near zero thicknesses, the unit of dimensionless thickness t is reduced by a factor of 10^5 compared with its definition; $\Delta\omega/\Gamma$ = (b) 1, (c) –1, (d) 0. The synchrotron radiation beam is incident in a direction along the normal.

dependent and can be found as the product $d\omega/dk$. As a result, we have

$$v_g = \frac{c\sqrt{\varepsilon_M}}{1 + \Delta\varepsilon_M + \omega\varepsilon'/2}, \qquad (29)$$

where $\varepsilon = d\varepsilon/d\omega$, and $\Delta\varepsilon_M$ is the contribution of the nuclear resonance interaction of synchrotron radiation quanta to the permittivity (see equation (2)).

The synchronization condition (10) [6] now becomes

$$\frac{\sqrt{\varepsilon_M}}{1 + \Delta\varepsilon_M + \omega\varepsilon'/2} = \frac{1}{\sqrt{\varepsilon_e}} \qquad (30)$$

and can be satisfied for a definite frequency of the absorbed synchrotron radiation photon. This means that the amplitude of the ICMS component under study increases linearly with sample thickness only for absorption of photons with a definite, synchronous, frequency by the nuclei. As in the preceding case examined above, this means that this ICMS component is suppressed in the transmitted beam and it can be detected more efficiently in the reflected beam.

Using the expression (29), we find that for the elasticinelastic ICMS components the critical angles for reflection and transmission are the same, they depend on the frequency of the absorbed synchrotron radiation photon, and they are determined by the relation

$$\cos\varphi_s = \cos\varphi_c = \frac{\sqrt{\varepsilon_e\varepsilon_M}}{1 + \Delta\varepsilon_M + \omega\varepsilon'/2}. \qquad (31)$$

It should be noted that the investigation of the elasticinelastic ICMS component in the reflected beam is also preferable because the generation of this component in the sample as a result of strong absorption of synchrotron radiation photons with frequencies near the Mössbauer resonance occurs at small thicknesses, determined by the Mössbauer absorption length, and its investigation in the transmitted beam on thick samples is ineffective.

11. CONCLUSIONS

The above analysis of ICMS by an isotopic boundary demonstrates that most of the features found for this optics as compared with conventional, specifically, the difference of the critical angles for transmission and reflection ICMS, can be observed experimentally, since

the corresponding angular and energy ranges of the effects are experimentally resolvable. Moreover, the ICMS maxima found in reflection and transition could be of interest for Mössbauer filtration of synchrotron radiation. However, it is very important that in ICMS in transmission, i.e., forward, the spectral range of ICMS is strongly limited by phase matching requirements, which results in suppression of this scattering channel and a serious limitation of the frequency-integrated forward-scattering intensity. This limitation does not occur for ICMS at a large angle, i.e., in reflection.

We note that for a plate-shaped sample and grazing angles φ_0 for a synchrotron radiation beam less than the critical angle for reflection, i.e., for $\varphi_0 < \varphi_s$, there is no transmitted ICMS beam. However, if the sample has the form of a wedge whose angle φ_s is large compared with the critical angle φ_0 for reflection, then for certain ICMS frequencies (see Fig. 2) there exists an ICMS beam from the sample, right up to a zero grazing angle φ_0 of the synchrotron radiation beam. As noted above, this opens up additional possibilities for Mössbauer filtration of synchrotron radiation in the transmission geometry.

The entire analysis performed above concerned a layer of matter containing a Mössbauer isotope and bounded by an isotopic boundary. However, the phenomenon studied also occurs for a sample placed in a vacuum. The difference arising here is that now there exists a nonresonant reflection of the synchrotron radiation beam at the boundaries for all frequencies represented in the beam. It is a source of the background (which in an experiment can be eliminated by using the time-delay technique [4, 5]). In addition, the form of the expression for the critical angle for ICMS reflection changes (for a plate in vacuum $\cos\varphi_s = \sqrt{\varepsilon_e}$, $\varphi_s = \sqrt{1 - \sqrt{\varepsilon_e}} = \omega_p/\omega$). This angle is now identical to the critical angle for total internal reflection of a synchrotron radiation beam at the boundary of the sample with the vacuum. This latter angle is not related with Mössbauer scattering. We also note that phenomena similar to those studied above also occur in other ICMS components, specifically, in inelastic coherence scattering, where reemission of a photon is accompanied by recoil processes. As noted above, however, the spectral density of the corresponding scattering channels is much lower, and for this reason they were not studied in detail here. On the whole, the results obtained support the view which has formed in the last few years that Mössbauer optics investigations of surface phenomena (see, for example, [13–17]) are an important direction of investigations using synchrotron radiation.

ACKNOWLEDGMENTS

This work was supported by the Russian Foundation for Basic Research (project no. 96-02-18812) and the Russian State Scientific Program “Fundamental metrology” as part of the project “Synchrotron radiation.”

REFERENCES

1. M. Seto, Y. Yoda, S. Kikuta, *et al.*, Phys. Rev. Lett. **74**, 3828 (1995).
2. A. I. Chumakov, A. Q. R. Baron, R. Rüffer, *et al.*, Phys. Rev. Lett. **76**, 4258 (1996); A. I. Chumakov, R. Rüffer, A. Q. R. Baron, *et al.*, Phys. Rev. B **54**, R9596 (1996).
3. B. Fultz, C. C. Ahn, E. E. Alp, *et al.*, Phys. Rev. Lett. **79**, 937 (1997).
4. G. V. Smirnov, Preprint No. IAÉ-5907/9 (Institute of Atomic Energy, Moscow, 1995).
5. A. Chumakov and R. Rüffer, Hyperfine Interact. **113**, 59 (1998).
6. V. A. Belyakov, Pis’ma Zh. Éksp. Teor. Fiz. **67**, 9 (1998) [JETP Lett. **67**, 8 (1998)].
7. V. A. Belyakov, *Diffraction Optics of Complex-Structured Periodic Media* (Nauka, Moscow, 1988; Springer, New York, 1992), Ch. 10, p. 333.
8. M. A. Andreeva and R. N. Kuzmin, *Mössbauer Gramma Optics* (Mosk. Univ., Moscow, 1982); *Mössbauer and X-ray Optics of Surface* (Izd. Obshchenatsional’noĭ Akademii Znaniĭ, Moscow, 1996).
9. *Anomalous Resonance X-Ray Scattering*, Ed. by G. Materlik (Springer, Berlin, 1994).
10. V. A. Belyakov, Zh. Éksp. Teor. Fiz. **108**, 741 (1995) [JETP **81**, 405 (1995)].
11. V. A. Belyakov, Pis’ma Zh. Éksp. Teor. Fiz. **68**, 269 (1998) [JETP Lett. **68**, 287 (1998)].
12. A. Q. R. Baron, J. Arthur, S. L. Ruby, *et al.*, Phys. Rev. B **50**, R10354 (1994).
13. L. Niesen, A. Mugarza, M. F. Rosu, *et al.*, Phys. Rev. B **58**, 8590 (1998).
14. V. A. Belyakov and I. V. Zhadenov, Phys. Lett. A **189**, 248 (1994).
15. V. A. Belyakov and S. V. Semenov, J. Synchrotron Radiat. **5**, 943 (1998).
16. M. A. Andreeva, Pis’ma Zh. Éksp. Teor. Fiz. **68**, 449 (1998) [JETP Lett. **68**, 480 (1998)].
17. V. G. Kon and A. I. Chumakov, Zh. Éksp. Teor. Fiz. **114**, 3 (1998) [JETP **87**, 1 (1998)].

Translation was provided by AIP

Journal of Experimental and Theoretical Physics, Vol. 90, No. 2, 2000, pp. 301–307.
Translated from Zhurnal Éksperimental'noĭ i Teoreticheskoĭ Fiziki, Vol. 117, No. 2, 2000, pp. 342–349.

Phase Transitions and Low-Frequency Dielectric Dispersion in Ferroelectric Langmuir–Blodgett Films of the Copolymer Vinylidene Fluoride with Trifluoroethylene

S. P. Palto[1, *], A. M. Lotonov[2], K. A. Verkhovskaya[1], G. N. Andreev[1], and N. D. Gavrilova[2]

[1]*Institute of Crystallography, Russian Academy of Sciences, Moscow, 117333 Russia*

[2]*Moscow State University, Moscow, 119899 Russia*

**e-mail: lev@glasnet.r*

Received June 9, 1999

Abstract—The dielectric properties of multilayer ferroelectric Langmuir–Blodgett films based on the copolymer vinylidene fluoride with trifluoroethylene with 70/30 composition are investigated. Good agreement with theoretical models on the basis of the phenomenological Landau–Ginzburg approach is demonstrated for the first time for ultrathin films. Expressions describing the temperature variation of the permittivity in the temperature range of hysteresis and giving quantitative agreement with experimental data are obtained. It is shown that the Langmuir–Blodgett films are conducting. This conductivity does not depend on the frequency of the field. The results are explained by the fact that the motion of charge in the films is not bounded by domain walls. The jumps observed in the frequency dispersion at volume and low-temperature (surface) phase transitions are explained by a sharp increase in the relaxation times at the transition into the ferroelectric state. *© 2000 MAIK "Nauka/Interperiodica".*

1. INTRODUCTION

The question of two-dimensional ferroelectricity in films of the copolymer vinylidene fluoride with trifluoroethylene (PVDF/TrFE), prepared by the Langmuir-Blodgett (LB) method, is now being widely discussed [1]. There are several reasons for the interest in these systems. In the first place, the question of proper two-dimensional ferroelectricity is now being discussed for the first time [2]. Thus far, the ferroelectric properties in several monomolecular layers have been investigated in detail only in free-standing films of smectic liquid crystals [3]. In the latter case, ferroelectricity is due to the smectic chiral C^* phase and therefore it is not proper ferroelectricity, but rather it arises as a result of the inclination of the chiral molecules in individual smectic layers. For PVDF/TrFE the order parameter of the ferroelectric phase transition is the electric polarization [4]. Its contribution to the free energy is decisive for the appearance of a ferroelectric state. It is obvious that the contribution of spontaneous polarization to the free energy can change strongly when one of the spatial directions is eliminated (transition to a two-dimensional monomolecular layer). As a result of this circumstance, there arose the question of whether or not proper ferroelectricity can actually exist in two-dimensional systems. The preparation of ferroelectric LB films and their first investigations made it possible to answer the latter question affirmatively [2]. The experimental results prove the existence of a ferroelectric state right up to thicknesses of tens of angstroms. In the second place, a surface phase transition is observed in PVDF/TrFE (70/30) LB films. In contrast to the volume phase transition observed at $T \simeq 115$°C, this transition occurs at room temperature near 20°C. Its most interesting features, which have been studied by direct and inverse photoemission, are that it is accompanied by pronounced changes in the crystal and electronic structure of the films, specifically, a change of "metallicity" and uniaxial doubling of the surface Brillouin zone are observed [5–7]. Finally, the possibility of practical applications of ultrathin ferroelectric films in electronic devices is significant in itself. On account of the small thickness of the films, the switching voltages can be lowered by a factor of 100 (from hundreds and thousands of volts, characteristic for bulk samples, to several volts).

Despite intense investigations of the properties of ferroelectric LB films by the most diverse methods, including IR- range Fourier spectroscopy [8], a quantitative analysis of the data according to their dielectric properties has still not been published. The present paper is the first attempt in this direction. We shall investigate phase transitions and the low-frequency dielectric properties of LB films with a thickness of 20 and 30 monolayers (100–150 Å). It is demonstrated quantitatively for the first time that Landau's phenomenological approach for describing phase transitions is applicable for such thin films.

1063-7761/00/9002-0301$20.00

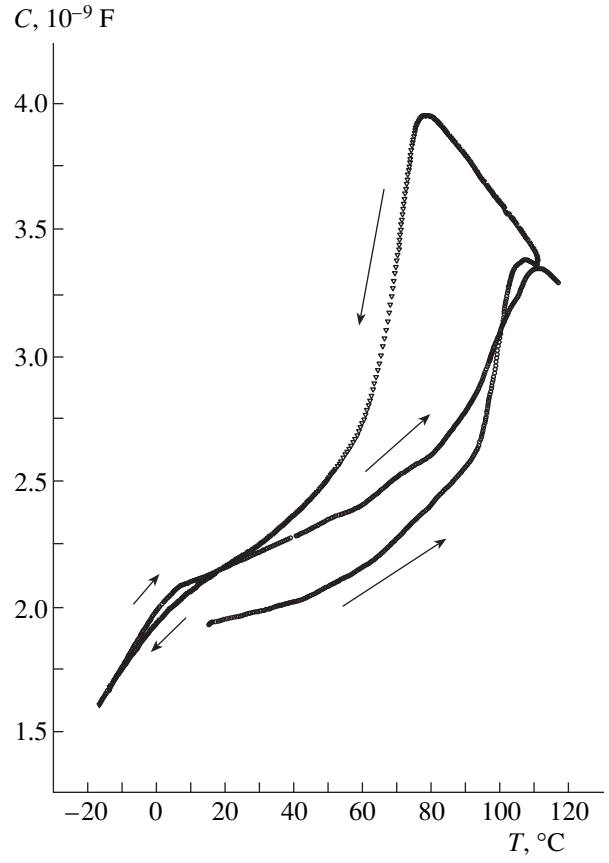

Fig. 1. Temperature dependences of the capacitance on heating and subsequent cooling of the sample of a PVDF/TrFE LB film with 70/30 composition. The dependences were measured at 1000 Hz. The film thickness is 100 Å (20 monolayers). The coverage of the electrodes is $S = 1 \pm 0.03$ mm^2. The arrows indicate the direction of temperature variation. The lower curve corresponds to the onset of the temperature cycle.

2. EXPERIMENTAL PROCEDURE

The PVDF/TrFE films investigated, which consisted of 20 and 30 monolayers, were obtained by the LB method by successively transferring monomolecular layers from the surface of water to the surface of a hard substrate. We employed glass substrates with a 300–500 Å thick previously deposited aluminum electrode. The monomolecular layers were transferred from the water surface at room temperature (20–22°C) and surface pressure 3 mN/m. At room temperature this pressure corresponds to a 5 Å thick close-packed monolayer, where the probability of local collapse (formation of a 10 Å thick bimolecular layer on individual locations on the surface of the water) is small. In the present work, instead of the horizontal lift method, which was used in [1], where the substrate surface is parallel to the water surface when the monolayer is transferred, we employed the classical LB method. Transfer occurred when the substrate was pulled out of the water (*Z*-type transfer), so that the normal to the substrate surface was oriented approximately parallel to the water surface [9]. A second aluminum electrode was deposited on the polymer film. Depending on the series of samples, the total area covering the electrodes ranged from 0.01 to 0.023 cm^2. The thickness of the polymer films calculated on the basis of the number of transfers and the thickness of the monomolecular layer was 100 and 150 Å for 20 and 30 monomolecular layers, respectively.

The measurements of the dielectric properties were performed using standard methods, implemented at Moscow State University (MSU) and at the Institute of Crystallography (IC RAN). At MSU the sample was placed in a thermostat, and the temperature and frequency dependences of the capacitance and the tangent of the dielectric loss angle were measured using an ac R-551 bridge. A measuring voltage not exceeding 0.1 V was applied to the sample. A static method for varying the temperature is used in the apparatus. The temperature was stabilized to within ≈0.005°. The sample could be held at a stable temperature for 30 min. The measurements of the real and imaginary parts of the permittivity were performed in the frequency range 100–20000 Hz and temperature range –25…+120°C, including both the volume and surface phase transitions. A similar method, based on the computer system PhysLab 4.5, making it possible to record temperature dependences in an automatic mode, was used at the IC RAN. Temperature scanning at the rate 0.05°C/s from –25°C up to +120°C was achieved by using Peltier elements.

3. MEASUREMENT RESULTS AND DISCUSSION

We were not able to observe a clear difference between the dielectric spectra of the samples containing 20 and 30 monolayers. For this reason, in discussing the results we omit a comparative analysis of the thickness dependences of the experimental LB films.

3.1. Characteristic Features in the Temperature Variation of the Real Part of the Complex Permittivity (Phase Transitions)

Figure 1 shows the temperature dependence of the capacitance. This dependence is characteristic for ferroelectric LB films based on PVDF/TrFE with 70/30 composition [1, 2]. On account of the small thickness of the LB films, the standard procedure cannot be used to determine the values of the real part ε' of the permittivity using the dependence obtained. Indeed, if direct calculations of the permittivity are made at temperature $T = 20$°C, starting from the values of the film thickness and capacitance of the sample, then the value ε' = 2.5 is obtained. This value is approximately five times smaller than the value measured for bulk PVDF/TrFE samples [10]. Moreover, the value obtained is approximately 1.5 times smaller than the instantaneous value ε'(∞), which, according to the data of [10], is 3–4. The reason for the discrepancy should be sought, first and

foremost, in the influence of the aluminum oxide film. This influence cannot be neglected, especially for ultrathin LB polymer films. In the general case, any ultrathin nonferroelectric film at the interface between the ferroelectric and the electrode can act as a parasitic capacitance. An additional contribution to the parasitic capacitance can also be due to the presence of a noncrystalline (amorphous) phase in the volume of the film as well as the near-electrode regions, where the spontaneous polarization is screened by charges injected from the electrodes. Thus, the values of the capacitance C measured in the experiment must be referred to two serially connected capacitances C_1 and C_2, referring, respectively, to the ferroelectric LB film and another parasitic capacitance. Despite the fact that the value of the parasitic capacitance C_2 cannot be measured, there still exists a correct method for taking account of the capacitance C_2. Let us consider the proposed procedure in greater detail. We are interested in the dependence $C_1(T)$, for which in the model where the capacitances are connected in series it is easy to obtain the relation

$$C_1(T) = \left[\frac{1}{C(T)} - \left(\frac{1}{C(T_x)} - \frac{1}{C_1(T_x)}\right)\right]^{-1}, \qquad (1)$$

where $C(T_x)$ and $C_1(T_x)$ are the capacitances of the sample and the polymer film at fixed temperature. In equation (1) we neglect the temperature dependence of the parasitic capacitance, using its value at a fixed temperature T_x. In our case this is justified, since, for example, for oxide films the temperature variations of the dielectric constants are small compared with the corresponding temperature variations in the ferroelectrics. In terms of the permittivity, the relation (1) can be written in the form

$$\varepsilon'(T) = \left[\frac{1}{\varepsilon'(T_x)} - \gamma(T, T_x)\right]^{-1}, \qquad (2)$$

where

$$\gamma(T, T_x) = \frac{\varepsilon_0 S}{d}\left[\frac{1}{C(T_x)} - \frac{1}{C(T)}\right], \qquad (3)$$

ε_0, S, and d are the permittivity of free space, the area of the intersection of the electrodes, and the thickness of the LB polymer film, respectively. We underscore that only measurable quantities appear in equation (3). Thus, to reconstruct the dependence $\varepsilon'(T)$ from equation (2) it is necessary to know the permittivity at only one point: $\varepsilon'(T_x)$. It is significant that in the procedure of finding of this point $\gamma(T)$ is in general a sign-alternating function, while $\varepsilon'(T)$ should be positive and not less than $\varepsilon(\infty) \approx 3$. Keeping the latter in mind, we obtain from equation (2) the condition for the admissible interval for $\varepsilon'(T_x)$:

$$\gamma_{\max} \leq \frac{1}{\varepsilon'(T_x)} \leq \frac{1}{\varepsilon(\infty)} \approx 0.3, \qquad (4)$$

where $\gamma_{\max}$ corresponds to the maximum value of γ in the entire temperature range.

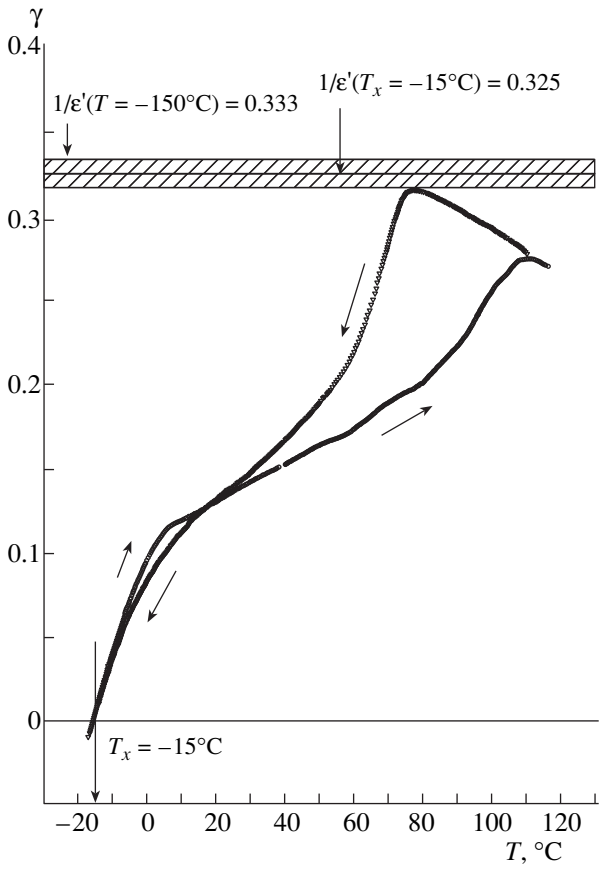

Fig. 2. Temperature dependences of the parameter γ (see text) on heating and subsequent cooling of the sample of a PVDF/TrFE LB film with 70/30 composition. The dependences were measured at 1000 Hz. The film thickness is 100 Å (20 monolayers). The arrows indicate the direction of temperature variation. The hatched region corresponds to the admissible range of values of $1/\varepsilon(T_x)$ (see text).

Since the measured capacitance decreases with temperature, as the temperature T_x decreases, the value of $\gamma_{\max}$ increases, and the admissible range (4) for $1/\varepsilon'(T_x)$ decreases. The upper limit of the admissible range can be determined more accurately by using data from low-temperature measurements performed for the copolymer PVDF/TrFE in [10]. According to [10], at $T = -150$°C and frequency 1000 Hz $\varepsilon' = 3.0$. Figure 2 shows the experimental temperature dependence $\gamma(T)$ for $T_x = -15$°C. The hatched horizontal region corresponds to the admissible values $1/\varepsilon'(T_x = -15°C) = 0.316–0.333$. Using the relation (4) and an approximately three-percent error in the absolute measurements of the coverage of the electrodes in the samples, we arrive at the conclusion that, to within the error limits, any value from the indicated range is correct. For definiteness, we choose the average value $1/\varepsilon'(T_x) = 0.325$, which is used for calculating the dependence $\varepsilon'(T)$ using equation (2).

The reconstructed temperature dependence $\varepsilon'(T)$ is displayed in Fig. 3. The data on the ordinate are presented on a logarithmic scale. The high-temperature

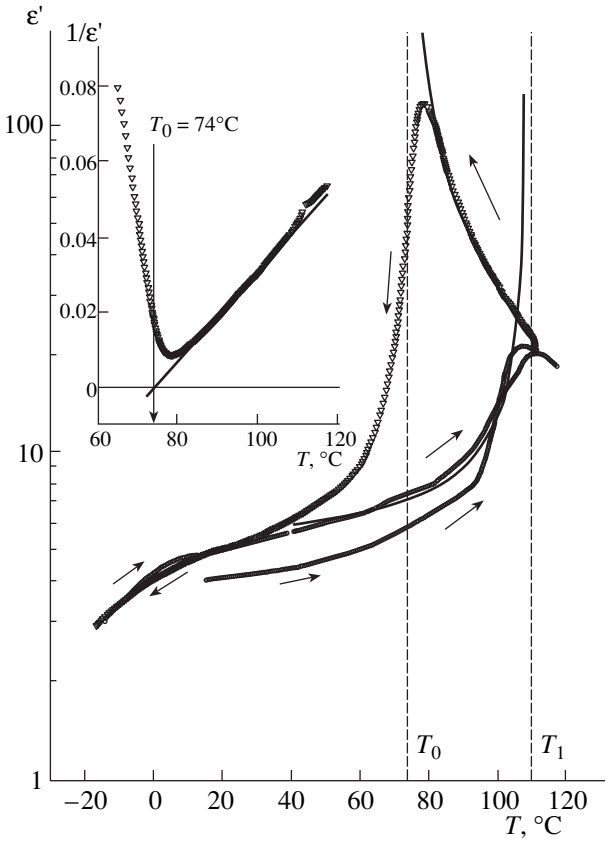

Fig. 3. Temperature dependences of the permittivity on heating and subsequent cooling of a PVDF/TrFE LB film with 70/30 composition. The dependences were measured at 1000 Hz. The film thickness is 100 Å (20 monolayers). The solid lines in the region of hysteresis (T_0 = 77.1°C, T_c = 112°C) of the high-temperature phase transition correspond to the theoretical curves. The arrows indicate the direction of temperature variation. Inset: data on the temperature dependence of the reciprocal of the permittivity on cooling from the paraelectric phase.

phase transition is very pronounced. On cooling, the permittivity grows rapidly, reaching values greater than 100, which exceeds the values ~80, observed by Furukawa [10] for bulk PVDF/TrFE samples. It should be noted that the maximum value at temperature 77°C depends on our choice of the value of $1/\varepsilon'(T_x)$ in the admissible range 0.316–0.333. In choosing $1/\varepsilon'(T_x) = \gamma_{max} = 0.316$, according to Eq. (2), we naturally obtain infinity, which would correspond to the fact that the measured capacitance at T = 77°C is exclusively the parasitic capacitance. It is important to note that, even though the arbitrariness in the choice of the value of $1/\varepsilon'(T_x)$ strongly influences the maximum value of ε' at 77°C, this influence on the fundamental characteristics of a transition, such as the Curie temperature and the Curie–Weiss constant, is weak and results in an additional error of only several percent.

Just as in bulk samples, hysteresis corresponding to a first-order phase transition is observed [4, 11]. The fact that the high-temperature phase transition is sharply pronounced makes it desirable to compare the behavior of the real part of the low-frequency permittivity to the prediction of the Landau–Ginzburg theory, which has been developed quite well for ferroelectrics [11].

Near the point of the phase transition the free-energy density F of the polymer film in an electric field E can be represented in the form of an expansion in powers of a small order parameter, which for proper ferroelectrics is the macroscopic polarization P,

$$F = \frac{1}{2}A_0(T - T_0)P^2 + \frac{1}{4}BP^4 + \frac{1}{6}CP^6 - EP, \qquad (5)$$

where A_0, B, and C are temperature-independent Landau coefficients, and T_0 is the Curie temperature. For a first-order phase transition $A > 0$, $B < 0$, and $C > 0$.

Minimizing the free energy (5), it is easy to find the equation of state in an electric field:

$$E = P[A_0(T - T_0) + BP^2 + CP^4]. \qquad (6)$$

For $E = 0$ the solutions of equation (6) that correspond to minima of the free energy determine the values of the spontaneous polarization P_s. Together with the trivial solution $P_s = 0$, equation (6) possesses nonzero solutions determined by the relation

$$P_s^2 = -\frac{B}{2C} + \sqrt{\frac{B^2}{4C^2} + -\frac{A_0}{C}(T - T_0)}. \qquad (7)$$

Since for a first-order phase transition $B < 0$ and $C > 0$, even for $T > T_0$ there exists, besides the trivial solution $P_s = 0$, a nonzero solution P_s (7). The solution $P_s = 0$ becomes unique and determines a unique minimum of the free energy only at temperatures above T_1 such that

$$T_1 = \frac{B^2}{4A_0C} + T_0. \qquad (8)$$

Thus, paraelectric ($P_s = 0$) and ferroelectric phases can coexist in the temperature interval $\{T_0, T_1\}$. A characteristic feature of the ferroelectric polymer PVDF/TrPE is that the range of temperature hysteresis is extremely wide ($\Delta T = T_1 - T_0 = 35$°C); see Fig. 3. Thus, we can infer that the formation of a new phase (paraelectric on heating and ferroelectric on cooling) is a slow process on a large fraction of the temperature range ΔT, with the exception of a small neighborhood $T_1 - \delta T$ ($\delta T > 0$, $\delta T \ll \Delta T$) on heating and $T_0 + \delta T$ on cooling. In the ideal case of "fast" variation of the temperature, when the formation of a new phase can be completely neglected, we have the following temperature behavior of the spontaneous polarization:

(i) on heating:

$$T \le T_1, \quad P_s^2 = \sqrt{\frac{A_0\Delta T}{C}}\left(1 + \sqrt{1 - \frac{T - T_0}{\Delta T}}\right), \qquad (9)$$
$$T > T_1, \quad P_s = 0;$$

(ii) on cooling:

$$T > T_0, \quad P_s = 0,$$
$$T \le T_0, \quad P_s^2 = \sqrt{\frac{A_0 \Delta T}{C}}\left(1 + \sqrt{1 - \frac{T - T_0}{\Delta T}}\right). \tag{10}$$

Differentiating the equation of state (6), using equations (9) and (10), it is easy to obtain the corresponding behavior of the permittivity:

on heating:

$$T \le T_1,$$
$$\varepsilon(T) = \varepsilon_b + \left\{4\varepsilon_0 A_0\left[\Delta T\left(1 + \sqrt{1 - \frac{T - T_0}{\Delta T}}\right) - (T - T_0)\right]\right\}^{-1}, \tag{11}$$

on cooling:

$$T \ge T_0, \quad \varepsilon(T) = \varepsilon_b + \frac{1}{\varepsilon_0 A_0 (T - T_0)}, \tag{12}$$

where ε_b is the temperature-independent background contribution far from a phase transition.

The experimental temperature dependence of the reciprocal of the permittivity on cooling from the paraelectric phase is shown in the inset in Fig. 3. As one can see, at $T > 80$°C there is a linear dependence corresponding to the expression (12) and reflecting satisfaction of the Curie–Weiss law with $A_0 = 1.4 \times 10^8$ J m C^{-2} K^{-1}, $T_0 = 74$°C. The same theoretical curve is superposed on the experimental points in the main figure. The experimental curve deviates from the theoretical curve near T_0, in a comparatively narrow temperature range ($\delta T = 6$°C), where the coexistence of two phases cannot be neglected, and the value of the permittivity is always finite. The data obtained in the temperature hysteresis range on heating from the ferroelectric phase likewise are described well by the dependence (11) (the lower solid curve in Fig. 3), where we used the value of A_0 found above and $T_1 \simeq 108$°C, corresponding to the maximum value of ε in the experiment. We note that no adjustable parameters are required, with the exception of $\varepsilon_b \simeq 4.3$, which corresponds to the experimental value of ε far from a phase transition at $T \simeq 6$°C. Just as in the case of cooling, substantial discrepancies from the theory occur only near the temperature T_1. Thus, in most of the temperature range ΔT there is very good quantitative agreement with the Landau–Ginzburg phenomenological model. Using the value of the spontaneous polarization $P_s \simeq 0.08$ C m^{-2}, measured at the temperature $T = 20$°C [12], it is easy to determine from equations (9) and (8) the remaining coefficients $C \simeq 7.9 \times 10^{14}$ J C^{-6} m^9, $B \simeq -3.9 \times 10^{12}$ J C^{-4} m^5, and from equation (5), setting $F = 0$, we obtain the transition temperature $T^* \simeq 107$°C.

A characteristic feature in the temperature dependence ε' is also observed in the temperature range 0–30°C. It should be noted that a similar feature but less pronounced was observed in [10] and in bulk PVDF/TrFE samples. It was attributed to microbrownian motions of noncrystalline polymer segments. Detailed investigations of LB films by electron spectroscopy show that a surface phase transition, characterized by doubling of the Brillouin zone, and changes in the electronic structure of crystalline LB films occur in this temperature range [6]. The fact that in this temperature range the permittivity does not undergo the sharp increase observed in the high-temperature range can be explained by the surface nature of this phase transition. Indeed, since this transition refers primarily to the boundary monolayers (an appreciable contribution from surface microcavities, which can exist in the bulk, should be expected only for thick films), the possible rapid growth of the permittivity in these surface layers is strongly masked by a stable volume contribution (once again arguments about the parasitic capacitance, to which the volume of the LB film itself will now contribute, can be used). The fact that this transition is accompanied by structural changes (for example, doubling of the Brillouin zone) casts doubt on the applicability of the phenomenological description in which the polarization is the only order parameter. We hope that a further detailed study of the surface transition will elucidate this problem.

According to our data, for LB films the values of ε' even at room temperature are close to $\varepsilon(\infty)$. An estimate of $\varepsilon(\infty)$ from our data, taking account of the low-temperature region, gives a value somewhat less than that obtained for bulk samples in [10] $\varepsilon = 3$. Thus, LB films possess a more pronounced crystallinity than bulk films obtained by conventional methods, for example, using a centrifuge.

3.2. Frequency Dispersion

LB films cannot be treated as ideal dielectrics. According to [5–7], an increase in the density of states near the Fermi level and a corresponding increase in conductivity are observed at a surface phase transition. For conducting materials, the frequency dependence of the complex permittivity

$$\varepsilon^*(\omega) = \varepsilon'(\omega) - i\varepsilon''(\omega) \tag{13}$$

contains a contribution associated with the conductivity, which likewise is a complex quantity:

$$\sigma^*(\omega) = \sigma'(\omega) + i\sigma''(\omega). \tag{14}$$

In turn, it follows from the Kramers–Kronig relations that the real and imaginary parts of the complex conductivity are related with the permittivity by the relations [13]

$$\varepsilon''(\omega) = \frac{\sigma'(\omega)}{\varepsilon_0 \omega} \equiv \varepsilon_d + \frac{\sigma_0}{\varepsilon_0 \omega}, \tag{15}$$

$$\varepsilon'(\omega) = \frac{\sigma''(\omega)}{\varepsilon_0 \omega} + \varepsilon(\infty). \tag{16}$$

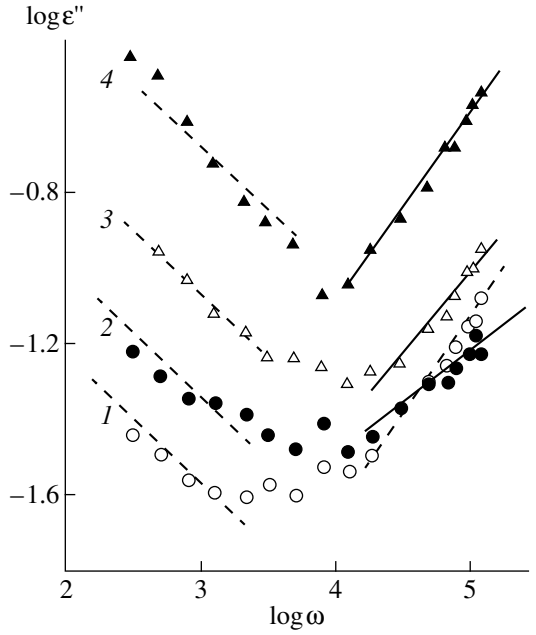

Fig. 4. Frequency dependences of the imaginary part ε" of the complex permittivity of a sample of a PVDF/TrFE LB film with 70/30 composition on heating: (*1*) 23.2°C, (*2*) 45.9°C, (*3*) 72.4°C, (*4*) 102.5°C. The film thickness is 150 Å (30 monolayers). The values of ε" correspond to the sample as a whole, including the parasitic capacitance (see text).

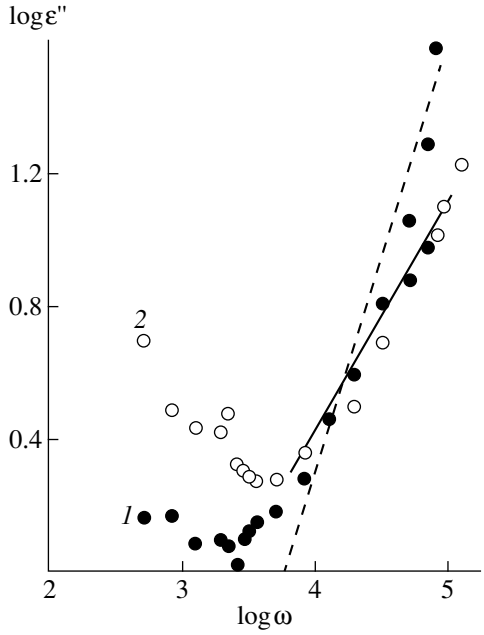

Fig. 5. Frequency dependences of the imaginary part ε" of the complex permittivity of a PVDF/TrFE LB film with 70/30 composition on cooling from the paraelectric phase after heating the sample above 120°C at temperatures 82.8 (*1*) and 109.8°C (*2*). The film thickness is 150 Å (30 monolayers). The values of ε" correspond to the sample as a whole, including the parasitic capacitance (see text).

The right-hand side in Eq. (15) is represented in the form of two contributions referring to the dipole relaxation and the conductivity σ_0 at zero frequency (dc current). This separation makes it possible to understand easily the experimental dependences ε"(ω) presented in Fig. 4 for various temperatures below the temperature T_1 of the volume phase transition. The contribution of the dc conductivity predominates at the lowest frequencies (up to 10 kHz). Indeed, the dependences presented on a logarithmic scale in Fig. 4 in the lowest frequency range are close to straight lines with slope −45°, which corresponds to the second term in the relation (15) (for $T = 23.2$°C, $\sigma_0 \approx 8 \times 10^{-8}\ \Omega^{-1}\ \mathrm{m}^{-1}$). The latter indicates a weak frequency dependence of the real part of the complex conductivity at low frequencies, where the contribution of the dipole relaxation is small. This result is not trivial. The typical situation for conducting polymer materials is that the real part of the conductivity increases strongly with increasing frequency of the field. For example, for the hopping mechanism of conductivity, the models and experimental results give quadratic growth of the real part of the conductivity at the lowest frequencies [13], which corresponds to linear growth of ε" with increasing frequency. The increase in the real part of the conductivity with increasing frequency is explained, for example, in [13] qualitatively as follows. In disordered polymer systems, where the hopping mechanism predominates, the conductivity should increase, since as the frequency of the field increases, a contribution arises from charge carriers moving in increasingly smaller regions (conducting clusters). In our case, on the whole, the frequency dependence of ε" up to 10 kHz has the opposite sign and corresponds to a constant conductivity. This attests to a high degree of crystallinity of the LB films consisting of quite large ordered clusters. In other words, over a period of variation of the electric field the motion of charges inside a cluster is not limited by its "walls." The negligible spikes in the frequency dependence near 2 and 10 kHz, which are especially pronounced with decreasing temperature, can indeed be attributed to smaller clusters.

We shall now discuss the dependences at frequencies above 10 kHz (Fig. 4). Here the contribution that should be attributed to the dipolar relaxation of a ferroelectric polymer predominates [10]. In our case, we note the sharpness of the low-temperature phase transition. As the temperature decreases from 100 to 45°C (curves *2–4*), the frequency dispersion (slope of the curves) decreases, while at 23.2°C a jump in the opposite direction occurs. Similar behavior is also observed near the high-temperature phase transition (Fig. 5). The curve *2* in Fig. 5 corresponds to the paraelectric state ($T = 110$°C, after heating up to 120°C), and the curve *1* corresponds to the onset of the transition into the ferroelectric state. Just as in the case of the surface phase transition, it is easy to see that the frequency dispersion increases near the volume phase transition on cooling from the paraelectric phase. Thus, an analogy is observed

between surface and volume phase transitions. On the hole, the jump in the frequency dispersion can be explained by a shift of the maximum of the curve $\varepsilon''(\omega)$ to lower frequencies at a transition into the ferroelectric state. This corresponds to an increase of the relaxation times (according [10], the maximum shifts from tens of megahertz to hundreds of kilohertz at a transition into the ferroelectric state). More detailed investigations require the use of a high-frequency measurement technique and are a subject of a separate work.

4. CONCLUSIONS

Our investigations of the dielectric properties of multilayer ferroelectric LB films demonstrate for the first time good agreement with theoretical models based on the Landau–Ginzburg phenomenological approach. We obtained expressions describing the temperature variation of the permittivity near hysteresis, and we found quantitative agreement with experiment. We have also confirmed the presence of conductivity in LB films. The frequency dispersion data show that this conductivity does not depend on the frequency of the field. This result is explained by the fact that the motion of charge in LB films is not bounded by the walls of crystalline domains. We observed a jump in the frequency dispersion both at volume and low-temperature (surface) phase transitions. This jump is explained by a sharp increase in the relaxation times accompanying a transition into the ferroelectric state.

ACKNOWLEDGMENTS

We are deeply grateful to N.N. Petukhova and S.G. Yudin for technical assistance in preparing the Langmuir-Blodgett films and to L.M. Blinov for extremely helpful suggestions in the course of a discussion of this work. We are also grateful to S. Ducharme, V.M. Fridkin, and A.V. Sorokin for helpful critical remarks. The group at the Institute of Crystallography is supported by the Russian Foundation for Basic Research (project no. 99-02-16484).

REFERENCES

1. S. Palto, L. Blinov, A. Bune, *et al.*, Ferroelectr. Lett. Sect. **19**, 65 (1995).
2. A. V. Bune, V. M. Fridkin, S. Ducharme, *et al.*, Nature **391**, 874 (1998).
3. E. I. Demikhov, S. Pikin, and E. S. Pikina, Phys. Rev. E **52**, 6250 (1995).
4. T. Furukawa, Phase Transit. **18**, 143 (1989).
5. J. Choi, P. Dowben, S. Pebley, *et al.*, Phys. Rev. Lett. **80**, 1328 (1998).
6. J. Choi, P. A. Dowben, A. V. Bune, *et al.*, Phys. Lett. A **249**, 505 (1999).
7. J. Choi, P. A. Dowben, C. N. Borca, *et al.*, Phys. Rev. B **59**, 1819 (1999).
8. V. V. Kochervinskiĭ, B. V. Lokshin, S. P. Palto, *et al.*, Vysokomol. Soedin., Ser. A **41**, 1290 (1999) [Pol. Sci., Ser. A **41**, 832 (1999)].
9. S. G. Yudin, S. P. Palto, V. A. Khavrichev, *et al.*, Thin Solid Films **210–211**, 46 (1992).
10. T. Furukawa and G. E. Johnson, J. Appl. Phys. **52**, 940 (1981).
11. G. A. Smolenskiĭ, V. A. Bokov, V. A. Isupov, N. N. Krainik, R. E. Pasynkov, A. I. Sokolov, and N. K. Yushin, *The Physics of Ferroelectric Phenomena* (Nauka, Leningrad, 1985).
12. S. Palto, L. Blinov, E. Dubovik, *et al.*, Europhys. Lett. **34**, 465 (1996).
13. S. Capaccioli, M. Lucchesi, P. A. Rolla, and G. Ruggeri, J. Phys.: Condens. Matter **10**, 5595 (1998).

Translation was provided by AIP

Journal of Experimental and Theoretical Physics, Vol. 90, No. 2, 2000, pp. 308–318.
Translated from Zhurnal Éksperimental'noĭ i Teoreticheskoĭ Fiziki, Vol. 117, No. 2, 2000, pp. 350–361.

SOLIDS
Structure

Localization of Acoustic Vibrational Modes in a Chain-Type Lattice

A. P. Zhernov[1, *] and E. P. Chulkin[2]

[1] *Russian Research Centre Kurchatov Institute , Moscow, 123182 Russia*
[2] *Physicotechnical Institute, Ural Division, Russian Academy of Sciences, Izhevsk, 426001 Russia*
**e-mail: zhernov@isssph.kiae.ru*
Received June 17, 1999

Abstract—The problem of weak localization of acoustic phonon modes in a nonideal chain-type crystal lattice is studied. An expression is obtained for the diffusion coefficient tensor *D*. The role of the back coherent scattering processes is investigated. It is established that on account of such processes a substantial renormalization of the diffusion coefficient *D* can occur in the relatively low-frequency range, where the dispersion laws for phonon modes exhibit quasi-one-dimensional properties. *© 2000 MAIK "Nauka/Interperiodica".*

1. INTRODUCTION

Definite attention is now being devoted in the literature to the problem of localization of phonon modes as well as sound and light waves in disordered systems under conditions where coherent multiple scattering processes are substantial. Here phenomena associated with coherent backscattering are of great interest. A number of questions have been investigated for weakly anisotropic three-dimensional lattices, including systems with resonantly scattering impurity centers (see, for example, [1–7]).

Localization phenomena should be more pronounced in low-dimensional systems than in conventional three-dimensional compounds. It is significant that under the conditions of diagonal disorder well-defined quasi-local modes do not arise in such lattices [8, 9]. As a result, when impurities are present, effects associated with weak localization could become important. For this reason, it is of interest to perform theoretical investigations of the localization of vibrational modes in layered and quasi-one-dimensional compounds. The possibility of localization of vibrational excitations in weakly anisotropic layered lattices has been discussed in [10]. Our objective in the present paper is to analyze the situation for nonideal chain-type crystals.

The problem of the localization of acoustic modes with displacement vectors parallel and perpendicular to the weakly coupled chains is studied. The vibrational modes of the first type are longitudinally polarized excitations (*l* modes). Modes of the second type are so-called bending excitations (*b* modes) [11]. In a quite wide low-frequency range, a strongly anisotropic chain-type crystal can manifest quasi-one-dimensional dynamical properties. Specifically, the frequency of the *l* mode is essentially independent of the transverse component of the quasi-momentum, and the frequency of the *b* mode is approximately proportional to the squared longitudinal component of the quasi-momentum. As far as the model of disorder is concerned, we shall confine our attention to diagonal disorder and we shall analyze the behavior of the diffusion coefficient tensor. It is assumed that the vibrational excitations are elastically scattered by point-like defects. The two-particle lattice Green's function, averaged over the impurity configurations, is determined taking account of the back coherent scattering processes.

We note that we use the phenomenological Born–Karman theory, in which the symmetry properties of the lattice are taken into account when determining the dynamical force parameters, to describe the dispersion laws of *l* and *b* modes. The force parameters in this theory are given as second-order derivatives of the real structure-dependent part E_{st} of the energy with respect to specific components of the atomic displacements. (The energy E_{st} is the sum of the energies of the ionic lattice and the configurational part of the electronic energy.) The force parameters determined in this manner contain contributions from pair and multiparticle interatomic interactions, and they also depend on the electron density distribution. The number of coordination spheres to which the interaction extends can be large. Confining ourselves to the qualitative aspect of the phenomenon, we take into account in the low-frequency representation for the *l* and *b* modes only the interaction between atoms located in the nearest chains. In principle, if the dispersion laws of specific harmonic modes (in a chain lattice) are known, then they can be approximated by the formulas presented in the next section.

In this connection, we call attention to the theoretical works on the problem of hydrogen in the metallic state [12–15]. In these works it was assumed that in metallic hydrogen the electrons are completely collectivized, so that the protons are stripped of orbital electrons. The form factor of the electron-ion interaction is

known exactly. In [12–15] the properties of the metallic state, both at zero pressure $p = 0$ [12] and under finite pressures [13–15], have been investigated in a microscopic approach. The authors employed perturbation theory with respect to the electron-ion interaction. They took account of the second-, third-, and fourth-order contributions. Thus, a situation where the interaction in the system is not only a pair interaction but also a nonpair (covalent type) interaction was studied. It was established that a metallic phase exists and that the system is dynamically stable. It is very interesting that structures with pronounced anisotropy are realized at $P = 0$. Specifically, filamentary structures (with proton chains) arise, and the minimum distance between the atoms along the chains is much shorter than the distance between the chains.

Physically, the appearance of a chain-like structure in hydrogen is due to compensation in the structure-dependent energy E_{st} of the contributions from the ionic lattice and from the second-order terms with respect to the form factor to the electron energy. The third-order terms strongly affect the structural properties. The effect of the fourth-order terms, including the terms associated with the renormalization of the chemical potential and Fermi energy, is comparatively small.

We underscore that the analysis of the phonon spectrum, which was studied in the entire Brillouin zone, revealed specific low-frequency modes of *l* and *b* types (see details in [12]).

One circumstance stimulating investigation of chain-type structures is a recently discovered new phase of carbon—carbolite [16]. Although the crystal structure of this phase has not been investigated in detail, there are grounds for believing that it consists of carbon chains which are coupled with one another by a weak van-der-Waals interaction. The anomalous behavior of the specific heat of carbolite at low temperatures can serve as an indirect confirmation of the quasi-one-dimensional structure of this material [17].

2. DYNAMICAL MODEL OF A CHAIN CRYSTAL

Dispersion laws. We shall assume that the effective force interaction between atoms in the crystal lattice along the *z* axis is much stronger than the interaction in the *xy* plane. Then one can talk about atomic chains in which the coupling is stronger than between individual chains. For simplicity, it is also assumed that the matrices of the force parameters are diagonal with respect to the Cartesian indices. Vibrations along the *z* axis and with displacement vector **u** in the *xy* plane are independent.

The lattice is assumed to be tetragonal with cell parameters $\{a, b\}$. Here the parameter *b* characterizes the distance between the atoms in a chain and the parameter *a* determines the distance between chains. Under the conditions of strong anisotropy of the interatomic interaction, the lattice parameters can be of different orders of magnitude.

We shall study vibrational modes with relatively low frequencies. It is assumed that $bk_z \ll 1$. The quantities ak_x and ak_y need not be small.

In the general case, the frequencies of the vibrational modes are eigenvalues of the Fourier components of the matrix of the second-order dynamical force components. This matrix is defined by a relation of the type

$$\Phi_{\alpha\alpha'}(\mathbf{k}) = \sum_{\mathbf{s}} \Phi_{\alpha\alpha'}^{0\mathbf{s}}[\cos(\mathbf{k}\cdot\mathbf{R}_{\mathbf{s}}) - 1]. \tag{2.1}$$

On this basis, we shall determine the dispersion law for an acoustic vibrational mode describing the displacements of atoms with mass M_0 parallel to the weakly coupled chains, i.e., along the *z* axis. We have

$$\begin{aligned} M_0\omega_l^2(\mathbf{k}) &= -\frac{1}{2}\sum_{\mathbf{s}_\perp} \Phi_{zz}^{0\mathbf{s}_\perp} R_{\mathbf{s}_\perp}^z R_{\mathbf{s}_\perp}^z \mathbf{k}_z^2 \\ &+ \frac{1}{2}\sum_{\mathbf{s}_\parallel} \Phi_{zz}^{0\mathbf{s}_\parallel}[\cos(\mathbf{k}_\parallel\cdot\mathbf{R}_{\mathbf{s}_\parallel}) - 1]. \end{aligned} \tag{2.2}$$

We note that the force parameters $\Phi_{zz}^{0\mathbf{s}_\perp}$ and $\Phi_{zz}^{0\mathbf{s}_\parallel}$ characterize the interaction along the *z* axis and in the *xy* plane, and

$$\left|\Phi_{zz}^{0\mathbf{s}_\parallel}\right| \ll \left|\Phi_{zz}^{0\mathbf{s}_\perp}\right|. \tag{2.3}$$

We shall take account of the dynamical interaction only between the nearest-neighbor atoms. Then, instead of equation (2.2), we obtain

$$\omega_l^2(\mathbf{k}) \approx \frac{\omega_\perp b^2}{2} k_z^2 + \omega_\parallel^2\left(\sin^2\frac{k_x a}{2} + \sin^2\frac{k_y a}{2}\right). \tag{2.4}$$

The frequencies $\omega_\perp$ and $\omega_\parallel$ can be expressed in terms of the parameters $\Phi_{zz}^{0\mathbf{s}_\perp}$ and $\Phi_{zz}^{0\mathbf{s}_\parallel}$. It is important that, according to equation (2.3), $\omega_\parallel^2 \ll \omega_\perp^2$.

We now consider bending modes. For vibrational modes of this type the displacement vectors are oriented perpendicular to the weakly coupled chains. Using the definition (2.1) and the condition $bk_z \ll 1$ we can write

$$\begin{aligned} M_0\omega_b^2(\mathbf{k}) &\approx -\frac{1}{2}\sum_{\mathbf{s}_\perp} \Phi_{xx}^{0\mathbf{s}_\perp}(R_{\mathbf{s}_\perp}^z)^2 k_z^2 \\ &+ \frac{1}{4}\sum_{\mathbf{s}_\perp} \Phi_{xx}^{0\mathbf{s}_\perp}(R_{\mathbf{s}_\perp}^z)^4 k_z^4 - \frac{1}{2}\sum_{\mathbf{s}_\parallel} \Phi_{xx}^{0\mathbf{s}_\parallel}\sin\frac{bk_\parallel}{2}. \end{aligned} \tag{2.5}$$

It is well known that in the absence of stresses in the crystal the force parameters satisfy a condition of the type (see, for example, [18, 19])

$$\sum_{\mathbf{s}_\parallel} \Phi_{zz}^{0\mathbf{s}_\parallel} R_{\mathbf{s}_\parallel}^x R_{\mathbf{s}_\parallel}^x = \sum_{\mathbf{s}_\perp} \Phi_{xx}^{0\mathbf{s}_\perp} R_{\mathbf{s}_\perp}^z R_{\mathbf{s}_\perp}^z. \tag{2.6}$$

Hence it follows that three characteristic force parameters should appear in the dispersion law for the bending modes (since the first term in equation (2.5) is redefined). Specifically, together with the parameters $\Phi_{xx}^{0\mathbf{s}_\perp}$ and $\Phi_{xx}^{0\mathbf{s}_\parallel}$, there also arises a parameter $\Phi_{zz}^{0\mathbf{s}_\parallel}$, where in the model adopted

$$\left|\Phi_{zz}^{0\mathbf{s}_\parallel}\right| \ll \left|\Phi_{xx}^{0\mathbf{s}_\parallel}\right| \ll \left|\Phi_{xx}^{0\mathbf{s}_\perp}\right|. \tag{2.7}$$

Thus, using equation (2.6), we obtain instead of equation (2.5) [11]

$$\omega_b^2(\mathbf{k}) = (\omega_1 a)^2 k_z^2 + \left(\frac{\omega_3 b}{\pi}\right)^2 k_z^4 + \omega_2^2\left(\sin^2\frac{k_x a}{2} + \sin^2\frac{k_y a}{2}\right). \tag{2.8}$$

The three characteristic frequencies appearing here correspond to three force parameters (2.7). The conditions $\omega_1^2 \ll \omega_2^2 \ll \omega_3^2$ are imposed on these frequencies. We note that $\omega_3 \approx \omega_\perp$ and $\omega_1 \approx \omega_\parallel$.

We shall now discuss the expressions for the anisotropic dispersion laws for the *l* and *b* modes, equations (2.4) and (2.8). Examination of these expressions shows that at the lowest frequencies, $\omega \le \omega_1$, the quantities ω_l and ω_b depend, generally speaking, on the quasi momentum components k_x, k_y, and k_z. If the frequency of the longitudinal mode lies in the range

$$2\omega_\parallel^2 \le \omega_l^2 < \omega_\perp^2, \tag{2.9}$$

then the second term in equation (2.4) is comparatively small. Therefore the quantity ω_l^2 is essentially independent of the transverse components of the quasi momentum, k_x and k_y, and the dispersion law for the *l* modes corresponds to the case of a quasi-one-dimensional lattice. At the same time, for a bending mode in the frequency range such that

$$2\omega_2^2 \ll \omega_b^2 < \omega_3^2, \tag{2.10}$$

the first and third terms in the expression (2.8) can be neglected. It is found that the frequency ω_b does not depend on the quasi momentum components k_x and k_y. It is proportional to k_z^2. Therefore the dispersion law for the *b* mode also exhibits quasi-one-dimensional behavior.

As noted in the introduction, bending modes were introduced into the analysis by I.M. Lifshits. However, he investigated their effect on the low-temperature behavior of the specific heat and the thermal expansion coefficient (see, for example, [11]).

Vibrational densities of states. We shall present concrete expressions for the densities of states of the *l* and *b* modes. They appear explicitly in the relations for the partial diffusion coefficients (see Section 3).

We start with the *l* mode. It can be shown that the squared density of phonon states in the frequency range $0 \le \omega^2 < 2\omega_\parallel^2$ is determined by an expression of the form

$$g_l(\omega^2) = \frac{b}{\pi^3\omega_\parallel^2}\int dk_z K\left(\sqrt{\xi^2(2-\xi^2)}\right), \qquad \xi^2 = \frac{\omega^2 - \dot{v}_\perp^{(l)2} k_z^2}{\omega_\parallel^2}. \tag{2.11}$$

Here K is the complete elliptic integral of the first kind, and $\dot{v}_\perp^{(l)} = b\omega_\perp/\sqrt{2}$ is the group velocity. In the limit $\omega \to 0$, when the dispersion law corresponds to the three-dimensional case, we have from equation (2.11)

$$g_l(\omega^2) = \frac{\sqrt{2}}{\pi^2}\frac{\omega}{\omega_\parallel^2\omega_\perp}\left(1 + \frac{\omega^2}{3\omega_\parallel^2} + \frac{\omega^4}{6\omega_\parallel^4} + \ldots\right). \tag{2.12}$$

In the quasi-one-dimensional range (2.9), as shown in Appendix A, the density of states can be expressed in terms of elliptic integrals:

$$g_l(\omega^2) = \frac{4\sqrt{2}}{\pi^3\omega_\perp}\frac{1}{\omega + \sqrt{\omega^2 - \omega_\parallel^2}} \times K'\left(\frac{\sqrt{\omega^2-\omega_\parallel^2} + \sqrt{\omega^2 - 2\omega_\parallel^2}}{\omega + \sqrt{\omega^2-\omega_\parallel^2}}\right) \times K\left(\frac{\sqrt{\omega^2-\omega_\parallel^2} - \sqrt{\omega^2 - 2\omega_\parallel^2}}{\omega + \sqrt{\omega^2-\omega_\parallel^2}}\right), \tag{2.13}$$

$$K'(k) = K(k'), \quad k' = \sqrt{1-k^2}. \tag{2.14}$$

Here k is the elliptic modulus, and k' is an additional elliptic modulus. If $\omega_l^2 \ll \omega_\perp^2$, then

$$g_l(\omega^2) \approx \frac{1}{\sqrt{2}\pi\omega_\perp\omega}\left(1 + \frac{\omega_\parallel^2}{4\omega^2} + \frac{5\omega_\parallel^4}{16\omega^4} + \ldots\right). \tag{2.13'}$$

Thus, in the frequency range (2.9) the density of states of longitudinal modes $g_l(\omega) = 2\omega q_l(\omega^2)$ depends weakly on the frequency.

The squared partial density of phonon states of b modes for $0 < \omega_b^2 < 2\omega_2^2$ is

$$g_b(\omega^2) = \frac{1}{\pi^2\omega_2^2}\sum_{k_z} K(\sqrt{\xi^2(2-\xi^2)}),$$
$$\xi^2 = \frac{\omega^2 - (\omega_1 a)^2 k_z^2}{\omega_2^2}. \quad (2.15)$$

In the limit $\omega \longrightarrow 0$ (more accurately, in the long-wavelength limit for $0 \le \omega^2 \ll 2(a/b)^4\omega_1^4/\omega_\perp^2$) it follows from the expression (2.15) that

$$g_b(\omega^2) = \frac{b\omega}{(2\pi)^2 a\omega_1\omega_2^2}\left(1 + \frac{1}{3}\frac{\omega^2}{\omega_2^2} + \frac{1}{6}\frac{\omega^4}{\omega_2^4} + \ldots\right), \quad (2.15')$$

i.e., the dependence is of a quasi-three-dimensional character. Finally, the frequency range $2\omega_2^2 < \omega^2 < \omega_\perp^2 \approx \omega_3^2$ we have according to the results of Appendix A:

$$g_b(\omega^2) = \frac{1}{8\pi^2\sqrt{\pi\omega_\perp\omega^3}}\Psi_0^{(b)}. \quad (2.16)$$

For $\omega_b^2 \gg \omega_2^2$ this expression assumes the form

$$g_b(\omega^2) = \frac{1}{8\sqrt{\pi\omega_\perp\omega^3}}\left(1 + \frac{3}{4}\frac{\omega_2^2}{\omega^2} + \frac{657}{1024}\frac{\omega_2^4}{\omega^4} + \ldots\right). \quad (2.16')$$

We call attention to the fact that the density of states $g_b(\omega) = 2\omega g_b(\omega^2)$ determined by equation (2.16') is a decreasing function of frequency.

We also note that the functions g_l and g_b are determined, respectively, by the relations (2.12)–(2.14) and (2.15), (2.16) in the entire range of low and intermediate frequencies.

Group velocities. The group velocities of the vibrational modes also enter in the expressions for the partial diffusion coefficients. A summary of the formulas is given below. In the first place, in the case of the l mode we have

$$v_\perp^{(l)}(\mathbf{k}) = \frac{\partial\omega_l(\mathbf{k})}{\partial k_z} = \frac{\dot{v}_\perp^{(l)2}k_z}{\omega_l(\mathbf{k})}, \quad (2.17)$$

where $\dot{v}_\perp^{(l)} = b\omega_\perp/\sqrt{2}$ and

$$v_{x(y)}^{(l)}(\mathbf{k}) = \frac{\partial\omega_l(\mathbf{k})}{\partial k_{x(y)}} = \frac{a\omega_\parallel^2}{\omega_l(\mathbf{k})}\sin(k_{x(y)}a). \quad (2.17')$$

The average velocities are given by expressions of the type

$$\sqrt{\langle v_{x(y)}^{(l)2}\rangle} = \frac{v_{x(y),\max}^{(l)}}{\sqrt{2}},$$
$$\langle v_\parallel^{(l)2}\rangle = \langle v_x^{(l)2}\rangle + \langle v_y^{(l)2}\rangle = \frac{\omega_\parallel^4 a^2}{4\omega_l^2(\mathbf{k})}. \quad (2.17'')$$

For the b modes we have

$$v_\perp^{(b)}(\mathbf{k}) = \frac{\partial\omega_b(\mathbf{k})}{\partial k_z} = \frac{2k_z^3 b^4\omega_\perp^2}{\omega_b^2(\mathbf{k})\pi^2} \approx \frac{2b}{\sqrt{\pi}}\sqrt{\omega_b(\mathbf{k})\omega_\perp}, \quad (2.18)$$

$$v_{x(y)}^{(b)}(\mathbf{k}) = \frac{\partial\omega_b(\mathbf{k})}{\partial k_{x(y)}} = \frac{a\omega_2^2}{4\omega_b(\mathbf{k})}\sin(k_{x(y)}a). \quad (2.18')$$

The corresponding average velocities are

$$\sqrt{\langle v_{x(y)}^{(b)2}\rangle} = \frac{v_{x(y),\max}^{(b)}}{\sqrt{2}},$$
$$\langle v_\parallel^{(b)2}\rangle = \langle v_x^{(b)2}\rangle + \langle v_y^{(b)2}\rangle = \frac{\omega_2^2}{4\omega_b^2(\mathbf{k})}\frac{\omega_2^2 a^2}{4}. \quad (2.18'')$$

On the single-site scattering matrix and mass operator. We shall now examine the characteristic features of the single-site t scattering matrix and mass operator $P(\omega)$ that are due to the elastic scattering of phonon modes by impurity atoms. We assumed that the disorder is diagonal and the impurity differ from the matrix atoms only with respect to mass. Here M and M_0 are the masses of the defect atoms and the atoms of the regular matrix, and c is the defect concentration. The value of the parameter $c\epsilon^2$, where $\epsilon = 1 - M/M_0$, is a measure of the disorder. We note that defect concentration c is assumed to be low ($c \ll 1$). In this situation the total perturbation is a sum of contributions from individual defects. To determine the mass operator, in practice it is sufficient to consider only terms of second order in the parameter c. The effect of the interaction of phonons with groups of more than two impurities should be weak because of lattice anharmonicity.

For vibrational modes with displacement vectors oriented parallel and perpendicular to the weakly coupled chains ($j = l, b$), the operator $P_j(\omega)$ is given by relations of the form

$$P_j(\omega) = ct_j(\omega)[1 + \Delta_j(\omega)], \quad (2.19)$$

where t_j is the single-site scattering matrix, and the form factor Δ_j describes the pair dynamical interaction of the impurities:

$$\Delta_j(\omega) = ct_j^2(\omega)\left[-\frac{\partial G_j^0}{\partial\omega^2} - G_j^{02}(\omega)\right]$$
$$+ \frac{c}{2}\sum_{\mathbf{s}\neq 0} G_{j,0\mathbf{s}}^{02}(\omega)t_j^2(\omega)\left[\frac{1 + e^{i\mathbf{k}\cdot\mathbf{s}}}{1 - t_j(\omega)C_{j,0\mathbf{s}}^0}\right] \quad (2.20)$$
$$+ \frac{c}{2}\sum_{\mathbf{s}\neq 0} G_{j,0\mathbf{s}}^{02}t_j^2(\omega)\frac{1 - e^{i\mathbf{k}\cdot\mathbf{s}}}{1 + t_j(\omega)G_{j,0\mathbf{s}}^0} + \ldots.$$

Here $G^0_{j,ss'}$ is the Green's function of the ideal lattice, and it is constructed from the operators of the components u^α_s of the dynamical atomic displacements ($\alpha = z, x(y)$), and G^0_j is the Green's function with equal site indices.

The matrix t_j is determined by the expression

$$t_j^{-1}(\omega) = V[1 - VG_j^0(\omega^2)]^{-1}, \quad V = \epsilon\omega^2. \tag{2.21}$$

The series for $P_j(\omega)$ (2.19) converges if

$$c\left|t_j^2(\omega)\frac{\partial G_j^0(\omega)}{\partial \omega^2}\right| \ll 1. \tag{2.22}$$

We now consider the behavior of the single-site t scattering matrix (2.21) at frequencies $w^2 \gg 2\omega_\parallel^2$, where the vibrational spectrum exhibits quasi-one-dimensional properties. For such frequencies

$$\begin{aligned} \mathrm{Im}G_l^0(\omega^2) &= \pi g_l(\omega^2) \approx \frac{1}{\sqrt{2}\omega_\perp\omega}, \\ \mathrm{Im}G_b^0(\omega^2) &= \pi g_b(\omega^2) \approx \frac{1}{\sqrt{\omega_3\omega^3}}. \end{aligned} \tag{2.23}$$

Using the relations (2.23) and the Kramers–Kronig relations, we obtain for the corresponding real parts of the Green's functions

$$\begin{aligned} \mathrm{Re}G_l^0(\omega^2) &= \int_0^\infty \frac{d\omega'^2}{\pi} P\frac{1}{\omega^2 - \omega'^2}\mathrm{Im}G_l^0(\omega'^2) \approx \frac{\sqrt{2}}{\pi\omega_\perp^2}, \\ \mathrm{Re}G_b^0(\omega^2) &= \int_0^\infty \frac{d\omega'^2}{\pi} P\frac{1}{\omega^2 - \omega'^2}\mathrm{Im}G_b^0(\omega'^2) \approx \frac{\sqrt{\pi}}{8}\frac{1}{\sqrt{\omega_3\omega^3}}. \end{aligned} \tag{2.24}$$

Thus, the total Green's functions are approximately

$$\begin{aligned} G_l^0(\omega^2) &\approx \frac{\sqrt{2}}{\pi\omega_\perp^2} + i\frac{1}{\sqrt{2}\omega_\perp\omega}, \\ G_b^0(\omega^2) &\approx \frac{\sqrt{\pi}}{8}\frac{1}{\sqrt{\omega_3\omega^3}}(1+i). \end{aligned} \tag{2.25}$$

We call attention to the fact that for the l modes $\mathrm{Re}G_l^0(\omega^2) \ll \mathrm{Im}G_l^0(\omega^2)$ in a wide frequency range. At the same time, for the b modes the real and imaginary parts of the function $G_l^0(\omega^2)$ are of the same order of magnitude.

Using the explicit form of the Green's functions $G^0_{l,b}(\omega^2)$ (2.25) and the diagonal perturbation operator $V = -\epsilon\omega^2$, we find that the denominators $R_{l,b}$ of the single-site t scattering matrix can be represented in the form

$$\begin{aligned} R_l(\omega^2) &= 1 - VG_l^0(\omega^2) \approx 1 - \frac{\sqrt{2}}{\pi}|\epsilon|\frac{\omega^2}{\omega_\perp^2} - i\frac{|\epsilon|\omega}{\sqrt{2}\omega_\perp}, \\ R_b(\omega^2) &\approx 1 - \frac{\sqrt{\pi}}{8}|\epsilon|\sqrt{\frac{\omega}{\omega_3}}(1+i), \end{aligned} \tag{2.26}$$

whence it is evident that the real parts of the t matrices in the case of strong disorder vanish for frequencies ω_r which are roots of the equations

$$\mathrm{Re}R_{l(b)}(\omega_r^2) = 0. \tag{2.27}$$

The frequencies themselves are given by the relations

$$\omega_r^{(l)2} \approx \frac{\pi}{\sqrt{2}}\frac{\omega_\perp^2}{|\epsilon|}, \quad \omega_r^{(b)} \approx \frac{64}{\pi}\frac{\omega_3}{\epsilon^2}. \tag{2.28}$$

The broadening of a level with characteristic frequency ω_r, by definition, is of the order of

$$\Gamma_r^{l(b)} = \frac{\mathrm{Im}R_{l(b)}(\omega_r^2)}{\dfrac{d}{d\omega}[\mathrm{Re}R_{l(b)}(\omega^2)]\Big|_{\omega=\omega_r}}. \tag{2.29}$$

Using the expressions presented for Γ_r we obtain

$$\Gamma_r^{(l)} \approx \frac{\pi}{4}\omega_\perp = \sqrt{2\pi|\epsilon|}\omega_r, \quad \Gamma_r^{(b)} \approx 2\omega_r^{(b)}. \tag{2.30}$$

Let us now compare the expressions (2.29) and (2.30). It turns out that for frequencies $\omega^2 \gg 2\omega_\parallel^2$ the condition $\Gamma_r/\omega_r \ll 1$ does not hold, as a result of which it makes no sense to talk about quasi-local levels existing in a narrow frequency range or about a resonant type scattering by such levels. (Quasi-local modes arise in quasi-one-dimensional crystals in the case of off-diagonal disorder and weakly coupled impurities [8, 9]. The case of one-dimensional crystals is examined in Appendix B.)

Using equations (2.19) and (2.20), we obtained specific estimates of the mass operator for the case of strong diagonal disorder, when $c \ll 1$ and at the same time $\epsilon^2 c \leq 1$. This was done in order to determine the approximate form of $\overline{G}^{(j)+}_{\mathbf{k}}(\omega)$, the spatial Fourier component of the single-particle Green's function of the j phonon mode with quasi momentum $\mathbf{k}$, averaged over the impurity configurations. The frequency range where the dispersion laws for the l and b modes exhibit quasi-one-dimensional behavior was examined. It turns out that the renormalization of the frequencies of the vibrational modes can be neglected. As far as damping is concerned, it is sufficient to retain the term linear in

the concentration c in the expression for the imaginary part of the mass operator. On this basis, we have

$$\overline{G}_{\mathbf{k}}^{(j)+}(\omega) \approx \left[\omega^2 - \omega^2(\mathbf{k}) - i\frac{\omega}{\tau_i^{(j)}(\omega)}\right]^{-1}. \tag{2.31}$$

Here $\omega/\tau_i(\omega)$ is the imaginary part of the mass operator, and (see, for example, [19])

$$\frac{\omega}{\tau_i^{(j)}(\omega)} = \frac{\pi}{2}c\epsilon^2\omega^2 g_j(\omega). \tag{2.32}$$

3. DIFFUSION COEFFICIENT AND WEAK LOCALIZATION

Diffusion coefficient and the two-particle Green's function. We base our definition of the diffusion coefficient tensor for phonons of a harmonic lattice on a strict Kubo-type expression for the lattice thermal conductivity. On this basis, we shall determine the thermal conductivity tensor κ for low temperatures, where the elastic scattering of phonons by defects determines the mean-free path length. The case of a layered crystal has been discussed in detail in [10]. Here we consider a chain crystal.

For a chain crystal the lattice possesses axial symmetry and the tensor κ possesses two principal values, which we denote as $\kappa_\parallel$ and $\kappa_\perp$. The corresponding expression for $\kappa_{\alpha\alpha}$ is a sum of the contributions of l and b modes. Similarly, as done in [10] it can be shown that

$$\kappa_{\alpha\alpha} = \frac{1}{NT^2} \times \sum_{\mathbf{k}j} \omega_j^2(\mathbf{k}) n(\omega_j(\mathbf{k}))[n(\omega_j(\mathbf{k})) + 1] D_{\alpha\alpha}^{(j)}(\omega_j(\mathbf{k})), \quad j = l, b. \tag{3.1}$$

In equation (3.1) D denotes the diffusion coefficient; $n(\omega)$ is the equilibrium Planck phonon distribution function; and, α is the Cartesian index. We have

$$D_{\alpha\alpha'}^{(j)}(\omega) = \frac{4}{\omega g_j(\omega)} \times \sum_{\mathbf{k}\mathbf{k}'} v_\alpha^{(j)}(\mathbf{k}) v_{\alpha'}^{(j)}(\mathbf{k}) \omega_j(\mathbf{k}) \omega_j(\mathbf{k}') G_2^{(j)}(\mathbf{k}; \mathbf{k}'; \omega). \tag{3.2}$$

We recall that in the expressions (3.1) and (3.2) the quantities $\omega_j(\mathbf{k})$ and $\mathbf{v}^{(j)} = \partial\omega_j(\mathbf{k})/\partial\mathbf{k}$ are the dispersion law and the group velocity of a phonon mode with quasi momentum $\mathbf{k}$; $g_j(\omega)$ is the partial density of vibrational states. The spatial Fourier component of the two-frequency Green's function G_2 can be expressed in terms of the single-particle Green's functions by means of the equation

$$G_2^{(j)}(\mathbf{k}, \mathbf{k}'; \omega, \Omega) = \lim_{\Omega \to 0} \langle G_{\mathbf{k},\mathbf{k}'}^{(j)+}(\omega) G_{\mathbf{k},\mathbf{k}'}^{(j)-}(\omega - \Omega)\rangle_c, \tag{3.3}$$

where $\langle \ldots \rangle_c$ denotes averaging over different impurity configurations. In our case, in the momentum representation the equation for the two-particle Green's function can be represented in the form of a Bethe–Salpeter type equation

$$G_2^{(j)}(\mathbf{k}, \mathbf{k}', \omega, \Omega) = \lim_{\Omega \to 0} \langle G_{\mathbf{k},\mathbf{k}'}^{(j)+}(\omega) G_{\mathbf{k},\mathbf{k}'}^{(j)-}(\omega - \Omega)\rangle_c = \lim_{\Omega \to 0}\left\{\overline{G}_{\mathbf{k}}^{(j)+}(\omega)\overline{G}_{\mathbf{k}}^{(j)-}(\omega - \Omega) \times \left[\delta_{\mathbf{k}\mathbf{k}'} + \sum_{\mathbf{k}_1} U_j(\mathbf{k}, \mathbf{k}_1; \omega, \Omega) G_2^{(j)}(\mathbf{k}_1, \mathbf{k}'; \omega, \Omega)\right]\right\}. \tag{3.4}$$

We are studying the role of the back coherent scattering processes (certain specific interference processes arising with scattering of phonons by fluctuations of the phonon density of states near defects). As is well known, they determine the weak-localization regime which arises when

$$ql^{(j)} \ll 1, \quad \Omega\tau_i^{(j)}(\omega) \ll 1, \tag{3.5}$$

where $l^{(j)} = v^{(j)}\tau_i^{(j)}(\omega)$ is the mean-free path of a j-type phonon, bounded by elastic scattering by impurities. In the case of interest to us, the vertex part U appearing in equation (3.4) is determined by "fan" type diagrams. It turns out that

$$U_j(\mathbf{k}, \mathbf{k}'; \omega, \Omega) = \Gamma_j[1 - J_j(\mathbf{q}, \omega, \Omega)]^{-1}, \quad J_j(\mathbf{q}, \omega, \Omega) = \frac{\Gamma_j}{N}\sum_{\mathbf{k}_1} \overline{G}_{\mathbf{k}_1}^{(j)+}(\omega)\overline{G}_{\mathbf{k}_1-\mathbf{q}}^{(j)-}(\omega + \Omega), \tag{3.6}$$

where $\mathbf{q} = \mathbf{k} + \mathbf{k}'$. For the initial vertex Γ_j we found (see also [10])

$$\Gamma_j^{-1}(\omega) = \frac{1}{N}\sum_{\mathbf{k}} \overline{G}_{\mathbf{k}}^{(j)+}(\omega)\overline{G}_{\mathbf{k}}^{(j)-}(\omega). \tag{3.7}$$

At relatively low frequencies (2.9) and (2.10), i.e., in the range where the lattice exhibits quasi-one-dimensional properties,

$$\Gamma_j(\omega) \approx \frac{\omega}{\pi\tau_i^{(j)}(\omega) g_j(\omega^2)}. \tag{3.7'}$$

Diffusion vertices. We shall consider only the frequency ranges where the phonon dispersion laws exhibit quasi-one-dimensional properties. We note that the calculation of the complete vertices $U_j(\mathbf{k}, \mathbf{k}'; \omega, \Omega)$ in the diffusion limit is comparatively difficult. As an illustration, the corresponding calculations are performed in Appendix C for the case $j = l$. The results are summarized below.

In the first place, for longitudinal l modes for the frequency range (2.9) we have, using equations (3.6)–

(3.7) and also equations (A.3) and (C.2) from the Appendix,

$$U_l(\mathbf{q};\,\omega,\Omega)\approx\frac{\Gamma_l}{\tau_i^{(l)}}\Bigg[-i\Omega+\left(1-\frac{2\omega_\parallel^2\Psi_2^{(l)}}{\omega^2\Psi_0^{(l)}}\right)\tau_i^{(l)}v_\perp^{(l)2}q_\perp^2 + \frac{4(\Psi_2^{(l)}-\Psi_4^{(l)})}{\Psi_0^{(l)}}\frac{\langle v_\parallel^{(l)2}\rangle\tau_i^{(l)}}{a^2}\left(\sin^2\frac{q_xa}{2}+\sin^2\frac{q_ya}{2}\right)\Bigg]^{-1}. \tag{3.8}$$

Here

$$\Psi_n^{(l)} = \Psi_n^{(l)}\left(\frac{\omega_\parallel}{\omega}\right) = \int_0^{\pi/2} du\sin^2\frac{nu}{2}f\left(u,\frac{\omega_\parallel}{\omega}\right)K\left(\frac{\omega_\parallel}{\omega}f\left(u,\frac{\omega_\parallel}{\omega}\right)\right), \tag{3.9}$$

$$n = 2, 4.$$

To simplify the equations, we have set

$$f\left(u,\frac{\omega_\parallel}{\omega}\right) = \frac{1}{\sqrt{1-(\omega_\parallel^2/\omega^2)\sin^2u}}.$$

When $\omega \gg \omega_\parallel$, the quantities $\Psi_n^{(l)}$ (3.9) are approximately

$$\Psi_0^{(l)}\approx\frac{\pi^2}{4},\quad \Psi_2^{(l)}\approx\frac{\pi^2}{8},\quad \Psi_4^{(l)}\approx\frac{3\pi^2}{32}. \tag{3.9'}$$

Then the expression for U_l (3.8) simplifies. It has the form

$$U_l(\mathbf{q};\,\omega,\Omega)\approx\frac{\Gamma_l}{\tau_i^{(l)}}\times\left[-i\Omega+D_\perp^{(l)0}q_\perp^2+\frac{D_\parallel^{(l)0}}{a^2}\left(\sin^2\frac{q_xa}{2}+\sin^2\frac{q_ya}{2}\right)\right]^{-1}, \tag{3.10}$$

where

$$D_\perp^{(l)0} = v_\perp^{(l)2}\tau_i^{(l)},\quad D_\parallel^{(l)0} = \langle v_\parallel^{(l)2}\rangle\tau_i^{(l)}/2.$$

For the case of the bending b modes the vertex U_b in the frequency range (2.10) is given by

$$U_b(\mathbf{q};\,\omega,\Omega)\approx\frac{\Gamma_b}{\tau_i^{(b)}}\Bigg[-i\Omega+\frac{4}{\pi}\frac{\Psi_1^{(b)}}{\Psi_0^{(b)}}\tau_i^{(b)}v_\perp^{(b)2}q_\perp^2 + \frac{4\Psi_2^{(b)}}{\Psi_0^{(b)}}\frac{\langle v_\parallel^{(b)2}\rangle\tau_i^{(b)}}{a^2}\left(\sin^2\frac{q_xa}{2}+\sin^2\frac{q_ya}{2}\right)\Bigg]^{-1}. \tag{3.11}$$

Here

$$\Psi_0^{(b)} = \Psi_0^{(b)}\left(\frac{\omega_2}{\omega}\right) = \int_0^{\pi/2}\int_0^{\pi/2} dudtP(u,t),$$

$$\Psi_1^{(b)} = \iint_0^{\pi/2} dudtP^{-1}(u,t),$$

$$\Psi_2^{(b)} = \iint_0^{\pi/2} dudt\sin^2(2u)P(u,t),$$

$$P(u,t) = \left[1-\frac{\omega_2^2}{\omega^2}(\sin^2u+\sin^2t)\right]^{-3/4}.$$

When $\omega \gg \omega_2$, the quantities $\Psi_n^{(b)}$ are approximately

$$\Psi_0^{(b)} = \Psi_1^{(b)} = \frac{\pi^2}{4},\qquad \Psi_2^{(b)} = \frac{\pi^2}{16}. \tag{3.11'}$$

As a result, instead of equation (3.11) we obtain

$$U_b(\mathbf{q};\,\omega,\Omega)\approx\frac{\Gamma_b}{\tau_i^{(b)}}\times\left[-i\Omega+D_\perp^{(b)0}q_\perp^2+\frac{D_\parallel^{(b)0}}{a^2}\left(\sin^2\frac{q_xa}{2}+\sin^2\frac{q_ya}{2}\right)\right]^{-1}, \tag{3.12}$$

where

$$D_\perp^{(b)0} = v_\perp^{(b)2}\tau_i^{(b)},\quad D_\parallel^{(b)0} = \langle v_\parallel^{(b)2}\rangle\tau_i^{(b)}/2.$$

We call attention to the fact that the partial densities of vibrational states can be expressed in terms of the functions $\Psi_0^{(l)}$ and $\Psi_0^{(b)}$:

$$g_l(\omega^2) = \frac{2\sqrt{2}}{\pi^3\omega_\perp}\Psi_0^{(l)},\qquad g_b(\omega^2) = \frac{1}{2\pi^{5/2}}\frac{\Psi_0^{(b)}}{\sqrt{\omega_\perp\omega^3}}. \tag{3.13}$$

Partial diffusion coefficients. We shall now determine the partial diffusion coefficients in the weak-localization regime. We shall determine the principal values of the tensor $D^{(j)}$ in the situation where the conditions (3.5) are satisfied. Using the relations (3.2) and (3.4) we have

$$\{D_\parallel^{(j)}, D_\perp^{(j)}\} = \{D_\parallel^{(j,1)}, D_\perp^{(j,1)}\} - \{D_\parallel^{(j,2)}, D_\perp^{(j,2)}\}, \tag{3.14}$$

where

$$\{D_{\parallel}^{(j,1)}, D_{\perp}^{(j,1)}\} = \frac{1}{\pi g_j(\omega)} \times \lim_{\Omega\to 0}\sum_{\mathbf{k}}\left\{\frac{\partial\omega_j^2(\mathbf{k})}{\partial k_{\parallel}}, \frac{\partial\omega_j^2(\mathbf{k})}{\partial k_z}\right\}\bar{G}_{\mathbf{k}}^{(j)+}(\omega)\bar{G}_{\mathbf{k}}^{(j)-}(\omega+\Omega), \tag{3.15}$$

$$\{D_{\parallel}^{(j,2)}, D_{\perp}^{(j,2)}\} = \frac{1}{\pi g_j(\omega)}\lim_{\Omega\to 0}\sum_{\mathbf{q}\le \mathbf{q}_j^{(\parallel)}, \mathbf{q}_j^{(\perp)}} U_j(\mathbf{q};\omega,\Omega) \times\sum_{\mathbf{k}}\left\{\frac{\partial\omega_j^2(\mathbf{k})}{\partial k_{\parallel}}\frac{\partial\omega_j^2(\mathbf{k})}{\partial k_z}\right\} \times\bar{G}_{\mathbf{k}}^{(j)+}(\omega)\bar{G}_{\mathbf{k}}^{(j)-}(\omega+\Omega)\bar{G}_{\mathbf{k}+\mathbf{q}}^{(j)+}(\omega)\bar{G}_{\mathbf{k}+\mathbf{q}}^{(j)-}(\omega+\Omega). \tag{3.16}$$

The first term in equation (3.14) determines the standard values of the diffusion coefficient. The second term in equation (3.16) determines the effect of the interference scattering processes near defects. In the case of a lattice with a strongly-anisotropic interatomic force interaction, which we are studying, the summation over $\mathbf{q}$ is bounded above by small quantities $q_j^{(\parallel,\perp)} \approx \pi/l_{\parallel,\perp}^{(j)}(\omega)$. If $a \approx b$, then $l_{\parallel,\perp}^{(j)} = v_{\parallel,\perp}^{(j)}\tau_i^{(j)}(\omega)$. However, if the unit cell parameters a and b are strongly different, i.e., $a \ll b$, then a situation where $q_j^{(\perp)} \approx \pi/b$ can occur.

We shall confine ourselves to the static case, where $\Omega \longrightarrow 0$. Using the relations (3.14)–(3.16) and the representation (2.31) for the Green's functions and (3.10) and (3.12) for the vertex parts, the partial diffusion coefficients can be calculated in the frequency range where the vibrational spectrum of the modes exhibits quasi-one-dimensional properties.

As an example, we shall determine the diffusion coefficient $D^{(l)}$ for the frequency range (2.9). We consider first the contribution given by equation (3.15) to $D^{(l)}$. In equation (3.15) we switch from summation to integration. The integration over dk_z must be performed through a pole and then over dk_x and dk_y directly. We find

$$\{D_{\perp}^{(l,1)}(\omega), D_{\parallel}^{(l,1)}(\omega)\} = 4b\tau_i^{(l)}(\omega)\frac{\Psi_0^{(l)}}{\pi^3 g_l(\omega)v_{\perp}} \times\left\{v_{\perp}^2\left(1-\frac{2\omega_{\parallel}^2\Psi_2^{(l)}}{\omega^2\Psi_0^{(l)}}\right), \frac{a^2\omega_{\parallel}^4}{4\omega^2}\frac{4(\Psi_2^{(l)}-\Psi_4^{(l)})}{\Psi_0^{(l)}}\right\} \tag{3.17}$$

(the functions $\Psi_n^{(l)}$ were determined by the relation (3.9)). Next, we switch to the interference term (3.16). Calculations similar to those described above yield

$$\{D_{\perp}^{(l,2)}(\omega,\Omega), D_{\parallel}^{(l,1)}(\omega,\Omega)\} = \{D_{\perp}^{(l,1)}(\omega), D_{\parallel}^{(l,1)}(\omega)\} \times\frac{\tau_i^{(l)2}}{2\omega^2}\sum_{\mathbf{q}} U_l(\mathbf{q};\omega,\Omega). \tag{3.18}$$

Using equations (3.17) and (3.18) we have

$$\{D_{\perp}^{(l)}(\omega,\Omega), D_{\parallel}^{(l)}(\omega,\Omega)\} = \{D_{\perp}^{(l,1)}(\omega,\Omega), D_{\parallel}^{(l,1)}(\omega,\Omega)\}F^{(l)}(\omega,\Omega), \tag{3.19}$$

where

$$F^{(l)}(\omega,\Omega) = 1-\frac{\tau_i^{(l)2}(\omega)}{2\omega^2}\sum_{\mathbf{q}} U_l(\mathbf{q};\omega,\Omega). \tag{3.20}$$

(The diffusion vertex U_l is given by the expression (3.8).)

For the frequency range $\omega^2 \gg \omega_{\parallel}^2$, using equations (3.9') and (2.13'), the expression (3.17) assumes the form

$$\{D_{\perp}^{(l,1)}(\omega), D_{\parallel}^{(l,1)}(\omega)\} \approx\left\{\tau_i^{(l)}v_{\perp}^2, \frac{a^2\omega_{\parallel}^4\tau_i^{(l)}}{8\omega^2}\right\} = \left\{\tau_i^{(l)}v_{\perp}^2, \frac{\langle v_{\parallel}^{(l)2}\rangle\tau_i^{(l)}}{2}\right\}. \tag{3.21}$$

For the factor $F^{(l)}$ (3.20), in the static limit $\Omega \longrightarrow 0$ and using equation (3.10) together with equation (3.21), we obtain a representation in the form

$$F^{(l)}(\omega) \approx 1-\Delta F^{(l)}, \quad \Delta F^{(l)} = \frac{c\epsilon^2}{\pi}\frac{\omega}{\omega_{\perp}}\frac{\omega^2}{\omega_{\parallel}^2}\frac{C_e}{\sqrt{1-\omega_{\parallel}^2/\omega^2}}, \tag{3.21'}$$

where

$$C_e = K(\sqrt{2}-1)K'(\sqrt{2}-1) = \sqrt{2}K^2(\sqrt{2}-1) \approx 3.83.$$

It can be shown similarly that for the bending b modes for $\omega^2 \gg \omega_2^2$ we have

$$\{D_{\perp}^{(b)}, D_{\parallel}^{(b)}\} \approx\left\{\left[\frac{4}{\pi}b^2\omega_3\omega\tau_i^{(b)}, \frac{a^2}{16\pi}\frac{\omega_2^4}{\omega^2}\tau_i^{(b)}(\omega)\right]F^{(b)}(\omega)\right\}, \tag{3.22}$$

where

$$F^{(b)}(\omega) = 1-\Delta F^{(b)}, \quad \Delta F^{(b)} = \sqrt{\pi}c\epsilon^2\frac{\omega^2}{\omega_2^2}\sqrt{\frac{\omega}{\omega_3}}\frac{C_e}{1-3\omega_2^2/4\omega^2}. \tag{3.22'}$$

We underscore that the deviation of the factor $F^{(l,b)}$ from 1 is due to the back coherent scattering processes. It follows directly from the expressions (3.21') and (3.22') that under the conditions of diagonal disorder, when $c\epsilon^2 \sim 0.1$, in certain intermediate frequency ranges (2.9) and (2.10) interference processes can strongly alter the partial diffusion coefficients. In principle, a gap appears in the spectrum $D(\omega)$, i.e., as the interaction between chains becomes weaker (when the frequencies

$\omega_\parallel$ and ω_2 decrease), the renormalization of the partial diffusion factors intensifies.

As already noted, $\omega_3 \approx \omega_\perp$, $\omega_1 \approx \omega_\parallel$, and $\omega_1 \ll \omega_2$. Therefore, since

$$\frac{\Delta F^{(b)}}{\Delta F^{(l)}} = \sqrt{\pi^3}\frac{\omega_\parallel^2}{\omega_2^2}\sqrt{\frac{\omega_\perp}{\omega}} \approx \sqrt{\pi^3}\frac{\omega_1^2}{\omega_2^2}\sqrt{\frac{\omega_\perp}{\omega}} < 1, \qquad (3.23)$$

the bending modes, as compared with longitudinal modes, start to localize at high values of the parameter $c\epsilon^2$.

4. CONCLUSIONS

In this paper, the possibility of weak localization of acoustic vibrational modes in an nonideal strongly anisotropic harmonic chain-type crystal lattice was analyzed. It was assumed that the coupling between atoms in the chains is much stronger than between atoms of individual chains and that the lattice exhibits quasi-one-dimensional properties. Longitudinally polarized excitations and excitations resembling bending waves in noninteracting chains were studied.

Analytic expressions for the diffusion coefficient tensors D of the modes were obtained for temperatures where the phonon free paths are determined by elastic scattering by point defects. It was shown that in certain frequency ranges, where the dispersion laws of the modes exhibit quasi-one-dimensional properties, for values of the disorder parameter near several tens substantial renormalization of the diffusion coefficient is possible on account of the back coherent scattering processes. In principle, a range of forbidden frequencies arises in the spectrum $D(\omega)$.

Let us compare the results for a chain crystal with the results for three-dimensional and layered crystals. For a three-dimensional crystal and diagonal disorder, quasi-local modes exist in the Debye low-temperature part of the spectrum. In other words, a system of resonantly scattering impurity centers arises. If the impurity concentration c exceeds a critical value c_{cr} and a low-frequency gap appears in the spectrum, then in regions where modes become localized arise at the edges of the gap. If $c < c_{cr}$ (no gap), localization processes are weak compared with the retardation effect [6]. The case of a layered crystal has been examined in [10]. If disorder is diagonal, then there are no quasi-local-type impurity modes in the region where the lattice exhibits quasi-two-dimensional (or quasi-one-dimensional) properties. According to [10], on account of the specific interference scattering processes, the gap in the spectrum $D(\omega)$ appears only with strong disorder, when $c\epsilon^2 \geq 1$. Thus, as expected, the back coherent scattering processes should be most strongly manifested for chain compounds.

Unfortunately, we know of no experimental data on the thermal conductivity of strongly disordered quasi-one-dimensional crystals. The search for the renormalization of the D tensor predicted in this paper requires special experiments on carbolite type compounds.

ACKNOWLEDGMENTS

We are grateful to the referee for very valuable remarks.

APPENDIX A

We shall determine the density of states of longitudinal and bending modes in regions where the lattice exhibits quasi-one-dimensional properties. In the first place, by definition

$$g_l(\omega^2) = \frac{1}{N}\sum_{\mathbf{k}}\delta(\omega^2 - \omega_l^2(\mathbf{k})). \qquad (A.1)$$

We switch in equation (A.1) from summation over $\mathbf{k}$ to integration over $d\mathbf{k}$. In doing so,

$$\frac{1}{N}\sum_{\mathbf{k}}\ldots = \frac{a^2 b}{(2\pi)^3}\iint_{-\pi/a}^{\pi/a} dk_x dk_y \int dk_z \ldots . \qquad (A.2)$$

For non-bending modes, if the frequency lies in the range $2\omega_\parallel^2 \leq \omega^2 < \omega_\perp^2$, taking account of equation (A.2) the density of states is given by the relations

$$g_l(\omega^2) = \frac{a^2 b}{(2\pi)^3}\iint_{-\pi/a}^{\pi/a} dk_x dk_y$$

$$\times \int dk_z \delta\left(\omega^2 - \dot{v}_\perp^2 k_z^2 - \omega_\parallel^2\left(\sin^2\frac{k_x a}{2} + \sin^2\frac{k_y a}{2}\right)\right)$$

$$= \frac{2\sqrt{2}a^2}{\pi^3\omega_\perp}\iint_0^{\pi/a} dxdy(\omega^2 - \omega_\parallel^2\sin^2 x)^{-1/2} \qquad (A.3)$$

$$\times\left(1 - \frac{\omega_\parallel^2}{\omega^2 - \omega_\parallel^2\sin^2 x}\sin^2 y\right)^{-1/2} = \frac{2\sqrt{2}}{\pi^3\omega_\perp\omega}\Psi_0^{(l)}\left(\frac{\omega_\parallel}{\omega}\right),$$

$$\Psi_0^{(l)}(w) = \int_0^{\pi/2} dx(1 - w^2\sin^2 x)^{-1/2} K\left(\sqrt{\frac{w^2}{1 - w^2\sin^2 x}}\right),$$

$$w^2 = \frac{\omega_\parallel^2}{\omega^2}.$$

We now make a change of variables in equation (A.3). We set

$$z = \frac{\sqrt{1 - w^2}}{\sqrt{1 - w^2\sin^2 x}}. \qquad (A.4)$$

As a result, instead of equation (A.3) we obtain

$$\Psi_0^{(l)}(\omega^2) = \int\limits_{\sqrt{1-w^2}}^{1} \frac{dzK\left(\frac{wz}{\sqrt{1-w^2}}\right)}{\sqrt{[z^2-(1-w^2)](1-z^2)}}. \quad \text{(A.5)}$$

The integral in equation (A.5) can be expressed in terms of elliptic functions. According to [20]

$$\Psi_0^{(l)}(\omega^2) = \frac{1}{1+\sqrt{1-w^2}} K'\left(\frac{\sqrt{1-w^2}\left(1+\sqrt{1-\frac{w^2}{1-w^2}}\right)}{1+\sqrt{1-w^2}}\right) \quad \text{(A.6)}$$

$$\times K\left(\frac{\sqrt{1-w^2}\left(1-\sqrt{1-\frac{w^2}{1-w^2}}\right)}{1+\sqrt{1-w^2}}\right).$$

For *b* modes, in the frequency range $2\omega_2^2 \le \omega^2 \ll \omega_3^2$, we have

$$g_b(\omega^2) = \frac{a^2 b}{(2\pi)^3}\iint\limits_{-\pi/a}^{\pi/a} dk_x dk_y \int dk_z \delta(\omega^2 - \omega_b(\mathbf{k})^2)$$

$$= \frac{1}{2\pi^3 \omega_\perp b}\iint\limits_{-\pi/a}^{\pi/a} dxdy \int \frac{d(k_z^2 \omega_\perp b^2)}{2k_z}$$

$$\times \delta\left[\left(\sqrt{\omega^2 - \omega_2^2(\sin^2 x + \sin^2 y)} - \frac{k_z^2 \omega_\perp b^2}{\pi}\right)\right. \quad \text{(A.7)}$$

$$\left.\times\left(\sqrt{\omega^2 - \omega_2^2(\sin^2 x + \sin^2 y)} + \frac{k_z^2 \omega_\perp b^2}{\pi}\right)\right]$$

$$= \frac{\Psi_0^{(b)}}{2\pi^2\sqrt{\pi\omega_\perp \omega^3}},$$

$$\Psi_0^{(b)} = \int\limits_0^{\pi/2} dx\left(1 - \frac{\omega_2^2}{\omega^2}\sin^2 x\right)^{-3/4}$$

$$\times \int\limits_0^{\pi/2} dy\left(1 - \frac{\omega_2^2}{\omega^2 - \omega_2^2 \sin^2 x}\sin^2 y\right)^{-3/4}.$$

APPENDIX B

We now consider a one-dimensional chain with the dispersion law

$$\tilde{\omega}_l^2(\mathbf{k}) = 2\omega_\perp^2 \sin^2 \frac{k_z b}{2} \quad \text{(B.1)}$$

and heavy impurities. In this case exact analytical expressions can be obtained for the Green's function $G_l^0(\omega^2)$ and for the parameters of a quasi-local level.

First, we have, using equation (B.1),

$$\frac{1}{\pi}\mathrm{Im}\tilde{G}_l^0(\omega^2) = \tilde{g}_l(\omega^2) = \frac{1}{N}\sum_{k_z}\delta(\omega^2 - \tilde{\omega}_l^2(\mathbf{k}))$$

$$= \frac{b}{2\pi\omega_\perp^2}\frac{1}{b}\int\frac{d\cos(k_z b)}{-\sin(k_z b)}\delta\left(\cos(k_z b) - \frac{\omega_\perp^2 - \omega^2}{\omega_\perp^2}\right) \quad \text{(B.2)}$$

$$= \frac{1}{\pi\omega}\frac{1}{\sqrt{2\omega_\perp^2 - \omega^2}}.$$

Second, by definition

$$\mathrm{Re}\tilde{G}_l^0(\omega^2) = \int\limits_0^\infty \frac{d\omega'^2}{\pi} P\frac{1}{\omega^2 - \omega'^2}\mathrm{Im}\tilde{G}_l^0(\omega^2). \quad \text{(B.3)}$$

The integral appearing in equation (B.3) can be calculated using the substitution

$$\omega'^2 = 2\omega_\perp^2 \sin^2 u. \quad \text{(B.4)}$$

We obtain

$$\mathrm{Re}\tilde{G}_l^0(\omega^2) = \frac{2}{\pi\omega}\frac{1}{\sqrt{2\omega_\perp^2 - \omega^2}}. \quad \text{(B.5)}$$

Using the relations (2.27) and (2.29) and equations (B.2) and (B.5), we can determine the characteristic frequency and width of a quasi-local level:

$$\tilde{\omega}_r = \frac{\pi}{\sqrt{2|\epsilon|}}\frac{\omega_\perp}{\sqrt{1+\pi/2|\epsilon|}},$$
$$\tilde{\Gamma}_r(l) = \frac{\pi}{2}\omega_r\left(1 - \frac{\omega_r^2}{2\omega_\perp^2}\right). \quad \text{(B.6)}$$

Let us now compare $\tilde{\omega}_r$ and $\tilde{\Gamma}_r(l)$. According to the relations (B.6), the condition for the existence of an impurity level, $\tilde{\Gamma}_r(l)/\tilde{\omega}_r \ll 1$, holds only near the upper limit of the spectrum, where $\tilde{\omega}_r \le 2\omega_\perp^2$.

APPENDIX C

We now consider the case of *l* modes, and we obtain a concrete expression for the factor $J_l(\mathbf{q}; \omega, \Omega)$ which appears in equation (3.6) for the vertex part in the Bethe–Salpeter equation for the two-particle Green's function. To this end, we switch in the expression for J_l from summation over **k** to integration over $d\mathbf{k}$, for which we employ the relation (A.2). We calculate the integral over dk_z, using the representation for the

Green's function in the form (2.31), using residues. We obtain

$$J_l(\mathbf{q};\,\omega,\Omega) = \frac{\sqrt{2}\pi a^2\tau_i^{(l)}}{2\pi^3\omega^2\omega_\perp}$$
$$\times\iint\limits_{-\pi/a}^{\pi/a}\frac{dk_x dk_y}{\sqrt{1-\frac{\omega_\parallel^2}{\omega^2}\left(\sin^2\frac{q_x a}{2}+\sin^2\frac{q_y a}{2}\right)}}$$
$$\times\left\{1+i\Omega\tau_i^{(l)}+i\frac{\tau_i^{(l)}\omega_\parallel^2}{2\omega}\right. \qquad \text{(C.1)}$$
$$\times\left[\sin^2\frac{q_x a}{2}\sin(k_x a)+\sin^2\frac{q_y a}{2}\sin(k_y a)\right]$$
$$\left.-i(\mathbf{v}_\perp\mathbf{q}_\perp)\tau_i^{(l)}\left[1-\frac{\omega_\parallel^2}{\omega^2}\left(\sin^2\frac{q_x a}{2}+\sin^2\frac{q_y a}{2}\right)\right]^{1/2}\right\}^{-1}.$$

In the situation where the back coherent scattering processes occur, the conditions $q_\perp l_i \ll 1$ and $\Omega\tau_i^{(l)}(\omega) \ll 1$ should be satisfied (here $l_i = \mathbf{v}_\perp\tau_i^{(l)}$ is the elastic mean free path length). We shall also consider frequency ranges such that $(\omega_\parallel^2\,\tau_i^{(l)}/\omega) \ll 1$ (we recall that $\omega_\parallel$ is a parameter characterizing the "entanglement" of the chains). On this basis, we represent the expression in the braces in equation (C.1) in the form of a geometric progression. The integrals of the odd functions vanish. As a result, we have

$$J_l(\mathbf{q};\,\omega,\Omega)\approx\frac{2\sqrt{2}\tau_i^{(l)}}{\pi^2\omega^2\omega_\perp}\{(1+i\Omega\tau_i^{(l)}-\tau_i^{l2}v_\perp^{(l)2}q_\perp^2)\Psi_0^{(l)}$$
$$-4(\Psi_2^{(l)}-\Psi_4^{(l)})\left(\frac{\tau_i^{(l)}\omega_\parallel^2}{2\omega}\right)^2\left(\sin^2\frac{q_x a}{2}+\sin^2\frac{q_y a}{2}\right) \qquad \text{(C.2)}$$
$$\left.+\Psi_2^{(l)}\frac{2\omega_\parallel^2}{\omega^2}v_\perp^{(l)2}\tau_i^{(l)2}q_\perp^2\right\}.$$

The functions $\Psi_n^{(l)}$ were determined above in the main part of the text.

REFERENCES

1. E. Akkermans and R. Maynard, Phys. Rev. B **32**, 7850 (1985).
2. T. R. Kirpatrik, Phys. Rev. B **31**, 5746 (1985).
3. J. E. Graebner, B. Golding, and L. C. Allen, Phys. Rev. B **34**, 5696 (1986).
4. Qian-Jin Chu and Zhao-Qing Zhag, Phys. Rev. B **38**, 4906 (1988).
5. H. Bottger and M. Theuerkauf, Phys. Status Solidi B **150**, 73 (1988).
6. A. P. Zhernov, E. I. Salamatov, and E. P. Chulkin, Phys. Status Solidi B **165**, 355 (1991); **168**, 81 (1991).
7. A. P. Zhernov and E. P. Chulkin, Zh. Éksp. Teor. Fiz. **109**, 602 (1996) [JETP **82**, 321 (1996)].
8. M. A. Ivanov and Yu. V. Skripnik, Fiz. Tverd. Tela (Leningrad) **32**, 2965 (1990) [Sov. Phys. Solid State **32**, 1722 (1990)].
9. M. A. Ivanov, A. M. Kosevich, E. S. Syrkin, *et al.*, Fiz. Nizk. Temp. **19**, 434 (1993) [Low Temp. Phys. **19**, 305 (1993)].
10. A. P. Zhernov and E. P. Chulkin, Zh. Éksp. Teor. Fiz. **113**, 930 (1998) [JETP **86**, 507 (1998)].
11. I. M. Lifshits, Zh. Éksp. Teor. Fiz. **22**, 475 (1952).
12. E. G. Brovman, Yu. M. Kagan, and A. Kholas, Zh. Éksp. Teor. Fiz. **61**, 2429 (1971) [Sov. Phys. JETP **34**, 1300 (1972)].
13. E. G. Brovman, Yu. M. Kagan, and A. Kholas, Zh. Éksp. Teor. Fiz. **62**, 1492 (1972) [Sov. Phys. JETP **35**, 783 (1972)].
14. Yu. M. Kagan and V. V. Pushkarev, Zh. Éksp. Teor. Fiz. **73**, 967 (1977) [Sov. Phys. JETP **46**, 511 (1977)].
15. N. W. Ashcroft, Phys. Rev. Lett. **21**, 1748 (1968).
16. S. Tanuma and A. V. Palnichenko, J. Mater. Res. **10**, 1120 (1995).
17. A. S. Gurov, V. N. Kopylov, and K. Kusano, Phys. Rev. B **56**, 11629 (1997).
18. G. Leibfried and W. Ludwig, *The Theory of Anharmonic Effects in Crystals* (Inostrannaya Literatura, Moscow, 1968).
19. G. Leibfried and N. Broier, *Point Defects in Metals. Introduction to the Theory* (Springer, Heidelberg, 1978; Mir, Moscow, 1981).
20. A. A. Prudnikov, Yu. A. Bychkov, and O. I. Marychev, *Integrals and Series. Supplement* (Nauka, Moscow, 1986), p. 184.

Translation was provided by AIP

Journal of Experimental and Theoretical Physics, Vol. 90, No. 2, 2000, pp. 319–323.
Translated from Zhurnal Éksperimental'noĭ i Teoreticheskoĭ Fiziki, Vol. 117, No. 2, 2000, pp. 362–367.

SOLIDS
Structure

Vibrational Spectra of the Ammonia Halides NH_4I and NH_4F at High Pressures

V. P. Glazkov[2], D. P. Kozlenko[1,] *, B. N. Savenko[1], and V. A. Somenkov[2]

[1] *Joint Institute for Nuclear Research, Dubna, 141980 Russia*

[2] *Russian Research Centre Kurchatov Institute, Moscow, 123182 Russia*

**e-mail: denk@nf.jinr.ru*

Received June 18, 1999

Abstract—The vibrational spectra of ammonium iodide NH_4I at pressures up to 4.1 GPa and ammonium fluoride NH_4F at pressures up to 4.7 GPa were investigated by inelastic incoherent neutron scattering. The pressure dependences of the transverse optical translational and librational modes were obtained. The behavior of the rotational potential barrier for the ammonium ion as a function of the lattice parameter for disordered and ordered cubic phases of ammonium halides with CsCl type structure were calculated. The results obtained confirm that the transition from an orientationally disordered cubic phase into an ordered cubic phase in ammonium halides occurs at close critical values of the positional parameter of hydrogen (deuterium). © *2000 MAIK "Nauka/Interperiodica".*

1. INTRODUCTION

The study of the effect of high pressures on ammonium halides is of interest for clarifying the changes in the structure and excitation spectra in order to determine the characteristics of the interaction potentials and the nature of phase transitions occurring with a change in volume [1].

One of the most important questions concerning the dynamics of ammonium halides is the behavior of the librational mode of the ammonium ion accompanying orientational phase transitions arising with a change in the external conditions (temperature and pressure). This question is best studied by neutron spectroscopy, which makes it possible to determine the position of the libration peak directly from the experimental data. In contrast to this, the optical infrared and Raman spectroscopy methods are insensitive to the librational mode, and it is determined only from the overtones and Raman modes, which can result in computational errors. However, the possibility of performing inelastic neutron scattering experiments at sufficiently high pressures appeared only very recently, because of the development of the anvil technique. Thus, in [2] the vibrational spectrum of NH_4Cl was studied at pressures up to 4 GPa. The pressure dependences of the librational and transverse optical translational modes were obtained, and it was shown that their intersection together with the appearance of a phase transition at higher temperatures is possible. Similar results were recently obtained for NH_4Br [3]. This made it interesting to study the behavior of these modes under pressure for the entire class of ammonium halides, specifically, for NH_4I and NH_4F.

Our early neutron diffraction investigations of ND_4Cl, ND_4Br, ND_4I, and ND_4F at pressures up to 4–5 GPa [4, 5] showed that the structural behavior of ammonium halides at high pressures is characterized by the presence of a single critical value of the positional parameter of deuterium (hydrogen) u_{cr}, determining the point of the orientational phase transition and tentatively attributed to the change in the relief of the potential as volume decreases [5]. The presence of an orientationally disordered cubic phase II with CsCl-type structure, which, as pressure increases to a certain value transforms into an orientationally ordered cubic phase IV (CsCl-type structure with ferromagnetic type ordering) in the case of NH_4Cl ($P \approx 0.6$ GPa [4]) and NH_4Br ($P \approx 2.5$ GPa [4]) or a tetragonal phase V (antiferromagnetic-type ordering) in the case of NH_4I ($P \approx 8.3$ GPa [6]) with approximately the same critical value of the positional parameter, is characteristic for all ammonium halides except NH_4F.

In contrast to other ammonium halides, NH_4F is characterized by the presence of several phases with hexagonal symmetry with a different type of ordering of the ammonium ions [5]. In NH_4F the value of the positional parameter initially is greater than the critical value, and for it there exists only an ordered cubic phase III, which is isostructural to the phase IV of other ammonium halides.

Our objective in the present work was to investigate the vibrational spectra of the cubic phases of NH_4I and NH_4F at high pressures by inelastic neutron scattering in order to obtain information about the characteristics of the rotational potential and the change in this potential at orientational phase transitions.

1063-7761/00/9002-0319$20.00

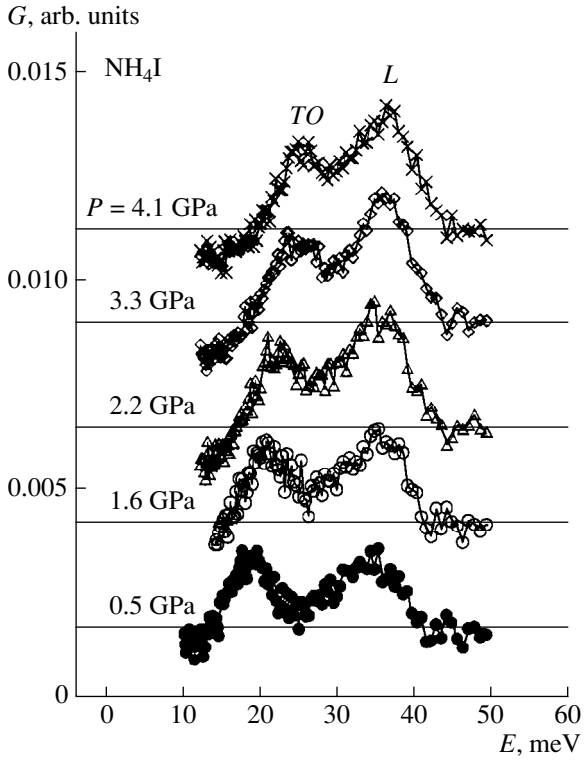

Fig. 1. Generalized density of vibrational states for NH_4I at various pressures.

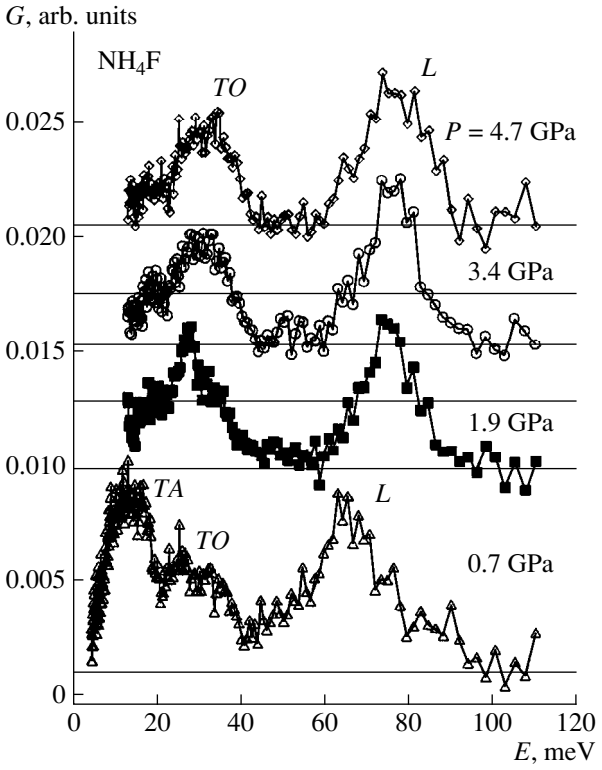

Fig. 2. Generalized density of vibrational states for NH_4F at various pressures.

2. DESCRIPTION OF THE EXPERIMENT

The experiments were performed at room temperature using a DN-12 spectrometer [7] in a pulsed high-flux IBR-2 reactor in the Laboratory of Neutron Physics at the Joint Institute of Nuclear Research (Dubna), using a high-pressure chamber with sapphire anvils [8]. The sample volume was $V \approx 2$ mm^3. The pressure in the chamber was measured according to the shift of the ruby luminescence line to within 0.05 GPa. A cooled beryllium filter positioned at the scattering angle $2\theta = 90°$ was used to analyze the neutron energy transfer [3]. The final energy of the detected neutrons was $E = 4$ meV, and the characteristic measurement time for one spectrum was 40 h.

3. BASIC RESULTS

The spectra of the generalized density of vibrational states $G(E)$ of the cubic phases of NH_4I and NH_4F (Figs. 1 and 2) contain two peaks corresponding to the transverse optical translational mode (*TO*) and the librational mode (*L*). For NH_4I the frequencies of these modes are close, and the corresponding peaks partially overlap. For NH_4F the peak of the *L* mode was shifted substantially to higher energies compared with NH_4I and no overlapping of the peaks of the *TO* and *L* modes is observed. The pressure dependences obtained for the frequencies of the *TO* and *L* modes for NH_4I and NH_4F are shown in Figs. 3 and 4. The experimental values of ν_i, obtained at different pressures from the data in this and other works, are presented in Table 1.

The NH_4I sample does not undergo phase transformations in the pressure range $0.05 < P < 8.3$ GPa, and the frequencies of the *TO* and *L* modes increase linearly with increasing pressure (Fig. 3), just as in NH_4Cl [2]. The dependence $\nu_{TO}(P)$ obtained agrees with the Raman spectroscopy data [10], and the dependence $\nu_L(P)$ differs somewhat from the dependence computed

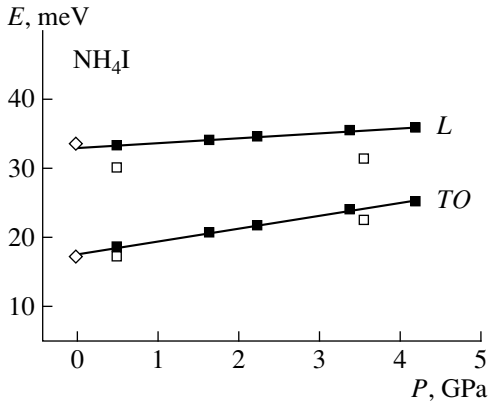

Fig. 3. Pressure dependences of the frequencies of the *TO* and *L* modes for NH_4I. (■) Data from this work; (◇) neutron spectroscopy data [9]; (□) Raman spectroscopy data [10].

from the data of [10]. Extrapolation of both dependences to $P = 0$ gives values of ν_{TO} and ν_L close to the values obtained in [9], which were measured for the NH_4I(II) phase at $T = -25°C$ and $P = 0$ (Fig. 3).

The Grüneisen parameters of the *TO* and *L* modes $\gamma_i = -(d\ln\nu_i/d\ln V)_T$, presented in Table 2 together with the values of the derivatives $d\nu_i/dP$, were calculated for the cubic phases NH_4I(II) at $P = 0.5$ GPa and NH_4F(III) at $P = 1.9$ GPa. The following values of the bulk modulus $B = B_0 + B_1P$ were used in the calculations: $B(P = 0.5\ \text{GPa}) = 16.8(7)$ GPa for NH_4I [11] and $B(P = 1.9\ \text{GPa}) = 93.4(7)$ GPa for NH_4F [4]. The value obtained $\gamma_i(\nu_{TO}) = 1.7(2)$ for NH_4I that is smaller than the value determined in [10] from the Raman spectra: $\gamma_i(\nu_{TO}) = 2.4(3)$.

At room temperature NH_4F possesses the wurtzite structure (NH_4F(I) phase, space group $P6_3mc$), which at $P = 0.45$ GPa transforms into a complicated rhombohedral structure containing 24 molecules in a hexagonal unit cell (NH_4F(II) phase, space group $R3c$) [5]. The transition into an ordered cubic phase of NH_4F(III) occurs at pressure $P = 1.15$ GPa [5].

The spectrum $G(E)$ of the rhombohedral phase of NH_4F(II) measured at $P = 0.7$ GPa has three peaks, corresponding to a transverse acoustic mode (*TA*) and *TO* and *L* modes. A characteristic feature of the spectrum is the very strong *TA* peak, whose intensity is higher than that of the other peaks.

For NH_4F a small increase of the frequency ν_{TO} of the transverse optical mode from 28.6 to 30.8 meV is observed at the I–II transition, after which it decreases to 27.2 meV at a II–III transition (Fig. 4). The librational mode behaves in the opposite manner: ν_L decreases from 68.9 to 65.2 meV at the I–II transition and increases to 74.7 meV at the II–III transition (Fig. 4). The values of ν_{TO} and ν_L at $P = 0$ are taken from [9]. In the III cubic phase, as the pressure increases further, the frequencies of both modes increase, and ν_L remains essentially pressure-independent. The value of ν_L for NH_4F(III), ν_L ($P = 1.9$ GPa) = 74.7 meV, is much greater than the similar values for other ammonium halides ($\nu_L \approx 40$ meV) in phases with similar structure. This could be due to the presence of strong hydrogen bonds in NH_4F [12].

The lower value of ν_L for the NH_4F(II) phase seems to be explained by the fact that this structure has stronger hydrogen bonds N-H-F than the NH_4F(I) and NH_4F(III) phases. The results of the neutron diffraction investigation of deuterated ammonium fluoride ND_4F(II) [12] have shown that the distance between D and F in this structure is approximately 5% greater than in ND_4F(I), and the N–D–F angles are distorted by approximately 10° compared with the corresponding value 180° for ND_4F(I) and ND_4F(III).

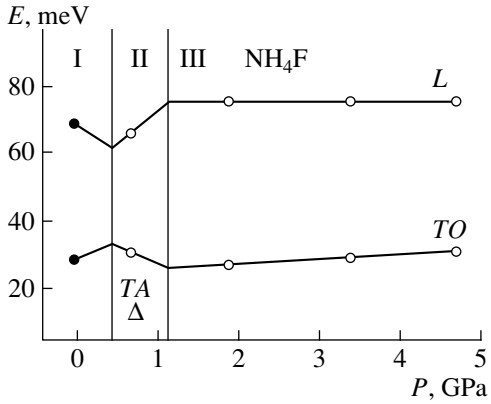

Fig. 4. Pressure dependences of the frequencies of the *TO* and *L* modes for NH_4F. (○) Data from this work; (●) neutron spectroscopy data [9]; (△) value of the *TA* mode for the rhombohedral phase of NH_4F(II).

4. DISCUSSION

There exist several models [13–15] that make it possible to establish a relation between the frequency of the librational mode and the rotational potential barrier for the ammonium ion in a cubic lattice. In [13] the vibrations of an anharmonic anisotropic oscillator in the field of

Table 1. Values of the frequencies of the *TO* and *L* modes in NH_4I and NH_4F at various pressures

P, GPa	ν_L, meV	ν_{TO}, meV
	NH_4I, II phase	
0 ($T = -25°C$) [9]	34.1(7)	17.1(7)
0.5	33.3(9)	18.6(9)
1.6	34.3(9)	20.8(9)
2.2	34.9(9)	22.0(9)
3.3	35.9(9)	24.0(9)
4.1	36.2(9)	25.4(9)
	NH_4F	
0 (I phase) [9]	68.9 ± 2.2	28.6(7)
0.7 (II phase)	65.2(9)	30.8(9)
1.9 (III phase)	74.7(9)	27.2(9)
3.4	75.6(9)	30.3(9)
4.7	76.1(9)	31.5(9)

Table 2. Grüneisen parameters of the *TO* and *L* modes for NH_4I at $P = 0.5$ GPa and NH_4F at $P = 1.9$ GPa

Mode	$d\nu_i/dP$, meV/GPa	γ_i
	NH_4I	
$\nu_{TO} = 18.6$ meV	1.89	1.7(2)
$\nu_L = 33.3$ meV	0.82	0.4(1)
	NH_4F	
$\nu_{TO} = 27.2$ meV	1.52	5.2(2)
$\nu_L = 74.7$ meV	0.5	0.63(1)

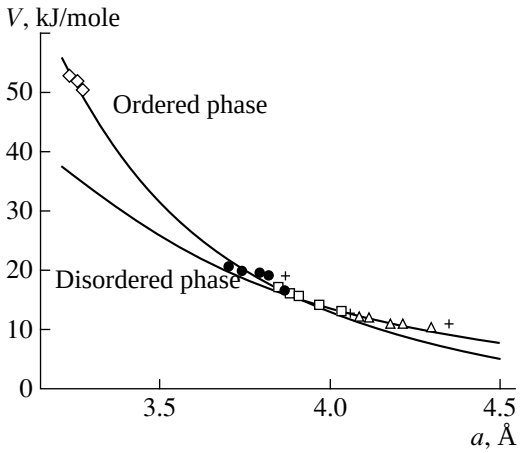

Fig. 5. Rotational potential barrier V_0 versus the lattice parameter for the orientationally disordered and ordered phases of ammonium halides. (△) NH_4I, (□) NH_4Br [3], (●) NH_4Cl [2], (◇) NH_4F, (+) values of the activation energy for NH_4Cl, NH_4Br, and NH_4I obtained by the NMR method [13].

a phenomenological electrostatic potential [16], corresponding to cubic symmetry of the crystal and tetragonal symmetry of the ammonium ion, were studied:

$$V = \frac{V_0}{2}\sum_{i=1}^{4}\left(\frac{x_i^4 + y_i^4 + z_i^4}{l_{\text{N–H}}^4} - \frac{3}{5}\right), \qquad (1)$$

where $l_{\text{N–H}}$ is the length of the N–H bond, and x_i, y_i, and z_i are the coordinates of the hydrogen atoms in the ammonium ion.

The height of the rotational potential barrier V_0 is determined by the length of the N–H bond and the unit-cell parameter:

$$V_0 = 46.8\left(\frac{e}{4}\right)^2 \frac{l_{\text{N–H}}^4}{a^5}. \qquad (2)$$

In this model the relation between V_0 and ν_L has the form

$$V_0 = \frac{1}{16}\frac{(\nu_L + 5h^2/2I)^2}{h^2/2I}, \qquad (3)$$

where h is Planck's constant, I is the moment of inertia of the ammonium ion, and ν_L is expressed in energy units.

Table 3. Values of the parameters B and C for the potential (3)

Parameter	Disordered phase	Ordered phase
B, kJ/mole	5.087×10^3	74.098×10^3
C	4.2(2)	6.2(2)

If the dependence $\nu_L(P)$ and the lattice parameter dependences $a(P)$ are known, the dependence $V_0(a)$, which characterizes V_0 as a function of the interionic distance in the crystal, can be calculated. It is known that the behavior of the librational mode changes at a II–IV orientational phase transition, which occurs in ammonium halides under pressure [2]. Figure 5 shows the dependences $V_0(a)$ for the disordered and ordered cubic phases of ammonium halides, calculated from the neutron spectroscopy data for $\nu_L(P)$ [2] (NH_4Cl), [8] (NH_4Br), and the results of the present work for NH_4I and NH_4F. The $a(T)$ data and the values of the II–IV transition pressures for NH_4Cl and NH_4Br are taken from [3, 4]. The values of V_0 for $P = 0$ agree with the values obtained for the activation energy of the NH_4^+ ion in ammonium halides by the nuclear magnetic resonance (NMR) method [13].

Both potentials intersect at the lattice parameter a_{cr} = 3.88(6) Å (Fig. 5). This is equivalent (for the same value of the N–H bond length) to approximately the same value of the positional parameter ($u_{cr} = l_{\text{N–H}}/a_{cr}\sqrt{3}$), characterizing the II–IV orientational phase transition, which occurs for values of the lattice parameter close to a_{cr}, a = 3.83 Å in NH_4Cl and a = 3.89 Å in NH_4Br [4].

Interpolation of the dependences $V_0(a)$ for the II and IV phases by a function of the type

$$V_0(a) = B/a^C \qquad (4)$$

(Fig. 5) gives the values for the parameters B and C presented in Table 3.

The value of the exponent for the disordered phase is close to C = 5. This shows that the relation (3) is a good approximation for determining V_0. At the same time, the value of C for the ordered phase is closer to C = 7, which is probably due to the fact that in this case the contribution of the octupole-octupole interaction of the ammonium ions to the energy of the system increases [17, 18], $V_{O–O} \sim I_3^2/a^7$, where I_3 is the octupole moment of the NH_4^+ ions. The magnitude of this contribution depends on the relative orientation of the NH_4^+ ions and is small for an orientationally disordered phase [18]. The fact that the exponents differ from C = 5 (for the disordered phase) and C = 7 (for ordered phase) shows that higher-order terms must be taken into account (anharmonicity, multipoles, and so on).

Thus, the results show that the dependence of the rotational potential of the barrier on the interatomic distance changes at an orientational phase transition. It is possible that a situation similar to that in ammonium halides also occurs for orientational transitions in other systems with molecular cations, where the compressibility is determined primarily by the anionic sublattice. In this case, assuming that

$$a_0 - (da/dP)P_{tr} = a_{cr},$$

we obtain a simple estimate for the transition pressure

$$P_{tr} = (a_{cr} - a_0)/\beta,$$

where a_0 is the lattice parameter at atmospheric pressure and $\beta = da/dP$ is the linear compressibility.

Interpolation of the pressure dependences $\nu_L(P)$ and $\nu_{TO}(P)$ for NH_4I to higher pressures indicates that they can intersect, $\nu_L = \nu_{TO}$ at $P \approx 14$ GPa. Since the ammonium ion participates in librational and translational motions, resonance between *TO* and *L* modes is possible and could result in structural instability and a phase transition at high pressures. Raman spectroscopy [10] at high pressures showed strong changes in the spectra, on the basis of which it was inferred that a phase transition into a new, previously unknown, high-pressure phase $NH_4(V)$ occurs at $P_V = 5.4(5)$ GPa. A neutron diffraction investigation of deuterated ammonium iodide ND_4I [5] showed that a real structural phase transition occurs only at a much higher pressure $P = 8.3$ GPa. Since at this pressure the difference of the frequencies of the *TO* and *L* modes should not exceed 5 meV, this could indicate the existence of an interaction between the *TO* and *L* modes, which changes the high-pressure dynamics of NH_4I and in consequence leads to a structural phase transition.

5. CONCLUSIONS

The results of this work, which were obtained by inelastic neutron scattering at high pressures, show that orientational phase transitions in ammonium halides can be described, using previously proposed theoretical models, on the basis of a change in the rotational potential as a function of the distance. The intersection of the potentials of the ordered and disordered phases at close values of the lattice parameter or positional parameter for different compounds explains the previously established characteristics of the structural behavior of ammonium halides and makes it possible to predict the behavior of other similar systems.

ACKNOWLEDGMENTS

We are grateful to N.N. Parshin and S.L. Platonov for assisting in the preparation and performance of the experiments.

This work was supported by the Russian Foundation for Fundamental Research (projects nos. 97-02-16622 and 97-02-17587) and the State program "Neutron investigations of condensed media."

REFERENCES

1. S. J. Jeon, R. F. Porter, and A. L. Ruoff, J. Raman Spectrosc. **19**, 179 (1988).
2. A. M. Balagurov, B. N. Savenko, A. V. Borman, *et al.*, High Press. Res. **14**, 55 (1995).
3. A. V. Balagurov, V. P. Glazkov, D. P. Kozlenko, *et al.*, Preprint No. R13-97-312 (Joint Institute of Nuclear Research, Dubna, 1997).
4. A. V. Balagurov, D. P. Kozlenko, B. N. Savenko, *et al.*, Fiz. Tverd. Tela (St. Petersburg) **40**, 142 (1998) [Phys. Solid State **40**, 127 (1998)].
5. V. P. Glazkov, D. P. Kozlenko, B. N. Savenko, *et al.*, Kristallografiya **44**, 55 (1999) [Crystallogr. Rep. **44**, 50 (1999)].
6. V. P. Glazkov, D. P. Kozlenko, B. N. Savenko, *et al.*, Physica B **265**, 92 (1999).
7. V. L. Aksenov, A. M. Balagurov, S. L. Platonov, *et al.*, High Press. Res. **14**, 181 (1995).
8. V. P. Glazkov and I. N. Goncharenko, Fiz. Tekh. Vys. Davleniĭ **1**, 56 (1991).
9. V. M. Myers, J. Chem. Phys. **46**, 4034 (1967).
10. A. M. Heyns, K. R. Hirsh, and W. B. Holzapfel, J. Chem. Phys. **73**, 105 (1980).
11. P. W. Bridgman, Proc. Am. Acad. Arts Sci. **74**, 21 (1940); **76**, 1 (1945).
12. A. C. Lawson, R. B. Roof, J. D. Jorgensen, *et al.*, Acta Crystallogr. **45**, 212 (1989).
13. H. S. Gutowsky, G. E. Pake, and R. Bersohn, J. Chem. Phys. **72**, 643 (1954).
14. G. Venkataraman, K. Usha Deniz, P. K. Iyengor, *et al.*, J. Phys. Chem. Solids **27**, 1103 (1966).
15. C. W. Garland and B. B. Weiner, J. Chem. Phys. **53**, 1609 (1970).
16. T. Nagamiya, Proc. Phys. Math. Soc. Jpn. **24**, 137 (1942).
17. Y. Ebisuzaki, J. Chem. Phys. **61**, 3170 (1974).
18. O. H. Seeck, D. Hupfeld, H. Krull, *et al.*, Phys. Rev. B **58**, 623 (1998).

Translation was provided by AIP

Journal of Experimental and Theoretical Physics, Vol. 90, No. 2, 2000, pp. 324–329.
Translated from Zhurnal Éksperimental'noĭ i Teoreticheskoĭ Fiziki, Vol. 117, No. 2, 2000, pp. 368–374.

SOLIDS
Structure

Anomalous Birefringence of Light in Free-Standing Samples of Porous Silicon

M. E. Kompan[1, *], J. Salonen[2], and I. Yu. Shabanov[1]

[1] *Ioffe Physicotechnical Institute, Russian Academy of Sciences, St. Petersburg, 194021 Russia*
**e-mail: kompan@solid.ioffe.rssi.ru*
[2] *Turku University, Finland*

Received July 15, 1999

Abstract—The birefringence of light in freely suspended samples of porous silicon is observed and investigated. The effect is interpreted as "shape birefringence," i.e., the effect caused by the structure of a material consisting of anisotropic formations with sizes less than the wavelength of the light and with a predominant orientation. It is checked experimentally that the samples do not possess optical activity or optical anisotropy in the plane of the porous-silicon film. It is determined that the effect is observed for polarization of incident light that rules out the possibility of observing birefringence in a uniform optical medium, and it is not observed in the conventional experimental geometry. Qualitative explanations are given for the anomalous character of the observed defect. © *2000 MAIK "Nauka/Interperiodica".*

1. INTRODUCTION

Increasingly more complicated objects are being studied in modern condensed-state physics. An example of such an object is porous silicon, which has been actively investigated in the last ten years in connection with the possibilities of producing a new generation of optoelectronic devices based on it [1]. We recall that according to current ideas porous silicon is a self-organizing formation consisting of silicon "quantum wires" with transverse dimensions of up to tens of angstroms. Since the cross sections of the wires are small, the properties of the wires (and the properties of the material as a whole) are largely determined by quantum confinement in the electronic and phonon subsystems [2, 3]. The character of the structure of a material consisting of individual filaments also influences the properties of the material and is a source of additional effects (see, for example, [4]).

Just as for other complicated objects, besides the "logical" and potentially helpful properties, porous silicon demonstrates unexpected effects, whose nature remains puzzling. Specifically, manifestations of ferromagnetism in porous silicon were reported in [5]. In [6], it was observed in an investigation of the magnetooptic Faraday effect in porous silicon that the magetooptic rotation decreases as light passes through the sample at an angle to the direction normal to the sample surface. It was inferred that the effect is due to detection of the magnetization component lying in the plane of the sample. However, subsequent investigations showed that when the sample is inclined, the polarization of the transmitted light changes irrespective of the presence of a magnetic field. Thus, the observed change in polarization of the transmitted light was found to be a result of the birefringence of light in porous silicon.

We know of no works on birefringence in porous silicon. The relative simplicity of the structural units (silicon atoms) and the cubic crystal lattice, just as in the initial crystalline silicon (see [1]), rule out the basic conventional reasons for the appearance of birefringence in crystals. At the same time, the mesoscopic structural elements—quantum wires—can easily be responsible for birefringence because of shape anisotropy, even if the material composing the wires is completely isotropic. There also exist specific mechanisms that can lead to birefringence in low-dimensional objects (see, for example, [7]).

In the present paper we describe the experimental results obtained from investigations of the basic manifestations of the birefringence observed in porous silicon.

2. EXPERIMENTAL TECHNIQUE AND SAMPLE PREPARATION

The samples for the investigations were obtained by anodic etching of standard silicon plates with resistivity 0.015–0.025 Ω/cm and (100) orientation in a 1 : 1 mixture of 40% HF with ethanol with no additional illumination of the samples. The anodization current was maintained at 70 mA/cm^2. After the layer was allowed to form under the indicated conditions for 6–16 min, the etch current density increased by an order of magnitude, which resulted in separation of the layer formed from the substrate. The samples obtained were 15–50 μm thick and possessed a porosity of about 65%. The samples were separated from the substrate (initial silicon crystal) by sharply increasing the anodization current. Under optical monitoring the samples demonstrated the

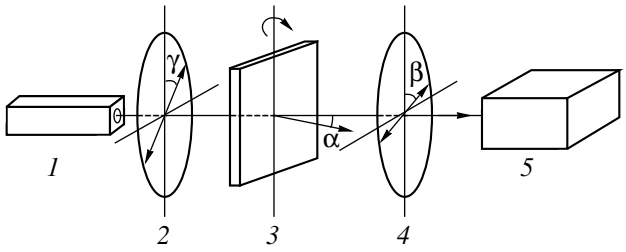

Fig. 1. Diagram of the experimental apparatus: (*1*) He-Ne laser; (*2*) additional polarizer; (*3*) sample; (*4*) analyzer; (*5*) photodetector. The letters indicate the following angles: (α) between the normal to the sample plane and the direction of incidence of the light; (β)angular position of the analyzer relative to the rotation axis of the sample; (γ) angular position of the polarizer relative to the same axis.

luminescence typical for porous silicon in the orange range of the spectrum and a shift of the Raman scattering band in the direction of lower energies by 8–10 cm $^{-1}$ as a result of confinement in the phonon subsystem.

The intensity of the light transmitted successively through a linear polarizer, a film sample of porous silicon, and an analyzer was recorded in the main body of the experiments as a function of the angular position of the analyzer. This method for describing the polarization of light, according to [8], is called the projection picture. The arrangement of the experiment and the notations for the angles used in this paper are presented in Fig. 1. In turn, the projection pictures were recorded for various angles between the normal to the sample surface and the direction of propagation of the light. Linearly polarized light, oriented in a different manner ($\gamma = 0°, 45°, 90°$) relative to the rotation axis of the sample, was used in the experiments. In the typical case the direction of the probe beam, the direction of the electric oscillations of the light wave, and the rotation axis were oriented along the Cartesian axes of the coordinate system. The experiments were performed with low-power radiation (2–4 mW) from an unfocused helium-neon laser at a wavelength of 6328 Å at room temperature.

Since the porous-silicon samples are not as perfect as conventional materials used for optical polarization investigations, the experiment showed a variance in the data and irregular deviations of the recorded dependences from the dependences dictated by the symmetry laws. Such deviations are very likely to be due to nonuniformities in the material and were not were not investigated. This article includes the regularly observable dependences, which are typical for a variety of samples.

3. EXPERIMENTAL RESULTS

1. It was observed in the experiments that rotation of the sample (see Fig. 1) changes the polarization of the light transmitted through it. The largest effect was observed in the cases where the vector **E** of the linearly polarized light incident on the sample was oriented in the direction of or perpendicular to the rotation axis of the sample, which lies in the plane of the sample. The difference in the results for these two cases was substantially smaller than the effect itself.

Figure 2 gives an idea of the character of the data directly recorded in the experiment. When the angle between the polarization plane of the incident light and the rotation axis of the sample was $\gamma = 45°$, virtually no change in polarization was observed. The corresponding dependence is presented in Fig. 2a. When the vector **E** of the light oscillations was oriented parallel or perpendicular to the rotation axis of the sample, the dependences were substantially different. The projection patterns obtained for several angles of inclination of the

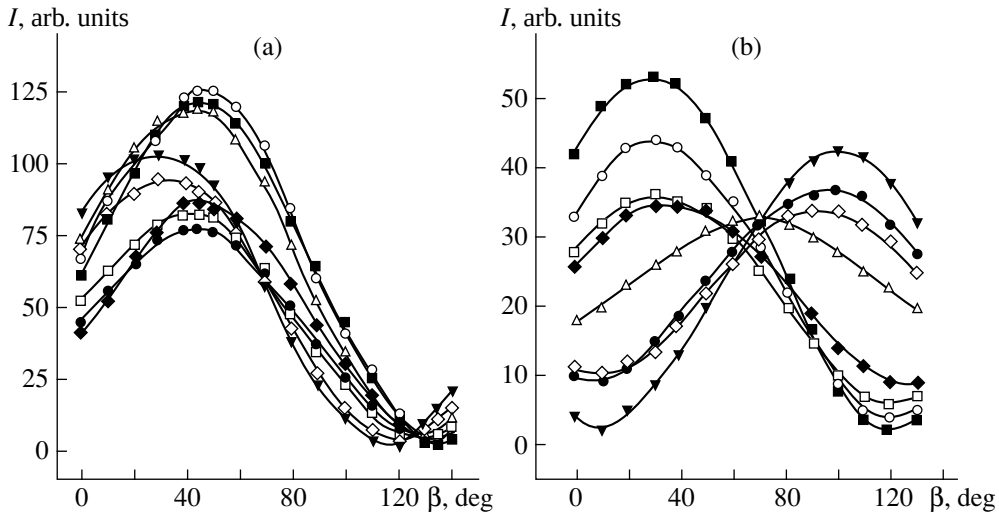

Fig. 2. Projection curves for the polarization of the light transmitted through a film sample of porous silicon for $\gamma = 45°$ (a), $\gamma = 90°$ (b), and for different angles α of rotation of the sample: ■, $\alpha = 0°$; ○, $\alpha = 10°$; △, $\alpha = 20°$; ▼, $\alpha = 30°$; ◇, $\alpha = 35°$; □, $\alpha = 40°$; ◆, $\alpha = 45°$; ●, $\alpha = 50°$.

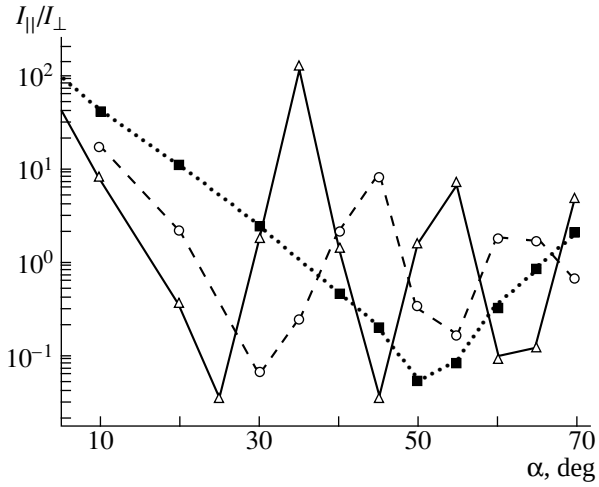

Fig. 3. Ratios of the intensities of the components with initial polarization $I_{\|}$ and the polarization component $I_{\perp}$ orthogonal to it as a function of the rotation angle α for three samples of porous silicon with thickness 15 (■), 30 (○), and 50 (△) μm. The plot demonstrates the effect of the sample thickness on the frequency of the change in polarization caused by rotation of the sample.

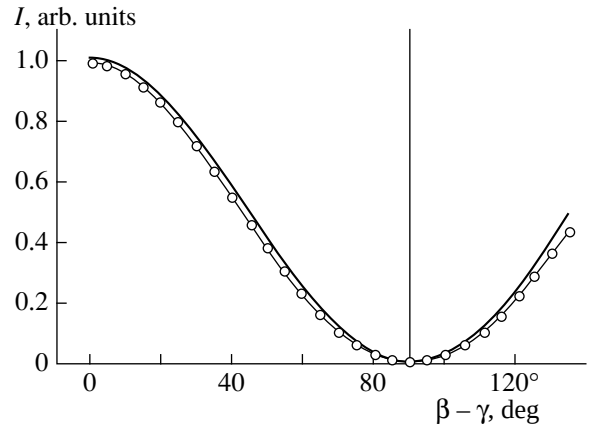

Fig. 4. Intensity of the light transmitted through the polarizer and analyzer as a function of the angle β – γ between the axes of maximum transmission with a sample of porous silicon between them (circles) and without the sample, i.e., Malus' law (solid curve). The plot demonstrates the absence of depolarization and optical activity in the sample in a direction normal to the surface.

sample ($0° < \alpha < 50°$) relative to the direction of light propagation are collected in Fig. 2b. The angle β of rotation of the analyzer relative to the position of crossing with the analyzer is plotted along the abscissa axis for all curves of the family $\gamma = 90°$, and the light intensity transmitted through the analyzer is plotted along the ordinate. The different curves in a family correspond to different angles of rotation of the sample. It is evident from the figure that as the sample rotates, the projection pattern characterizing the light polarization changes. It is important to note that as the sample rotates, the maxima and minima of the projection patterns change places, and for certain samples repeatedly, while there is almost no shift in the points of intersections of the curves.

The experiments showed that the character of the observed curves, specifically, the period of alternation of the maxima and minima, depends on the thickness of the sample. This is evident from the plots presented in Fig. 3: The period of the oscillations (as a function of the rotation angle of the sample) is smaller for thick samples.

To determine the nature of the observed effect the same series of experiments was repeated on one of the samples, after which the sample was impregnated with paraffin oil (the immersion medium for microscopes). Such treatment of the sample decreased the observed birefringence effect by approximately a factor of 2.

2. A series of additional experiments was performed in search of other manifestations of optical anisotropy. These experiments showed that the polarization of the light transmitted through the sample does not change if the light passes through the sample in a direction normal to the surface. It is evident in Fig. 4 that the light transmitted through the sample along this direction is completely extinguished by the linear analyzer. The position of the analyzer is, in this case, exactly the same as the position in which the probe beam in the absence of the sample is extinguished in the setup. The general behavior of the dependence quite accurately follows Malus' law (solid line), attesting to the fact that the light remained linearly polarized with the same direction of polarization which it had before passing through the sample.

When the polarizer and the analyzer are mutually oriented so as to achieve the maximum transmission and the sample lies between them so that the normal to the sample surface is directed along the light beam, rotation of the sample relative to the normal to its surface did not result in a periodic variation of the intensity of the light transmitted by the analyzer. In these experiments variations of intensity up to 30–40% were observed for some samples, but a characteristic angular dependence with the period π/4 was never observed (Fig. 5). It can be assumed on the basis of the latter circumstance that in the cases where a variation of the intensity was observed, it was simply caused by the inadequate optical quality of the samples and not by the presence of optical anisotropy in the plane of the sample.

We interpret the experimental results described in Section 2 as attesting unequivocally to the absence in our samples (free standing films of porous silicon) of (i) appreciable depolarization of the linearly polarized light, (ii) rotation of the polarization plane (nonmagnetic), and (iii) optical anisotropy (optic axis or its projection) lying in the plane of the films investigated. Since the samples were obtained from isotropic mate-

rial (silicon with its cubic lattice) using etching, the latter result is entirely natural.

4. DISCUSSION

The interpretation of the observed facts and the derivations can be uniquely divided into two groups.

1. In terms of its overall features, the observed effect is understandable, almost trivial. In a film material the directions along and perpendicular to the film can be nonequivalent. Characteristic oscillatory modes, which ordinarily have a different polarization, exist in anisotropic materials. These modes, usually called ordinary and extraordinary rays, propagate in the crystal without a change in the type of oscillation, but their propagation velocities are different, which corresponds to different refractive indices for these modes. When the angle of incidence of the light on the sample changes, the effective refractive indices and the optical path lengths for the ordinary and extraordinary rays change.

As a result, when the light leaves the sample, the superposition of modes can lead to light of a different polarization than the polarization at the entrance into the sample. Since the change in polarization arose because of the difference of the optical paths of the two components of the light in the sample, this change should increase as the sample thickness increases and as the angle between the normal to the sample and the direction of incidence of the light increases. Both these tendencies were clearly observed in the experiment, and the effects responsible for them can be easily described by the well-known formulas [9].

The phase shift between the components propagating with different velocity can be written in the form

$$\Delta\phi = \frac{2\pi}{\lambda} d(n_o - n_e).$$

Here $\Delta n = n_o - n_e$ is the difference of the refractive indices between the components of the light with different polarization, d is the geometric path length of the light in the sample ($d = t/\cos\theta$ for light passing through a sample of thickness t at angle θ). In turn, the angle θ can be found from the known angle of incidence and the refractive index. On the basis of previously obtained data [10], the average refractive index can be assumed to be known ($n = 1.75$ for porosity $P = 65\%$). Hence, having determined the rotation angle of the sample giving a rotation of the projection pattern by 90° (which corresponds to a transition from a maximum to a minimum in the projection pattern of the type presented in Fig. 2 or a phase shift of $\pi/2$ between components with different polarization), we obtain a difference of the coefficients for the two types of waves $\Delta n = 0.10$ that is much greater than, for example, in $ZnGeP_2$ [11] or (Al)GaInP [12]. The variance in the values of Δn obtained for different samples does not exceed 20–25%.

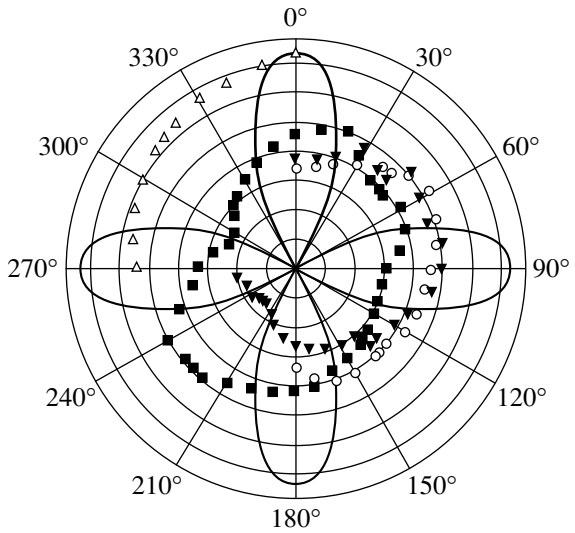

Fig. 5. Intensity of the light transmitted successively through a polarizer, the sample, and an analyzer as a function of the rotation angle of the sample with the sample rotated relative to the normal to its surface. The sample is oriented normally to the light beam, the analyzer and polarizer are initially placed in the position of maximum transmission. The curves represented by different symbols correspond to different samples. The solid curve shows the form of the dependence $\cos 4\varphi$ that would indicate the presence of an optic axis in the plane of the sample.

The experiment with a sample impregnated with paraffin oil indicates unequivocally the reason for the optical anisotropy. As indicated above, optical anisotropy in porous silicon could be due to the fact that the anisotropic elements forming the material of porous silicon have a predominant orientation. The presence of interior surfaces oriented in a definite manner in the material, taking account of the need to satisfy the boundary conditions for the light vector **E**, will cause the permittivity to be different in different directions, i.e., birefringence. The corresponding formulas and terminology are given in the well-known monograph by Born and Wolf [9]. It can be assumed that the sizes of the structural elements of porous silicon are comparable to or greater than the size of the oil molecules, so that the oil can penetrate into the porous material, equalizing the difference of the refractive indices between individual elements and the medium between them. (We note in addition that these anisotropic elements must nonetheless be smaller than the wavelength of the probing light; otherwise, the experiment would show scattering and depolarization but not birefringence.) The filling of the space between the anisotropic elements with a medium with refractive index (n_{oil}) falling between the refractive indices of the "quantum wire" material (n_{Si}) and the vacuum will obviously decrease the optical anisotropy and the birefringence which are due to the presence of anisotropic structural elements. For this reason, the result of the experiment with the impregnated sample proved that the observed anisotropy is due to the fact that the material consists of

anisotropic elements with a predominant orientation (so-called shape birefringence [9]). This result, without question, agrees with the existing ideas about the structure of porous silicon.

2. However, an attempt to give a more detailed interpretation of the results is dismayingly unproductive.

It must be kept in mind, first and foremost, that the effect is also observed for the directions of oscillations of the light vector **E** along the rotation axis of the sample. This fact renders meaningless the formal interpretation presented above, at least for the case of an optically uniform medium. Indeed, for the vector **E** of the electric oscillations of the light directed along the rotation axis of the sample ($\gamma = 0$, see Fig. 1), the direction of the vector **E** does not change either at the entrance of the light into or at the exit from the sample; **E** will lie in the plane of the sample. The vector will also have no components directed along the normal to the surface of the sample. In other words, there are no components with a different polarization and the same experimental arrangement. Under these conditions, changing the angle of incidence will change the optical path length and the phase of the outgoing light relative to the phase of the light that exited the sample in a direction normal to the surface. But since two components with different polarization for which an inclination of the sample would change the phase difference are not present, the polarization of the outgoing light also cannot change.

Such components could arise if the sample contained an optic axis making a nonzero angle with the rotation axis. However, the experiments described in Section 3.2 show unequivocally that there is no such axis.

One other possibility can be presented *a priori*: Birefringence coexists with rotation of the polarization plane in the material. In this case the direction of the oscillations of the vector **E** could be changed as a result of a rotation of the polarization plane. This would actually signify the appearance of a light oscillation with a different polarization, and a phase difference could appear between the two basic types of waves in accordance with the formulas presented above. However, this possibility is not confirmed experimentally—the data in Fig. 4 clearly show that there is no rotation of the polarization plane in the sample.

3. An interpretation of the observed effects can be proposed only at a qualitative level with a substantial complication of the model. One possibility is to assume that the sample is nonuniform, so that the light transmitted through it passes successively, for example, through regions with different directions of rotation of the polarization plane. In this case, the light transmitted through the sample normally can maintain the same polarization plane as for the incident light, just as in the experiment described above. At the same time, the polarization inside the sample makes an angle to the main directions, so that the rotation of the sample will result in the appearance of a phase shift between the components and, in this case, to a change in polarization.

The conjecture made above presumes, first and foremost, that porous silicon has a complex (hierarchical) structure. In itself, this conjecture does not contain any unusual hypotheses. In works on this material, experimental evidence is presented, for example, for a layered structure. Each layer in turn is formed by a collection of oriented "quantum wires" [13–15]. Such a structure could give, for example, rotation of the polarization plane at the entrance to the layer and a reverse rotation at the exit from the layer; the total rotation for light passing through a layer in a direction normal to the layer could be close to zero. But, even with oblique passage a layer with such properties could also demonstrate dichroism with dependences similar to those observed in our experiments.

This conjecture of a compensated rotation of the polarization plane makes it possible to relate the data from all experiments in a single model. However, in this case, the exact compensation of the contributions of separate regions is nontrivial. It is sufficient to recall that the demagnetization (on the average) of an ordinary piece of iron is due to a quite complicated system of phenomena that minimize the volume energy of the magnetic field. In principle, the complex hierarchical structure of porous silicon consisting of nano- and microobjects of different scale leaves another possibility—balanced combination of right- and left-hand rotations. The question is why nature chooses precisely this variant from the enormous number of possibilities.

With respect to porous silicon, this question is consistent and relevant, since the formation of porous silicon itself is a self-organization of a mass of nanosize elements, which at present is not fully understood (see, for example, [16]). However, up to now, attempts to analyze the situation have been made only for the process leading to the formation of the quantum wires themselves. The observation of birefringence of light in the present work shows that the organization of the quantum-size elements into a single material—porous silicon—is nontrivial and not accidental, and this question requires a special investigation.

5. CONCLUSIONS

Thus, in the present work birefringence of light in porous silicon was observed and investigated for the first time. The collection of results of observations can be easily interpreted formally as a manifestation of the birefringence of the experimental material. An experiment with an impregnated sample unequivocally shows that the observed birefringence is the socalled shape birefringence and is due to the structure of the material consisting of anisotropic objects which have a predominant orientation.

Nonetheless, a correct description of part of the experimental data using well-known formulas for bire-

fringence does not exhaust the questions concerning the nature of the observed defects. The results of different experiments can be explained as whole only qualitatively using quite complicated assumptions about the structure of the material.

REFERENCES

1. A. G. Cullis, L. T. Canham, and P. P. J. Calcott, J. Appl. Phys. **82**, 909 (1997).
2. L. T. Canham, Appl. Phys. Lett. **57**, 1046 (1990).
3. I. Gregora, B. Champagnon, and A. Halimaoui, J. Appl. Phys. **75**, 3034 (1994).
4. M. E. Kompan, V. B. Kulik, I. I. Novak, *et al.*, Pis'ma Zh. Éksp. Teor. Fiz. **67**, 95 (1998) [JETP Lett. **67**, 106 (1998)].
5. R. Laiho, E. Ladheranta, L. Vlasenko, *et al.*, J. Lumin. **57**, 197 (1993).
6. M. E. Kompan and I. Yu. Shabanov, Fiz. Tverd. Tela (St. Petersburg) **41**, 54 (1999) [Phys. Solid State **41**, 45 (1999)].
7. L. C. Lew Yan Voon, Appl. Phys. Lett. **70**, 2446 (1997).
8. W. A. Shurcliff, *Polarized Light: Production and Use* (Harvard University Press, Cambridge, 1962; Mir, Moscow, 1965).
9. M. Born and E. Wolf, *Principles of Optics* (Pergamon Press, Oxford, 1969, 4th ed.; Nauka, Moscow, 1970).
10. J. Salonen, K. Saarinen, J. Peuta, *et al.*, Mater. Res. Soc. Symp. Proc. **486**, 323 (1998).
11. D. W. Fisher and M. C. Omher, J. Appl. Phys. **81**, 4225 (1997).
12. R. Wirht, A. Moritz, C. Geng, *et al.*, Phys. Rev. B **55**, 1730 (1997).
13. V. I. Beklemishev, V. M. Gontar', V. V. Levenets, *et al.*, Élektronnaya Promyshlennost', No. 2, 36 (1994).
14. M. E. Kompan, V. E. Khatsiev, I. Yu. Shabanov, *et al.*, Fiz. Tverd. Tela **39**, 2137 (1997) [Phys. Solid State **39**, 1912 (1997)].
15. V. Parkhutik, in *Abstracts of PSST, International Conference on Porous Silicon—Science and Technology, Majorka, 1998*, p. 16.
16. M. E. Kompan, J. Salonen, and I. Yu. Shabanov, Electronic Journal "Issledovano v Rossii," http://zhurnal.mipt.rssi.ru/articles/1999/001.pdf (1999).

Translation was provided by AIP

Journal of Experimental and Theoretical Physics, Vol. 90, No. 2, 2000, pp. 330–340.
Translated from Zhurnal Éksperimental'noĭ i Teoreticheskoĭ Fiziki, Vol. 117, No. 2, 2000, pp. 375–386.

Effect of High Pressures on Exchange and Hyperfine Interactions in Rare-Earth Orthoferrites

A. G. Gavrilyuk[1], G. N. Stepanov[1], I. S. Lyubutin[2,] *, A. S. Stepin[2], I. A. Troyan[1], V. A. Sidorov[1], B. Palosz[3], S. Stel'makh[3], and M. Winzenick[4]

[1]*Institute of High-Pressure Physics, Russian Academy of Sciences, Troitsk, Moscow oblast, 142092 Russia*
[2]*Institute of Crystallography, Russian Academy of Sciences, Moscow, 117333 Russia*
[3]*High Pressure Research Center, Polish Academy of Sciences, Warsaw, Poland*
[4]*Univesität-G-H Paderborn, 33098 Paderborn, Germany*
**e-mail: lyubutin@magnet.crystal.msk.su*

Received July 26, 1999

Abstract—The effect of high pressures P on the Néel temperature T_N, the crystal lattice parameters, and the magnitude of the hyperfine magnetic field H^{Sn} at a nucleus of a diamagnetic tin atom was studied in pure and tin-doped orthoferrites $RFeO_3$ (R = Nd, Lu). The dependence of these quantities on the geometry of the exchange bonds, specifically, the angle and length of the chemical bond Fe–O–Fe(Sn), was analyzed. It was established that under pressure the angular contribution decreases and the radial contribution increases T_N and H^{Sn}, the radial contribution being greater than the angular contribution in absolute magnitude. Numerical estimates were obtained for the angular and radial contributions to T_N and H^{Sn}. In lutecium orthoferrite, at $P > 30$ GPa anomalies indicating a possible phase transition were observed in the behavior of the lattice parameters and the value of H^{Sn}. *© 2000 MAIK "Nauka/Interperiodica".*

1. INTRODUCTION

In the orthoferrites $RFeO_3$ (R is a rare-earth element) doped with diamagnetic tin ions Sn^{4+}, Mössbauer spectroscopy has revealed strong magnetic fields at ^{119}Sn nuclei, reaching 250 kOe [1]. These fields arise as a result of the transfer of spin density from the 3*d* shell of the Fe^{3+} ion into the *ns* shell of the Sn^{4+} ion, which is what produces the hyperfine magnetic field at a Sn nucleus via the Fermi contact interaction. Spin-density transfer occurs by the mechanism of indirect exchange with the participation of an intermediate oxygen ion along the chain Fe–O–Sn [2]. For this reason, the field produced by such a mechanism is called an indirect hyperfine interaction field or a supertransferred hyperfine magnetic field (H^{Sn}_{STHF}) [2]. Investigations have shown that the field H^{Sn}_{STHF} (which in what follows we denote by H^{Sn}) is very sensitive to the local magnetic and crystal structure and to the geometry of the exchange bonds [2–4]. In the series of orthoferrites $RFeO_3(Sn^{4+})$, as R changes from La to Lu the value of the field H^{Sn} decreases approximately by 100 kOe [1]. This decrease is due to the decrease in the angle of the exchange bond Fe–O–Fe (or Fe–O–Sn), which in turn is caused by the decrease in the ionic radius of the rare-earth element. This effect also explains the decrease in the Néel temperature T_N [4] and the field H^{Fe}_{STHF} at the ^{57}Fe nuclei.

The theoretical approach to this problem on the basis of the method of molecular orbitals (ligand field theory) was initially formulated in [5, 6] and later developed in [7–10]. Comparing the theoretical values of the field H_{STHF} with the experimental values makes it possible to estimate the transfer and overlap integrals and thereby obtain information about the covalency and exchange interaction parameters in a specific crystal structure. However, investigations performed for the perovskite, garnet, and spinel structures [2, 4, 7, 10, 11] have shown that the theory does not always explain and can explain only qualitatively the experimental results obtained under normal pressure.

High-pressure experiments can serve as a good test for checking and improving theoretical models. Lister and Benedek [12] have investigated the pressure dependence of the hyperfine magnetic field H^{Fe} at ^{57}Fe nuclei in octa- and tetrahedral sites of yttrium iron garnet and found that H^{Fe} is virtually independent of the lattice parameter. In [13] four orthoferrites and the ferrites-spinels $NiFe_2O_4$ and Fe_3O_4 were investigated. For the orthoferrites, it was found that H^{Fe} (296 K) increases with pressure, which the authors attributed to the increase in T_N with constant H^{Fe} (0 K). For the spinels $NiFe_2O_4$ and Fe_3O_4, it was found that H^{Fe} (0 K) decreases with increasing pressure. In [14], it was observed that in the spinel $MnFe_2O_4$ (Sn^{4+}) the field H^{Sn} at the tin nuclei increased substantially under pressure *P*. It was found that dH^{Sn} (296 K)/dP = +3 kOe/GPa.

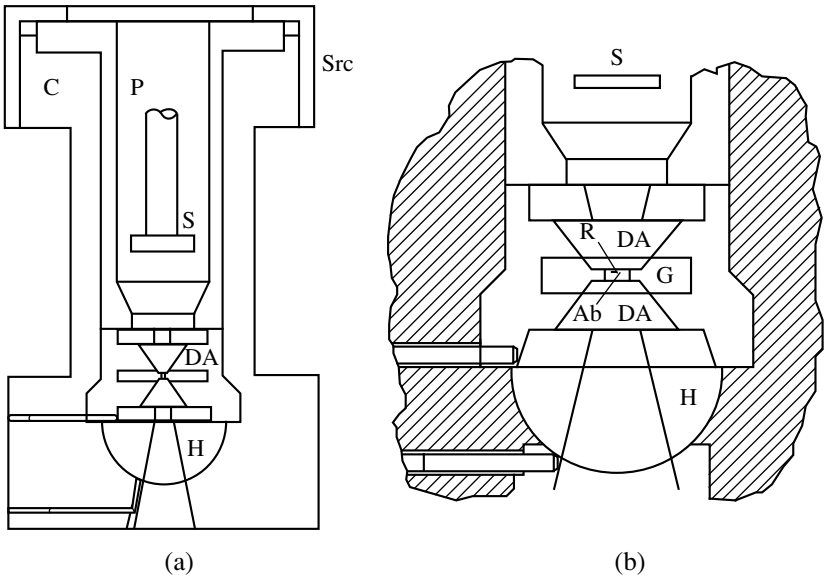

Fig. 1. (a) Schematic view of a typical high-pressure chamber with diamond anvils for Mössbauer and optical measurements: P, C, piston-cylinder, S, Mössbauer source or focusing lens, DA, diamond anvils, H, positioning hemisphere; Src, nut for fixing the load. (b) Enlarged view of the central part of the chamber: G, gasket, Ab, sample (absorber), R, ruby grain.

High-pressure investigations are very difficult, but they can yield information about the change occurring in the exchange interactions and the covalency parameters as a result of deformations of the crystal lattice. In the present work we used the high-pressure technique to investigate H^{Sn} and T_N accompanying a change in the interionic distances and angles of the exchange bond in the orthoferrites $NdFeO_3$ and $LuFeO_3$, pure and doped with Sn^{4+} ions.

2. EXPERIMENTAL PROCEDURE

2.1. High-Pressure Chamber with Diamond Anvils for Mössbauer, Optical, and X-ray Investigations

We conducted a series of investigations of the Mössbauer spectra, the optical absorption spectra, the Raman spectra, and the X-ray diffraction spectra using high-pressure chambers with diamond anvils. A schematic view of such a chamber is displayed in Fig. 1. Depending on the type of experiment and required maximum pressure, the diameter of the working area of the anvils varied in the range 300–800 μm. In the Mössbauer experiments, the diameter of the anvils was about 600 μm. The pressure in the chamber was measured according to the shift of a ruby fluorescence line using a special optical apparatus equipped with a He–Cd laser. A rhenium interlayer (gasket) was clamped between the diamond anvils. The initial thickness of the rhenium foil was 200 μm, and the final thickness of the indentation was about 50 μm. An opening with a diameter of ~200 μm was produced at the center of the gasket by means of a spark discharge. The opening was filled with powder of the experimental sample and ~10 μm ruby crystal grains were placed on top. Pressures exceeding 40 GPa can be generated using such a diamond chamber. The maximum pressure difference along the sample was 0.1 GPa.

The Mössbauer absorption spectra of the ^{119}Sn nuclei were measured on a standard spectrometer with a multichannel analyzer in the regime where gamma rays are transmitted through a sample. A small, specially produced, source based on $Ca^{119m}SnO_3$ with a ~3 mm in diameter active spot and a high specific activity served as the gamma-ray source. During the experiment the source was at room temperature. The acquisition time of each spectrum ranged from 1 to 4 weeks. Computer analysis of the Mössbauer spectra was performed using a program developed at the Institute of Crystallography of the Russian Academy of Sciences.

Diamond anvils with a diameter of about 300 μm were used in the optical absorption experiments. The opening at the center of the rhenium gasket was ~100 μm in diameter. A thin plate was prepared from the experimental sample by compressing powder between the anvils. A particle of this plate together with a ruby grain were placed on the surface of one of the anvils. Polyethylsiloxane liquid (PES-5) served as the pressure-transmitting medium. Pressures up to 100 GPa can be obtained in such a chamber. The optical setup for investigating the absorption spectra at high pressure makes it possible to perform measurements in the visible and near-IR ranges (from 0.2 up to 5 μm). We expect that interesting evolution of the optical absorption edge in rare-earth orthoferrites should be observed in the pressure range 30–100 GPa.

In the X-ray diffraction experiments, the diameter of the diamond anvils was about 400 μm. The experiment was performed using an energy-dispersion

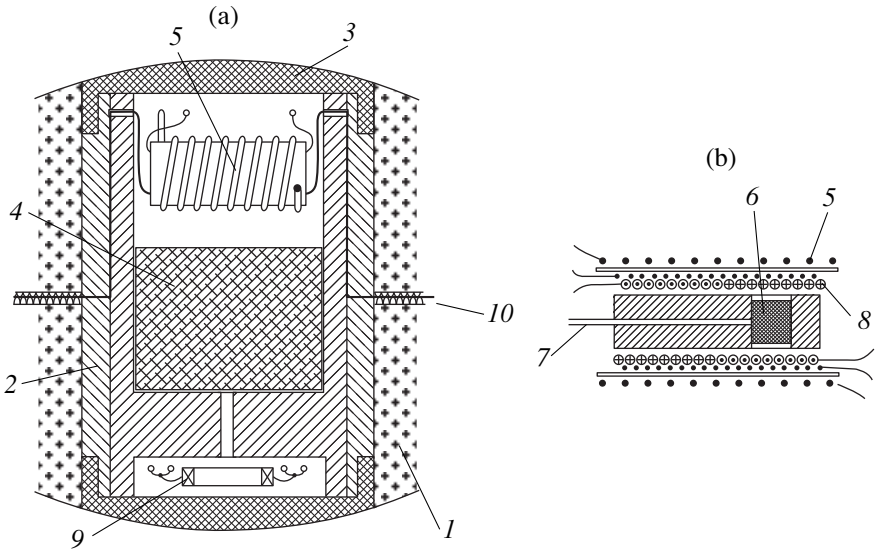

Fig. 2. (a) Overall view of the central part of the "Toroid" chamber with a teflon high-pressure cell. (b) Diagram of the assembly for measuring the magnetic susceptibility; *1*, interlayer (catlinite), *2*, teflon ampul, *3*, covers, *4*, thermal insulator, *5*, heater, *6*, sample, *7*, thermocouples, *8*, mica, *9*, strain gauge, *10*, manganin pressure gauge, *11*, electric leads.

scheme in the synchrotron source in Hamburg, Germany (HASYLAB/DESY, Hamburg) [15]. Mineral oil was used as the pressure-transmitting medium. This technique was used to investigate the compressibility and lattice parameters of orthoferrites up to 42 GPa pressure.

2.2. "Toroid" High-Pressure Chamber for Measurements by the Method of Differential-Thermal Analysis and Mössbauer Spectra

Measurements by the differential-thermal analysis (DTA) method were performed in a "Toroid" type high-pressure chamber [16, 17]. Hydrostatic pressures up to 10 GPa inside a liquid-filled teflon ampul can be produced in this chamber, and measurements of the compressibility (using resistance strain gauges) and magnetic susceptibility can be performed. Up to 10 electric leads can be introduced into the chamber, and various measurements can be performed at high temperatures up to 900 K. A general view of the central part of such a chamber with a high-pressure cell is displayed in Fig. 2a, and the assembly for the DTA measurements is shown in Fig. 2b. In measurements performed by this method, two 0.05 mm in diameter chromel-alumel thermocouples are placed inside the heater. One of them is in indirect contact with the experimental sample, and the other is separated from the sample by a mica interlayer. The sample with the thermocouples and the mica is placed in an additional copper thermal screen. In this setup the surrounding medium (a liquid) serves as a reference sample in the DTA measurements. The pressure inside the cell is measured continuously with a manganin probe. The pressure coefficient of the manganin wire was calibrated according to the phase transition in Bi at 2.55 and 7.7 GPa. The probe is placed in the cold zone of the ampul (Fig. 2a), and its temperature remains almost constant as the sample is heated up to 700 K. The pressure dependence of the Néel temperature (T_N) in orthoferrites was investigated by the DTA method in such a chamber, and part of the Mössbauer spectra at $T = 77$ and 296 K was investigated.

The DTA method is widely used for detecting first-order phase transitions accompanied by a jump in volume and release of latent heat. However, second-order transitions (for example, magnetic) can also be observed by this method, since the specific heat possesses a feature at the transition point (λ anomaly). The temperature dependence $\Delta T(T)$ obtained in a DTA experiment also has an anomaly, whose magnitude depends on the rate of heating or cooling of the sample. For high rates of heating (cooling) the anomaly is greater, but its position shifts by several degrees to higher (lower) temperatures. For this reason, the Néel temperature was measured during heating and cooling and its average value was determined. In our DTA investigations, for a $2 \times 2 \times 0.8$ mm^3 orthoferrite sample, the typical value of the anomalous part in the temperature dependence $\Delta T(T)$ was 1–2 μV, which corresponds to 0.05 K with heating rates 2–4 K/s. The indications of the thermocouples and the pressure sensor were measured with a digital voltmeter with 0.01 μV resolution. The data were accumulated and processed with a computer. The typical curves of the DTA signal $\Delta T(T)$ for $NdFeO_3$ for different pressures are shown in Fig. 3. The peak in $\Delta T(T)$ corresponds to the Néel point. The method of thermal measurements of magnetic transitions under pressure is described in greater detail in [18].

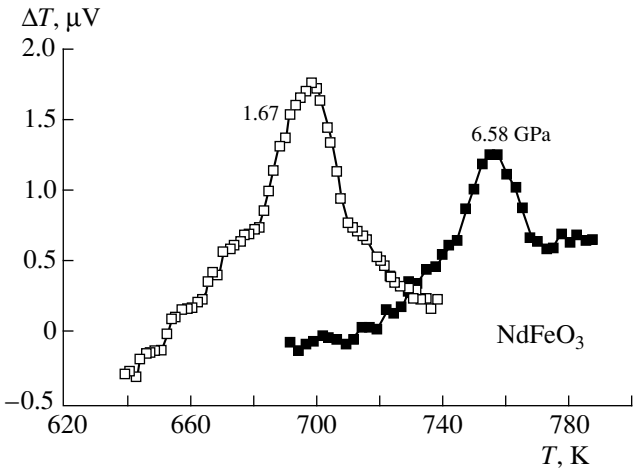

Fig. 3. Temperature dependences of the DTA signal for a single crystal of the orthoferrite $NdFeO_3$ at various pressures. The peak in $\Delta T(T)$ corresponds to the Néel point.

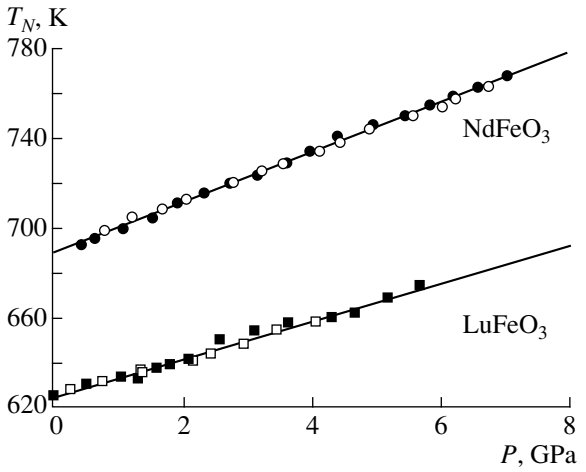

Fig. 4. Pressure dependence of the Néel temperature for single crystals of the orthoferrites $NdFeO_3$ and $LuFeO_3$. The filled and open circles refer to regimes with increasing and decreasing pressures, respectively.

2.3. Sample Preparation

A ceramic technology was used to prepare pure and tin-doped orthoferrites $NdFeO_3$ and $LuFeO_3$. Some of the investigations were also performed on single crystals of pure $NdFeO_3$ and $LuFeO_3$, grown at the Institute of Crystallography of the Russian Academy of Sciences by a hydrothermal method and by a fluxed solution method. Some iron ions Fe^{3+} in doped samples $(R_{1-x}Ca_x)[Fe_{1-x}Sn_x]O_3$ ($x = 0.05$ and 0.1) were replaced by tin ions Sn^{4+}, and the R^{3+} ions were replaced with Ca^{2+} to compensate the charge. To increase the accuracy of the Mössbauer investigations, tin enriched with the isotope ^{119}Sn to 93% was used to prepare the samples. An AFV-201-Toshiba X-ray diffractometer was used to make sure that the samples consisted of a single phase. All compounds possessed perovskite structure (space group *Pbnm*) and were isostructural to the orthoferrite $GdFeO_3$ [19]. The lattice parameters and Néel temperatures for pure and substituted orthoferrites at normal pressure are presented in the table.

3. EXPERIMENTAL RESULTS

3.1. Effect of Pressure on the Néel Temperature

Figure 4 displays the pressure dependence of the Néel temperature for single crystals of the pure orthoferrites $NdFeO_3$ and $LuFeO_3$. The values of T_N were measured by the DTA method in a "Toroid" chamber. A hydrostatic pressure of up to 7 GPa was attained inside a capsule filled with a mixture of pentane and petroleum ether. The pressure dependences $T_N = f(P)$ are identical with increasing and decreasing pressure and are fit well by a linear law at least up to $P = 7$ GPa (Fig. 4). The experimental values of the pressure coefficients dT_N/dP are 11.2 ± 0.12 and 8.45 ± 0.27 K/GPa, respectively, for $NdFeO_3$ and $LuFeO_3$. The value of T_N measured in this chamber at atmospheric pressure agrees to within 0.5 K with the values from the table.

3.2. Effect of Pressure on the Crystal Lattice Parameters

Figure 5 shows the typical X-ray spectra of the orthoferrite $LuFeO_3$, measured at room temperature by the energy-dispersion method, using a synchrotron source, in a chamber with diamond anvils. Together with the diffraction peaks of orthoferrite, whose positions and intensity agree well with known tabulated data, peaks due to gold, whose powder was present in the chamber together with the orthoferrite sample, are also seen in the spectra. The pressure in the chamber was determined according to the position of these peaks, using the well-known equation of state for gold [20]. As pressure increases, the diffraction peaks broaden as a result of the appearance of pressure gradients in the chamber and the closelying peaks start to overlap strongly. In addition, at high pressures, some of the peaks corresponding to the orthoferrite start to overlap with the peaks corresponding to gold. For this reason, the values of the unit-cell parameters *a*, *b*, and *c* of $LuFeO_3$ were calculated according to the position of the 002, 111, 211, 202, and 301 peaks, whose overlapping with other peaks is smaller.

Lattice parameters and Néel temperature T_N for pure and substituted orthoferrites under normal pressure

Compound	*a*, Å	*b*, Å	*c*, Å	T_N, K
$NdFeO_3$	5.441	5.573	7.753	687
$(Nd_{0.9}Ca_{0.1})[Fe_{0.9}Sn_{0.1}]O_3$	5.476	5.608	7.788	615
$LuFeO_3$	5.213	5.547	7.565	623
$(Lu_{0.9}Ca_{0.1})[Fe_{0.9}Sn_{0.1}]O_3$	5.262	5.580	7.620	555

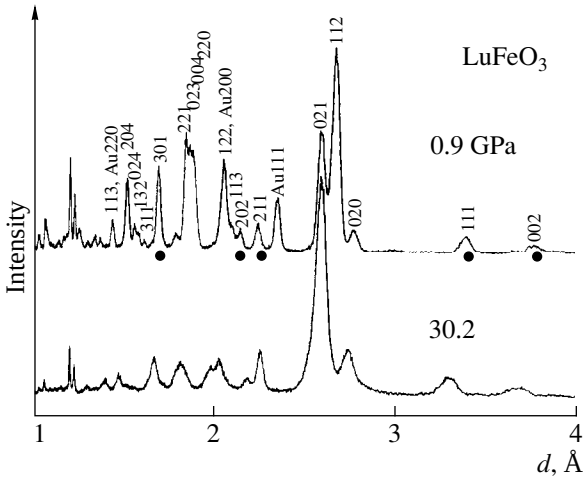

Fig. 5. Typical X-ray spectra of the orthoferrite $LuFeO_3$ at various pressures. The filled circles mark peaks used for calculating the unit-cell parameters.

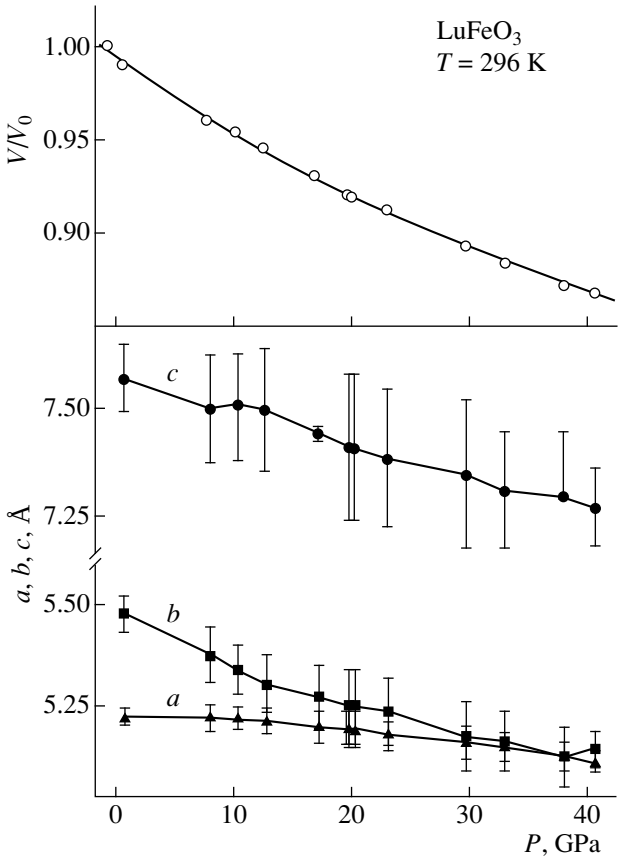

Fig. 6. Pressure dependence of the unit cell parameters and the relative volume of the unit cell for a single crystal of the orthoferrite $LuFeO_3$.

Figure 6 shows the pressure dependence of the unit-cell parameters in the orthoferrite $LuFeO_3$. As expected, the parameters *a*, *b*, and *c* decrease with increasing pressure. Despite the large experimental error, it is evident in Fig. 6 that the parameter *b* decreases more rapidly than the parameter *a*, and they become equal to one another at $P > 30$ GPa. This could signify a transition of the orthorhombic structure of the orthoferrite into a tetragonal structure. Such a transformation can be observed qualitatively in Fig. 5, where two of the three close-lying peaks 020, 112, and 021 (021 and 112) of the orthorhombic lattice completely merge at high pressure.

Figure 6 also shows the pressure dependence of the relative unit cell volume V/V_0 for $LuFeO_3$, measured up to 41 GPa. The values of the bulk modulus $K = -V_0(\partial V/\partial P)^{-1}$ were calculated from the experimental data. The parameters of the equation of state in the polynomial representation of the form $V/V_0 = 1 - P/K + \delta P^2$ were found to be $K = (220 \pm 10)$ GPa and $\delta = (3.3 \pm 0.4) \times 10^{-5}$ GPa^{-2}. The parameters for the equation of state in Murnagan's form $P = (K/K')[(V_0/V)^{K'} - 1]$ are $K = (212 \pm 16)$ GPa and $K' = 4.6 \pm 0.8$.

3.3. Mössbauer Spectra of ^{119}Sn Nuclei under Normal Pressure

At temperatures $T < T_N$ a magnetic hyperfine splitting is observed in the Mössbauer spectra of ^{119}Sn (see Fig. 7) as a result of the Zeeman interaction of 10 nuclei with the effective magnetic field H^{Sn}. The typical spectrum consists of six resonance lines, corresponding to transitions from an excited state of a ^{119}Sn nucleus (spin $I = 3/2$) into the ground state ($I = 1/2$). A calculation of the hyperfine interaction parameters showed that, for all compositions, to within the error limits there are no quadrupole shifts. The isomeric chemical shifts relative to the source are zero (for identical temperatures of the source and absorber). As the tin concentration *x* increases, additional components associated with the nearest-neighbor effects arise in the spectra of the $(R_{1-x}Ca_x)[Fe_{1-x}Sn_x]O_3$ samples (Fig. 7).

In the structure of orthoferrite all tin ions are located in oxygen octahedra, and their nearest cationic environment can be represented in the form $k_n = [(6-n)\text{Fe} + n\text{Sn}]$. For small *x* all Sn ions occupy equivalent positions with a configuration of the nearest neighbors $k_0 = (6\text{Fe} + 0\text{Sn})$. As *x* increases, together with k_0, the statistical weight of the local sites with the configuration $k_1 = (5\text{Fe} + 1\text{Sn})$ increases, which results in the appearance of a new subspectrum in the Mössbauer spectrum (Fig. 7). For large values of *x*, new satellites corresponding to configurations with $n = 2, 3, \ldots, 6$ appear, and a singlet (with zero magnetic field at the ^{119}Sn nucleus), due to Sn ions which do not have magnetic neighbors in the nearest-neighbor environment (for k_6), can appear at the center of the spectrum. This phenomenon has been investigated in detail in [11].

We found that for a tin ion in the coordination $k_0 = (6\text{Fe} + 0\text{Sn})$ the fields H^{Sn} (0 K) are (222 ± 1) and (160 ± 1) kOe, respectively, for neodymium and lutecium orthoferrites. Since under normal pressure the interionic

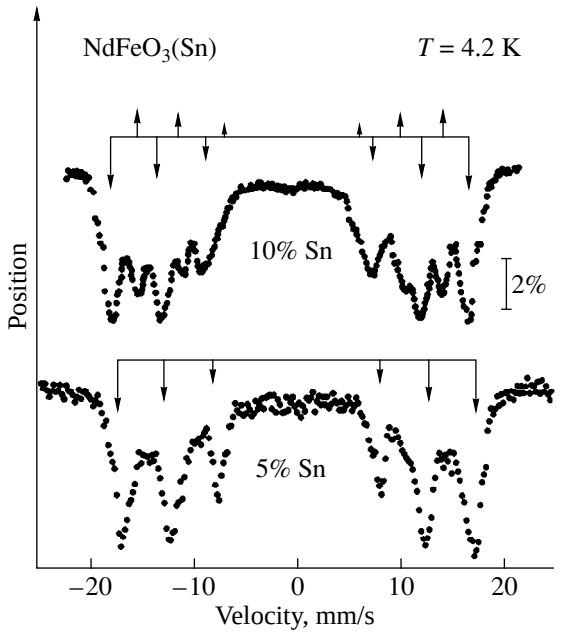

Fig. 7. Mössbauer spectra of ^{119}Sn nuclei at normal pressure in the orthoferrites $(Nd_{1-x}Ca_x)[Fe_{1-x}Sn_x]O_3$ for $x = 0.05$ and 0.1 at $T = 4.2$ K. The arrows show the positions of the resonance lines corresponding to Sn^{4+} ions in local sites with the coordination k_0 = (6Fe + 0Sn) (down arrows) and k_1 = (5Fe + 1Sn) (up arrows).

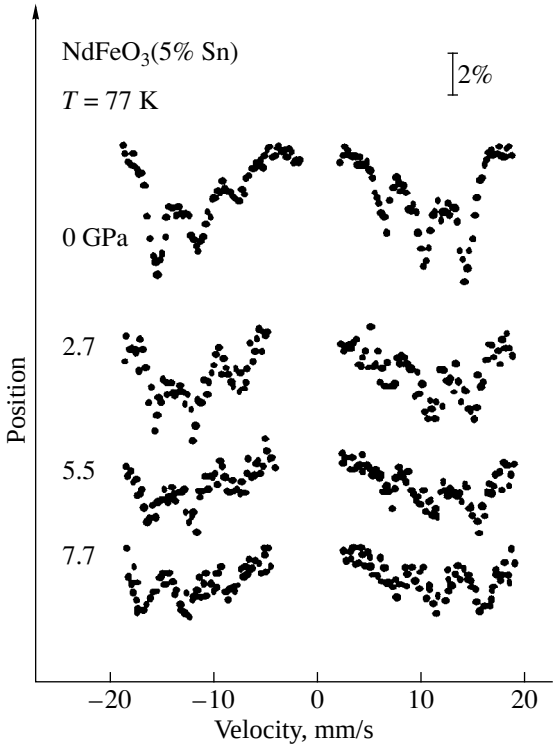

Fig. 8. Mössbauer spectra of ^{119}Sn nuclei in $NdFeO_3$ (5% Sn) at various pressures, measured in a "Toroid" chamber at $T = 77$ K.

distances Fe–O in the series $RFeO_3$ remain essentially unchanged as R varies from La to Lu, the observed decrease of the field H^{Sn} is due to the change in the angle φ of the exchange bond Fe–O–Fe (or Fe–O–Sn) [2], which decreases by 10.5° from $NdFeO_3$ to $LuFeO_3$. It was also found that for the configuration k_1 = (5Fe + 1Sn) the field H^{Sn} (0 K) in the orthoferrite $(Nd_{0.9}Ca_{0.1})[Fe_{0.9}Sn_{0.1}]O_3$ is 193 kOe. This means that the removal of one iron atom (out of six) from the nearest neighbor environment of tin decreases the field H^{Sn} by 29 kOe. Such a strong dependence of H^{Sn} on R and k_n shows that the ^{119}Sn nuclei are extremely sensitive to the local structural and magnetic environment.

3.4. Effect of Pressure on the Mössbauer Spectra of ^{119}Sn Nuclei

Figure 8 shows the evolution of the Mössbauer spectra for neodymium orthoferrite as a function of pressure in a "Toroid" chamber. For measurements at the center of the chamber, the opening in the catlinite interlayer was filled with powder of the experimental sample (instead of the teflon ampul in Fig. 2). Bismuth and barium wires were placed at the center of the sample between the top and bottom die. The wires were in electrical contact with the dies. An oil pump was used to regulate the load on the dies. The pressure-transmitting apparatus made it possible to cover completely with liquid helium the dies with the interlayer and the experimental sample. In the Mössbauer experiment, the gamma-ray source was located outside the high-pressure chamber. The direction of the radiation was in the plane of the catlinite interlayer and passed through the sample. The load on the dies was increased until the next phase transition in bismuth or barium was reached. These transitions were detected according to a jump in the resistance of the Bi or Ba wire. In the process of accumulating the Mössbauer spectrum, the pressure was maintained constant using an oil pump and a special control scheme. The spectra of $(Nd_{0.9}Ca_{0.1})[Fe_{0.9}Sn_{0.1}]O_3$ at room and nitrogen temperatures under pressures up to 7.7 GPa were measured in such a chamber.

All spectra were analyzed assuming two magnetic sextets and one singlet. We discovered that the magnetic field H^{Sn} on a tin nucleus increases with pressure. Figure 9 shows the pressure dependences of the field H^{Sn} for a k_0 configuration in neodymium and lutecium orthoferrites at $T = 296$ K. These dependences are fit well by a linear function

$$H(P) = H_0 + \frac{\partial H}{\partial P}P, \qquad (1)$$

where H_0 is the field H^{Sn} at normal pressure and room temperature. For k_0 coordination, the following values of the parameters were found in the orthoferrite $(Nd_{0.9}Ca_{0.1})[Fe_{0.9}Sn_{0.1}]O_3$: $H_0 = (196 \pm 2)$ kOe and

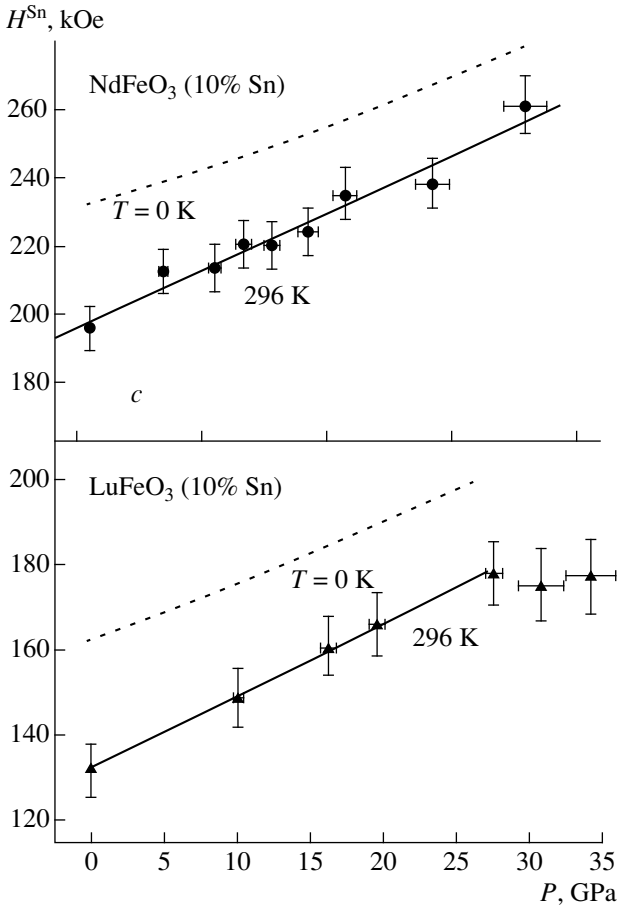

Fig. 9. Pressure dependence of the field H^{Sn} in the orthoferrites $NdFeO_3$ and $LuFeO_3$ at T = 296 K. Solid lines are linear fit, dashed lines are interpolation of the data using Eq. (2) to T = 0 K.

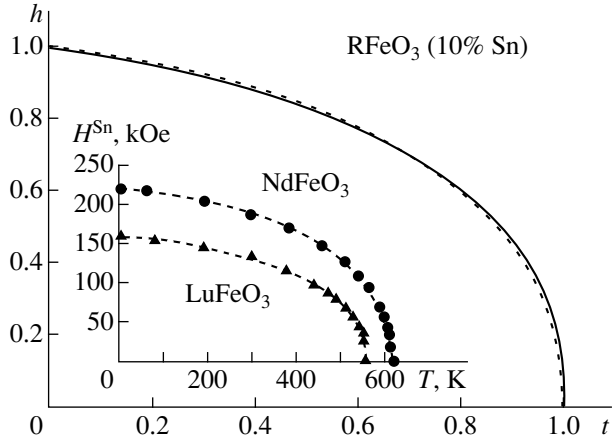

Fig. 10. Temperature dependences of the fields H^{Sn} in $NdFeO_3$ (10% Sn) and $LuFeO_3$ (10% Sn) in reduced coordinates. The solid and dashed lines show the fit of the expression (2) to the experimental data for neodymium and lutecium orthoferrites, respectively (see text). Inset: Experimental dependences H^{Sn} (T) at normal pressure, from [1].

$\partial H/\partial P = (1.98 \pm 0.16)$ kOe/GPa; for k_1 coordination: $H_0 = (170.8 \pm 1.5)$ kOe and $\partial H/\partial P = (1.66 \pm 0.14)$ kOe/GPa; orthoferrite $(Lu_{0.9}Ca_{0.1})[Fe_{0.9}Sn_{0.1}]O_3$, the following values were obtained for k_0 coordination: $H_0 = (132 \pm 2)$ kOe and $\partial H/\partial P = (1.68 \pm 0.10)$ kOe/GPa.

3.5. Extrapolation of the Field H^{Sn} to T = 0 K

Both the change of the Néel pressure with temperature and the change in the magnitude of the field H^{Sn} with pressure at T = 0 K affect the pressure dependence of the field H^{Sn} at T = 296 K. To analyze the experimental results theoretically, it is necessary to know the fields H^{Sn} at absolute zero temperature. Knowing the dependence $H^{Sn} = f(T)$ for normal pressure and the dependences H^{Sn} (296 K) = $f(P)$ and $T_N = f(P)$, the pressure dependence of the field H^{Sn} at T = 0 K, i.e., H^{Sn} (0 K) = $f(P)$, can be estimated. For this, we shall employ a scaling model and we shall represent the temperature dependence of the field H^{Sn} in a form that does not depend on the pressure:

$$h = \exp(-\alpha t)(1-t)^{\beta}. \quad (2)$$

Here $h = H^{Sn}(T)/H^{Sn}(0)$ and $t = T/T_N$, and the parameters α and β are determined by fitting the function (2) to the experimental temperature dependence $H^{Sn}(T)$ at normal pressure. The pressure dependence $H^{Sn}(P)$ at zero temperature $H_0(P)$ is found from the expression

$$H_0(P) = H(T_{RT}, P)\exp\left(\alpha\frac{T_{RT}}{T_N(P)}\right)\left(1-\frac{T_{RT}}{T_N(P)}\right)^{-\beta}. \quad (3)$$

Knowing $H_0(P)$, it is also easy to calculate the values of H^{Sn} for any pressure and temperature:

$$H(T, P) = H_0(P)\exp\left(-\alpha\frac{T}{T_N(P)}\right)\left(1-\frac{T}{T_N(P)}\right)^{\beta}. \quad (4)$$

The magnitude of the field H^{Sn} in the entire admissible (T, P) range can also be determined from its pressure dependence at room temperature:

$$H(T, P) = H(T_{RT}, P)\exp\left(\alpha\frac{T_{RT}-T}{T_N(P)}\right)\left(\frac{T_N(P)-T}{T_N(P)-T_{RT}}\right)^{\beta}. \quad (5)$$

We check the proposed extrapolation procedure for the orthoferrite $NdFeO_3$ (5% Sn) data first. Th extrapolation of the pressure dependence of H^{Sn} at T = 296 K to the pressure dependence at T = 77 K agreed well with the experimental values of the field at this temperature.

In a previous work [1], we measured in detail the temperature dependences of H^{Sn} in the orthoferrites $NdFeO_3$ (10% Sn) and $LuFeO_3$ (10% Sn) under normal pressure (see Fig. 10). Analyzing these data using the proposed extrapolation scheme, we found that the experimental values can be fit well by the empirical function (2) with the following values of the adjustable parameters:

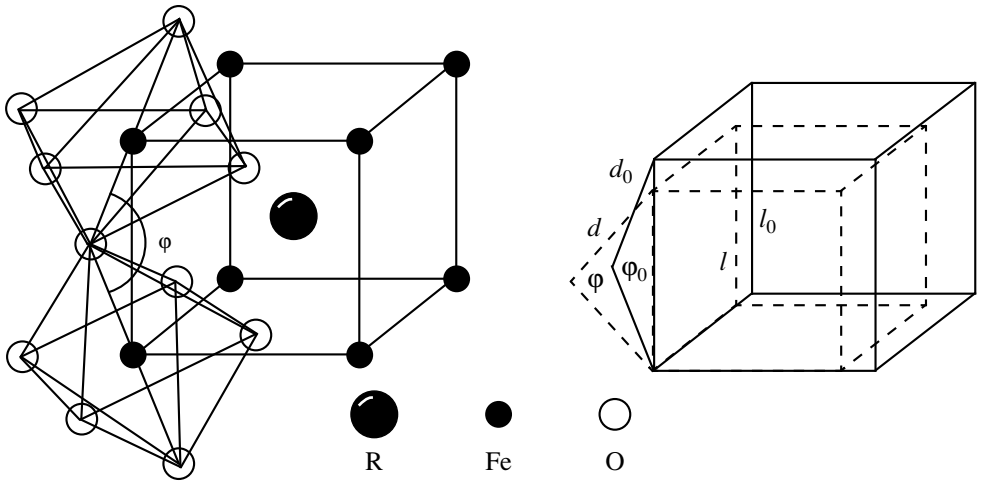

Fig. 11. Schematic view of the crystal structure of perovskite. The dashed lines show the changes in the parameters of the structure after application of pressure.

$\alpha = -0.261 \pm 0.008$, $\beta = 0.452 \pm 0.007$ for $NdFeO_3$ (10% Sn) and $\alpha = -0.207 \pm 0.008$, $\beta = 0.418 \pm 0.007$ for $LuFeO_3$ (10% Sn). As one can see in Fig. 10, the temperature dependences of H^{Sn} for the two different orthoferrites are very close. This confirms the universality of the form of the function $h = f(t)$.

The pressure dependences of H^{Sn} calculated using the proposed zero-temperature scheme for the orthoferrites $NdFeO_3$ (10% Sn) and $LuFeO_3$ (10% Sn) are shown in Fig. 9. For the neodymium orthoferrite the dependence $H_0^{Sn}(P)$ is approximately linear up to $P = 30$ GPa with slope $dH^{Sn}(0\ K)/dP \approx 1.56 \pm 0.03$ kOe/GPa. For the lutecium orthoferrite the linearity with coefficient $dH^{Sn}(0\ K)/dP \approx 1.41 \pm 0.03$ kOe/GPa remains up to $P \approx 27$ GPa, after which a kink appears. This probably indicates a phase transition.

4. DISCUSSION

4.1. Radial and Angular Pressure Dependences of the Field H^{Sn}

If the field H^{Sn} arises because of spin-density transfer from the 3*d* shell of the Fe^{3+} ion to the *ns* shell of the Sn^{4+} ion by the indirect exchange mechanism, then the field H^{Sn} should depend on the geometry of the Fe–O–Sn exchange bonds [2]. At high pressure, the length *d* of the chemical bond Fe–O (Sn–O) should decrease, and the angle between the lines of the Fe–O–Sn bond should also change. The angle φ should change because the bulk modulus K_{lat} of the lattice is different from the bulk modulus K_{oct} of the polyhedra (in this case octahedra) comprising this lattice. The bulk modulus for the oxygen octahedra can be estimated from published data [21]: $K_{oct} \sim 280$ GPa. The value of K_{lat} measured in the present work for lutecium orthoferrite $LeFeO_3$ is ~220 GPa.

We shall represent the change in the field $H^{Sn}(0\ K)$ under pressure as a sum of the radial and angular components:

$$\frac{\partial H}{\partial P} = \frac{\partial H}{\partial d}\frac{\partial d}{\partial P} + \frac{\partial H}{\partial \varphi}\frac{\partial \varphi}{\partial P} \tag{6}$$

and we shall estimate the magnitude of each component.

Figure 11 shows the schematic form of the crystal structure of the perovskite, where d_0, d, φ_0, φ, l_0, and l are parameters of the structure before and after the application of pressure, respectively. To a first approximation, the change in the lattice parameters under pressure is given by

$$\Delta d = \frac{d_0 P}{3K_{oct}}, \quad \Delta l = \frac{l_0 P}{3K_{lat}}. \tag{7}$$

We shall express the differential of the sine of the angle $\varphi/2$ in two ways: in terms of the increase in the angle

$$\Delta \sin\left(\frac{\varphi_0}{2}\right) = \frac{1}{2}\cos\left(\frac{\varphi_0}{2}\right)\Delta\varphi \tag{8}$$

and as a differential of a function of two variables *d* and *l*, using the fact that $\sin(\varphi_0/2) = l_0/2d_0$,

$$\begin{aligned}\Delta \sin\left(\frac{\varphi_0}{2}\right) &= \frac{1}{2d_0}\Delta l_0 - \frac{l_0}{2d_0^2}\Delta d_0 \\ &= \sin\left(\frac{\varphi_0}{2}\right)\left(\frac{1}{K_{lat}} - \frac{1}{K_{oct}}\right)\frac{P}{3}.\end{aligned} \tag{9}$$

Equating the right-hand sides of Eqs. (8) and (9), we obtain an expression for estimating the pressure derivative of the angle φ:

$$\frac{\partial\varphi}{\partial P} = \frac{2}{3}\tan\left(\frac{\varphi_0}{2}\right)\left(\frac{1}{K_{lat}} - \frac{1}{K_{oct}}\right). \quad (10)$$

The value of the derivative of the field with respect to the angle can be calculated from the experimental dependence $H^{Sn}(0\ K) = f(\varphi)$, which we obtained previously for normal pressure for a series of orthoferrites $RFeO_3(Sn^{4+})$ [4]. Such an estimate gives $\partial H/\partial\varphi = 5.9 \pm 0.5$ kOe/deg. Using Eqs. (7) and (10), we transform Eq. (6) into the form

$$\frac{\partial H}{\partial d} = \frac{3K_{oct}}{d}\left[\frac{dH}{dP} - \frac{2}{3}\tan\left(\frac{\varphi}{2}\right)\left(\frac{1}{K_{lat}} - \frac{1}{K_{oct}}\right)\frac{\partial H}{\partial\varphi}\right], \quad (11)$$

where dH/dP is an experimental quantity measured in this work. Substituting the numerical values of the parameters, we obtain estimates for the angular and radial contributions to the field H^{Sn} under the action of pressure. For neodymium orthoferrite

$$\frac{\partial H^{Sn}}{\partial\varphi}\frac{\partial\varphi}{\partial P} \approx -0.86\ \text{kOe/GPa},$$
$$\frac{\partial H^{Sn}}{\partial d}\frac{\partial d}{\partial P} \approx +2.42\ \text{kOe/GPa}. \quad (12)$$

For lutecium orthoferrite

$$\frac{\partial H^{Sn}}{\partial\varphi}\frac{\partial\varphi}{\partial P} \approx -0.65\ \text{kOe/GPa},$$
$$\frac{\partial H^{Sn}}{\partial d}\frac{\partial d}{\partial P} \approx +2.06\ \text{kOe/GPa}. \quad (13)$$

Thus the radial and angular contributions have different signs, and the radial contribution is greater in absolute magnitude than the angular contribution. In consequence, the resulting field H^{Sn} increases with pressure. For example, for neodymium orthoferrite estimates show that under 30 GPa pressure the angular contribution decreases the field H^{Sn} (0 K) by 26 kOe, and the radial contribution increases the field by 73 kOe.

4.2. Radial and Angular Dependences of the Néel Temperature under Pressure

The change in the geometry of the exchange bonds under pressure can also affect the Néel temperature. By analogy with the expression (6), we shall represent the pressure dependence of T_N as a sum of the radial and angular components:

$$\frac{dT_N}{dP} = \frac{\partial T_N}{\partial d}\frac{\partial d}{\partial P} + \frac{\partial T_N}{\partial\varphi}\frac{\partial\varphi}{\partial P}. \quad (14)$$

The dependence of T_N on the exchange-bond angle at normal pressure has been investigated for a series of orthoferrites $RFeO_3$, both pure and tin-doped [4]. An estimate of the angle derivative of T_N gives $\partial T_N/\partial\varphi = +6.0 \pm 0.3$ K/deg. Using the derivatives $\partial\varphi/\partial P$ and $\partial d/\partial P$ computed above, we can find the angular and radial contributions to the pressure dependence of T_N. For neodymium orthoferrite

$$\frac{\partial T_N}{\partial\varphi}\frac{\partial\varphi}{\partial P} \approx -0.87\ \text{K/GPa},$$
$$\frac{\partial T_N}{\partial d}\frac{\partial d}{\partial P} \approx +12.1\ \text{K/GPa}. \quad (15)$$

For lutecium orthoferrite

$$\frac{\partial T_N}{\partial\varphi}\frac{\partial\varphi}{\partial P} \approx -0.66\ \text{K/GPa},$$
$$\frac{\partial T_N}{\partial d}\frac{\partial d}{\partial P} \approx +9.1\ \text{K/GPa}. \quad (16)$$

Thus, just as for the behavior of the field H^{Sn} under pressure, the angular contribution decreases and the radial contribution increases T_N, and the resulting value of T_N increases with pressure. An estimate shows that the magnitudes of the relative changes occurring in T_N and H^{Sn} (0 K) as a result of a decrease in the interionic distances are close.

For neodymium orthoferrite

$$\frac{1}{T_N}\frac{\partial T_N}{\partial d}\frac{\partial d}{\partial P} \sim 0.019\ \text{GPa}^{-1},$$
$$\frac{1}{H}\frac{\partial H}{\partial d}\frac{\partial d}{\partial P} \sim 0.011\ \text{GPa}^{-1}. \quad (17)$$

For lutecium orthoferrite

$$\frac{1}{T_N}\frac{\partial T_N}{\partial d}\frac{\partial d}{\partial P} \sim 0.016\ \text{GPa}^{-1},$$
$$\frac{1}{H}\frac{\partial H}{\partial d}\frac{\partial d}{\partial P} \sim 0.013\ \text{GPa}^{-1}. \quad (18)$$

Hence it follows that in orthoferrites superexchange and the field H^{Sn} are of the same nature and depend similarly not only on the bond angle [4] but also on the interionic distance.

4.3. Pressure Dependence of the Field H^{Sn} in the LCAO Model

In the model of a linear combination of atomic orbitals, the field H^{Sn} and the Néel temperature T_N can be expressed in terms of the covalency parameters for an Fe–O–Sn chain [4, 7–10]. According to [4], we can write

$$H^{Sn}(0\ K) \sim A_{\sigma,\pi}^2\left[-\sum_{n=1}^{4} S_{ns}\Phi_{ns}(0) + a_{5s}\Phi_{5s}(0)\right]^2, \quad (19)$$

where $A_{\sigma,\pi} = [S_{\sigma,\pi} + B_{\sigma,\pi}]$; $S_\sigma = \langle p_z | d_{3z^2-r^2} \rangle$, $S_\pi = \langle p_x | d_{xz} \rangle$, and $S_{ns} = \langle p_z | \Phi_{ns} \rangle$ are overlap integrals; B_σ, B_π, and a_{5s} are transfer parameters of the type $pz \longrightarrow d_{3z^2-r^2}$, $p_{x,y} \longrightarrow d_{xz,yz}$, and $p_z \longrightarrow \Phi_{5s}$; $\Phi_{ns}(0)$ is the *ns* function of the Sn^{4+} ion near the nucleus; p_z is the 2*p* function of the O^{2-} ion; and, $d_{3z^2-r^2, xz, yz}$ is the 3*d* function of the Fe^{3+} ion. Analysis of various contributions in the field H^{Sn} (0 K) performed on the basis of the experimental data in [2] shows that the greatest contribution to this field is due to the covalent transfer of the polarized 2*p* electrons of the O^{2-} ion into the outer 5*s* shells of the Sn^{4+} ion. Then

$$H^{Sn}(0\ \mathrm{K}) \sim A^2_{\sigma,\pi} a^2_{5s} \Phi^2_{5s}(0). \tag{20}$$

The angular dependence of the field H^{Sn} has been analyzed in detail in [4] using the model of linear combination of atomic orbitals. Using the experimental results on the dependence of H^{Sn} on the interatomic distance under pressure, it is possible to estimate the change in the covalency parameter as a function of pressure. Differentiating the expression (20) with respect to pressure, we obtain

$$\frac{1}{a_{5s}}\frac{\partial a_{5s}}{\partial P} \approx \frac{1}{2H}\frac{\partial H}{\partial d}\frac{\partial d}{\partial P}. \tag{21}$$

Using Eqs. (17) and (18), we obtain for neodymium orthoferrite

$$\frac{1}{a_{5s}}\frac{\partial a_{5s}}{\partial P} \approx 0.005\ \mathrm{GPa}^{-1}$$

and for lutecium orthoferrite

$$\frac{1}{a_{5s}}\frac{\partial a_{5s}}{\partial P} \approx 0.006\ \mathrm{GPa}^{-1}.$$

It is also possible to compare the results of numerical calculations performed on the basis of the above-discussed model for the pair In^{3+}–O^{2-} with our calculations for tin, taking account of the fact that the In^{3+} and Sn^{4+} ions are isoelectronic. In [22] it was found on the basis of NMR data that in the spinel structure the parameter characterizing the transfer of an electron from a 2*p* orbital of the O^{2-} ion into a 5*s* orbital of the In^{3+} ion increases by 30% when the interatomic distance decreases by 10%. Hence

$$\frac{1}{a_{5s}}\frac{\partial a_{5s}}{\partial P} \approx \frac{3}{d}\frac{\partial d}{\partial P}. \tag{22}$$

The decrease of interionic distances under pressure is due to the compression of the oxygen octahedra and can be calculated using the formula (7). Assuming that the data for indium are also applicable for isoelectronic tin, and using the relations (7), (20), and (22), we can write an expression for the change in the field H^{Sn}(0 K) as a result of the decrease in the interatomic distances under pressure:

$$\frac{\partial H}{\partial d}\frac{\partial d}{\partial P} \approx \frac{2H}{a_{5s}}\frac{\partial a_{5s}}{\partial P} \approx \frac{6H}{d}\frac{\partial d}{\partial P}. \tag{23}$$

Hence we obtain an estimate for the pressure derivative of the field at tin:

$$\frac{1}{H}\frac{\partial H}{\partial d}\frac{\partial d}{\partial P} \approx \frac{6H}{d}\frac{\partial d}{\partial P} \approx \frac{2}{K_{oct}} \approx 0.007\ \mathrm{GPa}^{-1}. \tag{24}$$

This is approximately 1.5–2 times less than the estimates obtained on the basis of our experimental data (see Eqs. (17) and (18)). Several reasons can be given for this discrepancy, the main one being, apparently, the difference of the ionic radii of In^{3+} and Sn^{4+}. Nonetheless, the LCAO model can qualitatively explain the behavior of H^{Sn} at high pressure. From this model it followed that a decrease in the length of the exchange bond results in an increase of the transfer parameter a_{5s} and to an increase in the field H^{Sn}.

5. CONCLUSIONS

Under the action of pressure on the crystal lattice of orthoferrite the geometry of the exchange bonds changes in a manner so that the exchange interaction Fe–O–Fe intensifies with increasing pressure. The radial contribution increases and the angular contribution decreases the superexchange. In the experimental pressure range the dependences $T_N(P)$ and $H_0^{Sn}(P)$ were found to be linear to a first approximation. For neodymium orthoferrite the dependence $H_0^{Sn}(P)$ is linear up to the maximum pressure in the present measurements $P = 30$ GPa. In lutecium orthoferrite, where the measurements were performed up to 35 GPa, for $P > 30$ GPa anomalies were observed in the behavior of $H_0^{Sn}(P)$, indicating a possible phase transition. An anomaly in the behavior of the lattice parameters was observed in the same pressure range (see Fig. 4). In addition, an electronic transition accompanied by a change in the optical absorption edge has been observed in previous work in $LuFeO_3$ in the same pressure range [15]. Recently, Hearne *et al.* [23] observed in lanthanum orthoferrite $LaFeO_3$ approximately for the same pressures a spin-crossover transition of iron ions from a magnetic into a nonmagnetic state.

Probe nuclei of diamagnetic tin atoms demonstrate a higher sensitivity to the geometry of exchange bonds than the matrix nuclei (^{57}Fe). Fe ions have am intrinsic magnetic moment, which usually induces a strong field at the nucleus of this ion. For this reason, the subtle effects of supertransfer are "screened" by the strong magnetic field from the intrinsic electronic shell. For diamagnetic ions this difficulty does not occur, since in the ground state their electronic shells are spin-com-

pensated and the hyperfine magnetic field at the nucleus is completely determined by the covalent effect of delocalization and transfer of spin density to a given ion from paramagnetic neighbors.

ACKNOWLEDGMENTS

This work was supported by the Russian Foundation for Fundamental Research, projects nos. 98-02-17197a and 99-02-26932z.

REFERENCES

1. I. S. Lyubutin and Yu. S. Vishnyakov, Zh. Éksp. Teor. Fiz. **61**, 1962 (1971) [Sov. Phys. JETP **34**, 1045 (1971)].
2. I. S. Lyubutin, *Physical Crystallography* (Nauka, Moscow, 1992), p. 326.
3. P. B. Fabrichnyĭ, Zh. Vses. Khim. O–va im. D. I. Mendeleeva **30**, 143 (1985).
4. I. S. Lyubutin, T. V. Dmitrieva, and A. S. Stepin, Zh. Éksp. Teor. Fiz. **115**, 1070 (1999) [JETP **88**, 590 (1999)].
5. J. Owen and D. R. Taylor, Phys. Rev. Lett. **16**, 1164 (1966).
6. N. L. Huang, R. Orbach, E. Simanek, *et al.*, Phys. Rev. **156**, 383 (1967).
7. C. Boekema, F. van der Woude, and G. A. Sawatzky, Int. J. Magn. **3**, 341 (1972).
8. G. A. Sawatzky and F. van der Woude, Phys. Rev. B **4**, 3159 (1971).
9. A. S. Moskvin, N. S. Ovanesyan, and V. A. Trukhtanov, Hyperfine Interact. **1**, 265 (1975).
10. A. S. Moskvin, N. S. Ovanesyan, and V. A. Trukhtanov, Hyperfine Interact. **3**, 429 (1977); Hyperfine Interact. **5**, 13 (1977).
11. I. S. Lyubutin and Yu. S. Vishnyakov, Kristallografiya **17**, 968 (1972).
12. J. D. Lister and G. B. Benedek, J. Appl. Phys. **27**, 1320 (1966).
13. N. A. Halasa, G. De Pasquali, and H. G. Drickamer, Phys. Rev. B **10**, 154 (1974).
14. I. N. Nikolaev, V. P. Potapov, and I. S. Lyubutin, Fiz. Tverd. Tela (Leningrad) **20**, 3585 (1978) [Sov. Phys. Solid State **20**, 2072 (1978)].
15. A. G. Gavriliuk, G. N. Stepanov, I. A. Trojan, *et al.*, in *Proceedings of the MRS Symposium, 1998, High-Pressure Materials Research*, Vol. 499, p. 393.
16. L. G. Khvostantsev, L. F. Vereshchagin, and A. P. Novikov, High Temp.—High Press. **9**, 637 (1977).
17. L. G. Khvostantsev and V. A. Sidorov, Phys. Status Solidi A **82**, 389 (1984).
18. V. A. Sidorov, Appl. Phys. Lett. **72**, 2174 (1998).
19. S. Geller, J. Chem. Phys. **24**, 1236 (1956).
20. D. L. Heinz and R. Jeanloz, J. Appl. Phys. **55**, 885 (1984).
21. R. M. Hazen and L. W. Finder, *Comparative Crystal Chemistry* (Wiley, New York, 1982).
22. Y. Miyahara and S. Iida, J. Phys. Soc. Jpn. **37**, 1248 (1974).
23. G. R. Hearne, M. P. Pasternak, R. D. Taylor, *et al.*, Phys. Rev. B **51**, 11495 (1995).

Translation was provided by AIP

Journal of Experimental and Theoretical Physics, Vol. 90, No. 2, 2000, pp. 341–351.
Translated from Zhurnal Éksperimental'noĭ i Teoreticheskoĭ Fiziki, Vol. 117, No. 2, 2000, pp. 387–397.

SOLIDS
Structure

Electron Spin Resonance Study of the Dynamic Magnetic Susceptibility of CuO, $Cu_{1-x}Zn_xO$, and $Cu_{1-x}Li_xO$ Single Crystals

V. A. Ryzhov[1, *], A. V. Lazuta[1], I. A. Kiselev[1], I. D. Luzyanin[1], and T. I. Arbuzova[2, **]

[1] *Petersburg Konstantinov Institute of Nuclear Physics, Russian Academy of Sciences, Gatchina, Leningrad oblast, 188350 Russia*

[2] *Institute of Metal Physics, Ural Division, Russian Academy of Sciences, Yekaterinburg, 620219 Russia*

**e-mail: ryzhov@omrb.pnpi.spb.ru*
*** e-mail: magsemi@ifm.e-burg.su*

Received July 27, 1999

Abstract—Results are presented of studies of the dynamic magnetic susceptibility of CuO, $Cu_{1-x}Zn_xO$ ($x \approx 1.5\%$), and $Cu_{1-x}Li_xO$ ($x \approx 1\%$) single crystals. The orientational dependence of the ESR spectra was investigated at room temperature. The results for CuO are analyzed using a model of a quasi-one-dimensional antiferromagnet ($S = 1/2$) with anisotropic exchange interaction between Cu^{2+} spins in the chains and exchange coupling between the chains allowing for one-dimensional spin diffusion and spinon excitations. The estimated line width is of the same order of magnitude as the experimental data. Substituting Cu with Zn scarcely alters the spin dynamics of the Cu^{2+} ions, as in weakly diluted magnets. Lithium doping substantially increases the ESR line width and this is attributed to excess holes forming rapidly relaxing spin complexes with copper ions.

1. INTRODUCTION

Studies of CuO are attracting interest because the electronic and magnetic properties of this compound are similar to the properties of known undoped oxocuprates such as La_2CuO_4. The similarity of the properties is a consequence of the electronic state of Cu^{2+} ($S = 1/2$) and the equivalent oxygen coordination of copper (four oxygen atoms forming a slightly distorted square). Copper oxide is an insulator (semiconductor) with charge transfer [1]. Of its various transport properties, particular mention is made of the low carrier mobility and the activation nature of the *p*-type conductivity [2, 3].

The antiferromagnetic semiconductor CuO has a monoclinic crystal lattice. In the range between $T_{N1} \approx 230$ K and $T_{N2} \approx 212$ K we observe helicoidal magnetic ordering which for $T < T_{N2}$ is replaced by a collinear antiferromagnetic structure with the spins oriented along the *b* axis of the crystal [4, 5]. A characteristic feature of the magnetic interactions in CuO is the presence of chains in the $[\bar{1}01]$ direction with the (Cu–O–Cu) bond angle $\varphi \simeq 146°$, which ensures strong antiferromagnetic exchange $J \approx 800$ K. The bond angles in the other directions are close to 100° which leads to significantly weaker ferromagnetic exchange $V \approx J/20$ between the chains [6]. As a result for $T > T_{N1}$ CuO exhibits behavior characteristic of low-dimensional magnets: a broad $\chi(T)$ at $T \approx 540$ K [7, 8] and dominant antiferromagnetic fluctuations in the direction of the chains [9].

The magnetic resonance of the dominant CuO phase has been investigated in one study using a powder sample [10]. It was found that the line half-width $\Delta H_{1/2} \approx 8$ kOe depended weakly on temperature for $T_{N1} \le T \le 430$ K. The deviation of the line profile from Lorentzian at the wing $H - H_f \ge 2\Delta H_{1/2}$ ($f \approx 45$ GHz) was interpreted as the manifestation of one-dimensional effects. However, as we shall see, this conclusion cannot be considered to be definitive.

It should be stressed that no ESR signal is observed in the parent high-temperature superconducting compounds (i.e., undoped cuprates) [11]. The reasons for this are not completely clear since estimates of the rates of relaxation of the homogeneous magnetization, for example in La_2CuO_4, based on known values of the anisotropic and isotropic exchange interactions yield fully observable widths [12]. A possible additional relaxation channel may be observed, involving phonon modulation of Dzyaloshinskii–Morya interaction, which can substantially broaden the ESR line at high temperatures [13]. In this respect, the accessibility of resonance studies of CuO makes this a fairly unique compound in the copper oxide class.

Lithium doping of CuO to 4% ("charge" doping) offers interesting possibilities. In $Cu_{1-x}Li_xO$, the Li^+ ions replacing Cu^{2+} introduce additional holes into the CuO matrix which leads to increased conductivity without changing the semiconducting character [3]. The doping causes some drop in T_N to $T_N \approx 183$ K for

$x = 3.7\%$ [14, 15]. According to nuclear quadrupole resonance and NMR data, this substitution has no influence on the spin dynamics of Cu^{2+} in the paramagnetic phase. Substantial changes take place in the antiferromagnetic region where, for doped samples, a strong maximum is observed in the temperature dependence of the nuclear spin relaxation rate caused by the localization of excess holes [14]. Note that similar qualitative characteristics are observed in the behavior of the lithium-doped cuprate La_2CuO_4 [16]. In CuO it is also possible for Cu to be substituted by Zn atoms. The Zn^{2+} ion has $S = 0$ so that this "spin" doping is equivalent to the appearance of a vacancy in the antiferromagnetic matrix. In the antiferromagnet La_2CuO_4 this substitution yielded effects characteristic of the behavior of a dilute magnet. An exception was the low-temperature range $T < 100$ K where the nuclear quadrupole resonance spectra revealed characteristics interpreted as the cooperative freezing of local magnetic moments induced by zinc at Cu orbitals [17]. In CuO, only the influence of zinc doping on the static magnetic susceptibility has been studied [15].

In the present study we report resonance investigations of CuO, $Cu_{1-x}Zn_xO$ ($x \approx 1.5\%$), and $Cu_{1-x}Li_xO$ ($x \approx 1\%$) single crystals at room temperature. We studied the orientational dependences of the spectra which were accurately described by the Lorentz formula in CuO, slightly less accurately for zinc-doped copper oxide and satisfactorily for the lithium-doped oxide. It is shown that a characteristic feature of CuO which yields a Lorentzian line, despite the quasi-one-dimensional nature of the magnetic substance, is the fairly strong interchain bond. The rates of spin relaxation and the *g*-factors were determined. These results are used as the basis to study the influence of doping on the spin dynamics of CuO.

2. EXPERIMENTAL METHOD AND RESULTS

We investigated a CuO single crystal taken from a batch studied previously in [8]. According to the X-ray data, the crystal was single-phase with a monoclinic $C2/c$ structure. The lattice parameters and the static susceptibility of the crystal corresponded to those given in [8]. The crystal mass was 35.7 mg and the dimensions were approximately $1 \times 2 \times 4.2$ mm^3. The lattice parameters and the static susceptibility of the other two samples $Cu_{1-x}Li_xO$ ($x = 1\%$, $m \approx 6.4$ mg, $1 \times 1 \times 2$ mm^3) and $Cu_{1-x}Zn_xO$ ($x = 1.5$–2%, $m \approx 4.8$ mg, $1 \times 1.2 \times 1.5$ mm^3) agree with the data given in [15]. All the single crystals were prism-shaped with a parallelogram cross section and the *c* axis directed along the long edge.

The dynamic magnetic susceptibility of the samples was studied using ESR. The orientational dependence of the susceptibility was obtained at room temperature. For the experiments we used an *X*-range spectrometer ($f \approx 8.37$ GHz) developed to record broad dipole magnetic transitions and the Hall conductivity at a given frequency [18]. The main features of the spectrometer which can be used to observe broad ESR lines can be summarized as follows.

(1) The spectrometer uses a cylindrical two-mode balance resonator using the TE_{111} oscillation mode [19]. A static magnetic field **H** is directed along the axis of the cylinder (*z* axis). The sample is placed at the end of the resonator and is exposed to a linearly polarized alternating field $\mathbf{h}(t)$ (*x* axis) perpendicular to **H**. The receiving plane (*y* axis) is perpendicular to the plane of excitation and the signal received $M_y = \chi_{yx}h(t)$ is proportional to χ_{yx}, which is the off-diagonal element of the magnetic susceptibility tensor, i.e., the rotation of the plane of polarization of the microwave oscillations in the resonator is recorded. Provided that this resonator is frequency-degenerate (the frequency of its natural oscillations does not depend on the rotation of their plane of polarization), deep frequency-independent decoupling (≥ 40 dB) of the receiving mode from the excitation mode can be achieved. This means that a high-power ($P \approx 1$ W) microwave generator can be used without its frequency and amplitude noise being observed at the detector input, and thus the sensitivity of the spectrometer (under conditions far from saturation $\chi_{\min} \propto P^{-1/2}$ [20, 21]) is enhanced compared with a traditional one (klystron power ≤ 50 mW).

(2) The spectrometer uses periodic sweeping of the static magnetic field and synchronous signal acquisition. The large sweep amplitude ensures that the ESR line passes through the region of the maximum and ensures that the largest possible signal is recorded on each sweep of the field.

Note that in a conventional spectrometer using modulation of a static magnetic field, either the first derivative of the ESR line or its second derivative (using double modulation) are recorded. The optimum signal-to-noise ratio (the maximum of the derivative) is achieved under conditions where the modulation amplitude is approximately equal to the half-width of the ESR line [20, 21]. For broad lines this condition is not satisfied which leads to a loss of sensitivity.

Another important factor should also be discussed. In the existing field geometry in a cylindrical resonator using the TE_{111} oscillation mode where the exciting and receiving modes are shifted by 90°, the Kerr effect at the conducting bases of the resonator also leads to some rotation of the plane of polarization of the reflected electromagnetic wave [18, 22]. Since the field **H** directed along the resonator axis is perpendicular to the microwave currents of the exciting mode flowing between its ends, a Hall microwave current appears at the ends turned through 90° relative to the exciting-mode currents and giving a signal which depends linearly on *H*. This signal has in fact been observed experimentally, and its magnitude agreed with the theoretical estimate [18]. Thus, in order to determine the response

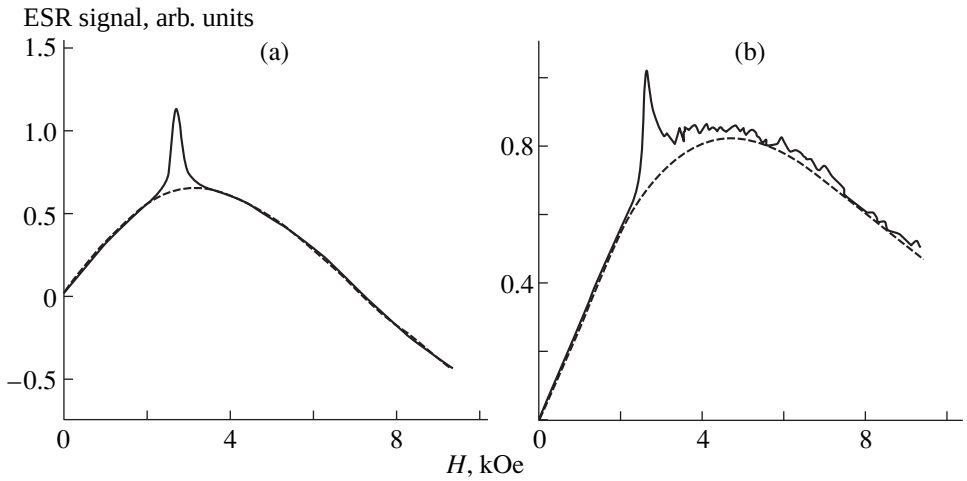

Fig. 1. Experimental (solid curves) and theoretical (dashed curves) ESR spectra of a CuO single crystal (T = 300 K, **H** ∥ **b**): a, **h** ∥ **a**; b, **h** ∥ **c**. The approximation is described in the text. The following parameters of the spectra were obtained: $g = 1.85 \pm 0.16$; $\Gamma_1 = 4.83 \pm 1.50$ kOe; $\Gamma_2 = 5.05 \pm 1.50$ kOe. The phase shifts are determined from the signals from isolated Cu^{2+} centers (peaks in the figures): $\varphi_1 = -6° \pm 10°$; $\varphi_2 = 30° \pm 11°$. The angular coefficients of the line representing the contribution of the Hall effect to the signal are: $k_1^{Hall} = -0.87 \pm 0.03$; $k_2^{Hall} = -0.28 \pm 0.01$.

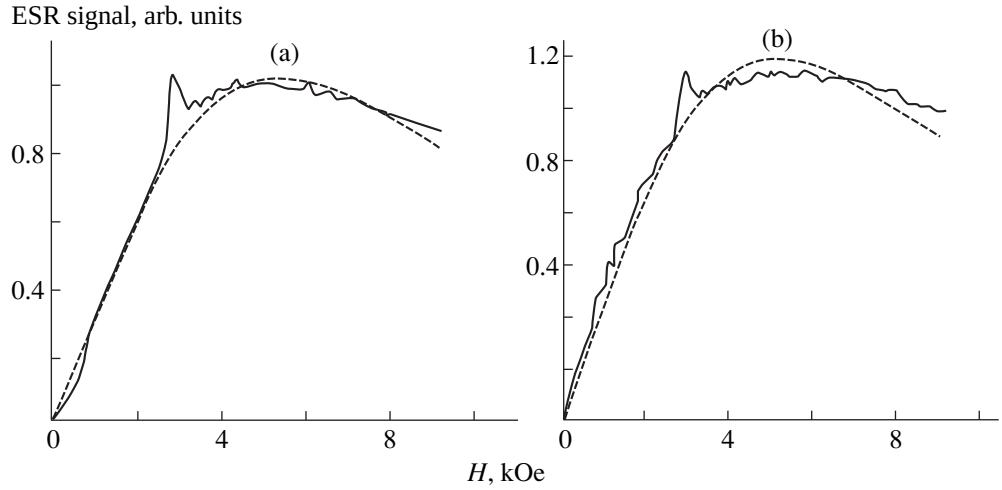

Fig. 2. As Fig. 1 for **H** ∥ **c**: a, **h** ∥ **a**; b, **h** ∥ **b**. The parameters are: $g = 2.20 \pm 0.15$; $\Gamma_1 = 7.20 \pm 1.45$ kOe; $\Gamma_2 = 7.15 \pm 1.45$ kOe; $\varphi_1 = 23° \pm 10°$; $\varphi_2 = 19.2° \pm 9.4°$; $k_1^{Hall} = 0.00 \pm 0.01$; $k_2^{Hall} = 0.00 \pm 0.01$.

of the sample, we need to subtract the signal from the resonator material. In order to calculate the weighting factor required for the subtraction we used a control sample, a polycrystalline nitroxyl radical (g = 2.0055, $\Delta H \approx 40$ Oe) containing a known quantity of spins. The accuracy of subtracting the signal from the resonator correlates with the accuracy of subtracting the control signal. This is almost absent in the difference spectra shown in Figs. 1–4, which indicates that the subtraction accuracy is good. If the sample is conducting and microwave currents are present, the Hall effect in the sample also gives rise to a signal which depends linearly on the static field.

An important characteristic of these compounds is their high permittivity at the frequency used; for example, $\varepsilon \approx 10$ in CuO for f = 9 GHz [2]. In this case, the wavelength of the field inside the sample is close to its dimensions. In addition, as a result of the electrical conductivity of the sample the value of ε is commensurate with $4\pi\sigma/\omega$. These two factors may lead to an appreciable difference between the phase of the alternating magnetic field inside the sample and the phase of the

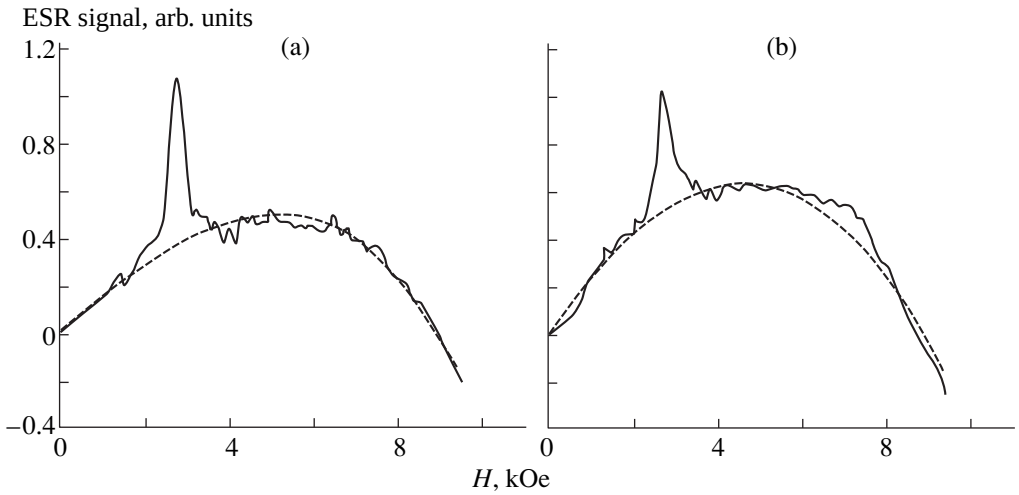

Fig. 3. As Fig. 1 for a $Cu_{1-x}Li_xO$ single crystal. The parameters are: $g = 2.20 \pm 0.15$; $\Gamma_1 = 13.7 \pm 1.5$ kOe; $\Gamma_2 = 15.24 \pm 1.80$ kOe; $\varphi_1 = 12.7° \pm 9.4°$; $\varphi_2 = 13.6° \pm 9.1°$; $k_1^{Hall} = -0.033 \pm 0.030$; $k_2^{Hall} = -2.85 \pm 0.06$.

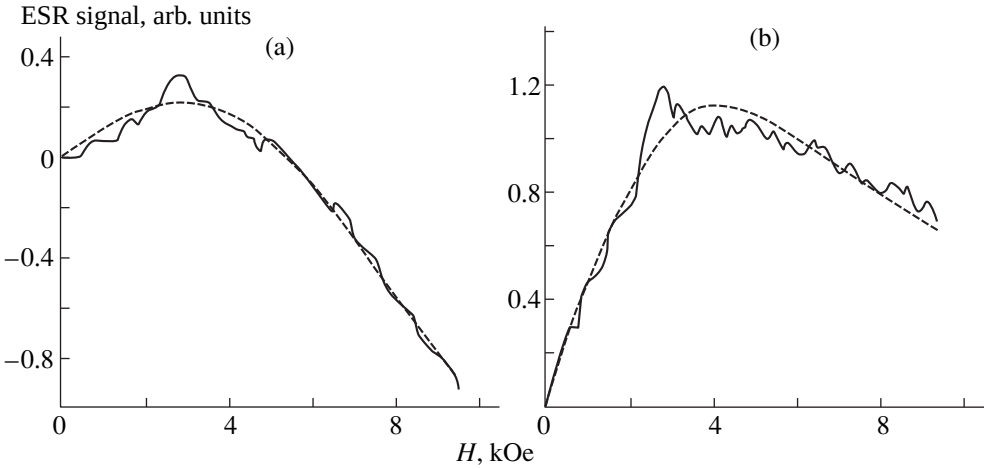

Fig. 4. As Fig. 1 for a $Cu_{1-x}Zn_xO$ single crystal. The parameters are: $g = 2.20 \pm 0.15$; $\Gamma_1 = 5.27 \pm 1.50$ kOe; $\Gamma_2 = 5.24 \pm 1.50$ kOe; $k_1^{Hall} = 0.00 \pm 0.02$; $k_2^{Hall} = -1.66 \pm 0.06$. The phase shifts were determined together with the other parameters by fitting: $\varphi_1 = 46.4° \pm 6.5°$; $\varphi_2 = 21° \pm 10°$.

field outside the sample, which must be taken into account in a quantitative analysis. This factor is particularly important for broad nonresonant lines (the spin relaxation rate is $\Gamma > 2\pi f$), when it is almost impossible to tune in to one of the components of the spectrum using the signal profile because of the small difference between the H-dependences $\mathrm{Re}\chi_{yx}(\omega, H)$ and $\mathrm{Im}\chi_{yx}(\omega, H)$, and the control signal must be used for tuning. We shall consider this in greater detail.

The wave vector in the medium is

$$k_i = \frac{\omega\sqrt{\varepsilon}}{c}\sqrt{1 + i\frac{4\pi\sigma}{\varepsilon\omega}}.$$

For $\varepsilon \approx 10$ and $\sigma = 10^{-2}\ \Omega^{-1}\ \mathrm{cm}^{-1}$, which correspond to CuO at $T = 300$ K [2], for $f = 8.34$ GHz we have

$$k_i = \frac{1}{0.18}\sqrt{1 + 0.22i}\ \mathrm{cm}^{-1}.$$

We assumed that the magnetic permeability is $\mu \approx 1$ since the susceptibility of CuO is low, $4\pi\chi \sim 10^{-3}$ [8]. In a sample with $l \geq |k_i|^{-1} \approx 2$ mm (this scale is close to the dimensions of the crystal being studied $l \approx 2$–4 mm) the magnetic field is distributed uniformly and acquires a phase shift relative to the external field because of the complex nature of k_i. Knowing the field distribution $\mathbf{h}(\mathbf{r})$, we can find the magnetization induced by this

field which, because of the low susceptibility, is given in the first order with respect to χ_{ij} by

$$m_i(\mathbf{r}, \omega) = \chi_{ij}(\omega)h_j(\mathbf{r}, \omega).$$

Here we use a homogeneous limit for χ_{ij} which does not depend on **r** since the size of the magnetic inhomogeneities in the system, which is related for example to the correlation length of the spin fluctuations, is negligible compared with the macroscopic scale $|k_i|^{-1}$ of variation of the field. From a comparison with the result for a uniform field it is clear that the effective field **h*** determining the magnetization of the sample has the form

$$\mathbf{h}^*(\omega) = \sum_{\mathbf{r}} \mathbf{h}(\mathbf{r}, \omega)V_0^{-1},$$

where V_0 is the sample volume.

For quantitative estimates we determine **h*** for a sphere of radius a in an alternating external magnetic field under conditions when $\lambda \gg a$ a but $|k_i|a \sim 1$. In this case, the field distribution is known [23] and for **h*** ∥ **h** (an obvious consequence of the symmetry) we find

$$h^*(k_i a) = \frac{3}{(k_i a)^2}[1 - (k_i a)\cot(k_i a)]h.$$

In the homogeneous limit $|k_i|a \ll 1$ we have $h^* = h$ whereas for $|k_i|a \geq 1$ the dependence $h^*(k_i a)$ exhibits resonant singularities attributable to diffraction at the sphere. Using the wave vector determined above $k_i = k_i' + ik_i''$ ($k_i' \approx 5.6$ cm^{-1}, $k_i''/k_i' \approx 0.1$) for the first resonance $k_i' a = \pi/2$, which is possible for $a \geq 0.28$ cm, we obtain $\mathrm{Im}h^*/\mathrm{Re}h^* \simeq 0.25$. This estimate determines the order of magnitude of the phase shift of the internal field which can be predicted for a sample with $k_i' l \sim 1$.

In the experiments, the phase of the reference voltage was set to record the component of the control signal proportional to $\mathrm{Re}\chi_{yx}(\omega, H)$. In order to calculate the true phase of the magnetic field inside the sample we used as an internal control the weak signal from isolated Cu^{2+} centers, which was present in the spectra of CuO and $Cu_{1-x}Li_xO$ as can be seen from Figs. 1–3. Isolated centers in CuO single crystals which contribute to the static susceptibility at low temperatures were investigated by ESR in an earlier study [24]. The phase of the alternating field inside the sample thus calculated differed from the value $\varphi = 0$ corresponding to the signal proportional to $\mathrm{Re}\chi_{yz}$. As a result, the response was a mixture of $\mathrm{Re}\chi_{yx}$ and $\mathrm{Im}\chi_{yx}$ with the weightings $\cos\varphi$ and $\sin\varphi$, respectively. This effect resulted in a substantially greater difference between the line profile and a Lorentzian one for $H < \omega_r$ compared with the region $H > \omega_r$ recorded in [10] and assigned to the influence of the anisotropy of the g-factor. An analysis shows that weak dispersion can be used to describe the spectrum observed in this study to be described over the entire range of variation of the static field, within the limits of a Lorentzian profile.

In the experiments one axis of the sample crystal was oriented in the direction of the static field **H** and the other two axes were oriented alternately in the direction of the alternating field **h**(t). Thus, two spectra were recorded when each of the crystal axes was oriented parallel to the static field (six spectra in total). In order to eliminate any additions to the signal of the symmetric component of the susceptibility tensor $\chi_{xx} \propto H^2$, we used the odd parity of $\chi_{yx}(\omega, H)$ with respect to H: the spectra of these samples were also recorded for the inverse orientation of the static field **H** and were then subtracted from the spectra obtained for the "direct" orientation of **H**. The sensitivity of the spectrometer is sufficient to observe the signal from the oxygen gas in the air contained in the resonator [18] so that all the spectra were obtained under conditions where argon or nitrogen was blown through the resonator.

Figures 1–4 show the spectra of the samples obtained by subtracting the signal attributable to the Hall effect in the resonator material. Figure 1 shows the signals from a CuO single crystal whose **b** axis is oriented parallel to the static field **H** in the cases **a** ∥ **h**(t) and **c** ∥ **h**(t). Also plotted are the theoretical spectra obtained as a result of fitting to the experimental ones (the procedure will be described below). Figure 2 gives the spectra for CuO and the result of an approximation for a different orientation of the crystal relative to the static field **c** ∥ **H**. Figures 3 and 4 show experimental and theoretical spectra for $Cu_{1-x}Li_xO$ and $Cu_{1-x}Zn_xO$ single crystals, respectively. The orientation of the crystals is the same as that for CuO in Fig. 1. Similar spectra were also obtained for different orientations of the samples. The parameters of the spectra determined as a result of the fitting are given in the captions to the figures.

3. DISCUSSION

We shall analyze the dynamic susceptibility of an anisotropic magnet. An expression for its transverse dynamic susceptibility with respect to **H**, valid in the range of H between $H = 0$ and $g\mu H \gg \Gamma$, can be obtained using the results of [25]. The fields are conveniently directed along the principal axes (**a**, **b**, **c**) of the tensor $\hat{\chi}$. The equations for the magnetization **m**(t) induced by a linearly polarized alternating field **h**(t) in the case **H** ∥ **a** and **h** ∥ **b** (with the indices obviously transposed for the different orientations) have the form

$$\frac{\partial m_b(t)}{\partial t} = i\omega_{bc}m_c(t) - \Gamma_b[m_b(t) - \chi_b h(t)], \quad (1)$$

$$\frac{\partial m_c(t)}{\partial t} = i\omega_{cb}m_b(t) - \Gamma_c m_c(t) - M_a\mu\frac{g_b g_c}{g_a}h(t), \quad (2)$$

$$\omega_{cb} = -i\mu g_b g_c M_a(g_a\chi_b)^{-1}, \quad \omega_{bc} = -\omega_{cb}\chi_b\chi_c^{-1}. \quad (3)$$

Here M_a and χ_b are the static magnetization and susceptibility, Γ_a and Γ_b are the spin relaxation rates, g_i are the g factors, and the indices correspond to the $\hat{\chi}$ axes. The "relaxation" term in equation (1) strongly influences the dependence of $\hat{\chi}(\omega)$ on H for broad lines ($\omega \sim \Gamma_i$). Its form is dictated by the known expression for $\hat{\chi}(\omega, H)$ for an isotropic magnet and the formula for the anisotropic situation where $H = 0$. From equations (1) and (2) we find an expression for $\chi_{cb}(\omega, H)$ which determines $m_c(t)$ for $h(t) \propto \exp(-i\omega t)$:

$$\chi_{cb}(\omega, H) = -\chi_{cb}(\omega, -H) = -i\omega M_a \mu \frac{g_b g_c}{g_a} \times [\omega^2 - \Omega_a^2(H) + i\omega(\Gamma_b + \Gamma_c) - \Gamma_b\Gamma_c]^{-1}, \quad (4)$$

$$\Omega_a^2 = \omega_{cb}\omega_{bc} = \left(\mu\frac{g_b g_c}{g_a}\right)^2 \frac{M_a^2}{\chi_b\chi_c}. \quad (5)$$

In CuO the weak anisotropy of χ at room temperature is most likely attributable to the anisotropy of the g-factor [26, 27] so that $\tilde{\chi} = \chi_i/g_i^2$ will not depend on the orientation. Under the experimental conditions $M \propto H$ and formula (5) is simplified: $M_a = \chi_a H$, $\Omega_a = g_a \mu H$. This last relationship makes it significantly easier to determine the values of the g-factors. The expressions obtained were used to approximate the experimental spectra.

The formulas given for the response when **H** ∥ **a** show that the components of the magnetization along **b** and **c** are involved in the precession. Thus, an approximation was made simultaneously for two spectra obtained for a fixed orientation of **H** and the alternating field directed alternately along the other two axes. In this case, as we have already noted we allowed for a shift of the phase φ of the alternating field inside the sample relative to the phase of the field outside the sample which leads to the appearance of an additional component $\mathrm{Im}\chi_{yx}$ with the weighting $\sin\varphi$ in the signal $\mathrm{Re}\chi_{yx}$ with the weighting $\cos\varphi$. For CuO and $Cu_{1-x}Li_x$ crystals this phase shift was determined using the signal from isolated Cu^{2+} centers present in the spectra and was taken into account as a fixed parameter. For $Cu_{1-x}Zn_xO$ where this signal was not observed, as can be seen from Fig. 4, the phase shift was the fitting parameter. The values of the phase shift φ depended on the orientation of the crystal and the two values φ_1 and φ_2, respectively, were determined to approximate the two spectra.

A linear contribution with respect to the field H, representing the Hall effect in the sample, was added to the theoretical spectrum during fitting, and for each of the two spectra being analyzed this was written in the form $k_j^{Hall} H/H_{\max}$, where $j = 1, 2$ and $H_{\max}$ is the maximum static field achieved experimentally. The spin relaxation rates obtained for each pair of spectra are indistinguishable since they appear symmetrically in expression (4) (we denote them by Γ_1 and Γ_2). In addition, their values were almost the same when the orientation of **H** was fixed. These two factors made it difficult to determine Γ_i ($i = a, b, c$) from a simple comparison of the rates for different orientations of the field. Under these conditions it was effective to use the values $\Gamma_{ik} = (\Gamma_i + \Gamma_k)/2$ for each orientation of the external field, from which the values of Γ_i could be determined for CuO:

$$\Gamma_c = 4.0 \pm 1.5 \text{ kOe}, \quad \Gamma_a = 6.0 \pm 1.5 \text{ kOe}, \quad \Gamma_b = 8.5 \pm 1.5 \text{ kOe},$$

for $Cu_{1-x}Zn_xO$:

$$\Gamma_c = 3.5 \pm 1.6 \text{ kOe}, \quad \Gamma_a = 7.0 \pm 1.5 \text{ kOe}, \quad \Gamma_b = 8.0 \pm 1.5 \text{ kOe},$$

and for $Cu_{1-x}Li_xO$:

$$\Gamma_c = 17.5 \pm 3.0 \text{ kOe}, \quad \Gamma_a = 11.0 \pm 3.0 \text{ kOe}, \quad \Gamma_b = 5.0 \pm 3.0 \text{ kOe}.$$

It can be seen from these results that the relationship $\Gamma_a \approx \Gamma_c < \Gamma_b$ is satisfied for CuO. We also give the values of the g-factors obtained as a result of fitting for CuO:

$$g_a = 2.26 \pm 0.14, \quad g_c = 2.20 \pm 0.15, \quad g_b = 1.85 \pm 0.16,$$

for $Cu_{1-x}Zn_xO$ and $Cu_{1-x}Li_xO$:

$$g_a \approx g_b \approx g_c = 2.20 \pm 0.15.$$

Note that the average values of the g-factor and the spin relaxation rate calculated from the data obtained for CuO agree with those obtained in [10].

When analyzing the spin dynamics of CuO in the homogeneous limit, we need to allow for the quasi-one-dimensional nature of this antiferromagnet at $T = 300$ K. Three-dimensional critical behavior caused by interchain isotropic exchange $V \approx J/20 \approx 40$ K is observed in the paramagnetic phase at lower temperatures in the range $T_N = 230 \text{ K} \le T \le 250$ K [14]. The relaxation of the homogeneous magnetization in CuO is determined by the fairly strong anisotropy of the exchange interaction in the chains $J^{an} \approx 10$ K [5]. Despite the fact that $J^{an} \ll J$, this interaction generally cannot be analyzed in terms of perturbation theory in one-dimensional magnets. However, in CuO the fairly strong coupling between the chains $V > J^{an}$ limits the region of purely one-dimensional behavior. After making adequate allowance for this interaction, perturbation theory with respect to J^{an} can be used to determine the low-frequency dynamics. We stress that we need to determine the influence of V on the fluctuation dynamics, which is important for $T \gg J$, and not on the static behavior. This

can be accomplished in the first approximation in the limits of mean field theory [28].

Before analyzing this aspect, we shall discuss the dynamics of a one-dimensional isotropic antiferromagnet of spin $S = 1/2$. When $T < J$, this magnet exhibits two regions of different dynamic behavior: a hydrodynamic region where the momentum in the direction of the chain is $q_\parallel a_\parallel \ll 1$ ($a_\parallel$ is the distance between the spins in the chain) and a region of antiferromagnetic fluctuations near the momentum $Q = \pi/a_\parallel$ [29, 30]. From the theoretical point of view, the question of the type of hydrodynamic excitations for $T \neq 0$ remains unanswered. For $T \ll J$, a method using a fermion representation for the spinon operators with a linearized spectrum followed by bosonization yields a propagating hydrodynamic mode with a linear spectrum which does not depend on T [30, 31]. This conclusion is clearly inconsistent with the conventional assumption that spin diffusion exists. However, the result of an analysis based on the Bethe ansatz is compatible with this hypothesis [32]. Recent studies using numerical methods also yield contradictory results. The calculations [33, 34] support the existence of a diffusion mode whereas in [35] the authors conclude that the behavior is more complex. At the same time the NMR and ESR data reliably confirm that spin diffusion exists in one-dimensional antiferromagnets having half-integer spin such as in Sr_2CuO_3 ($S = 1/2$) [36] and $((CH_3)_4NMnCl_3$ ($S = 5/2$) [37]. It is interesting to note that the diffusion mode is also present in the one-dimensional antiferromagnet $AgVP_2S_6$ with $S = 1$ [38] where, unlike one-dimensional antiferromagnets with half-integer spin, the ground state has a gap. The antiferromagnetic fluctuations are described by spinon excitations for which an explicit form of the pair correlation function is known for $T \ll J$ [39] which is confirmed by the neutron scattering data in the one-dimensional antiferromagnet $KCuF_3$ with $S = 1/2$ [40] and NMR data in Sr_2CuO_3 [36].

Thus, when analyzing Γ, we need to take into account the existence of spin diffusion, spinon excitations, and chain interaction. In order to determine Γ we shall use the theory of interacting modes which includes decoupling the four-spin correlation function to give products of pair correlation functions [37]. This approach allows for the simplest processes which contribute to Γ. Although the possibilities of this method as applied to a quasi-one-dimensional magnet have not yet been fully clarified, it can yield expressions for Γwhich are consistent with the experiments for $T > J$ in a one-dimensional antiferromagnet possessing anisotropy caused by dipole forces and the diffusion hydrodynamics under conditions when exchange coupling between the chains is negligible [37]. Since the accuracy of this approach improves as the dimensions increase, we predict that this approach can be used to reliably determine at least the order of magnitude of Γ when the chain interaction is significant. The result of perturbation theory in terms of J_{an} for Γ_i ($i = a, b, c$) has the form [41]

$$\Gamma_i = \frac{1}{4}G_0^{-1}\sum_{\mathbf{q}}[J_i^{an}(\mathbf{q}_\parallel)]^2\frac{1}{\pi}\int_{-\infty}^{\infty}\left(\frac{\mathrm{Im}G(\mathbf{q}, x)}{\sinh(x/2T)}\right)^2 dx. \quad (6)$$

Here we have $(J_i^{an}(\mathbf{q}_\parallel))_2 = [J_b(\mathbf{q}_\parallel) - J_c(\mathbf{q}_\parallel)]^2$ for $i = a$ and so on, $J_j(\mathbf{q}_\parallel)$ is the exchange interaction along the j axis in the chain, $G(\mathbf{q}, x)$ is the Green pair spin function, and G_0 is the Green static function for $q = 0$. The values of Γ_i contain contributions from the hydrodynamic region (Γ_i^D) and the spinon excitations (Γ_i^{sp}):

$$\Gamma_i = \Gamma_i^D + \Gamma_i^{sp}. \quad (7)$$

We shall first consider Γ_i^D assuming that spin diffusion exists. In the one-dimensional case, the contribution to Γ_i from the diffusion mode is singular in the region of low momentum [37]. This singularity is related to the scale of truncation determined by the interaction which limits the one-dimensional diffusion behavior in the limit $q_\parallel \longrightarrow 0$. In our case this is interchain coupling. In order to allow for three-dimensional effects, we shall use the relaxation expression for the dynamic form factor G:

$$G(\mathbf{q}, \omega) = i\Gamma(\mathbf{q})[\omega + i\Gamma(\mathbf{q})]^{-1}G_0, \quad (8)$$

$$\Gamma(\mathbf{q}) = Dq_\parallel^2 + \Gamma_\perp(\mathbf{q}_\perp). \quad (9)$$

Here $\Gamma_\perp(\mathbf{q}_\perp)$ describes the damping caused by the chain interaction and $\mathbf{q}_\perp$ is the momentum in the plane orthogonal to the chains. Using this expression from (6) provided that $x/T \ll 1$ we find

$$\Gamma_i^D = (J_i^{an}(0))^2 G_0 T\sum_{\mathbf{q}_\perp}\left(2\left(\frac{D}{a_\parallel}\right)^2\Gamma_\perp(\mathbf{q}_\perp)\right)^{-1/2}, \quad (10)$$

where in accordance with the hydrodynamic approximation $J_i^{an}(\mathbf{q}_\parallel)$ is taken for $q_\parallel = 0$. For $q_\perp a_\perp \ll 1$ ($a_\perp$ is the interchain spacing) we predict that $\Gamma_\perp(\mathbf{q}_\perp) = D_\perp q_\perp^2$ where $D_\perp$ is the coefficient of spin diffusion in the plane orthogonal to the chains. As a result, the expression for Γ_i^D is finite. In order to estimate this we need to find $\Gamma_\perp(\mathbf{q}_\perp)$. Using a procedure similar to the derivation of expression (6), where $\partial S_q^\alpha/\partial t$ is determined

by the interaction V and formulas (8) and (9) for G, we find

$$\Gamma_\perp(\mathbf{q}_\perp) = TG_0\sum_{\mathbf{p}_\perp}[V(\mathbf{q}_\perp-\mathbf{p}_\perp)-V(\mathbf{p}_\perp)]^2 \times\left(\frac{D}{a_\parallel^2}[\Gamma_\perp(\mathbf{q}_\perp-\mathbf{p}_\perp)+\Gamma_\perp(\mathbf{p}_\perp)]\right)^{-1/2}. \quad (11)$$

Here, as in formulas (8) and (10), $G_0(0)$ is used as the static Green function $G_0(\mathbf{q})$ since for $q_\parallel a \ll 1$ this function is not critical in the region $T \geq T_N$. From this equation which only allows for the diffusion contribution from the longitudinal mode, we can determine the value of $\Gamma_\perp(\mathbf{q}_\perp)$ which we denote by $\Gamma_\perp^D(\mathbf{q}_\perp)$. As we shall show below, the influence of spinons on $\Gamma_\perp(\mathbf{q}_\perp)$ does not alter the estimate for Γ_i^D which uses $\Gamma_\perp^D(\mathbf{q}_\perp)$.

Expressing $\Gamma_\perp^D(\mathbf{q}_\perp)$ in the form $\Gamma_\perp^D(\mathbf{q}_\perp) = \Gamma_\perp^D f^D(\mathbf{q}_\perp)$, where $f^D(\mathbf{q}_\perp)$ is a dimensionless function, from equation (11) we determine the scale $\Gamma_\perp^D$:

$$\Gamma_\perp^D = V\left(\frac{V}{D/a_\parallel^2}\right)^{1/3}(TG_0)^{2/3}. \quad (12)$$

This result allows us to obtain the following estimate from (10)

$$\Gamma_i^D \sim [J_i^{an}(0)]^2(TG_0)^{2/3}(V^{2/3}(D/a_\parallel^2)^{1/3})^{-1}. \quad (13)$$

We note that $\Gamma_i^D/\Gamma_\perp^D \sim [J_i^{an}(0)/V]^2 \approx 6\times10^{-2}$. The value of $\Gamma_\perp^D$ determines the boundary between the one-dimensional and three-dimensional dynamic behavior. In the homogeneous limit the Green function for $\omega \ll \Gamma_\perp^D$ has a Lorentzian form with the damping Γ_i typical of three-dimensional dynamics. By analyzing the dependence of $\Gamma_\perp^D(\mathbf{q})$ on ω, we can show that this function decays with frequency when $\omega \gg \Gamma_\perp^D$. In this regime the dynamic form factor will be determined by the one-dimensional dynamics. As a result, in this region of frequencies and magnetic fields the ESR spectrum may show some deviation from the Lorentzian line profile typical of a one-dimensional magnet [37].

The values of $\Gamma_\perp^D$ and Γ_i^D depend on the diffusion coefficient D whose value is not generally determined. For estimates we use the classical result for a chain:

$$\frac{D}{a_\parallel^2} = J\sqrt{\frac{2}{3}\pi S(S+1)},$$

which evidently gives the lower limit of D [36]. Bearing in mind that $G_0 \approx (J\pi^2)^{-1}$ at $T = 300$ K [42], we have $\Gamma_i^D \sim 0.1$ K and $\Gamma_\perp^D \sim 1.7$ K. The comparative smallness of these values is to a considerable extent attributable to the small factor $(TG_0)^{2/3} \approx 0.1$. Note that the relationship $\Gamma_\perp^D \ll T < J$ ensures that the region $Dq_\parallel^2 \gg \Gamma_\perp^D$ exists and that the inequality $\omega/T \ll 1$ is satisfied (for $\omega \sim \Gamma_\perp^D$). Both these conditions were used to determine $\Gamma_\perp^D$.

We now analyze the contribution to Γ made by spinon excitations which appear when $T < J$. Judging by the neutron scattering data [40], the Green spinon function obtained in the region $T \ll J$ comparatively accurately describes these modes in our case $T/J \approx 3/8$. To determine Γ^{sp} to within a numerical factor we can use the scaling representation for this function [34]:

$$G(\tilde{q}_\parallel, \omega) = \frac{A}{T}\Phi\left(\frac{C\tilde{q}_\parallel}{T}, \frac{\omega}{T}\right), \quad (14)$$

where $\tilde{q}_\parallel = q_\parallel - \pi/a_\parallel$, $C = J\pi/2a_\parallel$ is the spinon velocity, $A = 0.33$ to within a logarithmic factor, and $\Phi(0, 0) = 1$. Substituting this expression into formula (6) and taking $J_i^{an}(q)$ for $q = \pi/a_\parallel$, using a dimensional estimate we find $\Gamma_i^{sp} \propto T^{-1}$. This result holds if the integral in (6) is not singular for small $q_\parallel$ and x and does not diverge when $Cq_\parallel \gg T$, $x \gg T$. Using the explicit form of the function G [39], we can confirm that these conditions are satisfied and find the numerical factor. Bearing in mind that $|J_i^{an}(\pi/a_\parallel)| = |J_i^{an}(0)|$, we obtain

$$\Gamma_i^{sp} \approx [J_i^{an}(0)]^2/T. \quad (15)$$

Here the numerical factor is exactly unity since $(A\pi)^2 \approx 1$ where π^2 is the factor from $G_0^{-1} \approx J\pi^2$ and the remaining integral is close to unity.

Perturbation theory can definitely be applied in this case since Γ_i^{sp} is determined by the thermal spinons with $\omega \sim T$, $C\tilde{q}_\parallel \sim T$, and $\Gamma_i^{sp}/T \ll 1$.

We shall now consider the influence of spinons on the transverse modes which as we have seen are important for determining Γ_i^D Applying perturbation theory in terms of V, by analogy with the calculations of Γ_i^{sp} and $\Gamma_\perp^D$, we find

$$\Gamma_\perp^{sp}(\mathbf{q}_\perp) \approx \sum_{\mathbf{p}_\perp}[V(\mathbf{q}_\perp-\mathbf{p}_\perp)-V(\mathbf{p}_\perp)]^2T^{-1}. \quad (16)$$

The inequality $\Gamma_\perp^{sp}(\mathbf{q}_\perp)/T \leq (V/T)^2 \ll 1$ justifies the perturbation theory approach at $T = 300$ K. Estimating the value of $\Gamma_\perp^{sp}(\mathbf{q}_\perp)$ for $q_\perp a_\perp \sim 1$ which determines Γ_i^D in expression (10), we find $\Gamma_\perp^{sp} \sim V^2/T \approx 5$ K at $T = 300$ K.

Since $\Gamma_\perp^{sp} \sim \Gamma_\perp^D$ the spinon contribution does not change the order of magnitude of this estimate for Γ_i^D.

Note that the procedure for decoupling the four-spin correlation function into two spinon modes used to determine Γ_i^{sp} and $\Gamma_\perp^{sp}$ exhausts the spinon contribution to these quantities since the spinons are free. Bearing in mind that $\Gamma_i^{sp} \sim 0.33$ K, we finally have

$$\Gamma_i = \Gamma_i^D + \Gamma_i^{sp} \sim 3.5 \text{ kOe}. \quad (17)$$

Here an order-of-magnitude estimate is obtained mainly as a result of the diffusion contribution, which was determined allowing only for the simplest diffusion process. Provided that $(V/T)^2 \ll 1$, only this term depends explicitly on the chain interaction which was not specified above. In the compound CuO which is a monoclinic system these interactions are more complex [5] compared with the interaction in a simple tetragonal magnetic lattice. Since we are not claiming to make an exact quantitative estimate of Γ^D, it is merely important that the interactions between the chains do not differ substantially in magnitude. This condition is satisfied for CuO since, according to the neutron data for the magnon spectrum, the chain interactions in two mutually perpendicular directions in the plane orthogonal to the chains are 5 and 3 meV [6]. Finally we neglected the influence of interchain coupling on the static sublattice Green function, which leads to three-dimensional critical behavior of CuO. As has been noted, the corresponding three-dimensional effects begin to have an influence below $T = 250$ K.

The estimate obtained, $\Gamma \sim 3.5$ kOe, is close to the experimental value $\Gamma = 5$–7 kOe. In addition to the factor noted above, this difference may also be attributed to some indeterminacy of the exchange anisotropy, whose exact value along the different axes is unknown. We shall discuss this aspect in greater detail. Knowing Γ_i and using the proportionality $\Gamma_i \propto (J_i^{an}(0))^2$, we can determine the relationships between $J_i(0)$ which, however, do not agree with the inequality $J_b(0) > J_{a,c}(0)$ obtained because the **b** axis in CuO is the easy axis in the collinear phase [4]. This disparity may be attributed to the fact that the **a** and **c** crystallographic axes do not coincide with the principal axes of the tensor $\hat{J}$ and therefore $\hat{\chi}(\omega)$. In this case, the expression for the measurable response in the field **H** directed along the **a** and **c** axes includes all three Γ_i and is more complex than the result (4), which cannot be used to determine Γ_i in this geometry. At the same time, the **b** axis as the second-order axis in the monoclinic system must coincide with one of the principal axes of the tensor $\hat{\chi}(\omega)$ [23]. Thus, when **H** ∥ **b**, formula (4) holds for the response.

The formulated assumption is supported by the orientation of the helicoid plane in the incommensurate phase, which passes through the **b** axis and forms an angle of 28° with the **a** axis [5]. Since the exchange anisotropy is responsible for this orientation, we can conclude that although the two axes of the tensor $\hat{J}$ lie in the plane (**a**, **c**), they do not coincide with the **a** and **c** axes. Thus, the exact values of the spin relaxation rates and the *g*-factors in CuO obtained from the ESR spectra **H** ∥ **b** are

$$(\Gamma_a + \Gamma_c)/2 \approx 5 \pm 1.5 \text{ kOe}, \quad g_b = 1.85 \pm 0.16.$$

We shall now consider the results for samples where Cu is replaced by Zn and Li. The incorporation of zinc influences the spectra comparatively weakly. For instance, the value of $(\Gamma_a + \Gamma_c)/2 \approx 5$ kOe simply agrees with the result for CuO. This is naturally interpreted in terms of ordinary magnetic dilution. The stronger influence of the magnetic dilution on the line width is attributed to the one-dimensional diffusion length being limited to a value of the order of the average spacing between the impurities in the chain. However, as is readily established, in our case the zinc concentration (1.5%) is too low for this constraint to influence Γ^D for the selected value of *D*.

The appreciable broadening of the spectra in the lithium-doped crystal is attributed to the appearance of excess holes which strongly perturb the magnetic subsystem. Strong coupling between the holes and the spin system is indicated by the fact that the activation energy in the temperature dependence of the conductivity changes by approximately a factor of two on transition to the magnetically ordered state in pure CuO and in lithium-doped CuO [3]. Note that the increase in the conductivity by approximately two orders of magnitude in the Li-containing samples at $T = 300$ K compared with CuO does not change its character. The conductivity of CuO is satisfactorily described by small-radius polaron theory with incoherent hopping at $T = 300$ K [2]. In this case, the hole lifetime in the localized state $\tau_h \approx 10^{-10}$ s at $T \approx 300$ K is approximately the same as the reciprocal resonance frequency f^{-1}. Assuming that holes localized in a CuO_4 cluster form a Zhang–Rice singlet and thereby remove the matrix spin from resonance, hole hopping at the frequency $\tau_h^{-1} \approx f$ could lead to line broadening by a value of the order of itself. However, this simple broadening mechanism with strongly localized holes can occur when the hole concentration is comparable to the number of copper atoms in the matrix. By this reasoning, we can evidently eliminate this influence of hole mobility on the line width.

It should be stressed that the hole mobility is three-dimensional as is evidenced by the weak anisotropy of the CuO conductivity [2]. Hence, in lithium-doped CuO there is no reason to predict that the quasi-one-dimensional spin excitations will be strongly modified by mobile holes which could occur if the hole transport took place mainly along the chains.

Bearing in mind the comparatively long time spent by the holes in the bound state, a scenario where the motion of the holes is not a determining factor in the broadening seems more realistic. It may be predicted that the holes form an exchange-bound complex with several copper spins, for example with four copper ions in the unit cell. The rich spin spectrum of the complex and the strong phonon coupling can ensure a fairly high rate of spin–lattice relaxation considerably higher than the rate of spin–lattice relaxation of the matrix. Assuming that the complex is weakly bound to the matrix spins and has a susceptibility χ_{hc} substantially higher than the susceptibility of the matrix $\chi \propto (J\pi^2)^{-1}$, we can obtain line broadening in doped CuO commensurate with $\Delta H_{1/2}$ in CuO. Let us assume, for example, that the distance between the two lower levels of the complex is $\Delta E \simeq 300$ K $\approx J/3$. Then, $\chi_{hc} \sim 3(g\mu)^2/J$ and $x\chi_{hc}/\chi \sim 3\pi^2 x \approx 1/3$, where $x \approx 10^{-2}$ is the relative lithium concentration (excess holes). If the rate of spin relaxation of the complexes is $\Gamma_{hc} \sim (3–5)\Gamma$, their contribution to the width will be close to $\Delta H_{1/2}$ for the matrix. Quite clearly, in this case doping should increase the static susceptibility of the system below the hole localization temperature $T \approx 70$ K [14]. Unfortunately, data on χ for lithium-doped copper oxide [15] cannot be used to determine whether this 30% increase is caused by the fairly large diamagnetic contribution to the susceptibility of the ion cores. The hole mobility in this model simply limits the lifetime of the complexes to τ_h and is not fundamental if $\tau_h^c \geq \Gamma_{hc}^{-1}$.

The influence of doping on the magnetic system does not merely involve the effect described. We know that in lightly doped two-dimensional cuprates the incorporation of holes limits the two-dimensional correlation length of the spin fluctuations above T_N. This effect has been studied most comprehensively in La_2CuO_4 for various dopants including Li [16]. A certain universality of its dependence on the dopant concentration observed near T_N can be attributed to the formation of a collective hole structure. Quite clearly, lithium doping in CuO also limits the growth of one-dimensional spin fluctuations which should influence the critical increase in the spin relaxation rate near T_N. In view of this, it is suggested that experiments should be carried out to make a comparative analysis of the ESR line widths in pure and lithium-doped CuO near T_N.

The results relating to the Hall effect in these crystals were not analyzed in the present study. We merely note that the "hole" sign of the Hall signal corresponds to the polarity of the carriers (for electron conduction in the resonator material this is positive).

ACKNOWLEDGMENTS

The authors are grateful to V. A. Solov'ev for assistance with the experiments. This work was supported by the Russian Foundation for Basic Research, project no. 97-02-17097.

REFERENCES

1. W. Brening, Phys. Rep. **251**, 153 (1995).
2. A. A. Samokhvalov, N. A. Viglin, B. A. Gizhevskiĭ, *et al.*, Zh. Éksp. Teor. Fiz. **103**, 951 (1993) [JETP **76**, 463 (1993)].
3. B. A. Gizhevskiĭ, A. A. Samokhvalov, N. M. Chebotaev, *et al.*, Sverkhprovodimost' (KIAE) **4**, 827 (1991).
4. J. B. Forsyth, P. J. Brown, and B. M. Wanklin, J. Phys. C **21**, 2917 (1988).
5. M. Ain, A. Menelle, B. M. Wanklyn, *et al.*, J. Phys.: Condens. Matter **4**, 5327 (1992).
6. M. Ain, W. Reichardt, B. Hennion, *et al.*, Physica C **162–164**, 1279 (1989).
7. M. O'Keeffe and F. S. Stone, J. Phys. Chem. Solids **23**, 261 (1962).
8. T. I. Arbuzova, A. A. Samokhvalov, I. B. Smolyak, *et al.*, J. Magn. Magn. Mater. **95**, 168 (1991).
9. T. Chattopadhyay, G. J. McIntyre, P. J. Brown, *et al.*, Physica C **170**, 371 (1990).
10. K. Kindo, M. Honda, T. Kohashi, and M. Date, J. Phys. Soc. Jpn. **59**, 2332 (1990).
11. F. Mehran, Phys. Rev. B **46**, 5640 (1992).
12. A. V. Lazuta, Physica C **181**, 127 (1991).
13. P. Simon, J. M. Bassat, S. B. Oseroff, *et al.*, Phys. Rev. B **48**, 4216 (1993).
14. P. Carretta, M. Corti, and A. Rigamonti, Phys. Rev. B **48**, 3433 (1993).
15. T. I. Arbuzova, I. V. Smolyak, S. V. Naumov, *et al.*, Fiz. Tverd. Tela (St. Petersburg) **40**, 1876 (1998) [Phys. Solid State **40**, 1702 (1998)].
16. P. J. Suh, P. C. Hammel, Y. Yoshinari, *et al.*, Phys. Rev. Lett. **81**, 2791 (1998).
17. M. Corti, A. Rigamonti, F. Tabak, *et al.*, Phys. Rev. B **52**, 4226 (1995).
18. V. A. Ryzhov, E. I. Zavatskiĭ, V. A. Solov'ev, *et al.*, Zh. Tekh. Fiz. **65**, 133 (1995) [Tech. Phys. **40**, 71 (1995)].
19. V. V. Isaev-Ivanov and V. N. Fomichev, Prib. Tekh. Éksp., No. 3, 172 (1976).
20. G. Feher, Bell Syst. Tech. J. **36**, 449 (1957).
21. C. P. Poole, *Experimental Techniques in Electron Spin Resonance* (Wiley, New York, 1966; Mir, Moscow, 1970).
22. A. G. Redfield, J. Appl. Phys. **25**, 1021 (1954).
23. L. D. Landau and E. M. Lifshitz, *Electrodynamics of Continuous Media* (Pergamon, Oxford, 1984; Nauka, Moscow, 1992).
24. C. B. Azzolini, A. Paleari, and G. B. Parravicini, J. Phys.: Condens. Matter **4**, 1359 (1992).
25. D. L. Huber and M. S. Seehra, Phys. Status Solidi B **74**, 145 (1976).
26. U. Kobler and T. Chattopadhyay, Z. Phys. B **82**, 383 (1991).
27. T. I. Arbuzova, I. B. Smolyak, A. A. Samokhvalov, *et al.*, Zh. Éksp. Teor. Fiz. **113**, 1026 (1998) [JETP **86**, 559 (1998)].

28. H. J. Schulz, Phys. Rev. Lett. **77**, 2790 (1996).
29. I. Affleck, in *Fields, Strings and Critical Phenomena*, Ed. by E. Brezin and J. Zinn-Justin (North Holland, Amsterdam, 1990), p. 563.
30. S. Sachdev, Phys. Rev. B **50**, 13006 (1994).
31. B. N. Narozhny, Phys. Rev. B **54**, 3311 (1996).
32. X. Zotos, Phys. Rev. Lett. **82**, 1764 (1999).
33. M. Bohm, V. S. Viswanath, J. Stolze, *et al.*, Phys. Rev. B **49**, 15669 (1994).
34. O. A. Starykh, A. N. Sandvik, and R. R. P. Singh, Phys. Rev. B **55**, 14953 (1997).
35. K. Fabricius and B. M. McCoy, Phys. Rev. B **57**, 8340 (1998).
36. M. Takigawa, N. Motoyama, H. Fisaki, *et al.*, Phys. Rev. Lett. **76**, 4612 (1996).
37. T.-P. Boucher, M. A. Bakheit, M. Nechtschein, *et al.*, Phys. Rev. B **13**, 4098 (1976).
38. M. Takigawa, T. Asano, Y. Ajiro, *et al.*, Phys. Rev. Lett. **76**, 2173 (1996).
39. H. J. Schulz, Phys. Rev. B **34**, 6372 (1986).
40. D. A. Tennat, T. G. Perring, P. A. Cowley, *et al.*, Phys. Rev. Lett. **70**, 4003 (1993).
41. S. V. Maleev, Zh. Éksp. Teor. Fiz. **66**, 1809 (1974) [Sov. Phys. JETP **39**, 889 (1974)].
42. S. Eggert, I. Affleck, and M. Takahashi, Phys. Rev. Lett. **73**, 332 (1994).

Translation was provided by AIP

Journal of Experimental and Theoretical Physics, Vol. 90, No. 2, 2000, pp. 352–359.
Translated from Zhurnal Éksperimental'noĭ i Teoreticheskoĭ Fiziki, Vol. 117, No. 2, 2000, pp. 398–406.

SOLIDS
Electron Properties

Influence of an Electric Field on the Stability of Thermogravitational Flow in a Vertical Capacitor

S. A. Zhdanov, S. R. Kosvintsev*, and I. Yu. Makarikhin**
Perm State University, Perm, 614600 Russia
**e-mail: kosvintsev@psu.ru*
***e-mail: igor@psu.ru*
Received August 18, 1999

Abstract—An experimental and theoretical study is made of the influence of a transverse electric field on thermogravitational flow in a vertical capacitor filled with a barely conducting liquid. The boundaries of the capacitor are maintained at different temperatures. In the calculations it is assumed that the main contribution to ionization of the liquid, which is electrically neutral in the absence of the field, is made by the buildup of uncompensated charge accompanying the flow of electric current through a liquid having a nonuniform conductivity distribution. The latter is induced by the temperature gradient. This system is simulated experimentally by using a suitable working liquid–electrode material system. © *2000 MAIK "Nauka/Interperiodica".*

1. INTRODUCTION

The influence of an electric field on the equilibrium stability of a barely conducting liquid has recently formed the subject of numerous experimental and theoretical studies which are reviewed in [1, 2]. This problem has attracted interest because of the wide range of technical applications in which strong electric fields are used. One example is an electrohydrodynamic energy converter, in which electric field energy is converted directly into the kinetic energy of a liquid flow. Another important technical application is the possible of intensifying and, in some cases, controlling dynamically [3, 4] the heat and mass transfer in high-voltage devices. The problem of electroconvective instability is also interesting from the general theoretical point of view since it opens up possibilities for studying and using a new type of flow excitation, and also introduces a new type of interaction between electric and hydrodynamic fields. The main difficulty encountered in the description of electroconvective instability is that in the absence of an electric field, barely conducting liquids are electrically neutral and charge formation in these liquids is a complex physicochemical process whose description has not yet been completely clarified. The charge formation mechanisms are usually classified into several types [2, 5]. One of these is the formation of uncompensated bound charge as a result of nonuniform polarization of the liquid which can be induced, for example, by nonuniform heating of the barely conducting liquid. Many experimental investigations indicate that because of its smallness this mechanism negligibly influences the electroconvective instability in ordinary barely conducting liquids. The most hazardous mechanism for instability is electrification as a result of a local loss of equilibrium in the dissociation–recombination reaction of liquid molecules in the regions adjacent to the electrodes (physical injection). In this case, like electric charge forms around the electrode, and this can either relax as a result of Ohmic current and interaction with opposite liquid ions formed in the bulk, or it can induce electroconvective motion of the liquid. When the liquid is heated nonuniformly, uncompensated space charge may also form as a result of the temperature dependence of the ion mobilities (electroconductive mechanism). The influence of these types of charge formation on electroconvective instability has now been studied in fairly great detail with reference to problems involving the mechanical equilibrium instability of a nonuniformly heated, barely conducting liquid [2, 5]. However, a more complex and interesting problem from the theoretical point of view and in terms of technical applications is the study of flow stability in an electric field. Unlike problems of electroconvective equilibrium instability, the flow, which takes place even in the absence of the electric field, influences the equilibrium distribution of the electric charge. Few theoretical studies have examined this problem. Takashima and Hamabata [6] investigated the equilibrium of thermogravitational flow in a vertical capacitor with nonuniformly heated boundaries allowing for nonuniform polarization of the liquid dielectric. This study is merely of theoretical value because, as we have already noted, the influence of the ponderomotive force on electroconvective instability is doubtful. The problem of equilibrium stability of the thermogravitational flow in a vertical capacitor was solved most systematically by one of the present authors [7] for the electroconductive mechanism of charge formation. In this study, Makarikhin examined the electroconvective instability of the dominant steady-state plane-parallel flow in a vertical gap with ideal heat-conducting and electrically conducting

1063-7761/00/9002-0352$20.00

boundaries [7]. It is known [8] that the dominant flow appears in the absence of an electric field for an arbitrarily small temperature difference at the boundaries of the gap. The flow can be unstable for a certain value of the dimensionless Grashof number. Depending on the liquid parameters either a monotonic "cat's eye" instability mode or an oscillation mode, i.e., thermal waves, can occur. In [7] Makarikhin constructed stability maps in dimensionless coordinates by plotting Grashof number against Rayleigh electric number for limiting cases of small Prandtl numbers and an infinitely short electric charge relaxation time. Disregarding various qualitative experiments [9] in which the possibility of electroconvective instability was demonstrated, no experimental investigations have yet been made of flow instability.

The present paper is devoted to an experimental investigation of electroconvection in a vertical capacitor with nonuniformly heated boundaries under conditions where the electroconductive mechanism of electrification predominates. One of the aims of this study was to identify the ranges of experimental parameters where the electroconductive mechanism makes the main contribution to charge formation. Numerical investigations are made of electroconvection in a vertical capacitor for finite electric relaxation times and other physicochemical parameters similar to the real physical situation which was obtained experimentally.

2. EXPERIMENTAL

As was noted in the Introduction, several electrification mechanisms usually take place in a barely conducting liquid, the most hazardous generally being the injection mechanism. Thus, in order to isolate the electroconductive mechanism, we needed to use an electrode–liquid system in which the threshold potential for physical injection and the rate of charge relaxation in the electrode regions were as high as possible [5]. That is to say, the electrode material should have a fairly high electron work function from the metal, which must not oxidize in an electric field. The barely conducting liquid for its part should have a sufficiently high intrinsic conductivity so that the charge relaxation time is as short as possible but not so high that it influences the Joule heating of the liquid. After many preliminary experiments we selected a system using steel electrodes and Mazola corn oil from the US.

2.1. Physicochemical Parameters

Since the physicochemical parameters of this liquid are not described in the literature, we carried out preliminary experiments to measure these and the results are presented in table. The density ρ and coefficient β of the temperature dependence of the density were determined using densitometers which were lowered into a measuring cylinder containing thermostatically controlled working liquid. The temperature was maintained to within 0.05°C. The dynamic viscosity η as a function of temperature was determined by the Stokes method, which involved measuring the dropping time for small spheres of Wood's alloy in the thermostatically controlled measuring cylinder.

Table

ρ, g/cm^3	$\beta \times 10^4$, 1/°C	η, P	$k \times 10^3$, cm^2/s
0.9182	6.2 ± 0.4	$11.5 \times T^{-0.82}$	1.7 ± 0.1

The thermal diffusivity of the corn oil κ was determined by solving the standard convective problem of the equilibrium stability of a horizontal layer of liquid heated from below. We know [8] that the critical Rayleigh parameter for which stability is lost is $Ra^* = 1708$. The Rayleigh number is then determined by the conventional procedure: $Ra^* = \rho g \beta \theta^* h^3/\eta\kappa$, where θ^* is the critical temperature difference between the boundaries of the liquid layer, and g is the free-fall acceleration. Having measured θ^* and knowing the other liquid parameters, we can determine the thermal diffusivity. In order to measure the critical temperature difference, we constructed an experimental cell comprising a plane horizontal layer of liquid whose boundaries were maintained at different temperatures. This setup was used to compare the effective thermal conductivity of the liquid layer (molecular and convective) with the thermal conductivity of a thin Plexiglas plate through which we passed the same heat flux as in the liquid layer. When convective motion occurred, the ratio of these thermal conductivities changed and this allowed us to determine the corresponding critical temperature difference at the liquid layer.

2.2. Electroconvective Cell

The experimental cell was a vertical gap measuring $14 \times 8.0 \times 0.80$ cm^3 (Fig. 1). The cell was formed by a transparent Plexiglas frame and its sides were bounded by steel electrodes measuring $43 \times 10 \times 0.3$ cm^3. The temperature gradient in the layer was produced by heat exchangers *3* comprising solid aluminum blocks measuring $45 \times 14 \times 5.5$ cm^3, each containing 15 cylindrical channels *4*. Water from two thermostats was circulated through the channels. This solid structure allowed us to maintain the temperature of each heat exchanger to within 0.1°C and the temperature nonuniformity along its surface was less than 0.02°C. Thin electrically insulating plates *5* and *6* made of 0.10 cm thick Getinaks and 0.38 cm thick Plexiglas, respectively, were inserted between the heat exchangers and the electrodes. The experimental apparatus was fitted with a UPU-10 stabilized dc voltage source which could deliver a voltage in the range 200–10 000 V. The voltage was monitored using an S-56 electrostatic voltmeter to within 50 V. The Plexiglas spacer *6* was used as the constant thermal conductivity reference in the Schmidt–Milverton method of studying the equilibrium stability of a liquid [10]. This

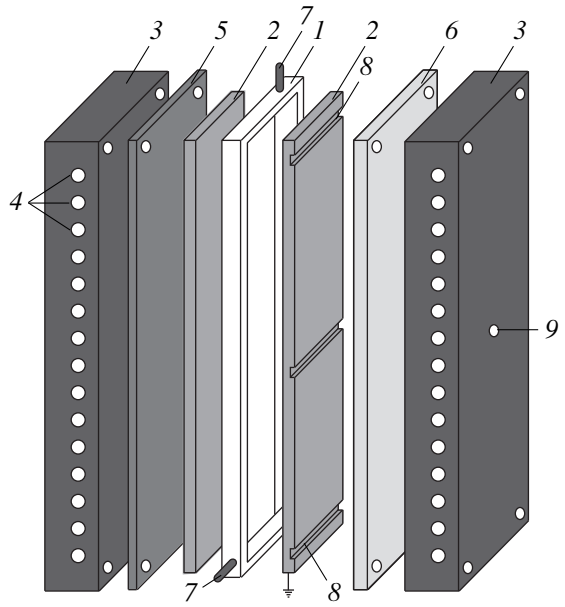

Fig. 1. Schematic of convective cell: *1*, plexiglas frame; *2*, steel electrodes; *3*, heat exchangers; *4*, channels for circulating water from thermostats; *5*, Getinaks insulating plate; *6*, Plexiglas insulating plate used as heat flux detector; *7*, tubes for filling with working liquid; *8*, *9*, channels for thermocouples.

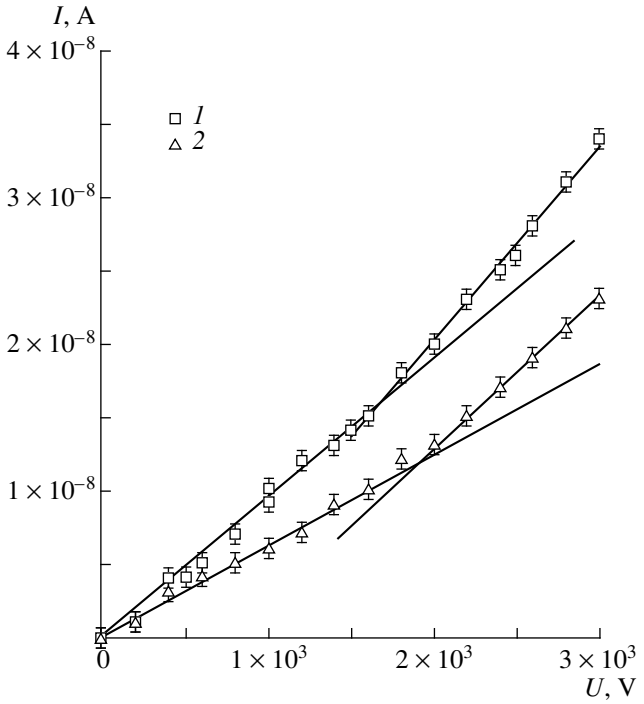

Fig. 2. Current–voltage characteristics of industrial corn oil (*1*) and heat-treated oil (*2*).

method involves comparing the thermal resistance of the liquid layer and the insulating spacer *6* by measuring the temperature gradients at the liquid layer T_s and at the insulating spacer T_p. If the electric field does not influence the dominant thermogravitational flow and the heat transport is only determined by the molecular thermal conductivity (as was shown in [8], the dominant flow does not create any additional heat flux across the layer), the ratio of the temperature gradient at the liquid layer T_s to the temperature gradient at the sample T_p will be constant for various temperature gradients between the heat exchangers. When electroconvective instability occurs, the effective thermal conductivity of the liquid increases and the ratio of the temperature gradients decreases. The constructed dependence of T_p on T_s was used to determine the critical temperature difference at the liquid layer T^* at which electroconvective instability occurs. Several copper–Constantan thermocouples were installed in the cell to measure the temperatures (two to monitor the temperature uniformity along the heat exchangers, two to measure the temperature gradient at the spacer and at the liquid layer, and one to measure the temperature gradient between the heat exchangers).

2.3. Investigation of Electrophysical Parameters

We know [11] that the electrophysical properties of a liquid–electrode system depend strongly on the quantity and qualitative composition of the impurities in the liquid, the time of interaction between the liquid and the charged metal electrode, and also on the interelectrode gap. As a result, the conductivity and the temperature dependence of the conductivity were measured directly using the model described above before the convective experiment. In addition, measurements of the current–voltage characteristics were carried out to show that the electroconductive mechanism of charge formation predominates in the experiments and injection ionization does not influence the electroconvective instability. In order to measure the current–voltage characteristics, a 12.4 kΩ reference resistance was connected in series in the low-voltage capacitor supply circuit and the voltage drop as a function of the voltage across the capacitor plates was measured experimentally at this resistance. The current–voltage characteristics were measured at a fixed temperature, which was the same for both heat exchangers.

The first series of experiments was devoted to studying the conductivity of the oil. Figure 2 (curve *1*) gives the current–voltage characteristic of oil which had not received any additional treatment. It can be seen that the dependence is essentially nonlinear and a kink is clearly visible. This nonlinearity can easily be attributed to the existence of injection conductivity, which is characterized by a quadratic dependence of current on voltage unlike the electroconductive mechanism for which Ohm's law is satisfied [11]. In Fig. 2 these dependences are clearly superposed. The relatively clear kink on the current–voltage characteristic indicates that isothermal electroconvective instability occurs. The increase in the current transport is evidently caused by

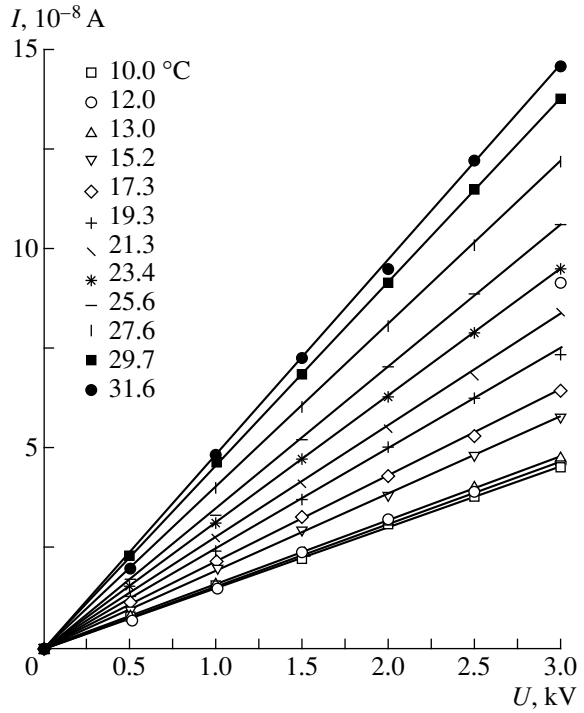

Fig. 3. Current–voltage characteristics of purified corn oil at various temperatures.

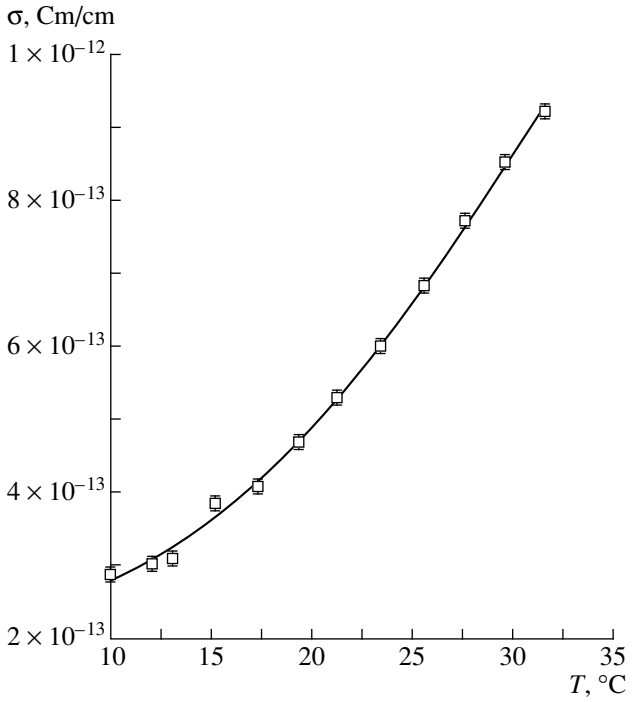

Fig. 4. Conductivity of corn oil versus temperature.

the convective current transport. In order to suppress the level of injection, the oil was subjected to heat treatment. For this purpose the oil was kept at a pressure of 1–10 Torr and a temperature of 70–80°C for two days. The current–voltage characteristics obtained after heat treatment are also plotted in Fig. 2 (curve *2*). It can be seen that despite the qualitative similarity between the characteristics of the treated and untreated oils, there is a substantial quantitative difference. First, the critical voltage at which electroconvective instability occurs increased to 2 kV. Second, the low-voltage conductivity decreased substantially. Third, the relative contribution of the isothermal electroconvective instability to the current transport decreased. Subsequently, we only used electrode voltages lower than 3 kV to identify the electroconductive convection mechanism.

The next step in the experiments was to measure the coefficient of the temperature dependence of the conductivity, for which we measured the current–voltage characteristics at various temperatures in the liquid layer. Figure 3 shows the current–voltage characteristics plotted at various temperatures of an isothermal layer of corn oil. It can be seen that these characteristics are linear which indicates that instability caused by the isothermal injection mechanism of charge formation is not observed in this electrode–liquid system for the given temperatures and voltages up to 3 kV.

The conductivities of the liquid were calculated from the slopes of the current–voltage characteristics for various temperatures using the formula $\sigma = h(k_f - k_e)/S$, where h and S are the layer thickness and the area of the capacitor plate, respectively, and k_f and k_e are the slopes of the current–voltage characteristic when the cell is filled with corn oil and when it is empty, respectively. As a result, we obtain the temperature dependence of the conductivity (Fig. 4). It can be seen that the conductivity increases nonlinearly with temperature, whereas the theoretical investigations [7] assume a linear dependence. However, in experiments to study the electroconvective instability with relatively small temperature gradients, for example, between 15 and 25°C, the difference of the dependence from linear does not exceed 1%, which suggests that the theoretical assumptions are adequate. The coefficient of the linear temperature dependence of the conductivity was determined as the slope of the tangent drawn to the experimental curve at the point $T = 23$°C and was found to be $\beta_\sigma = 0.058$ 1/°C.

2.4. Experimental Results

The experimental procedure was as follows. Thermostats were used to establish a specific temperature gradient between the heat exchangers in the cell with no applied voltage. Voltage was then applied to the electrodes and after a steady-state heat transfer regime had been established, which could be determined from the fact that the thermocouple readings were constant, measurements were made of the thermo-emf at the heat flux detector T_p and at the liquid layer T_s. The temperature gradient between the heat exchangers was then altered and the measurements repeated. The results

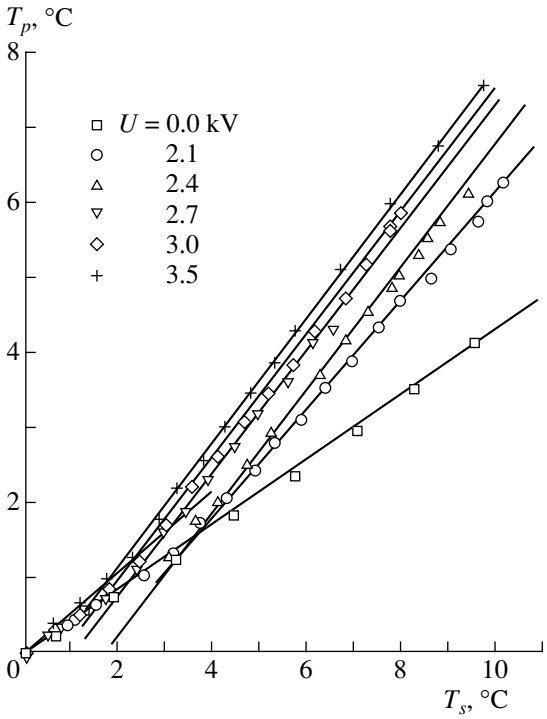

Fig. 5. Temperature gradient T_p at heat flux detector as a function of T_s for various voltages across the electrodes.

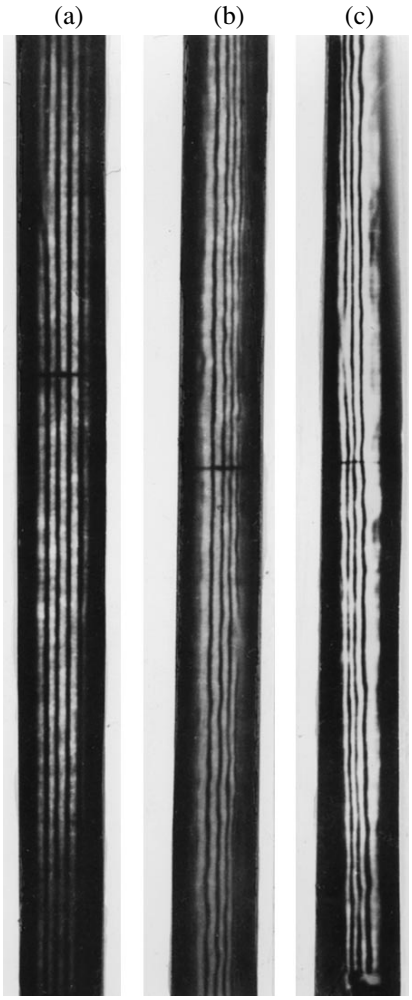

Fig. 6. Photographs of grating obtained for the same temperature difference at the layer boundary T_s = 7.5°C and different voltages across the electrodes (a, U = 0, b, U = 1600, c, U = 2000 V).

were used to construct dependences of the temperature gradient at the layer on the temperature gradient at the spacer. Similar measurements were made for other fixed potential differences between the electrodes between zero and 4.0 kV. Typical dependences for several voltages across the electrodes are plotted in Fig. 5. It can be seen that for zero voltage, the dependence is a straight line passing through the origin. This behavior is typical of the molecular heat transfer regime because the dominant thermogravitational flow does not transfer any heat across the layer. For small temperature gradients at the liquid layer, the dependence $T_p(T_s)$ in the presence of a field is the same as that for $U = 0$, which corresponds to the absence of any electroconvective instability. However, as the temperature gradient increases further, the dependence acquires a kink and the temperature gradient at the spacer increases more rapidly than that at the liquid layer. This indicates that electroconvective instability occurs in the model, which increases the thermal flux and therefore reduces the temperature gradient at the liquid layer. It can be seen that as the voltage increases, the critical temperature difference decreases. Moreover, most of the dependences for different voltages are parallel. This means that during electroconvective instability, only one type of supercritical motion is established in the liquid. The post-crisis line only has a significantly different slope at relatively low voltages. Thus, for a fixed voltage across the electrodes we determined the critical gradients at the liquid layer T^* which correspond to the point of inflection on the curves $T_p(T_s)$.

During the experiments we also made visual observations of the flow structure using a penumbral grating method. This involved making observations of a bright, uniformly illuminated grating of parallel equidistant fringes through the transparent side walls of the capacitor. When the flow exhibited electroconvective instability, the uniform distribution of the temperature gradient was perturbed and "stria" appeared, bending the ray path in the capacitor and distorting the grating lines. Figure 6 shows a photograph of a grating for the gradient T_s = 7.5°C at various voltages. At zero potential difference between the electrode the fringes remain parallel (Fig. 6a). When the voltage slightly exceeds the critical value (for a given temperature), the fringes begin to bend (Fig. 6b). At high voltages the electroconvection is so strong that the bending becomes appreciable (Fig. 6b). It should be noted that the observed pattern for a given

voltage and temperature gradient at the layer is steady-state under these conditions, which suggests that the convective structures are steady-state.

Using the measured parameters of the working liquid and these critical temperature gradients we constructed a thermogravitational flow stability diagram (Fig. 7) using dimensionless coordinates: the electric number B, which has the meaning of the ratio of the Coulomb forces to the Archimedes forces, and the Grashof number G. The dimensionless parameters were calculated using the formulas $G = \rho^2 g\beta\theta h^3/\eta^2$ and $B = eU^2\beta_\sigma/\rho g\beta h^3$. The stability diagram also gives the results of a theoretical analysis which will be discussed below.

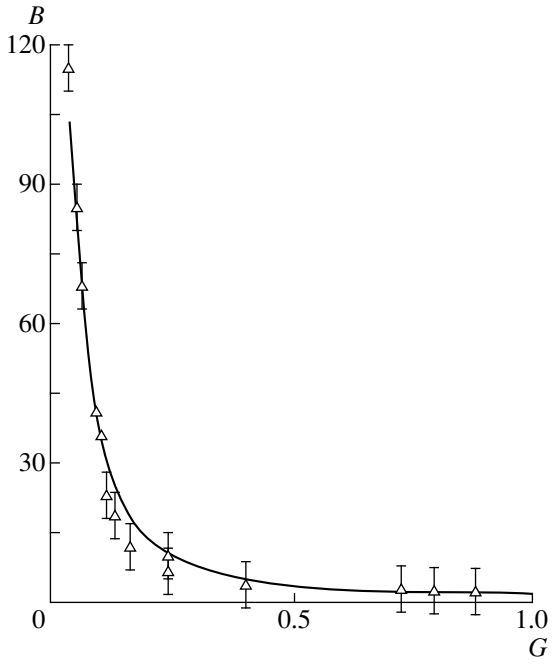

Fig. 7. Diagram of thermogravitational flow stability. The solid curve corresponds to the theoretical calculations.

3. THEORETICAL ANALYSIS

The problem of the stability of thermogravitational flow is formulated assuming that a barely conducting liquid fills a vertical capacitor whose boundaries are heated to different temperatures. We write a system of electroconvection equations consisting of the Navier–Stokes and heat transfer equations, the electric charge conservation law, the Gauss law, and the electric field potentiality condition:

$$\gamma\left(\frac{\partial \mathbf{v}}{\partial t} + (\mathbf{v}\nabla)\mathbf{v}\right) = -\nabla p + \gamma\nu\Delta\mathbf{v} - \gamma\beta T\mathbf{g} + \rho\mathbf{E},$$

$$\frac{\partial T}{\partial t} + \mathbf{v}\nabla T = \chi\Delta T, \quad \nabla\mathbf{v} = 0,$$

$$\frac{\partial \rho}{\partial t} + \nabla(\sigma\mathbf{E} + \rho\mathbf{v}) = 0, \quad \sigma = \sigma_0(1 + \beta_\sigma T), \tag{1}$$

$$\varepsilon(\nabla\mathbf{E}) = \rho, \quad \mathbf{E} = -\nabla\varphi,$$

Here γ, ν, ε, and σ are the density, kinetic viscosity, dielectric constant, and average conductivity of the liquid, β and β_σ are the temperature dependences of the density and conductivity, and $\mathbf{E}$ and φ are the electric field strength and potential. Assuming that the boundaries of the capacitor are solid and ideally conduct both heat and electric current, we obtain the boundary conditions:

$$x = \mp h, \quad \mathbf{v} = 0, \quad T = \pm\theta, \quad \varphi = \mp U, \tag{2}$$

where h is the half-width of the liquid layer, θ and U are half the temperature difference and potential difference at the boundaries of the liquid layer, respectively, and x is the coordinate axis having its origin at the center of the layer and perpendicular to the boundaries. The solution of the system (1) for the steady state in which all the time derivatives are zero gives the velocity field of the dominant thermogravitational flow and the corresponding distributions for all the parameters of the problem:

$$T_0 = -\theta\xi, \quad \xi = \frac{x}{h}, \quad \mathbf{v}_0 = \mathbf{v}_0(0, 0, v_0),$$

$$v_0 = \frac{\beta g\theta h^2}{\sigma\nu}\xi(\xi^2 - 1).$$

$$\mathbf{E}_0 = \mathbf{E}_0(E_0, 0, 0), \quad E_0 = \frac{2U\beta_\sigma\theta}{h\ln A}\frac{1}{(1 - \beta_\sigma\theta\xi)}, \tag{3}$$

$$\rho_0 = \frac{2\beta_\sigma^2\theta^2\varepsilon U}{h^2\ln A}\frac{1}{(1 - \beta_\sigma\theta\xi)^2}, \quad A = \ln\frac{1 - \beta_\sigma\theta}{1 + \beta_\sigma\theta}.$$

It was found that steady-state flow does not depend on the coordinate in the direction of the liquid layer, and that the electrical and hydrodynamic characteristics do not depend on one another. In particular, the velocity profile is the same as that in the absence of an electric field. We shall subsequently assume that the inhomogeneities of the density and conductivity are small and we write the system of equations (1) linearized about the steady state (3) for perturbations of all three parameters of the problem. We shall assume that, in accordance with [8], planar perturbations are the most hazardous from the point of view of equilibrium instability in the absence of a field. Thus, we shall only analyze those perturbations which depend on the x and y coordinates. The dimensionless linearized system of equations for the perturbations has the following form:

$$\frac{\partial\Delta\Psi}{\partial t} + G\left(v_0\frac{\partial\Delta\Psi}{\partial z} - \frac{\partial^2 v_0}{\partial x^2}\frac{\partial\Psi}{\partial z}\right) = \Delta\Delta\Psi + \frac{\partial\theta}{\partial x}$$

$$- G_e\left(\frac{\partial\Phi}{\partial z}\frac{\partial^2 F_0}{\partial x^2} - E_0\frac{\partial\Delta\Phi}{\partial z}\right),$$

$$\frac{\partial\theta}{\partial t} + G\left(v_0\frac{\partial\theta}{\partial z} - \frac{\partial T_0}{\partial x}\frac{\partial\Psi}{\partial z}\right) = \frac{1}{P}\Delta\theta,$$

$$\frac{\partial\Delta\Phi}{\partial t} + G\left(v_0\frac{\partial\Delta\Phi}{\partial z} + \frac{\partial^2 E_0}{\partial x^2}\frac{\partial\Psi}{\partial z}\right)$$

$$= \frac{1}{P_e}\left(S\frac{\partial E_0}{\partial x}\theta + SE_0\frac{\partial\theta}{\partial x} - \sigma(T_0)\Delta\Phi - \frac{\partial\sigma(T_0)}{\partial x}\frac{\partial\Phi}{\partial x}\right), \quad (4)$$

$$G = \frac{g\beta\theta h^3}{\nu^2}, \quad G_e = \frac{\varepsilon U^2}{\gamma g\beta\theta h^3}, \quad S = \beta_\sigma\theta,$$

$$P = \frac{\nu}{\chi}, \quad P_e = \frac{\varepsilon\nu}{\sigma_0 h^2},$$

$$x = \pm 1\colon \frac{\partial\Psi}{\partial x} = \frac{\partial\Psi}{\partial z} = \theta = \Phi = 0,$$

$$\sigma \ll \frac{1}{h}\left(\frac{\varepsilon}{\mu}\right)^{1/2}, \quad \frac{\omega}{2\pi} \ll \frac{c}{h}.$$

The units of measurement were selected as follows: h for length, h^2/ν for time, $\beta g\theta h^2/\nu$ for velocity, θ for temperature, $\gamma\beta g\theta h$ for pressure, and U for potential; G and P are the Grashof and Prandtl numbers, G_e is the Grashof electric number which gives the ratio of the Coulomb force and the viscous dissipative forces, and may be obtained from the electric number B used experimentally by multiplying this number by the Rayleigh number, and P_e is the Prandtl electric number which gives the ratio of the relaxation times of the velocity and charge perturbations. The velocity field and the electric field are written conventionally in terms of the current function and the electric potential. We considered planar normal perturbations periodic along the z axis and having the wave number k which was selected as follows. We first solved the standard problem of the stability of thermogravitational flow [8] in the absence of an electric field for the liquid parameters described in the experimental section (see Table 1). We determined the critical wave number k^* corresponding to the most hazardous perturbation mode. We then solved the problem in the presence of an electric field (4) with $k = k^*$ and determined the dependence of the critical parameter G_e for which electroconvective instability occurs for each selected value of G. For the physicochemical parameters corresponding to the experimental conditions ($P = 600$ and $P_e = 3.0$) the system (4) has a small parameter at one of the leading derivatives. Thus, a differential sweeping method was selected for the calculations. The results of the calculations for the parameters given above are plotted together with the experimental data in Fig. 7. It can be seen that the agreement between the experimental results and the theoretical analysis is more than satisfactory.

4. CONCLUSIONS

The good agreement between the experimentally and theoretically determined patterns of electroconvective instability of the thermogravitational flow in a vertical capacitor shows first that in the selected electrode–liquid system the electroconvective instability is caused by an electroconductive type of charge formation as a result of the temperature dependence of the conductivity and second indicates that the constructed theoretical model is adequate. However, steady-state convective structures are observed in the capacitor within the error limits of the penumbral flow visualization method. The theoretical analysis also predicts the presence of thermal waves along the layer. However, a more detailed analysis predicts that two thermal waves having the same wave number but propagating in opposite directions will be present simultaneously. In the range of small numbers B when the influence of the electric field is still insufficiently strong, the critical numbers B^+ and B^- for the generation of thermal waves propagating upward and downward differ substantially. For relatively large B and small G the critical numbers B^+ and B^- become equal and a superposition of these waves occurs in the liquid. The result of this superposition will evidently be a standing wave or steady-state convective structure. At this point, it should also be stressed that the visual observations of the convective structures were made at voltages slightly higher than the critical values, i.e., in the range of parameters where a linear stability analysis may be inadequate to describe convective structures.

As we noted in the Introduction, electroconductive electrification is only one of the possible mechanisms for the excitation of electroconvective instability. For the most commonly used electrode–liquid systems, injection ionization in the electrode regions is an important factor for the analysis of stability. Problems involving the influence of injection on the stability of thermogravitational flows and the contribution of all the mechanisms described for the electrification of a barely conducting liquid to electroconvective instability will form the subject of a separate publication.

ACKNOWLEDGMENTS

The authors are grateful to Yu.K. Bratukhin, B.L. Smorodin, and M.G. Velarde for fruitful discussions, and also to the Internet Center at Perm State University for supplying information.

These results are part of a study supported financially by the Russian Foundation for Basic Research (project no. 98-01-00507).

REFERENCES

1. S. R. Kosvintsev, Candidate's Dissertation in Physics and Mathematics (Perm State University, Perm, 1993).
2. A. Castellanos, P. Atten, and M. G. Velarde, Phys. Fluids **27**, 1607 (1984).

3. V. V. Berezhnov and S. R. Kosvintsev, Vestn. Perm. Gos. Univ., No. 4, 42 (1985).
4. S. R. Kosvintsev and M. G. Velarde, in *Abstracts of the International Workshop on Electrical Conduction, Convection and Breakdown in Fluids, Seville, Spain, 1998*, p. 109.
5. S. P. Kosvintsev, Vestn. Perm. Gos. Univ., No. 2, 128 (1992).
6. M. Takashima and H. Hamabata, J. Phys. Soc. Jpn. **53**, 1728 (1984).
7. I. Yu. Makarikhin, Izv. Ross. Akad. Nauk, Mekh. Zhidk. Gaza, No. 5, 35 (1994).
8. G. Z. Gershuni, E. M. Zhukhovitskiĭ, and A. A. Nepomnyashchiĭ, *Stability of Convective Flows* (Nauka, Moscow, 1989), p. 320.
9. S. R. Kosvintsev and A. I. Mizev, in *Optical Methods of Studying Flows* (Inst. Teplofiz. Sib. Otdel. Ross. Akad. Nauk, Novosibirsk, 1991), p. 208.
10. R. J. Schmidt and S. W. Milverton, Proc. R. Soc., London, Ser. A **152**, 586 (1935).
11. Yu. K. Stishkov and A. A. Ostapenko (Leningrad Gos. Univ., Leningrad, 1989), p. 52.

Translation was provided by AIP

Journal of Experimental and Theoretical Physics, Vol. 90, No. 2, 2000, pp. 360–362.
Translated from Zhurnal Éksperimental'noĭ i Teoreticheskoĭ Fiziki, Vol. 117, No. 2, 2000, pp. 407–410.

SOLIDS
Electron Properties

Quasi-Two-Dimensional Shubnikov–de Haas Effect

N. S. Averkiev, L. E. Golub*, and S. A. Tarasenko

Ioffe Physicotechnical Institute, Russian Academy of Sciences, St. Petersburg, 194021 Russia
** e-mail: golub@coherent.ioffe.rssi.ru*

Received July 2, 1999

Abstract—The theory of the Shubnikov–de Haas effect is generalized to the case of two-dimensional systems with several occupied size-quantization subbands. Possible interlevel scattering is taken into account. It is shown that the relative amplitudes of the Shubnikov–de Haas oscillations are determined not only by the occupancy of the subbands but also by the intensity of intersubband transitions. *© 2000 MAIK "Nauka/Interperiodica".*

1. INTRODUCTION

As we are well aware, in structures with a degenerate electron gas, oscillations of the resistance occur in a magnetic field and this is known as the Shubnikov–de Haas effect. These oscillations are caused by the systematic crossing of the Fermi level by the Landau levels in a quantizing magnetic field. However, the regions of the fields in which these oscillations are observed in the two-dimensional (2*D*) and three-dimensional (3*D*) cases differ appreciably. In bulk materials, oscillations occur in "classically strong" magnetic fields when $\omega_c\tau \gg 1$. Here ω_c is the cyclotron frequency and τ is the carrier relaxation time. In 2*D* structures on the other hand, the effect occurs in moderate fields when $\omega_c\tau \lesssim 1$ [1]. As the magnetic field increases further, the relative amplitude of the oscillations increases and when several Landau levels are situated below the Fermi level, the quantum Hall effect is observed. Consequently, in the region of the Shubnikov–de Haas effect in 3*D* materials it is possible to observe oscillations at several frequencies which are multiples of the fundamental harmonic. In ultraquantum 2*D* systems however, a rigorous theoretical analysis only yields conductivity oscillations at a single frequency.

A qualitatively new situation is encountered in quasi-two-dimensional structures in which two or more size-quantization levels are occupied. In this case, each subband can give conductivity oscillations with its own period. The amplitudes of the oscillations will be determined by the scattering probability, including that accompanied by transitions to other levels. This effect was observed experimentally in [2, 3]. However, the quantitative analysis of the experimental data was made incorrectly since the oscillation terms were taken into account inconsistently. In bulk materials oscillations with several periods have been observed in multivalley semiconductors under intensive intervalley scattering [4] and a theory was developed in [5]. However, these results cannot be applied to quasi-two-dimensional systems because, unlike the 3*D* case, the parameter $\omega_c\tau$ is not large.

The aim of the present study is to make systematic calculations of the quasi-two-dimensional Shubnikov–de Haas effect when two size-quantization levels are occupied. For simplicity, we consider the case of zero temperature and we neglect spin–magnetic field interaction. It is shown that even when the occupancy of the second level is relatively small, the resistance can oscillate with two periods which are determined by the occupancies of each subband. Since measurement of the Shubnikov–de Haas oscillations is one of the main methods of characterizing conducting 2*D* systems, the results can be used to determine not only the carrier concentrations but also their intra- and interlevel scattering times.

2. THEORY

In order to calculate the conductivity tensor at frequency ω in a static magnetic field *B*, we shall use the relationship [6]

$$\sigma_{\alpha\beta}(\omega, \mathbf{B}) = \frac{ine^2}{m\omega}\delta_{\alpha\beta} + \frac{e^2}{\omega}[\Pi_{\alpha\beta}(\omega, \mathbf{B}) - \Pi^{(0)}_{\alpha\beta}(\omega)], \quad (1)$$

where $\Pi_{\alpha\beta}(\omega, \mathbf{B})$ is the polarization operator of the system, $\Pi^{(0)}_{\alpha\beta}(\omega)$ is the polarization operator calculated neglecting scattering in a zero magnetic field, *n* is the carrier concentration, *e* and *m* are the charge and effective mass of the particles, α, β are Cartesian coordinates. The polarization operator $\Pi_{\alpha\beta}(\omega, \mathbf{B})$ is expressed in terms of the exact Green's function in the magnetic field which is obtained from the Dyson equation [6].

We shall calculate the conductivity of a quasi-two-dimensional structure in a magnetic field perpendicular to the plane of the quantum well when two size-quantization levels are occupied. We shall assume that scattering takes place at the short-range potential, each subband contains many Landau levels,

$$E_F, E_F - \Delta \gg \hbar\omega_c, \quad (2)$$

and the "good conductor" condition is satisfied for both subbands:

$$E_F\tau_1^{(B)},\ (E_F-\Delta)\tau_2^{(B)} \gg \hbar. \tag{3}$$

Here E_F is the Fermi energy, Δ is the energy gap between the size-quantization levels, ω_c is the cyclotron frequency, and $\tau_1^{(B)}$ and $\tau_2^{(B)}$ are the carrier relaxation times in the subbands in the magnetic field. The Green's function of the noninteracting particles in the Landau gauge may be written in the form

$$G_\varepsilon(\mathbf{r},\mathbf{r}') = \sum_{n,k_y}\sum_{i,j=1} a_{ij}(n,\varepsilon)\psi^{(i)}_{n,k_y}(\mathbf{r})\psi^{(j)*}_{n,k_y}(\mathbf{r}'), \tag{4}$$

where $\psi^{(j)}_{n,k_y}$ are the wave functions of the particles in the magnetic field allowing for size quantization, $i, j = 1, 2$ is the subband number, and n and k_y are the number of the Landau level and the wave vector in the plane of the well.

The coefficients a_{ij} are determined from the Dyson equation which is a 4×4 system. An analysis [7] shows that in the approximation of a large distance between the subbands ($\tau^{(B)}_{1,2}\Delta \gg \hbar$) the coefficients a_{12} and a_{21} are much smaller than the diagonal ones. Thus, the Green's function may be written in the form

$$G_\varepsilon(\mathbf{r},\mathbf{r}') = \sum_{n,k_y}\frac{\psi^{(1)}_{n,k_y}(\mathbf{r})\psi^{(1)*}_{n,k_y}(\mathbf{r}')}{\varepsilon - E_n + E_F + [i\hbar/2\tau_1^{(B)}]\mathrm{sign}\varepsilon} + \sum_{n,k_y}\frac{\psi^{(2)}_{n,k_y}(\mathbf{r})\psi^{(2)*}_{n,k_y}(\mathbf{r}')}{\varepsilon - E_n + E_F - \Delta + [i\hbar/2\tau_2^{(B)}]\mathrm{sign}\varepsilon}, \tag{5}$$

where $E_n = \hbar\omega_c(n + 1/2)$ is the energy of the Landau level, but the times $\tau_1^{(B)}$ and $\tau_2^{(B)}$ for intra- and intersubband scattering at the short-range potential are determined from a system of two algebraic equations. For $\omega_c\tau_j^{(B)} < 1$ the solution has the form

$$\tau_1^{(B)} = \tau_1\left[1+\left(1-\frac{\tau_1}{\tau_{12}}\right)\delta_1+\frac{\tau_1}{\tau_{12}}\delta_2\right],$$
$$\tau_2^{(B)} = \tau_2\left[1+\left(1-\frac{\tau_2}{\tau_{12}}\right)\delta_2+\frac{\tau_2}{\tau_{12}}\delta_1\right], \tag{6}$$

where τ_1, τ_2, and τ_{12} are the total relaxation times in the subbands and the intersubband relaxation time in the absence of a magnetic field, δ_1 and δ_2 are oscillating quantities,

$$\delta_1 = 2\cos\left(2\pi\frac{E_F}{\hbar\omega_c}\right)\exp\left(-\frac{\pi}{\omega_c\tau_1}\right),$$
$$\delta_2 = 2\cos\left(2\pi\frac{E_F-\Delta}{\hbar\omega_c}\right)\exp\left(-\frac{\pi}{\omega_c\tau_2}\right), \tag{7}$$

For the calculations we assumed that the Fermi level is fixed. Note that the time $\tau_1^{(B)}$ was calculated in [8] for the case where only one subband was occupied.

When calculating the conductivity tensor using formula (1), the difference between the polarization operators must be calculated jointly to eliminate any discrepancies. For the dissipative component we then obtain

$$\sigma_{xx} = \frac{n_1e^2\tau_1/m}{1+(\omega_c\tau_1)^2}\left\{1-2\frac{(\omega_c\tau_1)^2}{1+(\omega_c\tau_1)^2}\delta_1 + \frac{\tau_1}{\tau_{12}}\left[2\frac{(\omega_c\tau_1)^2}{1+(\omega_c\tau_1)^2}-1\right](\delta_1-\delta_2)\right\} + \frac{n_2e^2\tau_2/m}{1+(\omega_c\tau_2)^2}\left\{1-2\frac{(\omega_c\tau_2)^2}{1+(\omega_c\tau_2)^2}\delta_2 + \frac{\tau_2}{\tau_{12}}\left[2\frac{(\omega_c\tau_2)^2}{1+(\omega_c\tau_2)^2}-1\right](\delta_2-\delta_1)\right\}, \tag{8}$$

where n_1 and n_2 are the carrier concentrations in the subbands in zero magnetic field. The off-diagonal components of the conductivity tensor are given by the expression

$$\sigma_{xy} = -\frac{n_1e^2\tau_1^2\omega_c/m}{1+(\omega_c\tau_1)^2}\left\{1+\frac{1+3(\omega_c\tau_1)^2}{(\omega_c\tau_1)^2[1+(\omega_c\tau_1)^2]}\delta_1 + 2\frac{\tau_1}{\tau_{12}}\left[2\frac{(\omega_c\tau_1)^2}{1+(\omega_c\tau_1)^2}-1\right](\delta_1-\delta_2)\right\} - \frac{n_2e^2\tau_2^2\omega_c/m}{1+(\omega_c\tau_2)^2}\left\{1+\frac{1+3(\omega_c\tau_2)^2}{(\omega_c\tau_2)^2[1+(\omega_c\tau_2)^2]}\delta_2 + 2\frac{\tau_2}{\tau_{12}}\left[2\frac{(\omega_c\tau_2)^2}{1+(\omega_c\tau_2)^2}-1\right](\delta_2-\delta_1)\right\}. \tag{9}$$

The formulas (5)–(9) were obtained assuming $|\delta_1|$, $|\delta_2| \ll 1$ so that they are valid in fields $\exp(-\pi/\omega_c\tau_j) \ll 1$ and in this case the parameter $\omega_c\tau_j$ may be of the order of unity.

3. DISCUSSION OF RESULTS

In accordance with formulas (7) and (8), a characteristic feature of the quasi-two-dimensional effect is the existence of oscillations at frequency $(E_F - \Delta)/\hbar$ even when the second subband has a relatively low occupancy. The reason for this effect is that the probability of scattering of a particle from the main subband

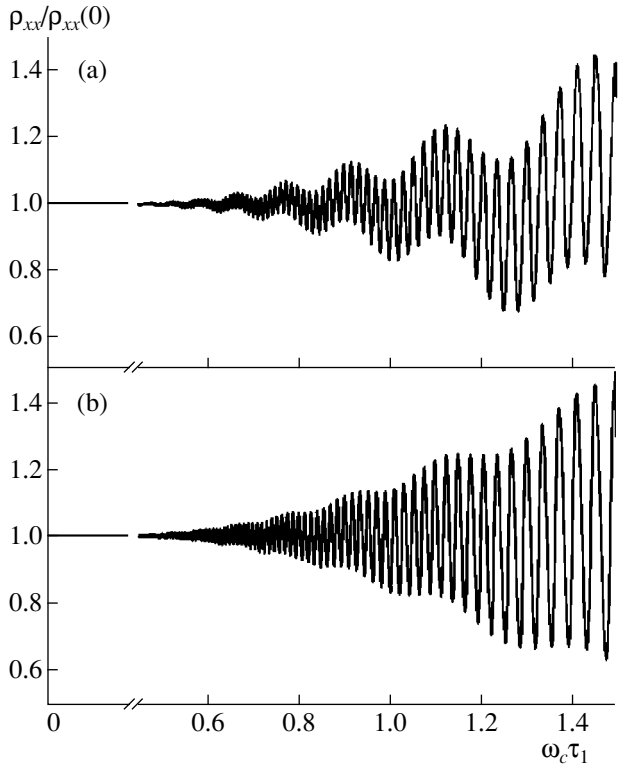

Fig. 1. Dependences of the dissipative component of the resistance ρ_{xx} on the magnetic field under conditions of the Shubnikov–de Haas effect for various intersubband scattering intensities: (a) $\tau_1/\tau_{12} = 0.5$, (b) $\tau_1/\tau_{12} = 0.05$.

oscillates with two periods (7) even when $n_2 \ll n_1$. Figure 1 gives dependences of $\rho_{xx} = \sigma_{xx}/(\sigma_{xx}^2 + \sigma_{xy}^2)$ on the magnetic field for the following parameters: $E_F\tau_1/\hbar = 50$, $(E_F - \Delta)\tau_2/\hbar = 5$, $\tau_1 = \tau_2$. Figure 1a corresponds to the case of intensive intersubband transitions ($\tau_1/\tau_{12} = 0.5$) and a low-frequency harmonic can be seen clearly against the background of high-frequency oscillations. If the intersubband transitions are suppressed (Fig. 1b), the low-frequency oscillations have a relatively small amplitude and only exist because the second subband is occupied ($n_2/n_1 = 0.1$).

The Shubnikov–de Haas effect at low temperatures was studied experimentally in [2, 3, 9] in GaAs/AlGaAs heterostructures under conditions when inequalities (2) and (3) were satisfied. The results of a Fourier analysis of the dependences of the resistance on the magnetic field made in [2, 3] and [9] differ qualitatively. In [2, 3] peaks were obtained at frequencies $E_F/\hbar\omega_c$ and $\Delta/\hbar\omega_c$ whereas in [9] they were obtained at $E_F/\hbar\omega_c$ and $(E_F - \Delta)/\hbar\omega_c$. According to the theory put forward these experiments may differ in terms of the parameters $\delta_{1,2}$: in [2, 3] $\delta_{1,2} \gtrsim 1$ and in [9] $\delta_{1,2} \ll 1$. However in the experiments [2, 3] the parameters $\delta_{1,2}$ could also be less than one since the dependences of the resistance on the magnetic field given in these studies are similar to the curves plotted in Fig. 1. Specifically, in [2, 3] oscillations were observed experimentally with two periods whose ratio was close to n_1/n_2. It should be noted that the parameters $\delta_{1,2}$ are extremely sensitive to the values of τ_1 and τ_2 [see (7)] and a detailed analysis of the specific scattering mechanisms is required to determine these times exactly.

With increasing magnetic field when δ_1 and δ_2 are no longer small but the conditions (2) and (3) still hold, the system for $\tau_j^{(B)}$ must be solve more exactly, i.e., the appropriate number of terms must be taken in the series $\exp(-\pi l/\omega_c\tau_j)$, l = 1, 2, …. Qualitatively, this has the result that the combination frequencies $\Omega = l_1E_F/\hbar\omega_c + l_2(E_F - \Delta)/\hbar\omega_c$ appear in the oscillations, where l_1 and l_2 are arbitrary integers. This behavior of the Shubnikov–de Haas effect was observed in quasi-two-dimensional Te layers in [10].

In the present study we have considered the case of zero temperature. When the temperature increases, the amplitudes of the harmonics at the combination frequency $\Omega = \Delta/\hbar\omega_c$ may increase relative to the others [7]. The temperature behavior of Shubnikov–de Haas oscillations was studied experimentally in [11].

ACKNOWLEDGMENTS

This work was supported by the Russian Foundation for Basic Research (project no. 98-02-18424) and the program “Physics of Solid-State Nanostructures.”

REFERENCES

1. A. Isihara and L. Smrčka, J. Phys. C **19**, 6777 (1986).
2. P. T. Coleridge, Semicond. Sci. Technol. **5**, 961 (1990).
3. D. R. Leadley, R. Fletcher, R. J. Nicholas, *et al.*, Phys. Rev. B **46**, 12439 (1992).
4. N. Ya. Minina and L. A. Kirakozova, Zh. Éksp. Teor. Fiz. **101**, 1663 (1992) [Sov. Phys. JETP **74**, 886 (1992)].
5. V. A. Kozlov, E. E. Narimanov, and K. A. Sakharov, Fiz. Tverd. Tela (St. Petersburg) **36**, 309 (1994) [Sov. Phys. Solid State **36**, 168 (1994)].
6. A. A. Abrikosov, L. P. Gor’kov, and I. E. Dzyaloshinskiĭ, *Methods of Quantum Field Theory in Statistical Physics* (Fizmatgiz, Moscow, 1962; Prentice-Hall, Englewood Cliffs, New York, 1963).
7. M. E. Raikh and T. V. Shahbazyan, Phys. Rev. B **49**, 5531 (1994).
8. T. Ando, J. Phys. Soc. Jpn. **37**, 1233 (1974).
9. W. de Lange, PhD Dissertation (Eindhoven University of Technology, Eindhoven, the Netherlands, 1993).
10. V. A. Berezovets, I. I. Farbshtein, and D. Schneider, Fiz. Tverd. Tela (St. Petersburg) **41**, 537 (1999) [Phys. Solid State **41**, 481 (1999)].
11. T. H. Sander, S. N. Holmes, J. J. Harris, *et al.*, Phys. Rev. B **58**, 13856 (1998).

Translation was provided by AIP

Journal of Experimental and Theoretical Physics, Vol. 90, No. 2, 2000, pp. 363–369.
Translated from Zhurnal Éksperimental'noĭ i Teoreticheskoĭ Fiziki, Vol. 117, No. 2, 2000, pp. 411–419.

SOLIDS
Electron Properties

Electron Spin Resonance with $g_{eff} \approx 4.2$ in $YBa_2Cu_3O_{6.35}$. Model of Chain Copper–Oxygen Fragments

M. V. Eremin[1, *], R. M. Eremina[2], M. R. Gafurov[1], V. A. Ivan'shin[1, 3], I. N. Kurkin[1], S. P. Kurzin[1], H. Keller[4], and M. Gutmann[5]

[1]*Kazan State University, Kazan, 420008 Russia*
[2]*Kazan Physicotechnical Institute, Kazan, 420029 Russia*
[3]*Experimentalphysik V, EKM, Institut für Physik, Universitat Augsburg, D-86159 Augsburg, Germany*
[4]*Physik-Institut der Universitat Zürich, CH-8057 Zürich, Switzerland*
[5]*Laboratory for Neutron Scattering, ETH Zürich & Paul Scherrer Institut, CH-5232 Villigen, Switzerland*
** e-mail: Mikhail.Eremin@ksu.ru*

Received May 11, 1999

Abstract—Systematic measurements are made of ESR spectra with $g \approx 4.2$ in $YBa_2Cu_3O_{6+y}$ compounds with various doping indices y. Temperature dependences of the spectrum intensity show that the ground states of the centers are singlet and the energies of the excited states $M_S = \pm 1$ correspond to 8–11 K. In general, the intensity of the ESR spectra varies with time and depends on the sample preparation technology. The most probable models for the paramagnetic centers studied are considered to be chain fragments of copper ions of variable valence. General laws governing the energy structure of these centers are described. *© 2000 MAIK "Nauka/Interperiodica".*

1. INTRODUCTION AND REVIEW OF PREVIOUS WORKS

Compounds having the composition $YBa_2Cu_3O_{6+y}$ are superconductors when $y > 0.35$ and have thus been investigated intensively by various methods including ESR. The ESR spectrum usually consists of a single line with $g \approx 2.0$–2.4 [1–5]. Depending on the sample preparation technology, the ESR spectrum is either observed at high temperatures [1–3] (we call this the high-temperature spectrum) or only when $T < 40$ K [1, 4, 5] (low-temperature spectrum). The nature of ESR centers with $g \approx 2$ has been repeatedly discussed in the literature although it has not yet been definitively clarified. In most studies, for want of a better model, this signal is arbitrarily attributed to isolated Cu^{2+} ions in the chains. Eremina *et al.* [5] assume that the low-temperature spectrum is attributable to copper–oxygen clusters with $S = 2$. The assumption that copper–oxygen centers with spins $S = 1/2$ and $S = 2$ are present in $YBa_2Cu_3O_{6+y}$ planes provides a good explanation of the temperature and field dependences of the specific heat in $YBa_2Cu_3O_{6+y}$ [6] at low temperatures.

Various publications have reported the observation of a signal at $g \approx 4.2$ in the ESR spectrum of YBaCuO compounds. It was naturally assumed and discussed that the ESR line at $g \approx 4.2$ is attributed to the presence of paramagnetic centers with $S \neq 1/2$, such as Cu^{3+} ions ($S = 1$), Cu^{2+}–Cu^{2+} ($S = 1$) pairs, or random Fe^{3+} ion impurities.

The observation of a single $g \approx 22$ line in the ESR spectrum allows various viewpoints to be advanced as to the structure of the center. In view of this, a study of the ESR spectrum of the line in the "half" field ($g \approx 4.2$) is more informative to determine the nature of the paramagnetic centers. We note various publications which either reported the observation of ESR at $g \approx 4.2$ or assumed that the ESR signal is attributed to ions with $S \neq 1/2$ [7–24].

The authors of [7–10, 15] assumed that in the samples studied, there are copper ions not only with the valence Cu^{2+} but also Cu^{3+} ($S = 1$). However, an ESR spectrum with $g \approx 4.2$ was not observed in these studies.

Likodimos *et al.* [11] studied the electron spin resonance of $Pr_{0.5}Y_{0.5}Ba_2Cu_3O_x$ and observed several ESR lines including a low-intensity line with $g = 4.19(1)$. These authors [11] assume that the ESR spectrum is attributable to pairs of Cu^{2+} ions with weak exchange interaction and the $g = 4.19$ line corresponds to the $\Delta M = \pm 2$ transition. They postulate that the Cu^{2+} pairs are located in Cu(1)O planes and are somehow magnetically isolated from the antiferromagnetically bound copper ions in the $Cu(2)O_2$ planes. As a rather improbable assumption the authors [11] assigned the $g = 4.19$ line to random Fe^{3+} ion impurities. It was also noted in [11] that the intensity of the $g = 4.19$ line was reduced substantially one month after preparation of the sample.

Guskos *et al.* [12] studied the electron spin resonance of $RBaCuFeO_5$ compounds (R = Eu, Y, Yb). Var-

ious lines were observed including the $g = 4.21(1)$ line of width $\Delta H = 3.1(1) \times 10^{-3}$ T. The authors [12] ascribe the ESR spectrum to two types of Fe^{3+} ion centers (one giving a signal at $g = 4.21$).

In [13] Guskos *et al.* studied the electron spin resonance of $LaBaSrCu_3O_{6+x}$ in the tetragonal phase. Apart from the ESR signal from the Cu^{2+} ions, these authors also observed a broad line with $g \approx 2.1$ and $\Delta B_{pp} = 0.19(1)$ T. In addition, at $T < 20$ K they also observe a narrow line with $g \approx 4.2$ and $\Delta B_{pp} = 5 \times 10^{-3}$ T The authors ascribe this signal to the$\Delta M = \pm 2$ transition in exchange-coupled Cu^{2+} pairs [13].

In the tetragonal phase of $Y_{0.5}Sm_{0.5}Ba_2Cu_3O_{6+x}$ the same authors observed ESR with $g = 4.22(1)$ and $\Delta H = 0.012(1)$ T [14]. The nature of this signal, as in [13] was ascribed to exchange-coupled pairs of Cu^{2+} ions. The specific pair model was not indicated since no reasonable model of this pair could be put forward. This is because the superexchange coupling parameter between the nearest copper ions should be approximately 1500 K [as in the Cu(2)O planes] and not 0.22 cm^{-1} as is required to explain the ESR spectrum in [11]. Assuming that this is a pair of second or third neighbors, it is unclear how the spins of this pair in the Cu(1) positions were isolated from those in the Cu(2) positions. According to the Goodenough–Kanamori rules, the coupling of the Cu(1)–Cu(2) spins via apical oxygen should be of the order of 100 K!

Misra and Misiak [16] investigated the electron spin resonance of $YBa_{1.9}K_{0.1}Cu_3O_x$ and observed an ESR line with $g \approx 4.5$ at $T < 40$ K. The nature of this signal was not discussed. Lyfar' *et al.* [17] observed a weak ESR signal with $g \approx 4.5$ at room temperature in YBaCuO compounds. Electron spin resonance was only observed in samples having outgrowths of "black" and "green" particles. The authors [17] attribute these signals to the Cu^{3+} ion (at $D > h\nu$, where D is the initial splitting parameter).

In $La_{1.85}Sr_{0.15}CuO_4$, ESR with $g \approx 4.18$ was observed in [18]. Citing [19], where authors are inclined to assume that the $g \approx 4$ line characterized the $S = 1$ triplet states formed by pairs of holes when these are in excess under strontium doping. This explanation is based on the observation that the intensity of the ESR signal increases as the quantity of strontium increases. However, an increase in the intensity of the $g \approx 4$ signal was also observed in [18] as a result of iron ion doping. Since the incorporation of iron reduces the concentration of holes, the explanation put forward in [19] is somewhat doubtful.

Kataev *et al.* [20] investigated $La_2CuO_{4-\delta}$ and observed a weak ESR signal with $g \approx 4$. The signal intensity obeys the Curie law. The authors [20] postulate that the $g \approx 4$ line is either assigned to ferromagnetic Cu^{2+} pairs or to Cu^{3+} ($S = 1$).

The compound $BaBiO_3$ has also been investigated [21] both without any additional impurities and with added Mg, Al, Co, Fe, and Mn. The compounds $Ba_{1-x}K_xBiO_3$ with $x = 0.1$ and 0.1% Co or 1% Al impurities have also been studied. In all the samples ESR was observed with $g \approx 4$–4.5. The very high-intensity ESR line in samples with added cobalt is undoubtedly attributable to the Co^{2+} ion. In other samples the intensity of the $g \approx 4.2$ signal was substantially weaker and the reason for this was not discussed.

In [22–24] an important characteristic of ESR with $g \approx 4.2$ was observed in $Ba_{1-x}K_xBiO_3$ and $BaPb_yBi_{1+y}O_3$ systems. On analyzing the temperature dependence of this ESR signal intensity, the authors [22–24] found that the ESR signal with $g \approx 4.2$ is observed from excited triplet states. These triplet states are presumably assigned to pairs of oxygen holes localized at apical oxygens.

We shall now turn our attention to [25] in which $YBa_2Cu_3O_x$ was investigated by ESR and where at $T < T_c$ the authors observed a high-intensity signal in a weak magnetic field (<100 Oe). The authors [25] attributed this signal to the formation of Cu^{2+}–Cu^{4+} pairs. This is an erroneous conclusion because the signal in a "zero" magnetic field is not ESR but nonresonant microwave absorption, characteristic of superconductors. However, their reasoning on the fluctuations (at the rate $<10^{10}$ s^{-1}) of the copper valence of the type $2Cu^{3+} \longrightarrow Cu^{4+} + Cu^{2+}$ and $2Cu^{+} \longrightarrow Cu^{2+} + Cu^{0}$ is interesting in the context of the models of variable-valence centers discussed below.

To conclude our review of the literature, we can conclude that although numerous publications have reported the observations of ESR lines in a half field, the experimental results are still contradictory and thus the conclusions and assumptions made by the authors on the nature of this signal, at least in $YBa_2Cu_3O_{6+y}$ are ambiguous. In many cases, this signal is attributed to the presence of external or specially introduced impurities (Fe^{3+}, Co^{2+}). However, this is evidently not the only reason for the appearance of ESR in a half field in $YBa_2Cu_3O_{6+y}$.

In the present paper we report an investigation of YBaCuO compounds with different oxygen contents and different sample preparation technologies in order to observe an ESR signal with $g \approx 4$. Measurements were made using nonoriented YBaCuO samples and samples oriented using an external magnetic field (quasi-single crystals). The temperature dependence of the $g \approx 4.2$ ESR signal intensity showed that ESR is observed from excited states with $S = 1$. The experimental results are most logically attributed to chain copper clusters of variable valence.

2. EXPERIMENT

In the present study, ESR was used to investigate compounds having the composition $YBa_2Cu_3O_{6+y}$ generally containing rare-earth ion impurities (Yb, Er). The investigations were carried out using an IRES-1003 ESR spectrometer (*X*-range, frequency 9.25–9.48 GHz) in the temperature range 4–100 K.

Three series of YBaCuO samples having different oxygen contents and prepared by different methods were studied.

Series A

The samples in this series were prepared by normal ceramic technology using the components Y_2O_3, R_2O_3 (1% relative to Y_2O_3, R = Er or Yb), $BaCO_3$, and CuO. Superconducting samples A1 (without R^{3+} impurities), A2 (with Yb^{3+} impurities), and A3 (with Er^{3+} impurities) were first prepared (the component mixture was ground for 1 h, slowly heated to 850°C, held for 15 h, rapidly cooled, reground, slowly heated to 900°C, held for 6 h, and slowly cooled). The entire procedure was carried out in air. The samples obtained, A1, A2, and A3, had $T_c \approx 85$ K and $x \approx 6.85$. Then nonsuperconducting samples, A4, A5, and A6, were prepared from portions of samples A1–A3 (samples A1–A3 were annealed in air at 900°C for 2.5 h, then quenched in nitrogen, and dried in a helium atmosphere). Samples A4–A6 were not superconducting (at $T \approx 10$ K) and the oxygen content estimated from measurements of the lattice parameter c was $x \approx 6.35$. We investigated the ESR of rare-earth ions (Er^{3+} and Yb^{3+}) in series A samples in [26]. These samples were prepared by R.Yu. Abdulsabirov and S.L. Korableva.

Series B

The samples in this series ($Y_{0.99}Er_{0.01}Ba_2Cu_3O_x$), like the series A samples, were prepared by solid-phase synthesis using the components Y_2O_3, Er_2O_3, $BaCO_3$, and CuO. However, a different temperature and atmospheric regime was used compared with series A. We first obtained compounds having an oxygen content $x \approx 7$ (the samples were first heated slowly in air and then in a nitrogen atmosphere to 940°C, held in nitrogen and then in oxygen for around 10 h, followed by slow three-stage cooling in oxygen to room temperature). The entire cycle continued for 110 h. Samples in this series having an oxygen index $x < 7$ were obtained from the $x = 7$ samples by annealing in a nitrogen atmosphere. The quantity of oxygen in the sample depends on the annealing temperature (T_{ann}). The higher T_{ann}, the lower the oxygen content. For example, at T_{ann} we obtained a sample with $x \approx 6.12$ and at $T_{ann} = 320$°C $x = 6.96$. The annealing time was around 30 h. Ten samples were obtained with different oxygen contents. Series B was grown by R.Sh. Zhdanov and M.B. Mityagin.

Series C

The preparation technology for samples in this series ($YBa_2Cu_3O_{6+y}$ containing 1% Er^{3+} ion impurities) differs substantially from that for samples in series A and B, and is described in detail in [27, 28]. At this point, we merely note that series C was prepared by sol gel technology and the initial materials are metal nitrates. The samples in this series had various oxygen indices between 6 and 7.

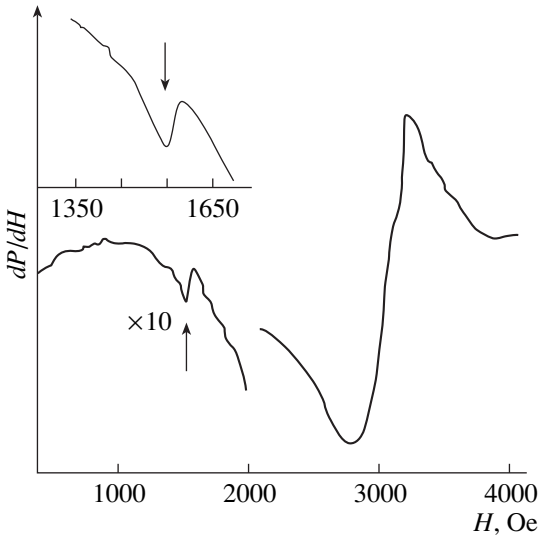

Fig. 1. Electron spin resonance spectrum of sample A5 ($YBa_2Cu_3O_{6.35}$) in the magnetic field range 400–4000 Oe, $T \approx 14$ K. The inset shows a fragment of the spectrum in the range 1300–1700 Oe, $T \approx 4$ K. The arrow indicates the $g \approx 4.2$ line.

All the samples in series A, B, and C were investigated by ESR to determine whether the $g \approx 4.2$ line was present. This line was observed in some samples and not in others. For instance, in the series A samples this signal was observed in the nonsuperconducting sample containing Yb^{3+} impurities (A5) and in the nonsuperconducting sample without impurities R^{3+} (A4) and was not observed in the superconductors A1, A2, A3, and in the Er^{3+}-doped nonsuperconducting sample (A6). Figure 1 shows the ESR spectrum of sample A5. The series A samples comprised powder in paraffin and were not oriented.

In the series B and series C samples no $g \approx 4$ signal was observed for any oxygen index between 6 and 7.

The ESR line with $g \approx 4.2$ was studied in the greatest detail for sample A5. This signal has a low intensity (see Fig. 1) and is only observed at $T < 100$ K. The value of $g = 4.24(2)$ does not depend on temperature. The line width depends weakly on temperature (in sample A5 $\Delta H_{pp} \approx 40$ Oe at $T \approx 5$ K and $\Delta H_{pp} \approx 50$ Oe at $T \approx 30$ K). An important factor was that the integrated intensity of this line exhibited an anomalous temperature dependence (not obeying the Curie law) (see Fig. 2). From this it follows that the ESR line with $g = 4.24$ can be ascribed to the excited states of the paramagnetic centers, not to the ground state (estimates of the excitation energy will be made below). In order to confirm that this anomalous temperature dependence of the integrated line intensity was not caused by the characteristics of the device or the properties of the sample,

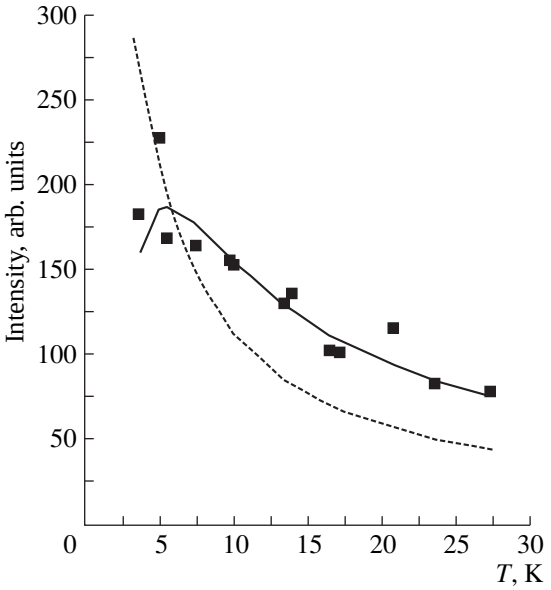

Fig. 2. Relative intensity of the ESR signal with $g \approx 4.2$ in sample A5. The solid curve gives the calculations using formula (2), the parameter is $\Delta \approx 9.5 \pm 1.5$ K, and the dashed curve gives the Curie law.

we measured the intensity of the ESR line with $g \approx 2$. At $T < 15$ K the Curie law is accurately satisfied for the $g \approx 2$ ESR line. It should also be noted that samples A4 and A5 for which ESR with $g \approx 4.2$ is observed are not superconductors. Finally we note another interesting circumstance. When the samples are stored for a long time at room temperature, changes occur in the ESR spectra. For samples A4 and A5 the intensity of the $g \approx 4.2$ lines decreases and disappears after a few years whereas the ESR signal with $g \approx 2$ conserves its high intensity, but the line profile changes. Particularly marked changes are observed in the series B and C samples having a low oxygen content, where the $g \approx 2$ line intensity increases catastrophically. No changes are observed for the R^{3+} ion lines in any of the samples. From this it is logical to conclude that the $g \approx 2$ and $g \approx 4$ ESR lines belong to different paramagnetic centers.

Summarizing the experimental facts, we can draw the following conclusions.

(1) Electron spin resonance with $g \approx 4.2$ was observed in quenched $YBa_2Cu_3O_{6+y}$ samples prepared by solid-phase synthesis and having $y \approx 0.35$. No ESR with $g \approx 4.2$ was observed in annealed YBaCuO samples obtained by solid-phase synthesis or in YBaCuO samples obtained by the sol gel method for any oxygen content.

(2) Electron spin resonance with $g \approx 4.2$ and ESR with $g \approx 2$ can be ascribed to different types of centers.

(3) Electron spin resonance with $g \approx 4.2$ has an anomalous temperature dependence (which corresponds to the recording of ESR at excited energy levels as in [22–24]).

3. ANALYSIS OF PARAMAGNETIC CENTER MODELS WITH $g \approx 4.2$

At first glance, following [22], the ESR line with $g \approx 4.2$ could be logically assigned to a pair of localized holes (O^-) at apical oxygen positions. In our case, however, it is incomprehensible that such a pair could be "isolated". We know that in $YBa_2Cu_3O_{6+y}$ the O^- ($S = 1/2$) states are strongly coupled with the copper spins. Copper–oxygen singlet states are formed which for simplicity we shall subsequently denote by "Cu^{3+} ($S = 0$)". It is impossible for triplet states to form only from these. Thus, we shall analyze copper–oxygen centers involving chain spins of copper Cu^{2+} ($S = 1/2$). Models for the formation of copper chain fragments with constant valence were discussed in [29]. Subsequently, for completeness of the following analysis we shall also briefly discuss chain fragments of variable-valence ions. Since the filling of O(4) positions with oxygen ions leads to a change in the valence of the copper ions in the chains and ultimately these chains are conducting, it is quite natural to assume that fragments of the following type form in the $YBa_2Cu_3O_{6+y}$ chains:

(1) Cu^{2+}–Cu^{+}–Cu^{2+} or Cu^{2+}–"Cu^{3+}"–Cu^{2+},

(2) Cu^{2+}–Cu^{+}–Cu^{2+}–Cu^{2+} or

Cu^{2+}–"Cu^{3+}"–Cu^{2+}–Cu^{2+}, and so on.

The excess "Cu^{3+}" (hole) or Cu^{+} (electron) charges can evidently migrate between various oxygen positions so that the states of fragments from two chains are triply degenerate in terms of the method of distributing Cu^{+} (or "Cu^{3+}") and the states of fragments from three chains are quadruply degenerate. The possible formation of impurity centers with effective spin $S = 1/2$ in $YBa_2Cu_3O_{6+y}$ chains was first noted in [30] using NMR of these compounds at low temperatures.

We shall first consider a variant where the singlet state is the "Cu^{3+} ($S = 0$)" ground state, as in the $YBa_2Cu_3O_{6+y}$ planes. According to the calculations [31–33], this type of singlet state corresponds to the superposition of the Zhang–Rice singlet states, trivalent copper Cu^{3+} ($S = 0$), and neutral oxygen. The energy levels of the hole and electron fragments can be calculated by diagonalizing the Hamiltonian

$$H = \sum t_{ij} a^{+}_{i\sigma} a_{i\sigma} + \sum J_{ij} \left[(S_i S_j) - \frac{n_i n_j}{4} \right], \qquad (1)$$

where J_{ij} is the superexchange coupling parameter of Cu^{2+} spins, t_{ij} is the transport integral of the Cu or "Cu^{3+}" states between the copper nearest neighbors, and n_i are the occupation numbers. In the first case, an electron migrates so that $J/t < 0$ and in the second case, a hole migrates and therefore $J/t > 0$. We can take $J = 1500$ K to be the same as that for the copper states in the $YBa_2Cu_3O_{6+y}$ planes [34] and $t \approx 330$ K, as was measured for Cr^{3+}–Cr^{2+} states in $KZnF_3$ [35]. Note that both the parameters of our model are greater than the

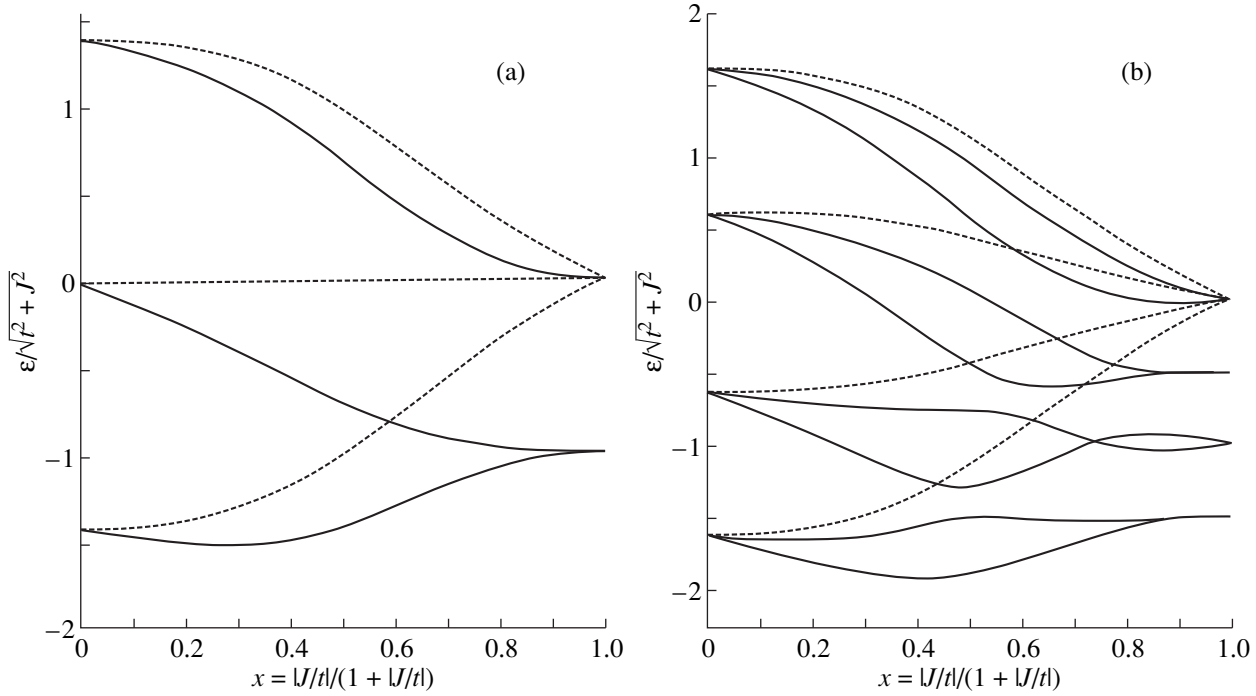

Fig. 3. Energy diagrams of the energy levels of variable-valence copper clusters for various values of the parameters t and J: (a) Cu^{2+}–"Cu^{3+}"–Cu^{2+} cluster, the solid curves correspond to $S = 0$ states, the dashed curves to $S = 1$ states; (b) Cu^{2+}–Cu^{2+}–"Cu^{3+}"–Cu^{2+} cluster, the solid curves correspond to $S = 1/2$ states, the dashed curves to $S = 3/2$ states.

exchange coupling integral of the Cu(1)–Cu(2) spins and thus the latter is not discussed at this point.

The Hamiltonian was diagonalized by a numerical technique and the results of the calculations are plotted in Fig. 3. As was predicted, the energy diagrams of the energy levels do not depend on whether a hole or an electron migrates. Only the absolute value of the parameter t is important. For a two-membered fragment, for arbitrary ratios between the parameters t and J, the ground state is a singlet whereas for a three-membered fragment the ground state is a doublet with effective spin $S = 1/2$. For convenience of representing the results, the dimensionless parameter $x = |J/t|/(1 + |J/t|)$ is plotted on the ordinate. Variation of the parameter x between zero and unity gives all possible values of the ratio J/t. Possible energy levels of the centers are plotted on the abscissa in units of $\sqrt{t^2 + J^2}$. This reasoning can easily be generalized to the case of chain fragments with an arbitrary number of members. The ground state of a fragment having an even number of members with one hole will be a singlet and that for an odd number of members will be a doublet with $S = 1/2$. Thus, we can conclude that in $YBa_2Cu_3O_{6+y}$ chains various centers with $S = 1/2$ can generally be formed. However, since the formation of the centers given above is most likely for low values of the doping index y in $YBa_2Cu_3O_{6+y}$, we shall confine our analysis to these models.

It can be seen from Figs. 3a and 3b that there are a fairly large number of low excited states, whose presence is required to explain the difference between the temperature dependences of the ESR signal intensities and the Curie law. In linear fragments of constant-valence ions the excited states are much higher, and the differences from the Curie law will be negligible. In this respect our models differ fundamentally from those considered in [29].

Thus, we shall assume that copper clusters of variable valence with the $S = 0$ ground state and $S = 1$ excited state are responsible for the ESR signals with $g \approx 4.2$ observed in $YBa_2Cu_3O_{6+y}$ and we shall analyze the temperature dependences of the ESR signals. Temperature dependences of the relative ESR signal intensities measured in the present study in a field of 1590 Oe are plotted in Fig. 2. If the $g \approx 4.2$ ESR line is attributed to the excited state of a paramagnetic center $S = 1$ (transition between the $M_S = +1$ and $M_S = -1$ states), its intensity should be given by

$$I = \text{const} \times \frac{\exp(-g\beta H/kT) - \exp(g\beta H/kT)}{1 + \exp(-g\beta H/kT) + \exp(g\beta H/kT) + \exp(\Delta/kT)}, \quad (2)$$

where Δ is the absolute value of the energy interval between the ground singlet and the excited triplet. Using the least squares method we find that $\Delta \approx 9$ K for $YBa_2Cu_3O_{6.35}$ using the experimental data plotted in Fig. 2. It can be seen from Fig. 3a that these intervals are considerably larger for values of the parameter t around 330 K. In view of this, the model of a Cu^{2+}–Cu^{+}–Cu^{2+} center is not suitable to explain our experiments. The

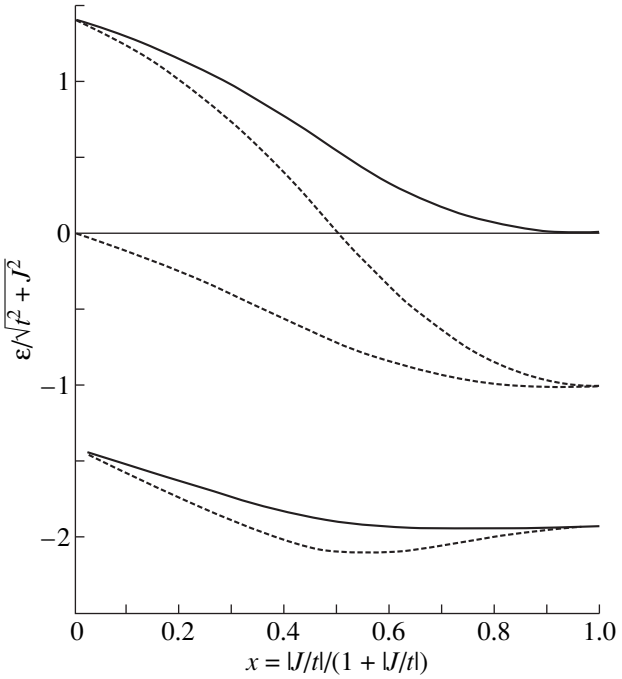

Fig. 4. Energy level diagrams of a Cu^{2+}–"Cu^{3+}"–Cu^{2+} cluster assuming $G_{pol} = -0.25$ eV. The solid curves correspond to $S = 0$ states and the dashed curves to $S = 1$ states.

Cu^{2+}–"Cu^{3+}"–Cu^{2+} model can be completely reconciled with the observed temperature dependence of the ESR signal with $g \approx 4.2$ if we take into account the nonequivalence of the position of the "Cu^{3+}" state at the center of the cluster and at its ends. Figure 4 shows the cluster energy levels when the difference between the polaron binding energy of "Cu^{3+}" at the center of the cluster and at its ends is $G_{pol} = -0.25$ eV. This is clearly a nontrivial important characteristic of the model. The $S = 1$ excited state is positioned near the ground singlet state although all three parameters t, J, and G_{pol} are considerably larger than this energy scale. In these models of paramagnetic centers three sources of anisotropic spin–spin interaction of the type $DS_z^2 + E(S_x^2 - S_y^2) + \ldots$ may be noted: dipole–dipole and pseudo-dipole interactions of Cu^{2+} spins as for pairs of isolated ions [36] and anisotropic exchange interaction of a hole spin at oxygen with copper spins. In our case, the latter evidently predominates. According to estimates [37] for copper–oxygen clusters where the ground singlet state lies in the CuO_2 planes, the anisotropy of the spin–spin interaction of oxygen holes and copper may lead to $D = 0.05$–0.2 meV. This conclusion also applies to our case and can explain the absence of any ESR signal from these clusters with $g \approx 2$.

We shall now discuss why ESR in a "half" magnetic field was only observed in quenched nonsuperconducting $YBa_2Cu_3O_{6.35}$ samples prepared by solid-phase synthesis. In our model ESR with $g \approx 4.2$ corresponds to the transition $|+1\rangle \longleftrightarrow |-1\rangle$ and is forbidden when these states contain no small component of the $|0\rangle$ state. This is the situation for an ideally ordered crystal lattice or for an isolated Cu^{2+}–"Cu^{3+}"–Cu^{2+} cluster and so ESR is not observed in a "half" field. However, the situation changes when we are dealing with samples having a nonuniform oxygen distribution at the interface between the tetragonal and the orthorhombic phase such as quenched $YBa_2Cu_3O_{6.35}$. These "poor" nonsuperconducting samples have the largest distortions of the local crystal fields which explains why the $\Delta M = \pm 2$ transition is partially allowed.

Note that the excited-state energies of paramagnetic centers with $M_S = \pm 1$ obtained by us from the temperature dependence do not contradict the data obtained from the specific heat [6], since the centers described "freeze out" at superconducting temperatures and make no contribution to the specific heat.

Generally, a linear chain fragment Cu^{3+} ($S = 1$)–Cu^{2+} ($S = 1/2$)–Cu^{2+} ($S = 1/2$)–Cu^{3+} ($S = 1$) has a similar structure of lower spin states, as our calculations have shown.[1] In order to describe the energy spectrum of this fragment we naturally need to go beyond the t–J model. As for the Cu^{2+} ($S = 1/2$)–"Cu^{3+} ($S = 0$)"–Cu^{2+} ($S = 1/2$) fragment, its ground state (for $x > 0.5$) is singlet and the excited triplet is comparatively close. When they are formed during the oxygen doping of the samples, neither type of fragment leads to the appearance of holes in CuO_2 planes and consequently they do not destroy the antiferromagnetic correlations of the Cu(2) spins. Both center models can explain the following experimental observation made by us: in samples A4 and A5 the intensity of the $g \approx 4.2$ ESR line decreases with time. A few years after preparation of the samples this line disappears, whereas the $g \approx 2$ ESR signal persists but its line profile changes. All these observations are a natural result of the diffusion and ordering of oxygen. Cu^{2+}–"Cu^{3+}"–Cu^{2+} chain fragments are the most probable and interesting for the physics of charge ordering of transition-metal oxides. Recently they were proposed independently to explain the specific heat, NMR/NQR, and spin susceptibility of quasi-one-dimensional copper chains in $Sr_{2.5}Ca_{11.5}Cu_{24}O_{41}$[39. 40]. [2]

4. CONCLUDING REMARKS

From the reasoning put forward above, it therefore follows that the most natural model of an ESR center with $g \approx 4.2$ in $YBa_2Cu_3O_{6.35}$ is that of chain copper–oxygen clusters of variable valence. The isolated fragments of variable-valence ions Cu^{2+}–"Cu^{3+} ($S = 0$)"–Cu^{2+} in $YBa_2Cu_3O_{6.35}$ and $Sr_{2.5}Ca_{11.5}Cu_{24}O_{41}$ [39, 40] have analogs in other transition-metal oxides, as has recently become apparent. It has been found that the variable-valence fragments Ni^{2+} ($S = 1/2$)–Ni^{3+} ($S = 1$)–Ni^{2+} ($S = 1/2$) form the structural unit of the stripe structure in the

[1] An analysis of the force of the crystal field at triply coordinated copper showed that its ground state is more likely to be Cu^{3+} ($S = 1$) than "Cu^{3+} ($S = 0$)".

[2] This paper was submitted in May 1999 and was presented at the Ampere Colloquium in Pisa in June 1999 [38].

$La_2NiO_{4.17}$ nickelates [41, 42]. Zigzag structures of Mn^{3+}–Mn^{4+}–Mn^{3+} triplets are found in manganites ($La_{1-x}Sr_xMnO_3$) (see the review [43]). A tendency to form structural fragments of variable valence is clearly a common property of doped Mott–Hubbard insulators. In this respect, the importance of the conclusions reached in the present study goes far beyond the problem of ESR in a half field.

ACKNOWLEDGMENTS

The authors are grateful to M.A. Teplov for continuous interest and discussions of the problem of magnetic centers in high-temperature superconductors at the initial stage of these investigations and to A.Yu. Yakubovskiĭ for critical comments.

This work was partly supported by the Russian Foundation for Basic Research (projects nos. 97-02-18598 and 98-02-17687), the State Science and Technology Program "Superconductivity" (project no. 98014), and the Swiss National Science Foundation (grant no. 7SUPJ048660).

REFERENCES

1. J. Genossar, D. Shaltiel, V. Zevin, *et al.*, J. Phys.: Condens. Matter **1**, 9471 (1989).
2. I. A. Garifullin, N. N. Garif'yanov, N. E. Alekseevskiĭ, *et al.*, Physica C **179**, 9 (1991).
3. B. I. Kochelaev, J. Sichelschmidt, B. Elschner, *et al.*, Phys. Rev. Lett. **79**, 4274 (1997).
4. J. Stankowski, W. Kempinski, and Z. Trybula, Acta Phys. Pol. A **80**, 571 (1991).
5. R. M. Eremina, M. R. Gafurov, and I. N. Kurkin, Fiz. Tverd. Tela (St. Petersburg) **39**, 432 (1997) [Phys. Solid State **39**, 374 (1997)].
6. J. P. Emerson, D. A. Wright, B. F. Woodfield, *et al.*, Phys. Rev. Lett. **82**, 1546 (1999).
7. D. H. A. Blank, J. Flokstra, G. J. Gerritsma, *et al.*, Physica B **145**, 222 (1987).
8. U. Straub, D. Krug, Ch. Zieglez, *et al.*, Mater. Res. Bull. **24**, 681 (1989).
9. M. D. Glinchuk and A. P. Pecheniy, Physica C **220**, 233 (1994).
10. A. P. Pechoniy, M. D. Glinchuk, V. A. Mineev, *et al.*, Phase Transit. **29**, 105 (1990).
11. V. Likodimos, N. Guskos, G. Palios, *et al.*, Phys. Rev. B **52**, 7682 (1995).
12. N. Guskos, V. Likodimos, J. Kuriata, *et al.*, Phys. Status Solidi B **181**, K69 (1994).
13. N. Guskos, V. Likodimos, J. Kuriata, *et al.*, Phys. Status Solidi B **180**, 491 (1993).
14. N. Guskos, V. Likodimus, G. Palios, *et al.*, Phys. Status. Solidi B **184**, K31 (1994).
15. N. Guskos, Th. Leventouri, Ch. Trikalinos, *et al.*, Phys. Status Solidi B **152**, K9 (1989).
16. S. K. Mistra and L. E. Misiak, Solid State Commun. **72**, 1207 (1989).
17. D. L. Lyfar', D. P. Moiseev, A. A. Motuz, *et al.*, Fiz. Nizhk. Temp. **13**, 876 (1987) [Sov. J. Low Temp. Phys. **13**, 503 (1987)].
18. A. Sienkiewicz, M. Z. Cieplak, G. Xiao, and C. L. Chien, J. Less-Common Met. **164–165**, 870 (1990).
19. H. Thomann and R. A. Klemm, Phys. Rev. B **38**, 6552 (1988).
20. V. E. Kataev, E. F. Kukovitskiĭ, Yu. I. Talanov, *et al.*, Pis'ma Zh. Éksp. Teor. Fiz. **48**, 96 (1988) [JETP Lett. **48**, 101 (1988)].
21. G. Wubbeler, *Elektronenspinresonanz-Untersuchungen und Cu-frein Hochtemperatursupraleitern* (Electron Spin Resonance Studies and Cu-free High-Temperature Superconductors) (Osnabruck Univ., Osnabruck, 1990).
22. A. Yakubovskiĭ, S. Gudenko, A. Rusakov, *et al.*, Physica C **282–287**, 1929 (1997).
23. A. I. Golovashkin, A. Yu. Yakubovskiĭ, S. V. Gudenko, and A. P. Rusakov, Physica C **317–318**, 432 (1999).
24. A. Yu. Yakubovskiĭ, S. V. Gudenko, N. V. Anshukova, *et al.*, Zh. Éksp. Teor. Fiz. **115**, 1326 (1999) [JETP **88**, 732 (1999)].
25. M. D. Sastry, A. G. I. Dalvi, Y. Babu, *et al.*, Nature **330**, 49 (1987).
26. R. Yu. Abdulsabirov, R. Sh. Zhdanov, Ya. S. Izygzon, *et al.*, Sverkhprovodimost' (KIAE) **2**, 52 (1989).
27. V. A. Ivanshin, M. R. Gafurov, I. N. Kurkin, *et al.*, Physica C **307**, 61 (1998).
28. P. Meuffels, B. Rupp, and E. Porschke, Physica C **156**, 441 (1988).
29. G. Uimin, Phys. Rev. B **50**, 9531 (1994).
30. M. A. Teplov, O. N. Bakharev, A. V. Dooglav, *et al.*, in *Abstracts of the 13th Workshop of International School Solid State Physics, Erice, Italy, 1998.*
31. A. S. Moskvin, N. N. Loshkareva, Yu. P. Sukhorukov, *et al.*, Zh. Éksp. Teor. Fiz. **105**, 967 (1994) [JETP **78**, 518 (1994)].
32. R. Martin, Phys. Rev. B **53**, 15501 (1996).
33. M. V. Eremin, S. G. Solov'yanov, and S. V. Varlamov, Zh. Éksp. Teor. Fiz. **112**, 1763 (1997) [JETP **85**, 963 (1997)].
34. Guo-Meng Zhao, K. Conder, H. Keller, and K. A. Muller, Nature **381**, 676 (1996).
35. M. V. Eremin, S. I. Nikitin, N. I. Silkin, *et al.*, Pis'ma Zh. Éksp. Teor. Fiz. **61**, 599 (1995) [JETP Lett. **61**, 612 (1995)].
36. J. Owen and E. A. Harris, in *Electron Paramagnetic Resonance* (Plenum, New York, 1972), p. 427.
37. M. Eremin and E. Sigmund, Solid State Commun. **90**, 765 (1994).
38. M. Eremin, R. Eremina, M. Gafurov, *et al.*, in *Abstracts of the AMPERE Specialized Colloquium, Pisa, Italy, 1999*, p. 123.
39. K. Kumagai, S. Tsuji, R. Nishikawa, *et al.*, in *Abstracts of LT22, Helsinki, Finland, 1999*, p. 238.
40. S. Ohsugi, Y. Kitaoka, K. Magishi, *et al.*, in *Abstracts of LT22, Helsinki, Finland, 1999*, p. 238.
41. I. M. Abu-Shiekah, O. O. Bernal, H. B. Brom, *et al.*, cond-mat/9805124; submitted to Phys. Rev. Lett.
42. P. Wochner, J. M. Tranquada, D. J. Buttrey, *et al.*, Phys. Rev. B **57**, 1066 (1998).
43. D. I. Khomskiĭ and G. A. Sawatzky, Solid State Commun. **102**, 87 (1997).

Translation was provided by AIP

Journal of Experimental and Theoretical Physics, Vol. 90, No. 2, 2000, pp. 370–377.
Translated from Zhurnal Éksperimental'noĭ i Teoreticheskoĭ Fiziki, Vol. 117, No. 2, 2000, pp. 420–428.

SOLIDS
Electron Properties

Formation of an Effective Electric Field in Track Regions During the Stopping of Fast Heavy Charged Particles in Materials

E. V. Metelkin* and A. I. Ryazanov**

Kurchatov Institute Russian Research Centre, Moscow, 123182 Russia
**e-mail: e.v.metelkin@mtu-net.ru*
***e-mail: ryazanov@cityline.ru*

Received July 1, 1999

Abstract—A microscopic approach is used to study the formation of an electric field near the trajectories of fast heavy charged particles propagating in various materials. The analysis is based on determining the space–time distribution function of the fast δ-electrons generated when heavy ions are stopped in materials and the electric current produced by them. The spatial dependence of the electric field strength is determined at various times. The results are used to analyze the process of electric field energy transfer to the ionic subsystem. The spatial distribution of the energy acquired by the ionic subsystem from the electric field is determined over its characteristic lifetime. A mechanism is proposed to explain the formation of track regions both as a result of the higher local heating of the ionic subsystem and as a result of the possible irreversible displacement of the atoms from nodal points. *© 2000 MAIK "Nauka/Interperiodica".*

1. When fast heavy charged particles having energies $E \geq 1$ MeV/nucleus are stopped in materials, as a result of direct interaction with atomic nuclei and electrons their kinetic energy is predominantly transferred to the electronic subsystem and only a small fraction is transferred to the ionic subsystem. Subsequent processes associated with electron and ion heat conduction and also electron–phonon interaction [1] lead to relaxation of the electron and ion temperatures near the heavy particle trajectory [2]. In metals, for example, as a result of the higher electron heat conduction the energy transferred to the electronic subsystem over the characteristic electron–phonon interaction times ($\tau_{ep} \simeq 10^{-13}$ s) can propagate over fairly large distances. Further heating of the ionic subsystem may occur as a result of electron–phonon interaction and is caused by energy being transferred from the electronic to the ionic subsystem over distances substantially greater than the lattice period.

The theory of track formation has been considered in numerous studies [2–7]. These may be divided into two groups, one based on the thermal *T*-spike model [2–4] and the other based on the "ion explosion" model [5–7]. In the thermal spike model the heating of the track region and the ionic subsystem near the heavy particle trajectory is considered to be the result of energy transfer from the electronic to the ionic subsystem. The ion explosion model considers the electrostatic repulsion of stripped ions over the characteristic lifetimes of the electron-depleted regions $t \simeq \omega_p^{-1} \simeq 10^{-15}$–$10^{-16}$ s (ω_p is the plasma frequency). However, no accurate calculations of the effective electric fields formed over these times have been reported in the literature.

Recent experimental investigations of stopping processes of fast heavy charged particles by various materials have yielded various new results. These results particularly relate to the formation of point defects near the heavy particle trajectory: the number of these defects is substantially greater than the corresponding values obtained as a result of calculations based on elastic scattering of stopped ions at the ionic subsystem [8, 9]. A similar process of primary point defect formation is determined by the electron stopping losses and depends strongly on them. Another phenomenon is the anisotropic growth of amorphous alloys under heavy ion irradiation [10–13]. This process also depends strongly on the electron stopping losses of the moving ion.

Numerical results [3, 4] obtained recently using the *T*-spike model and based on solving a system of nonlinear equations describing the change in the temperatures of the electronic and ionic subsystems allowing for electron–phonon interaction cannot explain these experiments. The temperatures of the ionic subsystem obtained on this basis are comparatively low. Existing ion explosion models [5, 7] are predominantly qualitative and contain no accurate calculations of the resulting electric fields.

However, we know that near the trajectory of a moving ion, fast δ-electrons form whose directions of propagation are predominantly perpendicular to the trajectory of the moving ion [7]. The ensuing cascade of electron collisions becomes isotropic over fairly large distances, which leads to the appearance of radial electric currents

1063-7761/00/9002-0370$20.00

and the formation of a radial electric field. In the present study, a kinetic approach is employed to analyze electron current formation processes and the formation of an effective electric field near the trajectory of a moving heavy ion. The results are used as the basis to propose a model to estimate typical values of the energy obtained by the material ions from the electric field and to explain the appreciable increase in the temperature of the ionic subsystem near the moving ion trajectory.

2. We shall determine the current generated by fast δ-electrons formed as a result of the interaction between a moving ion and target atoms near its trajectory. The current generated by the secondary electrons will be neglected because of their low velocity. To simplify the following calculations we shall assume that when they interact with target electrons, the δ-electrons lose energy (on average $\Delta(\varepsilon)$ for an isolated collision) but their direction of motion does not change. In this case, in the continuous slowing approximation the Green function for the electron flux has the following form (see [14]):

$$\Phi(\varepsilon, \mathbf{r}, \mathbf{\Omega}, t, \varepsilon_0, \mathbf{r}', \mathbf{\Omega}', t') = \frac{1}{\Delta(\varepsilon)\Sigma(\varepsilon)} \times \delta\left(t - t' - \int_{\varepsilon}^{\varepsilon_0} \frac{d\varepsilon'}{v'\Delta(\varepsilon')\Sigma(\varepsilon')}\right) \times \delta\left(\mathbf{r} - \mathbf{r}' - \mathbf{\Omega}'\int_{\varepsilon}^{\varepsilon_0} \frac{d\varepsilon'}{\Delta(\varepsilon')\Sigma(\varepsilon')}\right)\delta(\mathbf{\Omega} - \mathbf{\Omega}'), \quad (1)$$

where ε is the kinetic energy of the electrons, v is their velocity, $\Sigma(\varepsilon)$ is the cross section for interaction of δ-electrons with target electrons, and $\Delta(\varepsilon)$ is the average loss of δ-electron energy as a result of an isolated collision.

Expression (1) describes the unsteady-state spatial–angular and energy distribution of the flux of electrons at time t and point $\mathbf{r}$ after these were initially generated at time t' and point $\mathbf{r}'$ having the energy ε_0 and the direction of motion $\mathbf{\Omega}'$.

We shall further assume that the δ-electrons are generated instantaneously over the entire path of the propagating heavy charged particle. The direction of motion of the knock-on electrons is related to the direction of motion of a heavy charged particle by the well-known expression [15]:

$$\cos\theta = \sqrt{\frac{\varepsilon_0}{\varepsilon_m}}, \quad (2)$$

where θ is the angle between the directions of motion of the knock-on electron and the moving charged particle, $\varepsilon_m = 4mE_1/M$ is the maximum energy which can be acquired by a knock-on δ-electron, m is the electron mass, and M and E_1 are the mass and energy of the heavy charged particle.

Taking this reasoning into account, the Green function for a flux of electrons generated instantaneously on a straight line parallel to the z axis and passing through the point having the coordinates x', y' is given by

$$\Phi_1(\varepsilon, \mathbf{r}, \mathbf{\Omega}, t, \varepsilon_0, \mathbf{r}') = \frac{1}{\Delta(\varepsilon)\Sigma(\varepsilon)} \times \delta\left(t - \int_{\varepsilon}^{\varepsilon_0} \frac{d\varepsilon'}{v'\Delta(\varepsilon')\Sigma(\varepsilon')}\right)\frac{1}{2\pi}\delta\left(\Omega_z - \sqrt{\frac{\varepsilon_0}{\varepsilon_m}}\right) \times \delta\left(\sqrt{(x-x')^2 + (y-y')^2} - \sqrt{1-\Omega_z^2}\right) \times \int_{\varepsilon}^{\varepsilon_0} \frac{d\varepsilon'}{\Delta(\varepsilon')\Sigma(\varepsilon')}\Bigg)\left[2\pi\sqrt{(x-x')^2 + (y-y')^2}\right]^{-1}. \quad (3)$$

For the following calculations we convert to coordinates where the z' axis is parallel to the z axis and passes through the point having the coordinates x', y'. In these coordinates the function Φ_1 possesses axial symmetry and has the form

$$\Phi_1(\varepsilon, \rho, \mathbf{\Omega}, t, \varepsilon_0) = \frac{1}{\Delta(\varepsilon)\Sigma(\varepsilon)}\delta\left(t - \int_{\varepsilon}^{\varepsilon_0} \frac{d\varepsilon'}{v'\Delta(\varepsilon')\Sigma(\varepsilon')}\right) \times \frac{1}{2\pi}\delta\left(\Omega_z - \sqrt{\frac{\varepsilon_0}{\varepsilon_m}}\right)\delta\left(\rho - \sqrt{1-\Omega_z^2}\int_{\varepsilon}^{\varepsilon_0} \frac{d\varepsilon'}{\Delta(\varepsilon')\Sigma(\varepsilon')}\right)\frac{1}{2\pi\rho}, \quad (4)$$

where ρ is the distance between the z' axis and the point of observation (cylindrical geometry).

We shall neglect the component of the δ-electron current along the z' axis because the average cosine of the angle between the direction of motion of the knock-on δ-electrons and the direction of motion of the heavy charged particle is small. Using (4) we obtain the following expression for the radial component of the δ-electron current:

$$j_{\rho}^{(1)}(\varepsilon, \rho, t, \varepsilon_0) = e\frac{\sqrt{1-(\varepsilon_0/\varepsilon_m)}}{\Delta(\varepsilon)\Sigma(\varepsilon)}\,\delta\left(t - \int_{\varepsilon}^{\varepsilon_0} \frac{d\varepsilon'}{v'\Delta(\varepsilon')\Sigma(\varepsilon')}\right) \times \delta\left(\rho - \sqrt{1 - \frac{\varepsilon_0}{\varepsilon_m}}\int_{\varepsilon}^{\varepsilon_0} \frac{d\varepsilon'}{\Delta(\varepsilon')\Sigma(\varepsilon')}\right)\frac{1}{2\pi\rho}. \quad (5)$$

Then, using well-known relationships we derive an expression for the Green function of the radial component of the δ-electron current in the initial coordinates:

$$j_{\rho} = j_{\rho}^{(1)}(x-x', y-y') \times \frac{(x-x')x + (y-y')y}{\sqrt{(x-x')^2 + (y-y')^2}\sqrt{x^2+y^2}}, \quad (6)$$

where the function $j_\rho^{(1)}(x - x', y - y')$ is determined by formula (5) in which we need to set $\rho = \sqrt{(x-x')^2 + (y-y')^2}$.

In cylindrical coordinates, the Green function (6) has the following form:

$$j_\rho(\rho, \varphi, \varepsilon, t, \rho', \varphi', \varepsilon_0) = e\frac{\sqrt{1-(\varepsilon_0/\varepsilon_m)}}{\Delta(\varepsilon)\Sigma(\varepsilon)} \times \delta\left(t - \int_\varepsilon^{\varepsilon_0} \frac{d\varepsilon'}{v'\Delta(\varepsilon')\Sigma(\varepsilon')}\right) \times \frac{\delta(\sqrt{\rho^2 + \rho'^2 - 2\rho\rho'\cos(\varphi - \varphi_0)} - r(\varepsilon, \varepsilon_0))}{2\pi r(\varepsilon, \varepsilon_0)} \times \frac{\rho^2 - \rho\rho'\cos(\varphi - \varphi_0)}{r(\varepsilon, \varepsilon_0)\rho}, \quad (7)$$

where the function $r(\varepsilon, \varepsilon_0)$ is described by

$$r(\varepsilon, \varepsilon_0) = \sqrt{1 - \frac{\varepsilon_0}{\varepsilon_m}\int_\varepsilon^{\varepsilon_0} \frac{d\varepsilon'}{\Delta(\varepsilon')\Sigma(\varepsilon')}}. \quad (8)$$

3. The energy distribution of the number of electrons n knocked on from target atoms by a moving ion per unit length of its trajectory is given by the following semi-empirical relationship [16, 17]:

$$\frac{d^2n}{d\varepsilon dz} = \sum_j \frac{4\pi N_j Z_1^{*2} e^4}{\varepsilon_m(\varepsilon + I_j)^2}, \quad (9)$$

where the subscript j refers the jth electron shell of the atom, N_j is the electron density at the jth shell, I_j is the corresponding ionization energy, Z_1^* is the effective charge of a moving ion, which is given by

$$Z_1^* = Z_1\left[1 - \exp\left(-\frac{v}{v_0 Z_1^{2/3}}\right)\right]. \quad (10)$$

Here v_0 is the Bohr velocity, v is the ion velocity, and Z_1 is its atomic number.

After integrating expression (9) over energy between zero and $\varepsilon_m - I_j$, we obtain (assuming $\varepsilon_m \gg I_j$)

$$\frac{dn}{dz} = \frac{4\pi e^4}{\varepsilon_m} Z_1^{*2} Z_2 N\left\langle\frac{1}{I}\right\rangle, \quad (11)$$

where N and Z_2 are the density and atomic number of the target atoms, and the value of $\langle 1/I\rangle$ is determined by the equality

$$Z_2\left\langle\frac{1}{I}\right\rangle = \sum_j \frac{N_j}{N I_j}. \quad (12)$$

Note that estimates made using formula (12) in [7] for iron yielded $\langle 1/I\rangle = (1/8)\ \text{eV}^{-1}$.

In order to simplify the following calculations, we shall assume that the number of electrons knocked on from target atoms by a moving ion per unit length of its trajectory is described by the energy distribution [see (9)]

$$\frac{d^2n}{d\varepsilon dz} = \frac{4\pi Z_2 Z_1^{*2} e^4}{\varepsilon_m \varepsilon^2}, \quad (13)$$

whose lower energy limit is determined by the effective ionization potential I:

$$I = \left(\left\langle\frac{1}{I}\right\rangle\right)^{-1}. \quad (14)$$

For iron (see above) we clearly have $I = 8$ eV.

This approach appreciably simplifies the following calculations and gives a total number of electrons knocked on from target atoms by a moving ion per unit path length which agrees with expression (11). This is readily established after integrating expression (13) over energy between I and ε_m.

Estimates made using formula (11) for ions having energies of 10 MeV/nucleus propagating in iron yielded the result

$$\frac{dn}{dz} \simeq 3.27 \times 10^{-2} Z_1^{*2}\ [\text{Å}^{-1}], \quad (15)$$

which shows that as the atomic number of the moving ion increases from $Z_1 = 8$ (oxygen) to $Z_1 = 92$ (uranium), the number of knock-on electrons increases from 2.1 Å^{-1} to 1.1×10^2 Å^{-1}. From this it follows that the region of ionization produced by direction interaction between a fast ion and target atoms should have a finite transverse dimension.

We shall estimate the characteristic transverse dimension of this region. The impact parameter ρ is related to the energy ε transferred to an electron by a heavy ion by [15]

$$\rho^2 = 4(Z_1^{*2} e)^2 \frac{\varepsilon_m - \varepsilon}{\varepsilon_m^2 \varepsilon}. \quad (16)$$

Quite clearly, the maximum transverse dimension (ρ_{max}) will be determined by the minimum imparted energy sufficient for ionization ($\varepsilon_{min} \simeq I$):

$$\rho_{max} \simeq 2Z_1^* e^2 \frac{1}{\varepsilon_m}\sqrt{\frac{\varepsilon_m}{I}}. \quad (17)$$

Estimates made using formula (17) for ions having energies of 10 MeV/nucleus propagating in iron showed that as the atomic number of the moving ion increases from $Z_1 = 8$ to $Z_1 = 92$, the dimension ρ_{max} increases from 0.62 Å to 4.5 Å

Taking this into account, the spatial energy distribution of electrons knocked on from target atoms by a

moving ion will be described by the following expression [see (13) and (16)]:

$$S(\varepsilon_0, \rho') = \frac{4\pi N Z_2 Z_1^{*2} e^4}{\varepsilon_m \varepsilon_0^2} \times \delta\left(\rho' - 2\frac{Z_1^* e^2}{\varepsilon_m}\sqrt{\frac{\varepsilon_m}{\varepsilon_0} - 1}\right)\frac{1}{2\pi\rho'}. \quad (18)$$

4. Contracting the Green function (7) with the source function (18) and integrating the resulting expression over energy, we determine the space–time distribution of the current generated by the δ-electrons knocked by a moving charged particle from the target atoms:

$$J_\rho(\rho, t) = \int_I^{\varepsilon_m} d\varepsilon \int_\varepsilon^{\varepsilon_m} d\varepsilon_0 \int_0^{2\pi} d\varphi' \times \int_0^\infty d\rho' \rho' j_\rho(\rho, \varphi, t, \varepsilon, \rho', \varphi', \varepsilon_0) S(\varepsilon_0, \rho'). \quad (19)$$

Integrating over the angle φ' and the coordinate ρ' in Eq. (19), we find

$$J_\rho(\rho, t) = \frac{eS_0}{\pi^2}\int_I^{\varepsilon_m}\frac{d\varepsilon_0}{\varepsilon_0^2}\int_I^{\varepsilon_0} d\varepsilon \frac{\sqrt{1-\varepsilon_0/\varepsilon_m}}{\Delta(\varepsilon)\Sigma(\varepsilon)} \times \delta\left(t - \int_\varepsilon^{\varepsilon_0}\frac{d\varepsilon'}{v'\Delta(\varepsilon')\Sigma(\varepsilon')}\right)\frac{1}{r(\varepsilon, \varepsilon_0)} \times \frac{\rho - [\rho^2 + r_0^2(\varepsilon_0) - r^2(\varepsilon, \varepsilon_0)]/2\rho}{\sqrt{r^2(\varepsilon, \varepsilon_0) - [\rho - r_0(\varepsilon_0)]^2}\sqrt{[\rho + r_0(\varepsilon_0)]^2 - r^2(\varepsilon, \varepsilon_0)}} \times \eta(r^2(\varepsilon, \varepsilon_0) - [\rho - r_0(\varepsilon_0)]^2) \times \eta([\rho + r_0(\varepsilon_0)]^2 - r^2(\varepsilon, \varepsilon_0)), \quad (20)$$

where $r(\varepsilon, \varepsilon_0)$ is described by expression (8), $S_0 = 4\pi N Z_2 Z_1^{*2} e^4/\varepsilon_m$; $\eta(x)$ is the Heaviside function, and $r_0(\varepsilon_0) = 2(Z_1^* e^2/\varepsilon_m)\sqrt{\varepsilon_m/\varepsilon_0 - 1}$.

5. In order to determine the strength of the electric field generated by the heavy ion motion, we use the Maxwell equation:

$$\frac{\partial E_\rho}{\partial t} + 4\pi(J_\rho + \sigma E_\rho) = 0, \quad (21)$$

where σ is the conductivity of the target material.

For times shorter than the relaxation time the solution of equation (21) has the form

$$E_\rho(\rho, t) = -4\pi\int_0^t dt' J_\rho(\rho, t'). \quad (22)$$

Substituting (20) into (22), we find the space–time distribution of the electric field:

$$E_\rho(\rho, t) = \frac{4e}{\pi}S_0\int_I^{\varepsilon_m}\frac{d\varepsilon_0}{\varepsilon_0^2}\int_{\varepsilon_1(t,\varepsilon_0)}^{\varepsilon_0} d\varepsilon \frac{\sqrt{1-\varepsilon_0/\varepsilon_m}}{\Delta(\varepsilon)\Sigma(\varepsilon)}\frac{1}{r(\varepsilon, \varepsilon_0)} \times \frac{\rho - [\rho^2 + r_0^2(\varepsilon_0) - r^2(\varepsilon, \varepsilon_0)]/2\rho}{\sqrt{r^2(\varepsilon, \varepsilon_0) - [\rho - r_0(\varepsilon_0)]^2}\sqrt{[\rho + r_0(\varepsilon_0)]^2 - r^2(\varepsilon, \varepsilon_0)}} \times \eta(r^2(\varepsilon, \varepsilon_0) - [\rho - r_0(\varepsilon_0)]^2) \times \eta([\rho - r_0(\varepsilon_0)]^2 - r^2(\varepsilon, \varepsilon_0)), \quad (23)$$

where e is the absolute value of the electron charge, and the function $\varepsilon_1(t, \varepsilon_0)$ is the solution of the equation

$$t - \int_{\varepsilon_1}^{\varepsilon_0}\frac{d\varepsilon'}{v'\Delta(\varepsilon')\Sigma(\varepsilon')} = 0. \quad (24)$$

In order to simplify the calculations, we convert to the new variable in expression (23)

$$u = r(\varepsilon, \varepsilon_0), \quad du = -\sqrt{1 - \frac{\varepsilon_0}{\varepsilon_m}}\frac{d\varepsilon}{\Delta(\varepsilon)\Sigma(\varepsilon)}. \quad (25)$$

As a result, we obtain

$$E_\rho(\rho, t) = \frac{4e}{\pi}S_0\int_I^{\varepsilon_m}\frac{d\varepsilon_0}{\varepsilon_0^2}\int_0^{r_1(\varepsilon_0, t)}\frac{du}{u} \times \frac{\rho - [\rho^2 + r_0^2(\varepsilon_0) - u^2]/2\rho}{\sqrt{u^2 - [\rho - r_0(\varepsilon_0)]^2}\sqrt{[\rho + r_0(\varepsilon_0)]^2 - u^2}} \times \eta(u^2 - [\rho - r_0(\varepsilon_0)]^2)\eta([\rho + r_0(\varepsilon_0)]^2 - u^2), \quad (26)$$

where the function $r_1(\varepsilon_0, t)$ is described by

$$r_1(\varepsilon_0, t) = \sqrt{1 - \frac{\varepsilon_0}{\varepsilon_m}}\int_{\varepsilon_1(t,\varepsilon_0)}^{\varepsilon_0}\frac{d\varepsilon}{\Delta(\varepsilon)\Sigma(\varepsilon)}. \quad (27)$$

6. In order to perform numerical calculations using formula (26), we need to determine the form of the functions contained in the expressions in the integrand in (24) and (27). The product of the functions Δ(ε) and Σ(ε) evidently gives the energy lost by a moving electron per unit length. Then, using the differential cross

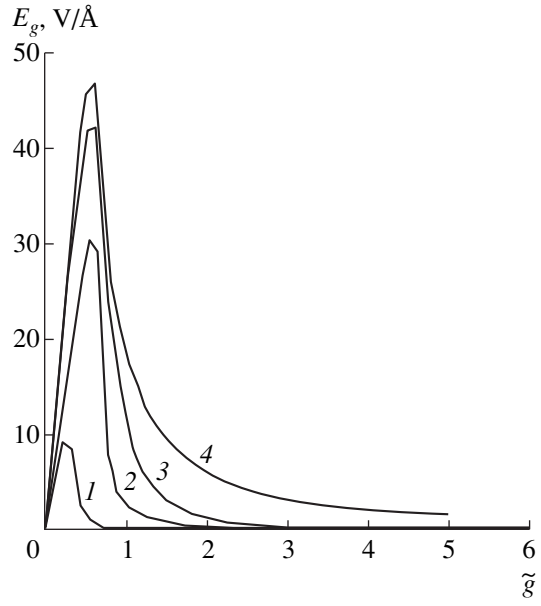

Fig. 1. Spatial dependences of the electric field formed as a result of the propagation of oxygen ions in iron at various times: *1*—$t/t_r = 0.01$, *2*—$t/t_r = 0.05$, *3*—$t/t_r = 0.1$, and *4*—$t/t_r = 1$.

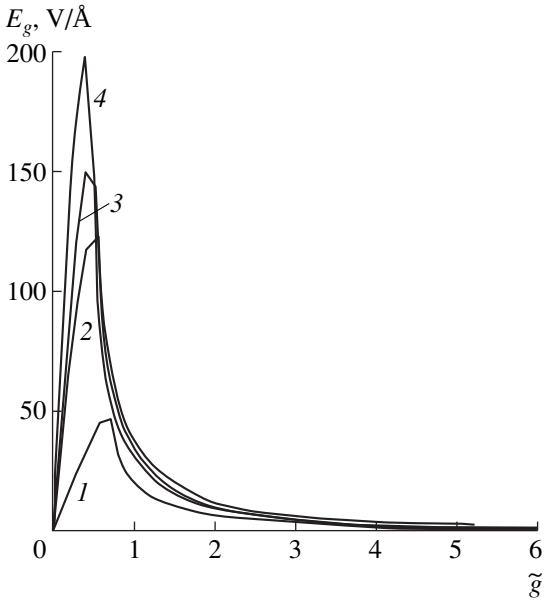

Fig. 2. Spatial dependences of the electric field formed as a result of the propagation of various ions in iron at times t_r: *1*—$Z_1 = 8$, *2*—$Z_1 = 36$, *3*—$Z_1 = 54$, and *4*—$Z_1 = 92$.

section for scattering of a δ-electron by material electrons in the form [15]

$$d\Sigma(\varepsilon' \longrightarrow \varepsilon) = \frac{\pi Z_2 N e^4}{\varepsilon'} \frac{dT}{T^2} \tag{28}$$

(where T is the energy imparted by a moving electron to electrons of the target atoms), we find

$$\Delta(\varepsilon)\Sigma(\varepsilon) = \frac{\pi Z_2 N e^4}{\varepsilon} \ln\frac{\varepsilon}{I}. \tag{29}$$

Substituting (29) into (24), we obtain the following equation to determine the dimensionless function $\tilde{\varepsilon}_1(t, \tilde{\varepsilon}_0) = \varepsilon_1/I$:

$$1 - \frac{I^2}{\pi Z_2 e^4 v_I t} \int_{\tilde{\varepsilon}_1}^{\tilde{\varepsilon}_0} \frac{dx\sqrt{x}}{\ln x} = 0 \tag{30}$$

where $\tilde{\varepsilon}_0 = \varepsilon_0/I$, $v_I = \sqrt{2I/m}$.

Similarly for the function $r_1(\varepsilon_0, t)$ we find

$$r_1(\tilde{\varepsilon}_0, t) = \frac{I^2}{\pi Z_2 N e^4} \sqrt{1 - \frac{\tilde{\varepsilon}_0}{\tilde{\varepsilon}_m}} \int_{\tilde{\varepsilon}_1(t, \tilde{\varepsilon}_0)}^{\tilde{\varepsilon}_0} \frac{x dx}{\ln x}. \tag{31}$$

Making the distance dimensionless by dividing by ρ_{max} [see (17)] and the energy dimensionless by dividing by the effective ionization potential I, we obtain the following definitive result for the space–time distribution of the electric field:

$$E_\rho(\tilde{\rho}, t) = E_0 \tilde{\rho} \int_1^{\tilde{\varepsilon}_m} \frac{d\tilde{\varepsilon}_0}{\tilde{\varepsilon}_0^2} \times \int_0^{\tilde{r}_1^2(\tilde{\varepsilon}_0, t)} \frac{dx}{x} \frac{1 - (\tilde{\rho}^2 + \tilde{r}_0^2 - x)/2\tilde{\rho}^2}{\sqrt{x - (\tilde{\rho} - \tilde{r}_0)^2}\sqrt{(\tilde{\rho} + \tilde{r}_0)^2 - x}} \times \eta(x - (\tilde{\rho} - \tilde{r}_0)^2)\eta((\tilde{\rho} + \tilde{r}_0)^2 - x), \tag{32}$$

where $\tilde{r}_1 = r_1/\rho_{max}$, $\tilde{r}_0 = r_0/\rho_{max} = \sqrt{1/\tilde{\varepsilon}_0 - 1/\tilde{\varepsilon}_m}$, and $E_0 = 2eNZ_2\rho_m$ is the characteristic electric field strength.

7. Formula (32) was used to make numerical calculations of the electric field formed near the track of heavy charged particles having energies of 10 MeV/nucleus stopped in iron.

Figure 1 gives spatial dependences of the electric field formed as a result of the propagation of oxygen ions ($Z_1 = 8$) at times $t/t_r = 0.01$, 0.05, 0.1, 1 ($t_r = 10^{-16}$ s is the characteristic relaxation time). It can be seen that with increasing time $t = t_r$ the size of the region occupied by the electric field and its strength increase, reaching a maximum of ≃47 V/Å.

Figure 2 gives spatial dependences of the electric field formed when oxygen ($Z_1 = 8$), krypton ($Z_1 = 36$), xenon ($Z_1 = 54$), and uranium ($Z_1 = 92$) irons are stopped in iron at time $t = t_r$. It can be seen that as the atomic number of the moving ion increases, the electric field increases, reaching a maximum of ≃198 V/Å for uranium ions. Moreover, the maximum electric field is achieved at points which lie within the maximum dimension of the electron source ρ_{max} [see (17)]. Figure 3

shows the same dependences as a function of the distance in angstrom. It can be seen that the electric field can reach high values at considerable distances from the track of a moving charged particle.

The energy lost by a heavy charged particle per unit length of its trajectory can be determined using expression (13)

$$\frac{dE_1}{dz} = \int_I^{\varepsilon_m} d\varepsilon \varepsilon \frac{d^2n}{d\varepsilon dz} = \frac{4\pi e^4 N Z_2 Z_1^{*2}}{\varepsilon_m} \ln\frac{\varepsilon_m}{I}. \quad (33)$$

We compare this value with the energy of the electric field formed at time $t = t_r$ as a result of the motion of heavy charged particles having energies of 10 MeV/nucleus. The electric field energy W_E per unit length of the moving particle trajectory can be obtained using expression (32)

$$\frac{dW_E}{dz} = W_0 \int_0^{\infty} d\tilde{\rho}\,\tilde{\rho}\,\tilde{E}_\rho^2(\tilde{\rho}, t = t_r), \quad (34)$$

where $W_0 = E_0^2 \rho_m^2/4$, $\tilde{E}_\rho = E_\rho/E_0$.

Results of calculations made using formulas (33) and (34) for moving particles having atomic numbers Z_1 = 8, 36, 54, and 92 are given in Table. These results show that as the atomic number of the moving particle increases, the fraction of its energy converted into electric field energy increases (26% for uranium ions). This is because the electric field energy increases more rapidly as the charge of the moving ion increases. For example, we find $(dE_1/dz) \sim (Z_1^*)^2$ and $(dW_E/dz) \sim W_0 \sim (Z_1^*)^4$.

Since an appreciable fraction of the heavy charged particle energy can be converted into electric field energy, leading to the formation of large electric fields, this factor must be borne in mind when determining the distribution function of the electrons knocked by a heavy particle from the target atoms, i.e., the influence of the generated electric field on the motion of the knock-on electrons must be taken into account self-consistently in the calculations.

We shall analyze the reason for the formation of large electric fields in greater detail. For this purpose we find the density of the electrons knocked on by a heavy charged particle:

$$\frac{dn}{dV} = \int_I^{\varepsilon_m} d\varepsilon_0 S(\varepsilon_0, \rho), \quad (35)$$

where the function $S(\varepsilon_0, \rho)$ is described by expression (18) and is the number of electrons of energy ε_0 formed by a heavy particle per unit volume per unit energy range. Substituting (18) into (35), we obtain

$$\frac{dn}{dV} = NZ_2\eta(\rho_{\max} - \rho), \quad (36)$$

where $\rho_{\max}$ is given by formula (17).

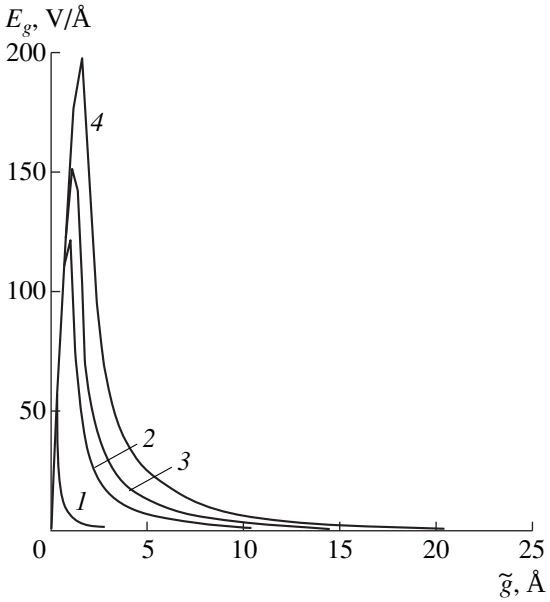

Fig. 3. Spatial dependences of the electric field formed as a result of the propagation of various ions in iron at times t_r: *1*—Z_1 = 8, *2*—Z_1 = 36, *3*—Z_1 = 54, and *4*—Z_1 = 92.

It follows from this last result that as it moves, a heavy charged particle in fact completely "strips" the target atoms in the region $\rho \le \rho_{\max}$. As a result of the drift of knock-on atoms from this region, the nuclei of the target atoms are "exposed," which leads to the formation of a large positive charge and consequently to large electric fields. If all the knock-on electrons could leave the region of action of the source by the time $t = t_r$, the positive charge density in this region would evidently be eNZ_2. In this case, in accordance with the Gauss theorem, the electric field strength in this region would increase linearly

$$E_\rho^{(1)} = 2\pi eNZ_2\rho, \quad (37)$$

reaching a maximum at its boundary:

$$E_{\rho,\max}^{(1)} = 2\pi eNZ_2\rho_{\max}. \quad (38)$$

Estimates made using formula (38) for various ions with Z_1 = 8, 36, 54, 92 and energies of 10 MeV/nucleus propagating in iron yielded the following results: $E_{\rho,\max}^{(1)}$ = 108, 411, 553, and 782 V/Å, respectively.

Results of calculations using formulas (33) and (34)

Value	$Z_1 = 8$	$Z_1 = 36$	$Z_1 = 54$	$Z_1 = 92$
dE_1/dz, keV/Å	0.130	1.90	3.44	6.88
dW/dz, keV/Å	0.004	0.26	0.63	1.80
$\frac{dW/dz}{dE_1/dz}$	0.03	0.14	0.18	0.26

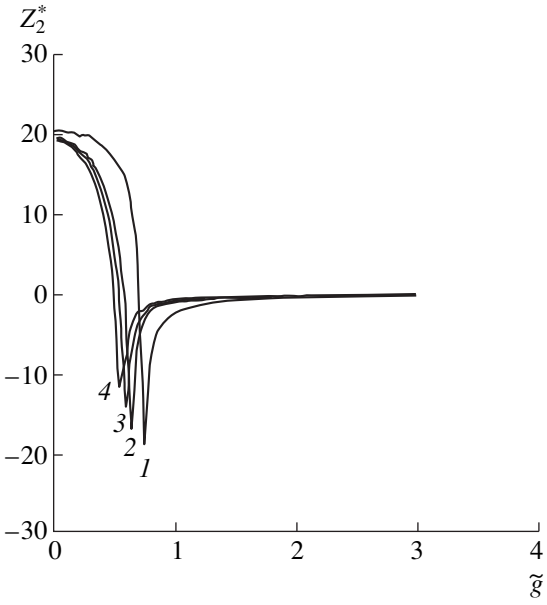

Fig. 4. Spatial dependences of Z_2^* formed as a result of the propagation of various ions in iron at times t_r: *1*—$Z_1 = 8$, *2*—$Z_1 = 36$, *3*—$Z_1 = 54$, and *4*—$Z_1 = 92$.

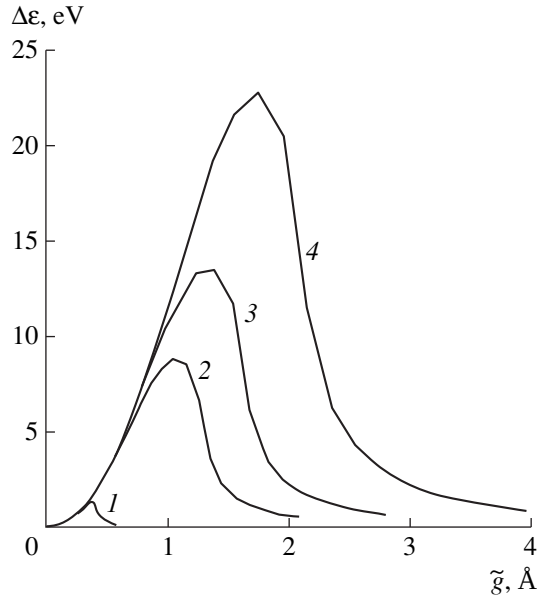

Fig. 5. Spatial distribution of the energy acquired by the lattice ions from the electric field during the propagation of various ions in iron: *1*—$Z_1 = 8$, *2*—$Z_1 = 36$, *3*—$Z_1 = 54$, and *4*—$Z_1 = 92$.

These estimates are higher than the maximum values of the electric field obtained in the numerical calculations (see Figs. 2 and 3).This difference arises because not all the knock-on electrons can leave the region of action of the source ($\rho \le \rho_{max}$) by the time $t = t_r$.

We shall assess the situation having determined the electric charge density using the well-known relationship:

$$\sigma = \frac{1}{4\pi}\mathrm{div}\mathbf{E}(\rho, t = t_r). \quad (39)$$

Figure 4 gives dependences of $Z_2^* = \sigma/eN$ on distance calculated using formulas (32) and (39) for ions having atomic numbers $Z_1 = 8$, 36, 54, and 92 and energies of 10 MeV/nucleus. The value of Z_2^* is the effective ion charge (in units of e) at the lattice points. If all the electrons were to leave the region $\rho \le \rho_{max}$, the relationship $Z_2^* = 26$ would be satisfied. However, we can see (see Fig. 4) that the value of Z_2^* is lower and decreases with increasing distance, changing sign. Negative values of Z_1^* clearly correspond to an excessive number of electrons around the lattice atoms formed as a result of displacement from the central region. These results also explain the differences between the maximum values of the electric field discussed above.

8. The short-lived action of high-power electric fields on positive target ions having the charge eZ_2 in the region $\rho \le \rho_{max}$ causes considerable momentum and therefore considerable energy to be transferred to these ions. We shall give a rough estimate of this energy.

It can be seen from Fig. 1 that over the time interval between $0.1t_r$ and t_r in the region $\tilde{\rho} \le 1$ the electric field varied very slightly. In this case, we shall assume that an electric field $E_\rho(\rho, t = t_r)$ acts on the target ions during the time $t_r = 10^{-16}$ s. The force acting on a lattice ion from the electric field is given by

$$F = eZ_2E_\rho. \quad (40)$$

As a result of the action of this force, over the time t_r the lattice ion receives the momentum

$$\Delta p = Ft_r = eZ_2E_\rho t_r \quad (41)$$

and the energy

$$\Delta\varepsilon = \frac{(\Delta p)^2}{2M_2} = \frac{e^2Z_2^2t_r^2}{2M_2}E_\rho^2, \quad (42)$$

where M_2 is the mass of a lattice ion.

Figure 5 shows the distribution of the energy acquired by lattice ions in the region $\rho \le \rho_{max}$ plotted using formula (42) and the results obtained above (see Figs. 2 and 3). The calculations were made for heavy ions ($Z_1 = 8$, 36, 54, 92) having energies of 10 MeV/nucleus propagating in iron. It can be seen from the figure that the lattice ions receive appreciable energy from the electric field. As the atomic number of the moving ion (Z_1) increases, the imparted energy increases substantially and may reach the binding energies of the atoms in the lattice sites (see the curve for $Z_1 = 92$). This leads

to substantial heating of the lattice ions in the region $\rho \le \rho_{max}$.

9. Thus, as fast heavy charged particles propagate in matter, they knock electrons from atoms. The electric current generated by the knock-on δ-electrons leads to the formation of an electric field which increases with time near the heavy particle trajectory. Quite clearly, the field will increase over times shorter than the characteristic relaxation time t_r.

Calculations made above for fast charged particles having energies of 10 MeV/nucleus propagating in iron showed that these electric fields may reach a high intensity, which increases as the atomic number (Z_1) of the moving particle increases. For example, when Z_1 increases from 8 (oxygen) to 92 (uranium), the maximum electric field increases from 47 V/Å to 200 V/Å. Moreover, as Z_1 increases the fraction of the energy concentrated in the electric field increases compared with the energy lost by the moving particle as a result of electron stopping, reaching 26% for uranium ions. This factor indicates that the influence of this electric field on the motion of the knock-on electrons must be taken into account self-consistently.

The action of high-power electric fields on positive target ions, even for a short time interval ($t = t_r$), causes an appreciable transfer of energy to these ions which may reach the binding energy of the atoms in lattice sites. This leads to stronger heating of the lattice ions and also creates conditions for the irreversible displacement of atoms from lattice sites and the formation of point defects near the moving particle trajectory.

REFERENCES

1. M. I. Kaganov, I. M. Lifshitz, and L. V. Tanatarov, Zh. Éksp. Teor. Fiz. **31**, 232 (1957) [Sov. Phys. JETP **4**, 173 (1957)].
2. I. M. Lifshitz, M. I. Kaganov, and L. V. Tanatarov, At. Energ. **6**, 391 (1959).
3. T. Toulemonde, C. Dufour, and E. Paumier, Phys. Rev. B **46**, 14362 (1992).
4. K. Yasui, Nucl. Instrum. Methods Phys. Res. B **90**, 409 (1994).
5. R. L. Fleiscker, B. B. Price, and R. M. Walger, J. Appl. Phys. **36**, 3645 (1965).
6. S. Klaumunzer, Ming-Dong Hou, and G. Schumacher, Phys. Rev. Lett. **57**, 850 (1986).
7. D. Leseur and A. Dunlop, Radiat. Eff. Defects Solids **126**, 163 (1993).
8. A. Dunlop and D. Leseur, Radiat. Eff. Defects Solids **126**, 132 (1993).
9. A. Iwase and T. Iwata, Nucl. Instrum. Methods Phys. Res. B **90**, 322 (1994).
10. S. Klaumunzer, Changlin Li, and G. Schumacher, Appl. Phys. Lett. **51**, 97 (1987).
11. S. Klaumunzer *et al.*, Radiat. Eff. Defects Solids **108**, 131 (1989).
12. A. I. Ryazanov, A. E. Volkov, and S. Klaumunzer, Phys. Rev. B **51**, 12107 (1995).
13. H. Trinkaus and A. I. Ryazanov, Phys. Rev. Lett. **74**, 5072 (1995).
14. A. I. Isakov, M. V. Kazarnovskiĭ, Yu. A. Medvedev, *et al.*, *Nonsteady-State Neutron Stopping. Fundamental Relationships and Various Applications* (Nauka, Moscow, 1984).
15. L. D. Landau and E. M. Lifshitz, *Mechanics* (Nauka, Moscow, 1973; Pergamon, Oxford, 1973).
16. R. H. Ritchie and C. Claussen, Nucl. Instrum. Methods **198**, 133 (1982).
17. E. J. Kobetich and R. Katz, Phys. Rev. **170**, 391 (1968).

Translation was provided by AIP

Journal of Experimental and Theoretical Physics, Vol. 90, No. 2, 2000, pp. 378–388.
Translated from Zhurnal Éksperimental'noĭ i Teoreticheskoĭ Fiziki, Vol. 117, No. 2, 2000, pp. 429–439.

SOLIDS
Electron Properties

Microscopic Theory of Auger Recombination in Quantum Wires

E. B. Dogonkin*, G. G. Zegrya, and A. S. Polkovnikov*****

Ioffe Physicotechnical Institute, Russian Academy of Sciences, St. Petersburg, 194021 Russia

**e-mail: eugen@theory.ioffe.rssi.ru*

***e-mail: zegrya@theory.ioffe.rssi.ru*

****e-mail: tol@theory.ioffe.rssi.ru*

Received July 27, 1999

Abstract—An analysis is made of mechanisms for Auger recombination of nonequilibrium carriers in cylindrical quantum wires. It is shown that two different Auger recombination mechanisms take place in these wires: a quasi-threshold and a nonthreshold mechanism. Both mechanisms are associated with the presence of heterobarriers but are of a different nature. The quasi-threshold mechanism is attributed to the spatial confinement of the carrier wave functions to the region of the quantum wire and in this case the quasi-momentum conservation law is violated and the Auger recombination process is intensified. As the radius of the wire increases, the quasi-threshold Auger recombination process goes over to a threshold process. The nonthreshold mechanism is caused by the scattering of an electron (hole) at the heterojunction; the rate of this nonthreshold Auger recombination tends to zero in the limit of an infinite-radius wire. © *2000 MAIK "Nauka/Interperiodica"*.

1. INTRODUCTION

In narrow-gap homogeneous III–V semiconductors two main Auger recombination processes predominate. The first involves the recombination of an electron and a heavy hole and the excitation of another electron (CHCC) while the other Auger process involves the transition of a heavy hole to a spin–orbit split-off subband (CHHS). In the first order of perturbation theory in terms of electron–electron interaction, both Auger processes are threshold ones (except for semiconductors in which the spin–orbit splitting constant is close to the band gap) and the Auger recombination rate has an exponential temperature dependence [1].

Unlike homogeneous semiconductors, in heterostructures the quasi-momentum component normal to the interface is not conserved which leads to the appearance of a nonthreshold mechanism for Auger recombination [2]. This mechanism has been studied fairly comprehensively in quantum-well heterostructures [3–5]. Nonradioactive recombination processes in narrow-band semiconductors and in heterostructures control the lifetimes of nonequilibrium carriers when their concentration is high. In addition, Auger recombination processes strongly influence the characteristics of optoelectronic devices and in particular, the threshold currents of heterolasers. No detailed analysis has yet been made of Auger recombination mechanisms for quantum wires. The aim of the present study is to make a theoretical analysis of Auger recombination mechanisms of nonequilibrium carriers in semiconducting quantum wires.

In order to describe the spectrum and wave functions of the carriers in a quantum wire, we use the model of a cylindrical rectangular quantum well of finite depth for electrons in the conduction band and holes in the valence band. It was shown in [5] that three Auger recombination mechanisms exist in rectangular planar quantum wells, i.e., threshold, quasi-threshold, and nonthreshold mechanisms. In the present study we show that the quasi-threshold mechanism is also present in quantum wires and is converted into a three-dimensional threshold process in the limit of an infinite-radius wire.[1] A fundamental difference compared with the situation in quantum wells is observed for the nonthreshold mechanism of Auger recombination. A quantum wire has two channels for nonthreshold Auger recombination: (1) transfer of a large quasi-momentum to an excited carrier (as for planar quantum wells); (2) transfer of large angular momentum to this carrier. This last process is the only nonthreshold mechanism of Auger recombination in quantum dots [6]. The two nonthreshold Auger recombination mechanisms have different dependences on the heterobarrier height for electrons and holes, and also on the wire radius. The rates of the nonthreshold and quasi-threshold Auger recombination processes are power functions of temperature which makes Auger recombination in quantum-wire heterostructures more effective than that in homogeneous semiconductors.

[1] Unlike quantum wells, the threshold Auger recombination process in quantum wire is naturally considered as a constituent part of the quasi-threshold Auger process.

2. FUNDAMENTAL EQUATIONS

In order to analyze recombination processes we need to know the wave equations of the carriers. The wave equations and the carrier spectrum in narrow-gap III–V semiconductors are most accurately described using the four-band Kane model.

2.1. Kane Equations

For most III–V semiconductors the wave functions of electrons in the conduction band at the center of the Brillouin zone are accurately described by the Γ_6^+ representation and in the valence band by the Γ_7^+ and Γ_8^+ representations. The first two are doubly degenerate and the third is fourfold degenerate. The basis wave functions of the conduction band and the valence band are usually taken in the form of eigenfunctions of the angular momentum [7, 8] but for the case of cylindrical symmetry it is natural to select a different basis [9]:

$$\begin{aligned} &|s\uparrow\rangle, |s\downarrow\rangle, |p_+\uparrow\rangle, |p_+\downarrow\rangle,\\ &|p_-\uparrow\rangle, |p_-\downarrow\rangle, |p_z\uparrow\rangle, |p_z\downarrow\rangle, \end{aligned} \tag{1}$$

where

$$\begin{aligned} |p_+\rangle &= 1/\sqrt{2}|(p_x + ip_y)\rangle,\\ |p_-\rangle &= 1/\sqrt{2}|(p_x - ip_y)\rangle, \end{aligned}$$

and $|s\rangle$ and $|p_x\rangle$, $|p_y\rangle$, $|p_z\rangle$ are *s*- and *p*-type Bloch functions with angular momenta of 0 and 1, respectively. The first functions describe the state of the conduction band and the second ones describe the valence band at the Γ point. The arrows indicate the direction of spin. This choice corresponds to basis functions for which the projections of the quasi-momentum and angular momentum on the wire axis have particular values corresponding to the symmetry of a cylindrical wire. In this basis, the dependence of the Bloch amplitudes on the *z* coordinate (the *z* axis is parallel to the wire axis) and the axial angle has a simple form. The carrier wave function ψ may be expressed in the form

$$\psi = \psi_s|s\rangle + \boldsymbol{\psi}|\mathbf{p}\rangle,$$

where ψ_s and $\boldsymbol{\psi}$ are spinors. We write the Kane equations in differential form which allows integration across the interface [5]:

$$\begin{cases} (E_g + \delta - E)\psi_s - i\hbar\nabla\boldsymbol{\psi} = 0,\\ -E\boldsymbol{\psi} - i\hbar\gamma\nabla\psi_s + \dfrac{\hbar^2}{2m_0}\nabla[6\tilde{\gamma}_2\nabla\boldsymbol{\psi}]\\ + \dfrac{\hbar^2}{2m_0}\dfrac{\partial}{\partial x_k}(\tilde{\gamma}_1 - 2\tilde{\gamma}_2)\dfrac{\partial}{\partial x_k}\boldsymbol{\psi} + i\delta\boldsymbol{\sigma}\times\boldsymbol{\psi} = 0. \end{cases} \tag{2}$$

Here γ is the Kane matrix element [9] having the dimensions of velocity, $\tilde{\gamma}_1$ and $\tilde{\gamma}_2 = \tilde{\gamma}_3$ are generalized Luttinger parameters [9], $\delta = \Delta_{so}/3$, Δ_{so} is the spin–orbit splitting constant, E_g is the band gap, m_0 is the free electron mass, and $\boldsymbol{\sigma} = (\sigma_x, \sigma_y, \sigma_z)$ are the Pauli matrices. If the heavy-hole mass m_h describing the interaction with higher bands is introduced phenomenologically instead of the Luttinger parameters, the equations (2) yield those obtained in [10]. It can be confirmed that the equations (2) do not differ from those usually used in the literature [8–11]. In the first equation in the system (2) for the electrons we neglect the term containing the heavy mass for the electrons [12]. Using the probability flux density conservation law, we can obtain boundary conditions for the envelopes of the wave functions at the interface [5]. In the approximation $\tilde{\gamma}_1$, $\tilde{\gamma}_2$ = const, assuming that the effective mass of the heavy holes is much greater than the electron mass, we can obtain the continuity condition for the following functions:

$$\boldsymbol{\psi}, \frac{d\psi_z}{d\rho}, m_l^{-1}\mathrm{div}\boldsymbol{\psi}, \tag{3}$$

where

$$m_l^{-1} = \frac{2\gamma^2}{E_g - E} + m_0^{-1}(\tilde{\gamma}_1 + 4\tilde{\gamma}_2).$$

2.2. Carrier Spectra in a Homogeneous Semiconductor

By Fourier transforming the Kane equations (2), we can obtain the spectra for the electrons and three hole branches [5]:

(a) heavy holes

$$E_h = -\frac{\hbar^2k^2}{2m_k},$$

where

$$m_h^{-1} = m_0^{-1}(\tilde{\gamma}_1 - 2\tilde{\gamma}_2),$$

(b) light holes and spin-split-off holes

$$\begin{aligned} E_{l,so} &= -\frac{3\delta}{2} - \frac{\hbar^2k^2}{4}(m_l^{-1} + m_h^{-1})\\ &\pm\sqrt{2\delta^2 + \left(\frac{\delta}{2} - \frac{\hbar^2k^2}{4}(m_l^{-1} - m_h^{-1})\right)^2}, \end{aligned} \tag{4}$$

(c) electrons

$$k^2 = \frac{\mathscr{E}}{\hbar^2\gamma^2} + \frac{\mathscr{E}^2 + \mathscr{E}(2E_g + 3\delta) + (E_g + 3\delta)E_g}{E_g + \mathscr{E} + 2\delta}$$

(k is the quasi-momentum of the carriers). Here the hole energy E is measured from the edge of the valence band and the electron energy $\mathscr{E}$ is measured from the bottom of the conduction band.

2.3. Wave Functions in a Homogeneous Semiconductor

In cylindrical coordinates the wave functions of heavy holes obtained from the Kane equations (2) in the basis (1) may be expressed in the form

$$\psi_{h1}(\rho, \phi, z) = H_1 \times \begin{bmatrix} 0 \\ 0 \\ -2iqJ_{m-3/2}(k_h\rho)e^{i(m-3/2)\phi} \\ k_hJ_{m-1/2}(k\rho)e^{i(m-1/2)\phi} \\ 0 \\ -k_hJ_{m+3/2}(k_h\rho)e^{i(m+3/2)\phi} \\ \sqrt{2}k_hJ_{m-1/2}(k_h\rho)e^{i(m-1/2)\phi} \end{bmatrix} e^{iqz}, \quad (5)$$

$$\psi_{h2}(\rho, \phi, z) = H_2 \times \begin{bmatrix} 0 \\ 0 \\ -k_hJ_{m-3/2}(k_h\rho)e^{i(m-3/2)\phi} \\ 0 \\ k_hJ_{m+1/2}(k\rho)e^{i(m+1/2)\phi} \\ -2iqJ_{m+1/2}(k_h\rho)e^{i(m+3/2)\phi} \\ 0 \\ \sqrt{2}k_hJ_{m+1/2}(k_h\rho)e^{i(m+1/2)\phi} \end{bmatrix} e^{iqz}, \quad (6)$$

where J_m are mth-order Bessel functions, H_1 and H_2 are normalization constants, q and k_h are the projections of the quasi-momentum parallel and perpendicular to the axial axis, and m is the projection of the total momentum on the axial axis which has half-integer values. Inside the quantum wires the wave functions have the form of a linear combination of (5) and (6). If a heavy hole is localized, above the barrier its wave function is similar to (5) and (6) except that the Bessel function J_m should be replaced by the Macdonald function K_m with k_h replaced by ik_h.

For light and spin-orbit split-off holes we can write:

$$\psi_{i1}(\rho, \phi, z) = A_1 \times \begin{bmatrix} \frac{\sqrt{2}\hbar(k_i^2 + q^2)\gamma}{E_g - E}J_{m-1/2}(k\rho)\, e^{i(m-1/2)\phi} \\ 0 \\ -k_i(1 + \lambda_i)J_{m-3/2}(k_h\rho)e^{i(m-3/2)\phi} \\ 2iqJ_{m-1/2}(k\rho)e^{i(m-1/2)\phi} \\ k_i(\lambda_i - 1)J_{m+1/2}(k\rho)e^{i(m+1/2)\phi} \\ 0 \\ \sqrt{2}iqJ_{m-1/2}(k_h\rho)e^{i(m-1/2)\phi} \\ -\sqrt{2}k_i\lambda_iJ_{m+1/2}(k_h\rho)e^{i(m+1/2)\phi} \end{bmatrix} e^{iqz} \quad (7)$$

and

$$\psi_{i2}(\rho, \phi, z) = A_2 \times \begin{bmatrix} \frac{\sqrt{2}\hbar(k_i^2 + q^2)\gamma}{E_g - E}J_{m+1/2}(k\rho)\, e^{i(m+1/2)\phi} \\ 0 \\ k_i(\lambda_i - 1)J_{m-1/2}(k\rho)e^{i(m-1/2)\phi} \\ 2iq\lambda_iJ_{m+1/2}(k\rho)e^{i(m+1/2)\phi} \\ k_i(1 + \lambda_i)J_{m+3/2}(k_h\rho)e^{i(m+3/2)\phi} \\ -\sqrt{2}k_i\lambda_iJ_{m-1/2}(k_h\rho)e^{i(m-1/2)\phi} \\ \sqrt{2}iqJ_{m+1/2}(k_h\rho)e^{i(m+1/2)\phi} \end{bmatrix} e^{iqz}, \quad (8)$$

where $i = l, s$ corresponds to light and spin-split-off holes, A_1 and A_2 are normalization constants, and $\lambda_i = \delta/(E + 4\delta - \hbar^2(k_i^2 + q^2)/2m_h)$.

The electron wave functions are exactly the same as the wave functions for light and spin-orbit split-off holes except that the substitution $E \longrightarrow E_g + \mathscr{E}$ must be made.

2.4. Carrier States in a Quantum Wire

Since, in the selected basis, the projections of the momentum and the angular momentum of the carriers on the z axis have specific values, the variables z, ρ, and ϕ in equation (2) are separated. Hence, the eigenstates of the carriers in a quantum wire are determined by a dispersion equation which has a radial dependence of the wave functions for certain values of q and m. Unlike quantum wells [5], in a quantum wire the states cannot be separated in terms of parity even for heavy holes so that the dispersion equations are cumbersome. For heavy holes this equation has the form

$$\left(\frac{K_{m-3/2}(\kappa_hR)}{J_{m-3/2}(k_hR)} - \frac{K_{m+1/2}(\kappa_hR)}{J_{m+1/2}(k_hR)}\right)$$

$$\times\left(\frac{K_{m+3/2}(\kappa_h R)}{J_{m+3/2}(k_h R)}-\frac{K_{m-1/2}(\kappa_h R)}{J_{m-1/2}(k_h R)}\right)$$
$$=\frac{4q^2}{\kappa_h^2 k_h^2}\left(k_h\frac{K_{m-3/2}(\kappa_h R)}{J_{m-3/2}(k_h R)}-\kappa_h\frac{K_{m-1/2}(\kappa_h R)}{J_{m-1/2}(k_h R)}\right) \quad (9)$$
$$\times\left(k_h\frac{K_{m+3/2}(\kappa_h R)}{J_{m+3/2}(k_h R)}-\kappa_h\frac{K_{m+1/2}(\kappa_h R)}{J_{m+1/2}(k_h R)}\right).$$

Here R is the wire radius, and k_h and κ_h are the moduli of the quasi-momentum components normal to the interface in the well and in the barrier region, respectively. The quasi-momenta are uniquely interrelated by the dispersion law. In the limit of an infinitely wide or deep well we can obtain a simplified dispersion equation for the heavy holes:

$$\left(\frac{J_m(k_h R)}{J_{m-2}(k_h R)}-1\right)\left(\frac{J_{m-1}(k_h R)}{J_{m+1}(k_h R)}-1\right)=\frac{4q^2}{k_h^2}. \quad (10)$$

For light holes we derive the following dispersion equation:

$$q^2\left[\frac{m_l}{\tilde{m}_l}\left(\frac{\kappa_l^2+q^2}{k_l^2+q^2}\right)-\left(\frac{2\tilde{\lambda}_l-1}{2\lambda_l-1}\right)^2\right]$$
$$=\left[\kappa_l^2\left(\frac{2\tilde{\lambda}_l-1}{2\lambda_l-1}\right)^2+k_l^2\left(\frac{m_l}{\tilde{m}_l}\right)^2\left(\frac{\kappa_l^2+q^2}{k_l^2+q^2}\right)^2\right.$$
$$-\kappa_l k_l\frac{m_l}{\tilde{m}_l}\left(\frac{\kappa_l^2+q^2}{k_l^2+q^2}\right)\left(\frac{2\tilde{\lambda}_l-1}{2\lambda_l-1}\right) \quad (11)$$
$$\times\left(\frac{K_{jz-1/2}(\kappa_l R)}{J_{jz-1/2}(k_l R)}\frac{J_{jz+1/2}(k_l R)}{K_{jz+1/2}(\kappa_l R)}\right.$$
$$\left.\left.+\frac{K_{jz+1/2}(\kappa_l R)}{J_{jz+1/2}(k_l R)}\frac{J_{jz-1/2}(k_l R)}{K_{jz-1/2}(\kappa_l R)}\right)\right].$$

The dispersion equation for the electrons in the conduction band is slightly simpler since it is divided into two equations (this separation does not occur in quantum wells [5]):

$$k_c\frac{\sqrt{\lambda_c^2-1}}{Z}\sqrt{\frac{J_{m-1/2}(k_c R)J_{m+3/2}(k_c R)}{J_{m+1/2}^2(k_c R)}}$$
$$=\kappa_c\frac{\sqrt{\tilde{\lambda}_c^2-1}}{\tilde{Z}}\sqrt{\frac{K_{m-1/2}(\kappa_c R)K_{m+3/2}(\kappa_c R)}{K_{m+1/2}^2(\kappa_c R)}} \quad (12)$$

or

$$k_c\frac{\sqrt{\lambda_c^2-1}}{Z}\sqrt{\frac{J_{m+1/2}(k_c R)J_{m-3/2}(k_c R)}{J_{m-1/2}^2(k_c R)}}$$
$$=\kappa_c\frac{\sqrt{\tilde{\lambda}_c^2-1}}{\tilde{Z}}\sqrt{\frac{K_{m+1/2}(\kappa_c R)K_{m-3/2}(\kappa_c R)}{K_{m-1/2}^2(\kappa_c R)}}, \quad (13)$$

where $\mathscr{E}$ is the electron energy measured from the edge of the conduction band inside the wire,

$$\lambda_c=\frac{\delta}{E_g+2\delta+\mathscr{E}},$$

$$Z=\frac{\mathscr{E}^2+\mathscr{E}(2E_g+3\delta)+(E_g+3\delta)E_g}{\mathscr{E}+E_g+2\delta},$$

$\tilde{\lambda}$ and $\tilde{Z}$ are the same values but in the region below the barrier. The wave functions corresponding to equation (12) have an even-valued projection of the orbital moment of the Bloch envelopes on the z axis while in the case (13) this projection has an odd value. The following calculations of the matrix elements will be made assuming that an electron localized in a wire is in the size-quantization ground level whose energy is determined from:

$$k_c\frac{\sqrt{\lambda_c^2-1}}{Z}\frac{J_1(k_c R)}{J_0(k_c R)}=\kappa_c\frac{\sqrt{\tilde{\lambda}_c^2-1}}{\tilde{Z}}\frac{K_1(\kappa_c R)}{K_0(\kappa_c R)}. \quad (14)$$

3. MATRIX ELEMENT OF AUGER RECOMBINATION

3.1. Auger Recombination Probability

In the limits of the first order of perturbation theory in terms of electron–electron interaction the Auger recombination probability per unit time is given by

$$W_{i\to f}=\frac{2\pi}{\hbar}|M_{fi}|^2\delta(\varepsilon_f-\varepsilon_i). \quad (15)$$

In this case the matrix element of the transition has the form:[2]

$$M_{fi}=\left\langle\psi_f(\mathbf{r}_1,\mathbf{r}_2,\nu_1,\nu_2)\left|\frac{e^2}{\kappa_\infty|\mathbf{r}_1-\mathbf{r}_2|}\right|\psi_i(\mathbf{r}_1,\mathbf{r}_2,\nu_1,\nu_2)\right\rangle, \quad (16)$$

where $\mathbf{r}_1$ and $\mathbf{r}_2$ are the carrier coordinates, ν_1 and ν_2 are the spin variables, e is the electron charge, and κ_∞ is the rf permittivity of the semiconductor [1]. Allowing for the antisymmetrization of the wave functions, the

[2] It was shown in [5] that allowance for the mapping potential as a correction to the Coulomb potential introduces negligibly small corrections to the matrix element and the Auger recombination rate.

matrix element of the Auger transition may be expressed in the form

$$M_{fi} = M_{\mathrm{I}} - M_{\mathrm{II}}, \tag{17}$$

where

$$\begin{aligned} M_{\mathrm{I}} &= \left\langle \psi_3(\mathbf{r}_1, \nu_1)\psi_4(\mathbf{r}_2, \nu_2)\left|\frac{e^2}{\kappa_\infty|\mathbf{r}_1 - \mathbf{r}_2|}\right| \right. \\ &\quad \left. \times \psi_1(\mathbf{r}_1, \nu_1)\psi_2(\mathbf{r}_2, \nu_2)\right\rangle, \\ M_{\mathrm{II}} &= \left\langle \psi_3(\mathbf{r}_1, \nu_1)\psi_4(\mathbf{r}_2, \nu_2)\left|\frac{e^2}{\kappa_\infty|\mathbf{r}_1 - \mathbf{r}_2|}\right| \right. \\ &\quad \left. \times \psi_1(\mathbf{r}_2, \nu_2)\psi_2(\mathbf{r}_1, \nu_1)\right\rangle. \end{aligned} \tag{18}$$

In accordance with [5], when the condition $\Delta_{so} \gg T$ is satisfied in heterostructures (which holds for most III–V semiconductors) the mixing of spin-split-off holes with heavy holes is negligible, and mixing of light and heavy holes is insignificant when $m_c \ll m_h$. Under these conditions we can use the generally accepted terminology for Auger recombination processes in homogeneous semiconductors. For simplicity here we shall mainly confine our analysis to the CHCC Auger recombination process. When the condition $E_g - \Delta_{so} \gg T$ is satisfied, which is the case for most III–V semiconductors, all the qualitative conclusions will also hold for the CHHS process.

3.2. Auger Recombination Mechanisms in Quantum Wires

The carrier wave functions are the eigenfunctions of the projections of the quasi-momentum and angular momentum operators on the z axis. Consequently, the matrix element of the Auger recombination automatically satisfies the momentum and angular momentum conservation laws and in the cylindrical coordinates ρ, ϕ, z has the form

$$\begin{aligned} M_{\mathrm{I}} &= \frac{e^2}{\kappa_\infty}\int_0^\infty \rho_1 d\rho_1 \int_0^\infty \rho_2 d\rho_2 \int_0^{2\pi} d\phi_1 \int_0^{2\pi} d\phi_2 \\ &\quad \times \int_{-\infty}^{\infty} dz_1 \int_{-\infty}^{\infty} dz_2 \frac{e^{im(\phi_1 - \phi_2) + iq(z_1 - z_2)}}{|\mathbf{r}_1 - \mathbf{r}_2|} \\ &\quad \times (\mathbf{R}_2^*(\rho_1)\mathbf{R}_3(\rho_1))(\mathbf{R}_1^*(\rho_2)\mathbf{R}_4(\rho_2)), \end{aligned} \tag{19}$$

where $\mathbf{R}_1$, $\mathbf{R}_2$, $\mathbf{R}_3$, and $\mathbf{R}_4$ are the radial components of the particle wave functions and

$$\begin{cases} m = m_2 - m_3 = m_4 - m_1 \\ q = q_2 - q_3 = q_4 - q_1 \end{cases}$$

are the imparted axial projections of the angular momentum and the quasi-momentum. The matrix element M_{II} is obtained from M_{I} by transposing the subscripts 1 and 2 of the wave functions $\mathbf{R}_1$ and $\mathbf{R}_2$. The function $\mathbf{R}_1$ corresponds to a localized carrier and $\mathbf{R}_4$ corresponds to a carrier in the excited state; a recombining heavy hole–electron pair corresponds to the wave functions $\mathbf{R}_2$ and $\mathbf{R}_3$. For the CHCC process $\mathbf{R}_1$ and $\mathbf{R}_4$ correspond to electrons in the conduction band whereas in the description of the CHHS process $\mathbf{R}_1$ corresponds to a heavy hole and $\mathbf{R}_4$ to a spin-orbit split-off hole.

Fourier transforming the Coulomb potential with respect to the coordinates ρ and ϕ, we obtain

$$\begin{aligned} &\int_0^{2\pi} d\phi \int_{-\infty}^{\infty} dz \frac{e^{im\phi + iqz}}{|\mathbf{r}_1 - \mathbf{r}_2|} \\ &= \begin{cases} 4\pi I_m(q\rho_1)K_m(q\rho_2), & \rho_1 \le \rho_2, \\ 4\pi I_m(q\rho_2)K_m(q\rho_1), & \rho_1 > \rho_2 \end{cases} \end{aligned} \tag{20}$$

(where I_m is a modified mth-order Bessel function). Since the heavy-hole mass is large ($m_h \gg m_c$), its wave function decays rapidly below the barrier compared with the electron wave function and the below-barrier region of overlap of the heavy-hole and electron wave functions can be neglected. It should be noted that this by no means implies that the problem can be solved using the approximation of an unbounded potential barrier for the heavy hole, since its energy levels are obtained from the exact boundary conditions (3). As noted above, we shall also assume that the recombining electron is in the size-quantization ground level. This assumption is justified even for fairly broad quantum wires because of the comparatively low electron mass. Under these conditions the matrix element has the form

$$\begin{aligned} M_{\mathrm{I}} &= \frac{4\pi e^2}{\kappa_0}\int_0^R \rho_1 d\rho_1 \mathbf{R}_2^*(\rho_1)\mathbf{R}_3(\rho_1) \sum_{\eta = s, \mathbf{p}} \left[a_{1\eta}a_{4\eta} \right. \\ &\quad \times \int_0^{\rho_1} \rho d\rho K_m(q\rho_1)I_m(q\rho) J_{m_{4\eta}}(k_4\rho) J_{m_{1\eta}}(k_1\rho) \\ &\quad + a_{1\eta}a_{4\eta}\int_{\rho_1}^{R} \rho d\rho I_m(q\rho_1)K_m(q\rho) J_{m_{4\eta}}(k_4\rho) J_{m_{1\eta}}(k_1\rho) \\ &\quad \left. + b_{1\eta}b_{4\eta}\int_R^{\infty} \rho d\rho I_m(q\rho_1)K_m(q\rho) J_{m_{4\eta}}(\kappa_4\rho) J_{m_{1\eta}}(\kappa_1\rho) \right], \end{aligned} \tag{21}$$

where η corresponds to the number of the basis function and allowing for the spin has eight values, $a_{i\eta}$ are

the factors of the Bessel functions for the radial components of the wave functions:

$$R_{1\eta}(\rho) = \begin{cases} a_{1\eta}J_{m_{1\eta}}(k_1\rho), & \rho \le R \\ b_{1\eta}K_{m_{1\eta}}(\kappa_1\rho), & \rho > R, \end{cases}$$

$$R_{4\eta}(\rho) = \begin{cases} a_{4\eta}J_{m_{4\eta}}(k_4\rho), & \rho \le R \\ b_{4\eta}J_{m_{4\eta}}(\kappa_4\rho), & \rho > R. \end{cases}$$

In the matrix element (21) we can identify two different contributions. This first is associated with discontinuities of the wave functions and their derivatives at the heterojunction (at the point $\rho = R$. The process determined by this contribution corresponds to scattering at the heterobarrier. For the case of a single barrier this scattering leads to the appearance of a nonthreshold Auger recombination channel [2] and a similar situation occurs in quantum wells [3–5]. The rate of the nonthreshold Auger recombination process tends to zero in the limit of an infinite-radius wire. The second contribution in (21) is associated with scattering at the short-range Coulomb potential [5]. In the CHCC Auger recombination process the electron is excited either to the continuous or the discrete part of the spectrum corresponding to $\mathscr{E} = E_g$. In the first case, the electron either acquires a large quasi-momentum perpendicular to the interface or has a large projection of the angular momentum on the z axis. In the second case, the electron acquires a large quasi-momentum directed along the axis of the wire. This last process is clearly a threshold one since it requires the hole to have the same quasi-momentum. In quantum wells only the transition to the discrete spectrum corresponds to the threshold process [5] but this statement does not hold for quantum wires. On transition to the continuous spectrum with increasing angular momentum the threshold is not lifted. For this reason it is meaningless to isolate the threshold process and this is more conveniently considered as a constituent part of the quasi-threshold process. Thus, separating the nonthreshold and quasi-threshold mechanisms of Auger recombination in quantum wires, we write the matrix element for Auger recombination in the form

$$M_1 = M^{(1)} + M^{(2)}, \tag{22}$$

where $M^{(1)}$ and $M^{(2)}$ are the nonthreshold and quasi-threshold matrix elements, respectively. In the limit of a large-radius wire, the quasi-threshold Auger recombination mechanism is converted to the threshold mechanism.

3.3. Matrix Element of the Nonthreshold Auger Process

The nonthreshold Auger process involves scattering of carriers at the heterojunction. The corresponding matrix element is determined by the discontinuities of the wave functions and their derivatives at $\rho = R$. Detailed calculations of the nonthreshold matrix element are given in Appendix A where the following result is obtained:

$$M^{(1)} = \frac{8\pi e^2}{\kappa_0(q^2 + k_4^2)}R_{1s}(R)R_{4s}(R)$$

$$\times\left\{qRK_{m-1}(qR)\left[\frac{3V_c + V_v}{4E_g}\right] + mK_m(qR)\frac{3V_c}{4E_g}\right\} \tag{23}$$

$$\times\int_0^R(\mathbf{R}_2^*(\rho)\mathbf{R}_3(\rho))I_m(q\rho)\rho d\rho.$$

The first term in braces is proportional to q and corresponds to the nonthreshold process in a quantum well [5], the second term is proportional to m and corresponds to the nonthreshold Auger recombination channel in quantum dots [6]. It can be seen from (23) that the two contributions to $M^{(1)}$ have different dependences on the barrier height for electrons in the conduction band and holes in the valence band.

3.4. Matrix Element of the Quasi-Threshold Auger Process

The quasi-threshold process is associated with the confinement of the region of overlap of the wave functions within the volume of the quantum wire. In accordance with the Heisenberg uncertainty principle, this has the result that the δ-function in the quasi-momentum conservation law is replaced by a function which tends to it in the limit $R \longrightarrow \infty$. Calculations of the quasi-threshold matrix element are given in Appendix B; the final expression for $M^{(2)}$ has the form

$$M^{(2)} = \frac{4\pi e^2}{\kappa_0(q^2 + k_4^2)}$$

$$\times\int_0^R(\mathbf{R}_2^*(\rho)\mathbf{R}_3(\rho))(\mathbf{R}_1^*(\rho)\mathbf{R}_4(\rho))\rho d\rho. \tag{24}$$

In the limit $R \longrightarrow \infty$ and subject to the condition k_1, $k_2 \ll k_3$, k_4 this matrix element becomes proportional to $\delta(k_4 - k_3)$, i.e., the quasi-threshold process is converted to the threshold Auger recombination process. In fact, the quasi-threshold matrix element is proportional to the integral of four Bessel functions:

$$M^{(2)} \propto \int_0^R J_0(k_1\rho)J_0(k_2\rho)J_m(k_3\rho)J_m(k_4\rho)\rho d\rho. \tag{25}$$

Assuming that k_3, $k_4 \gg k_1$, k_2, this integral can be expanded as a series in terms of the primitive

$J_m(k_3\rho)J_m(k_4\rho)$. Retaining the first term of the series, we obtain

$$M^{(2)} \propto \frac{R}{k_4^2 - k_3^2} J_0(k_1 R) J_0(k_2 R)(k_3 J_{m-1}(k_3 R) \times J_m(k_4 R) - k_4 J_m(k_3 R) J_{m-1}(k_4 R)). \quad (26)$$

For large R the Bessel functions can be replaced by their asymptotic expressions for a large argument:

$$J_m(z) \approx \sqrt{\frac{2}{\pi z}} \cos\left(z - \frac{\pi m}{2} + \frac{\pi}{4}\right). \quad (27)$$

Substituting this expression into (26), we finally obtain

$$M^{(2)} \propto \frac{\sin(k_4 - k_3)R}{k_4 - k_3}. \quad (28)$$

In the limit $R \longrightarrow \infty$ this expression squared gives a δ-function multiplied by the radius of the quantum wire:

$$\frac{\sin(k_4 - k_3)R^2}{(k_4 - k_3)^2} \longrightarrow \frac{\pi R}{2}\delta(k_4 - k_3).$$

4. AUGER RECOMBINATION COEFFICIENT

In order to calculate the Auger recombination coefficient in the first order of perturbation theory, the transition probabilities (15) should be averaged over the initial states and summed over the final ones:

$$G = \frac{3\pi}{\hbar} \sum_{\mathbf{k}_1, \mathbf{k}_2, \mathbf{k}_3, \mathbf{k}_4} \langle M^2 \rangle f_1 f_2 (1 - f_3)(1 - f_4) \times \delta(E_3 + E_4 - E_1 - E_2). \quad (29)$$

Here f_1, f_2 are the carrier distribution functions in the initial state, and f_3 and f_4 are those in the final state, and $\langle M^2 \rangle$ is the sum of the squares of the matrix elements of the Auger transition over the spin variables of the initial and final states. The contributions to the Auger recombination rate from the quasi-threshold and nonthreshold processes cannot be separated because interference takes place between them. For small wire radii this interference is particularly strong because both processes are nonthreshold ones [5]. For large-radius quantum wires the interference between $M^{(1)}$ and $M^{(2)}$ can be neglected because unlike nonthreshold processes, the main quasi-threshold transitions involve heavy holes having a high longitudinal quasi-momentum or angular momentum. Taking the above reasoning into account, it is clear that neglecting interference gives an almost accurate result for large-radius wires and an order-of-magnitude result for thin wires. The Auger recombination rate thus obtained has correct dependences on the quantum wire parameters (radius, barrier heights for holes and electrons) and on the temperature.

We introduce the Auger recombination coefficient C which is related to the rate G by

$$G = Cn^2 p,$$

where n and p are the one-dimensional concentrations of electrons and holes. Neglecting interference between the contributions of the various processes, we write

$$C = C^{(1)} + C^{(2)}, \quad (30)$$

where the coefficients $C^{(1)}$ and $C^{(2)}$ correspond to nonthreshold and quasi-threshold Auger processes having the matrix elements M_1 and M_2, respectively.

An expression for the nonthreshold Auger recombination coefficient may be obtained by substituting (23) into (29), which gives

$$C_1 \approx \frac{24 e^4 \hbar^3 \gamma^4}{\kappa_\infty^2} \frac{F(\Delta_{so}/E_g)}{E_g^5 R^5} \times \frac{k_c^5 J_0^4(k_c R)}{(J_0^2(k_c R) + J_1^2(k_c R) + K_0^2(\kappa_c R) + K_1^2(\kappa_c R))^2} \times \left\langle \left(\left[\frac{3V_c + V_v}{4E_g} \right]^2 + \frac{m^2}{q^2 R^2} \left[\frac{3V_c}{4E_g} \right]^2 \right) \frac{k_h^2 q^2}{(q^2 + k_4^2)^3 k_f(q)} \right\rangle, \quad (31)$$

where

$$F(x) = \frac{(1 + x/3)(1 + x)}{(1 + 2x/3)(1 + x/2)} \frac{1 + 7x/9 + x^2/6}{1 + x/4 + x^2/6},$$

$$k_f(q) = \sqrt{\frac{2E_g^2}{\hbar^2 \gamma^2} \frac{1 + \Delta_{so}/2E_g}{1 + \Delta_{so}/3E_g} - q^2}.$$

The angular brackets denote averaging over the heavy-hole distribution function. For a Boltzmann distribution, which is usually valid for holes, this averaging has the form

$$\langle f(q_h, k_{mn}) \rangle = \frac{1}{Z} \sum_{n,m} \int_0^\infty dq_h f(q_h, k_{mn}) \exp\left(-\frac{k_{mn}^2 + q_h^2}{q_T^2} \right),$$

where

$$Z = \frac{q_T \sqrt{\pi}}{2} \sum_{n,m} \exp\left(-\frac{k_{mn}^2}{q_T^2} \right),$$

n is the level number of the holes, m is the projection of the angular momentum, k_c and κ_c are the quasi-momenta of a ground-state electron above and below

the barrier, perpendicular to the interface; q_T is the thermal momentum of the heavy holes:

$$q_T = \sqrt{\frac{2m_hT}{\hbar^2}},$$

and k_{mn} is the quasi-momentum corresponding to the size-quantization level of the holes which for an infinitely deep quantum well and heavy holes has the value:

$$k_{mn} = R/\gamma_{mn},$$

where γ_{mn} is the nth root of the Bessel function J_m.

For the coefficient of the quasi-threshold Auger process we have

$$C_2 \approx \frac{6e^4\hbar^3\gamma^4}{\kappa_\infty^2}\frac{F(\Delta_{so}/E_g)}{E_g^5}\frac{1}{R^5}$$

$$\times\frac{k_c^2J_0^4(k_cR)}{(J_0^2(k_cR)+J_1^2(k_cR)+K_0^2(\kappa_cR)+K_1^2(\kappa_cR))^2} \quad (32)$$

$$\times\left\langle\frac{k_h^2}{(q_h^2+k_h^2)k_f}\frac{\sin^2(k_f-k_h)R}{(k_f(q)-k_h)^2}\right\rangle.$$

In the limit of an infinite-radius wire, the expression for the coefficient of the quasi-threshold Auger recombination process yields that for the Auger recombination coefficient in a homogeneous semiconductor. Assuming that the size-quantization levels of the carriers merge into the continuous spectrum and integrating over them, we obtain

$$C_2\pi^2R^4 \longrightarrow \frac{16\sqrt{2}\pi^{5/2}}{3}\frac{e^4\hbar^3}{\kappa_\infty^2}$$
$$\times\frac{F(\Delta_{so}/E_g)}{E_g^{5/2}T^{1/2}m_c^{1/2}m_h^{3/2}}\exp\left(-\frac{E_{th}}{T}\right), \quad (33)$$

where E_{th} is the threshold energy of the CHCC process in a homogeneous semiconductor; in the Kane model $E_{th} \approx (2m_c/m_h)E_g$. Note that for broad wells we need to take into account not only the process with $k_f = k_h + k_{c1} + k_{c2}$ but another three processes corresponding to $k_f = k_h + k_{c1} - k_{c2}$, $k_f = k_h - k_{c1} + k_{c2}$, and $k_f = k_h - k_{c1} - k_{c2}$. Expression (33) may be compared with the well-known Gel'mont result [13] obtained for the Auger recombination coefficient in a homogeneous semiconductor:

$$C_{3D} = 6\sqrt{2}\pi^{5/2}\frac{e^4\hbar^3}{\kappa_0^2}\frac{1}{E_g^{5/2}T^{1/2}m_c^{1/2}m_h^{3/2}}\exp\left(-\frac{E_{th}}{T}\right). \quad (34)$$

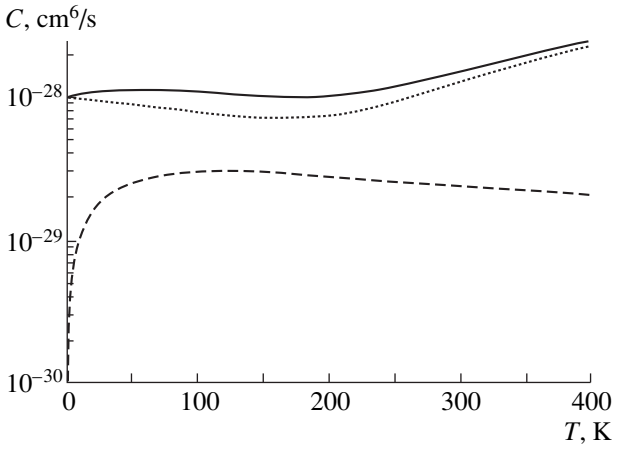

Fig. 1. Temperature dependence of the coefficient of Auger recombination for the CHCC process for two mechanisms of Auger recombination: nonthreshold ($C_1\pi^2R^4$, dashed curve) and quasi-threshold ($C_2\pi^2R^4$, dotted curve) for a thin wire (of radius R = 50 Å). The solid curve gives the total Auger recombination coefficient ($(C_1 + C_2)\pi^2R$).

A small difference in the numerical coefficient is attributed to the assumption $\Delta_{so} \gg E_g$ made in [13].

5. DISCUSSION OF RESULTS

An analysis of Auger recombination processes in quantum-wire semiconductor structures has shown that two different mechanisms exist: nonthreshold and quasi-threshold Auger recombination. The nonthreshold process has two channels involving scattering of the longitudinal component of the quasi-momentum and the angular momentum. The first channel is similar to the nonthreshold Auger process in quantum wells, while the second is similar to the nonthreshold Auger recombination channel in quantum dots. The coefficients for these channels have different dependences on the barrier heights for electrons and holes. This factor particularly impedes the suppression of Auger recombination in type 2 quantum-wire semiconducting structures unlike quantum-well structures [14]. In quantum wells the threshold CHCC Auger recombination process involved the transition of an excited electron to the discrete spectrum. For wires, as we have shown, there is also a threshold process involving an electron transition to the continuous spectrum. For this reason in wires it is meaningless to separate the quasi-threshold and threshold processes into two separate processes.

In order to analyze the Auger recombination coefficients we used a typical InGaAsP heterostructure with band gap E_g = 1 eV.

It can be seen from Figs. 1 and 2 that the coefficient C_1 for nonthreshold Auger recombination is a weak function of temperature for narrow quantum wires and decreases with temperature for broad wires. However, the quasi-threshold Auger recombination coefficient C_2

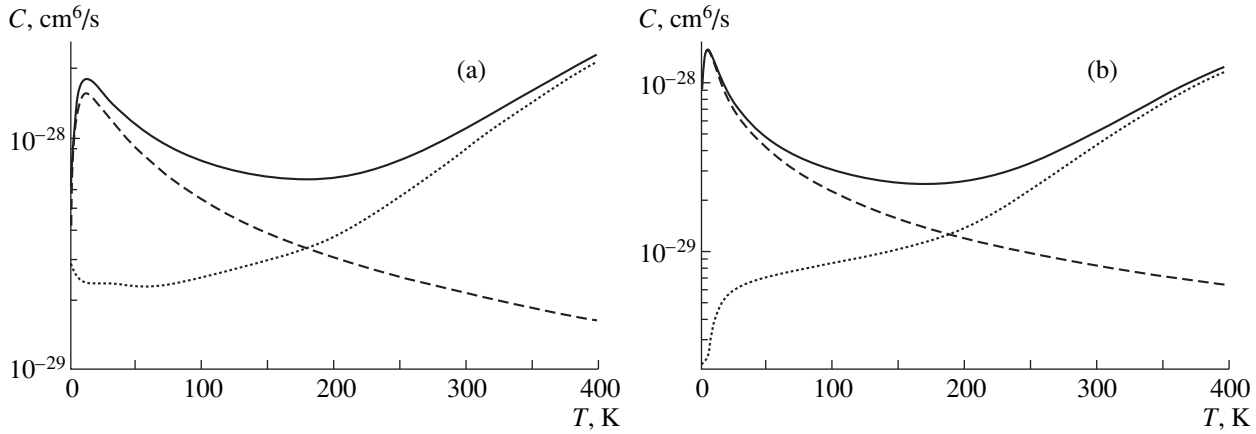

Fig. 2. Temperature dependence of the coefficient of Auger recombination for the CHCC process for two mechanisms of Auger recombination: nonthreshold ($C_1\pi^2R^4$, dashed curve) and quasi-threshold ($C_2\pi^2R^4$, dotted curve) for broad wires with R = 150 (a) and R = 250 (b). The solid curve gives the total Auger recombination coefficient ($(C_1 + C_2)\pi^2R^4$).

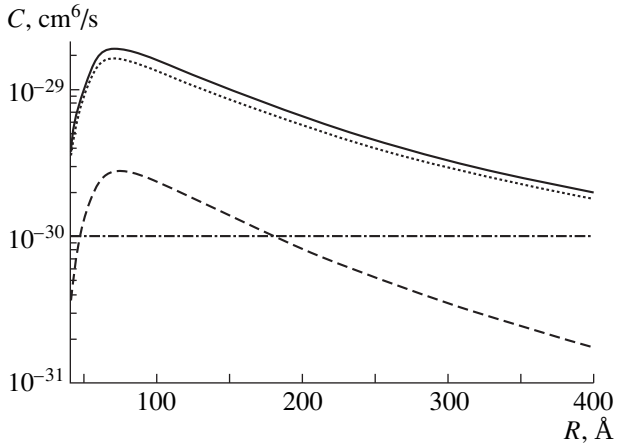

Fig. 3. Dependence of the coefficient of Auger recombination for the nonthreshold ($C_1\pi^2R^4$, dashed curve) and quasi-threshold ($C_2\pi^2R^4$, dotted curve) processes on the radius of the quantum wire at T = 300 K. The solid curve gives the total Auger recombination coefficient ($(C_1 + C_2)\pi^2R^4$) and the horizontal dot-dash line gives the three-dimensional coefficient of the CHCC process.

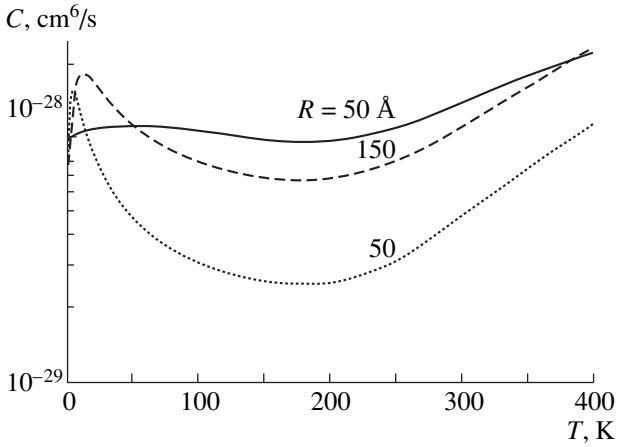

Fig. 4. Temperature dependence of the total Auger recombination coefficient for quantum wires of various radii.

increases with temperature. For thin wires C_2 is also a weak function of temperature (Fig. 1). As the wire radius R increases, the dependence of C_2 on temperature becomes stronger and approaches the threshold (exponential) dependences in bulk semiconductors (Fig. 2). The quantitative relationship between C_1 and C_2 also changes: C_1 decreases more rapidly with increasing R compared with C_2 so that the effective three-dimensional coefficient $C_{3D}^1 = C_1(\pi R^2)^2$ vanishes for $R \longrightarrow \infty$, whereas $C_{3D}^2 = C_2(\pi R^2)^2$ approaches the bulk coefficient of Auger recombination C_{3D} (Fig. 3). For thin wires, the Auger coefficients of the quasi-threshold and nonthreshold processes are considerably higher than the three-dimensional coefficient C_{3D} relative to the square of the area of the cylindrical cross section of the wire ($(\pi R^2)^2$). The Auger recombination coefficient is a nonmonotonic function of the wire radius over a wide range of temperature (Fig. 4). For narrow wires the Auger coefficient is initially small because of the small overlap of the wave functions of electrons and holes in bound states. As the radius of the wire increases, the influence of the heterobarriers on the Auger recombination processes diminishes and the threshold nature of these processes becomes apparent. Thus, for large-radius wires the Auger recombination coefficient decreases to the value corresponding to the three-dimensional Auger coefficient of a homogeneous semiconductor.

It follows from this analysis that the Auger recombination mechanisms in quantum wires are broadly similar to those in quantum wells [5] and only differ quantitatively.

For homogeneous semiconductors, the first order of perturbation theory in terms of interelectron interaction is inadequate to calculate the Auger recombination coefficient. This is because the threshold Auger recombination process is strongly influenced by electron–

phonon and electron–electron relaxation processes, which partially remove the Auger recombination threshold. However, the first order of perturbation theory gives a qualitatively correct result for semiconductor structures with quantum wires and quantum wells, since the influence of the heterobarriers on the Auger recombination processes is more important than the relaxation processes if the characteristic sizes of the heterostructure are smaller than the mean free path of the carriers [15, 16].

ACKNOWLEDGMENTS

In conclusion the authors would like to thank V. Golovach for discussions of various results. This work was partly supported financially by the Russian Foundation for Basic Research (projects nos. 97-02-18151, 98-07-90336, and 99-02-16796) and also by the program "Physics of Solid-State Nanostructures" of the Russian Ministry of Science (projects nos. 97-1035 and 97-33).

APPENDIX

A. Calculation of the Nonthreshold Matrix Element

The nonthreshold matrix element may be written in the form

$$M^{(1)} = \frac{4\pi e^2}{\kappa_\infty} \times \int_0^R \rho_1 d\rho_1 I_m(q\rho_1)\mathbf{R}_2^*(\rho_1)\mathbf{R}_3(\rho_1)J^{(1)}, \tag{35}$$

where

$$J^{(1)} = \sum_{\eta = s,\mathbf{p}} \left[a_{1\eta}a_{4\eta}\int_0^R \rho d\rho K_m(q\rho)J_{m_{4\eta}}(k_4\rho)J_{m_{1\eta}}(k_1\rho) + b_{1\eta}b_{4\eta}\int_R^\infty \rho d\rho K_m(q\rho)J_{m_{4\eta}}(\kappa_4\rho)K_{m_{1\eta}}(\kappa_1\rho)\right], \tag{36}$$

η corresponds to the number of the basis function and taking into account the spin has eight values. Since $k_4 \gg k_1$ for the nonthreshold process, the integrals can be expanded as a series in terms of the primitive $K_m(q\rho)J_{m_{4\eta}}(k_4\rho)$. Retaining only linear terms with respect to V_c/E_g and V_v/E_g (V_c and V_v are the barrier heights for the electrons and holes, respectively), we expand (36) as a series in terms of q and m. The assumption $((V_c, V_v) \ll E_g$ usually holds for a broad class of heterostructures. Subject to these assumptions we can write

$$J^{(1)} = [\mathbf{F}_{4s}^1 R_{1s}]_R - [\mathbf{F}_{4\rho}^2 R_{2\rho}^{*\prime}]_R + [\mathbf{F}_{4s}^3 R_{1s}^{\prime\prime}]_R. \tag{37}$$

Here the subscripts number the particle and the basis state (s, $\mathbf{p}$) and the brackets denote a discontinuity of the function at the point $\rho = R$. The primitive of the product $K_m(q\rho)J_{m_{4\eta}}(k_4\rho)$ of order n is denoted by $\mathbf{F}_4^n$. The component ρ in the basis (1) has the form $F_\rho = \sqrt{-2F_{p^+}F_{p^-}}$. Substituting into (37) the specific form of the wave functions (7), we obtain (23).

B. Calculation of the Quasi-Threshold Matrix Element

The quasi-threshold matrix element for Auger recombination has the form

$$M^{(2)} = \frac{4\pi e^2}{\kappa_\infty}\int_0^R \rho_1 d\rho_1 \mathbf{R}_2^*(\rho_1)\mathbf{R}_3(\rho_1) \times \sum_{\eta = s,\mathbf{p}} a_{1\eta}a_{4\eta}\left[\int_0^{\rho_1} \rho d\rho K_m(q\rho_1) + I_m(q\rho)J_{m_{4\eta}}(k_4\rho)J_{m_{1\eta}}(k_1\rho) + \int_{\rho_1}^\infty \rho d\rho I_m(q\rho_1)K_m(q\rho)J_{m_{4\eta}}(k_4\rho)J_{m_{1\eta}}(k_1\rho)\right]. \tag{38}$$

If the condition $k_4^2 + q^2 \gg k_1^2$ is satisfied, we can assume that at least one of the functions $J_m(k_4\rho)$, $I_m(q\rho)$ varies rapidly compared with $J_0(k_1\rho)$. It is then easy to show that the first nonvanishing term of the expansion in terms of the parameter $k_1/(k_4^2 + q^2)^{1/2}$ gives

$$M^{(2)} = \frac{4\pi e^2}{\kappa_\infty}a_{1s}a_{4s}\int_0^R \rho_1 d\rho_1 \mathbf{R}_2^*(\rho_1)\mathbf{R}_3(\rho_1) \times \frac{\rho_1}{k_4^2 + q^2}J_0(k_1\rho_1)[K_m(q\rho_1)(qI_{m-1}(q\rho_1)J_m(k_4\rho_1) - k_4 I_m(q\rho_1)J_{m-1}(k_4\rho_1) - \frac{m}{\rho_1}I_m(q\rho_1)J_m(k_4\rho_1)) + I_m(q\rho_1)(qK_{m-1}(q\rho_1)J_m(k_4\rho_1) + k_4 K_m(q\rho_1) \times J_{m-1}(k_4\rho_1) - \frac{m}{\rho_1}K_m(q\rho_1)J_m(k_4\rho_1)]. \tag{39}$$

Using the relationship

$$K_m(q\rho_1)I_{m-1}(q\rho_1) + K_{m-1}(q\rho_1)I_m(q\rho_1) = \frac{2}{q\rho_1} \tag{40}$$

(which can easily be obtained by differentiating its left-hand side), we obtain expression (23) for the matrix element.

REFERENCES

1. B. N. Abakumov, V. I. Perel', and I. N. Yassievich, *Nonradiative Recombination in Semiconductors* (PIYaF, Gatchina, 1997).
2. G. G. Zegrya and V. A. Kharchenko, Zh. Éksp. Teor. Fiz. **101**, 327 (1992) [Sov. Phys. JETP **74**, 173 (1992)].
3. M. I. Dyakonov and V. Yu. Kachorovskiĭ, Phys. Rev. B **49**, 17130 (1994).
4. G. G. Zegrya, A. D. Andreev, N. A. Gun'ko, *et al.*, Proc. SPIE **2399**, 307 (1995).
5. A. S. Polkovnikov and G. G. Zegrya, Phys. Rev. B **58**, 4039 (1998); G. G. Zegrya and A. S. Polkovnikov, Zh. Éksp. Teor. Fiz. **113**, 1491 (1998) [JETP **86**, 815 (1998)].
6. G. G. Zegrya and A. S. Polkovnikov, in *Abstracts of the 2nd Russian Conference on Physics of Semiconductors, 1996*, Vol. 1, p. 95.
7. B. A. Foreman, Phys. Rev. B **49**, 1757 (1994).
8. G. L. Bir and G. E. Pikus, *Symmetry and Strain-Induced Effects in Semiconductors* (Nauka, Moscow, 1972; Wiley, New York, 1974).
9. P. C. Sercel and K. J. Vahala, Phys. Rev. B **42**, 3690 (1990).
10. R. A. Suris, Fiz. Tekh. Poluprovodn. **20**, 2008 (1986) [Sov. Phys. Semicond. **20**, 1258 (1986)].
11. M. G. Burt, J. Phys.: Condens. Matter **4**, 6651 (1992).
12. B. A. Foreman, Phys. Rev. B **56**, 12748 (1997).
13. B. L. Gel'mont, Zh. Éksp. Teor. Fiz. **75**, 536 (1978) [Sov. Phys. JETP **48**, 268 (1978)].
14. G. G. Zegrya and A. D. Andreev, Zh. Éksp. Teor. Fiz. **109**, 615 (1996) [JETP **82**, 328 (1996)].
15. A. S. Polkovnikov, E. B. Dogonkine, and G. G. Zegrya, in *Abstracts of the 7th Int. Symposium on Nanostructures: Physics and Technology, St. Petersburg, 1999*, p. 386.
16. A. S. Polkovnikov and G. G. Zegrya, submitted to Phys. Rev.

Translation was provided by AIP

Journal of Experimental and Theoretical Physics, Vol. 90, No. 2, 2000, pp. 389–396.
Translated from Zhurnal Éksperimental'noĭ i Teoreticheskoĭ Fiziki, Vol. 117, No. 2, 2000, pp. 440–448.

SOLIDS
Electron Properties

Centers of Charge Nonuniformity in Absorption Spectra of Lanthanum Manganites

N. N. Loshkareva[1], Yu. P. Sukhorukov[1, *], E. A. Neifel'd[1], V. E. Arkhipov[1], A. V. Korolev[1], V. S. Gaviko[1], E. V. Panfilova[1], V. P. Dyakina[1], Ya. M. Mukovskiĭ[2], and D. A. Shulyatev[2]

[1]*Institute of Metal Physics, Ural Division, Russian Academy of Sciences, Yekaterinburg, 620219 Russia*
[2]*Moscow State Institute of Steels and Alloys, Moscow, 117936 Russia*
**e-mail: suhorukov@imp.uran.ru*

Received August 4, 1999

Abstract—In order to study the microscopic nature of the phase separation in lanthanum manganites, experimental investigations were made of the optical, electrical, and magnetic properties of $La_{1-\delta}MnO_3$ and $La_{0.9}Sr_{0.1}MnO_3$ lanthanum manganite single crystals. The infrared absorption spectra revealed two bands at 0.14 eV and 0.35 eV whose intensity was sensitive to the magnetic order. The different temperature dependence of the electrical resistivity (semiconducting) and the transmission (metallic) below the Curie ferromagnetic temperature indicates that an insulator–metal transition takes place in various regions of the insulating matrix, i.e., phase separation occurs. Characteristic features of the properties and the nature of the phase separation in these compounds can be explained using a model of polar (hole $[MnO_6^{8-}]_{JT}$ and electron $[MnO_6^{10-}]_{JT}$) pseudo-Jahn–Teller clusters which form centers of charge nonuniformity in the crystal. © *2000 MAIK "Nauka/Interperiodica".*

1. INTRODUCTION

Lanthanum manganites are attracting interest because of the colossal magnetoresistance observed in these materials. The characteristic features of the properties of manganites depend on the concentration of Mn^{4+} ions formed by doping $LaMnO_3$ with divalent alkaline-earth ions (Ca, Ba, Sr) or as a result of intrinsic defects such as a lanthanum deficit La_xMnO_3 [1, 2]. It has been suggested [3, 4] that increasing the doping level to the percolation threshold is accompanied by phase separation, i.e., the formation of conducting ferromagnetic regions in the insulating antiferromagnetic matrix. Methods used to study phase separation in lanthanum manganites, such as NMR [5] or neutron scattering [6] provide information on the magnetic state of the material. The electronic aspect is also of interest, i.e., studying the conductivity of the conducting regions and the insulating matrix. This information is provided by jointly studying the optical and electrical properties. The absorption of light in the carrier interaction region in an $La_{1-x}Ca_xMnO_3$ polycrystal with $x = 0.1$ reveals an insulator–metal transition which takes place in various regions of the crystal, whereas the temperature dependence of the electrical resistivity reveals no such transition [7]. This observation provides direct evidence of electronic phase separation. At low dopant concentrations, optical methods can be used to identify various localized centers and to study the nucleation of the phase separation process.

The aim of the present paper is to study the electronic structure and the microscopic nature of the phase separation using data on the optical, electrical, and magnetic properties of two single crystals: lanthanum manganite containing only intrinsic vacancies and strontium-doped (10%) lanthanum manganite.

The optical conductivity spectra obtained by processing the reflection spectra using the Kramers–Kronig method are usually used for highly absorbing materials. It has been shown that for $La_{0.9}Sr_{0.1}MnO_3$ the reflection spectra of the polished and cleaved single crystals differ substantially [8]. In particular, damage to the surface during polishing leads to a reduction in the Drude weight and therefore yields incorrect conclusions on the carrier parameters. In the present study we used a direct method of measuring the absorption spectra of 40 μm thick single crystals. In this case, the contribution from the damaged surface was negligible. Apart from [9], the literature contains no data on the absorption spectra of lanthanum manganite single crystals.

2. EXPERIMENTAL METHODS

Single crystals of $La_{0.9}MnO_3$ and $(La_{0.9}Sr_{0.1})_{0.9}MnO_3$ (formulas by weight) were prepared by zone refining using radiative heating. The weights were selected bearing in mind the characteristic features of the preparation technology for crystals having real composi-

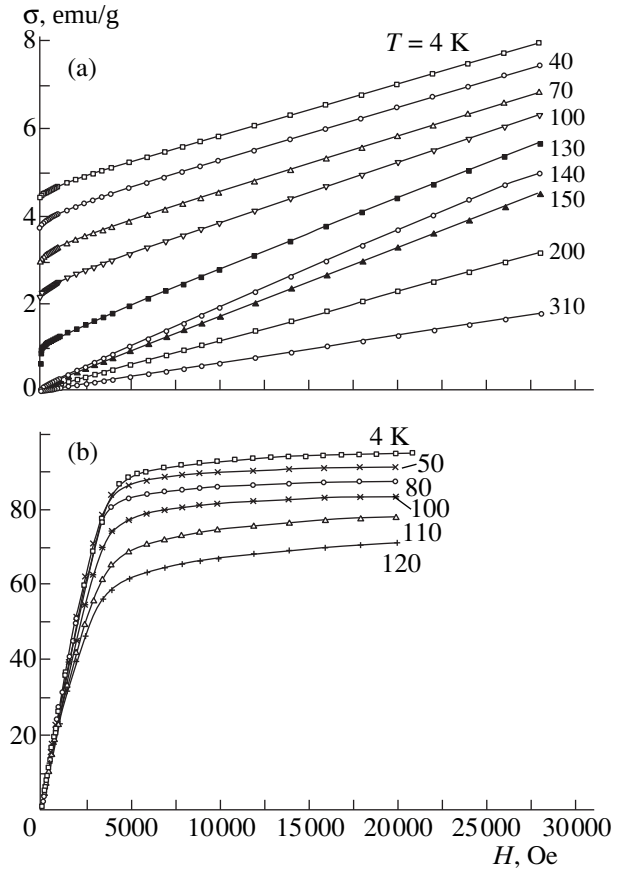

Fig. 1. Dependences of the magnetization on the magnetic field at various temperatures for LMO (a) and LSMO (b) single crystals.

tions close to $LaMnO_3$ (LMO) and $La_{0.9}Sr_{0.1}MnO_3$ (LSMO).

A structural analysis was made for powders using automatic DRON x-ray diffractometers fitted with a vacuum chamber for the temperature investigations (77–370 K) and using monochromatic K_α Cr radiation.

The absorption spectra of the lanthanum manganites were studied using an automatic IKS-21 spectrometer in the 0.09–0.9 eV energy range and an MDR-4 monochromator in the 1.0–3.6 eV range. Temperature measurements of the spectra were made in the range 80–293 K and the magnetic field was varied up to 8 kOe.

The temperature dependence of the dc electrical resistivity was measured by a four-probe method using Indium contacts prepared by ultrasonic soldering.

The magnetic measurements were made using an MPMS-5XL magnetometer (Quantum Design).

3. RESULTS OF MEASUREMENTS

Structural analyses of an LMO single crystal show that at room temperature and below this compound has an orthorhombic structure. At 127 K a transition takes place within the orthorhombic structure, which is accompanied by an abrupt decrease in volume (0.5%). The structure of an $(La_{0.9}Sr_{0.1})_{0.9}MnO_3$ (LSMO) single crystal at room temperature is also orthorhombic. A transition from the orthorhombic to the pseudorhombic modification takes place at 100 K [10].

The field dependences of the specific magnetization σ plotted in Fig. 1 reveal substantial differences between the magnetic properties of LMO and LSMO. For LMO, linear dependences $\sigma(H)$ are observed over a wide range of magnetic fields and at temperatures below 140 K some remanent magnetization is observed. This behavior indicates that the magnetism in LMO is predominantly antiferromagnetic with a ferromagnetic contribution. The ferromagnetic contribution can be treated in several ways. One possible explanation is the presence of a canted spin structure in the homogeneous crystal. Another explanation is the existence of magnetic heterogeneity, i.e., ferromagnetic regions in an antiferromagnetic matrix. Similar $\sigma(H)$ curves for the iodine-doped degenerate magnetic semiconductor EuTe are taken as the clearest evidence of magnetic heterogeneity or phase separation [3]. It is also possible for ferromagnetic regions to exist in a matrix with a canted spin structure. This is confirmed by neutron scattering experiments in lightly doped manganites [6]. At high temperatures the dependence $\chi(T)$ ($\chi = \sigma/H$ is the magnetic susceptibility) for LMO begins to depart from the Curie–Weiss law at $T < 260$ K in a weak magnetic field of 20 Oe.

Unlike the curves for LMO, the $\sigma(H)$ curves for LSMO are typical of a ferromagnet. The Curie temperature of LSMO determined from the *ac* susceptibility peak is 159 K. For both samples, in magnetic fields up to 50 kOe at low temperatures differences are observed in the magnetizations during cooling with and without a magnetic field, i.e., indications of spin-glass behavior are detected. These differences disappear at temperatures above the structural transition temperature. Thus, data on the dependences $\sigma(H)$ for LMO and the change in the magnetic state of the samples during cooling in a strong magnetic field (50 kOe) indicate that the samples are magnetically heterogeneous, with LMO being predominantly antiferromagnetic and LSMO predominantly ferromagnetic.

The room-temperature electrical resistivity ρ of the Sr-doped crystal is an order of magnitude lower than the crystal containing La vacancies (Fig. 2). The curves of $\rho(T)$ for LMO and LSMO reveal significant differences. For LMO in the temperature range 130–260 K the curve of $\rho(T)$ has a nonmonotonic complex profile and increases steeply at temperatures below the structural transition temperature ($T_s = 127$ K). Note that the dependence $\rho(T)$ is accurately reproduced in repeated measurements. The $\rho(T)$ curve for LSMO is smoother. The resistivity increases during cooling to $T_C = 159$ K, in the range 125–159 K the $\rho(T)$ curve has a plateau, and as the temperature drops further, the resistivity increases again. The structural transition from the

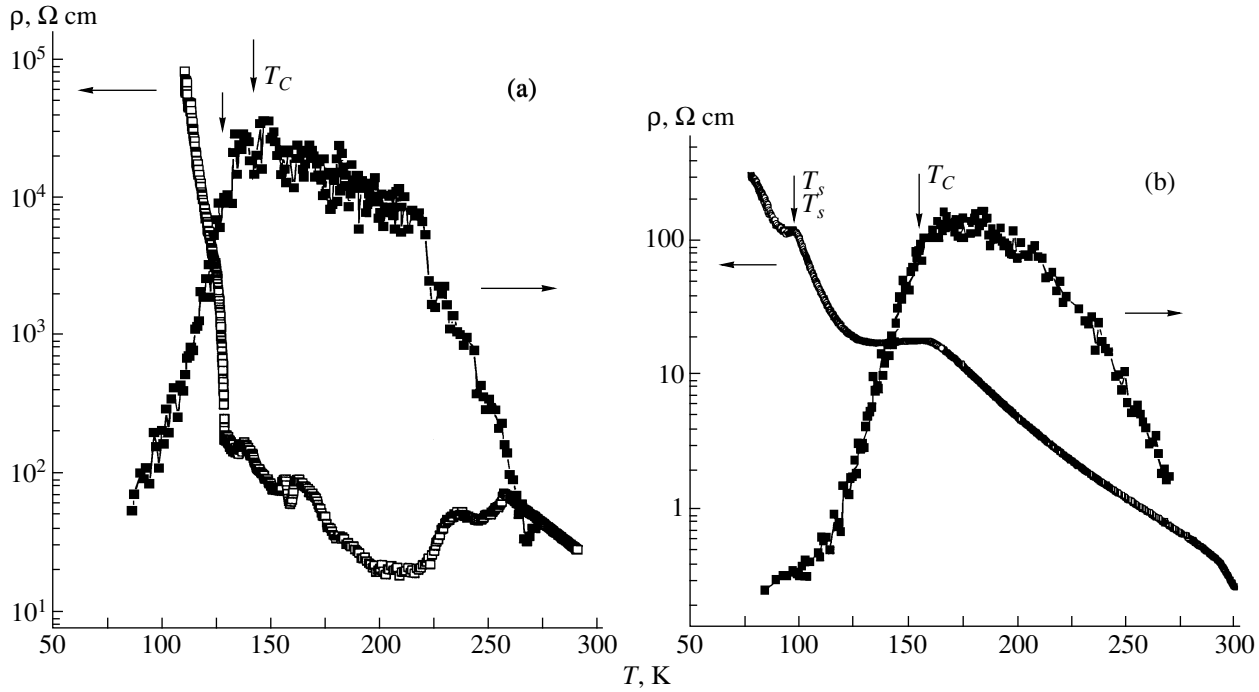

Fig. 2. Temperature dependences of the electrical resistivity and transmission at 0.14 eV for (a) LMO and (b) LSMO single crystals.

orthorhombic to a pseudo-cubic lattice at T_s = 100 K introduces a significant singularity into ρ(T) against a background of increasing resistivity, which is observed as a narrow plateau.

The absorption spectra of LMO and LSMO single crystals are shown in Figs. 3 and 4. A common feature of the spectra is the presence of an absorption band having a complex structure near 0.12–0.16 eV (left insets to Figs. 3 and 4). At high energies (right inset to Fig. 3) an absorption band at 1.75 eV is clearly observed for LSMO. The energy of this band in LMO is clearly lower and its intensity is higher than that in LSMO.

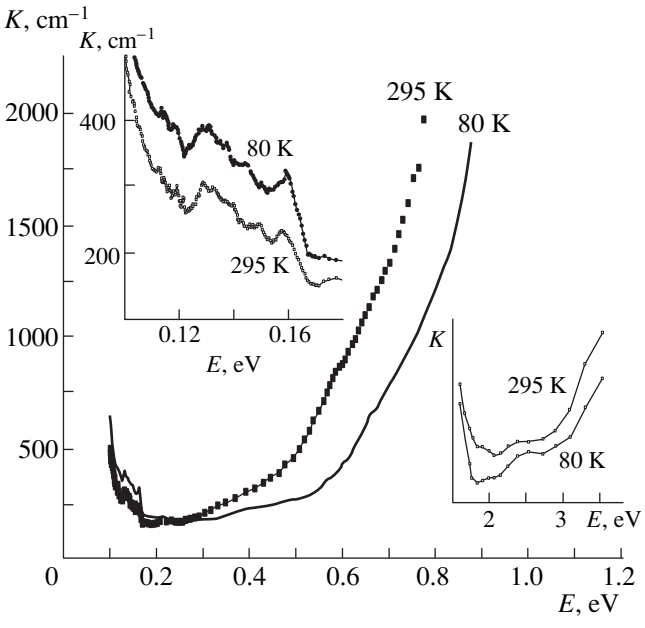

Fig. 3. Absorption spectra of an LMO single crystal at 80 and 295 K. The insets show the spectra in the low-energy (left) and high-energy (right) ranges.

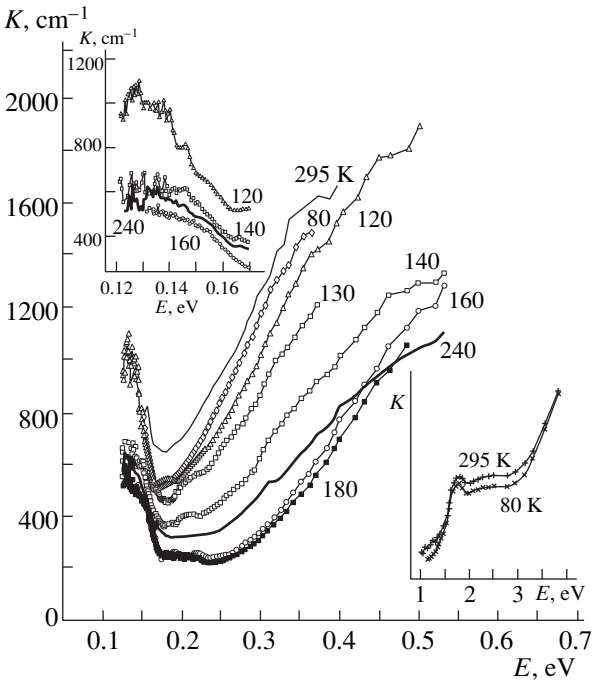

Fig. 4. Absorption spectra of an LSMO single crystal at various temperatures. The insets show the spectra in the low-energy (left) and high-energy (right) ranges.

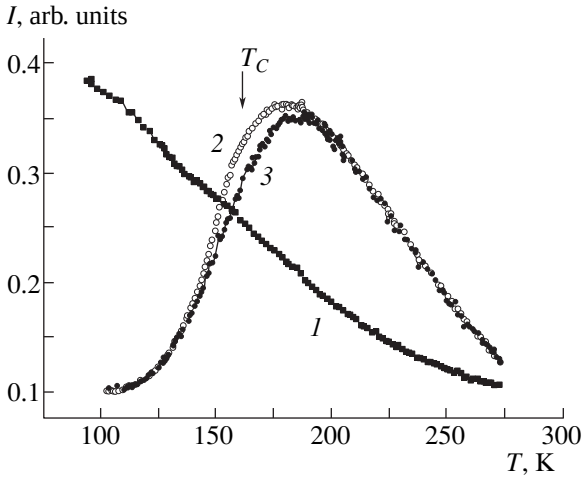

Fig. 5. Temperature dependences of the transmission of LMO single crystals at 0.6 eV (*1*) and LSMO single crystals at 0.3 eV in a field of 8 kOe (*3*) and without a field (*2*).

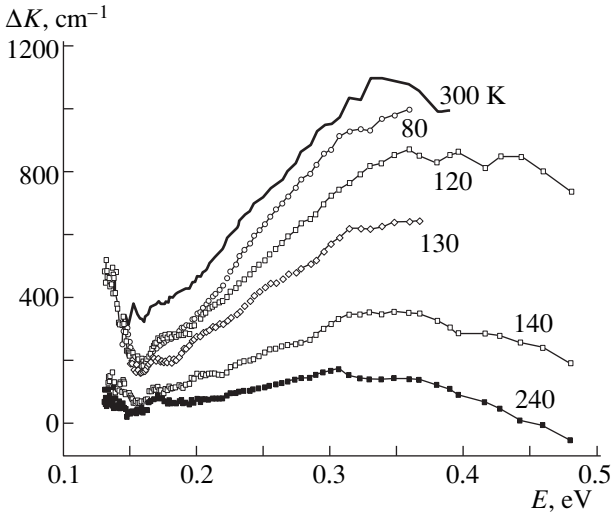

Fig. 6. Differences between the absorption spectra $\Delta K = K(T) - K$ (180 K) for LSMO single crystals at various temperatures.

(Appreciable absorption prevented us from determining the position of the band peak.)

The main difference between the spectra of the two crystals is the different temperature variation of the spectra in the energy range 0.2–0.8 eV. For the LMO single crystal (Fig. 3) cooling shifts the edge of the absorption band at approximately 1.5 eV toward higher energies (blue shift) which is typical of ordinary semiconductors. The temperature dependence of the intensity of the transmitted light (transmission) at 0.6 eV plotted in Fig. 5 (curve *1*) is monotonic. A similar dependence is observed at all energies in the range 0.3–0.8 eV.

The absorption of an LSMO single crystal in the range 0.09–0.6 eV decreases during cooling from room temperature to 180 K and then increases again as the temperature drops further. This exchange of a blue shift for a red one has already been observed by us [9] for $La_{0.9}Sr_{0.1}MnO_3$ single crystals. Figure 6 shows the differences between the absorption spectra at different temperatures and the absorption at 180 K which corresponds to the minimum absorption (highest transmission) $\Delta K = K(T) - K$ (180 K). It can be seen that the largest change in the spectra with temperature is observed at energies around 0.35 eV and 0.13 eV. It can be postulated that there is an absorption band at 0.35 eV whose intensity has a strong nonmonotonic temperature dependence, but this is not resolved in the spectra because of the high absorption coefficient. An optical conductivity band with a similar increase in intensity below T_C was observed at 0.4 eV for an $La_{7/8}Sr_{1/8}MnO_3$ polycrystal [11]. We note that in [11] no data are given on the band at energies around 0.14 eV. Figure 5 shows temperature dependences of the transmission at 0.3 eV without a magnetic field and in a field of 8 kOe for an LSMO single crystal (curves *2* and *3*). Unlike the monotonic dependence of the LMO transmission, the transmission of LSMO decreases from temperatures slightly above T_C. The magnetic field acts in the same way as a drop in temperature, as in the case described in [9]. The strongest dependence of the transmission on the magnetic field is observed at the Curie temperature. The negative magnetotransmission $(I(H) - I(H = 0))/I(H = 0)$ in a field of 8 kOe at T_C is 25%.

We shall now study the region of the low-energy band. Figures 2a and 2b show the temperature dependences of the transmission at 0.14 eV for both single crystals compared with the temperature dependences of the electrical resistivity. The energy 0.14 eV corresponds to the region where light interacts with the carriers, which can be seen most clearly from the LMO spectrum (inset to Fig. 3). For this sample the absorption band at 0.14 eV is positioned against a background of increasing absorption with decreasing energy which is typical of the interaction with free carriers. Note that light begins to interact with phonons at 0.09 eV [12], i.e., outside the range under study. The transmission of the LMO crystal increases as the temperature drops to approximately 150 K (slightly above T_C) and then decreases. This behavior is also observed for the transmission of LSMO, which increases as far as 180 K and then decreases. Except for a region of nonmonotonic $\rho(T)$, the dependences of the transmission and $\rho(T)$ for LSMO and LMO crystals during cooling to $\sim T_C$ are broadly similar, which is usual for semiconductors. Below T_C, however, ρ and the transmission have opposite temperature dependences.

Note that the temperature dependences of the transmission at 0.14 eV (Fig. 2) and 0.3 eV (Fig. 5) for an LSMO crystal are exactly the same. Figure 7 gives the temperature dependence of the thermo-emf for an LSMO single crystal. In the paramagnetic region the positive thermo-emf increases with decreasing temper-

ature, reaches a broad maximum around 185 K, i.e., above T_C, and then decreases again. A change in sign is observed at 137 K.

4. DISCUSSION

The optical conductivity (optical absorption) spectra of transition-metal oxides have some common features. In the middle infrared bands corresponding to localized states, so-called middle infrared (MIR) bands, are observed. As a result of doping with nonisovalent ions, some redistribution of the spectral density from the high-energy range (charge-transfer transitions) to the low-energy range (range of MIR bands and the Drude contribution) is observed in the optical conductivity spectra. This is manifest most clearly in the spectra of copper-oxide-based high-temperature superconducting compounds [13]. Studies of lanthanum manganites doped with various divalent ions reveal similar changes in the spectra [8, 14]. The existence of MIR bands and redistribution of the spectral density are common features of strongly correlated systems [15]. Despite many years of studying MIR bands, for example, in high-temperature superconducting compounds, there is no common viewpoint on the nature of these bands. The existence of local centers at high carrier concentrations created by doping cannot be explained using the single-electron band model. The most acceptable methods of solving the problems associated with the multielectron nature of the problem are cluster methods. A polar center phase model based on the cluster approach [16] can successfully explain the properties of copper–oxygen high-temperature superconductors and copper oxides. The basic assumptions of this model can be applied to lanthanum manganites [15].

In terms of the model [15] lanthanum manganites are considered as unstable systems toward the disproportionation reaction

$$2MnO_6^{9-} \longrightarrow [MnO_6^{8-}]_{JT} + [MnO_6^{10-}]_{JT}$$

involving the formation of polar hole $[MnO_6^{8-}]_{JT}$ and electron $[MnO_6^{10-}]_{JT}$ pseudo-Jahn–Teller centers characterized by a "local boson", i.e., a pair of electrons bound in a completely occupied molecular shell. Transitions in the majority $[MnO_6^{9-}]_{JT}$ clusters form the fundamental absorption band while transitions in the hole and electron centers correspond to the MIR bands. The MIR bands owe their origin to the strong correlation effect when an additional hole (electron) is introduced into the majority cluster, which lowers the energy of a charge-transfer transition. The energy states of the polar centers of lanthanum manganites are determined by the charge, spin, and orbital degrees of freedom. The $[MnO_6^{8-}]_{JT}$ and $[MnO_6^{10-}]_{JT}$ clusters, which formally correspond to Mn^{4+} and Mn^{2+} ions, are essentially Jahn–Teller magnetic polarons.

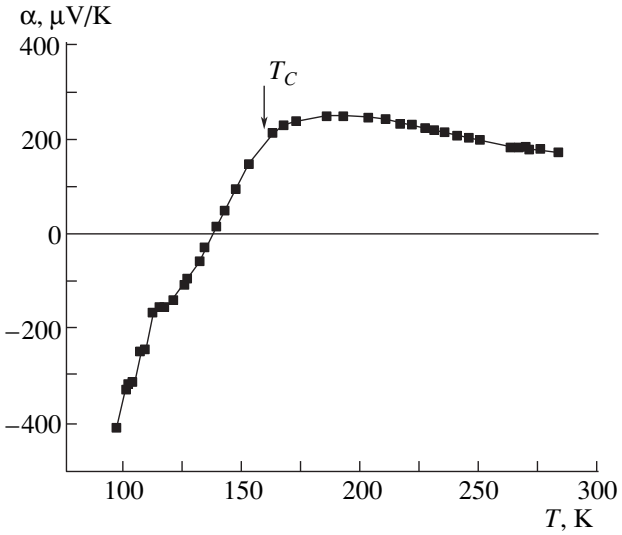

Fig. 7. Temperature dependence of the thermo-emf of an LSMO single crystal.

In this model the redistribution of the spectral weight in the optical conductivity spectra observed as the degree of doping increases is attributed to the formation of electron and hole clusters by majority matrix clusters. The disproportionation reaction approach has been used by other authors, for example, to explain the thermo-emf results in $La_{1-x}Ca_xMnO_3$ [17] and the simultaneous structural and metal–insulator transitions in $YNiO_3$ [18]. Hole and electron clusters form centers of charge nonuniformity which can have a complex structure and contain different numbers of clusters. The nucleation of these clusters is caused by local potential nonuniformities formed as a result of nonisovalent substitution or vacancy formation. The disproportionation reaction in lanthanum manganites can be accompanied by static or dynamic phase separation of a classical and/or quantum nature [15].

The results present here can be explained in terms of this model. In the spectral range under study three absorption bands are observed. The high-energy band with a peak at 1.75 eV in LSMO, and also present in LMO but shifted toward lower energies, is possibly attributed to an $e_g^1(Mn^{3+})$–$e_g^2(Mn^{3+})$ transition between states split by Jahn–Teller interaction. The optical transition is allowed because of the strong hybridization of e_g states with O2p states. Strontium doping suppresses static Jahn–Teller distortions and reduces the intensity of this band compared with that in LMO. Charge-transfer transitions in MnO_6^{9-} clusters begin at energies higher than 3 eV.

The MIR bands observed at 0.14 eV and 0.35 eV are probably attributable to transitions in polar (hole and electron) centers. The difference between the local potentials when trivalent lanthanum is replaced by divalent stron-

tium and a triply charged lanthanum vacancy is created are responsible for the different characteristics of the nonuniformity centers. As a result, the optical spectra for LMO only contain a low-energy band (0.14 eV) whereas that for LSMO contains both low-energy (0.14 eV) and high-energy (0.35 eV) bands. It can be seen from Fig. 4 that both bands in LSMO are well separated. The fact that their intensities have the same temperature dependences (Figs. 2 and 5) may indicate that they are assigned to the same formation, charge nonuniformity centers.

The results of studying the thermo-emf of lanthanum manganites with a lanthanum deficit La_xMnO_3 gives positive values of the thermo-emf for all values of x [2]. For manganites doped with divalent ions the thermo-emf can have both polarities. For our LSMO crystal, the thermo-emf is negative in the ferromagnetic region, as can be seen from Fig. 7. Assuming that the polarity of the thermo-emf depends on the ratio of hole and electron centers, a comparison of the spectra with the thermo-emf data suggests that the low-energy band (0.14 eV) in the absorption spectrum of both crystals is attributed to transitions in the hole MnO_6^{8-} center while the high-energy (0.35 eV) band is assigned to transitions in the electron MnO_6^{10-} center.

It has been noted that the MIR bands in the optical spectra of manganites can be considered to be a manifestation of magnetic polarons. A characteristic feature of the spectra of semiconductors with polaron conductivity is that phonon replicas are superposed on the "polaron" bands. The superposition of phonon replicas on the low-energy absorption band in LMO can be seen in the inset to Fig. 3. In the theory of electrostatic polarons [19] the position of the optical conductivity maximum $E_{\max}$ determines the activation energy of polaron mobility E_u, $E_{max} = 4E_u$, and the polaron binding energy $E_p = 2E_u$. For a polaron formed by a hole polar center, the binding energy is approximately 0.07 eV whereas for a polaron formed by an electron center this is –0.18 eV. The higher binding energy of the electrostatic polaron corresponds to a higher-intensity optical conductivity (absorption) band, as is observed experimentally, i.e., the intensity of the band attributed to an electron center is significantly higher than that assigned to a hole center.

The existence of two type of carrier, mobile holes (of effective mass $0.6m_0$) and barely mobile electrons (of mass $14m_0$), was established when calculating the band structure of $La_{0.7}Ba_{0.3}MnO_3$ manganites [20]. This is consistent with data on the relatively higher binding energy of "electron" polarons compared with "hole" polarons.

Note that the absence of a band corresponding to transitions in an electron center in the LMO spectrum does not generally imply that these centers are absent. Optical transitions in the center may be forbidden. A similar situation was encountered in copper oxide CuO, in which a transition in the CuO_4^{7-} electron center was only allowed in the presence of strong local distortions caused by ion bombardment of the crystal [21].

The intensity of the absorption band is usually related to the transition probability and the concentrations of centers in which the transition takes place. The increase in the intensity of the MIR bands below the Curie temperature is evidently attributed to an increase in the number of polarons in the charge nonuniformity center and/or an increase in the size of this center as a result of the polarization of the spins of nearest Mn ions. Jung *et al.* [11] suggest that for an $La_{7/8}Sr_{1/8}MnO_3$ sample the increase in the intensity of the optical conductivity band at 0.4 eV at temperatures below T_C is caused by the crossover of a small polaron to a large one. It should be noted that no data on the 0.4 eV band in the paramagnetic region are given in [11]. Our data indicate that the intensity of the MIR bands is high at room temperature, decreases substantially as the temperature drops to the Curie temperature, and then increases steeply. In general the intensity of the polaron absorption band reflects the conductivity in the polaron system.

It can be seen from the inset to Fig. 3 that for LMO the low-energy MIR band is observed against a background of increasing absorption at energies below 0.17 eV which is typical of the interaction of light with free carriers. Formally fitting the spectrum at $T = 295$ K using the Drude formula gives good agreement with the experiment for carrier relaxation times of 5×10^{-16} cm^{-3}. The carrier mobility assuming equal effective mass m_0 is obtained as 0.7 cm^2/(V s). The existence of a Drude contribution at room temperature and below, when the crystal resistivity is relatively high (Fig. 2), is quite surprising. The Drude contribution, a nonactivation charge transfer process, is possibly caused by tunneling in the polaron system, i.e., in the charge nonuniformity centers. An increase in the number of polarons should increase the number of tunneling transitions. The temperature dependence of the transmission for LMO at all energies in the range 0.10–0.17 eV is the same as in Fig. 2a for 0.14 eV, i.e., the transmission increases with decreasing temperature as far as $\sim T_C$ and then decreases below T_C. We can postulate that the MIR band and the Drude contribution have the same temperature dependences. Data obtained previously for $La_{1-x}Ca_xMnO_3$ polycrystals at 0.09 eV, far from the 0.14 eV band, had a similar transmission dependence [22]. The decrease in the transmission below T_C was attributed to an insulator–metal transition and its existence in lightly doped samples (below the percolation threshold) indicated that this takes place in isolated regions, or droplets. It was thus demonstrated that electronic phase separation exists.

In the crystals studied the doping level is far from the percolation threshold, as can be seen from the temperature dependence of the electrical resistivity (Fig. 2). Centers of charge nonuniformity formed near charged

defects are distributed some distance apart in the fundamental matrix. This is responsible for the difference at $T < T_C$ in the temperature dependences of the dc electrical resistivity and the optical transmission measured at 0.14 eV (Fig. 2). At temperatures above T_C the behavior of the $\rho(T)$ curves and the transmission broadly agrees which reflects the usual semiconducting dependence of the resistivity of the matrix and the charge nonuniformity centers. The decrease in the transmission at $T < T_C$ can most likely be treated as a manifestation of an insulator–metal transition in the charge nonuniformity centers (metal droplets) with the matrix remaining semiconducting. Below the structural transition temperature the electrical resistivity of the crystal increases more rapidly than before the transition which is evidently caused by additional carrier localization processes in the matrix, possibly as a result of charge ordering [22]. Thus, the optical data for LMO and LSMO crystals give an increase in the conductivity below T_C in isolated regions of the crystal, i.e., charge nonuniformity centers, while semiconducting conductivity is conserved in the matrix, i.e., these data indicate electronic phase separation.

The appreciable negative magnetotransmission (25%) is the optical analog of the negative magnetoresistance and provides additional confirmation that the absorption bands are associated with the carrier system.

The significant nonmonotonicity of the curve $\rho(T)$ for LMO (Fig. 2a) at temperatures below 260 K for which the dependence $\chi(T)$ also departs from the Curie–Weiss law, can be explained if we assume that this LMO crystal contains a set of charge nonuniformity centers of different sizes, possessing different electrical and magnetic characteristics, and therefore different paramagnetic–ferromagnetic and metal–insulator transition temperatures. The maximum Curie temperature for homogeneous La_xMnO_3 with a large La deficit ($x \approx 0.8$) is 260 K [23]. The electrical resistivity of an LSMO single crystal is an order of magnitude lower than that of LMO, i.e., the doping level of LSMO is higher. The smooth $\rho(T)$ curve clearly indicates that as the doping level increases, approaching the percolation threshold, not only does the number of charge nonuniformity centers increase but their sizes and characteristics become similar.

Returning to the magnetic properties of these crystals, we can postulate that the presence of charge nonuniformity centers is responsible for the magnetic heterogeneity of lanthanum manganites. Polar centers, or localized states, exist at low temperatures (an optical conductivity band at 0.4 eV can be seen at 10 K [11]) and they should conserve their spin individuality to some extent. This may well be the reason for the indications of spin glass behavior observed at low temperatures in lightly doped lanthanum manganites.

5. CONCLUSIONS

We have investigated the optical absorption spectra and the electrical and magnetic characteristics of a lanthanum manganite single crystal containing lanthanum vacancies $La_{1-\delta}MnO_3$ and a strontium-doped $La_{0.9}Sr_{0.1}MnO_3$ single crystal. The observed characteristics of the properties are explained using a model of polar (hole $[MnO_6^{8-}]_{JT}$ and electron $[MnO_6^{10-}]_{JT}$ pseudo-Jahn–Teller clusters which form charge nonuniformity centers. We observed two MIR absorption bands whose intensity exhibits a strong nonmonotonic temperature dependence which are an optical "portrait" of the polar centers. A comparison between the optical, electrical, and magnetic properties of the crystals indicates that below the ferromagnetic Curie temperature an insulator–metal transition takes place in the charge nonuniformity centers while the semiconducting conductivity of the matrix is conserved. The electronic and magnetic phase separation is attributed to the presence of charge nonuniformity centers.

ACKNOWLEDGMENTS

The authors would like to thank A.S. Moskvin, N.G. Bebenin, and B.A. Gizhevskiĭ for useful discussions.

This work was partly supported by the Russian Foundation for Basic Research (project no. 99-02-16280).

REFERENCES

1. A. Chainani, M. Mathew, and D. D. Sarma, Phys. Rev. B **47**, 15397 (1993).
2. R. Mahendiran, S. K. Tiwary, A. K. Raychaudhuri, *et al.*, Phys. Rev. B **54**, R9604 (1996).
3. E. L. Nagaev, Phys. Status Solidi B **186**, 9 (1994).
4. S. Yunoki, A. Moreo, and E. Dagotto, Phys. Rev. Lett. **81**, 5612 (1998).
5. G. Papavassiliou, M. Fardis, F. Milia, *et al.*, Phys. Rev. B **55**, 15000 (1997).
6. M. Hennion, F. Moussa, G. Biotteau, *et al.*, Phys. Rev. Lett. **81**, 1957 (1998).
7. N. N. Loshkareva, Yu. P. Sukhorukov, S. V. Naumov, *et al.*, Pis'ma Zh. Éksp. Teor. Fiz. **68**, 89 (1998) [JETP Lett. **68**, 97 (1998)].
8. K. Takenaka, K. Iida, Y. Sawaki, *et al.*, cond-mat/9810035 (1998).
9. N. N. Loshkareva, Yu. P. Sukhorukov, B. A. Gizhevskiĭ, *et al.*, Phys. Status Solidi A **164**, 863 (1997).
10. V. S. Gaviko, V. E. Arkhipov, A. V. Korolev, *et al.*, Fiz. Tverd. Tela (St. Petersburg) **41**, 1064 (1999) [Phys. Solid State **41**, 969 (1999)].
11. J. H. Jung, K. H. Kim, H. J. Lee, *et al.*, Phys. Rev. B **59**, 3793 (1999).
12. T. Arima and Y. Tokura, J. Phys. Soc. Jpn. **64**, 2488 (1995).

13. S. Usida, T. Udo, and H. Takagi, Phys. Rev. B **43**, 7042 (1991).
14. J. H. Jung, K. H. Kim, T. W. Noh, *et al.*, Phys. Rev. B **57**, R11043 (1998).
15. A. S. Moskvin, Physica B **252**, 186 (1998).
16. A. S. Moskvin, N. N. Loshkareva, and Yu. P. Sukhorukov, Zh. Éksp. Teor. Fiz. **105**, 967 (1994) [JETP **78**, 518 (1994)].
17. M. F. Hundley and J. J. Neumeier, Phys. Rev. B **55**, 11511 (1997).
18. J. A. Alonso, J. L. García-Munoz, M. T. Fernández-Díaz, *et al.*, Phys. Rev. Lett. **82**, 3871 (1999).
19. *Polarons*, Ed. by Yu. A. Firsov (Nauka, Moscow, 1975).
20. W. E. Pickett and D. J. Singh, J. Magn. Magn. Mater. **172**, 237 (1997).
21. N. N. Loshkareva, Yu. P. Sukhorukov, B. A. Gizhevskiĭ, *et al.*, Fiz. Tverd. Tela (St. Petersburg) **40**, 419 (1998) [Phys. Solid State **40**, 383 (1998)].
22. Y. Yamada, O. Hino, S. Nohdo, *et al.*, Phys. Rev. Lett. **77**, 904 (1996).
23. V. Ferris, L. Brohan, M. Ganne, *et al.*, Eur. J. Solid State Inorg. Chem. **32**, 131 (1995).

Translation was provided by AIP

Journal of Experimental and Theoretical Physics, Vol. 90, No. 2, 2000, pp. 397–399.
Translated from Zhurnal Éksperimental'noĭ i Teoreticheskoĭ Fiziki, Vol. 117, No. 2, 2000, pp. 449–451.

SOLIDS
Electron Properties

Two-Dimensional Electrons in Spirally Rolled-Up Quantum Wells

A. I. Vedernikov and A. V. Chaplik*

Novosibirsk State University, Novosibirsk, 630090 Russia
Institute of Semiconductor Physics, Siberian Division, Russian Academy of Sciences, Novosibirsk, 630090 Russia
**e-mail: chaplik@isp.nsc.ru*

Received September 1, 1999

Abstract—An effective Hamiltonian is obtained to describe the motion of a one-dimensional quantum particle along an arbitrary plane curve. Calculations are made of the energy levels and the polarization dependence of the electromagnetic wave absorption in a spirally rolled-up quantum well. © *2000 MAIK "Nauka/Interperiodica".*

1. INTRODUCTION

The success achieved in modern nanostructure technology has made it possible to develop systems having fairly complex geometric shapes. Typical examples are the so-called "quantum rolls" fabricated using an original method developed in [1, 2]. A strained structure consisting of quantum films of various materials (such as GaAs/InAs) curls up after being released from the substrate as a result of the relaxation of elastic stresses, as shown schematically in Fig. 1. The two-dimensional electron gas in one of the layers is thus on a cylindrical surface whose cross section is fairly accurately approximated by an Archimedes spiral: $\rho = L\varphi$, where ρ and φ are cylindrical coordinates in the plane perpendicular to the cylinder axis z. By varying the thickness of the layers and the lattice mismatch of the initial materials, it is possible to vary the radius of curvature of this structure almost continuously between a few tens of angstrom and a few micron. This system will be called a spirally rolled-up quantum well. In the present paper we investigate its electronic properties: the energy spectrum and the optical absorption in the infrared. We immediately stress a characteristic feature which distinguishes this system from planar quantum wells and nanotubes: this system is inhomogeneous in one of the directions of the cylindrical surface and is therefore broadly anisotropic in the XY plane. This factor is observed in the polarization dependences of the optical absorption.

2. EFFECTIVE ONE-DIMENSIONAL HAMILTONIAN

Since the complete wave function depends on the z coordinate as a plane wave, the problem reduces to the motion of an electron in a planar spiral waveguide. Assuming that the thickness of the initial quantum film δ is small compared with the longitudinal de Broglie wavelength (two-dimensional limit), we must assume that the motion across the waveguide is fast compared with that along it. We shall use a well-known method of adiabatic separation of fast and slow degrees of freedom and obtain an effective one-dimensional wave equation.

We shall first consider the general problem of the motion of a quantum particle along an arbitrary plane curve. We write the equation for the curve in the parametric form:

$$\mathbf{r} = \mathbf{r}(s),$$

where $\mathbf{r}$ is the plane vector (x, y) and s is the arc length measured from a certain initial point on the curve. We introduce the new variables h and s instead of x and y (Fig. 2) where h is measured along the normal to the curve so that the unit vectors (h, s, z) form a right triplet of vectors $(\mathbf{e}_h, \mathbf{e}_s, \mathbf{e}_z) = 1$. The square of a length element in the new coordinates is given by

$$\begin{aligned} dl^2 &= dh^2 + H_s^2 ds^2, \\ H_s &= 1 + h/R(s). \end{aligned} \tag{1}$$

where $R(s)$ is the radius of curvature. The coordinates h and s are clearly orthogonal and can be uniquely introduced for fairly small h. This constraint does not play

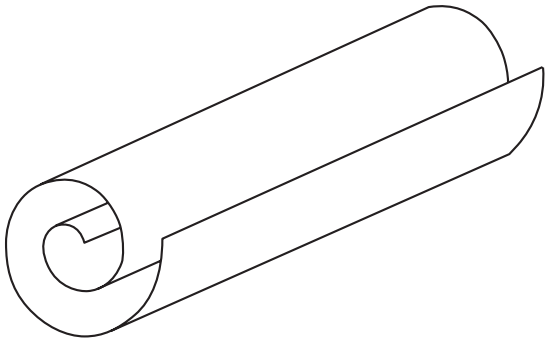

Fig. 1. "Quantum roll," spirally rolled-up film.

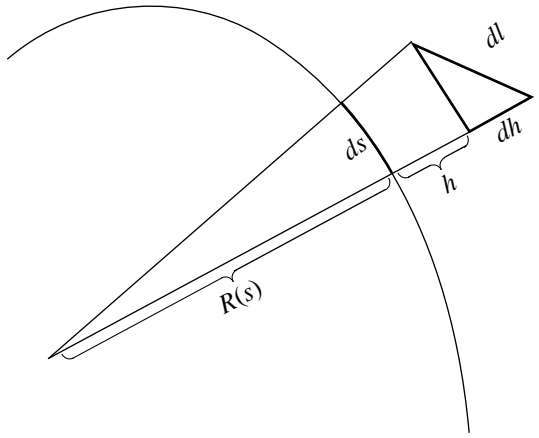

Fig. 2.

any part in the following analysis since we are interested in the region $0 < h < \delta$ (in the limit $\delta \longrightarrow 0$).

We now write the Schrödinger equation in the new variables also allowing for a homogeneous magnetic field parallel to the axis of the cylinder. We take the symmetric vector-potential gauge: $\mathbf{A} = [\mathbf{B}\mathbf{r}]/2$. In terms of the variables h, s, and z we obtain

$$A_s = \frac{1}{2}Bh + \frac{1}{2}B\dot{\mathbf{r}}(s)[\mathbf{e}_z\mathbf{r}(s)],$$

$$A_h = -\frac{1}{2}B\dot{\mathbf{r}}(s)\cdot\mathbf{r}(s), \qquad (2)$$

$$A_z = 0,$$

where the dot over the vector indicates a derivative of s and $\mathbf{e}_z$ is the unit vector along the z axis. The condition $\mathrm{div}\mathbf{A} = 0$ has the form

$$\frac{\partial A_s}{\partial s} + \frac{A_h}{R(s)} = 0. \qquad (3)$$

The Schrödinger equation ($\hbar = 1$) has the form:

$$-\frac{1}{2m}\left\{\frac{1}{H_s}\frac{\partial}{\partial h}\left(H_s\frac{\partial\Psi}{\partial h}\right) + \frac{1}{H_s}\frac{\partial}{\partial s}\left(\frac{1}{H_s}\frac{\partial\Psi}{\partial s}\right)\right\}$$
$$+\frac{ie}{mc}\left(\frac{A_s}{H_s}\frac{\partial\Psi}{\partial s} + A_h\frac{\partial\Psi}{\partial h}\right) + \frac{e^2\mathbf{A}^2}{2mc^2}\Psi = E\Psi. \qquad (4)$$

Table 1

ϵ	$\varphi_{\max}$		
	2π	4π	6π
ϵ_1	−0.001877	−0.007305	−0.007306
ϵ_2	0.05656	−0.00019	−0.0013
ϵ_3	0.1600	0.006223	−0.00005

At the waveguide boundaries $h = 0$, $h = \delta$the wave function vanishes: $\psi(s, 0) = \psi(s, \delta) = 0$. In accordance with the adiabatic approximation, we fix s and describe the motion along the h coordinate by the wave function of a rectangular well with solid walls (in order to eliminate the first derivative with respect to h this function must be multiplied by $1/\sqrt{H_s}$). We then make a gauge transformation which can eliminate the magnetic field in the limit $\delta \longrightarrow 0$. The final form of the complete wave function is as follows:

$$\Psi(h, s) = \sqrt{\frac{2}{\delta}}\frac{1}{\sqrt{H_s}}\sin\frac{\pi h}{\delta}\exp\left\{-i\frac{eBh}{2c}\dot{\mathbf{r}}(s)\cdot\mathbf{r}(s)\right\}$$
$$\times\exp\left[i\frac{e}{c}\int_{s_0}^{s}A_0 ds\right]\chi(s). \qquad (5)$$

Here we have

$$A_0 = A_s(s, h = 0) \equiv \frac{1}{2}B\dot{\mathbf{r}}(s)[\mathbf{e}_z\mathbf{r}(s)],$$

s_0 is the arbitrary origin of the arc length and $\chi(s)$ is the adiabatic wave function of the longitudinal motion. The equation for this is obtained by the usual procedure: equation (4) must be averaged over the dominant mode of the transverse motion (with the weightings H_s). After fairly cumbersome calculations, assuming everywhere possible that $\delta = 0$ we obtain:

$$-\frac{1}{2m}\frac{d^2\chi}{ds^2} - \frac{1}{8mR^2(s)}\chi = E_\parallel\chi, \qquad (6)$$

where $E_\parallel = E - \pi^2/2m\delta^2$ is the energy of the longitudinal motion.

Hence, the adiabatic potential of a one-dimensional electron on the curve of a line corresponds to attraction to points of maximum curvature. The magnetic field is only in phase with the wave function, so that the energy levels can only depend on the field for closed curves when Ψ satisfies the periodicity condition (then the result only contains the magnetic flux across the circuit). In particular, an electron in a spiral with free ends does not "sense" the magnetic field perpendicular to its plane regardless of the number of turns of the spiral (no captured flux).

3. NUMERICAL RESULTS FOR AN ARCHIMEDES SPIRAL. BOUND STATES

The compact form of equation (6) is useful for analyzing the general properties of the energy spectrum. For instance, it is easy to establish that for an Archimedes spiral the number of bound states is infinite since the asymptotic form of the adiabatic potential is a Coulomb one $U(s \longrightarrow \infty) \approx 1/16mLs$. For a quantum wire bent into a parabola or a hyperboloid we obtain $U \sim 1/s^3$ and $U \sim 1/s^6$, respectively.

However, because of the complex form of the dependence $R(s)$, it is more convenient to convert to a different variable to obtain quantitative results. We made numerical calculations of the energy levels and waves functions for an Archimedes spiral $\rho = L\varphi$, introducing the polar angle φ as the argument of the wave function. In the zeroth order with respect to the parameter δ/L the Schrödinger equation has the form

$$\frac{1}{1+\varphi^2}\frac{d^2\chi}{d\varphi^2} + \frac{2\varphi}{(1+\varphi^2)^2}\frac{d\chi}{d\varphi} - \frac{2+9\varphi^2+\varphi^4}{4(1+\varphi^2)^3} = 2mL^2E_{\|}\chi \equiv \varepsilon\chi. \quad (7)$$

As the boundary conditions we assume that χ vanishes at the end points of the spiral, i.e., at $\varphi = 0$ and $\varphi = \varphi_{max}$; the values $\varphi_{max} = 2\pi$, 4π, and 6π were selected. Equation (7) was transformed to give a difference equation and the problem was reduced to finding the eigenvalues and eigenvectors of the corresponding matrix. The bottom of the first transverse quantization subband was taken as the energy origin [see (6)]. The values of the first three energy levels are given in table for a spiral with one, two, and three turns ($\varphi_{max} = 2\pi$, 4π, and 6π).

States localized near the beginning of the spiral have negative energies; the number of these states naturally increases with increasing length. For a spiral having the minimum radius of curvature $R_{min} = L/2 = 50$ Å the depth of the ground level is 0.7 K.

4. INFRARED ABSORPTION

Let us assume that an electromagnetic wave propagates along the Z axis of the spiral. Transitions between the levels obtained above are determined by the electric field component of the wave tangent to the spiral. Quite clearly, as a result of the nonuniformity of the system with respect to φ, it is predicted that the infrared absorption intensity will have a strong polarization dependence. The probabilities of transitions between the three lowest levels w_{12}, w_{13}, and w_{23} were calculated numerically. Their dependences on the angle φ between the electric vector of the wave and the X axis (i.e., the tangent to the spiral at its beginning where $\varphi = 0$) are plotted in Fig. 3 for a three-turn spiral.

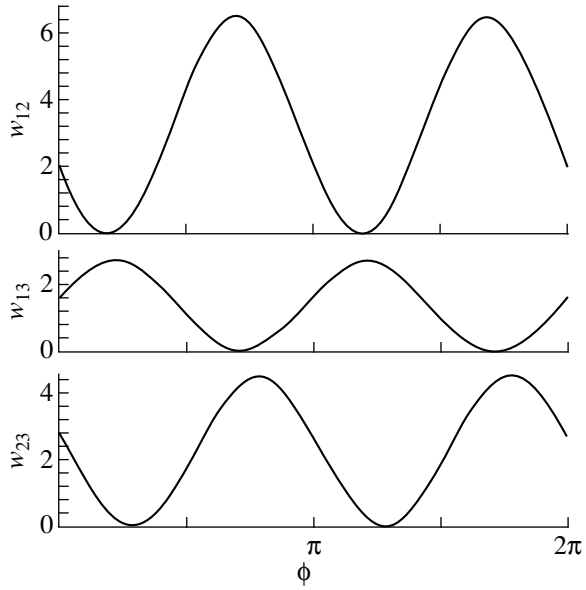

Fig. 3.

Note that for each transition there is a direction of polarization for which no absorption occurs. In classical terms this implies that the work of the external field performed on an electron in different parts of the spiral is compensated.

ACKNOWLEDGMENTS

This work was supported financially by the Russian Foundation for Basic Research (project no. 99-02-17127) and by the program "Physics of Solid-State Nanostructures" of the Russian Ministry of Science.

REFERENCES

1. V. Ya. Prinz, V. A. Seleznev, V.A. Samoylov, *et al.*, Microelectron. Eng. **30**, 439 (1996).
2. V. Ya. Prinz, V. A. Seleznev, and A. K. Gutakovsky, in *Abstracts of the 24th International Conference on Semiconductor Physics, Jerusalem, Israel, 1998.*

Translation was provided by AIP

Journal of Experimental and Theoretical Physics, Vol. 90, No. 2, 2000, pp. 400–403.
Translated from Zhurnal Éksperimental'noĭ i Teoreticheskoĭ Fiziki, Vol. 117, No. 2, 2000, pp. 452–456.

SOLIDS
Electron Properties

High-Frequency Hopping Conductivity and Permittivity in Compensated Semiconductors

V. D. Kagan*

Ioffe Physicotechnical Institute, Russian Academy of Sciences, St. Petersburg, 194021 Russia
**e-mail: victorkagan@pop.ioffe.rssi.ru*

Received September 6, 1999

Abstract—In semiconductors, high-frequency conductivity is caused by polarization reversal of the collective states of a pair of impurity atoms under the action of the random electric fields of all the impurities. A Coulomb correlation which appreciably increases the conductivity is established as a result of the statistical distribution of the particles over four levels of the diatomic system. The relaxation absorption and the permittivity of the entire pair system are calculated allowing for these statistics. *© 2000 MAIK "Nauka/Interperiodica".*

At low temperatures, a semiconductor containing donor and acceptor impurities is a disordered system in which all the electronic states are localized. Drift of electrons from majority to minority carriers creates empty sites among the majority carriers to which electrons hop from occupied majority impurities. In this way hopping conduction takes place in compensated semiconductors. In a static electric field an electron can cover macroscopic distances, having made a large number of hops. This is only possible when an enormous cluster of mutually bound states is formed in the system. If the electric field varies harmonically with time at high frequency ω, the analysis can be confined to a single electron hop over a distance considerably greater than the hopping length in a static field. At this hopping distance a dipole moment appears, which varies in phase with the alternating electric field which excites it. The polarization of the entire sample is produced by the additive contribution of all the pairs. Allowance for relaxation processes leads to some delay of this polarization relative to the alternating field and thus leads to absorption of this field. The theory of this relaxation absorption developed in the sixties was reviewed by Éfros and Shklovskiĭ [1].

An electron situated in a charge state at an isolated pair is exposed to the action of random electric fields from other impurities, so that this electron has a large energy spread. An electron positioned at a site having the coordinate $\mathbf{r}_1$ has the energy ϕ_1 and an electron with the coordinate $\mathbf{r}_2$ has the energy ϕ_2. These energies vary widely and differ from one another. In addition, there is the overlap energy of the states which, at large distances, depends exponentially on the distance between the atoms in the pair $\mathbf{r} = \mathbf{r}_1 - \mathbf{r}_2$, $r = |\mathbf{r}|$:

$$J(r) = J\exp(-r/a), \tag{1}$$

where a is the radius of the localized state. If both sites having the coordinates $\mathbf{r}_1$ and $\mathbf{r}_2$ are charged, we should have Coulomb repulsion. The complete Hamiltonian of the system has the form

$$\begin{aligned} H &= \phi_1 a_1^+ a_1 + \phi_2 a_2^+ a_2 \\ &+ J(r)(a_1^+ a_2 + a_2^+ a_1) + \frac{e^2}{kr} a_1^+ a_1 a_2^+ a_2, \end{aligned} \tag{2}$$

where a_1 and a_2 are the electron annihilation operators at points 1 and 2, a_1^+ and a_2^+ are the electron creation operators at these points, and k is the permittivity of the semiconductor.

We know that the Hamiltonian without the last term is diagonalized by the linear transformation

$$\begin{aligned} \alpha_1 &= a_1\cos\theta + a_2\sin\theta, \\ \alpha_2 &= -a_1\sin\theta + a_2\cos\theta, \\ \tan\theta &= \frac{J(r)}{\sqrt{\left(\frac{\phi_1 - \phi_2}{2}\right)^2 + J^2(r)}}, \end{aligned} \tag{3}$$

as a result of which we obtain the mixed energies of the single-electron states:

$$E_{1,2} = \frac{\phi_1 + \phi_2}{2} \mp \sqrt{\left(\frac{\phi_1 - \phi_2}{2}\right)^2 + J^2(r)}. \tag{4}$$

Applying the transformation (3) to the complete Hamiltonian (2) shows that this is also diagonalized and has the simple form:

$$H = E_1\alpha_1^+\alpha_1 + E_2\alpha_2^+\alpha_2 + \frac{e^2}{kr}\alpha_1^+\alpha_1\alpha_2^+\alpha_2. \tag{5}$$

Éfros and Shklovskiĭ drew attention to the fact that the Hamiltonian (5) has four energy levels: the single-electron levels (4) are supplemented by a zero level

with no electrons and a two-electron level having the energy

$$E_3 = E_1 + E_2 + \frac{e^2}{kr} = \phi_1 + \phi_2 + \frac{e^2}{kr}. \quad (6)$$

In order to find the equilibrium statistical distribution of a diatomic system, we require all the energy levels. According to [2], the equilibrium occupation numbers n_s^0 are given by

$$n_s^{(0)} = A^{-1}\exp[(\mu - E_s)/T]. \quad (7)$$

Here μ is the chemical potential of the electron system and T is the temperature in energy units. The normalization factor A is given by

$$A = 1 + \exp[(\mu - E_1)/T] + \exp[(\mu - E_2)/T] + \exp[(2\mu - E_3)/T]. \quad (8)$$

As the frequency increases, relaxation absorption is supplemented by another absorption process, i.e., resonant absorption caused by the transition of an electron between levels having the energies E_1 and E_2 provided that

$$E_2 - E_1 = \hbar\omega. \quad (9)$$

The concept of a Coulomb correlation was encountered in the resonant absorption theory developed by Shklovskiĭ and Éfros [2]. The Coulomb correlation is a statistical effect and may be perceived in formulas (7) and (8). Since the energy E_3 is increased as a result of the Coulomb repulsion energy, this reduces the occupation probability n_3. As a result of the common normalization factor, the occupation numbers $n_{1,2}$ are higher than the occupation numbers of a four-level system of uncharged particles. This is the Coulomb correlation. Note that the indirect influence of the Coulomb repulsion of two electrons on the occupation numbers of the single-electron states in which no direct Coulomb interaction takes place, is manifest in the Coulomb correlation.

The resonant absorption is proportional to the difference between the occupation numbers $n_1^0 - n_2^0$. Taking into account (9), this difference may be assumed to depend only on one energy E_1:

$$n_1^0 = \left\{\exp\left(\frac{E_1 - \mu}{T}\right) + 1 + \exp\left(-\frac{\hbar\omega}{T}\right) + \left[\left(\mu - \frac{e^2}{kr} - E_1 - \hbar\omega\right)\frac{1}{T}\right]\right\}^{-1}, \quad (10)$$

$$n_2^0 = n_1^0\exp(-\hbar\omega/T). \quad (11)$$

At low temperatures we find $\hbar\omega > T$, $n_2 = 0$, and the occupation number n_1 differs appreciably from the single-particle Fermi distribution: this number is one for energies E_1 between μ and $\mu - e^2/(kr) - \hbar\omega$ and zero outside this interval. Thus, the Coulomb correlation determines the energy interval $e^2/(kr)$ which contributes to the resonant absorption and may appreciably exceed the energy interval of the order $\hbar\omega$ used in the theory, which neglects the Coulomb correlation [2].

The Coulomb correlation significantly increases the magnitude of the relaxation absorption. However, no systematic theory of the relaxation absorption of a four-level system has yet been constructed. The aim of the present study is to construct such a theory in order to correct some of the results of the earlier two-level theory [1], particularly for high frequencies. Calculations of the contribution of soft pairs to the permittivity will also be presented.

An external alternating electric field $\mathbf{E}(t)$ can be incorporated very easily in the Hamiltonian (2). To do this we replace the energy ϕ_i by $\psi_i = \phi_i - e\mathbf{E}(t)\cdot\mathbf{r}_i$ in expression (2), we then diagonalize and obtain the energies $\bar{E}_i$ in which ϕ_i is replaced by ψ_i, which takes into account the influence of the electric field on the energy levels of a soft pair. The nonequilibrium occupation numbers are determined by the kinetic equations, in which we only allow for transitions within a single pair:

$$\frac{dn_1(t)}{dt} + \frac{1}{\tau_1}n_1(t) - \frac{1}{\tau_2}n_2(t) = 0,$$
$$\frac{dn_2(t)}{dt} + \frac{1}{\tau_2}n_2(t) - \frac{1}{\tau_1}n_1(t) = 0. \quad (12)$$

The transition probabilities are determined by the interaction of localized electrons with phonons [3]:

$$\frac{1}{\tau_0} = \nu_{ph}\exp\left(-\frac{2r}{a}\right)\left(\bar{E}_2 - \frac{\bar{E}_1}{T}\right)^s,$$
$$\frac{1}{\tau_1} = \frac{1}{\tau_0}N(\bar{E}_2 - \bar{E}_1), \quad (13)$$
$$\frac{1}{\tau_2} = \frac{1}{\tau_0}[N(\bar{E}_2 - \bar{E}_1) + 1],$$

$N(E) = [\exp(E/T) - 1]^{-1}$ is the Planck distribution function and the probability ν_{ph} and the exponent s are determined by the electron–phonon coupling mechanism ($s = 1$ for the deformation mechanism and $s = -1$ for the piezoelectric mechanism) [3]. The transition probabilities are necessarily proportional to the square of the overlap integral so that the transition probability has an exponential dependence on the coordinates which is written explicitly by us in formula (13). The

time dependence of the occupation numbers $n_i(t)$ is determined by the dependence of the energies $\bar{E}_i$ on the electric field.

We shall solve a linear problem for the electric field so that we can take this in the complex form $\mathbf{E}(t) = \mathbf{E}\exp(-i\omega t)$. Linearizing the equations (12) for $\delta n_i = n_i(t) - n_i^0$ we obtain

$$\delta n_1 - \delta n_2 = \frac{\phi_2 - \phi_1}{\sqrt{(\phi_2 - \phi_1)^2 + 4J^2(r)}} \frac{2/\tau}{(-i\omega + 1/\tau)} \times \frac{(e\mathbf{E}(t)\cdot\mathbf{r})}{T} n_1^0, \quad \frac{1}{\tau} = \frac{1}{\tau_1} + \frac{1}{\tau_2}. \tag{14}$$

The denominator (14) contains the total relaxation time of both levels which is the characteristic frequency dispersion of the occupation numbers.

The total dipole moment of the pair **d**, nonlinearized with respect to the electric field, is given by

$$\mathbf{d} = \frac{e\mathbf{r}}{2} \frac{(\psi_2 - \psi_1)^2}{(\psi_2 - \psi_1)^2 + 4J^2(r)} [n_2(t) - n_1(t)]. \tag{15}$$

The second factor in this formula is associated with the difference between the nodal states and the electron states in the pair. It is equal to $\cos^2\bar{\theta}$, and is the projection of the pair states on the nodal states, where $\bar{\theta}$ is the angle [see formula (3)] which depends on the total energies $\bar{E}_i$ and thus on the electric field.

When the dipole moment is linearized, two terms appear. The first, "equilibrium" term appears when the second factor in formula (15) is linearized and we keep the occupation numbers in it in equilibrium. In the second, "nonequilibrium" term we only allow for the electric field in the nonequilibrium occupation numbers. In order to find the electric current, we must differentiate the dipole moment with respect to time which, for us, is equivalent to multiplying (15) by $-i\omega$. Average expressions for the complex dipole moment and electric current are obtained after multiplying the individual contribution of a single pair by the density of states of the random energies $g(\phi_1)$ and $g(\phi_2)$ and integrating over all values of the random energies and over all coordinates. The real part of the electric current determines the electrical conductivity and the real part of the dipole moment determines the dielectric susceptibility and the imaginary part of the electrical conductivity which differs from this by the factor ω. The equilibrium term only contributes to the susceptibility. In the simple model of an amorphous semiconductor [1] the density of states is constant.

The complete electrical conductivity σ of the soft pairs is given by

$$\sigma = \frac{2e^2g^2}{dT} \int d^d r r^2 \int_{-\infty}^{\infty} d\phi_1 \times \int_{\phi_1}^{\infty} d\phi_2 \frac{(\phi_2 - \phi_1)^3}{[(\phi_2 - \phi_1)^2 + 4J^2(r)]^{3/2}} \frac{\omega^2/\tau_1}{(\omega^2 + 1/\tau_2)} n_1^0. \tag{16}$$

Here d is the spacial dimension (2 or 3).

Formula (16) for the high-frequency electrical conductivity is transformed differently for relatively low or high frequencies since in each case different spacings between the particles forming the soft pair are significant in the integral. For low frequencies the dependence on the spacings is determined by the relaxation denominator which isolates the characteristic spacings

$$r_\omega = \frac{a}{2} \ln \frac{\nu_{ph}}{\omega}.$$

The other coordinate dependence in the integrand associated with the overlap energy can be neglected. Hence, the classical case of low frequencies is determined by the inequalities

$$\frac{J}{T} \gg 1, \quad \frac{J}{T} \exp\left(-\frac{r_\omega}{a}\right) = \frac{J}{T}\sqrt{\frac{\omega}{\nu_{ph}}} \ll 1. \tag{17}$$

Converting from the energies $\phi_i$to the sum and difference variables, we can easily take the integral over the sum variable. For $d = 2$ the electrical conductivity is given by

$$\sigma = 2\pi e^2 g^2 \int_0^\infty dr r^3 \int_0^\infty d\phi \frac{\omega^2/\tau}{\omega^2 + 1/\tau^2} \times \left[2\cosh\frac{\phi}{2T}\sqrt{\cosh^2\left(\frac{\phi}{2T} - \beta\right)}\right]^{-1} \times \left[\frac{e^2}{2krT} + \ln\left(\cosh\frac{\phi}{2T} + \sqrt{\cosh^2\frac{\phi}{2T} - \beta}\right)\right]. \tag{18}$$

Here we have $\beta = \exp[-e^2/krT]$. Now to within logarithmic accuracy we take the integral over the coordinate:

$$\sigma = \pi^2 e^2 g^2 a r_\omega^3 \omega \int_0^\infty d\phi \left[4\cosh\frac{\phi}{2T}\sqrt{\cosh\left(\frac{\phi}{2T} - \beta_\omega\right)}\right]^{-1} \times \left[\frac{e^2}{2kr_\omega T} + \ln\left(\cosh\frac{\phi}{2T} + \sqrt{\cosh^2\frac{\phi}{2T} - \beta_\omega}\right)\right]. \tag{19}$$

Here we have $\beta_\omega = \beta(r_\omega)$. For $d = 3$ the expression contains the additional factor $4r_\omega/3$. The function in the integrand in (19) is the energy distribution function in the subsystem of two single-particle levels belonging to a four-level system. In the studies made by Efros [1, 4] this function was taken from the theory of two-level systems with a single electron and the author attempted to find the number of these, allowing partly for the

existence of four levels. As a result, an expression was put forward for the distribution function

$$f\left(\frac{\phi}{2T}\right) = \left(16\cosh^2\frac{\phi}{2T}\right)^{-1}\left(\frac{e^2}{kr_\omega T} + \frac{\phi}{2T}\right), \qquad (20)$$

which differs from expression (19). However, in the most interesting case of a strong Coulomb correlation

$$\frac{e^2}{kr_\omega T} \gg 1,$$

these expressions are functionally the same and only differ by a factor of two. The electrical conductivity is given by

$$\sigma = \frac{\pi^2 e^4}{4\,k} g^2 a\omega r_\omega^2. \qquad (21)$$

At high temperatures when the Coulomb correlation is insignificant we have

$$\sigma = \frac{\pi^4}{16} e^2 g^2 a\omega T r_\omega^3. \qquad (22)$$

Formula (19) describes a gradual change in the frequency dependence from (21) to (22).

We shall now analyze the quantum case achieved when the inequality the opposite of the second inequality from (17) is satisfied. In this case, the relaxation time in the denominator can be neglected so that the electrical conductivity becomes independent of frequency. The integral over the coordinates is now determined by the coordinate dependence of the overlap energy which over distances $r_T = a\ln(2J/T)$ decreases to levels of the order of T. Pairs having a shoulder of the order of r_T are soft and their contribution to the high-frequency electrical conductivity is summed.

The electrical conductivity depends on the electron–phonon interaction mechanism. We consider the case $d = 2$; for $d = 3$ we need to add the corresponding factor $4r_T/3$. When the Coulomb correlation is significant, $e^2/kr_T \gg T$,

$$\sigma = \frac{\pi e^4 g^2 \nu_{ph} a r_T^2 T^3}{16kJ^2}\int_0^\infty dx \frac{x^{2+s}}{\sinh x}, \qquad (23)$$

and when the Coulomb correlation is insignificant we have

$$\sigma = \frac{\pi e^2 g^2 \nu_{ph} a r_T^3 T^4}{32J^2}\int_0^\infty dx \frac{x^{3+s}}{\sinh^2(x/2)}. \qquad (24)$$

In the two-dimensional case the soft pairs interact with each other and it is meaningful to calculate their nonequilibrium contribution to the dielectric susceptibility or the proportional imaginary electrical conductivity. However, in the quantum case the imaginary electrical conductivity is much smaller than the real part so that this calculation is only made in the classical case. We note a difference in the calculations of the real and imaginary parts of the nonequilibrium electrical conductivity. For the imaginary electrical conductivity the integral over the coordinates is logarithimically large. However, since this is the integral of the power of the logarithm, apart from the large logarithmic factor the denominator also contains a number equal to the power of r_ω which appears in the result. This substantially reduces the final expression. In the Éfros article [4] this factor was omitted in the calculations of the imaginary part of the electrical conductivity. If the Coulomb correlation is significant we have

$$-\mathrm{Im}\sigma = \frac{\pi e^4 g^2 \omega r_\omega^3}{3k}. \qquad (25)$$

In this same article [4] Éfros attempted to allow for both the Coulomb correlation and the Coulomb gap in the density of single-particle states. In our view, this is not necessary. Using two-particle statistics shows that the electrical conduction process is collective and all the Coulomb interaction is taken into account in the distribution (7). The single-particle Coulomb gap has no relevance to this process.

Finally we consider the equilibrium dipole moment and the related imaginary part of the electrical conductivity. This dipole moment is not associated with relaxation and has no analog in the real part of the electrical conductivity. In this case, the integral over the coordinates may be determined by the overlap energy and therefore by the distance r_T. It is calculated as in the quantum case of electrical conduction. If the Coulomb correlation is significant, this part of the imaginary electrical conductivity given by

$$-\mathrm{Im}\sigma = \frac{\pi e^4 g^2 \omega r_T^3}{k}, \qquad (26)$$

is added as a term to the imaginary part of the electrical conductivity (25) and its value is completely comparable to this.

ACKNOWLEDGMENTS

This work was supported by the Russian Foundation for Basic Research, projects nos. 98-02-18280 and 97-02-18286.

REFERENCES

1. A. L. Éfros and B. I. Shklovskiĭ, in *Electron-Electron Interactions in Disordered Systems*, Ed. by A. L. Éfros and M. A. Pollak (North-Holland, Amsterdam, 1985), p. 201.
2. B. I. Shklovskiĭ and A. L. Éfros, Zh. Éksp. Teor. Fiz. **81**, 406 (1981) [Sov. Phys. JETP **54**, 218 (1981)].
3. Yu. A. Galperin, V. L. Gurevich, and D. A. Parshin, in *Hopping Transport in Solids*, Ed. by M. A. Pollak and B. I. Shklovskiĭ (North-Holland, Amsterdam, 1991), p. 81.
4. A. L. Éfros, Zh. Éksp. Teor. Fiz. **85**, 1834 (1985) [Sov. Phys. JETP **62**, 1057 (1985)].

Translation was provided by AIP

Journal of Experimental and Theoretical Physics, Vol. 90, No. 2, 2000, pp. 404–406.
Translated from Zhurnal Éksperimental'noĭ i Teoreticheskoĭ Fiziki, Vol. 117, No. 2, 2000, pp. 457–460.

SOLIDS
Electron Properties

Forbidden Optical Transitions Between Impurity Levels in Silicon and Gallium Phosphide

Ya. E. Pokrovskiĭ*, O. I. Smirnova, and N. A. Khval'kovskiĭ
Institute of Radio Engineering and Electronics, Russian Academy of Sciences, Moscow, 103907 Russia
**e-mail: yaep@mail.cplire.ru*
Received September 9, 1999

Abstract—Experimental estimates are made of absorption cross sections for forbidden optical transitions from the ground state to long-lived excited states of P, As, Sb, In, and Ga impurities in silicon and Te impurities in gallium phosphide. The results can be used to predict the possibility of long-wavelength stimulated emission being excited as a result of the population inversion of long-lived impurity states in these materials. © *2000 MAIK "Nauka/Interperiodica".*

1. INTRODUCTION

In a series of studies (see [1, 2] and the literature cited therein) the present authors have established that in semiconductors having a complex band structure (diamond, silicon, germanium, and gallium phosphide) some simple donor and acceptor impurities have deep excited states in which the lifetimes τ^* of electrons and holes are many orders of magnitude greater than the free carrier lifetimes τ. These states are split off from the ground states by valley–orbit or spin–orbit interactions and have the same parity as the impurity ground states. Hence, dipole optical transitions between long-lived excited and ground states (*1*, *2*, and *5* in Fig. 1) are forbidden. When semiconductors doped with these impurities are subjected to impurity photoexcitation, carriers accumulate in long-lived excited states during the cascade relaxation process. In silicon at low temperatures a significant buildup of carriers occurs, even under the action of the room-temperature background radiation present in optical experiments. In particular, the filling of excited states with this background leads to the appearance of long-wavelength absorption bands attributed to their photoionization (transitions *3*, *4*, and *6* in Fig. 1). It is predicted that the long lifetimes $\tau^* \sim 10^{-3}$ s in silicon and GaP can be used to achieve population inversion of long-lived states and to excite stimulated infrared emission. However, an important factor here is that the probabilities of radiative transitions from these states to the ground state are not too low. These probabilities can be estimated from the optical absorption cross sections σ for transitions from the ground to split-off states. This cross section is only known for Bi donor impurities in silicon ($\sigma \sim 10^{-16}$ cm^2 [3]) for which no electrons accumulate in long-lived excited states [1]. The present study shows that for other impurities the absorption cross sections for forbidden transitions were considerably lower.

2. EXPERIMENT

Absorption was studied using an LAFS-1000 Fourier spectrometer. The samples were placed in the helium bath of a cryostat with silicon windows. The transmission spectra were recorded using photoresistors positioned behind the samples in the cryostat. The absorption coefficient k was determined by normalizing the transmission spectra to the photodetector response spectra and the sample thickness. We used Ge photodetectors doped with Sb or Zn, or an Si photodetector doped with B which possessed high sensitivity in the 9–40, 32–50, and 45–70 meV ranges, respectively. We note that the results show good agreement in the regions where the sensitivities of the various photodetectors overlap. The intensity of the room-temperature background radiation passing through the cryostat windows and reaching the samples and the photodetectors was much higher than the intensity of the spectrometer radiation. Thus, the background determined the concentrations of nonequilibrium carriers in different states and this caused additional absorption. The

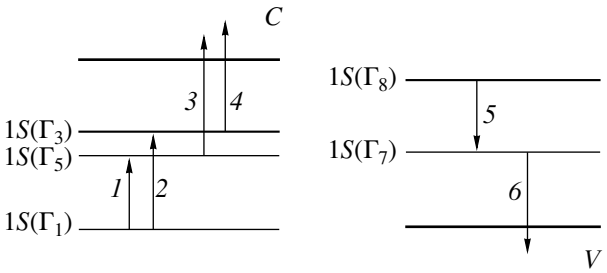

Fig. 1. Optical transitions involving long-lived excited states in semiconductors with a complex band structure. Excitation of electrons from the $1S(\Gamma_1)$ donor ground state to the following states: *1*—$1S(\Gamma_5)$, *2*—$1S(\Gamma_3)$; to the conduction band C from the states: *3*—$11S(\Gamma_5)$, *4*—$1S(\Gamma_3)$. Excitation of holes from the acceptor ground state $1S(\Gamma_8)$ to state *5*—$1S(\Gamma_7)$; *6*—from the $1S(\Gamma_7)$ state to the valence band V.

absorption cross sections for some impurities could only be determined in highly doped (~10^{17} cm^{-3}) crystals using samples 1–4 cm thick.

3. RESULTS AND DISCUSSION

Figure 2 gives spectral dependences of the absorption coefficient k of silicon doped with P and As donor impurities. Also plotted are results for Bi impurities from [3]. It can be seen that the spectra exhibit sharp peaks at 11.7 and 12.8 meV for P impurities and at 21.1 and 22.5 meV for As impurities. These values corresponds to the energies of forbidden optical transitions from the nondegenerate ground state of the donors $1S(\Gamma_1)$ to the triply degenerate $1S(\Gamma_5)$ and doubly degenerate $1S(\Gamma_3)$ excited states split off by valley–orbit interaction [4]. The absorption cross sections σ determined from Fig. 2 for transitions between the $1S(\Gamma_1)$) and $1S(\Gamma_5)$ states are 10^{-18} and 2.5×10^{-18} cm^2, respectively, for P and As impurities. It can also be seen from Fig. 2 that the spectrum of silicon doped with a lower concentration of As has a stepped absorption band in the energy range 32–38 meV, which corresponds to the ionization of long-lived excited states filled with background radiation (transitions *3* and *4* in Fig. 1 [1]). At high concentrations the absorption in this band becomes too strong and only the initial part of this step can be recorded. In the long-wavelength part of the spectrum Fig. 2 also shows additional absorption which depends weakly on energy and is evidently attributable to the formation of D^- centers [5]. We were unable to determine the cross section σ for Sb because of the lack of sufficiently large silicon samples highly doped with this impurity. The spectra of the samples investigated revealed no significant characteristics higher than the noise level in the 9–13 meV range which corresponds to the predicted energy of the forbidden transitions for Sb impurities. From this it follows that σ does not exceed 10^{-18} cm^2.

These results show that the intracenter absorption cross sections for forbidden transitions of P, As, and Bi donor impurities in silicon increase substantially as the valley–orbit splitting of the $1S$ state increases. The magnitude of this splitting is related to the difference between the real potential of the donor impurity and the potential of a point electric charge. This difference partially lifts the degeneracy of the $1S$ state and possibly determines the contribution of weak interactions accompanied by emission for which, unlike dipole interactions, parity-conserving optical electronic transitions are allowed.

The forbidden optical absorption cross sections for transitions in silicon from the doubly degenerate acceptor ground state $1S(\Gamma_8)$ to the long-lived nondegenerate excited state $1S(\Gamma_7)$ split off by spin–orbit interaction were substantially lower than those for donors. For B acceptor impurities, the energy for excitation of a hole to this state and its ionization energy are almost the same (23 meV [1, 4]). Thus, it is impossible to isolate

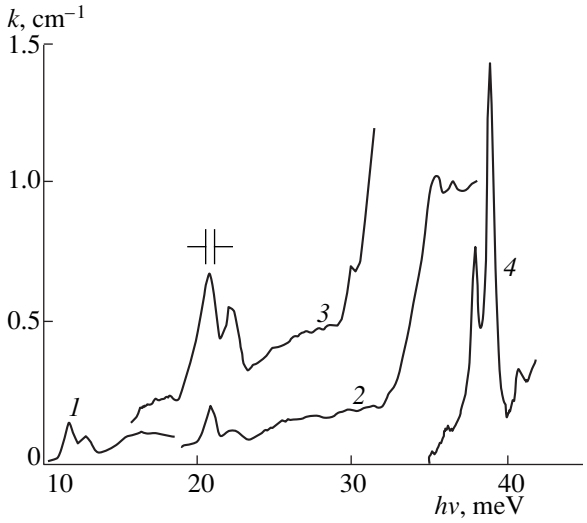

Fig. 2. Spectral dependences of the absorption coefficients k of silicon doped with various concentrations of donors: *1*—P, $N = 8 \times 10^{16}$ cm^{-3}; *2*—As, $N = 5 \times 10^{16}$ cm^{-3}; *3*—As, $N = 2 \times 10^{17}$ cm^{-3}; *4*—Bi, $N = 10^{16}$ cm^{-3} (from [3]).

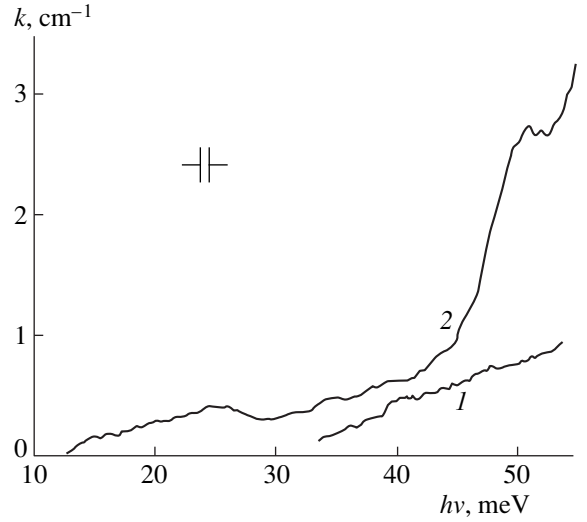

Fig. 3. Spectral dependences of the absorption coefficients k of silicon doped with various concentrations N of acceptors: *1*—In, $N = 7 \times 10^{16}$ cm^{-3}; *2*—Ga, $N = 2 \times 10^{17}$ cm^{-3}.

the contribution of selective excitation against the strong absorption background caused by the ionization of an excited state filled by the background. Figure 3 shows the absorption spectra of silicon doped with In and Ga. In the case of In, according to [6], absorption associated with a forbidden transition should be predicted at energies of 43–44 meV. However, no significant characteristics appear in this spectral range. From this it follows that the forbidden transition cross section for In impurities does not exceed 10^{-18} cm^2. For Ga impurities in silicon the energy position of the $1S(\Gamma_7)$ level is unknown although it may be estimated from

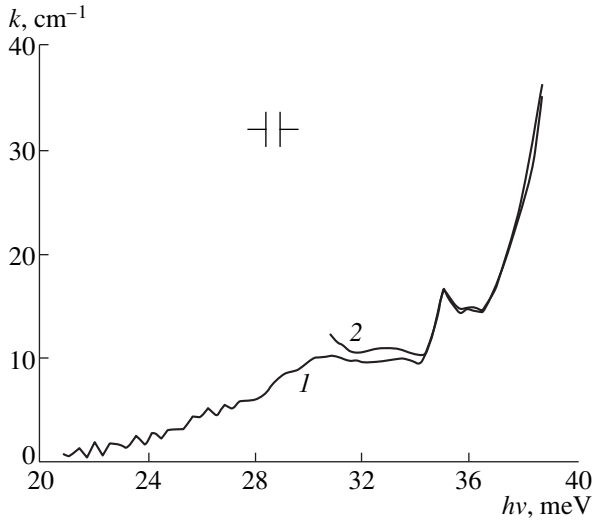

Fig. 4. Spectral dependence of the absorption coefficient k of gallium phosphide doped with Te to a concentration of 4×10^{17} cm^{-3}. The photoresistors used for recording were: *1*—Ge[Sb]; *2*—Ge[Zn].

Fig. 3. In fact, Fig. 3 shows a stepped absorption band which begins at around 48 meV. This absorption known for various other impurities in silicon [1] is naturally attributed to ionization of the $1S(\Gamma_7)$ state (transitions *6* in Fig. 1) filled with background radiation. Note that unlike B and In, for Ga impurities in silicon the long-lived excited state is not observed in the microwave hopping photoconductivity [1]. An appreciable buildup of holes in this state is impeded by the rapid relaxation of the excitation as a result of the emission of an optical phonon whose energy is close to that of the higher $2\Gamma_8$ state [4]. Nevertheless, some relatively weak filling of the $1S(\Gamma_7)$ state may occur as a result of the cascade relaxation of the excitation. Then, since the energies of the Ga ground state (74 meV [4]) and the edge of the absorption step (48 meV) are known, the appearance of forbidden absorption should be predicted at around 26 meV. It can be seen from Fig. 3 that no significant characteristics are observed in this spectral range. From this we can conclude that for Ga impurities in silicon $\sigma < 10^{-18}$ cm^2.

The energy spectrum of Te donor impurities in GaP has been investigated in various studies (see [7] and the literature cited therein). This spectrum is similar to the spectrum of simple donors in silicon although the strong lattice absorption, including bands of residual radiation in the range 40–50 meV [8], makes it very difficult to obtain reliable results. According to [7], the ionization energy of the $1S(\Gamma_1)$ ground state is 90.5 meV and the $1S(\Gamma_3)$ excited state is split off from the ground state by 40.7 meV, i.e., it falls within the region of strong lattice absorption. A state having this energy can hardly be long-lived since it can undergo rapid relaxation as a result of optical phonon emission. The $1S(\Gamma_5)$ state can be long-lived ($\tau^* = 8$ ms [2]) if its excitation energy lies outside the region of the residual radiation. Figure 4 gives the spectral dependence of the absorption coefficient of a 0.375 mm thick GaP wafer doped with Te. At 35.1 meV the spectrum exhibits a characteristic peak which can naturally be assigned to a transition from the ground to the $1S(\Gamma_5)$ excited state. The absorption cross section corresponding to this cross section is then close to 1.5×10^{-17} cm^2. It can also be seen from Fig. 4 that this peak is observed against a background of strong continuous absorption which can probably be attributed to the excitation of short-wavelength acoustic phonons [3]. This factor may prove an obstacle for the amplification of stimulated emission.

4. CONCLUSIONS

These experimental results can be used to assess the possibility of exciting stimulated infrared emission as a result of the population inversion of long-lived excited states. Silicon highly doped with As may prove the most useful material since the forbidden selective absorption in this material has a comparatively high intensity and substantially exceeds the background (Fig. 2). Estimates made using the well-known Einstein relationships show that the radiative lifetime of the $1S(\Gamma_5)$ excited state may be close to 1 s (for $\tau^* \sim 0.5$ ms [1]) and the active-medium gain for a population inversion of 10^{17} cm^{-3} is of the order of 0.1 cm^{-1}. For a radiation quantum yield of around 10^{-3} it is quite possible for long-wavelength stimulated infrared emission to be excited in high-Q resonators.

ACKNOWLEDGMENTS

This work was supported financially by the Russian Foundation for Basic Research (project no. 99-02-16078) and the Support Program for leading Scientific Schools (project no. 96-15-96701).

REFERENCES

1. Ya. E. Pokrovskiĭ, O. I. Smirnova, and N. A. Khval'kovskiĭ, Zh. Éksp. Teor. Fiz. **112**, 221 (1997) [JETP **85**, 121 (1997)].
2. Ya. E. Pokrovskiĭ, O. I. Smirnova, and N. A. Khval'kovskiĭ, Zh. Éksp. Teor. Fiz. **114**, 2204 (1998) [JETP **87**, 1201 (1998)].
3. W. E. Krag, W. H. Kleiner, and H. J. Zeiger, in *Abstracts of the X International Conference on the Physics of Semiconductors, Cambridge, 1970*, p. 271.
4. A. K. Ramdas and S. Rodríguez, Rep. Prog. Phys. **44**, 1287 (1981).
5. Ya. E. Pokrovskiĭ, O. I. Smirnova, and N. A. Khval'kovskiĭ, Pis'ma Zh. Éksp. Teor. Fiz. **66**, 224 (1997) [JETP Lett. **66**, 241 (1997)].
6. W. Scott, Appl. Phys. Lett. **32**, 540 (1978).
7. W. Scott, J. Appl. Phys. **50**, 472 (1979).
8. D. A. Kleinmann and W. G. Spitzer, Phys. Rev. **118**, 110 (1960).

Translation was provided by AIP